Multinucleon Transfer Reactions and Quasifission Processes in Time-Dependent Hartree-Fock Theory

Kazuyuki Sekizawa
Doctoral Program in Physics

Submitted to the Graduate School of
Pure and Applied Sciences
in Partial Fulfillment of the Requirements
for the Degree of Doctor of Philosophy in
Science

at the
University of Tsukuba

To My Dearest Family
and Sweet Petit

Preface

The atomic nucleus is a tiny ($\sim 10^{-14}$ m) quantum object composed of two kinds of fermions, neutrons and protons (nucleons), interacting through nuclear force. To study properties of atomic nuclei, nucleus-nucleus collision experiments utilizing a huge heavy-ion-accelerator is indispensable. By producing unstable nuclei which do not exist naturally on the earth as well as stable nuclei as an outcome of the nuclear reaction, we can study properties of nuclei composed of different numbers of neutrons and protons. From this point of view, we may consider that the nuclear reaction experiment plays an essential role as a means to study various kinds of atomic nuclei. Because it is basically a complex quantum many-body problem, however, it is not obvious how we experimentally produce objective nuclei and we need theoretical considerations. The main aims of this study are (i) to understand microscopic reaction mechanisms of low-energy heavy ion reactions and (ii) to theoretically predict optimum reactions, *i.e.* projectile-target combinations and incident energies, to experimentally produce objective nuclei. In this thesis, we focus on multinucleon transfer (MNT) and quasifission (QF) processes which have recently been considered to be a useful means to produce unstable nuclei.

We regard the atomic nucleus as a finite, non-relativistic, self-bound, quantum many-body system composed of neutrons and protons. Although scales of length and energy as well as interactions governing the system are very much different from those in atomic/molecular physics or condensed matter physics, we may expect analogous physics as a many-fermion system. From this point of view, we consider that MNT and QF processes in low-energy heavy ion reactions would provide us a unique opportunity for studying a non-equilibrium quantum many-body problem, where structural properties and time-dependent reaction dynamics are strongly related to each other reflecting the finiteness of the system and the complexity of the nuclear force. Thus this study is expected to provide us interdisciplinary information on non-equilibrium quantum transport phenomena in many-fermion systems.

In this thesis, we investigate MNT and QF processes in low-energy heavy ion reactions at energies around the Coulomb barrier using a microscopic framework of the time-dependent Hartree-Fock (TDHF) theory. Although we use a conventional terminology, "TDHF", it has recently been referred to as time-dependent density functional theory (TDDFT) or time-dependent energy density functional approach (TD-EDF). This is because the formalism of the TDHF theory with an effective nucleon-nucleon interaction has a correspondence to that of the density functional theory which has achieved great successes in atomic/molecular physics, condensed matter physics, and in the field of quantum chemistry. To clarify our theoretical formalism, I explain this point in the main text of the thesis.

Despite the fact that continuous efforts have been devoted for improving the method and for extending applications of the TDHF theory, limitation of the theory in various applications is not yet clear. This study aims to reveal applicability of the TDHF theory in describing low-energy heavy ion reactions at around the Coulomb barrier by performing a number of calculations using massively parallel supercomputers. We consider that to know the limit of applicability of the TDHF theory will be useful for developing our understanding of the atomic nuclei and for developing new theoretical frameworks and experimental conditions for the future investigations. In this thesis, we investigate MNT and QF processes which, before this work, had not been sufficiently studied in the microscopic framework of the TDHF theory.

Both MNT and QF processes involve transfer of many nucleons between two colliding nuclei. In this sense, the QF processes may be regarded as a special case of the MNT processes. Their transfer dynamics is expected to depend on projectile-target combinations, relative orientations if projectile and/or target are deformed, angular momenta, and incident energies. In addition, as described in the main text of the thesis, we found that the amount of transferred nucleons in MNT and QF processes depends much on the dynamics of a neck formation and its breaking, that is, a time-dependent dynamics of shape evolution in a composite system of projectile and target nuclei. When the composite system dissociates, a thick and long neck structure is often observed in TDHF calculations of MNT and QF processes. We found that a scission point of the neck changes suddenly when we slightly change the initial condition. The change in the scission point of the neck results in different number/direction of transfer of many nucleons involved inside the neck region. We will refer to this transfer mechanism as a *neck breaking transfer dynamics*. We anticipate that, if we can control the scission point of the neck, we may be able to produce objective nuclei by choosing the scission point of the neck to induce transfer of nucleons toward the desired direction. Then, we may regard it as *nuclear chemistry*, where we produce objective nuclei as we want through the controlled neck breaking transfer dynamics. We expect that this work will open the door to study heavy ion reactions along this direction in which we may access a new generation of *nuclear chemistry* as one of the subjects of low-energy nuclear physics.

Part of the thesis is based on results reported in publications listed below:

1. *Particle-number projection method in time-dependent Hartree-Fock theory: Properties of reaction products*,
   <u>K. Sekizawa</u> and K. Yabana, Phys. Rev. **90**, 064614 (2014); arXiv:1409.1083 [nucl-th].

2. *Time-dependent Hartree-Fock calculations for multinucleon transfer processes in $^{40,48}Ca+^{124}Sn$, $^{40}Ca+^{208}Pb$, and $^{58}Ni+^{208}Pb$ reactions*,
   <u>K. Sekizawa</u> and K. Yabana, Phys. Rev. C **88**, 014614 (2013); arXiv:1303.0552 [nucl-th].

3. *Strong Orientation Dependence of Multinucleon Transfer Processes in $^{238}U+^{124}Sn$ Reaction*,
   <u>K. Sekizawa</u> and K. Yabana, to appear in JPS Conference Proceedings; arXiv:1409.8612 [nucl-th].

4. *Time-dependent Hartree-Fock calculations for multi-nucleon transfer processes: Effects of particle evaporation on production cross sections*,
   <u>K. Sekizawa</u> and K. Yabana, EPJ Web of Conferences **86**, 00043 (2015); arXiv:1403.2862 [nucl-th].

This work was performed in collaboration with Professor Kazuhiro Yabana, the supervisor of this Ph.D. work at the University of Tsukuba.

Kazuyuki Sekizawa

Tsukuba
January 2015

Abstract

Multinucleon transfer (MNT) reactions and quasifission (QF) processes in low-energy heavy ion reactions may be regarded as a non-equilibrium quantum many-body dynamics. They have attracted much interests associated with curiosity for their microscopic reaction mechanisms which may reflect both static and dynamical properties of colliding nuclei. Recently, they have also attracted much interests as a new means to produce unstable nuclei whose production is difficult by other methods. The main aims of this study are to understand microscopic reaction mechanisms of the MNT and QF processes and to theoretically predict optimum reactions to produce objective unstable nuclei. To this end, we investigate the MNT and QF processes in low-energy heavy ion reactions employing a microscopic framework of the time-dependent Hartree-Fock (TDHF) theory.

In this thesis, we first explain the theoretical framework of the TDHF theory and its relation to the time-dependent density functional theory, TDDFT. We present how to numerically simulate heavy ion reactions in the TDHF theory and how to implement it into a computational code utilizing MPI and OpenMP parallelization techniques.

After giving our theoretical framework, we describe results of the TDHF calculations for the MNT and QF processes as a main part of the thesis. We divide it into two parts. The first part (Part I) is devoted to show that the applicability of the TDHF theory in describing the MNT reaction. Before our study, it was not known whether the TDHF theory can describe the MNT reaction quantitatively or not. We present our progresses of this work step by step in Part I.

To examine to what extent the TDHF theory describes MNT cross sections quantitatively, we analyze MNT processes in ^{40,48}Ca+^{124}Sn, ^{40}Ca+^{208}Pb, and ^{58}Ni+^{208}Pb reactions, for which precise experimental data are available. To calculate MNT cross sections, we extract transfer probabilities from the TDHF wave function after collision employing the particle-number projection (PNP) technique. From the results, effects of the neutron-to-proton ratio, N/Z, and the charge product, $Z_\mathrm{P} Z_\mathrm{T}$, on transfer dynamics are discussed. We show that the TDHF theory combined with the PNP technique can describe MNT cross sections quantitatively, with an accuracy comparable to existing successful theories, GRAZING, Complex WKB, and a dynamical model based on Langevin-type equations of motion.

Reaction products generated through MNT reactions can be highly excited, and subsequent de-excitation processes by particle evaporation should be taken into account. To include the effect of particle evaporation, we use a statistical model of particle evaporation putting excitation energy of reaction products evaluated from the TDHF wave function after collision as an input. To evaluate the excitation energy of reaction products, we develop a theoretical framework to calculate expectation values of operators in a particle-number projected TDHF wave function after collision. Because the method enables us to investigate microscopic reaction mechanisms which could not be seen from ordinary expectation values without the PNP, we demonstrate usefulness of the method taking ^{24}O+^{16}O reaction as an illustrative example. We then present MNT cross sections including effects of particle evaporation. We further discuss possible origins of discrepancies and several ways to improve the description.

From the thorough analyses presented in Part I, we have obtained a confidence that the TDHF theory provides a reasonable description of the MNT reaction with a certain predictive power in a

sense that the theory microscopically describes many-body dynamics without any adjustable parameter specific to the reaction. In the second part of the thesis (Part II), we further extend its application to reactions involving more heavier nuclei such as ^{238}U, where we expect a significant effect of the QF process in reactions at small impact parameters.

In Part II, we first investigate the MNT processes in ^{64}Ni+^{238}U reaction for which precise measurements of MNT cross sections were performed. From comparisons between MNT cross sections calculated by the TDHF theory combined with the PNP and those of the measurements, we again find reasonable agreements. In particular, the TDHF theory describes not only proton-stripping but also proton-pickup processes. This fact indicates that a reasonable description is possible for a transitional regime from quasielastic to more complex reactions in a small impact parameter region. The TDHF theory also describes QF processes involving transfer of several tens of nucleons in dissipative collisions at small impact parameters. For the ^{64}Ni+^{238}U system, measurements of total kinetic energy (TKE) of outgoing fragments as well as fragment mass (A) distributions in such a dissipative collision were achieved. By comparing the measured TKE-A distribution with that of the TDHF calculation, we find a good agreement between them. We investigate the orientation dependence as well as the incident energy dependence of the QF dynamics in head-on collisions of ^{64}Ni+^{238}U. We observe a capture process forming a superheavy nucleus with $Z = 120$ in the side collisions, while it never observed in the tip collisions.

As a next application of the TDHF theory to reactions involving ^{238}U, we analyze ^{238}U+^{100,124,132}Sn reactions. For the ^{238}U+^{124}Sn reaction, production cross sections involving many-proton transfer from ^{238}U to ^{124}Sn were measured. From the TDHF calculation, we find a strong orientation dependence of the reaction dynamics in ^{238}U+^{124}Sn. When ^{238}U collides from its tip, a thick and long neck structure is formed, while the neck formation is substantially suppressed when ^{238}U collides from its side. Because the neck structure is composed of both neutrons and protons, an absorption of the neck region when the dinuclear system dissociates results in transfer of both neutrons and protons toward the same direction. The measured many-proton transfer from ^{238}U to ^{124}Sn might be originated from the tip collision in which a thick and long neck formation followed by subsequent absorption of nucleons inside the neck region results in the many-proton transfer. We also investigate the orientation and incident energy dependence as well as the N/Z ratio dependence of the QF dynamics in head-on collisions of ^{238}U+^{100,124,132}Sn. We find the so called *inverse* QF process in the tip collisions, where a largely deformed transuranium nucleus is generated as a primary product in the TDHF calculation.

As a final topic of the thesis, we investigate the MNT and QF processes in ^{136}Xe+^{198}Pt reaction which has recently been considered as a candidate to produce neutron-rich unstable nuclei around the $N = 126$ region. We conduct a systematic TDHF calculation for ^{136}Xe+^{198}Pt reactions at various incident energies and impact parameters. From the results, we find that the reaction dynamics shows a similar behavior if we classify the reaction according to the distance of closest approach of the Rutherford trajectory, although it shows a complicated dependence on the incident energy and impact parameter. We also find that the *inverse* QF process emerges at certain initial conditions, which may be related to a large binding energy of doubly-magic ^{208}Pb.

From the thorough analyses of the MNT and QF processes in low-energy heavy ion reactions, we conclude that the TDHF theory provides a unified microscopic description of not only MNT processes in peripheral reactions but also QF processes in dissipative collisions without any adjustable parameters specific to the reaction. We thus consider that the TDHF theory will be a promising tool to investigate the microscopic reaction mechanisms of the MNT and QF processes and to predict optimum reactions as well as a novel reaction dynamics to produce exotic unstable nuclei which have never been produced by other known reactions.

Contents

List of Figures

List of Tables

Abbreviations

BCS	Bardeen-Cooper-Schrieffer
BEC	Bose-Einstein Condensation
CHF	Constrained Hartree-Fock
CN	Compound Nucleus
CWKB	Complex Wentzel-Kramers-Brillouin
DFT	Density Functional Theory
DIC	Deep Inelastic Collision
EDF	Energy Density Functional
EvR	Evaporation Residue
GCM	Generator Coordinate Method
HF	Hartree-Fock
HK	Hohenberg and Kohn / Hohenberg-Kohn
HPCI	High Performance Computing Infrastructure
IOI	Island of Inversion
IOS	Island of Stability
KS	Kohn and Sham / Kohn-Sham
MAD	Mass-Angle Distribution
MNT	Multinucleon Transfer
MPI	Message Passing Interface
OpenMP	Open Multi-Processing
PES	Potential Energy Surface
PLF	Projectile-Like Fragment
PNP	Particle-Number Projection
QF	Quasifission
RG	Runge and Gross / Runge-Gross
RI	Radioactive Ion
r process	rapid neutron-capture process
SH	Superheavy
Skyrme (TD)HF theory	(TD)HF theory with a Skyrme effective interaction
TDDFT	Time-Dependent Density Functional Theory
TDDM	Time-Dependent Density Matrix
TD-EDF	Time-Dependent Energy Density Functional approach
TDGCM	Time-Dependent Generator Coordinate Method
TDHF	Time-Dependent Hartree-Fock
TDHFB	Time-Dependent Hartree-Fock-Bogoliubov
TDKS	Time-Dependent Kohn-Sham
TDRPA	Time-Dependent Random Phase Approximation
TKE(L)	Total Kinetic Energy (Loss)
TLF	Target-Like Fragment

Chapter 1

INTRODUCTION

Starting from the finding of an atomic nucleus by Rutherford in 1911 [1], we human begins have explored physics of the atomic nuclei. Within the period of about 100 years, both experimental and theoretical studies have been extensively developed. Thanks to recent developments of experimental facilities, equipments, and techniques for nuclear reaction experiments, we are now entering a new era that we examine properties of unstable nuclei far from stability.

We are interested in nuclear reactions as a quantum many-body dynamics. One of the biggest goals of our study is to predict optimum reactions to produce objective nuclei based on a microscopic quantum many-body theory. Such theoretical predictions may provide us an opportunity to study unstable nuclei which have not been produced so far. This work aims to achieve the goal by developing our microscopic understanding of low-energy heavy ion reactions, especially, multinucleon transfer (MNT) and quasifission (QF) processes.

1.1 Our Interests for the Atomic Nuclei

1.1.1 Atomic nucleus as a finite quantum many-body system

The atomic nucleus is a tiny ($\sim 10^{-14}$m) massive entity locating at the center of an atom, which is responsible for almost all the mass of the atom. The atomic nucleus is composed of neutrons and protons (nucleons). We distinguish the atomic nucleus according to the number of neutrons (the neutron number, N) and the number of protons (the proton/atomic/charge number, Z). Each of them is referred to as a *nuclide*. We symbolically express a nuclide as $^A_Z X_N$, where A denotes the total number of nucleons (the mass number, $A = N + Z$) and X stands for the symbol for a corresponding element to the atomic number Z; *e.g.* a helium nucleus having two neutrons, known as an α particle, is expressed as $^4_2 He_2$ (We often omit subscripts of the proton and neutron numbers for simplicity). Nuclei which have the same atomic number Z but have a different neutron number N are called *isotopes*, while nuclei which have the same neutron number N but have a different atomic number Z are called *isotones*. Nuclei having the same mass number A are called *isobars*.

We may regard the atomic nucleus as a finite, non-relativistic, self-bound quantum many-body system composed of two kinds of fermions (neutrons and protons) interacting through the nuclear force. Unlike the atom, there is no core inside the nucleus and it is self-bounded through the nuclear attractive interaction. The nuclear force is of finite-range with an attractive part up to $d \sim 1.4$ fm and a repulsive part at short distance $d \lesssim 0.5$ fm (d is the internucleon distance). It shows unique properties, *e.g.*, existence of exchange interactions, strong spin-orbit and tensor couplings, spin and isospin dependences, and significance of the three-body force, and so on [2]. The atomic nucleus shows a number of interesting properties such as *magic numbers* [3, 4, 5], saturation properties of the
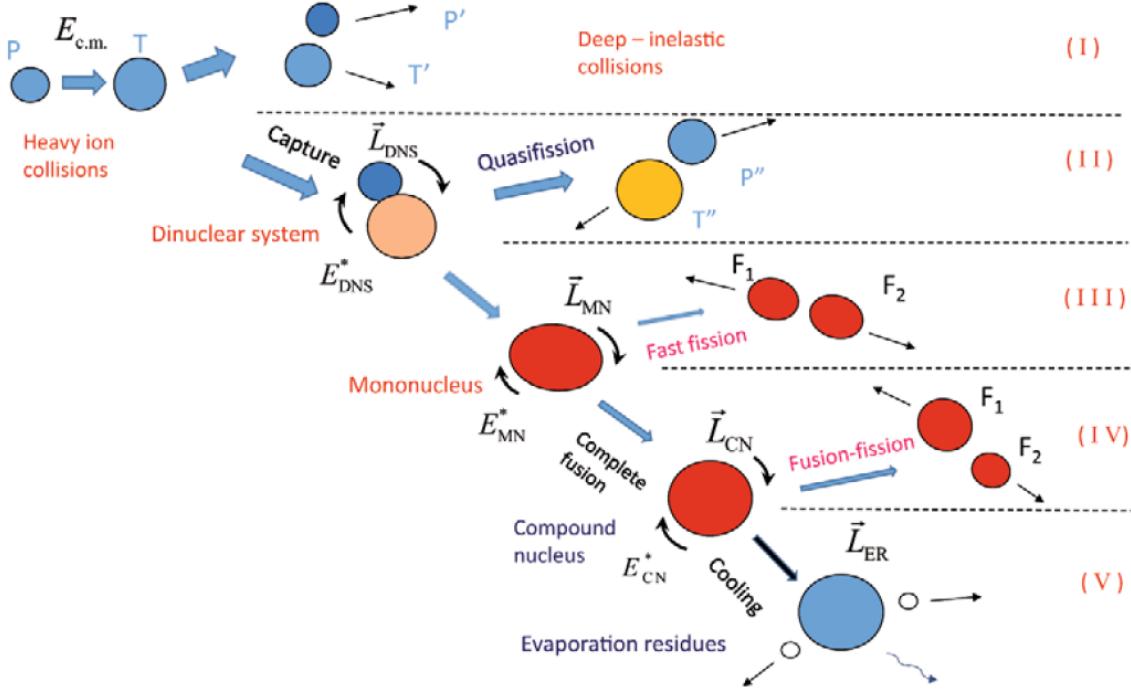
Figure 1.1: Representative processes in low-energy heavy ion reactions, deep inelastic collision (I), quasifission (II), fast fission (III), fusion-fission (IV), and evaporation residue formation (V), are schematically shown. The figure was taken from Ref. [8].

nuclear density ($\rho_0 \sim 0.16$ fm^{-3}) and the binging energy ($B/A \sim 8$ MeV) [6], strong quantum nature in a sense that the binding energy is relatively week compared with the zero-point kinetic energy [7], competition between the pairing and the quadrupole correlations [2], and so on. We are interested in various phenomena in nuclei as a unique finite quantum many-body system.

1.1.2 Heavy ion reactions

To study properties of the atomic nuclei, nuclear reaction experiments utilizing a heavy-ion accelerator are indispensable. Since, in such experiments, atomic nuclei whose surrounding electrons are removed are accelerated, we often refer to the nuclear reaction as the heavy ion reaction.

In heavy ion reactions at low energies around the Coulomb barrier, various different processes take place depending on the angular momentum (or the impact parameter) and the incident energy. Several representative processes are schematically shown in Fig. 1.1. When two nuclei do not approach enough to each other, elastic and quasielastic reactions take place. The latter may include a small excitation of reaction products and transfer of few nucleons. When two nuclei are touched, a dinuclear system is formed connected with a neck structure. Several nucleons are exchanged through the neck structure. Such processes including transfer of more than one nucleons could be referred to as MNT reactions. When the incident energy is sufficiently high compared with the Coulomb barrier, two nuclei collide deeply producing highly-excited reaction products having similar masses to those of the projectile and target nuclei. Such a process is referred to as a deep inelastic collision (DIC) which corresponds to a process shown in Fig. 1.1 (I). If two nuclei overcome or tunnel through the Coulomb barrier, they get a chance to fuse forming a compound nucleus (CN), which is referred to as a fusion reaction. However, on the way to fusion before the CN formation, the dinuclear system can dissociate into two individual nuclei having different masses compared with those of the projectile and target nuclei. Such a process is referred to as a QF process which is shown in Fig. 1.1 (II). The composite system survived against the QF process may form a mononuclear shape rather than a dinuclear shape because of a long contact
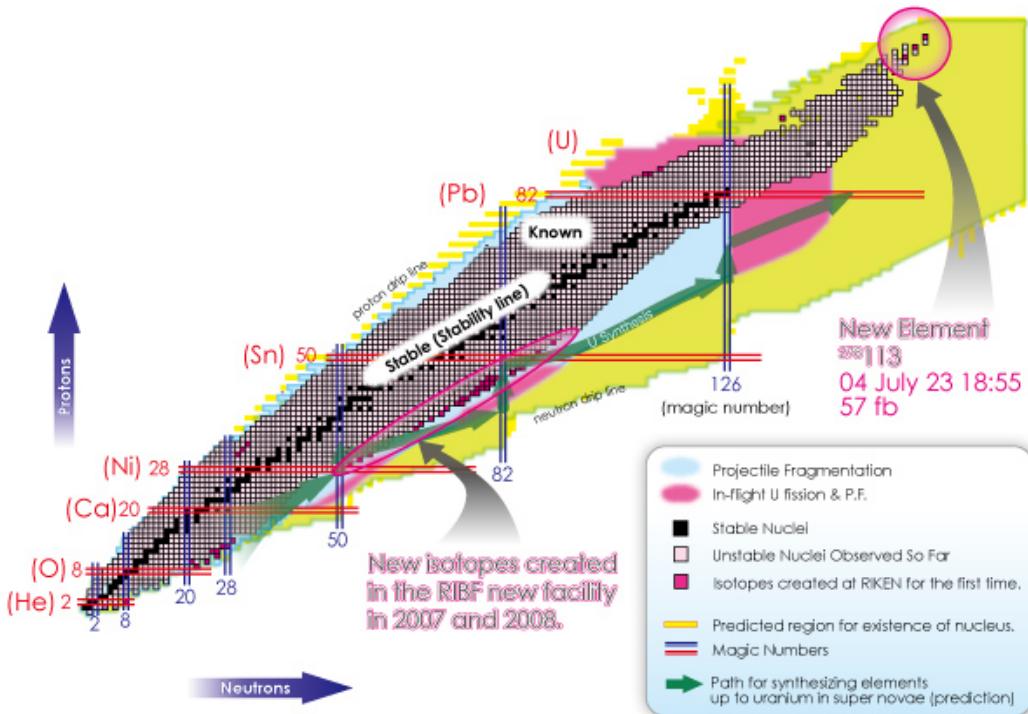
Figure 1.2: Chart of nuclides specified by the number of neutrons (horizontal axis) and the number of protons (vertical axis). Each box corresponds to an atomic nucleus. Black filled boxes denote stable nuclei which exist naturally on the earth. Gray colored boxes show unstable nuclei which were successfully produced experimentally in the past. Pink filled boxes exhibit unstable nuclei which were produced at RIKEN for the first time. Cyan shaded area represents nuclei which are expected to be produced by a projectile fragmentation. Pink shaded area represents nuclei which are expected to be produced by in-flight fission of uranium nucleus. Yellow shaded area indicates a region where corresponding nuclei are expected to exist in nature. Neutron (proton) magic numbers, 2, 8, 20, 28, 50, 82, 126, are indicated by blue (red) vertical (horizontal) lines. A possible r-process path is schematically represented by green arrows. The figure was taken from Ref. [9].

time. It may disintegrate through nuclear fission before or after the CN formation, which are referred to as fast fission (Fig. 1.1 (III)) and fusion-fission (CN-fission) (Fig. 1.1 (IV)), respectively. The survived product nucleus against these processes (I-IV) as well as deexcitation processes of particle evaporation is called an evaporation residue (EvR) which is usually measured to get an evidence of the CN formation (Fig. 1.1 (V)).

We may regard these reaction processes as quantum many-body dynamics which reflects both static properties of colliding nuclei and time-dependent dynamics during the collision. We are very much interested in microscopic mechanisms underlying those complex quantum many-body dynamics. In this thesis, we will focus on the MNT and QF processes which have recently been expected to be a promising tool to produce unstable nuclei whose production is difficult by other methods.

1.1.3 Physics of unstable nuclei

Because of the continuous advances in experimental equipments and techniques, nowadays, radioactive ions (RIs) can be used as a projectile in nuclear reaction experiments. For instance, RIs are produced by a nuclear spallation reaction induced by a uranium ($_{92}$U) beam irradiated on a beryllium ($_{4}$Be) or carbon ($_{6}$C) target. After the nuclear spallation reaction, radioactive unstable nuclei are produced. In RI beam facilities, produced RIs are re-accelerated and are irradiated on a secondary target. It enables
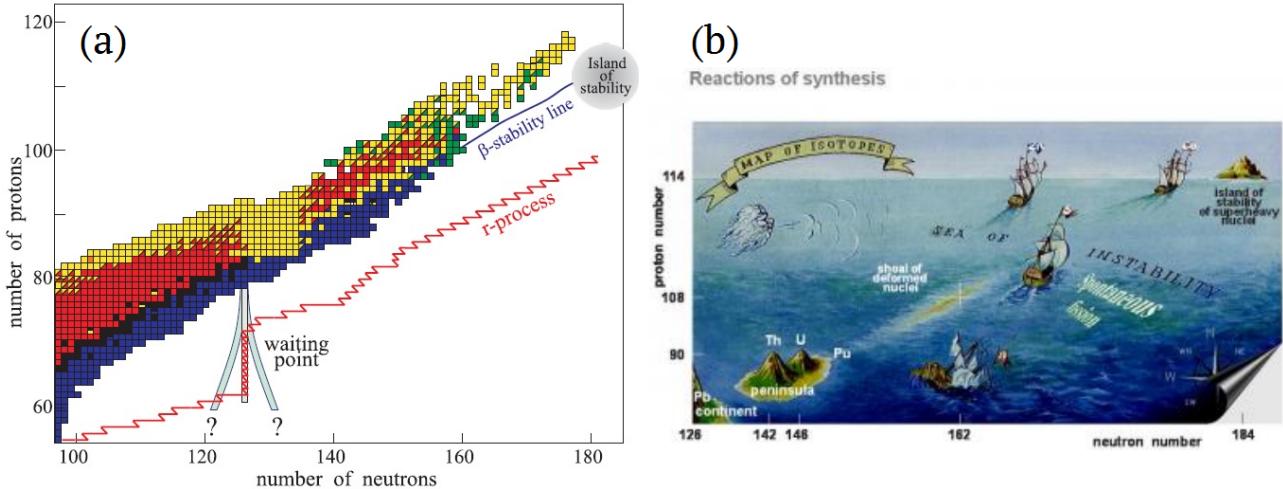
Figure 1.3: (a): The *north east* part of the nuclear chart. Each colored box represents an atomic nucleus which was produced experimentally. *r*-process path, β-stability line, and island of stability are shown schematically. (b): An illustration of voyages from the mainland (left bottom) toward the island of stability (right top). The most advancing ship represents hot fusion in reactions of calcium on an actinide target, the second one represents cold fusion, and the third one represents hot fusion induced by light ions. The sinking ship represents neutron capture reactions. The left figure was taken from Ref. [29]. The right figure was taken from Ref. [30].

us to explore more abundant kinds of reactions and nuclei which cannot be studied by experiment with a stable projectile. In Fig. 1.2, we show the nuclear chart in which newly produced nuclides at RIKEN are indicated, as an illustrative example.

One of the most striking examples of physics of unstable nuclei would be the finding of neutron *halo* structure of ^{11}Li, which was revealed, for the first time, by Tanihata *et al.* [10]. In the experiment, various isotopes of lithium ($_3$Li) and beryllium ($_4$Be) were produced as a secondary beam through a projectile fragmentation process and interaction cross sections were measured. From the measured interaction cross sections, matter root-mean-square radius was deduced. The deduced radius showed a noticeably-large value for ^{11}Li nucleus suggesting a spatially-extended tail of loosely-bound valence neutrons. Nowadays, such a spatially-extended neutron distribution is referred to as neutron *halo*, in an analogy like a halo of the moon, and has extensively studied [11]. Because neutron halo nuclei may have normal- and low-density regions at the center and the surface of the nucleus, respectively, they are expected to have both BCS- and BEC-type paired nucleons and have attracted much interests for those internucleon correlations [12] (BCS: Bardeen-Cooper-Schrieffer, BEC: Bose-Einstein Condensation).

Another example is the so called *shell evolution*. Recent measurements have revealed that the magic numbers of the atomic nuclei would be appeared/disappeared as the number of neutrons increases, toward neutron-rich nuclei far from the stability line. For example, for neutron-rich oxygen ($_8$O) isotopes, ^{28}O ($N = 20$) was found to be unbound and the neutron drip-line was established to be ^{24}O ($N = 16$) [13]. Moreover, Ozawa *et al.* found that an appearance of a new magic number $N = 16$ for ^{24}O from a systematic measurement of the one-neutron separation energy and the interaction cross section for neutron-rich *sd*- and *pf*-shell nuclei [14]. Also, $N = 34$ [15] was found to be a new magic number. For neutron-rich nuclei around sodium ($_{11}$Na), magnesium ($_{12}$Mg), and aluminum ($_{13}$Al) region, neutron-rich nuclei around $N = 20$ were found to be deformed indicating disappearance of the $N = 20$ magic number [16, 17, 18]. This region is called *island of inversion* (IOI) regarding a significance of the intruder states in those deformed $N \sim 20$ nuclei. Significant role of the tensor force for the shell evolution has recently been advocated based on shell-model calculations [19, 20, 21].

Production of superheavy (SH) nuclei is also of great interests. The heaviest element exists on the earth is plutonium ($_{94}$Pu), and thus elements with the atomic number larger than 94 were produced artificially in nuclear reaction experiments. The limit of existence and chemical properties of SH nuclei are of crucial interests. Theoretically, the next magic numbers ware predicted as $N = 184$ and $Z = 114$ [22, 23, 24], which is located on the *north east* part of the nuclear chart. The region in the nuclear chart around these magic numbers is called *island of stability* (IOS) which is schematically shown in Fig. 1.3 (a). These interests have urged us to synthesize and study physics of SH nuclei. To synthesize SH nuclei, the so called *cold fusion* reactions in which $^{208}_{82}$Pb$_{126}$ or $^{209}_{83}$Bi$_{126}$ target is utilized [25, 26, 27] and the so called *hot fusion* reactions in which an actinide target is bombarded by $^{48}_{20}$Ca$_{28}$ projectile [28] have been a useful tool. The situation toward the IOS is represented by a cartoon shown in Fig. 1.3 (b). The island seen at distance represents the IOS. Each ship represents different reaction: The first and third ships represent hot fusion reactions with ^{48}Ca beam and those with light-ion beam, respectively. The second ship represents cold fusion reactions. The fourth sinking ship represents neutron capture reactions, because neutron capture reactions with a nuclear reactor as a neutron source could synthesize SH nuclei up to fermium ($_{100}$Fm) isotopes.

As can be seen from Figs. 1.2 and 1.3 (a), however, there still remain many unknown nuclei which have not been produced so far. Recently, the MNT and QF processes have been considered to be useful to produce those unstable nuclei. To expand our research field as far as possible from the stability line and to develop our understanding of the atomic nuclei, this study aims to theoretically predict how to make those unstable nuclei using the MNT and QF processes.

1.2 New Means to Produce Unstable Nuclei

1.2.1 Multinucleon transfer reactions

In the last three decades, measurements of MNT processes were achieved extensively in heavy ion reactions at energies around the Coulomb barrier [31, 32, 33, 34, 35, 36, 37, 38, 39, 40, 41, 42, 43, 44, 45, 46, 47, 48, 49, 50, 51, 52, 53, 54, 55]. We may regard the MNT reaction as a non-equilibrium quantum transport phenomenon which reflect both static properties and time-dependent dynamics of colliding nuclei.

Besides fundamental interests in its mechanisms, the MNT reaction has recently considered to be useful as a means to produce unstable nuclei whose production is difficult by other methods. For example, a possibility to produce neutron-rich heavy nuclei using RI beam induced MNT reactions was pointed out by Dasso *et al.* [56, 57]. A production of neutron-rich nuclei around $A \sim 200$ along the neutron magic number $N = 126$ has been discussed [29, 58, 59]. The knowledge on structural properties of those nuclei is crucially important to understand a detail scenario of heavy elements synthesis in the rapid neutron-capture process (*r*-process) of the nucleosynthesis [60, 61]. An experiment to produce such neutron-rich unstable nuclei along $N = 126$ is now in progress in the reactions of Xe isotopes on ^{198}Pt [62]. A theoretical prediction by Zagrebaev [29] for the production of such neutron-rich nuclei is shown in Fig. 1.4 (a). The figure shows production cross sections of $N = 126$ isotones as a function of the charge number of the produced nuclei. Red circles connected with dotted lines show cross sections associated with high-energy proton-removal processes. While blue squares connected with solid lines show cross sections for MNT processes in ^{136}Xe+^{208}Pb reaction. As can be seen from the figure, cross sections of the MNT reaction is much larger than those of proton-removal reactions. Recently, a production of neutron-rich light nuclei through MNT reactions has also been discussed by Zagrebaev [63] and the results are shown in Fig. 1.4 (b). The figure shows production cross sections of MNT reactions (red squares) and of fragmentation processes (gray circles) as a function of the atomic
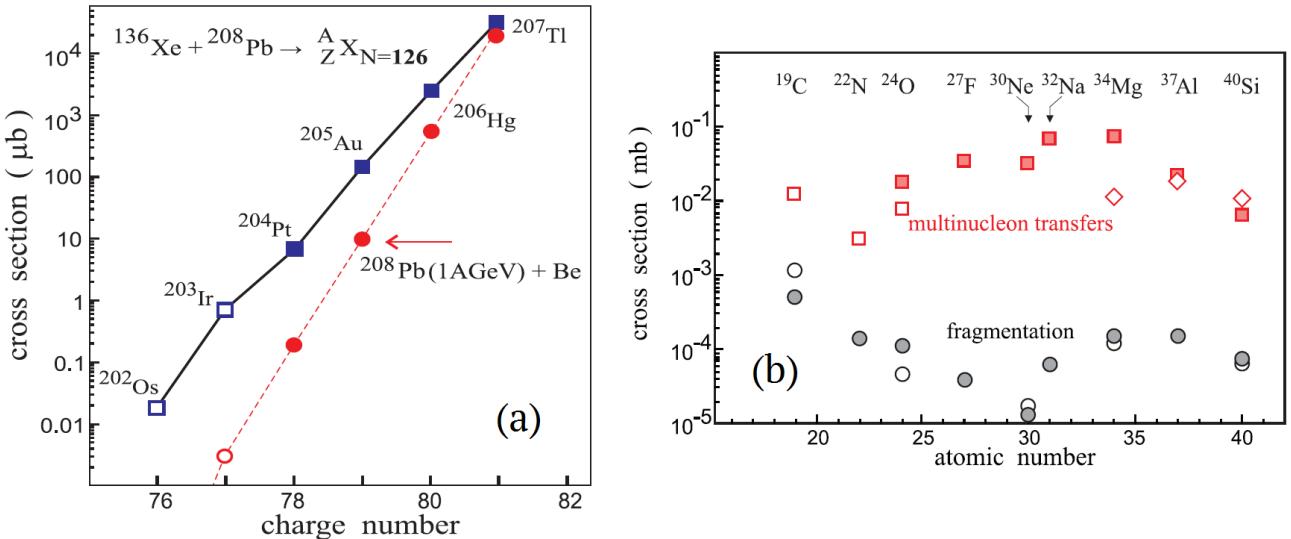
Figure 1.4: Cross sections calculated by a dynamical model based on Langevin-type equations of motion in comparison with measured cross sections. (a): Production cross sections of nuclei along the neutron magic number $N = 126$ for MNT processes in ^{136}Xe+^{208}Pb reaction at center-of-mass energy of 450 MeV (blue squares connected with solid lines) are shown. Measured cross sections associated with high-energy proton removal processes in ^{208}Pb+Be reaction [64] are also shown (red circles connected with dotted lines). (b): Production cross sections of light neutron-rich nuclei for MNT processes in ^{18}O+^{238}U (open squares), ^{26}Mg+^{238}U (filled squares), and ^{36}S+^{238}U (open diamonds) reactions are shown. Experimental cross sections associated with fragmentation processes of ^{48}Ca+^{181}Ta at $E_{\text{lab}} = 128$ MeV/nucleon [65] (gray filled circles) and ^{48}Ca+^{9}Be at $E_{\text{lab}} = 345$ MeV/nucleon [66] (black open circles) are also shown. The figure shown in (a) was taken from Ref. [29]. The figure shown in (b) was taken from Ref. [63].

number of the produced nuclei. Again the cross sections of MNT reactions show much larger values than those of fragmentation processes.

To describe MNT processes theoretically, models based on a direct reaction picture such as GRAZING [67] and Complex WKB (CWKB) [68] have been extensively developed and applied [39, 40, 43, 44, 45, 46, 47, 49, 50, 51]. In these models, MNT processes are treated statistically, using single-nucleon transfer probabilities calculated by the first-order perturbation theory. A dynamical model based on Langevin-type equations of motion has also been developed [69, 70]. This model describes not only MNT processes but also DICs, QF, fusion-fission, and fusion reactions in a unified way [29, 58, 69, 70, 71, 72, 73]. The results shown in Fig. 1.4 were calculated by the Langevin model.

Although the above mentioned approaches have shown reasonable successes, these models are not fully microscopic but include some model assumptions. To get a fundamental understanding of the reaction dynamics and to present a reliable prediction for the cross sections, it is highly desired to develop a fully microscopic description for the MNT processes with minimum assumptions on the dynamics. To this end, in this thesis, we conduct microscopic investigations of the MNT reaction employing the time-dependent Hartree-Fock (TDHF) theory.

1.2.2 Quasifission processes

In low-energy heavy ion reactions, fusion reactions take place forming the CN either passing over or tunnel through the Coulomb barrier. The CN is a composite system of projectile and target nuclei combined through the nuclear attractive interaction. Because the nuclear interaction makes the
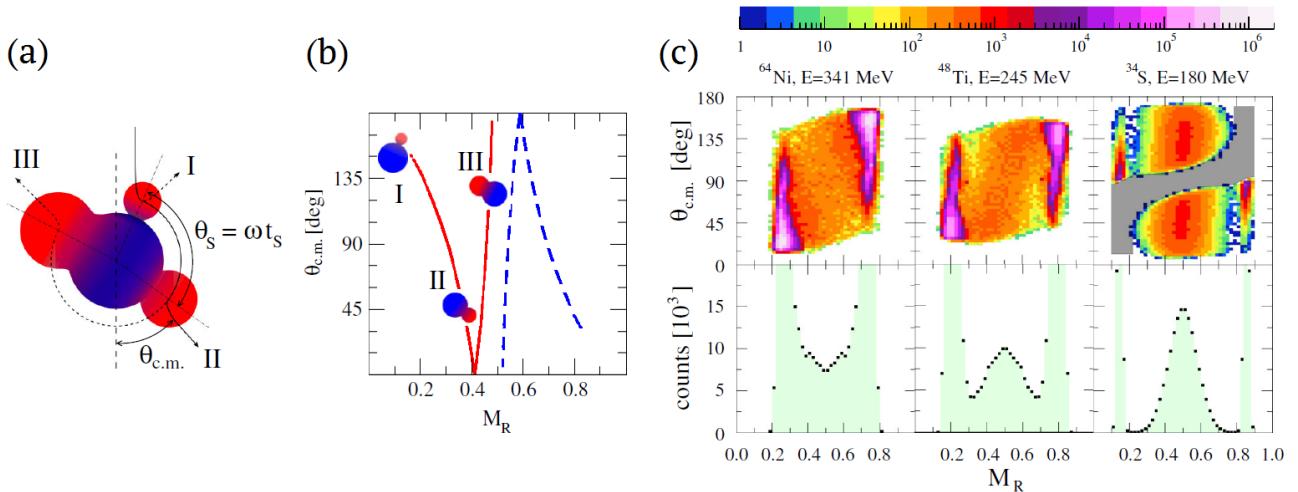
Figure 1.5: (a) and (b): Mass symmetrizing process in a dinuclear system and its correspondence in a mass-angle distribution (MAD) plot are shown schematically. (c): Experimental MAD (upper panels) and its projection onto M_R axis (lower panels) for ^{64}Ni+^{184}W at E_{lab} = 341 MeV (left), ^{48}Ti+^{184}W at E_{lab} = 245 MeV (middle), and ^{34}S+^{184}W at E_{lab} = 180 MeV (right). These figures were taken from Ref. [77].

composite system excited with chaotically complex configurations, any information of the entrance-channel, that is, information of the projectile and target nuclei before the collision, is lost after the CN formation. Because the CN is highly excited, it would suffer from subsequent deexcitation processes, particle evaporation and fission. In distinction from the latter process, fusion-fission, there is another fission process which takes place before the CN formation, the so called QF process.

The QF process hinders the CN formation and thus hinders the occurrence of the fusion reaction. Especially for heavy systems with the charge product, $Z_P Z_T$, greater than a critical value around 1600-1800, the fusion reaction is known to be suppressed, because of the strong Coulomb repulsion and dynamical effects on the barrier penetration process [74, 75]. For example, for $^{40}_{18}$Ar$_{22}$+$^{180}_{72}$Hf$_{108}$ ($\rightarrow^{220}_{90}$Th$_{130}$) reaction with $Z_P Z_T$ = 1296, the experimentally extracted fusion probability agrees with a prediction of one-dimensional barrier penetration model, where the fusion probability becomes 0.5 when the incident relative energy and the barrier-top energy coincide. While for $^{124}_{50}$Sn$_{74}$+$^{96}_{40}$Zr$_{56}$ ($\rightarrow^{220}_{90}$Th$_{130}$) reaction with $Z_P Z_T$ = 2000, which forms the same CN as the above mentioned reaction, the fusion probability was found to be substantially suppressed by several orders of magnitude [76]. Such a heavy system with $Z_P Z_T \gtrsim$ 1600 requires additional energy to form the CN compared with the estimation of the one-dimensional barrier penetration model. Such an energy is called *extra-push energy* [74, 75]. This fission process before the CN formation originated from the fusion hindrance phenomenon in heavy systems would be regarded as the QF process.

Because the QF process takes place in a much shorter timescale than that of fusion-fission, there is a characteristic correlation between the fragment mass and the scattering angle. Figure 1.5 shows typical examples of such a mass-angle correlation. In Fig. 1.5 (a), a reaction process after the touching configuration is illustrated. After two nuclei touched, a dinuclear system connected with a neck structure is formed. This dinuclear system rotates with symmetrizing the mass of each subsystem. Thus, if the dinuclear system dissociates before it rotates as large as 360 degree, there will be a visible correlation between the fragment mass and the scattering angle as schematically illustrated in Fig. 1.5 (b). The vertical axis is the scattering angle in the center-of-mass frame, while the horizontal axis is the mass ratio, $M_R \equiv M_{\mathrm{PLF(TLF)}}/(M_P + M_T)$. Red solid (blue dashed) line represents values for the lighter (heavier) fragment. This plot is called the mass-angle distribution (MAD) plot. In
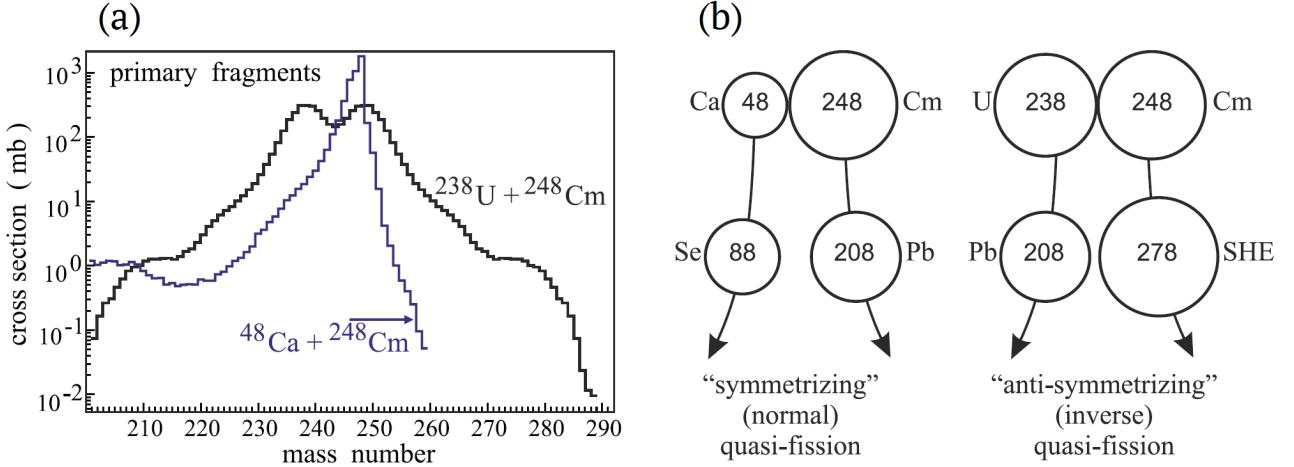
Figure 1.6: (a): Primary production cross sections of heavy fragment nuclei calculated by a dynamical model based on Langevin-type equations of motion. Blue solid line shows results for ^{48}Ca+^{248}Cm reaction at center-of-mass energy of 220 MeV, while black solid line shows results for ^{238}U+^{248}Cm reaction at center-of-mass energy of 770 MeV. (b): Schematic pictures of normal- and inverse-QF processes are schematically illustrated. The figure was taken from Ref. [84].

Fig. 1.5 (c), measured MAD plots for ^{64}Ni+^{184}W ($Z_P Z_T = 2072$), ^{48}Ti+^{184}W ($Z_P Z_T = 1628$), and ^{34}S+^{184}W ($Z_P Z_T = 1184$) reactions are shown, from left to right. As seen from the figure, for two systems with a large $Z_P Z_T$ value (left and middle panels), we find the mass-angle correlation. While, for the system with a small $Z_P Z_T$ (right panels), the mass-angle correlation is lost indicating a longer sticking time. From the MAD plot combined with an exponential decay model, the timescale of the QF process was deduced to be 10^{-20}–10^{-21} sec [77, 78, 79, 80]. On the other hand, measurements of the timescale of the QF process based on a crystal blocking technique indicated a timescale of 10^{-18} sec [81, 82]. Although the origin of discrepancy has not been fully understood, a possible relevance to the quantum decoherence phenomena has been advocated [83].

The QF process attracts much interests for several aspects. First one is the interest for its microscopic mechanisms as in the case of the MNT process, where we may expect much more complicated reaction dynamics than the MNT process in such a dissipative collision. Second one is related to synthesis of SH nuclei. Since the QF process hinders the CN formation, to understand the mechanisms of the QF process would have a crucial importance for investigating how to effectively synthesize SH nuclei. Another interest is a production of unstable nuclei. Since the QF process accompanies a transfer of many nucleons, it would be possible to apply it as a tool to produce unstable nuclei. Especially, an *inverse* (or *antisymmetrizing*) QF process has recently been considered to be useful to produce neutron-rich transuranium nuclei. A typical example is shown in Fig. 1.6. Figure 1.6 (a) shows primary production cross sections for heavier fragments in ^{48}Ca+^{248}Cm (blue solid line) and ^{238}U+^{248}Cm (black solid line) reactions as a function of the mass number of the fragment nuclei. In the case of ^{48}Ca+^{248}Cm reaction, there appears a shoulder structure at around $A = 208$. This corresponds to the QF process driven by the stabilization effect of doubly-magic ^{208}Pb in heavier fragments. On the other hand, in the case of ^{238}U+^{248}Cm reaction, the stabilization effect of doubly-magic ^{208}Pb affects to smaller fragments (initial ^{238}U nucleus). In this case, about 10 protons and 20 neutrons are transferred from ^{238}U to ^{248}Cm forming SH nuclei heavier than ^{248}Cm, which corresponds to the inverse QF process. These normal- and inverse-QF processes are schematically illustrated in Fig. 1.6 (b).

The dynamical model based on Langevin-type equations of motion has been extensively applied and had great successes [29, 58, 69, 70, 71, 72, 73]. However, the Langevin model contains several

model parameters. To make a reliable prediction of cross sections in the QF process, it is desirable to adequately describe not only complex reaction dynamics (energy dissipations, nucleon exchanges, deformations, surface vibrations, and so on) but also quantum effects with minimum parameters specific to the reaction. In this thesis, we thus investigate the QF process in the microscopic framework of the TDHF theory.

1.3 About this Study

1.3.1 Method: The TDHF theory

The TDHF theory is a microscopic theory for nuclear dynamics. The theory of the TDHF was first proposed by Dirac in 1930 [85]. Applications of the TDHF theory to nuclear collision dynamics started in 1970s [86, 87, 88, 89, 90, 91, 92, 93]. Progresses in the early stage were summarized in Ref. [94]. Since then, continuous efforts have been devoted for improving the method and extending applications [95, 96, 97, 98, 99, 100, 101, 102, 103, 104, 105, 106, 107, 108, 109, 110, 111, 112, 113, 114, 115, 116, 117, 118, 119, 120, 121, 122, 123, 124, 125, 126]. At present, three-dimensional calculations with full Skyrme functionals including time-odd components are routinely conducted. In most TDHF calculations, Skyrme-type interactions [127] are used. Since parameters of Skyrme interactions are determined to reproduce nuclear properties for a wide mass region, there is no empirical parameter specific to the reaction.

The TDHF theory may describe both peripheral and central collisions. In peripheral collisions, the mean-field of the collision partner works as a time-dependent perturbation for the orbitals. This picture of the transfer dynamics is similar to that in direct reaction models where single-particle transfer probabilities are calculated either by the perturbation theory [67, 68] or by solving numerically the time-dependent Schrödinger equation [128, 129, 130]. In collisions at smaller impact parameters, the TDHF theory describes macroscopic dynamics such as fusion [91, 95, 97, 102, 106, 109, 118, 121], QF [112, 113, 120, 121, 124, 125], and DICs [87, 88, 89, 90, 92, 93, 114, 121]. Nucleons are exchanged between projectile and target nuclei through the neck formation. This description of the MNT processes is similar to the Langevin-type description [69, 70]. In this way, the TDHF theory is expected to be capable of describing quite different transfer mechanisms in a unified way.

1.3.2 Aims

One of the main aims of this study is to reveal microscopic reaction mechanisms of the MNT and QF processes in low-energy heavy ion reactions. As explained in Sec. 1.2, the MNT and QF processes have recently been considered to be a useful means to produce unstable nuclei whose production is difficult by other methods. Utilizing the microscopic understanding of these reactions, we aim to theoretically predict optimum reactions, *i.e.* projectile-target combinations and incident energies, to produce objective unstable nuclei.

The semiclassical theories, GRAZING and CWKB, have achieved great successes in describing MNT reactions, while the dynamical Langevin model has recently been extensively developed and successfully applied to both MNT and QF processes. Their successes are noteworthy and they provide us substantial developments of our understanding of the reactions and related physics. However, a possible weak point of those successful models is that they are not fully microscopic and contain some model parameters and assumptions in describing the reaction. To obtain a microscopic understanding of the MNT and QF processes and to provide a reliable prediction for producing objective unstable nuclei, we aim to elucidate the feasibility of the TDHF theory as a possible candidate of a fully microscopic theory with smallest parameters and assumptions in describing the reaction dynamics.

In order to accomplish the aims of this study, we investigate the MNT and QF processes in a microscopic framework of the TDHF theory. Although there have been substantial efforts in studying low-energy heavy ion reactions employing the TDHF theory, applicability of the theory to study the MNT and QF processes was unclear (Very recently, the applicability of the TDHF theory to describe the QF process has been becoming noticeable [124, 125]). Because there is no adjustable parameter specific to the reaction dynamics in the TDHF theory, we do not know *a priori* that how reasonably it works in describing those complex reaction dynamics. To show that whether the TDHF theory describes MNT cross sections quantitatively, we shall make a direct comparison between experimental and theoretical cross sections. To this end, we calculate transfer probabilities and cross sections from the TDHF wave function after collision using a particle-number projection (PNP) technique [115]. By performing a systematic TDHF calculation for various systems for which precise experimental data of MNT and/or QF processes are available, we will shed light on the feasibility of the TDHF theory in describing the MNT and QF processes.

Although the TDHF theory provides us a fully microscopic description of nuclear many-body dynamics, it is, of course, not exact but an approximate framework for the nuclear many-body problem (Even though it has a connection to the time-dependent density functional theory (TDDFT) as explained in Chapter 2, we do not know a *special* density-functional which provides an exact description for various reaction channels). We thus consider that to extend its application as far as possible is quite important, because it will reveal the limit of application of the theory and will help us when we develop more sophisticated framework to describe the reaction dynamics. Receiving a benefit from extensive developments of high performance computing infrastructure (HPCI) which enables us a massively parallel computing on a supercomputer, we perform TDHF calculations for various systems at a number of initial conditions in order to achieve the aims and, hopefully, to elucidate a novel reaction dynamics in the TDHF theory.

1.3.3 Outline of the thesis

The thesis is organized as follows. In Chapter 2, we first give the theoretical formalisms of the Hartree-Fock (HF) and TDHF theories. A relation of them to the density functional theory (DFT) and the TDDFT is explained. Computational techniques to simulate heavy ion reactions numerically employing the TDHF theory is given.

We divide the main part of the thesis into two parts, Part I composed of Chapters 3, 4, and 5 and Part II composed of Chapters 6, 7, 8, and 9. The first part of the thesis (Part I) is devoted to show that the applicability of the TDHF theory to the MNT reactions taking into account effects of particle evaporation from primary reaction products. In the second part of the thesis (Part II), we examine a further extension of the application of the TDHF theory to reactions involving more heavier nuclei such as ^{238}U, where a significant contribution of the QF process is expected because of a substantially large $Z_{\mathrm{P}}Z_{\mathrm{T}}$ value.

In Chapter 3, we show results of the TDHF calculations for MNT reactions. To the author's knowledge, it was the first serious study of the MNT reaction employing the TDHF theory. We first explain how the MNT processes are described in the TDHF theory as well as the formalism of the PNP technique. We then apply the TDHF theory to reactions of ^{40}Ca+^{124}Sn at $E_{\mathrm{lab}} = 170$ MeV, ^{48}Ca+^{124}Sn at $E_{\mathrm{lab}} = 174$ MeV, ^{40}Ca+^{208}Pb at $E_{\mathrm{lab}} = 235$ and 249 MeV, and ^{58}Ni+^{208}Pb at $E_{\mathrm{lab}} = 328.4$ MeV, for which precise experimental data are available. From direct comparisons of MNT cross sections between calculated and measured ones, we show that the TDHF theory can describe MNT cross sections quantitatively. We also compare our results with those of other theoretical predictions. We find that the TDHF theory quantitatively describes MNT cross sections with an accuracy comparable to existing theories. We discuss dependence of MNT processes on the neutron-

to-proton ratio, N/Z, and the charge product, $Z_P Z_T$, of colliding nuclei. Light is shed on the existence of two types of transfer mechanisms, quantum tunneling and neck breaking dynamics, in the MNT reactions.

Reaction products produced by MNT processes can be highly excited. Because of this fact, MNT cross sections would be affected by particle evaporation processes. To include effects of particle evaporation, we need to evaluate excitation energy of reaction products in each transfer channel. To evaluate excitation energy of reaction products, we have developed a formalism to calculate expectation values of operators in a particle-number projected TDHF wave function after collision. This method is useful not only for evaluating excitation energy of reaction products but also for investigating reaction mechanisms which could not be examined by ordinary expectation values without the PNP. In Chapter 4, we explain an idea and the formalism of the method. We then apply it to ^{24}O+^{16}O reaction as an illustrative example to show usefulness of our method. The effects of particle evaporation on MNT cross sections are examined in Chapter 5.

From the analysis presented in Part I (Chapters 3, 4, and 5) we get a confidence that the TDHF theory describes the MNT reaction reasonably well without any adjustable parameter specific to the reaction. In Part II (Chapters 6, 7, 8, and 9), we extend its application to MNT and QF processes in reactions involving more heavier nuclei, as a next step of the study.

We first investigate ^{64}Ni+^{238}U reaction at $E_{\text{lab}} = 390$ MeV, for which measurements of MNT cross sections were achieved. From a comparison between measured cross sections and calculated ones, we show that the TDHF theory nicely reproduces measured cross sections both proton-stripping and proton-pickup channels. It is remarkable that cross sections for the proton-pickup channels were underestimated by the existing semiclassical theory, GRAZING, may be due to an insufficient assumption of the strong absorption of flux from transfer channels to fusion at a small impact parameter region. This fact may indicate that the TDHF theory would correctly describe the transitional regime from quasielastic to more complex reaction mechanisms. In addition, TDHF calculations show abundant cross sections for QF induced MNT processes. In such QF processes, we find that a scission point of a neck changes suddenly depending on the impact parameter and the relative orientation. To get further information on the QF dynamics, we examine energy dependence of QF dynamics in head-on collisions of ^{64}Ni+^{238}U. From the calculation, we find a significant effect of the relative orientation of colliding nuclei on the QF dynamics. In Chapter 6, we show these results and discuss possible structural effects of the composite system on the QF dynamics.

We next investigate ^{238}U+^{124}Sn reaction at $E_{\text{lab}} = 1356.6$ MeV. Measurements of MNT cross sections in ^{238}U+^{124}Sn induced dissipative collision were achieved in 1985, where measured MNT cross sections indicate that many protons (up to around 10) are transferred from ^{238}U to ^{124}Sn. From the TDHF calculations, we show that the measured many-proton transfer from ^{238}U to ^{124}Sn might be originated from the neck breaking dynamics, where a thick neck is formed between two colliding nuclei and its dissociation and subsequent absorption of the neck region results in transfer of many nucleons. In Chapter 7, the neck breaking transfer dynamics as well as significant effects of the relative orientation in ^{238}U+^{124}Sn reaction are discussed. To examine effects of the incident energy and the N/Z asymmetry on the QF dynamics, head-on collisions of ^{238}U+^{100,124,132}Sn are investigated, where we find inverse QF processes producing transuranium nuclei for certain initial conditions.

In Chapter 8, as a final topic of the thesis, we present tentative results of the application of the TDHF theory toward a prediction to produce objective unstable nuclei. We show results of a systematic TDHF calculation for ^{136}Xe+^{198}Pt reactions at various initial conditions. This reaction is considered to be useful to produce neutron-rich unstable nuclei around the neutron magic number $N = 126$. From the calculation, we find that the direction and amount of transfer at different initial conditions show a similar behavior as a function of distance of closest approach, although it shows quite complex behavior as functions of the impact parameter. We find that there appear inverse QF

processes at initial conditions corresponding to a certain region of the distance of closest approach. We discuss MNT and QF processes in ^{136}Xe+^{198}Pt reactions in comparisons with the other cases ^{64}Ni+^{238}U and ^{238}U+^{100,124,132}Sn reactions, in Chapter 8.

Finally, a summary of the thesis and a future prospect of the study are presented in Chapter 9.

Chapter 2

TDHF THEORY AND TDDFT, AND THEIR APPLICATION TO HEAVY ION REACTIONS

In this Chapter, we present theoretical formalisms which will be used to study MNT and QF processes in low-energy heavy ion reactions in the subsequent Chapters. In Sec. 2.1, we explain the HF theory and its time-dependent extension (the TDHF theory) with a Skyrme-type effective interaction. We refer them as the Skyrme HF theory and the Skyrme TDHF theory, respectively. Although the Skyrme (TD)HF theory has been developed as an approximate framework to describe many-nucleon systems, we may regard it as the DFT and the TDDFT. In Sec. 2.2, we thus explain basic concepts of the DFT and the TDDFT, where the Skyrme (TD)HF theory is regarded as the Kohn-Sham scheme based on the (TD)DFT. In Sec. 2.3, we describe computational techniques for simulating heavy ion reactions employing the TDHF theory.

2.1 TDHF Theory with a Skyrme Effective Interaction

In this Section, we recapitulate theoretical formalisms of the HF and TDHF theories. In Sec. 2.1.1, we first explain a basic concept of the HF theory. In Sec. 2.1.2, we introduce a Hamiltonian with a Skyrme-type effective interaction which has widely been used to study properties of many-nucleon systems. We will utilize the Skyrme Hamiltonian in our TDHF calculations of heavy ion reactions. In Secs. 2.1.3 and 2.1.4, we present the Skyrme energy density functional (EDF) and the Skyrme HF equation, respectively. In Sec. 2.1.5, we explain the theoretical framework of the TDHF theory.

2.1.1 Hartree-Fock theory

The Schrödinger equation for an N-particle system,

$$\hat{H}\Psi(\boldsymbol{r}_1, \cdots, \boldsymbol{r}_N) = E\Psi(\boldsymbol{r}_1, \cdots, \boldsymbol{r}_N), \tag{2.1.1}$$

can be derived according to the variational principle:

$$\frac{\delta}{\delta\langle\Psi|} \left[\frac{\langle\Psi|\hat{H}|\Psi\rangle}{\langle\Psi|\Psi\rangle} \right] = 0. \tag{2.1.2}$$

Here and hereafter, we often use the bracket notation, $e.g.$ $\langle\Psi|\hat{H}|\Psi\rangle \equiv \int d\boldsymbol{r}_1 \cdots \int d\boldsymbol{r}_N \Psi^*(\boldsymbol{r}_1, \cdots, \boldsymbol{r}_N)$ $\hat{H}\Psi(\boldsymbol{r}_1, \cdots, \boldsymbol{r}_N)$, to simplify equations. We temporary omit the spin and isospin degrees of freedom

for simplicity. Since it is computationally too demanding to solve the Schrödinger equation exactly, we need to introduce some approximations in describing the many-body problem. The HF theory [131, 132] is one of the approximations to treat a many-body problem, which is based on the variational principle. In the HF theory, the trial function $|\Psi\rangle$ for the variation is taken to be a single Slater determinant,

$$\Phi(\boldsymbol{r}_1, \cdots, \boldsymbol{r}_N) = \frac{1}{\sqrt{N!}} \det\{\phi_i(\boldsymbol{r}_j)\}, \tag{2.1.3}$$

where $\phi_i(\boldsymbol{r})$ $(i = 1, \cdots, N)$ denotes a single-particle wave function of ith orbital. These single-particle wave functions are orthonormal to each other, $\langle \phi_i|\phi_j\rangle \equiv \int d\boldsymbol{r}\phi_i^*(\boldsymbol{r})\phi_j(\boldsymbol{r}) = \delta_{ij}$. The many-body wave function Eq. (2.1.3) is thus normalized to unity in the whole space, $\langle \Phi|\Phi\rangle = 1$. The variation of Eq. (2.1.2) using the Slater determinant $|\Phi\rangle$ with a constraint on the orthonormalization condition for the single-particle wave functions,

$$\frac{\delta}{\delta\phi_\alpha^*(\boldsymbol{r}\sigma)} \left[\langle\Phi|\hat{H}|\Phi\rangle - \sum_{ij} \varepsilon_{ij}\Big(\langle\phi_i|\phi_j\rangle - \delta_{ij} \Big) \right] = 0, \tag{2.1.4}$$

leads the HF equation. ε_{ij} denote Lagrange multipliers for the constraint on the orthonormalization condition. We summarize details of the derivation in Appendix A.4. The HF equation takes the following form:

$$\int d\boldsymbol{r}' \, \hat{h}_{\mathrm{HF}}(\boldsymbol{r}, \boldsymbol{r}')\phi_i(\boldsymbol{r}') = \varepsilon_i\phi_i(\boldsymbol{r}) \quad (i = 1, \cdots, N), \tag{2.1.5}$$

$$\hat{h}_{\mathrm{HF}}(\boldsymbol{r}, \boldsymbol{r}') = \left[\hat{t}(\boldsymbol{r}) + \Gamma_{\mathrm{H}}(\boldsymbol{r})\right]\delta(\boldsymbol{r} - \boldsymbol{r}') - \Gamma_{\mathrm{F}}(\boldsymbol{r}, \boldsymbol{r}'). \tag{2.1.6}$$

The Hartree potential, $\Gamma_{\mathrm{H}}(\boldsymbol{r})$, and the Fock potential, $\Gamma_{\mathrm{F}}(\boldsymbol{r}, \boldsymbol{r}')$, are defined by

$$\Gamma_{\mathrm{H}}(\boldsymbol{r}) \equiv \int d\boldsymbol{r}'\hat{v}(\boldsymbol{r}, \boldsymbol{r}')\rho(\boldsymbol{r}'), \qquad \rho(\boldsymbol{r}) \equiv \sum_{i=1}^{N}\big|\phi_i(\boldsymbol{r})\big|^2, \tag{2.1.7}$$

$$\Gamma_{\mathrm{F}}(\boldsymbol{r}, \boldsymbol{r}') \equiv \hat{v}(\boldsymbol{r}, \boldsymbol{r}')\rho(\boldsymbol{r}, \boldsymbol{r}'), \qquad \rho(\boldsymbol{r}, \boldsymbol{r}') \equiv \sum_{i=1}^{N}\phi_i(\boldsymbol{r})\phi_i^*(\boldsymbol{r}'). \tag{2.1.8}$$

The Slater determinant is invariant under arbitrary unitary transformations for the single-particle wave functions $\{\phi_i\}$. We used this gauge degree of freedom to diagonalize the single-particle Hamiltonian, i.e. $\varepsilon_i \equiv \varepsilon_{ii}$.

In this way, the Schrödinger equation Eq. (2.1.1) is reduced to N coupled non-linear integro-differential equations in the HF theory. The Hartree-Fock theory is often referred to as a *mean-field* approximation, because Eq. (2.1.5) may be regarded as an equation for independent particles under a non-local potential which is generated by all the particles in the system.

2.1.2 Skyrme effective interaction

The Skyrme effective interaction [127, 133] has been used widely, starting from applications by Vautherin and Brink [134, 135], and had great successes in describing structural properties of nuclei in a wide mass region [136, 137]. Since the Skyrme effective interaction is a contact-type interaction $(v(\boldsymbol{r}, \boldsymbol{r}') \propto \delta(\boldsymbol{r} - \boldsymbol{r}'))$, the non-local Fock-potential in the HF equation is reduced to a local potential. The computational cost for the Skyrme HF theory is reduced significantly because of this locality. The Skyrme Hamiltonian is given by

$$\hat{H}_{\mathrm{Skyrme}} = \hat{T} + \sum_{i<j} \hat{v}_{ij} + \sum_{i<j<k} \hat{v}_{ijk} + \hat{V}_{\mathrm{Coul}}. \tag{2.1.9}$$

$\hat{T}$ denotes the kinetic energy operator,

$$\hat{T} = \sum_{i=1}^{N} \frac{\hat{\boldsymbol{p}}_i^2}{2m}, \tag{2.1.10}$$

where m denotes the nucleon mass and $\hat{\boldsymbol{p}}_i = -\mathrm{i}\hbar\boldsymbol{\nabla}_i$. $\hat{V}_{\mathrm{Coul}}$ denotes the Coulomb interaction between protons,

$$\hat{V}_{\mathrm{Coul}} = \sum_{i<j} \frac{e^2}{|\boldsymbol{r}_i - \boldsymbol{r}_j|} \delta_{q_i p} \delta_{q_j p}. \tag{2.1.11}$$

The three-body interaction is usually renormalized into the two-body interaction as a density dependent interaction [6]. The two-body interaction with the density-dependent effective three-body interaction is given by

$$
\begin{aligned}
\hat{v}_{ij} = \ \hat{v}(\boldsymbol{r}_i\sigma_i, \boldsymbol{r}_j\sigma_j) \ = \ & t_0\big(1 + x_0\hat{P}_\sigma\big)\delta(\boldsymbol{r}_i - \boldsymbol{r}_j) + \frac{1}{6}t_3\, \rho^\alpha\Big(\frac{\boldsymbol{r}_i + \boldsymbol{r}_j}{2}\Big)\big(1 + x_3\hat{P}_\sigma\big)\delta(\boldsymbol{r}_i - \boldsymbol{r}_j) \\
& + \frac{1}{2}t_1\big(1 + x_1\hat{P}_\sigma\big)\Big\{\delta(\boldsymbol{r}_i - \boldsymbol{r}_j)\hat{\boldsymbol{k}}^2 + \hat{\boldsymbol{k}}'^2\delta(\boldsymbol{r}_i - \boldsymbol{r}_j)\Big\} \\
& + t_2\big(1 + x_2\hat{P}_\sigma\big)\hat{\boldsymbol{k}}' \cdot \delta(\boldsymbol{r}_i - \boldsymbol{r}_j)\hat{\boldsymbol{k}} + \mathrm{i}W_0\left(\hat{\boldsymbol{\sigma}}_i + \hat{\boldsymbol{\sigma}}_j\right) \cdot \big\{\hat{\boldsymbol{k}}' \times \delta(\boldsymbol{r}_i - \boldsymbol{r}_j)\hat{\boldsymbol{k}}\big\}.
\end{aligned}
\tag{2.1.12}
$$

$\hat{\boldsymbol{\sigma}}$ denotes the ordinary Pauli spin matrices and $\hat{P}_\sigma = \frac{1}{2}(1 + \hat{\boldsymbol{\sigma}}_i \cdot \hat{\boldsymbol{\sigma}}_j)$ denotes the spin exchange operator. The operators of the relative wave vector, $\hat{\boldsymbol{k}}$ and $\hat{\boldsymbol{k}}'$, are defined by

$$\hat{\boldsymbol{k}} = \frac{\overrightarrow{\boldsymbol{\nabla}}_i - \overrightarrow{\boldsymbol{\nabla}}_j}{2\mathrm{i}}, \qquad \hat{\boldsymbol{k}}' = -\frac{\overleftarrow{\boldsymbol{\nabla}}_i - \overleftarrow{\boldsymbol{\nabla}}_j}{2\mathrm{i}}. \tag{2.1.13}$$

The operator $\hat{\boldsymbol{k}}$ acts on spatial functions located its right side, while the operator $\hat{\boldsymbol{k}}'$ acts on spatial functions located its left side. The parameters t_0, t_1, t_2, t_3, x_0, x_1, x_2, x_3, W_0, and α are determined so as to reproduce static properties of nuclei and some representative properties of nuclear matter (*e.g.* binding energy, root-mean-square radius, fission barrier height, properties of the equation of state, and so on) (see, *e.g.*, Refs. [138, 139, 140, 141, 142, 143, 144, 145, 146, 147]).

In our study, we employ Skyrme SLy5 parameter set [141] in Chapters 3, 4, 6, 7, and 8 and Skyrme SLyIII.0.8 parameter set [146] in Chapter 5. The SLy5 parameter set was made to reproduce, *e.g.* the binding energies and root-mean-square radii (when experimentally known) of doubly magic nuclei (^{40,48}Ca, ^{56}Ni, ^{132}Sn, and ^{208}Pb) and properties of infinite nuclear matter (the saturation properties $\rho_0 \approx 0.16$ fm^{-3} and $E/A \approx -16$ MeV, the incompressibility $K_\infty \approx 230$ MeV, the symmetry energy $a_S \approx 32$ MeV, and so on). In addition, the $\overleftrightarrow{J}^2$ term of the Skyrme EDF is included in the fitting procedure, which was usually neglected other parameter sets. The SLyIII.0.8 parameter set was made starting from the SLy5 parameter set with a particular constraint on the density-dependent term in the Skyrme EDF. Usually, a fractional-power density-dependence ρ^α ($\alpha = 1/3$ or $1/6$) has been utilized to reproduce the incompressibility of nuclear matter. However, there arises a problem when we evaluate an EDF kernel by applying the PNP and/or the angular momentum projection. The fractional-power density-dependence provides multi-poles in the complex plane and we cannot know which pole corresponds to the physical anzats (for detailed discussions, see, *e.g.*, Refs. [148, 149, 150] and references therein). Thus the SLyIII.0.8 parameter set was made constraining $\alpha = 1$ to avoid the problem. Since we will evaluate the energy expectation value with the PNP, the SLyIII.0.8 parameter set will be used in Chapter 5. (The number "0.8" indicates a value of the isoscalar effective mass, m_0^*/m. There are other parameter sets of SLyIII.*x.x* with *x.x* = 0.7, 0.9, and 1.0.) The SLy5 and SLyIII.0.8 parameter sets are shown in Table 2.1.

Table 2.1:   Values of the Skyrme SLy5 [141] and SLyIII.0.8 [146] parameter sets.

parameters	SLy5	SLyIII.0.8
t_0 (MeV fm^3)	-2484.88	-1100.272
t_1 (MeV fm^5)	483.13	359.568
t_2 (MeV fm^5)	-549.40	-210.840
t_3 (MeV fm$^{3+3\alpha}$)	13763.0	13653.845
x_0	0.778	$0.445\,280$
x_1	-0.328	$0.224\,693$
x_2	-1.000	$-0.615\,015$
x_3	1.267	$0.639\,947$
W_0 (MeV fm^5)	126.0	110.828
α	$1/6$	1

2.1.3 Skyrme energy density functional

In the Skyrme HF theory, an EDF, $E_{\rm SHF}$, and a Hamiltonian density, $\mathcal{H}(\boldsymbol{r})$, are defined as the energy expectation value of the Skyrme Hamiltonian:

$$E_{\rm SHF}[\rho, \tau, \boldsymbol{j}, \boldsymbol{s}, \boldsymbol{T}, \overleftrightarrow{J}] = \langle \Phi | \hat{H}_{\rm Skyrme} | \Phi \rangle = \int d\boldsymbol{r}\, \mathcal{H}(\boldsymbol{r}). \qquad (2.1.14)$$

We now introduce the spin and isospin degrees of freedom. We denote the single-particle wave functions as $\phi_i(\boldsymbol{r}\sigma)$, where σ denotes the spin coordinate. In the standard HF theory, each single-particle wave function is assumed to have its own intrinsic isospin, q_i, where $q_i = n$ is used for neutrons, while $q_i = p$ is used for protons. The Hamiltonian density is given by (a detailed derivation is given in Appendix B.2)

$$\begin{aligned}
\mathcal{H}(\boldsymbol{r}) =\ & \frac{\hbar^2}{2m}\tau(\boldsymbol{r}) + B_1\rho^2(\boldsymbol{r}) + B_2\sum_q \rho^{(q)2}(\boldsymbol{r}) \\
& + B_3\Big[\rho(\boldsymbol{r})\tau(\boldsymbol{r}) - \boldsymbol{j}^2(\boldsymbol{r})\Big] + B_4\sum_q\Big[\rho^{(q)}(\boldsymbol{r})\tau^{(q)}(\boldsymbol{r}) - \boldsymbol{j}^{(q)2}(\boldsymbol{r})\Big] \\
& + B_5\rho(\boldsymbol{r})\,\triangle\,\rho(\boldsymbol{r}) + B_6\sum_q \rho^{(q)}(\boldsymbol{r})\,\triangle\,\rho^{(q)}(\boldsymbol{r}) + B_7\rho^\alpha(\boldsymbol{r})\rho^2(\boldsymbol{r}) + B_8\rho^\alpha(\boldsymbol{r})\sum_q\rho^{(q)2}(\boldsymbol{r}) \\
& + B_9\Big[\rho(\boldsymbol{r})\boldsymbol{\nabla}\cdot\boldsymbol{J}(\boldsymbol{r}) + \boldsymbol{s}(\boldsymbol{r})\cdot(\boldsymbol{\nabla}\times\boldsymbol{j}(\boldsymbol{r})) + \sum_q\Big\{\rho^{(q)}(\boldsymbol{r})\boldsymbol{\nabla}\cdot\boldsymbol{J}^{(q)}(\boldsymbol{r}) + \boldsymbol{s}^{(q)}(\boldsymbol{r})\cdot\Big(\boldsymbol{\nabla}\times\boldsymbol{j}^{(q)}(\boldsymbol{r})\Big)\Big\}\Big] \\
& + B_{10}\boldsymbol{s}^2(\boldsymbol{r}) + B_{11}\sum_q\boldsymbol{s}^{(q)2}(\boldsymbol{r}) + B_{12}\rho^\alpha(\boldsymbol{r})\boldsymbol{s}^2(\boldsymbol{r}) + B_{13}\sum_q\rho^{(q)\alpha}(\boldsymbol{r})\boldsymbol{s}^{(q)2}(\boldsymbol{r}) \\
& + B_{14}\Big[\boldsymbol{s}(\boldsymbol{r})\cdot\boldsymbol{T}(\boldsymbol{r}) - \overleftrightarrow{J}^2(\boldsymbol{r})\Big] + B_{15}\boldsymbol{s}(\boldsymbol{r})\cdot\triangle\boldsymbol{s}(\boldsymbol{r}) \\
& + B_{16}\sum_q\Big[\boldsymbol{s}^{(q)}(\boldsymbol{r})\cdot\boldsymbol{T}^{(q)}(\boldsymbol{r}) - \overleftrightarrow{J}^{(q)2}(\boldsymbol{r})\Big] + B_{17}\sum_q\boldsymbol{s}^{(q)}(\boldsymbol{r})\cdot\triangle\boldsymbol{s}^{(q)}(\boldsymbol{r}) + \mathcal{H}_{\rm Coul}(\boldsymbol{r}), \qquad (2.1.15)
\end{aligned}$$

where the Coulomb energy density, $\mathcal{H}_{\rm Coul}(\boldsymbol{r})$, is defined by

$$\mathcal{H}_{\rm Coul}(\boldsymbol{r}) = \frac{e^2}{2}\rho^{(p)}(\boldsymbol{r})\left\{ \int d\boldsymbol{r}'\, \frac{\rho^{(p)}(\boldsymbol{r}')}{|\boldsymbol{r}-\boldsymbol{r}'|} - \frac{3}{2}\left(\frac{3}{\pi}\right)^{\frac{1}{3}}\big[\rho^{(p)}(\boldsymbol{r})\big]^{\frac{1}{3}} \right\}. \qquad (2.1.16)$$

The so called Slater approximation [151] was used for the exchange term. In practice, we use the Hockney's method [152] to evaluate the Coulomb potential in the direct term, in which the Fourier

transformation is achieved in a grid of a box two times larger than that utilized to express the single-particle wave functions. Some details of the method is given in Appendix D. The coefficients $B_1, \cdots, B_{17}$ are defined as follows:

$$B_1 = \frac{1}{2}t_0\left(1 + \frac{1}{2}x_0\right), \quad B_2 = -\frac{1}{2}t_0\left(\frac{1}{2} + x_0\right), \quad B_3 = \frac{1}{4}\left\{t_1\left(1 + \frac{1}{2}x_1\right) + t_2\left(1 + \frac{1}{2}x_2\right)\right\},$$

$$B_4 = -\frac{1}{4}\left\{t_1\left(\frac{1}{2} + x_1\right) - t_2\left(\frac{1}{2} + x_2\right)\right\}, \quad B_5 = -\frac{1}{16}\left\{3t_1\left(1 + \frac{1}{2}x_1\right) - t_2\left(1 + \frac{1}{2}x_2\right)\right\},$$

$$B_6 = \frac{1}{16}\left\{3t_1\left(\frac{1}{2} + x_1\right) + t_2\left(\frac{1}{2} + x_2\right)\right\}, \quad B_7 = \frac{1}{12}t_3\left(1 + \frac{1}{2}x_3\right), \quad B_8 = -\frac{1}{12}t_3\left(\frac{1}{2} + x_3\right),$$

$$B_9 = -\frac{1}{2}W_0, \quad B_{10} = \frac{1}{4}t_0x_0, \quad B_{11} = -\frac{1}{4}t_0, \quad B_{12} = \frac{1}{24}t_3x_3, \quad B_{13} = -\frac{1}{24}t_3,$$

$$B_{14} = \frac{1}{8}\left(t_1x_1 + t_2x_2\right), \quad B_{15} = -\frac{1}{32}\left(3t_1x_1 - t_2x_2\right), \quad B_{16} = -\frac{1}{8}\left(t_1 - t_2\right), \quad B_{17} = \frac{1}{32}\left(3t_1 + t_2\right).$$

We have introduced several densities ρ, τ, $\boldsymbol{j}$, $\boldsymbol{s}$, $\boldsymbol{T}$ and $\overleftrightarrow{\mathcal{J}}$ defined as follows [153]:

(i) particle density

$$\begin{aligned}
\rho(\boldsymbol{r}) &= \rho(\boldsymbol{r}, \boldsymbol{r}) \\
&= \sum_{i,\sigma} \phi_i^*(\boldsymbol{r}\sigma)\phi_i(\boldsymbol{r}\sigma),
\end{aligned} \tag{2.1.17}$$

(ii) kinetic energy density

$$\begin{aligned}
\tau(\boldsymbol{r}) &= (\boldsymbol{\nabla} \cdot \boldsymbol{\nabla}')\rho(\boldsymbol{r}, \boldsymbol{r}')\Big|_{\boldsymbol{r}=\boldsymbol{r}'} \\
&= \sum_{i,\sigma} \boldsymbol{\nabla}\phi_i^*(\boldsymbol{r}\sigma) \cdot \boldsymbol{\nabla}\phi_i(\boldsymbol{r}\sigma),
\end{aligned} \tag{2.1.18}$$

(iii) spin density

$$\begin{aligned}
\boldsymbol{s}(\boldsymbol{r}) &= \boldsymbol{s}(\boldsymbol{r}, \boldsymbol{r}) \\
&= \sum_{i,\sigma_1,\sigma_2} \phi_i^*(\boldsymbol{r}\sigma_1)\phi_i(\boldsymbol{r}\sigma_2)\langle\sigma_1|\hat{\boldsymbol{\sigma}}|\sigma_2\rangle,
\end{aligned} \tag{2.1.19}$$

(iv) current

$$\begin{aligned}
\boldsymbol{j}(\boldsymbol{r}) &= \frac{1}{2\mathrm{i}}\left(\boldsymbol{\nabla} - \boldsymbol{\nabla}'\right)\rho(\boldsymbol{r}, \boldsymbol{r}')\Big|_{\boldsymbol{r}=\boldsymbol{r}'} \\
&= \sum_{i,\sigma} \frac{1}{2\mathrm{i}}\left\{\phi_i^*(\boldsymbol{r}\sigma)\boldsymbol{\nabla}\phi_i(\boldsymbol{r}\sigma) - \phi_i(\boldsymbol{r}\sigma)\boldsymbol{\nabla}\phi_i^*(\boldsymbol{r}\sigma)\right\} \\
&= \sum_{i,\sigma} \Im\left[\phi_i^*(\boldsymbol{r}\sigma)\boldsymbol{\nabla}\phi_i(\boldsymbol{r}\sigma)\right],
\end{aligned} \tag{2.1.20}$$

(v) spin kinetic energy density

$$\begin{aligned}
\boldsymbol{T}(\boldsymbol{r}) &= \left(\boldsymbol{\nabla} \cdot \boldsymbol{\nabla}'\right)\boldsymbol{s}(\boldsymbol{r}, \boldsymbol{r}')\Big|_{\boldsymbol{r}=\boldsymbol{r}'} \\
&= \sum_{i,\sigma_1,\sigma_2} \left\{\boldsymbol{\nabla}\phi_i^*(\boldsymbol{r}\sigma_1) \cdot \boldsymbol{\nabla}\phi_i(\boldsymbol{r}\sigma_2)\right\}\langle\sigma_1|\hat{\boldsymbol{\sigma}}|\sigma_2\rangle,
\end{aligned} \tag{2.1.21}$$

(vi) spin current pseudotensor

$$\begin{aligned}
\overleftrightarrow{\mathcal{J}}(\boldsymbol{r}) &= \frac{1}{2\mathrm{i}}\left(\boldsymbol{\nabla} - \boldsymbol{\nabla}'\right) \otimes \boldsymbol{s}(\boldsymbol{r}, \boldsymbol{r}')\Big|_{\boldsymbol{r}=\boldsymbol{r}'} \\
&= \sum_{i,\sigma_1,\sigma_2} \frac{1}{2\mathrm{i}}\left\{\phi_i^*(\boldsymbol{r}\sigma_1)\boldsymbol{\nabla}\phi_i(\boldsymbol{r}\sigma_2) - \phi_i(\boldsymbol{r}\sigma_2)\boldsymbol{\nabla}\phi_i^*(\boldsymbol{r}\sigma_1)\right\} \otimes \langle\sigma_1|\hat{\boldsymbol{\sigma}}|\sigma_2\rangle \\
&= \sum_{i,\sigma_1,\sigma_2} \Im\left[\phi_i^*(\boldsymbol{r}\sigma_1)\boldsymbol{\nabla}\phi_i(\boldsymbol{r}\sigma_2)\right] \otimes \langle\sigma_1|\hat{\boldsymbol{\sigma}}|\sigma_2\rangle.
\end{aligned} \tag{2.1.22}$$

These densities are real by definition. Density and spin-density matrices are defined by $\rho(\boldsymbol{r},\boldsymbol{r}') \equiv \sum_\sigma \rho(\boldsymbol{r}\sigma,\boldsymbol{r}'\sigma)$ and $\boldsymbol{s}(\boldsymbol{r},\boldsymbol{r}') \equiv \sum_{\sigma_1,\sigma_2} \rho(\boldsymbol{r}\sigma_1,\boldsymbol{r}'\sigma_2)\langle\sigma_2|\hat{\boldsymbol{\sigma}}|\sigma_1\rangle$, respectively, where $\rho(\boldsymbol{r}\sigma,\boldsymbol{r}'\sigma') \equiv \sum_i \phi_i(\boldsymbol{r}\sigma)\phi_i^*(\boldsymbol{r}'\sigma')$. Densities ρ, τ, and $\overleftrightarrow{J}$ are even under the time-reversal operation, while $\boldsymbol{s}$, $\boldsymbol{T}$, and $\boldsymbol{j}$ are odd. $\overleftrightarrow{J}(\boldsymbol{r})$ is a rank-2 tensor having components $J_{\mu\nu}(\boldsymbol{r}) = \sum_{i\sigma_1\sigma_2} \Im\big[\phi_i^*(\boldsymbol{r}\sigma_1)\nabla_\mu\phi_i(\boldsymbol{r}\sigma_2)\big]\langle\sigma_1|\hat{\sigma}_\nu|\sigma_2\rangle$. The density $\boldsymbol{J}(\boldsymbol{r}) = \big(J_1(\boldsymbol{r}), J_2(\boldsymbol{r}), J_3(\boldsymbol{r})\big)$ in Eq. (2.1.15) is the anti-symmetric part of the tensor $\overleftrightarrow{J}(\boldsymbol{r})$, which has components $J_\lambda(\boldsymbol{r}) = \sum_{\mu\nu}\varepsilon_{\mu\nu\lambda}J_{\mu\nu}(\boldsymbol{r})$. We note that an inner product of these tensors is defined by $\overleftrightarrow{J}^2(\boldsymbol{r}) = \sum_{\mu\nu}\big(J_{\mu\nu}(\boldsymbol{r})\big)^2$. $\triangle\boldsymbol{s}(\boldsymbol{r})$ in Eq. (2.1.15) denotes a vector function having components $\triangle s_\nu(\boldsymbol{r})$ ($\nu = 1, 2, 3$), that is, the Laplacian acts on each component of $\boldsymbol{s}(\boldsymbol{r})$.

2.1.4 Skyrme Hartree-Fock equation

By performing the variation of Eq. (2.1.4) with the Skyrme Hamiltonian, we obtain the Skyrme HF equation for the single-particle wave functions (a detailed derivation is given in Appendix B.3):

$$\sum_{\sigma'} \hat{h}_{\mathrm{SHF}}^{(q_i)}(\boldsymbol{r}\sigma\sigma')\phi_i(\boldsymbol{r}\sigma') = \varepsilon_i\,\phi_i(\boldsymbol{r}\sigma), \tag{2.1.23}$$

where the single-particle Hamiltonian has the following form [153, 154],

$$\hat{h}_{\mathrm{SHF}}^{(q)}(\boldsymbol{r}\sigma\sigma') = -\frac{\hbar^2}{2m}\triangle\,\delta_{\sigma\sigma'} + \hat{h}_{\mathrm{even}}^{(q)}(\boldsymbol{r}\sigma\sigma') + \hat{h}_{\mathrm{odd}}^{(q)}(\boldsymbol{r}\sigma\sigma'). \tag{2.1.24}$$

The time-even and time-odd parts of the single-particle Hamiltonian are defined by

$$\hat{h}_{\mathrm{even}}^{(q)}(\boldsymbol{r}\sigma\sigma') = -\overrightarrow{\boldsymbol{\nabla}}\cdot M^{(q)}(\boldsymbol{r})\overrightarrow{\boldsymbol{\nabla}}\delta_{\sigma\sigma'} + U^{(q)}(\boldsymbol{r})\delta_{\sigma\sigma'} + \frac{1}{2\mathrm{i}}\left(\overleftrightarrow{\nabla\sigma}_{\sigma\sigma'}\cdot\overleftrightarrow{B}^{(q)}(\boldsymbol{r}) + \overleftrightarrow{B}^{(q)}(\boldsymbol{r})\cdot\overleftrightarrow{\nabla\sigma}_{\sigma\sigma'}\right), \tag{2.1.25}$$

$$\hat{h}_{\mathrm{odd}}^{(q)}(\boldsymbol{r}\sigma\sigma') = -\overrightarrow{\boldsymbol{\nabla}}\cdot\big(\boldsymbol{\sigma}_{\sigma\sigma'}\cdot\boldsymbol{C}^{(q)}(\boldsymbol{r})\big)\overrightarrow{\boldsymbol{\nabla}} + \boldsymbol{\sigma}_{\sigma\sigma'}\cdot\boldsymbol{\Sigma}^{(q)}(\boldsymbol{r}) + \frac{1}{2\mathrm{i}}\big(\overrightarrow{\boldsymbol{\nabla}}\cdot\boldsymbol{I}^{(q)}(\boldsymbol{r}) + \boldsymbol{I}^{(q)}(\boldsymbol{r})\cdot\overrightarrow{\boldsymbol{\nabla}}\big)\delta_{\sigma\sigma'}. \tag{2.1.26}$$

We introduced a shorthand notation, $\boldsymbol{\sigma}_{\sigma\sigma'} \equiv \langle\sigma|\hat{\boldsymbol{\sigma}}|\sigma'\rangle$. We defined two rank-2 tensors, $\overleftrightarrow{\nabla}$ which denotes a tensor having components $\nabla_{\mu\nu} \equiv \sum_\lambda \varepsilon_{\mu\nu\lambda}\nabla_\lambda$ and $\overleftrightarrow{\nabla\sigma}$ which denotes a tensor having components $\nabla_\mu\sigma_\nu$. We note that the differential operators, $\boldsymbol{\nabla}$ and $\triangle$, act only on a neighboring spatial function, while $\overrightarrow{\boldsymbol{\nabla}}$ acts all the spatial functions sitting on the right side of $\overrightarrow{\boldsymbol{\nabla}}$. Time-even mean-field potentials are defined by

$$M^{(q)}(\boldsymbol{r}) = B_3\rho(\boldsymbol{r}) + B_4\rho^{(q)}(\boldsymbol{r}), \tag{2.1.27}$$

$$\begin{aligned}
U^{(q)}(\boldsymbol{r}) = {}& 2\Big\{B_1\rho(\boldsymbol{r}) + B_2\rho^{(q)}(\boldsymbol{r})\Big\} + B_3\tau(\boldsymbol{r}) + B_4\tau^{(q)}(\boldsymbol{r}) \\
& + 2\Big\{B_5\triangle\rho(\boldsymbol{r}) + B_6\triangle\rho^{(q)}(\boldsymbol{r})\Big\} + B_9\boldsymbol{\nabla}\cdot\big\{\boldsymbol{J}(\boldsymbol{r}) + \boldsymbol{J}^{(q)}(\boldsymbol{r})\big\} \\
& + B_7(\alpha+2)\rho^{\alpha+1}(\boldsymbol{r}) + B_8\Big\{\alpha\rho^{\alpha-1}(\boldsymbol{r})\big(\rho^{(n)2}(\boldsymbol{r}) + \rho^{(p)2}(\boldsymbol{r})\big) + 2\rho^\alpha(\boldsymbol{r})\rho^{(q)}(\boldsymbol{r})\Big\} \\
& + \alpha\rho^{\alpha-1}(\boldsymbol{r})\Big\{B_{12}\boldsymbol{s}^2(\boldsymbol{r}) + B_{13}\big(\boldsymbol{s}^{(n)2}(\boldsymbol{r}) + \boldsymbol{s}^{(p)2}(\boldsymbol{r})\big)\Big\} + V_{\mathrm{Coul}}(\boldsymbol{r})\,\delta_{qp}, \tag{2.1.28}
\end{aligned}$$

$$\overleftrightarrow{B}^{(q)}(\boldsymbol{r}) = -2\big\{B_{14}\overleftrightarrow{J}(\boldsymbol{r}) + B_{16}\overleftrightarrow{J}^{(q)}(\boldsymbol{r})\big\} - B_9\overleftrightarrow{\nabla}\big\{\rho(\boldsymbol{r}) + \rho^{(q)}(\boldsymbol{r})\big\}, \tag{2.1.29}$$

where the Coulomb potential $V_{\mathrm{Coul}}(\boldsymbol{r})$ is given by

$$V_{\mathrm{Coul}}(\boldsymbol{r}) = e^2 \left\{ \int d\boldsymbol{r}' \frac{\rho^{(p)}(\boldsymbol{r}')}{|\boldsymbol{r} - \boldsymbol{r}'|} - \left(\frac{3}{\pi} \right)^{\frac{1}{3}} \left[\rho^{(p)}(\boldsymbol{r}) \right]^{\frac{1}{3}} \right\}. \tag{2.1.30}$$

While time-odd mean-field potentials are defined by

$$\boldsymbol{I}^{(q)}(\boldsymbol{r}) = -2 \left\{ B_3 \boldsymbol{j}(\boldsymbol{r}) + B_4 \boldsymbol{j}^{(q)}(\boldsymbol{r}) \right\} + B_9 \boldsymbol{\nabla} \times \left\{ \boldsymbol{s}(\boldsymbol{r}) + \boldsymbol{s}^{(q)}(\boldsymbol{r}) \right\}, \tag{2.1.31}$$

$$\boldsymbol{C}^{(q)}(\boldsymbol{r}) = B_{14} \boldsymbol{s}(\boldsymbol{r}) + B_{16} \boldsymbol{s}^{(q)}(\boldsymbol{r}), \tag{2.1.32}$$

$$\begin{aligned}
\boldsymbol{\Sigma}^{(q)}(\boldsymbol{r}) = \; & 2 \left\{ B_{10} \boldsymbol{s}(\boldsymbol{r}) + B_{11} \boldsymbol{s}^{(q)}(\boldsymbol{r}) \right\} + B_{14} \boldsymbol{T}(\boldsymbol{r}) + B_{16} \boldsymbol{T}^{(q)}(\boldsymbol{r}) \\
& + 2 \left\{ B_{15} \triangle \boldsymbol{s}(\boldsymbol{r}) + B_{17} \triangle \boldsymbol{s}^{(q)}(\boldsymbol{r}) \right\} + B_9 \boldsymbol{\nabla} \times \left\{ \boldsymbol{j}(\boldsymbol{r}) + \boldsymbol{j}^{(q)}(\boldsymbol{r}) \right\} \\
& + 2 \rho^{\alpha}(\boldsymbol{r}) \left\{ B_{12} \boldsymbol{s}(\boldsymbol{r}) + B_{13} \boldsymbol{s}^{(q)}(\boldsymbol{r}) \right\}.
\end{aligned} \tag{2.1.33}$$

In the static HF calculation, all the time-odd mean-field potentials vanish because of the time-reversal symmetry. These time-odd components have non-zero values in the case of dynamical Skyrme TDHF calculations.

2.1.5 Time-dependent Hartree-Fock theory

The TDHF theory [85] is the time-dependent extension of the static HF theory. The TDHF equation can be derived in an analogous manner to the derivation of the HF equation. By performing the time-dependent variation of an action,

$$\frac{\delta}{\delta \phi_{\alpha}^*(\boldsymbol{r}\sigma, t)} \left[\int dt' \langle \Phi(t) | \, \mathrm{i}\hbar \frac{\partial}{\partial t} - \hat{H} \, | \Phi(t) \rangle \right] = 0, \tag{2.1.34}$$

using a single Slater determinant as a trial function, we can derive the TDHF equation. In the case of the Skyrme Hamiltonian, we obtain

$$\mathrm{i}\hbar \frac{\partial \phi_i(\boldsymbol{r}\sigma, t)}{\partial t} = \sum_{\sigma'} \hat{h}_{\mathrm{SHF}}^{(q_i)}(\boldsymbol{r}\sigma\sigma', t) \phi_i(\boldsymbol{r}\sigma', t). \tag{2.1.35}$$

The time-dependent single-particle Hamiltonian has the same form as in the static HF equation defined by Eqs. (2.1.24)-(2.1.33) with the time-dependent densities composed of $\{\phi_i(\boldsymbol{r}\sigma, t)\}$.

The Skyrme TDHF equation Eq. (2.1.35) guarantees some conservation laws. The hermiteness of the single-particle Hamiltonian leads the conservation of the overlap between two single-particle wave functions:

$$\begin{aligned}
\mathrm{i}\hbar \frac{\partial}{\partial t} \langle \phi_i(t) | \phi_j(t) \rangle = \; & \sum_{\sigma} \int d\boldsymbol{r} \left\{ \left(\mathrm{i}\hbar \frac{\partial \phi_i^*(\boldsymbol{r}\sigma, t)}{\partial t} \right) \phi_j(\boldsymbol{r}\sigma, t) + \phi_i^*(\boldsymbol{r}\sigma, t) \left(\mathrm{i}\hbar \frac{\partial \phi_j(\boldsymbol{r}\sigma, t)}{\partial t} \right) \right\} \\
= \; & \sum_{\sigma, \sigma'} \int d\boldsymbol{r} \left\{ - \left(\hat{h}_{\mathrm{SHF}}^{(q_i)}(\boldsymbol{r}\sigma\sigma', t) \phi_i(\boldsymbol{r}\sigma', t) \right)^* \phi_j(\boldsymbol{r}\sigma, t) \right. \\
& \left. \qquad\qquad + \phi_i^*(\boldsymbol{r}\sigma, t) \left(\hat{h}_{\mathrm{SHF}}^{(q_i)}(\boldsymbol{r}\sigma\sigma', t) \phi_j(\boldsymbol{r}\sigma', t) \right) \right\} \\
= \; & \sum_{\sigma, \sigma'} \int d\boldsymbol{r} \, \phi_i^*(\boldsymbol{r}\sigma) \left[-\hat{h}_{\mathrm{SHF}}^{(q_i)\dagger}(\boldsymbol{r}\sigma'\sigma, t) + \hat{h}_{\mathrm{SHF}}^{(q_i)}(\boldsymbol{r}\sigma\sigma', t) \right] \phi_j(\boldsymbol{r}\sigma') \\
= \; & 0. \tag{2.1.36}
\end{aligned}$$

Eq. (2.1.36) automatically ensures the Pauli exclusion principle during a time evolution. The total energy is also conserved:

$$
\begin{aligned}
\mathrm{i}\hbar\frac{\partial}{\partial t}\langle\Phi(t)|\hat{H}_{\mathrm{SHF}}|\Phi(t)\rangle &= \sum_{i,\sigma}\left[\frac{\delta E_{\mathrm{SHF}}}{\delta\phi_i(\boldsymbol{r}\sigma,t)}\left(\mathrm{i}\hbar\frac{\partial\phi_i(\boldsymbol{r}\sigma,t)}{\partial t}\right) + \frac{\delta E_{\mathrm{SHF}}}{\delta\phi_i^*(\boldsymbol{r}\sigma,t)}\left(\mathrm{i}\hbar\frac{\partial\phi_i^*(\boldsymbol{r}\sigma,t)}{\partial t}\right)\right] \\
&= \sum_{i,\sigma}\left[\frac{\delta E_{\mathrm{SHF}}}{\delta\phi_i(\boldsymbol{r}\sigma,t)}\frac{\delta E_{\mathrm{SHF}}}{\delta\phi_i^*(\boldsymbol{r}\sigma,t)} - \frac{\delta E_{\mathrm{SHF}}}{\delta\phi_i^*(\boldsymbol{r}\sigma,t)}\frac{\delta E_{\mathrm{SHF}}}{\delta\phi_i(\boldsymbol{r}\sigma,t)}\right] \\
&= 0, \tag{2.1.37}
\end{aligned}
$$

where we regarded $E_{\mathrm{SHF}} = \langle\Phi|\hat{H}_{\mathrm{Skyrme}}|\Phi\rangle$ as a functional of $\{\phi_i\}$ and $\{\phi_i^*\}$. We can also show that the expectation value of any one-body operator which have no intrinsic time-dependence is conserved in the TDHF theory [94]. For example, the expectation values of the linear momentum and the total angular momentum operators are conserved, if the two-body interaction is Galilean invariant, $[\hat{H}_{\mathrm{SHF}}, \hat{\boldsymbol{P}}] = 0$ and $[\hat{H}_{\mathrm{SHF}}, \hat{\boldsymbol{J}}] = 0$, where $\hat{\boldsymbol{P}} = \sum_{i=1}^N \hat{\boldsymbol{p}}_i$ and $\hat{\boldsymbol{J}} = \sum_{i=1}^N(\hat{\boldsymbol{r}}_i \times \hat{\boldsymbol{p}}_i + \hat{\boldsymbol{s}}_i)$.

In the TDHF theory, a time evolution of a many-particle system is described microscopically from degrees of freedom of constituent particles of the system. Every particle moves under the time-dependent *mean-field* potential which is generated by all the particles in the system. Because the TDHF equation is the first-order differential equation with respect to time t, the many-body wave function after the time evolution is uniquely determined by a given initial condition.

As explained in this Section, the HF and TDHF theories are an approximated framework to describe a many-particle system by a single Slater determinant. However, the Skyrme (TD)HF theory may be regarded as an *exact* framework based on the (TD)DFT, if we regard the Skyrme (TD)HF equation as the (TD)KS equation with a *universal* density-functional expressed as the Skyrme EDF. To make the connection between the Skyrme (TD)HF theory and the (TD)DFT clear, we explain the basic concepts of the (TD)DFT in the next Section.

2.2 Basic Concepts of DFT and TDDFT

2.2.1 Density functional theory

We present basic concepts of the DFT. The DFT is based on a theorem of Hohenberg and Kohn [155] which states that there is a one-to-one correspondence between an external potential and a one-body density. We first explain the Hohenberg-Kohn (HK) theorem in Sec. 2.2.1 (a) for a many-particle system like atoms, molecules, and solids, where an external potential (Coulomb potential of atomic nuclei) exists which characterizes the system. A constrained search method of Levy [156] is explained in Sec. 2.2.1 (b) which supports basic concepts of the DFT. An elegant scheme of Kohn and Sham [157] is explained in Sec. 2.2.1 (c) which is quite useful for practical calculations based on the DFT. Because an atomic nucleus is a self-bound finite system without an external potential, we need some modifications of the original HK theorem. We will describe this point in Sec. 2.2.1 (d) and introduce recent progresses.

(a)   Hohenberg-Kohn theorem

The DFT is based on the theorem of Hohenberg and Kohn [155] which states a one-to-one correspondence between an external potential $v(\boldsymbol{r})$ and the one-body density $\rho(\boldsymbol{r})$: $v(\boldsymbol{r}) \Leftrightarrow \rho(\boldsymbol{r})$. The proof is given as follows.

Let us consider two external potentials, $v(\boldsymbol{r})$ and $v'(\boldsymbol{r})$, which deffer by more than a constant, $v(\boldsymbol{r}) - v'(\boldsymbol{r}) \neq \mathrm{const}$. The ground states under these external potentials will be different because

they obey different Schrödinger equations. It can be shown by *reductio ad absurdum.* We define the Hamiltonian $\hat{H} = \hat{T} + \hat{W} + \hat{V}$ and $\hat{H}' = \hat{T} + \hat{W} + \hat{V}'$. $\hat{T}$ is the kinetic energy and $\hat{W}$ is two-particle interactions. $\hat{V} = \sum_{i=1}^{N} v(\boldsymbol{r}_i)$ and $\hat{V}' = \sum_{i=1}^{N} v'(\boldsymbol{r}_i)$ denote the external potentials. Let us assume that they provide the same ground state $|\Psi_0\rangle$ with eigenvalues E_0 and E_0', respectively:

$$\hat{H}|\Psi_0\rangle = E_0|\Psi_0\rangle, \tag{2.2.1}$$

$$\hat{H}'|\Psi_0\rangle = E_0'|\Psi_0\rangle. \tag{2.2.2}$$

The subtraction of Eq. (2.2.2) from Eq. (2.2.1) leads $V - V' = E_0 - E_0' = $ const. which is inconsistent with the assumption that the external potentials differ by more than a constant. It means that there is a one-to-one correspondence between the external potential (regarding $v(\boldsymbol{r}) + $ const. as a same potential) and its ground state: $v(\boldsymbol{r}) \Leftrightarrow |\Psi_0\rangle$.

We next prove a one-to-one correspondence between the ground state $|\Psi_0\rangle$ and the density $\rho(\boldsymbol{r})$: $|\Psi_0\rangle \Leftrightarrow \rho(\boldsymbol{r})$. The proof can again be given by *reductio ad absurdum.* Let us assume that two different wave functions, $|\Psi_0\rangle$ and $|\Psi_0'\rangle$, provide the same density $\rho(\boldsymbol{r})$. According to the variational principle (Rayleigh-Ritz's minimal principle), there holds an inequality

$$
\begin{aligned}
E_0 = \langle\Psi_0|\hat{H}|\Psi_0\rangle &< \langle\Psi_0'|\hat{H}|\Psi_0'\rangle \\
&= \langle\Psi_0'|\hat{H}'|\Psi_0'\rangle + \langle\Psi_0'|\hat{V} - \hat{V}'|\Psi_0'\rangle \\
&= E_0' + \int d\boldsymbol{r}\, \rho(\boldsymbol{r})\{v(\boldsymbol{r}) - v'(\boldsymbol{r})\}.
\end{aligned}
\tag{2.2.3}
$$

The same argument holds for E_0' giving another inequality

$$E_0' < E_0 + \int d\boldsymbol{r}\, \rho(\boldsymbol{r})\{v'(\boldsymbol{r}) - v(\boldsymbol{r})\}. \tag{2.2.4}$$

The addition of Eqs. (2.2.3) and (2.2.4) leads inconsistency $E_0 + E_0' < E_0 + E_0'$ which verifies the one-to-one correspondence between the ground state and the density: $|\Psi_0\rangle \Leftrightarrow \rho(\boldsymbol{r})$. This completes the proof.

To summarize, the proven theorem in the above shows that there hold one-to-one correspondences, $v(\boldsymbol{r}) \Leftrightarrow |\Psi_0\rangle \Leftrightarrow \rho(\boldsymbol{r})$. Thus it states the one-to-one correspondence between the external potential and the density: $v(\boldsymbol{r}) \Leftrightarrow \rho(\boldsymbol{r})$. This theorem is called the 1st Hohenberg-Kohn (HK) theorem. As a corollary of this theorem, an important consequence is obtained. The 1st HK theorem indicates a fact that the many-body wave function of the system can be given by a functional of the density, $|\Psi\rangle = |\Psi[\rho]\rangle$. It means that any physical observables can also be given by a functional of the density: $\mathcal{O}[\rho] = \langle\Psi[\rho]|\hat{\mathcal{O}}|\Psi[\rho]\rangle$. Therefore, the energy of the system is also given by a functional of the density as $E[\rho]$ (we will refer $E[\rho]$ as an EDF) and a variation of $E[\rho]$ with respect to the density will lead the energy as well as the density of the ground state:

$$E_0 = E[\rho_0] = \min_{\rho} E[\rho]. \tag{2.2.5}$$

The statement represented in Eq. (2.2.5) is called the 2nd HK theorem. The 2nd HK theorem indicates that we can use the density $\rho(\boldsymbol{r})$ as a basic variable to describe the N-body system. This theorem thus provides a substantial reduction of the number of coordinates, from $3N$ to 3, in describing the N-body system.

(b)   Levy's constrained search method

Up to now, we showed the basic concept of the HK theorem which forms a theoretical foundation of the DFT. In the proof shown above, however, we implicitly assumed the existence of an external

potential $v(\boldsymbol{r})$ as well as an N-body wave function $|\Psi\rangle$ which actually generate the density $\rho(\boldsymbol{r})$. The former is referred to as v-representability, while the latter is referred to as N-representability. The v-representability is a strong requirement. Indeed, it was proven that there exists a reasonably-behaved non-v-representable density [158]. The N-representability is more weaker requirement. Indeed, it was proven that any non-negative ($\rho(\boldsymbol{r}) > 0$) differentiable density normalized as $N = \int d\boldsymbol{r}\rho(\boldsymbol{r})$ would be N-representable [159, 160]. Thus, a constrained search method proposed by Levy [156] has been a useful prescription to avoid the v-representability problem in performing the minimization of $E[\rho]$ with respect to the density $\rho(\boldsymbol{r})$.

The Levy's constrained search method consists of two minimization procedures. We first minimize the EDF $E[\rho]$ within a subspace of the Hilbert space in which the sate $|\Psi\rangle$ generates the trial density $\rho(\boldsymbol{r})$. After that, we minimize the $E[\rho]$ with respect to the density $\rho(\boldsymbol{r})$. The procedure is expressed by

$$E_0 = E[\rho_0] = \min_{\rho}\left[\ \min_{\Psi \to \rho} E[\rho]\ \right]. \tag{2.2.6}$$

This method mathematically justifies that we can perform the variation of $E[\rho]$ with respect to the density $\rho(\boldsymbol{r})$ which gives us the ground state energy E_0 at the true density $\rho_0(\boldsymbol{r})$ [156, 158].

(c) Kohn-Sham scheme

To describe the shell effect in the atom as well as the atomic nucleus, we need to adequately treat the kinetic energy of constituent particles of the system. An elegant prescription was proposed by Kohn and Sham [157] which magically provides a useful scheme where an auxiliary non-interacting reference system is introduced whose solution is *exactly* equivalent to the interacting system of interest.

According to the HK theorem, the energy of the interacting system described by $\hat{H} = \hat{T} + \hat{W} + \hat{V}$ can be expressed as a functional of the density

$$E_v[\rho] = \langle\Psi[\rho]|\hat{H}|\Psi[\rho]\rangle = F[\rho] + \int d\boldsymbol{r}\, v(\boldsymbol{r})\rho(\boldsymbol{r}), \tag{2.2.7}$$

where $F[\rho] \equiv \langle\Psi[\rho]|\hat{T} + \hat{W}|\Psi[\rho]\rangle$ is a *universal* density-functional which contains information of the N-body interacting system independent from the external potential. Then, Kohn and Sham rewrote the EDF $E_v[\rho]$ using the kinetic energy of a non-interacting system $T_0[\rho]$ (which can be a functional of the density because of the HK theorem) as

$$E_v[\rho] = T_0[\rho] + G[\rho] + \int d\boldsymbol{r}\, v(\boldsymbol{r})\rho(\boldsymbol{r}), \tag{2.2.8}$$

where $G[\rho] \equiv F[\rho] - T_0[\rho]$. The variational principle for this interacting system with the energy $E_v[\rho]$ leads

$$\frac{\delta E_v[\rho]}{\delta\rho} = \frac{\delta T_0[\rho]}{\delta\rho} + v_{\mathrm{KS}}(\boldsymbol{r}) = 0, \tag{2.2.9}$$

$$v_{\mathrm{KS}}(\boldsymbol{r}) = v_{\mathrm{KS}}[\rho(\boldsymbol{r})] \equiv \frac{\delta G[\rho]}{\delta\rho} + v(\boldsymbol{r}). \tag{2.2.10}$$

One would notice that the condition Eq. (2.2.9) is equivalent to a necessary condition to minimize energy of a non-interacting system described by $\hat{H}_{\mathrm{KS}} = \hat{T} + \sum_{i=1}^{N} v_{\mathrm{KS}}(\boldsymbol{r}_i)$. Therefore, the solution of simultaneous equations for orbital functions $\{\phi_i\}$ in the non-interacting reference system,

$$\left[-\frac{\hbar^2}{2m}\triangle + v_{\mathrm{KS}}(\boldsymbol{r})\right]\phi_i(\boldsymbol{r}) = \varepsilon_i\phi_i(\boldsymbol{r}), \tag{2.2.11}$$

$$v_{\mathrm{KS}}(\boldsymbol{r}) = \frac{\delta G[\rho]}{\delta\rho} + v(\boldsymbol{r}), \tag{2.2.12}$$

is *exactly* equivalent to the solution of Eqs. (2.2.9) and (2.2.10) for the interacting system of interest. The density is now given by $\rho(\boldsymbol{r}) = \sum_{i=1}^{N} |\phi_i(\boldsymbol{r})|^2$. The kinetic energy is given by $T_0[\rho] = -\frac{\hbar^2}{2m} \sum_{i=1}^{N} \int d\boldsymbol{r} \phi_i^*(\boldsymbol{r}) \triangle \phi_i(\boldsymbol{r})$ in terms of the orbitals $\{\phi_i\}$. We note that Eqs. (2.2.11) and (2.2.12) must be solved self-consistently, because the KS potential is given as a functional of the density $v_{\mathrm{KS}}(\boldsymbol{r}) = v_{\mathrm{KS}}[\rho(\boldsymbol{r})]$ which itself depends on the solution of Eq. (2.2.11).

In this way, the Kohn-Sham scheme provides a quite useful formalism to solve *exactly* the N-body interacting system in a solvable way. The functions $\{\phi_i\}$ are called the KS orbitals and the simultaneous equations for them, Eqs. (2.2.11) and (2.2.12), are called the KS equations. The KS equations look very similar to the HF equation. While the KS scheme is an *exact* method based on the DFT, the HF theory is just an approximation for the N-body system. The main difference is the one-body mean-field-like potential. In the KS scheme, the KS potential $v_{\mathrm{KS}}(\boldsymbol{r})$ contains a *universal* density-functional $G[\rho]$ which implicitly includes information of the interacting system of interest. We note that we do not know *a priori* the exact form of the universal density-functional $G[\rho]$.

(d)   Application to the atomic nucleus

As we mentioned earlier, we need some modifications of the HK theorem to treat the atomic nucleus, because the atomic nucleus is a self-bound finite system without an external potential. In practice, we usually describe an *intrinsic* state which violates the translational invariance and also the rotational invariance in case of a deformed nucleus. The original HK theorem is actually treating the density in the laboratory frame. We thus need a modified HK theorem for the intrinsic state (a wave-packet state) localized in space which verifies an existence of a *universal* density-functional with respect to the density of the intrinsic state.

Recently, extensive efforts have been paid for establishing a theoretical foundation of the DFT for the atomic nucleus [7, 161, 162, 163, 164, 165]. Indeed, in Ref. [164], it was shown that there exists a density functional for an intrinsic state. The proof can be done in a similar manner as described in Sec. 2.1.1. (a)-(c). We have to pay, however, a particular attention for decomposing the wave function into a product of intrinsic and spurious components. It can be performed exactly for the case of translational motion, while it cannot be done exactly for other cases such as rotational motion. For details of the proof, we recommend reader to see the proof in Refs. [7, 164]. Anyhow, the modified HK theorem justifies the DFT for the atomic nucleus and the KS scheme provides an *exact* self-consistent mean-field-like description for the atomic nucleus at the limit of zero external potential, $v(\boldsymbol{r}) \rightarrow 0$.

2.2.2   Time-dependent density functional theory

The DFT provides an *exact* formalism to calculate properties of the ground state of an N-body system. There is a time-dependent version of the DFT which enables us to calculate excitation, response, and reaction properties of a many-particle system. The TDDFT is based on the theorem of Runge and Gross [166] and we explain it in Sec. 2.2.2 (a). In practice, we use time-dependent version of the KS scheme. The van Leeuwen's theorem [167] guarantees the existence of a non-interacting reference system which provides the same time-dependent density $\rho(\boldsymbol{r}, t)$ as the interacting system of interest. The van Leeuwen's theorem is explained in Sec. 2.2.2 (b).

(a)   Runge-Gross theorem

We consider the time-dependent Hamiltonian, $\hat{H}(t) = \hat{T} + \hat{W} + \hat{V}(t)$ and $\hat{H}'(t) = \hat{T} + \hat{W} + \hat{V}'(t)$. We assume that the system is in the same ground state $|\Psi_0\rangle = |\Psi(t_0)\rangle$ at the initial time $t = t_0$. We also assume that the external potentials $v(\boldsymbol{r}, t)$ and $v'(\boldsymbol{r}, t)$ are an analytic function of time t so that they are Taylor expandable about $t = t_0$. The Runge-Gross (RG) theorem states that, for

v-representable densities $\rho(\boldsymbol{r}, t)$, there holds a one-to-one correspondence between the time-dependent external potential $v(\boldsymbol{r}, t)$ and the density $\rho(\boldsymbol{r}, t)$.

To prove the theorem, we first show that there is a one-to-one correspondence between the time-dependent external potential $v(\boldsymbol{r}, t)$ and the one-body current $\boldsymbol{j}(\boldsymbol{r}, t)$: $v(\boldsymbol{r}, t) \Leftrightarrow \boldsymbol{j}(\boldsymbol{r}, t)$. The one-body current is defined by

$$\boldsymbol{j}(\boldsymbol{r}, t) = \frac{\hbar N}{2\mathrm{i}m} \int d\boldsymbol{r}_2 \cdots \int d\boldsymbol{r}_N \big\{ \Psi^*(t)\boldsymbol{\nabla}\Psi(t) - \Psi(t)\boldsymbol{\nabla}\Psi^*(t) \big\}, \tag{2.2.13}$$

where we have abbreviated the spatial coordinates $\{\boldsymbol{r}_1, \cdots, \boldsymbol{r}_N\}$. We note that the differential operator $\boldsymbol{\nabla}$ acts only for the 1st coordinates, $\boldsymbol{r} \equiv \boldsymbol{r}_1$. The time derivative of the current $\boldsymbol{j}(\boldsymbol{r}, t)$ at $t = t_0$ can be written as

$$\partial_t \boldsymbol{j}(\boldsymbol{r}, t)\big|_{t=t_0} = \frac{N}{2m} \int d\boldsymbol{r}_2 \cdots \int d\boldsymbol{r}_N \big\{ (\hat{H}\Psi_0^*)\boldsymbol{\nabla}\Psi_0 - \Psi_0^*\boldsymbol{\nabla}(\hat{H}\Psi_0) + (\hat{H}\Psi_0)\boldsymbol{\nabla}\Psi_0^* - \Psi_0\boldsymbol{\nabla}(\hat{H}\Psi_0^*) \big\}, \tag{2.2.14}$$

where the time-dependent Schrödinger equation, $\mathrm{i}\hbar\partial_t\Psi = \hat{H}\Psi$, (and its complex conjugate) was used. The difference $\partial_t\big[\boldsymbol{j}(\boldsymbol{r}) - \boldsymbol{j}'(\boldsymbol{r})\big]\big|_{t=t_0}$ eliminates the common part proportional to $\hat{T} + \hat{W}$ leading a relation

$$\partial_t\big[\boldsymbol{j}(\boldsymbol{r}, t) - \boldsymbol{j}'(\boldsymbol{r}, t)\big]\big|_{t=t_0} = -\frac{1}{m}\rho(\boldsymbol{r}, t_0)\boldsymbol{\nabla}\big[v(\boldsymbol{r}, t_0) - v'(\boldsymbol{r}, t_0)\big], \tag{2.2.15}$$

where $\rho(\boldsymbol{r}, t_0) = N \int d\boldsymbol{r}_2 \cdots \int d\boldsymbol{r}_N |\Psi_0|^2$ and we used an equality $\boldsymbol{\nabla}V(t) = \boldsymbol{\nabla}\sum_{i=1}^N v(\boldsymbol{r}_i, t) = \boldsymbol{\nabla}v(\boldsymbol{r}, t)$. The Eq. (2.2.15) means that, if the time-dependent external potentials, $v(\boldsymbol{r}, t)$ and $v'(\boldsymbol{r}, t)$, differ by more than a time-dependent constant, $v(\boldsymbol{r}, t) - v'(\boldsymbol{r}, t) \neq c(t)$, the first time-derivative of the currents, $\boldsymbol{j}(\boldsymbol{r}, t)$ and $\boldsymbol{j}'(\boldsymbol{r}, t)$, at $t = t_0$ must be different. Therefore, $\boldsymbol{j}(\boldsymbol{r}, t)$ and $\boldsymbol{j}'(\boldsymbol{r}, t)$ must be different at a certain instant $t > t_0$. In the same way, we can calculate a difference between a higher-order (more than one) time-derivative of the currents $\boldsymbol{j}(\boldsymbol{r}, t)$ and $\boldsymbol{j}'(\boldsymbol{r}, t)$. For the $(k+1)$th time-derivative, we obtain

$$\partial_t^{k+1}\big[\boldsymbol{j}(\boldsymbol{r}, t) - \boldsymbol{j}'(\boldsymbol{r}, t)\big]\big|_{t=t_0} = -\frac{1}{m}\rho(\boldsymbol{r}, t_0)\boldsymbol{\nabla}w_k(\boldsymbol{r}), \tag{2.2.16}$$

where $w_k(\boldsymbol{r}) \equiv \partial_t^k\big[v(\boldsymbol{r}, t) - v'(\boldsymbol{r}, t)\big]\big|_{t=t_0}$. Since the external potentials, $v(\boldsymbol{r}, t)$ and $v'(\boldsymbol{r}, t)$, differ by more than a time-dependent constant, $v(\boldsymbol{r}, t) - v'(\boldsymbol{r}, t) \neq c(t)$, the right hand side of Eq. (2.2.16) must again have a non-zero value. Therefore, the Taylor expansion of the currents $\boldsymbol{j}(\boldsymbol{r}, t)$ and $\boldsymbol{j}'(\boldsymbol{r}, t)$ must be different at a certain order and it guarantees that $\boldsymbol{j}(\boldsymbol{r}, t) \neq \boldsymbol{j}'(\boldsymbol{r}, t)$. This proves the one-to-one correspondence between the time-dependent external potential (regarding $v(\boldsymbol{r}, t) + c(t)$ as a same potential) and the current: $v(\boldsymbol{r}, t) \Leftrightarrow \boldsymbol{j}(\boldsymbol{r}, t)$.

We next prove the one-to-one correspondence between the time-dependent external potential and the density: $v(\boldsymbol{r}, t) \Leftrightarrow \rho(\boldsymbol{r}, t)$. We take the divergence of Eq. (2.2.16) to get a relation for the densities:

$$\partial_t^{k+1}\boldsymbol{\nabla}\cdot\big[\boldsymbol{j}(\boldsymbol{r}, t) - \boldsymbol{j}'(\boldsymbol{r}, t)\big]\big|_{t=t_0} = -\partial_t^{k+2}\big[\rho(\boldsymbol{r}, t) - \rho'(\boldsymbol{r}, t)\big]\big|_{t=t_0} = -\frac{1}{m}\boldsymbol{\nabla}\cdot\big[\rho(\boldsymbol{r}, t_0)\boldsymbol{\nabla}w_k(\boldsymbol{r})\big], \tag{2.2.17}$$

where we used the continuity equation, $\partial_t\rho(\boldsymbol{r}, t) = -\boldsymbol{\nabla}\cdot\boldsymbol{j}(\boldsymbol{r}, t)$. If the right hand side has non-zero value, it means that the $(k+2)$th time-derivative of the densities, $\rho(\boldsymbol{r}, t)$ and $\rho'(\boldsymbol{r}, t)$, must be different. It can be shown by considering the following equation:

$$\int d\boldsymbol{r}\, \boldsymbol{\nabla}\cdot\big[w_k(\boldsymbol{r})\rho(\boldsymbol{r}, t_0)\boldsymbol{\nabla}w_k(\boldsymbol{r})\big] = \int d\boldsymbol{r}\, \rho(\boldsymbol{r}, t_0)\big[\boldsymbol{\nabla}w_k(\boldsymbol{r})\big]^2 + \int d\boldsymbol{r}\, w_k(\boldsymbol{r})\boldsymbol{\nabla}\cdot\big[\rho(\boldsymbol{r}, t_0)\boldsymbol{\nabla}w_k(\boldsymbol{r})\big]. \tag{2.2.18}$$

The left hand side of Eq. (2.2.18) vanishes according to the Gauss's divergence theorem assuming that $\rho(\boldsymbol{r}, t_0) \xrightarrow{\boldsymbol{r}\to\infty} 0$. Since the first term in the right hand side of Eq. (2.2.18) must have a non-zero value, the second term in the right hand side must also have a non-zero value. Therefore, from Eqs. (2.2.17)

and (2.2.18), we can conclude that a certain-order time-derivative of the densities, $\rho(\boldsymbol{r},t)$ and $\rho'(\boldsymbol{r},t)$, at $t=t_0$ must be different. Thus $\rho(\boldsymbol{r},t)$ and $\rho'(\boldsymbol{r},t)$ must be different at a certain instant $t>t_0$ if $v(\boldsymbol{r},t)-v'(\boldsymbol{r},t)\neq c(t)$. This conpletes the proof.

The RG theorem elucidates that the external potential $v(\boldsymbol{r},t)$ [*modulo* $c(t)$] is a functional of the density and the initial state. It means that the time-dependent many-body wave function can be expressed as a functional of the density multiplied by a merely phase factor, $\big|\Psi(t)\big\rangle=e^{-i\alpha(t)}\big|\Psi[\rho(t)]\big\rangle$ with $\dot{\alpha}(t)=c(t)$. Thus, any physical observables can be written as a functional of the density, $\mathcal{O}[\rho(t)]=\big\langle\Psi[\rho(t)]\big|\hat{\mathcal{O}}\big|\Psi[\rho(t)]\big\rangle$, because the phase does not affect the expectation value.

In practice, we use a time-dependent version of the KS scheme. The time-dependent Kohn-Sham (TDKS) equations are defined by

$$\mathrm{i}\hbar\frac{\partial}{\partial t}\phi_i(\boldsymbol{r},t)=\left[-\frac{\hbar^2}{2m}\triangle+v_{\mathrm{KS}}(\boldsymbol{r},t)\right]\phi_i(\boldsymbol{r},t). \tag{2.2.19}$$

The density is expressed as $\rho(\boldsymbol{r},t)=\sum_{i=1}^{N}\big|\phi_i(\boldsymbol{r},t)\big|^2$. Because the RG theorem does not tell us a specific form of the KS potential, how to define the time-dependent KS potential $v_{\mathrm{KS}}(\boldsymbol{r},t)$ would be a problem. Usually the so called *adiabatic approximation* is used where the same form of the KS potential as in the ground state DFT (except for the time-dependent external potential $v(\boldsymbol{r},t)$) is utilized for $t\geq t_0$, which is composed of the TDKS orbitals $\{\phi_i(\boldsymbol{r},t)\}$. Extensive discussions for the determination of the time-dependent KS potential can be found in Ref. [168]. One of the most important theorems was proven by van Leeuwen [167] which can be regarded as an extension of the RG theorem. The theorem guarantees that there exists an external potential $v'(\boldsymbol{r},t)$ for a system obeying a different two-particle interaction $\hat{W}'$ which provides the density $\rho(\boldsymbol{r},t)$ that coincides with the density in the system with $\hat{W}$ for all times. Because the non-interacting limit $W'\to0$ guarantees the existence of the non-interacting reference system, we shall follow the van Leeuwen's theorem in the next Section.

(b)   Van Leeuwen's theorem

In the case of the DFT, the KS scheme provides an elegant formalism which is quite useful for practical applications. Because the RG theorem is not based on the variational principle, we need to carefully prove the existence of an auxiliary non-interacting reference system which provides the same density as the interacting system for all times, $t\geq t_0$. It was proven by van Leeuwen [167] that there exists a system which gives the same time-dependent density $\rho(\boldsymbol{r},t)$, albeit that they have different interactions, $\hat{W}$ and $\hat{W}'$, and different external potentials, $\hat{V}(t)$ and $\hat{V}'(t)$. Since the theorem is valid even for the non-interacting limit $\hat{W}'\to0$, it guarantees the existence of the non-interacting reference system which provides the same density $\rho(\boldsymbol{r},t)$ as the interacting system of interest, $\hat{W}\neq0$.

We first derive a relation between the density $\rho(\boldsymbol{r},t)$ and the external potential $v(\boldsymbol{r},t)$ (Eq. (2.2.23)) which will be used to prove the theorem. We again start with a time-derivative of the current,

$$\partial_t j_\mu(\boldsymbol{r},t)\;=\;\frac{N}{2m}\int d\boldsymbol{r}_2\cdots\int d\boldsymbol{r}_N\big\{(\hat{H}\Psi^*(t))\partial_\mu\Psi(t)-\Psi^*(t)\partial_\mu(\hat{H}\Psi(t))$$
$$+(\hat{H}\Psi(t))\partial_\mu\Psi^*(t)-\Psi(t)\partial_\mu(\hat{H}\Psi^*(t))\big\}.$$

Here, we focus on a μ component of the current $j_\mu(\boldsymbol{r},t)$, $\boldsymbol{j}(\boldsymbol{r},t)=\big(j_1(\boldsymbol{r},t),j_2(\boldsymbol{r},t),j_3(\boldsymbol{r},t)\big)$. By putting $\hat{H}=\hat{T}+\hat{W}+\hat{V}$, we obtain [169]

$$m\,\partial_t j_\mu(\boldsymbol{r},t)=\rho(\boldsymbol{r},t)\partial_\mu v(\boldsymbol{r},t)-\sum_\nu\partial_\nu T_{\nu\mu}(\boldsymbol{r},t)-W_\mu(\boldsymbol{r},t), \tag{2.2.20}$$

where we define $W_\mu(\mathbf{r},t)$ and the momentum-stress tensor (part of the energy-momentum tensor) $T_{\mu\nu}(\mathbf{r},t)$ as

$$W_\mu(\mathbf{r},t) \equiv N \int d\mathbf{r}_2 \cdots \int d\mathbf{r}_N \Psi^*(t) \left[\partial_\mu \hat{W} \right] \Psi(t), \tag{2.2.21}$$

$$T_{\mu\nu}(\mathbf{r},t) \equiv \frac{\hbar^2 N}{2m} \int d\mathbf{r}_2 \cdots \int d\mathbf{r}_N \left\{ \left[\partial_\mu \Psi^*(t) \right] \left[\partial_\nu \Psi(t) \right] + \left[\partial_\mu \Psi(t) \right] \left[\partial_\nu \Psi^*(t) \right] - \frac{1}{2} \partial_\mu \partial_\nu \left[\Psi^*(t) \Psi(t) \right] \right\}. \tag{2.2.22}$$

By taking the divergence of Eq. (2.2.20) and using the continuity equation, we obtain the relation between the density and the external potential,

$$m\,\partial_t \nabla \cdot \mathbf{j}(\mathbf{r},t) = -m\,\partial_t^2 \rho(\mathbf{r},t) = -\nabla \cdot \left[\rho(\mathbf{r},t) \nabla v(\mathbf{r},t) \right] - q(\mathbf{r},t), \tag{2.2.23}$$

where $q(\mathbf{r},t) \equiv \sum_{\mu\nu} \partial_\mu \partial_\nu T_{\nu\mu}(\mathbf{r},t) + \sum_\mu \partial_\mu W_\mu(\mathbf{r},t)$.

Here, we introduce another system which obeys a different Hamiltonian $\hat{H}' = \hat{T} + \hat{W}' + \hat{V}'(t)$ with a wave function $\left| \Psi'(t) \right\rangle$. We prove that there exists an external potential $v'(\mathbf{r},t)$ which provides the same density $\rho(\mathbf{r},t)$ as the system of $\hat{H} = \hat{T} + \hat{W} + \hat{V}(t)$ for all times. Let us assume that we have solved the time-dependent Schrödinger equation with the initial wave function $\left| \Psi_0 \right\rangle$ so that we know the density $\rho(\mathbf{r},t)$ for all times. We then require $\rho'(\mathbf{r},t) = \rho(\mathbf{r},t)$ for all times and shall prove that we can construct $v'(\mathbf{r},t)$ which satisfies the requirement. Because of the requirement, there folds

$$\rho'(\mathbf{r},t_0) = \rho(\mathbf{r},t_0). \tag{2.2.24}$$

That is, the initial state of these systems, $\left| \Psi_0 \right\rangle$ and $\left| \Psi_0' \right\rangle$, has the same density. Since the relation Eq. (2.2.23) is a second-order differential equation with respect to time t, we also require a condition

$$\partial_t \rho'(\mathbf{r},t) \Big|_{t=t_0} = \partial_t \rho(\mathbf{r},t) \Big|_{t=t_0}, \tag{2.2.25}$$

which is equivalent to $\nabla \cdot \mathbf{j}'(\mathbf{r},t_0) = \nabla \cdot \mathbf{j}(\mathbf{r},t_0)$ because of the continuity equation. Then, the relation Eq. (2.2.23) for these systems gives the following equations:

$$m\,\partial_t^2 \rho(\mathbf{r},t) = \nabla \cdot \left[\rho(\mathbf{r},t) \nabla v(\mathbf{r},t) \right] + q(\mathbf{r},t), \tag{2.2.26}$$

$$m\,\partial_t^2 \rho(\mathbf{r},t) = \nabla \cdot \left[\rho(\mathbf{r},t) \nabla v'(\mathbf{r},t) \right] + q'(\mathbf{r},t). \tag{2.2.27}$$

The subtraction of Eq. (2.2.27) from Eq. (2.2.26) leads

$$\nabla \cdot \left[\rho(\mathbf{r},t) \nabla \omega(\mathbf{r},t) \right] = \zeta(\mathbf{r},t), \tag{2.2.28}$$

where we define two functions, $\omega(\mathbf{r},t) \equiv v(\mathbf{r},t) - v'(\mathbf{r},t)$ and $\zeta(\mathbf{r},t) \equiv q'(\mathbf{r},t) - q(\mathbf{r},t)$. This type of differential equation is known as the Sturm-Liouville type and we can, in principle, uniquely solve the equation under a boundary condition, $\omega(\mathbf{r},t) \overset{r\to\infty}{\longrightarrow} 0$, if $\rho(\mathbf{r},t)$ and $\zeta(\mathbf{r},t)$ are given.

Using the determination equation of Eq. (2.2.28), we can show that the existence of $v'(\mathbf{r},t)$ as follows. For $t = t_0$, we have

$$\nabla \cdot \left[\rho(\mathbf{r},t_0) \nabla \omega(\mathbf{r},t_0) \right] = \zeta(\mathbf{r},t_0). \tag{2.2.29}$$

Because of the requirements, we know the density $\rho(\mathbf{r},t_0)$. We may calculate $\zeta(\mathbf{r},t_0)$ from the wave functions $\left| \Psi_0 \right\rangle$ and $\left| \Psi_0' \right\rangle$. Thus, in principle, we can obtain $\omega(\mathbf{r},t_0)$ by solving Eq. (2.2.29). We then also obtain the external potential $v'(\mathbf{r},t_0) = v(\mathbf{r},t_0) - \omega(\mathbf{r},t_0)$ as well.

Next, we take a time-derivative of Eq. (2.2.28) at $t = t_0$. We then find

$$\boldsymbol{\nabla} \cdot \left[\rho(\boldsymbol{r}, t_0) \boldsymbol{\nabla} \partial_t \omega(\boldsymbol{r}, t) \Big|_{t=t_0} \right] = \partial_t \zeta(\boldsymbol{r}, t) \Big|_{t=t_0} - \boldsymbol{\nabla} \cdot \left[\partial_t \rho(\boldsymbol{r}, t) \Big|_{t=t_0} \boldsymbol{\nabla} \omega(\boldsymbol{r}, t_0) \right]. \qquad (2.2.30)$$

We already know $\rho(\boldsymbol{r}, t_0)$ and $\partial_t \rho(\boldsymbol{r}, t) \big|_{t=t_0}$ (by the assumptions), $\zeta(\boldsymbol{r}, t_0)$, and $w(\boldsymbol{r}, t_0)$. Since we have obtained $v'(\boldsymbol{r}, t_0)$ by solving Eq. (2.2.29), we may evaluate $\partial_t \zeta(\boldsymbol{r}, t) \big|_{t=t_0}$ by solving the time-dependent Schrödinger equation. Thus, we can, in principle, calculate $\partial_t \omega(\boldsymbol{r}, t) \big|_{t=t_0}$ by solving the Sturm-Liouville type equation of Eq. (2.2.30) and can obtain $\partial_t v'(\boldsymbol{r}, t) \big|_{t=t_0} = \partial_t v(\boldsymbol{r}, t) \big|_{t=t_0} - \partial_t \omega(\boldsymbol{r}, t) \big|_{t=t_0}$.

By repeating this procedure for the 2nd, 3rd, $\cdots$, kth time-derivatives of Eq. (2.2.28), we obtain

$$\boldsymbol{\nabla} \cdot \left[\rho(\boldsymbol{r}, t) \boldsymbol{\nabla} \partial_t^k \omega(\boldsymbol{r}, t) \Big|_{t=t_0} \right] = Q^{(k)}(\boldsymbol{r}), \qquad (2.2.31)$$

where we define the inhomogeneity

$$Q^{(k)}(\boldsymbol{r}) \equiv \partial_t^k \zeta(\boldsymbol{r}, t) \Big|_{t=t_0} - \sum_{l=0}^{k-1} {}_k C_l \, \boldsymbol{\nabla} \cdot \left\{ \partial_t^{k-l} \rho(\boldsymbol{r}, t) \Big|_{t=t_0} \boldsymbol{\nabla} \partial_t^l \omega(\boldsymbol{r}, t) \Big|_{t=t_0} \right\}. \qquad (2.2.32)$$

We can calculate an arbitrary-order time-derivative of $v'(\boldsymbol{r}, t)$ at $t = t_0$ through this procedure. Thus, we can construct the external potential $v'(\boldsymbol{r}, t)$ by the Taylor series

$$v'(\boldsymbol{r}, t) = \sum_{k=0}^{\infty} \frac{1}{k!} \partial_t^k v'(\boldsymbol{r}, t) \Big|_{t=t_0} \left(t - t_0 \right)^k, \qquad (2.2.33)$$

which actually generates the density $\rho(\boldsymbol{r}, t_0)$ in the system of $\hat{H}'(t_0) = \hat{T} + \hat{W}' + \hat{V}'(t_0)$. After an infinitesimal time evolution, $|\Psi(t_0)\rangle \to |\Psi(t_1)\rangle$, within the convergence radius of the Taylor expansion, we can conduct the same argument at $t = t_1$ as for the $t = t_0$ case. Therefore, we can construct the external potential $v'(\boldsymbol{r}, t)$ in the system of $\hat{H}'(t) = \hat{T} + \hat{W}' + \hat{V}'(t)$ for all times which generates the density $\rho(\boldsymbol{r}, t)$ that coincides with the density in the system of $\hat{H}(t) = \hat{T} + \hat{W} + \hat{V}(t)$ for all times. This completes the proof.

In the case of $\hat{W}' = \hat{W}$, the van Leeuwen's theorem corresponds to the RG theorem. Because the van Leeuwen's theorem is also valid for the non-interacting system ($\hat{W}' \to 0$), it guarantees the existence of the non-interacting reference system which can be regarded as the time-dependent version of the KS system.

As we saw in this Section, the KS scheme based on the (TD)DFT provides a powerful and quite useful theoretical formalism for describing a many-particle system. The (TD)KS equations have a very similar form as the (TD)HF equation. We may actually regard the Skyrme (TD)HF theory as the (TD)DFT regarding the Skyrme EDF as an approximated representation of the *universal* density-functional. Moreover, since the Skyrme Hamiltonian with the density-dependent effective three-body interaction contains ρ^α in the two-body interaction (*cf.* Eq. (2.1.12)), it is not a many-body Hamiltonian in a strict sense. This fact also exhibits the DFT-like character of the Skyrme (TD)HF theory. Indeed, properties of thousands of nuclei in a wide mass region have been successfully described by a *single* Skyrme-parameter-set which is adjusted to reproduce properties of several representative nuclei and the nuclear matter. Let us use, however, the conventional terminology, "the HF theory" and "the TDHF theory", to express our theoretical framework throughout the thesis.

2.3 Application to Nuclear Reactions

In this Section, we present computational techniques which will be used in our study of heavy ion reactions employing the TDHF theory. In Sec. 2.3.1, we explain a detailed procedure to construct an initial condition for the simulation of heavy ion reactions in the TDHF theory. Several computational methods are presented in Sec. 2.3.2.

2.3.1 Initial condition

(a) Ground-state calculation: Imaginary-time method

To simulate heavy ion reactions, we need to prepare the many-body wave function of the projectile and target nuclei in the HF ground state. We use the imaginary-time method to calculate the HF ground state. In the imaginary-time method, the total energy of the system is minimized by iterative updates of the single-particle wave functions and the mean-field potential.

Here, we present a basic concept of the imaginary-time method. Let us consider a case where the system obeys the Schrödinger equation,

$$\hat{H}\big|\Psi_n\big\rangle = E_n\big|\Psi_n\big\rangle. \tag{2.3.1}$$

$\big|\Psi_0\big\rangle$ denotes the ground state, while $\big|\Psi_n\big\rangle$ $(n > 0)$ denotes excited states. Because the eigenfunctions $\{\Psi_n\}$ form a complete set, an arbitrary state $\big|\xi\big\rangle$ can be expanded by using these eigenfunctions as

$$\big|\xi\big\rangle = \sum_{n=0}^{\infty} C_n\big|\Psi_n\big\rangle. \tag{2.3.2}$$

A multiplication of the imaginary-time evolution operator for a small imaginary-time step $\Delta\tau \equiv \mathrm{i}\Delta t$, $e^{-\hat{H}\Delta\tau/\hbar}$, to the state $\big|\xi\big\rangle$ may be written as

$$
\begin{aligned}
e^{-\hat{H}\Delta\tau/\hbar}\big|\xi\big\rangle &= \sum_{n=0}^{\infty} C_n e^{-\hat{H}\Delta\tau/\hbar}\big|\Psi_n\big\rangle \\
&= \sum_{n=0}^{\infty} C_n e^{-E_n\Delta\tau/\hbar}\big|\Psi_n\big\rangle \\
&= e^{-E_0\Delta\tau/\hbar}\sum_{n=0}^{\infty} C_n e^{(E_0-E_n)\Delta\tau/\hbar}\big|\Psi_n\big\rangle.
\end{aligned}
\tag{2.3.3}
$$

We will reach the ground state wave function $\big|\Psi_0\big\rangle$ after a sufficiently long imaginary-time propagation:

$$\lim_{n\to\infty}\left[e^{-\hat{H}\Delta\tau/\hbar}\right]^n\big|\xi\big\rangle \propto \big|\Psi_0\big\rangle. \tag{2.3.4}$$

Excited states $\big|\Psi_n\big\rangle$ $(n > 0)$ will be dumped exponentially in a much faster way than the ground state $\big|\Psi_0\big\rangle$, because $E_n > E_0$ $(n > 0)$ by definition. This is the basic concept of the imaginary-time method.

In the case of the Skyrme HF theory, small changes in the single-particle orbitals $\phi_i(\boldsymbol{r}\sigma) + \delta\phi_i(\boldsymbol{r}\sigma)$ $(i = 1, \cdots, N)$ vary the EDF, $E_{\mathrm{SHF}}[\Phi] = \big\langle\Phi\big|\hat{H}_{\mathrm{Skyrme}}\big|\Phi\big\rangle$, up to the first-order of $\delta\phi_i(\boldsymbol{r}\sigma)$ to

$$E_{\mathrm{SHF}}[\Phi + \delta\Phi] = E_{\mathrm{SHF}}[\Phi] + \sum_{i,\sigma}\int d\boldsymbol{r}\,\frac{\delta E_{\mathrm{SHF}}[\Phi]}{\delta\phi_i(\boldsymbol{r}\sigma)}\delta\phi_i(\boldsymbol{r}\sigma) + \sum_{i,\sigma}\int d\boldsymbol{r}\,\frac{\delta E_{\mathrm{SHF}}[\Phi]}{\delta\phi_i^*(\boldsymbol{r}\sigma)}\delta\phi_i^*(\boldsymbol{r}\sigma). \tag{2.3.5}$$

If we take the small variation, $\delta\phi_i(\boldsymbol{r}\sigma)$, as

$$\delta\phi_i(\boldsymbol{r}\sigma) \equiv -\frac{\Delta\tau}{\hbar}\frac{\delta E_{\mathrm{SHF}}[\Phi]}{\delta\phi_i^*(\boldsymbol{r}\sigma)} = -\frac{\Delta\tau}{\hbar}\sum_{\sigma'}\hat{h}_{\mathrm{SHF}}^{(q_i)}(\boldsymbol{r}\sigma\sigma')\phi_i(\boldsymbol{r}\sigma'), \tag{2.3.6}$$
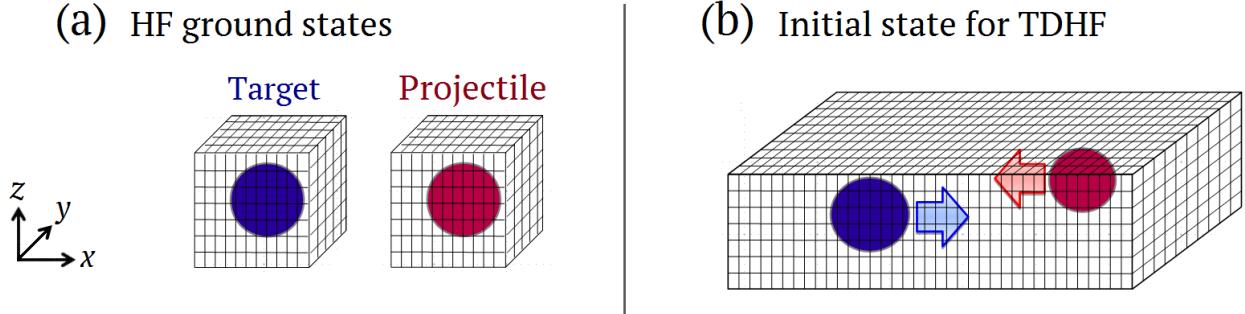
Figure 2.1: Schematic figures of the three-dimensional Cartesian grid for the HF calculation (a) and for the TDHF calculation (b). (a): The HF ground states of projectile and target nuclei are calculated separately. Because we do not impose any spatial symmetry, those nuclei can be spontaneously deformed to minimize the energy. (b): We use a rectangular box to calculate reaction dynamics. The ground states of the projectile and target nuclei are putted inside the box. We note that, the center-of-mass correction is neglected to use a consistent single-particle Hamiltonian in both HF and TDHF calculations.

a monotonic decrease of the total energy is guaranteed:

$$E_{\mathrm{SHF}}[\Phi + \delta\Phi] = E_{\mathrm{SHF}}[\Phi] - \frac{2\Delta\tau}{\hbar} \sum_{i,\sigma} \int d\boldsymbol{r} \left| \frac{\delta E_{\mathrm{SHF}}[\Phi]}{\delta\phi_i(\boldsymbol{r}\sigma)} \right|^2 < E_{\mathrm{SHF}}[\Phi]. \tag{2.3.7}$$

In practice, we use three-dimensional Cartesian grid representation to express the single-particle wave functions without any symmetry restrictions as schematically shown in Fig. 2.1 (a). We separately calculate the HF ground state of projectile and target nuclei. We start with an arbitrary Slater determinant composed of N Gaussian wave packets whose position is determined by a random number. We then repeat the imaginary-time propagation with a sufficiently small imaginary time-step, $\Delta\tau$. We perform the Schmidt's orthonormalization for the single-particle wave functions at each time-step to ensure $\langle\phi_i|\phi_j\rangle \equiv \sum_\sigma \int d\boldsymbol{r}\phi_i^*(\boldsymbol{r}\sigma)\phi_j(\boldsymbol{r}\sigma) = \delta_{ij}$. Since we deal with an intrinsic wave packet state, the HF ground sate spontaneously breaks the translational symmetry and the rotational symmetry in case of a deformed nucleus. Moreover, there may exist local minima on the potential energy surface as functions of deformation parameters [6, 170]. We indeed perform the imaginary-time calculation with certain constraints on the center-of-mass position and the principal axes as well as the deformation parameters. Such a calculation is called the constrained Hartree-Fock (CHF) method [6]. We first perform the CHF calculations with constraints on the deformation parameters, $\beta = 0$ and $\beta = 0.1$ and 0.2 with $\gamma = 0°$, 30°, and 60°. Then, we release those constraints and re-minimize the energy. We regard the least energy state as the HF ground state. Some details of the CHF method are summarized in Appendix C. In usual static HF calculation for nuclear structure, the center-of-mass correction is taken into account by replacing the kinetic energy operator as $\hat{T} \to \hat{T} - \hat{\boldsymbol{P}}^2/(2mA)$, where $\hat{\boldsymbol{P}} = \sum_i \hat{\boldsymbol{p}}_i$ and A is the mass number of the nucleus [136]. We note that, however, the center-of-mass correction is neglected in both the HF calculation of the projectile and target nuclei and the TDHF reaction calculation, because how to treat the center-of-mass correction in a colliding system is not at all trivial [102].

(b) Evaluation of the relative momentum

We simulate heavy ion reactions based on the TDHF theory. To save the computational cost in practice, we solve the TDHF equation using a finite-size numerical-box (typically, several tens of fm)

(a) Lab frame at $t=0$

(b) Initial configuration

(c) Wave vectors: $\boldsymbol{K}_{\mathrm{P}} + \boldsymbol{K}_{\mathrm{T}} = 0$
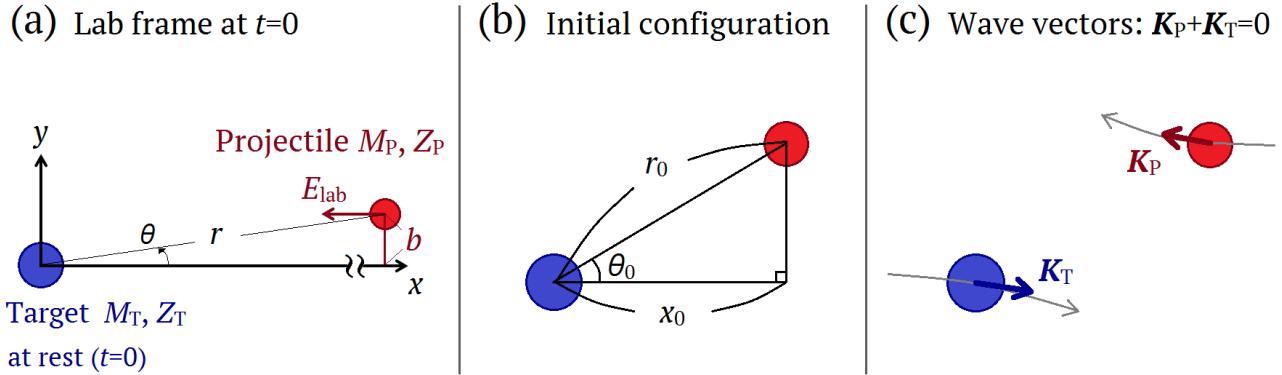
Figure 2.2: Schematic figures to explain our approach to evaluate the position and the relative wave vector for the TDHF calculation. (a): Geometric situation of the scattering problem is shown. (b): The initial configuration at a given separation distance in the x-direction, x_0, is illustrated. (c): The wave vectors of the two colliding nuclei at the initial configuration are illustrated in the center-of-mass frame.

for the reaction calculation as schematically shown in Fig. 2.1 (b). The initial separation distance, r_0, between the projectile and target nuclei at the initial stage of the TDHF calculation must be sufficiently shorter than the size of the box. In practice, we place the projectile and target nuclei in their HF ground state inside the numerical box assuming the Rutherford trajectory neglecting any Coulomb excitations before they reach the initial separation distance.

Let us denote the mass and charge of the projectile and target nuclei as $M_{\mathrm{P}}, Z_{\mathrm{P}}$ and $M_{\mathrm{T}}, Z_{\mathrm{T}}$, respectively. We use the mass simply given by $M_{\mathrm{P}} = m N_{\mathrm{P}}$ and $M_{\mathrm{T}} = m N_{\mathrm{T}}$, where $N_{\mathrm{P(T)}}$ denotes the total number of nucleons in the projectile (target) nucleus. We consider a situation that the projectile nucleus is coming from infinity with an incident energy E_{lab} and an impact parameter b in the laboratory frame. The target nucleus is considered to be at rest initially. We note that the target nucleus will start to move because of the recoil effect by the Coulomb repulsion. We set the incident direction parallel to the negative-x direction and the impact parameter vector parallel to the positive-y direction. The reaction plane is the xy-plane. This situation is schematically illustrated in Fig. 2.2 (a). It is well known that we can reduce this two-body scattering problem to the one-body problem with respect to the relative coordinate $\boldsymbol{r} = \boldsymbol{r}_{\mathrm{P}} - \boldsymbol{r}_{\mathrm{T}}$ with the reduced mass $\mu = M_{\mathrm{P}} M_{\mathrm{T}} / (M_{\mathrm{P}} + M_{\mathrm{T}})$, where the trivial center-of-mass translational motion is removed from the problem. For the reduced one-body problem, we have the equation of trajectory [171]

$$r(\theta) = \frac{l}{-1 + \varepsilon \cos(\theta - \alpha)}, \tag{2.3.8}$$

where several quantities are defined by

$$l = \frac{2Eb^2}{k} = \frac{k}{2E}(\varepsilon^2 - 1) \geq 0, \tag{2.3.9}$$

$$\varepsilon = \sqrt{1 + \left(\frac{2Eb}{k}\right)^2} \geq 1, \tag{2.3.10}$$

$$k = Z_{\mathrm{P}} Z_{\mathrm{T}} e^2. \tag{2.3.11}$$

$E \equiv \frac{M_{\mathrm{T}}}{M_{\mathrm{P}} + M_{\mathrm{T}}} E_{\mathrm{lab}}$ denotes the incident relative energy. Because of the initial condition $r(\theta = 0) \to \infty$, the angle α is determined to be $\alpha = \cos^{-1}\left(\frac{1}{\varepsilon}\right)$.

To evaluate the position and the relative momentum of the projectile and target nuclei, we first specify the initial separation distance parallel to the x-axis, which we denote as x_0, as schematically

illustrated in Fig. 2.2 (b). Using an equality $r_0 \cos\theta_0 = x_0$ and the equation of trajectory Eq. (2.3.8), we find

$$\cos\theta_0 = \frac{-c_0 c_1 \pm c_2 \sqrt{c_1^2 + c_2^2 - c_0^2}}{c_1^2 + c_2^2}, \tag{2.3.12}$$

where $c_0 \equiv x_0$, $c_1 \equiv l - x_0$, and $c_2 \equiv x_0(\varepsilon^2 - 1)^{1/2}$. Because the initial relative distance r_0 ($= x_0/\cos\theta_0$) must be positive ($r_0 > 0$), we select the positive sign in the denominator of Eq. (2.3.12). In this algorithm, we can arbitrary choose the position of the center-of-mass of the two colliding nuclei, $\boldsymbol{R}_{\mathrm{c.m.}}$. The initial position of the projectile and target nuclei inside the numerical box is then uniquely determined by x_0 and $\boldsymbol{R}_{\mathrm{c.m.}}$ for a given $M_{\mathrm{P(T)}}$, $Z_{\mathrm{P(T)}}$, E_{lab}, and b.

Ones we obtain the initial relative distance r_0, we can evaluate the relative velocity from the conservation rows for the relative angular momentum and the energy:

$$v_\theta(r_0) = \frac{b}{r_0} v_0, \tag{2.3.13}$$

$$v_r(r_0) = \sqrt{\left[1 - \left(\frac{b}{r_0}\right)^2\right] v_0^2 - \frac{2}{\mu}\frac{k}{r_0}}, \tag{2.3.14}$$

$$v_x(r_0) = v_r(r_0)\cos\theta_0 + v_\theta(r_0)\sin\theta_0, \tag{2.3.15}$$

$$v_y(r_0) = -v_r(r_0)\sin\theta_0 + v_\theta(r_0)\cos\theta_0, \tag{2.3.16}$$

where $v_0 = \sqrt{2E/\mu}$ denotes the initial relative velocity. $v_r(r_0)$, $v_\theta(r_0)$, $v_x(r_0)$, and $v_y(r_0)$ denote the radial, azimuthal, x, and y components of the relative velocity at the initial relative distance r_0, respectively. From the relative velocity, we define the relative wave vector at the initial separation distance by $\boldsymbol{K}_{\mathrm{rel}}(r_0) = \big(\mu v_x(r_0)/\hbar,\ \mu v_y(r_0)/\hbar\big)$.

To describe the whole reaction dynamics within a limited-size spatial box, we choose the center-of-mass frame, $\boldsymbol{K}_{\mathrm{P}} + \boldsymbol{K}_{\mathrm{T}} = 0$, where $\boldsymbol{K}_{\mathrm{P(T)}}$ denotes the wave vector of the projectile (target) in the center-of-mass frame. From an equality for the kinetic energy

$$\frac{\hbar^2 \boldsymbol{K}_{\mathrm{rel}}^2}{2\mu} = \frac{\hbar^2 \boldsymbol{K}_{\mathrm{P}}^2}{2M_{\mathrm{P}}} + \frac{\hbar^2 \boldsymbol{K}_{\mathrm{T}}^2}{2M_T} = \frac{\hbar^2 \boldsymbol{K}_{\mathrm{P(T)}}^2}{2\mu},$$

we see that $\big|\boldsymbol{K}_{\mathrm{P}}\big| = \big|\boldsymbol{K}_{\mathrm{T}}\big| = \big|\boldsymbol{K}_{\mathrm{rel}}\big|$. We thus distribute the relative wave vector to the projectile and target nuclei as

$$\boldsymbol{K}_{\mathrm{P}}(r_0) = \left(-\frac{\mu v_x(r_0)}{\hbar},\ +\frac{\mu v_y(r_0)}{\hbar}\right), \tag{2.3.17}$$

$$\boldsymbol{K}_{\mathrm{T}}(r_0) = \left(+\frac{\mu v_x(r_0)}{\hbar},\ -\frac{\mu v_y(r_0)}{\hbar}\right). \tag{2.3.18}$$

These wave vectors are schematically illustrated in Fig. 2.2 (c).

(c) Galilean boost

After the evaluation of the initial relative momentum, we give the momentum for the projectile and target nuclei. In the TDHF theory, the translational motion of a nucleus is represented by a collective translational motion of nucleons inside the nucleus. To see this, we consider a transformation for the single-particle wave functions $\{\phi_i(\boldsymbol{r}\sigma)\}$

$$\phi_i'(\boldsymbol{r}\sigma) = \exp\left[\frac{1}{N}\mathrm{i}\boldsymbol{K}\cdot\hat{\boldsymbol{r}}\right]\phi_i(\boldsymbol{r}\sigma), \tag{2.3.19}$$

where $\phi_i'(\boldsymbol{r}\sigma)$ represents the transformed single-particle wave function which has the translational momentum $\hbar\boldsymbol{K}/N$. The many-body wave function constructed from the transformed single-particle wave function takes the following form:

$$
\begin{aligned}
\Phi'(\boldsymbol{r}_1\sigma_1, \cdots, \boldsymbol{r}_N\sigma_N) &= \frac{1}{\sqrt{N!}} \det\{\phi_i'(\boldsymbol{r}_j\sigma_j)\} \\
&= \frac{1}{\sqrt{N!}} \begin{vmatrix} e^{\mathrm{i}\boldsymbol{K}\cdot\boldsymbol{r}_1/N}\phi_1(\boldsymbol{r}_1\sigma_1) & \cdots & e^{\mathrm{i}\boldsymbol{K}\cdot\boldsymbol{r}_N/N}\phi_1(\boldsymbol{r}_N\sigma_N) \\ \vdots & & \vdots \\ e^{\mathrm{i}\boldsymbol{K}\cdot\boldsymbol{r}_1/N}\phi_N(\boldsymbol{r}_1\sigma_1) & \cdots & e^{\mathrm{i}\boldsymbol{K}\cdot\boldsymbol{r}_N/N}\phi_N(\boldsymbol{r}_N\sigma_N) \end{vmatrix} \\
&= \exp\left[\mathrm{i}\boldsymbol{K}\cdot\left\{\frac{1}{N}\sum_{i=1}^N \boldsymbol{r}_i\right\}\right] \Phi(\boldsymbol{r}_1\sigma_1, \cdots, \boldsymbol{r}_N\sigma_N) \\
&= \exp\left[\mathrm{i}\boldsymbol{K}\cdot\boldsymbol{R}\right] \Phi(\boldsymbol{r}_1\sigma_1, \cdots, \boldsymbol{r}_N\sigma_N). \quad (2.3.20)
\end{aligned}
$$

$\boldsymbol{R} = \frac{1}{N}\sum_{i=1}^N \boldsymbol{r}_i$ is the center-of-mass coordinate of the nucleus. The transformed many-body wave function Eq. (2.3.20) may be regarded as a state boosted with the momentum $\hbar\boldsymbol{K}$.

In practice, we first perform the transformation for each single-particle wave function

$$
\phi_i'(\boldsymbol{r}\sigma) = \exp\left[\frac{1}{N_\mu}\mathrm{i}\boldsymbol{K}_\mu\cdot\hat{\boldsymbol{r}}\right]\phi_i(\boldsymbol{r}\sigma) \quad \text{for } i \in \mu \, (= \mathrm{P} \text{ or } \mathrm{T}),
$$

where $\boldsymbol{K}_\mu$ is the relative wave vector defined by Eqs. (2.3.17) and (2.3.18) and N_μ is the number of nucleons in each nucleus. "$i \in \mu$" means that the ith orbital initially belongs to either the projectile ($\mu = \mathrm{P}$) or the target ($\mu = \mathrm{T}$) at the initial stage of the TDHF calculation. In our code, 1st, $\cdots$, (N_P)th orbitals initially belong to the projectile, while $(N_\mathrm{P}+1)$th, $\cdots$, $(N_\mathrm{P}+N_\mathrm{T})$th orbitals initially belong to the target. After that, we construct a *single* Slater determinant by the boosted orbitals $\{\phi_i'\}$ ($i = 1, \cdots, N_\mathrm{P}+N_\mathrm{T}$). We then calculate a real-time evolution by solving the TDHF equation using the transformed single Slater-determinant composed of $\{\phi_i'\}$ as an initial wave function. We note that the TDHF wave function (a single Slater determinant) is invariant under arbitrary unitary transformations for the single-particle wave functions. Therefore, we may not be able to discuss any physics, in a strict sense, in terms of the information that which orbitals belonged to which nuclei at the initial stage of the TDHF calculation, because it is not gauge invariant.

2.3.2 Computational methods

(a) Real-space method

We employ three-dimensional Cartesian grid representation to express the single-particle wave functions. We use a uniform orthogonal mesh having a mesh spacing H. We set $H = 0.8$ fm in practical calculations. We have a discreet complex value at each grid point which represents the discretized single-particle wave function $\phi_\alpha(x_i, y_j, z_k, \sigma, t)$ at $x_i \equiv iH$, $y_j \equiv jH$, and $z_k \equiv kH$, where i, j, and k are zero or positive integers.

To calculate the first and second derivatives, we employ the high-order finite-difference method. For example, the νth x-derivative of the single-particle wave function at a grid point (x_i, y_j, z_k) is given by [172]

$$
\frac{\partial^\nu \phi_\alpha(x_i, y_j, z_k, \sigma, t)}{\partial x^\nu} \approx \frac{1}{b_N^{(\nu)}H^\nu}\sum_{n=-N}^{N} c_{N,n}^{(\nu)}\phi_\alpha(x_i + nH, y_j, z_k, \sigma, t). \quad (2.3.21)
$$

The same formula is utilized for the y- and z-derivative. In practice, we use 11-point finite-difference formula ($N = 5$). The coefficients, $b_N^{(\nu)}$ and $c_{N,n}^{(\nu)}$, are shown in Table 2.2 for $\nu = 1$ and 2 with $N = 5$.

Table 2.2:   Coefficients in the high-oder finite-difference formula Eq. (2.3.21), $b_N^{(\nu)}$ and $c_{N,n}^{(\nu)}$, for the first ($\nu = 1$) and second ($\nu = 2$) derivatives with $N = 5$ (the 11-point formula) [172].

11-point formula ($N = 5$)						
ν	$b_5^{(\nu)}$	$c_{5,0}^{(\nu)}$	$c_{5,\pm 1}^{(\nu)}$	$c_{5,\pm 2}^{(\nu)}$	$c_{5,\pm 3}^{(\nu)}$	$c_{5,\pm 4}^{(\nu)}$	$c_{5,\pm 5}^{(\nu)}$
1	2520	0	± 2100	∓ 600	± 150	∓ 25	± 2
2	25200	-73766	42000	-6000	1000	-125	8

All operations of the gradient, divergence, rotation, and Laplacian in the Skyrme HF equation are evaluated according to Eq. (2.3.21).

(b)   Real-time method

Using the wave function prepared as described in Sec. 2.3.1 as an initial TDHF wave function, we can simulate heavy ion reactions numerically. To calculate a real-time evolution, we employ the Taylor expansion method. In the method, a time evolution from time t to $t + \Delta t$ of the single-particle wave functions obeying the TDHF equation is calculated as

$$\phi_i(\boldsymbol{r}\sigma, t + \Delta t) \approx \sum_{k=0}^{k_{\max}} \frac{1}{k!} \left(\frac{\Delta t}{\mathrm{i}\hbar} \right)^k \sum_{\sigma'} \left[\hat{h}_{\mathrm{SHF}}^{(q_i)} \left(\boldsymbol{r}\sigma\sigma', t + \tfrac{\Delta t}{2} \right) \right]^k \phi_i(\boldsymbol{r}\sigma', t), \qquad (2.3.22)$$

where Δt and $k_{\max}$ denote a small time-step and the maximum order of the Taylor expansion, respectively. We set $\Delta t = 0.2$ fm/c and $k_{\max} = 4$ in our practical calculations. For the time evolution from time t to $t + \Delta t$, we use $\hat{h}_{\mathrm{SHF}}^{(q_i)}(\boldsymbol{r}\sigma\sigma', t + \Delta t/2)$ which is the single-particle Hamiltonian associated with the single-particle wave functions at time $t + \Delta t/2$ to increase numerical accuracy. This corresponds to the first-order predictor-corrector method. We note that we encountered a numerical instability just after a short real-time propagation if we omit the predictor-corrector step. In Fig. 2.3, the time-evolution scheme with the first-order predictor-corrector method is illustrated. Because the mean-field potentials in the single-particle Hamiltonian are constructed from the orbitals at each time-step, we need to calculate the time evolution in a self-consistent manner. A time evolution of the orbitals causes some changes of the densities and the mean-field potentials. The changes in the mean-field potentials affect the next time-evolution of the orbitals. In this way, complex many-body reaction processes, not only single-particle excitations but also corrective excitations, are described microscopically in a self-consistent manner from nucleons' degrees of freedom in the TDHF theory.

(c)   Parallelization

The recent remarkable progress in computational sciences, not only computational methods but also architecture, enables us to solve computationally-tough problems numerically on a massively-parallel supercomputer. Thus, we can now explore new physics by performing large-scale calculations and/or systematic calculations, which cannot be realized without abundant computational resources and the massively-parallel supercomputer powered by HPCI systems. It has been recognized that computational sciences have been one of the essential approaches to study physics in the nature in addition to the experimental and the theoretical approaches.

In order to perform a large number of TDHF calculations using a full Skyrme EDF including all the time-odd components without any symmetry restrictions, we parallelize our computational

code using a hybrid parallelization technique with the massage passing interface (MPI) and the open multi-processing (OpenMP). Since the time evolution of each single-particle wave function can be performed independently, we parallelize the code with respect to the single-particle wave functions. Our parallelization procedure is schematically illustrated in Fig. 2.4. We distribute N single-particle wave functions ϕ_i ($i = 1, \cdots, N = N_{\rm P} + N_{\rm T}$) to M MPI processes. To optimize the load balance of every processor, the number of single-particle wave functions per MPI process is determined as equal as possible. If we can adopt several CPUs with a shared memory to each MPI process, we further parallelize the calculation using the OpenMP. We note that communications between MPI processes are required at each time-step, because we need to update the single-particle Hamiltonian as shown in Fig. 2.3 (The densities/mean-fields are constructed from all the single-particle wave functions at each time-step).
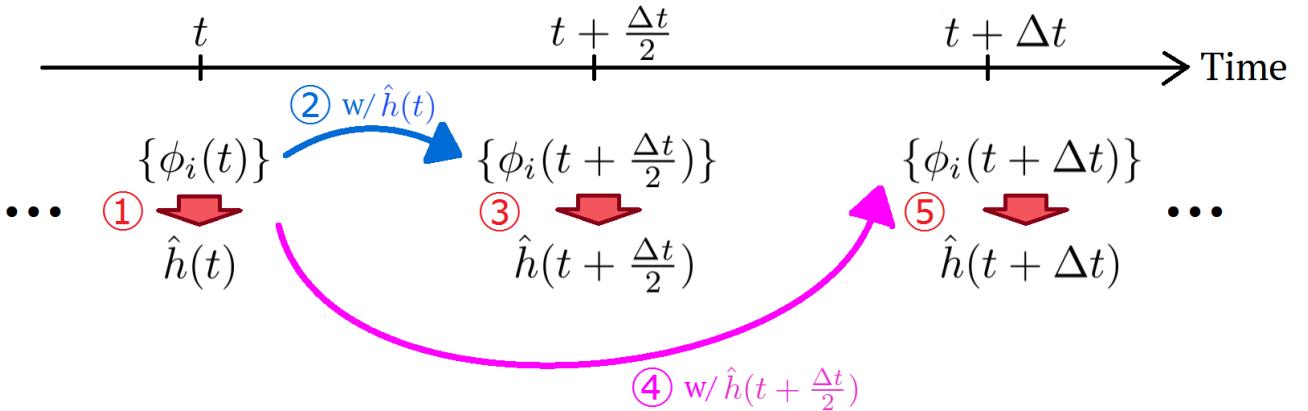
Figure 2.3: Time-evolution scheme from time t to $t + \Delta t$ with the first-order predictor-corrector method is illustrated schematically. The circled numbers indicate the order of procedures. The red down-arrows at step 1, 3, and 5 represent evaluation of the densities, the mean-field potentials, and the single-particle Hamiltonian using the single-particle wave functions at each time. The blue solid curry-arrow at step 2 represents a time evolution from time t to $t + \Delta t/2$ using the single-particle Hamiltonian at time t. While the pink solid curry-arrow at step 4 represents a time evolution from time t to $t + \Delta t$ using the single-particle Hamiltonian at time $t + \Delta t/2$.
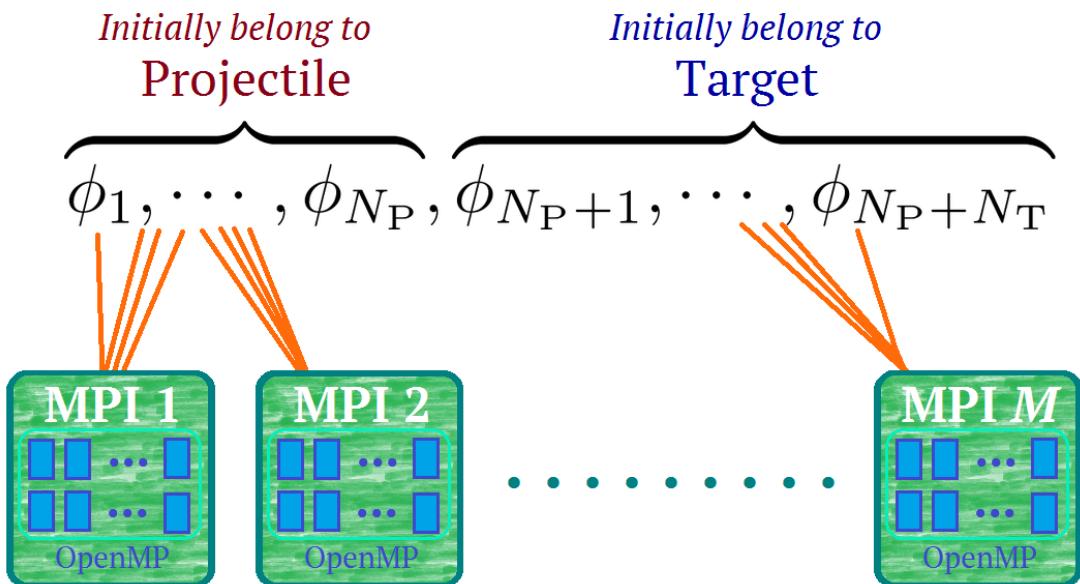
Figure 2.4: Concept of our MPI-OpenMP hybrid parallelization is illustrated. Green boxes represent MPI processes to which we may distribute several CPUs with a shared memory. Those CPUs are represented by blue small boxes inside the green box. We distribute N single-particle wave functions $\phi_i(\boldsymbol{r}\sigma, t)$ $(i = 1, \cdots, N = N_{\mathrm{P}} + N_{\mathrm{T}})$ to M MPI processes. The each MPI process is designed to perform the OpenMP parallelization with respect to the single-particle wave functions utilizing the CPUs with the shared memory.

Part I

Application of the TDHF theory to MNT reactions

Chapter 3

TDHF CALCULATIONS FOR MNT REACTIONS

In this first part of the thesis (Part I), we shed light on the feasibility of the TDHF theory combined with the PNP technique in describing MNT cross sections.

In this Chapter, we investigate MNT processes in reactions of ^{40}Ca+^{124}Sn at E_{lab} = 170 MeV, ^{48}Ca+^{124}Sn at E_{lab} = 174 MeV, ^{40}Ca+^{208}Pb at E_{lab} = 235 and 249 MeV, and ^{58}Ni+^{208}Pb at E_{lab} = 328.4 MeV, for which precise measurements of MNT cross sections were achieved [40, 43, 47, 50][*].

In addition to the fact that extensive experimental data are available for these systems, analyses and comparisons of these systems are of much interest because reactions in these systems are expected to show qualitatively different features. While ^{48}Ca+^{124}Sn has almost the same neutron-to-proton ratio, N/Z, between the projectile and target nuclei, other three systems have different N/Z ratios. We expect that transfer processes toward the charge equilibrium take place in reactions with a large N/Z asymmetry [116, 119, 174]. Moreover, it is well known that the basic feature of the low-energy heavy ion reactions depends much on the product of the charge numbers of the projectile and target nuclei, $Z_{\text{P}}Z_{\text{T}}$. Fusion reactions beyond the critical value, $Z_{\text{P}}Z_{\text{T}} \sim$ 1600-1800, are known to accompany an extra-push energy [75, 121]. Analyses of the fusion-hindrance phenomena in the TDHF theory have been reported in Refs. [117, 121], showing that the extra-push energy in the TDHF calculation is in good agreement with that of the Swiatecki's extra-push model [74]. The four systems to be analyzed have different $Z_{\text{P}}Z_{\text{T}}$ values, 1000 for ^{40,48}Ca+^{124}Sn, 1640 for ^{40}Ca+^{208}Pb, and 2296 for ^{58}Ni+^{208}Pb.

It has been considered that the success of the TDHF theory is limited to observables expressed as expectation values of one-body operators. Indeed, the particle-number fluctuation in DICs has been found to be substantially underestimated in the TDHF calculations [88, 89, 93]. Since transfer probabilities in the TDHF calculation may not be given as expectation values of any one-body operators, it is not at all obvious whether the TDHF calculation provides a reasonable description for MNT processes. One of the main purposes of this work is to clarify usefulness and limitation of the TDHF calculation for the MNT processes. We note that Simenel has recently presented a calculation using the Barian-Vénéroni variational principle [175] and concluded that the particle-number fluctuation may not be affected much by the correlation effects beyond the TDHF theory for reactions that are not as violent as DICs [176].

This Chapter is organized as follows. In Sec. 3.1, we describe a formalism to calculate transfer probabilities from the TDHF wave function after collision. We also describe our computational method. In Sec. 3.2, we present results of our TDHF calculations for four systems and compare them with measurements. In Sec. 3.3, we compare our results with those by other theories. In Sec. 3.4, a

---

[*] This Chapter is essentially based on our publication of Ref. [173].

summary and concluding remarks on this Chapter are presented.

3.1 Formulation

3.1.1 Definition of transfer probabilities

We consider a collision of two nuclei described by the TDHF theory. The projectile is composed of N_P nucleons and the target is composed of N_T nucleons. The total number of nucleons is $N = N_\mathrm{P} + N_\mathrm{T}$. In the TDHF calculation, a time evolution of single-particle orbitals, $\phi_i(\boldsymbol{r}\sigma, t)$ $(i = 1, \cdots, N)$, is calculated where $\boldsymbol{r}$ and σ denote the spatial and the spin coordinates, respectively. The total wave function is given by the Slater determinant composed of the orbitals:

$$\Phi(x_1, \cdots, x_N, t) = \frac{1}{\sqrt{N!}} \det\{\phi_i(x_j, t)\}, \tag{3.1.1}$$

where x is a set of the spatial and the spin coordinates, $x \equiv (\boldsymbol{r}, \sigma)$. For the moment, we will develop a formalism for a many-body system composed of identical fermions. An extension to the actual nuclei composed of two kinds of fermions, neutrons and protons, is simple and obvious.

Before the collision, two nuclei are separated spatially. We divide the whole space into two, the projectile region, V_P^i, and the target region, V_T^i. After the collision, we assume that there appear two nuclei, a projectile-like fragment (PLF) and a target-like fragment (TLF). We ignore channels in which nuclei are separated into more than two fragments after the collision. We again introduce a division of the whole space into two, the projectile region, V_P^f, which includes the PLF, and the target region, V_T^f, which includes the TLF.

We define the number operator of each spatial region as

$$\hat{N}_\tau = \int_\tau d\boldsymbol{r} \sum_{i=1}^{N} \delta(\boldsymbol{r} - \boldsymbol{r}_i) = \sum_{i=1}^{N} \Theta_\tau(\boldsymbol{r}_i), \tag{3.1.2}$$

where τ specifies the spatial region either $V_\mathrm{P}^{i(f)}$ or $V_\mathrm{T}^{i(f)}$. We introduce the space division function, $\Theta_\tau(\boldsymbol{r})$, defined as

$$\Theta_\tau(\boldsymbol{r}) = \begin{cases} 1 & \text{for} \quad \boldsymbol{r} \in \tau, \\ 0 & \text{for} \quad \boldsymbol{r} \notin \tau. \end{cases} \tag{3.1.3}$$

The sum of the two operators, $\hat{N}_{V_\mathrm{P}^{i(f)}}$ and $\hat{N}_{V_\mathrm{T}^{i(f)}}$, is the number operator of the whole space, $\hat{N} = \hat{N}_{V_\mathrm{P}^i} + \hat{N}_{V_\mathrm{T}^i} = \hat{N}_{V_\mathrm{P}^f} + \hat{N}_{V_\mathrm{T}^f}$. In ordinary TDHF calculations, an initial wave function is the direct product of the ground state wave functions of two nuclei boosted with the relative velocity. The single-particle orbitals, $\phi_i(x, t)$, are localized in one of the spatial regions, V_P^i or V_T^i, at the initial stage of the calculation. Therefore, the initial wave function is the eigenstate of both operators, $\hat{N}_{V_\mathrm{P}^i}$ and $\hat{N}_{V_\mathrm{T}^i}$, with eigenvalues, N_P and N_T, respectively. At the final stage of the calculation after the collision, each single-particle orbital extends spatially to both spatial regions of V_P^f and V_T^f. Because of this fact, the Slater determinant at the final stage is not an eigenstate of the number operators, $\hat{N}_{V_\mathrm{P}^f}$ and $\hat{N}_{V_\mathrm{T}^f}$, but a superposition of states with different particle-number distributions.

The probability that n nucleons are in the spatial region V_P^f and $N - n$ nucleons are in the spatial region V_T^f is defined as follows. We start with the normalization relation of the final wave function after the collision,

$$\int dx_1 \cdots \int dx_N \, |\Psi(x_1, \cdots, x_N)|^2 = 1, \tag{3.1.4}$$

where $\int dx \equiv \sum_\sigma \int d\boldsymbol{r}$. Here and hereafter, we denote the many-body wave function at the final stage of the calculation as $\Psi(x_1, \cdots, x_N) = \det\{\psi_i(x_j)\}/\sqrt{N!}$, and omit the time index. We also omit the

suffix f from V_{P}^f and V_{T}^f. The normalization relation, Eq. (3.1.4), includes an N-fold integral over the whole spatial region. We divide each spatial integral into two integrals over the subspaces, V_{P} and V_{T}. We then classify the 2^N terms, generated by the divisions of the spatial regions, according to the number of V_{P} and the number of V_{T} included in the integral:

$$
\begin{aligned}
1 &= \int_{V_{\mathrm{P}}+V_{\mathrm{T}}} dx_1 \cdots \int_{V_{\mathrm{P}}+V_{\mathrm{T}}} dx_N \, |\Psi(x_1, \cdots, x_N)|^2 \\
&= \sum_{n=0}^{N} \sum_{s(\{\tau_i\}:V_{\mathrm{P}}^n V_{\mathrm{T}}^{N-n})} \int_{\tau_1} dx_1 \cdots \int_{\tau_N} dx_N |\Psi(x_1, \cdots, x_N)|^2,
\end{aligned}
\tag{3.1.5}
$$

where each subscript τ_i $(i = 1, \cdots, N)$ represents either V_{P} or V_{T}. The notation $s(\{\tau_i\} : V_{\mathrm{P}}^n V_{\mathrm{T}}^{N-n})$ means that the sum should be taken for all possible combinations of τ_i on condition that, in the sequence of $\tau_1, \cdots, \tau_N$, V_{P} appears n times and V_{T} appears $N-n$ times. The number of the combinations equals to $_NC_n$. From this expression, we find the probability that n nucleons are in the V_{P} and $N-n$ nucleons are in the V_{T} is given by

$$
P_n = \sum_{s(\{\tau_i\}:V_{\mathrm{P}}^n V_{\mathrm{T}}^{N-n})} \int_{\tau_1} dx_1 \cdots \int_{\tau_N} dx_N |\Psi(x_1, \cdots, x_N)|^2.
\tag{3.1.6}
$$

Equation (3.1.5) ensures the relation, $\sum_{n=0}^{N} P_n = 1$. From the probability P_n, we may obtain nucleon transfer probabilities. For example, the probability of n-particle transfer from the projectile to the target is given by $P_{N_{\mathrm{P}}-n}$.

3.1.2 Particle-number projection operator

Above expression of the probability P_n can be represented as an expectation value of the PNP operator $\hat{P}_n$, i.e. $P_n = \langle \Psi | \hat{P}_n | \Psi \rangle$. This operator extracts a component of the wave function with particle number n in the V_{P} and $N-n$ in the V_{T} from the final wave function $\Psi(x_1, \cdots, x_N)$. From Eq. (3.1.6), we obtain the following expression for the PNP operator,

$$
\hat{P}_n = \sum_{s(\{\tau_i\}:V_{\mathrm{P}}^n V_{\mathrm{T}}^{N-n})} \Theta_{\tau_1}(\boldsymbol{r}_1) \cdots \Theta_{\tau_N}(\boldsymbol{r}_N).
\tag{3.1.7}
$$

The projected wave function, $\hat{P}_n \Psi$, is the eigenstate of the number operators, $\hat{N}_{V_{\mathrm{P}}}$ and $\hat{N}_{V_{\mathrm{T}}}$, with eigenvalues, n and $N-n$, respectively. From Eq. (3.1.5), there follows

$$
\sum_{n=0}^{N} \hat{P}_n = \prod_{i=1}^{N} \Big(\Theta_{V_{\mathrm{P}}}(\boldsymbol{r}_i) + \Theta_{V_{\mathrm{T}}}(\boldsymbol{r}_i) \Big) = 1.
\tag{3.1.8}
$$

Recently, Simenel has provided an alternative expression for the PNP operator [115] which is given by

$$
\hat{P}_n = \frac{1}{2\pi} \int_0^{2\pi} d\theta \, e^{\mathrm{i}(n-\hat{N}_{V_{\mathrm{P}}})\theta}.
\tag{3.1.9}
$$

We can easily show that this expression, Eq. (3.1.9), is equivalent to Eq. (3.1.7) as follows:

$$
\begin{aligned}
\hat{P}_n &= \frac{1}{2\pi} \int_0^{2\pi} d\theta \, e^{i(n-\hat{N}_{V_P})\theta} \\
&= \frac{1}{2\pi} \int_0^{2\pi} d\theta \, e^{in\theta} \prod_{i=1}^{N} \Big(\Theta_{V_T}(\boldsymbol{r}_i) + e^{-i\theta}\Theta_{V_P}(\boldsymbol{r}_i) \Big) \\
&= \sum_{n'=0}^{N} \frac{1}{2\pi} \int_0^{2\pi} e^{i(n-n')\theta} d\theta \sum_{s(\{\tau_i\}:V_P^{n'} V_T^{N-n'})} \Theta_{\tau_1}(\boldsymbol{r}_1) \cdots \Theta_{\tau_N}(\boldsymbol{r}_N) \\
&= \sum_{s(\{\tau_i\}:V_P^{n} V_T^{N-n})} \Theta_{\tau_1}(\boldsymbol{r}_1) \cdots \Theta_{\tau_N}(\boldsymbol{r}_N).
\end{aligned}
$$

3.1.3 Computation of transfer probabilities

Two expressions for the PNP operator $\hat{P}_n$, Eq. (3.1.7) and Eq. (3.1.9), have been utilized to calculate transfer probabilities in the TDHF theory. When we use Eq. (3.1.7), the probability P_n is expressed in terms of the single-particle orbitals as

$$
\begin{aligned}
P_n &= \int dx_1 \cdots \int dx_N \, \psi_1^*(x_1) \cdots \psi_N^*(x_N) \hat{P}_n \det\{\psi_i(x_j)\} \\
&= \sum_{s(\{\tau_i\}:V_P^{n} V_T^{N-n})} \sum_{\xi} \mathrm{sgn}(\xi) \langle \psi_1 | \psi_{\xi_1} \rangle_{\tau_1} \cdots \langle \psi_N | \psi_{\xi_N} \rangle_{\tau_N} \\
&= \sum_{s(\{\tau_i\}:V_P^{n} V_T^{N-n})} \det\{\langle \psi_i | \psi_j \rangle_{\tau_i}\},
\end{aligned} \tag{3.1.10}
$$

where the summation over ξ is taken for all possible permutations of the index ξ_i $(i = 1, \cdots, N)$, and $\mathrm{sgn}(\xi)$ is a sign depending on the number of permutations. $\langle \psi_i | \psi_j \rangle_{\tau} \equiv \int_\tau dx \, \psi_i^*(x)\psi_j(x)$ denotes an overlap integral in the spatial region τ.

When we use Eq. (3.1.9), we obtain

$$
\begin{aligned}
P_n &= \frac{1}{2\pi} \int_0^{2\pi} d\theta \, e^{in\theta} \langle \Psi | \prod_{i=1}^{N} e^{-i\Theta_{V_P}(\boldsymbol{r}_i)\theta} | \Psi \rangle \\
&= \frac{1}{2\pi} \int_0^{2\pi} d\theta \, e^{in\theta} \det\{\langle \psi_i | \psi_j \rangle_{V_T} + e^{-i\theta} \langle \psi_i | \psi_j \rangle_{V_P}\}.
\end{aligned} \tag{3.1.11}
$$

Two expressions, Eq. (3.1.10) and Eq. (3.1.11), should give equivalent results. We indeed confirmed that both expressions give the same results for light systems. However, the computational cost is rather different between two methods. Let us first consider the computational cost of Eq. (3.1.10),

$$
P_n = \sum_{s(\{\tau_i\}:V_P^{n} V_T^{N-n})} \det\{\langle \psi_i | \psi_j \rangle_{\tau_i}\}.
$$

In this expression, it is necessary to calculate the determinants of dimension N many times. For example, to calculate the probabilities of all possible processes, P_0 to P_N, we need to calculate determinants of dimension N for 2^N times. Even for the calculation of the probability without any particle transfer, we need to calculate the determinants as many as $_N C_{N_P}$. The calculation in this way soon becomes impossible as N increases and is useful only for light systems. This method has been used in the ^{40}Ca+^{40}Ca reaction in Ref. [88]. It has also been used in the electron transfer processes in atomic collisions [177, 178].

When we use the expression of Eq. (3.1.11),

$$P_n = \frac{1}{2\pi} \int_0^{2\pi} d\theta\, e^{\mathrm{i}n\theta}\, \det\{\langle \psi_i | \psi_j \rangle_{V_{\mathrm{T}}} + e^{-\mathrm{i}\theta} \langle \psi_i | \psi_j \rangle_{V_{\mathrm{P}}}\},$$

the computational cost can be significantly small. In this expression, we achieve integral over θ employing the trapezoidal rule discretizing the interval $[0, 2\pi]$ into M equal grids. To calculate all the probabilities, P_0 to P_N, we need to calculate the determinants of dimension N for M times. We find $M = 200$ is sufficient for systems presented in this Chapter. In our calculations shown below, we employ Eq. (3.1.11).

3.1.4   Transfer cross sections

We next derive the formula for cross sections of transfer reactions. We assume that both projectile and target nuclei are spherical, so that the reaction is specified by the incident energy E and the impact parameter b.

Up to this point, we derived expressions of transfer probabilities for a system composed of identical fermions. Since the TDHF wave function is a direct product of Slater determinants for neutrons and protons, the reaction probability is also given by the product of the probabilities for neutrons and protons. Let us denote the probability that N neutrons are included in the V_{P} as $P_N^{(n)}(b)$ and Z protons are included in the V_{P} as $P_Z^{(p)}(b)$. Then, the probability that N neutrons and Z protons are included in the V_{P} is given by

$$P_{N,Z}(b) = P_N^{(n)}(b)\, P_Z^{(p)}(b). \tag{3.1.12}$$

We calculate the transfer cross section for the channel where the PLF is composed of N, Z nucleons by integrating the probability $P_{N,Z}(b)$ over the impact parameter,

$$\sigma_{\mathrm{tr}}(N, Z) = 2\pi \int_{b_{\min}}^{\infty} b\, P_{N,Z}(b)\, db. \tag{3.1.13}$$

The minimum of the integration over the impact parameter is the border dividing fusion and binary reactions. In practice, we first examine the maximum impact parameter in which fusion reactions take place for a given incident energy. We will call it the fusion critical impact parameter and denote it as b_{f}. We then repeat reaction calculations at various impact parameters for the region, $b > b_{\mathrm{f}}$, and calculate the cross section by numerical quadrature according to Eq. (3.1.13).

3.1.5   Computational details

We have developed our own computational code of the TDHF theory for heavy ion reactions extending the code developed for the real-time linear response calculations [99]. As described in Chapter 2, we employ a uniform spatial grid in the three-dimensional Cartesian coordinate to represent single-particle orbitals without any symmetry restrictions. The grid spacing is taken to be 0.8 fm. We take a box size of $60 \times 60 \times 26$ grid points (48 fm × 48 fm × 20.8 fm) for reaction calculations, where the reaction plane is taken to be the xy-plane. The initial wave functions of projectile and target nuclei are prepared in a box with $26 \times 26 \times 26$ grid points.

We have tested the accuracy of the code by comparing our results with those by other codes. We have confirmed that the fusion critical impact parameters of the reactions of $^{16}\mathrm{O}+^{16}\mathrm{O}$ and $^{16}\mathrm{O}+^{28}\mathrm{O}$ reported in Ref. [102] are reproduced within 0.1 fm accuracy by our code. We have also calculated the fluctuation of exchanged nucleons for $^{40}\mathrm{Ca}+^{40}\mathrm{Ca}$ head-on collisions and confirmed that results reported in Ref. [179] are reproduced accurately.

3.2 Results

In this Section, we show calculated results for the reactions of ^{40}Ca+^{124}Sn at the incident energy of 170 MeV, ^{48}Ca+^{124}Sn at 174 MeV, ^{40}Ca+^{208}Pb at 235, 249 MeV, and ^{58}Ni+^{208}Pb at 328.4 MeV.

As for the energy density functional and potential, we use the Skyrme functional including all time-odd terms [154] except for the second derivative of the spin densities, $\triangle s^{(n,p)}$. We encounter numerical instability in the time evolution calculation if we include the term in the potential. All the results reported in this Chapter are calculated using the Skyrme SLy5 parameter set [141]. This interaction has been utilized in the fully three-dimensional TDHF calculations for heavy ion reactions [102, 109, 118].

In the ground state calculations, we find the ground states of ^{40}Ca, ^{48}Ca and ^{208}Pb are spherical. The ground state of ^{124}Sn is oblately deformed with $\beta \sim 0.11$. The ground state of ^{58}Ni is prolately deformed with $\beta \sim 0.11$.

We take the incident direction parallel to the x-axis and the impact parameter vector parallel to the y-axis. The reaction is specified by the incident energy and the impact parameter. As an initial condition, the two colliding nuclei are placed with the distance 16-18 fm in the x-direction. Before starting the TDHF calculation, we assume the centers of the two colliding nuclei follow the Rutherford trajectory. For the deformed nuclei, we placed the nucleus with the symmetry axis being set parallel to the z-axis.

We stop time evolution calculations when two nuclei are separated by 20-26 fm, if binary fragments are produced. If the colliding nuclei fuse and do not separate, we continue time evolution calculations more than 3000 fm/c after two nuclei touch. We have not found any reactions in which more than two fragments are produced after collision.

For each collision system, we first find the fusion critical impact parameter $b_{\rm f}$. We find them by repeating calculations changing the impact parameter by 0.01 fm step. We then calculate reactions for various impact parameters outside the critical value. At an impact parameter region smaller than 7 fm, we calculate reactions of impact parameters with 0.25 fm step. At an impact parameter region larger than 7 fm, we calculate reactions of $b = 7.5, 8, 9$, and 10 fm. Close to the fusion critical impact parameter, we calculate reactions in 0.05 fm and 0.01 fm impact parameter steps. All these calculations are used to evaluate the transfer cross sections. In calculating transfer cross sections according to Eq. (3.1.13), the upper limit of the integral over b is set to 10 fm.

3.2.1 ^{40,48}Ca+^{124}Sn reactions

In this Subsection, we present results for the reactions of ^{40}Ca+^{124}Sn at $E_{\rm lab} = 170$ MeV ($E_{\rm c.m.} \simeq 128.5$ MeV) and ^{48}Ca+^{124}Sn at $E_{\rm lab} = 174$ MeV ($E_{\rm c.m.} \simeq 125.4$ MeV), for which MNT cross sections have been measured experimentally [40, 43]. The neutron-to-proton ratio, N/Z, is different between the projectile and the target for ^{40}Ca+^{124}Sn, while it is almost the same for ^{48}Ca+^{124}Sn. Therefore, we expect different features in the transfer process. As we mentioned in the introduction, the product of charge numbers of the projectile and the target is important for the fusion dynamics. The present systems have $Z_{\rm P}Z_{\rm T} = 1000 < 1600$, so that no fusion-hindrance is expected to occur.

To estimate the Coulomb barrier height, we calculate the nucleus-nucleus potential using the frozen-density approximation neglecting the Pauli blocking effect [110, 180, 181]. The potential is given by $V(R) = E[\rho_{\rm P} + \rho_{\rm T}](R) - E_{\rm g.s.}[\rho_{\rm P}] - E_{\rm g.s.}[\rho_{\rm T}]$, where R is the distance between the centers-of-masses of the two nuclei, $\rho_{\rm P}$ ($\rho_{\rm T}$) denotes nuclear density of the projectile (target) in their ground state. $E[\rho_{\rm P} + \rho_{\rm T}](R)$ denotes the total energy when two nuclei are separated by the relative distance R. $E_{\rm g.s.}[\rho_{\rm P}]$ and $E_{\rm g.s.}[\rho_{\rm T}]$ denote the ground state energy of each nucleus. In the calculation, the Coulomb barrier height is estimated as $V_{\rm B} \approx 116.3$ MeV for ^{40}Ca+^{124}Sn and $V_{\rm B} \approx 115.1$ MeV for ^{48}Ca+^{124}Sn,
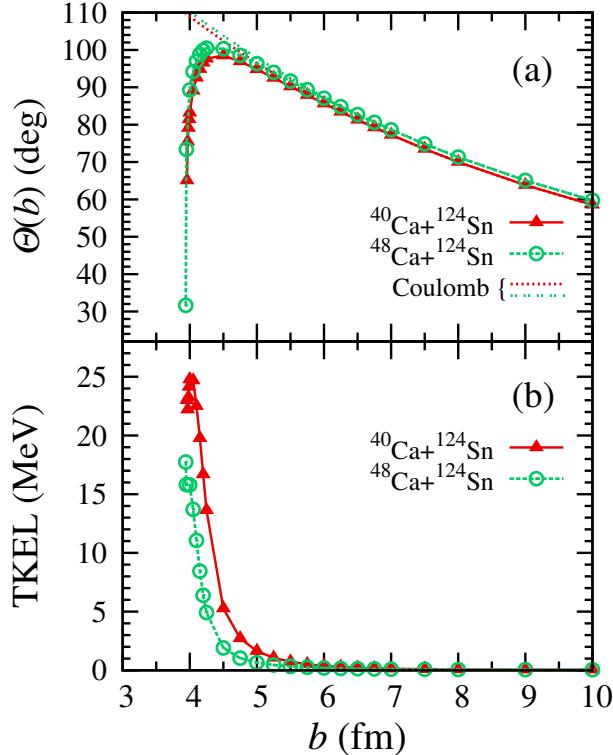
Figure 3.1:   Deflection function (a) and total kinetic energy loss (b) as functions of impact parameter b for the reactions of ^{40}Ca+^{124}Sn at $E_{\text{lab}} = 170$ MeV and ^{48}Ca+^{124}Sn at $E_{\text{lab}} = 174$ MeV. Results for the ^{40}Ca+^{124}Sn reactions are denoted by red filled triangles connected with solid lines, while results for the ^{48}Ca+^{124}Sn reactions are denoted by green open circles connected with dashed lines. In (a), we also show deflection functions for the pure Coulomb trajectories by a red dotted line for the ^{40}Ca+^{124}Sn reactions and by a green two-dot chain line for the ^{48}Ca+^{124}Sn reactions. The figure was taken from Ref. [173].

respectively. Since the initial relative energies are higher than the Coulomb barrier heights, we find the fusion critical impact parameter, $b_{\text{f}} = 3.95$ fm for ^{40}Ca+^{124}Sn and $b_{\text{f}} = 3.93$ fm for ^{48}Ca+^{124}Sn, respectively.

(a)   Overview of the reactions

Before showing detailed analyses of transfer reactions, we first present an overview of the reaction dynamics. In Fig. 3.1, we show the deflection function, $\Theta(b)$, in (a) and the total kinetic energy loss (TKEL) in (b), as functions of impact parameter b. Results for the ^{40}Ca+^{124}Sn reactions are denoted by red filled triangles connected with solid lines, while results for the ^{48}Ca+^{124}Sn reactions are denoted by green open circles connected with dotted lines. In Fig. 3.1 (a), we also show deflection functions of the pure Coulomb trajectories by a red dotted line for ^{40}Ca+^{124}Sn and by a green two-dot chain line for ^{48}Ca+^{124}Sn.

In practice, the deflection function and the TKEL are calculated in the following way. We denote the center-of-mass coordinate of the PLF (TLF) and the relative coordinate as $\boldsymbol{R}_{\text{PLF (TLF)}}(t)$ and $\boldsymbol{R}(t) = \boldsymbol{R}_{\text{PLF}}(t) - \boldsymbol{R}_{\text{TLF}}(t)$, respectively. We also denote the mass, charge number, and the reduced mass at the final stage of the calculation as $M_{\text{PLF (TLF)}}$, $Z_{\text{PLF (TLF)}}$, and $\mu_f = M_{\text{PLF}}M_{\text{TLF}}/(M_{\text{PLF}} + M_{\text{TLF}})$. The relative velocity at the final stage of the calculation, $t = t_f$, is calculated by $\dot{\boldsymbol{R}}(t_f) = (\boldsymbol{R}(t_f+\Delta t) - \boldsymbol{R}(t_f-\Delta t))/2\Delta t$. We evaluate the TKEL by TKEL $= E_{\text{c.m.}} - \frac{1}{2}\mu_f \dot{\boldsymbol{R}}(t_f)^2 - Z_{\text{PLF}}Z_{\text{TLF}}\, e^2/ |\boldsymbol{R}(t_f)|$, where $E_{\text{c.m.}}$ is the initial incident energy in the center-of-mass frame. The angle between
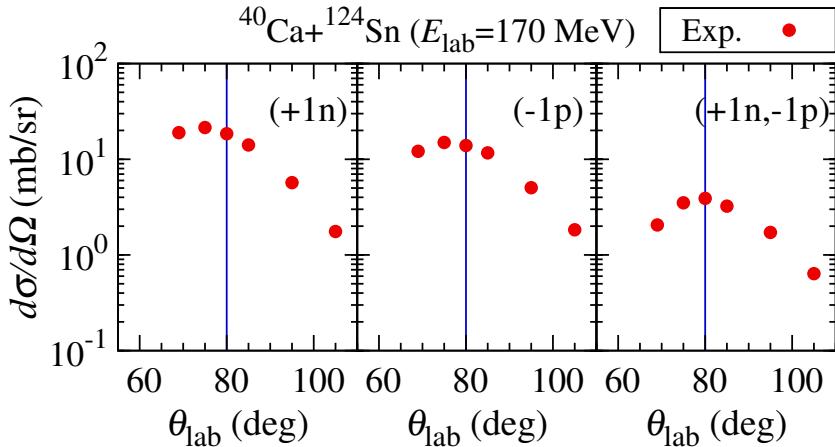
Figure 3.2:   Differential cross sections of representative transfer channels as functions of scattering angle in the laboratory frame for the ^{40}Ca+^{124}Sn reaction at $E_{\text{lab}} = 170$ MeV. The Coulomb rainbow angle obtained from the TDHF trajectories is denoted by blue solid vertical lines, and is compared with measured differential cross sections, red filled circles, which have been reported in Ref. [40]. The figure was taken from Ref. [173].

the vector $\boldsymbol{R}(t_f)$ and the x-axis, or the angle between the vector $\dot{\boldsymbol{R}}(t_f)$ and the x-axis, provides approximate value of the deflection angle. We estimate the correction for it assuming that both the PLF and the TLF follow the Rutherford trajectory specified by the coordinates and the velocities at the final time, t_f.

The TKEL increases rapidly as the impact parameter decreases in the region $b < 4.5$ fm, where the deflection function, $\Theta(b)$, decreases appreciably by the nuclear attractive interaction. The deflection function shows a maximum at $b \sim 4.25$ fm and decreases inside this impact parameter. The maximum deflection angle corresponds to the Coulomb rainbow angle, θ_{r}. It is given by 99° for ^{40}Ca+^{124}Sn and 100° for ^{48}Ca+^{124}Sn. In Fig. 3.2, we compare the Coulomb rainbow angle for the ^{40}Ca+^{124}Sn reaction with measured differential cross sections reported in Ref. [40]. Red filled circles denote measured cross sections and blue solid vertical lines denote the Coulomb rainbow angle in the laboratory frame. As seen from the figure, the peak positions of the measured cross sections roughly coincide with the Coulomb rainbow angle by the TDHF calculation.
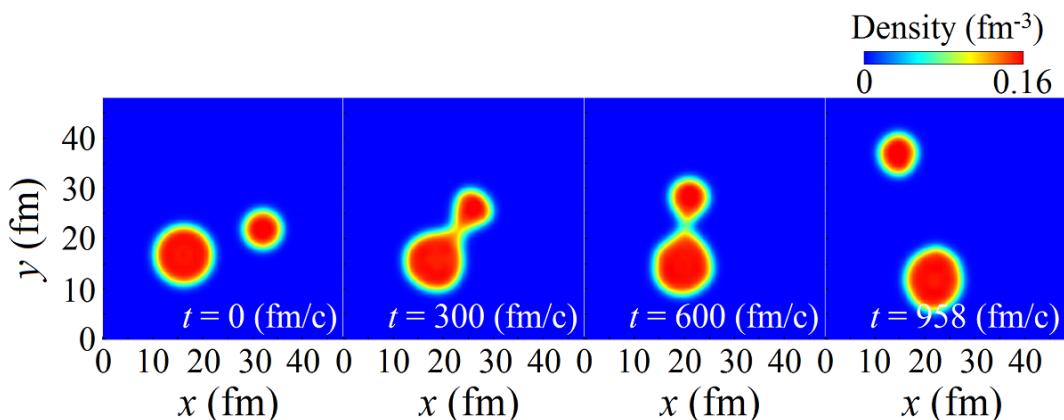
Figure 3.3:   Snapshots of density distribution of the ^{40}Ca+^{124}Sn reaction at $E_{\text{lab}} = 170$ MeV and $b = 3.96$ fm, just outside the fusion critical impact parameter. The figure was taken from Ref. [173].

In Fig. 3.3, we show snapshots of density distribution for the ^{40}Ca+^{124}Sn reaction at $b = 3.96$ fm, just outside the fusion critical impact parameter, b_{f}. We find a formation of a neck between the projectile and the target during the collision. As will be shown later, several nucleons are exchanged between the projectile and the target at this impact parameter. We find the formation of a neck for the impact parameter region smaller than $b \sim 4.25$ fm where the TKEL becomes appreciable.

We next consider the average number of transferred nucleons and its fluctuation. We denote the average number of nucleons in the PLF as $N_{\mathrm{PLF}}^{(q)}$ ($q = n$ for neutrons, p for protons), which is calculated from the density distribution at the final stage of the calculation,

$$N_{\mathrm{PLF}}^{(q)} = \int_{\mathrm{around\,PLF}} d\boldsymbol{r}\ \rho^{(q)}(\boldsymbol{r}), \tag{3.2.1}$$

where $\rho^{(q)}(\boldsymbol{r})$ is the density distribution of neutrons ($q = n$) or protons ($q = p$). The spatial integration is achieved over a sphere whose center coincides with the center-of-mass of the PLF. The radius of the sphere is taken to be 10 fm. We calculate the average number of nucleons in the TLF in the same way taking the radius of 14 fm for the TLF. We summarize various expressions for the average number and the fluctuation of transferred nucleons in Appendix A.

We denote the neutron (proton) number of the projectile and the target as $N_{\mathrm{P}}^{(q)}$ and $N_{\mathrm{T}}^{(q)}$, respectively. In general, there holds $N_{\mathrm{PLF}}^{(q)} + N_{\mathrm{TLF}}^{(q)} < N_{\mathrm{P}}^{(q)} + N_{\mathrm{T}}^{(q)}$, since some nucleons are emitted to the continuum by the breakup process. As will be shown later, however, the number of nucleons emitted to the continuum is very small in the present calculations. The average number of transferred nucleons from the target to the projectile, $N_{\mathrm{tr}}^{\mathrm{P}(q)}$, is given by

$$N_{\mathrm{tr}}^{\mathrm{P}(q)} = N_{\mathrm{PLF}}^{(q)} - N_{\mathrm{P}}^{(q)}. \tag{3.2.2}$$

Figure 3.4 shows the average number of transferred nucleons, $N_{\mathrm{tr}}^{\mathrm{P}(q)}$, in (a) and (e), the neutron-to-proton ratios, N/Z, of the PLF and the TLF after collision in (b) and (f), the average number of nucleons emitted to the continuum in (c) and (g), and the fluctuation of the transferred nucleon number in (d) and (h), as functions of impact parameter b for $^{40,\,48}$Ca+^{124}Sn reactions.

In Fig. 3.4 (a) and (e), the average number of transferred neutrons is shown by filled symbols connected with solid lines, while the average number of transferred protons is shown by open symbols connected with dotted lines. Positive values indicate the increase of the projectile nucleons (transfer from ^{124}Sn to $^{40,\,48}$Ca) and negative values indicate the decrease (transfer from $^{40,\,48}$Ca to ^{124}Sn). As seen from Fig. 3.4 (a) and (e), a large value of average number of transferred nucleons is seen for ^{40}Ca+^{124}Sn at the impact parameter region close to the fusion critical impact parameter, while the average number of transferred nucleons is small for ^{48}Ca+^{124}Sn.

We show in Fig. 3.4 (b) and (f) the neutron-to-proton ratios, N/Z, of the PLF and the TLF. For the PLF, it is given by $N_{\mathrm{PLF}}^{(n)}/N_{\mathrm{PLF}}^{(p)}$, and for the TLF by $N_{\mathrm{TLF}}^{(n)}/N_{\mathrm{TLF}}^{(p)}$. Before the collision, the N/Z ratio is given by 1.00 for ^{40}Ca, 1.40 for ^{48}Ca, and 1.48 for ^{124}Sn. The N/Z ratio of the PLF (TLF) is denoted by filled (open) symbols connected with solid (dotted) lines. We also denote the N/Z ratio of the total system by a horizontal dashed line in the figure, 1.34 for ^{40}Ca+^{124}Sn and 1.46 for ^{48}Ca+^{124}Sn. We find the nucleons are transferred toward the direction of the charge equilibrium. Namely, protons are transferred from ^{40}Ca to ^{124}Sn, while neutrons are transferred from ^{124}Sn to ^{40}Ca in the ^{40}Ca+^{124}Sn reaction. The N/Z ratios of the projectile and the target do not differ much for ^{48}Ca+^{124}Sn, and we find a small number of transferred nucleons on average for this reaction. The average number of transferred nucleons decreases rapidly as the impact parameter increases. For the impact parameter region larger than $b \sim 6$ fm, the average number of transferred nucleons almost vanishes.

In Fig. 3.4 (c) and (g), we show the average number of nucleons emitted to the continuum, $N_{\mathrm{break\text{-}up}}^{(q)} \equiv (N_{\mathrm{P}}^{(q)} + N_{\mathrm{T}}^{(q)}) - (N_{\mathrm{PLF}}^{(q)} + N_{\mathrm{TLF}}^{(q)})$, during the time evolution. The average number of
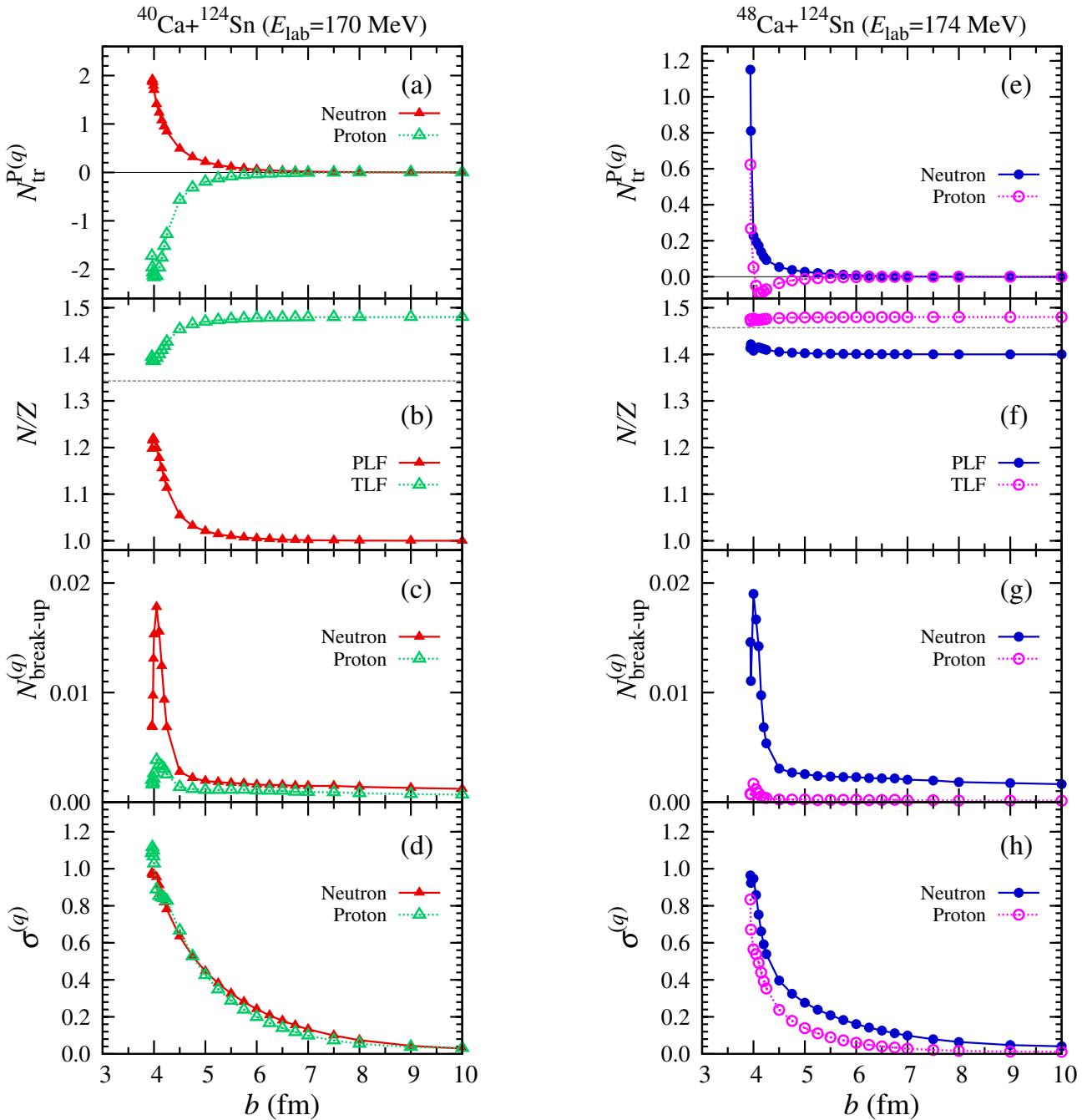
Figure 3.4: Left panels for ^{40}Ca+^{124}Sn at $E_{\text{lab}} = 170$ MeV and right panels for ^{48}Ca+^{124}Sn at $E_{\text{lab}} = 174$ MeV. (a) and (e): Average number of transferred nucleons from the target to the projectile. (b) and (f): Neutron-to-proton ratios, N/Z, of the PLF and the TLF after collision. (c) and (g): Average number of nucleons emitted to the continuum. (d) and (h): Fluctuation of transferred nucleon number. The horizontal axis is the impact parameter b. In (b) and (f), the equilibrium N/Z value of the total system is indicated by a horizontal dashed line. The figure was taken from Ref. [173].
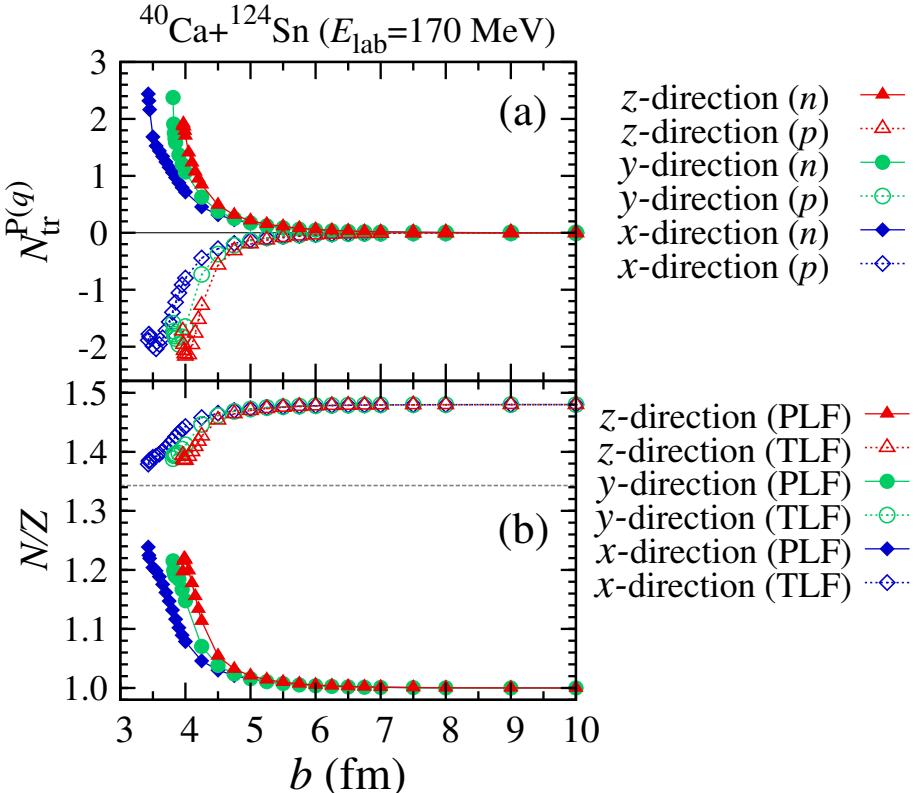
Figure 3.5: Comparison of calculated results for different initial orientations of ^{124}Sn in the ^{40}Ca+^{124}Sn reaction at E_{lab} = 170 MeV. (a): Average number of transferred nucleons from the target to the projectile. (b): Neutron-to-proton ratios, N/Z, of the PLF and the TLF after collision. The horizontal axis is the impact parameter b. The initial orientations of ^{124}Sn are indicated in legends. The figure was taken from Ref. [173].

neutrons (protons) emitted to the continuum is denoted by filled (open) symbols connected with solid (dotted) lines. As seen in the figure, the number of emitted nucleons is very small. The maximum value, about 0.02, is seen at the impact parameter close to the fusion critical impact parameter.

In Fig. 3.4 (d) and (h), we show the fluctuation of the transferred nucleon number. The expression for the fluctuation is given by Eq. (A.5.9). The fluctuation of the transferred neutron (proton) number is denoted by filled (open) symbols connected with solid (dotted) lines. We find the fluctuation decreases as the impact parameter increases. The fluctuation decreases more slowly than the average number of transferred nucleons as a function of impact parameter. We also find the fluctuation of ^{48}Ca+^{124}Sn is somewhat smaller than but comparable in magnitude to that of ^{40}Ca+^{124}Sn, although the average number is vanishingly small for ^{48}Ca+^{124}Sn.

As mentioned in the beginning of this Section, we placed the ^{124}Sn nucleus which is oblately deformed with $\beta \sim 0.11$ so that the symmetry axis is perpendicular to the reaction plane in the initial configuration. Namely, the symmetry axis of ^{124}Sn is set parallel to the z-axis. To take fully account of the deformation effect, we should achieve an average over initial orientations of the ^{124}Sn. However, since calculations of a number of initial orientations require huge computational costs, we do not achieve the orientation average but show results of a specific initial orientation. We here briefly discuss the difference of the reaction dynamics depending on the initial orientations.

In Fig. 3.5, we show the average number of transferred nucleons in (a) and the neutron-to-proton ratios, N/Z, of the PLF and the TLF after collision in (b), for three cases of different initial orientations of ^{124}Sn in the ^{40}Ca+^{124}Sn reaction. Red triangles are the same results as those shown in Fig. 3.4 (a)
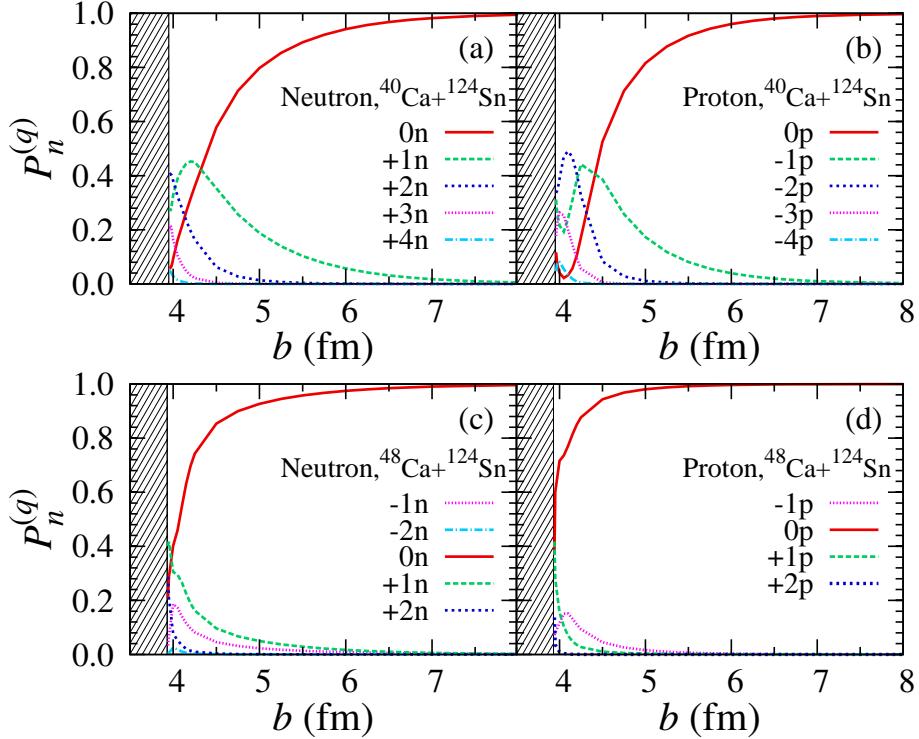
Figure 3.6: Neutron (left panels) and proton (right panels) transfer probabilities as functions of impact parameter b. (a) and (b): Results for the reactions of ^{40}Ca+^{124}Sn at $E_{\text{lab}} = 170$ MeV. (c) and (d): Results for the reactions of ^{48}Ca+^{124}Sn at $E_{\text{lab}} = 174$ MeV. The positive (negative) number of transferred nucleons represents the number of nucleons added to (removed from) the projectile. Shaded regions at small impact parameter ($b \leq 3.95$ fm for ^{40}Ca+^{124}Sn and $b \leq 3.93$ fm for ^{48}Ca+^{124}Sn) correspond to the fusion reactions. The figure was taken from Ref. [173].

and (b) where the symmetry axis of ^{124}Sn is chosen parallel to the z-axis. Green circles correspond to the cases of the symmetry axis set parallel to the y-axis (the direction of impact parameter vector). Blue diamonds correspond to the cases of the symmetry axis set parallel to the x-axis (the incident direction).

From the figure, we find a rather small difference among three cases of different initial orientations of ^{124}Sn. The prominent difference appears only at small impact parameter region. It comes from the difference of the fusion critical impact parameters. Since ^{124}Sn is oblately deformed, the Coulomb barrier height is the largest when the symmetry axis of the ^{124}Sn is parallel to the x-axis (the incident direction).

(b) Transfer probabilities

We next show transfer probabilities as functions of impact parameter which are obtained from the final wave functions using the PNP technique of Eq. (3.1.11). The nucleon transfer probabilities, $P_n^{(q)}(b)$, are shown in Fig. 3.6 (linear scale) and in Fig. 3.7 (logarithmic scale). Top panels of Fig. 3.6 ((a) and (b)) and top panels of Fig. 3.7 ((a), (b), (c), and (d)) show results of the ^{40}Ca+^{124}Sn reaction, while lower panels of Fig. 3.6 ((c) and (d)) and lower panels of Fig. 3.7 ((e), (f), (g), and (h)) show results of the ^{48}Ca+^{124}Sn reaction. In these figures, shaded regions at small impact parameter ($b \leq 3.95$ fm for ^{40}Ca+^{124}Sn and $b \leq 3.93$ fm for ^{48}Ca+^{124}Sn) correspond to the fusion reactions. The positive (negative) number of transferred nucleons represents the number of nucleons added to (removed from) the projectile.
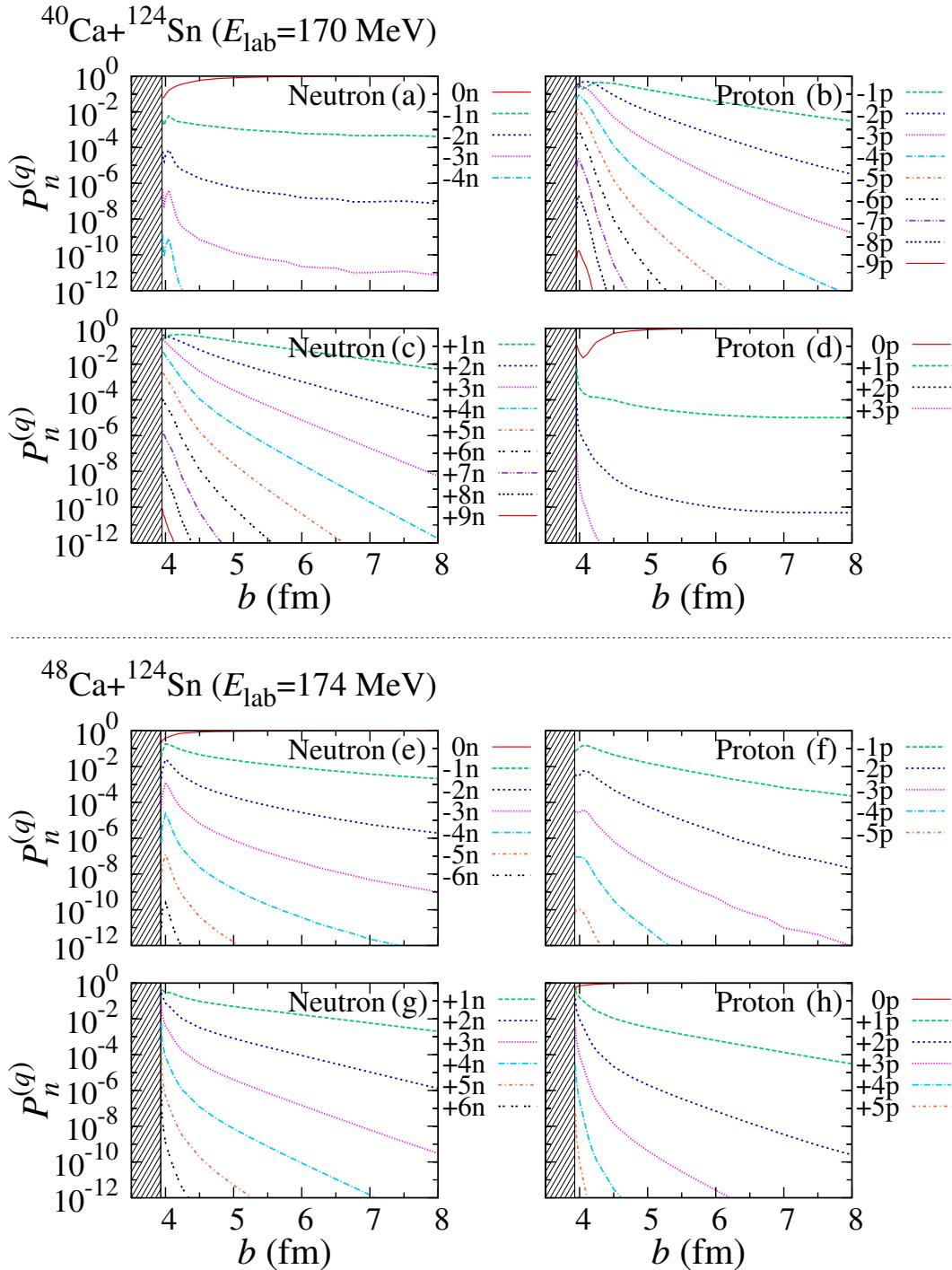
Figure 3.7: Transfer probabilities in Fig. 3.6 are shown in logarithmic scale. Nucleon transfer probabilities opposite to the direction of the charge equilibrium, which are not included in Fig. 3.6, are shown as well. The figure was taken from Ref. [173].
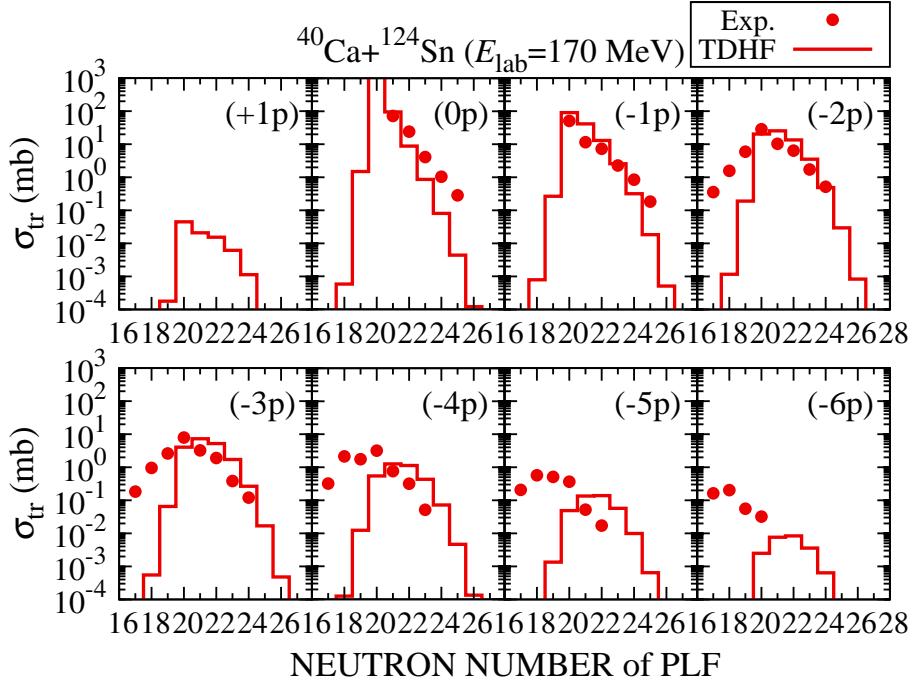
Figure 3.8: Cross sections for transfer channels classified according to the change of the proton number of the PLF from ^{40}Ca, as functions of neutron number of the PLF for the ^{40}Ca+^{124}Sn reaction at $E_{\mathrm{lab}} = 170$ MeV. Red filled circles denote measured cross sections and red solid lines denote results of the TDHF calculations. The number of transferred protons is indicated as $(x\mathrm{p})$ ($-6 \leq x \leq +1$). The measured cross sections have been reported in Ref. [40]. The figure was taken from Ref. [173].

From the figure, we find that probabilities of single-nucleon transfer (green dashed lines) extend to a large impact parameter region. As the number of transferred nucleons increases, the reaction probability is sizable only at a small impact parameter region, close to the fusion critical impact parameter.

The directions of the transfer processes are the same as those we observed in the average number of transferred nucleons in Fig. 3.4 (a) and (e). Namely, in the case of ^{40}Ca+^{124}Sn (Fig. 3.6 (a) and (b)), protons are transferred from ^{40}Ca to ^{124}Sn and neutrons are transferred from ^{124}Sn to ^{40}Ca, the directions toward the charge equilibrium. We note that the transfer probabilities toward the opposite directions, proton transfer from ^{124}Sn to ^{40}Ca and neutron transfer from ^{40}Ca to ^{124}Sn, are very small and are hardly seen in the linear scale figure (Fig. 3.6 (a) and (b)). In the logarithmic scale (Fig. 3.7 (a), (b), (c), and (d)), we find the transfer probabilities toward the opposite direction to the charge equilibrium are smaller than those toward the charge equilibrium by at least an order of magnitude. In the case of ^{48}Ca+^{124}Sn reaction (Fig. 3.6 (c) and (d), Fig. 3.7 (e), (f), (g), and (h)), the transfer probabilities toward both directions are the same order of magnitude. This is consistent with the fact that the average number of transferred nucleons is very small as shown in Fig. 3.4 (e).

(c) Transfer cross sections

Integrating the transfer probabilities over impact parameter, we obtain transfer cross sections. The results are shown in Fig. 3.8 for ^{40}Ca+^{124}Sn and in Fig. 3.9 for ^{48}Ca+^{124}Sn.

We first examine the ^{40}Ca+^{124}Sn reaction. Figure 3.8 shows the transfer cross sections classified according to the change of the proton number of the PLF from ^{40}Ca, as functions of neutron number of the PLF. Red filled circles denote measured cross sections and red solid lines denote results of the TDHF calculations. We show transfer cross sections of one proton added to (+1p) through six proton
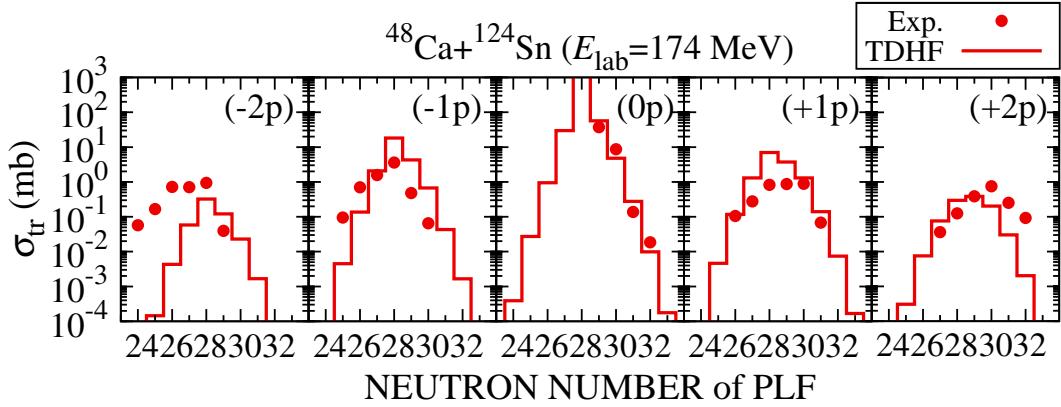
Figure 3.9: Cross sections for transfer channels classified according to the change of the proton number of the PLF from ^{48}Ca, as functions of neutron number of the PLF for the ^{48}Ca+^{124}Sn reaction at $E_{lab} = 174$ MeV. Red filled circles denote measured cross sections and red solid lines denote results of the TDHF calculations. The number of transferred protons is indicated as (xp) $(-2 \leq x \leq +2)$. The measured cross sections have been reported in Ref. [43]. The figure was taken from Ref. [173].

removed from $(-6p)$ ^{40}Ca.

We find the experimental data are reasonably reproduced by the TDHF calculations for cross sections without proton transfer shown in (0p) panel, although the cross sections are somewhat underestimated as the number of transferred neutrons increases. Zero- to four-neutron pick-up channels shown in $(-1p)$, $(-2p)$, and $(-3p)$ panels are also reproduced reasonably. The calculated cross sections toward the direction opposite to the charge equilibrium are small, consistent with the observation in transfer probabilities shown in Fig. 3.7 (a) and (d).

As the number of transferred protons increases, there appear some discrepancies between the TDHF calculations and the measurements. When more than one protons are transferred, the TDHF calculation underestimates measured cross sections of neutron removal channels $(N < 20)$. For five- and six-proton removal channels, $(-5p)$ and $(-6p)$, the TDHF cross sections become too small compared with the measurements. We also find a shift of the peak position toward the larger neutron number.

In Ref. [40], cross sections calculated by the GRAZING code [67] were compared with the measurements. In the GRAZING calculation, a similar discrepancy was observed. As the origin of the discrepancy, the significance of the evaporation effects has been mentioned [40]. We will compare our results with those of the GRAZING calculations in Sec. 3.3.

We note that particle evaporation processes are not taken into account sufficiently in the present calculation. In Fig. 3.1 (b), we find the TKEL of as large as 25 MeV at a small impact parameter region where appreciable MNT probabilities are found. The amount of the TKEL is sufficiently large to emit some nucleons to the continuum. However, as we saw in Fig. 3.4 (c), the average number of nucleons emitted to the continuum is very small, the maximum value is only 0.02. Although we have not yet estimated the number of evaporated nucleons, the inclusion of the evaporation processes is expected to reduce the discrepancy as follows. Neutron evaporation processes will shift the peak position of the transfer cross sections toward the smaller neutron number (left direction in Fig. 3.8). We may also expect that proton evaporation processes will shift cross section of n-proton removal channels to $(n + 1)$-proton removal channels.

Figure 3.9 shows transfer cross sections of ^{48}Ca+^{124}Sn reaction. The cross sections obtained from the TDHF calculations are in good agreement with the experimental data for zero- and one-proton transfer channels, (0p) and $(\pm 1p)$. For two-proton transfer channels $(\pm 2p)$, however, our TDHF
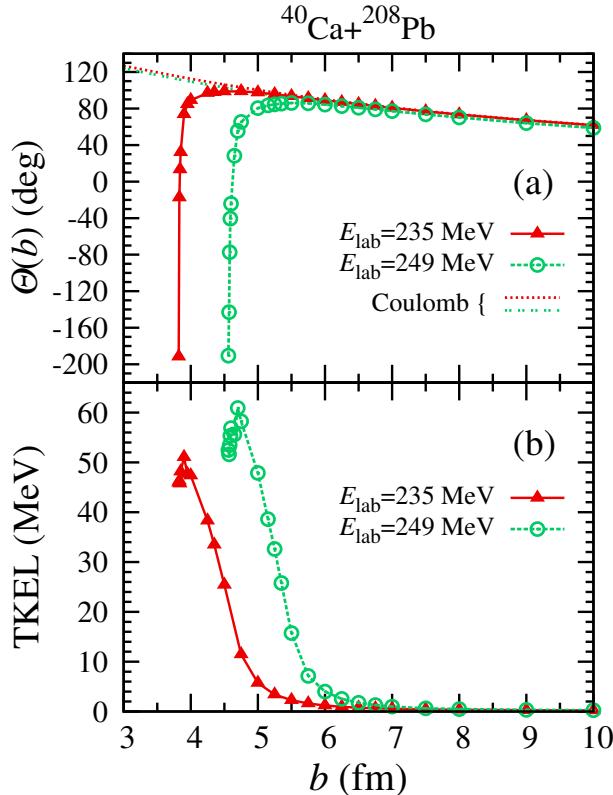
Figure 3.10: Deflection function (a) and total kinetic energy loss (b) as functions of impact parameter b for the reactions of ^{40}Ca+^{208}Pb at $E_{\text{lab}} = 235$ and 249 MeV. Results for the reactions at $E_{\text{lab}} = 235$ MeV are denoted by red filled triangles connected with solid lines, while results for the reactions at $E_{\text{lab}} = 249$ MeV are denoted by green open circles connected with dashed lines. In (a), we also show deflection functions for the pure Coulomb trajectories at $E_{\text{lab}} = 235$ MeV by a red dotted line and at $E_{\text{lab}} = 249$ MeV by a green two-dot chain line. The figure was taken from Ref. [173].

calculations underestimate the cross sections. In the case of two-proton removal channels (-2p), the peak position shifts toward larger neutron number, while in the case of two-proton pickup channels ($+2$p), the peak position shifts toward smaller neutron number. The underestimation in the (-2p) channels may be remedied by taking into account the neutron evaporation processes as in the case of ^{40}Ca+^{124}Sn reaction. However, the underestimation in the ($+2$p) channels may not. A similar discrepancy was reported in the GRAZING calculation [43]. In Ref. [43], more complex mechanisms such as neutron-proton pair transfer and/or α-cluster transfer have been advocated for the origin of the discrepancy.

3.2.2 ^{40}Ca+^{208}Pb reaction

In this Subsection, we present results for the reactions of ^{40}Ca+^{208}Pb at $E_{\text{lab}} = 235$ and 249 MeV ($E_{\text{c.m.}} \simeq 197.1$ and 208.8 MeV), for which measurements have been reported in Ref. [50]. This system has $Z_{\text{P}}Z_{\text{T}} = 1640$, close to 1600. Therefore, we expect an appearance of the indication of the fusion-hindrance. We estimate the Coulomb barrier height of this system using the frozen-density approximation, giving $V_{\text{B}} \approx 178.4$ MeV. Since the collision energies are higher than the barrier height, we find finite values of the fusion critical impact parameter b_{f}, as in the ^{40,48}Ca+^{124}Sn reactions. They are given by $b_{\text{f}} = 3.81$ and 4.55 fm at $E_{\text{lab}} = 235$ and 249 MeV, respectively.
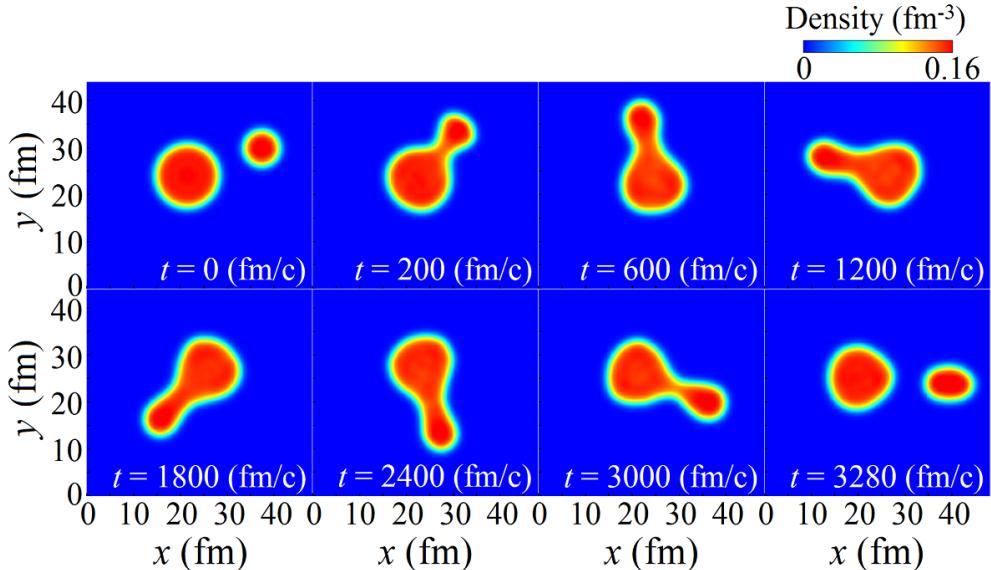
Figure 3.11: Snapshots of density distribution of the ^{40}Ca+^{208}Pb reaction at $E_{\mathrm{lab}} = 249$ MeV and $b = 4.56$ fm, just outside the fusion critical impact parameter. The figure was taken from Ref. [173].

(a) Overview of the reactions

We first present an overview of the reaction dynamics. In Fig. 3.10, we show the deflection function in (a) and the TKEL in (b), as functions of impact parameter. Results for the reaction at $E_{\mathrm{lab}} = 235$ MeV are denoted by red filled triangles connected with solid lines, while results for the reaction at $E_{\mathrm{lab}} = 249$ MeV are denoted by green open circles connected with dotted lines. In Fig. 3.10 (a), we also show deflection functions for the pure Coulomb trajectories at $E_{\mathrm{lab}} = 235$ MeV by a red dotted line and at $E_{\mathrm{lab}} = 249$ MeV by a green two-dot chain line. In this system, we find an increase of the TKEL up to around 50 MeV and 60 MeV for the incident energies of 235 MeV and 249 MeV, respectively. This maximum value of TKEL is about a factor of two larger than the case of ^{40,48}Ca+^{124}Sn reactions. We find the difference of the TKEL between these systems, ^{40}Ca+^{208}Pb and ^{40,48}Ca+^{124}Sn, comes from properties of the neck whose formation is observed when the TKEL becomes substantial.

In Fig. 3.11, we show snapshots of density distribution for the ^{40}Ca+^{208}Pb reaction at $E_{\mathrm{lab}} = 249$ MeV and $b = 4.56$ fm, just outside the fusion critical impact parameter. The neck is seen to be formed solidly for a long period from $t = 200$ fm/c to 3000 fm/c. This process may be regarded as a QF. As will be shown below, a number of nucleons are transferred from ^{208}Pb to ^{40}Ca at this impact parameter.

The period of the neck formation is longer in the present ^{40}Ca+^{208}Pb case than that in the ^{40,48}Ca+^{124}Sn cases. We find the neck formation for the periods of 1000-3000 fm/c and more for the present system depending on the impact parameter, while it is at most 300 fm/c in the ^{40,48}Ca+^{124}Sn systems. We consider this difference is related to the different $Z_{\mathrm{P}}Z_{\mathrm{T}}$ values of these systems. Since $Z_{\mathrm{P}}Z_{\mathrm{T}} \gtrsim 1600$ in the present system, fusion reactions are hindered by the QF process. Namely, there appears a certain impact parameter region in which binary final fragments are produced after a rather solid neck formation during the collision.

The Coulomb rainbow angle is $\theta_{\mathrm{r}} \simeq 99°$ for the reaction at $E_{\mathrm{lab}} = 235$ MeV and $\theta_{\mathrm{r}} \simeq 86°$ for the reaction at $E_{\mathrm{lab}} = 249$ MeV, respectively. The deflection function becomes negative at the small impact parameter region, reaching $-200°$ just outside b_{f}. In Fig. 3.12, we compare the Coulomb rainbow angles for the ^{40}Ca+^{208}Pb reactions at $E_{\mathrm{lab}} = 235$ and 249 MeV with measured differential cross sections which have been reported in Ref. [50]. Red filled triangles denote measured cross sections for $E_{\mathrm{lab}} = 235$ MeV, while green open circles denote those for $E_{\mathrm{lab}} = 249$ MeV. The Coulomb rainbow
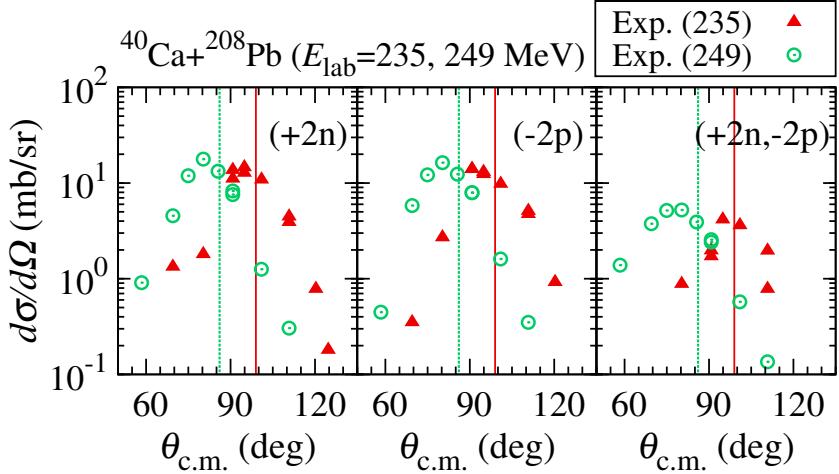
Figure 3.12:   Differential cross sections of representative transfer channels as functions of scattering angle in the center-of-mass frame for the ^{40}Ca+^{208}Pb reactions at $E_{\text{lab}} = 235$ and 249 MeV. The Coulomb rainbow angle obtained from the TDHF trajectories is denoted by red solid (green dotted) vertical lines for $E_{\text{lab}} = 235$ (249) MeV. They are compared with measured differential cross sections, red filled triangles (green open circles) for $E_{\text{lab}} = 235$ (249) MeV, which have been reported in Ref. [50]. The figure was taken from Ref. [173].

angle obtained from the TDHF trajectories is denoted by red solid (green dotted) vertical lines for $E_{\text{lab}} = 235$ (249) MeV. We find the peak positions of measured angular distributions are reasonably reproduced by the TDHF calculation.

Figure 3.13 shows the average number of transferred nucleons in (a), the N/Z ratios of the PLF and the TLF in (b), the average number of nucleons emitted to the continuum in (c), and the fluctuation of the transferred nucleon number in (d), as functions of impact parameter. In each panel, triangles represent results for $E_{\text{lab}} = 235$ MeV and circles represent results for $E_{\text{lab}} = 249$ MeV.

In Fig. 3.13 (a), the average number of transferred neutrons is shown by filled symbols connected with solid lines, while the average number of transferred protons is shown by open symbols connected with dotted lines. Positive values indicate the increase of the projectile nucleons (transfer from ^{208}Pb to ^{40}Ca) and negative values indicate the decrease (transfer from ^{40}Ca to ^{208}Pb). As seen from the figure, the average number of transferred protons shows a minimum at a certain impact parameter ($b = 4.0$ fm for $E_{\text{lab}} = 235$ MeV and $b = 5.0$ fm for $E_{\text{lab}} = 249$ MeV). Outside this impact parameter, the nucleon transfer process proceeds toward the direction of the charge equilibrium of the projectile and the target. Inside this impact parameter, neutrons are still transferred toward the same direction. However, the number of transferred protons decreases and becomes positive, which corresponds to the transfer from ^{208}Pb to ^{40}Ca.

At first sight, the direction of the proton transfer at small impact parameter region is opposite to the direction of the charge equilibrium. However, it is not the case as can be understood from Fig. 3.13 (b) which shows the neutron-to-proton ratios, N/Z, of the PLF (filled symbols connected with solid lines) and the TLF (open symbols connected with dotted lines), which are obtained from the average numbers of the nucleons shown in Fig. 3.13 (a). Before collision, the N/Z ratio is given by 1.00 for ^{40}Ca and 1.54 for ^{208}Pb. In Fig. 3.13 (b), the N/Z ratio of the total system, 1.43, is shown by a horizontal dashed line. As seen from the figure, the nucleon transfer processes proceed toward the direction of the charge equilibrium for both the PLF and the TLF at all impact parameter region outside the fusion critical impact parameter. Even though the average number of transferred protons shows complex behavior at small impact parameter region, the N/Z ratios of the PLF and the TLF

monotonically approach to the fully equilibrated value of 1.43 as the impact parameter decreases.
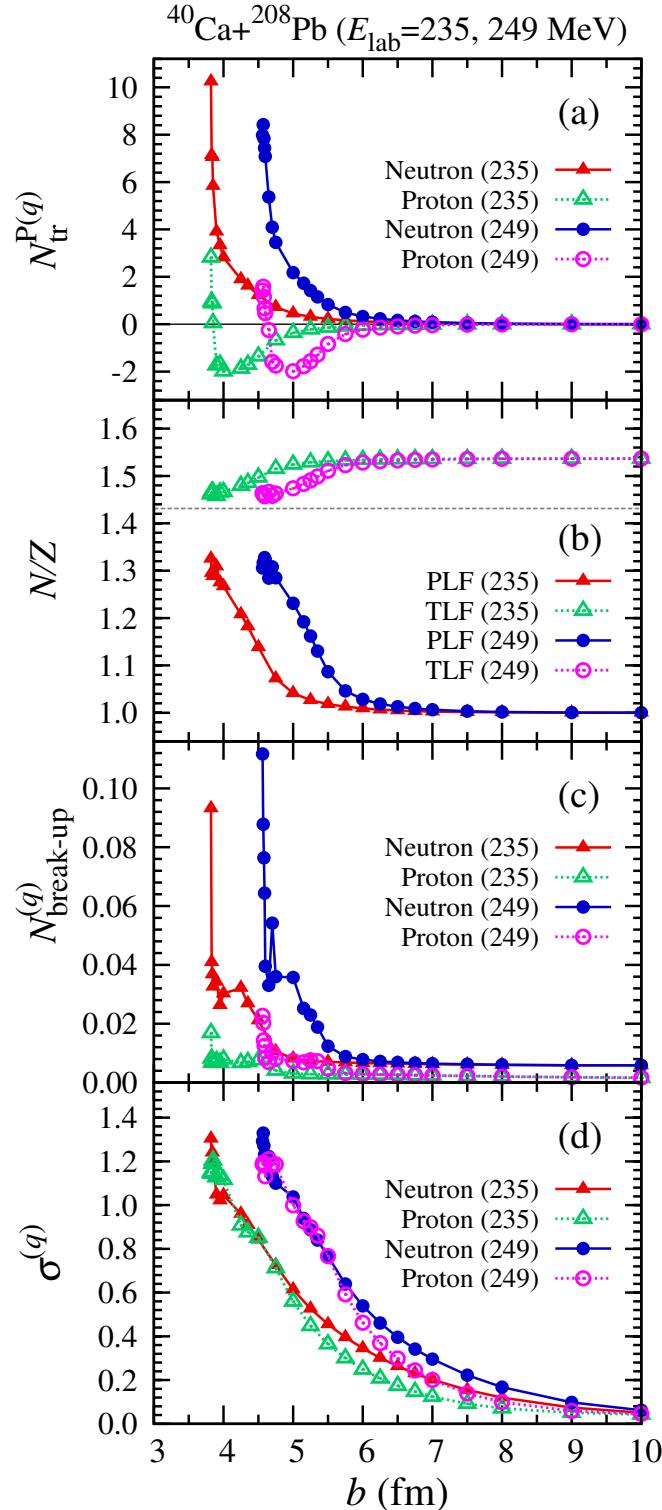
Figure 3.13: The ^{40}Ca+^{208}Pb reactions at E_{lab} = 235 and 249 MeV. (a): Average number of transferred nucleons from the target to the projectile. (b): Neutron-to-proton ratios, N/Z, of the PLF and the TLF after collision. (c): Average number of nucleons emitted to the continuum. (d): Fluctuation of transferred nucleon number. The horizontal axis is the impact parameter b. Results for the reactions at E_{lab} = 235 MeV are denoted by triangles, while results for the reactions at E_{lab} = 249 MeV are denoted by circles. In (b), the equilibrium N/Z value of the total system, 1.43, is indicated by a horizontal dashed line. The figure was taken from Ref. [173].

The change of sign of the average number of transferred protons at small impact parameter region is found to be related to the formation of a rather solid neck. When the neck is broken, we find that most part of the neck is absorbed by the lighter fragment (*cf.* Fig. 3.11). Since the neck is composed of both neutrons and protons, the absorption of the nucleons in the neck region results in the increase of average number of nucleons in the PLF for both neutrons and protons (see Fig. 3.13 (a)).

In Fig. 3.13 (c), we show the average number of nucleons emitted to the continuum during the time evolution. The average number of neutrons (protons) emitted to the continuum is denoted by filled (open) symbols connected with solid (dotted) lines. We count it by subtracting the number of nucleons inside a sphere of 14 fm for the TLF and that inside a sphere of 10 fm for the PLF from the total number of nucleons, 248. The average number of emitted nucleons is again very small, at most 0.1 around the fusion critical impact parameter.

In Fig. 3.13 (d), we show the fluctuation of the transferred nucleon number. The fluctuation of transferred neutron (proton) number is denoted by filled (open) symbols connected with solid (dotted) lines. The fluctuation increases monotonically as the impact parameter decreases, reaching the maximum value roughly 1.3 around the fusion critical impact parameter. Although the average number of transferred protons is small at the small impact parameter region, the fluctuation of transferred proton number has value as large as that of neutrons. This fact indicates that single-particle wave functions of protons are exchanged actively between the projectile and the target, although the number of transferred protons is small on average.

(b)   Transfer probabilities

The nucleon transfer probabilities, $P_n^{(q)}(b)$, are shown in Fig. 3.14. Top panels ((a), (b), (c), and (d)) show results at $E_\mathrm{lab} = 235$ MeV, while lower panels ((e), (f), (g), and (h)) show results at $E_\mathrm{lab} = 249$ MeV. In the figure, shaded regions at small impact parameter ($b \leq 3.81$ fm for $E_\mathrm{lab} = 235$ MeV and $b \leq 4.55$ fm for $E_\mathrm{lab} = 249$ MeV) correspond to the fusion reactions. The positive (negative) number of transferred nucleons represents the number of nucleons added to (removed from) the projectile. In the left panels ((a), (c), (e), and (g)), we show transfer probabilities, (0n) to (+4n) for neutrons and (0p) to (−4p) for protons. In the right panels ((b), (d), (f), and (h)), we show transfer probabilities, (+1n) to (+9n) for neutrons and (−4p) to (+4p) for protons, at small impact parameter regions just outside the fusion critical impact parameter. Probabilities of neutron transfer from ^{40}Ca to ^{208}Pb are very small and are not shown.

As in the case of $^{40, 48}$Ca+^{124}Sn reactions, we find that probabilities of single-nucleon transfer (green dashed lines) extend to a large impact parameter region. Reaction probabilities for MNT processes become appreciable at a small impact parameter region close to the fusion critical impact parameter. The transfer probabilities toward the charge equilibrium are large in most cases. At a small impact parameter region just outside the fusion critical impact parameter, however, we find substantial probabilities for the proton transfer processes opposite to the charge equilibrium as seen in the right panels of Fig. 3.14 ((b), (d), (f), and (h)). This is related to the increase of the average number of transferred protons at small impact parameter region which was seen in Fig. 3.13 (a).
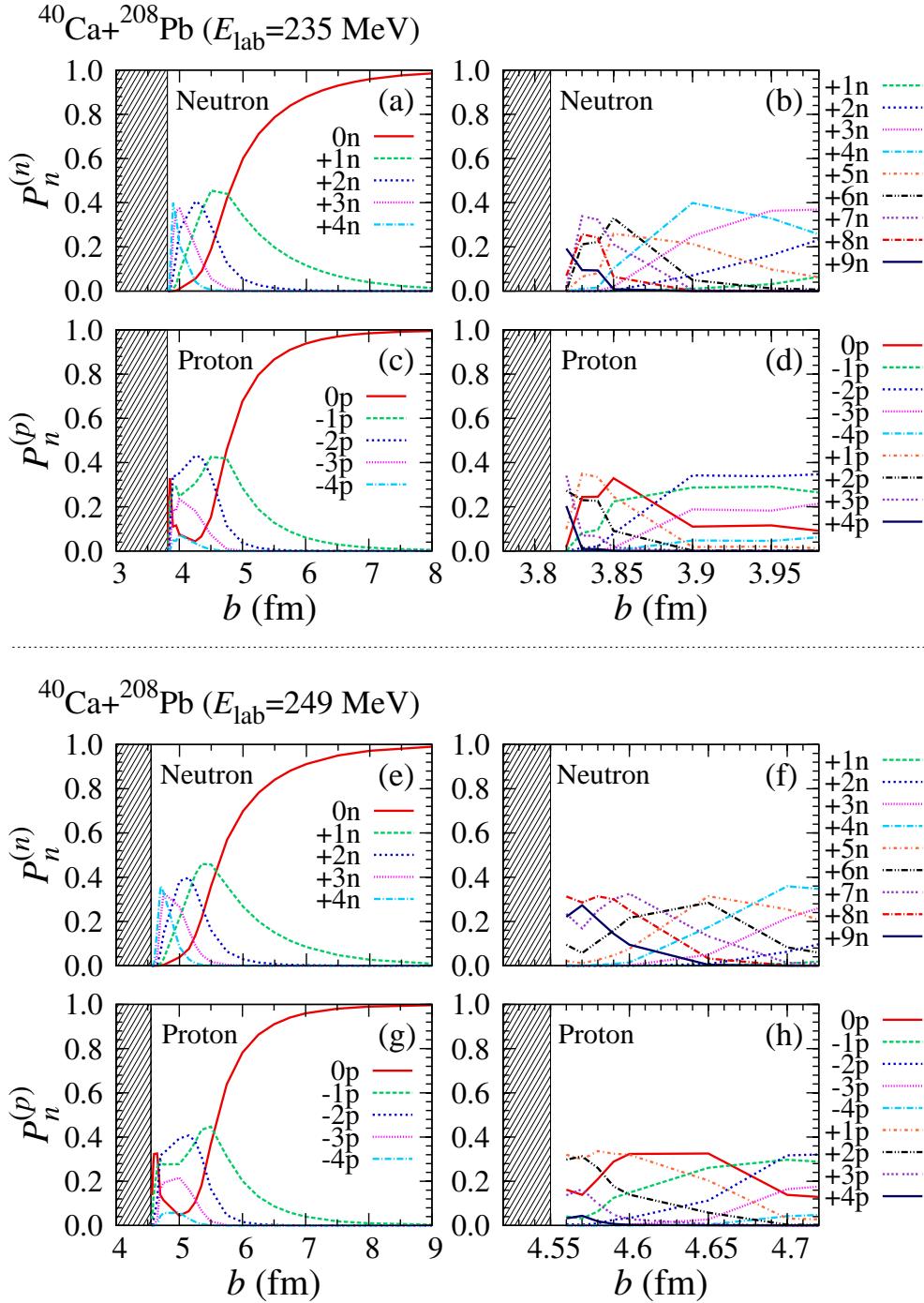
Figure 3.14: Neutron and proton transfer probabilities as functions of impact parameter b for the ^{40}Ca+^{208}Pb reactions. (a), (b), (c), and (d): Results at $E_{\text{lab}} = 235$ MeV. (e), (f), (g), and (h): Results at $E_{\text{lab}} = 249$ MeV. The positive (negative) number of transferred nucleons represents the number of nucleons added to (removed from) the projectile. Note that horizontal scales are different between the left and the right panels. Shaded regions at small impact parameter ($b \leq 3.81$ fm for $E_{\text{lab}} = 235$ MeV and $b \leq 4.55$ fm for $E_{\text{lab}} = 249$ MeV) correspond to the fusion reactions. The figure was taken from Ref. [173].
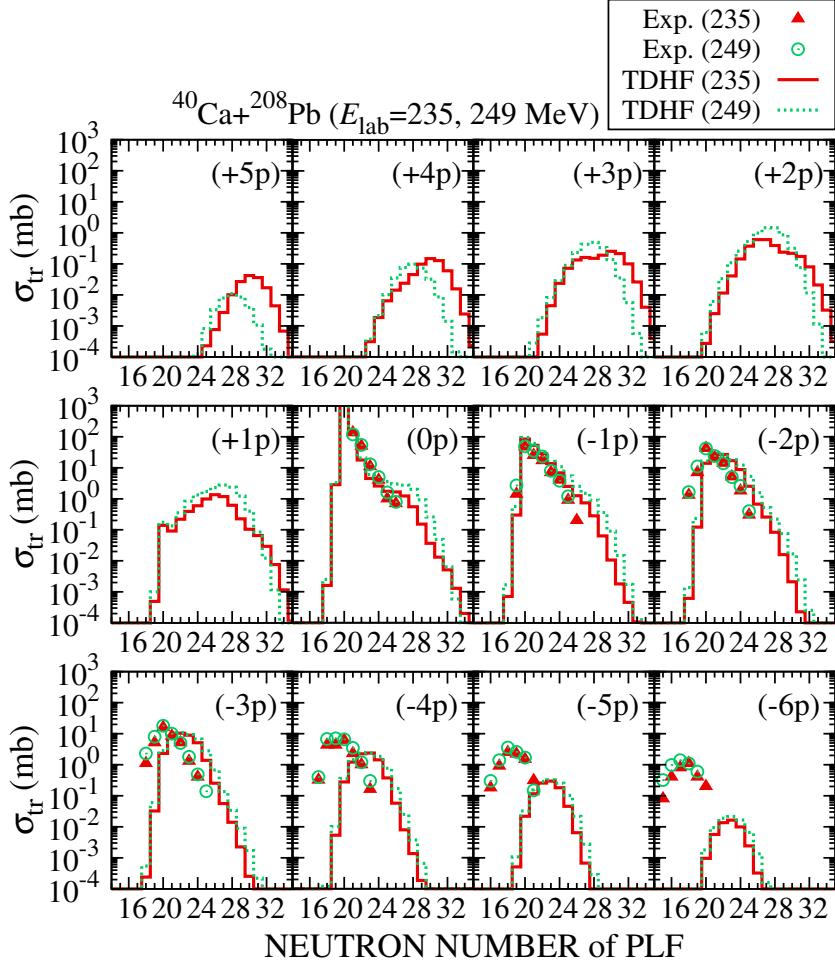
Figure 3.15: Transfer cross sections for the ^{40}Ca+^{208}Pb reactions at $E_{\mathrm{lab}} = 235$ and 249 MeV. Red filled triangles (green open circles) denote measured cross sections at $E_{\mathrm{lab}} = 235$ (249) MeV. Red solid (green dotted) lines denote results of the TDHF calculations at $E_{\mathrm{lab}} = 235$ (249) MeV. The number of transferred protons (positive number for the transfer from ^{208}Pb to ^{40}Ca) is indicated as $(x\mathrm{p})$ ($-6 \leq x \leq +5$). The measured cross sections have been reported in Ref. [50] The figure was taken from Ref. [173]**.

(c) Transfer cross sections

We show transfer cross sections in Figs. 3.15 and 3.16. Each panel of Fig. 3.15 shows cross sections classified according to the change of the proton number of the PLF from ^{40}Ca which is indicated by $(x\mathrm{p})$ ($-6 \leq x \leq +5$), as functions of neutron number of the PLF. Each panel of Fig. 3.16 shows cross sections classified according to the change of the neutron number of the PLF from ^{40}Ca which is indicated by $(x\mathrm{n})$ ($-5 \leq x \leq +9$), as functions of proton number of the PLF. Red filled triangles denote measured cross sections for $E_{\mathrm{lab}} = 235$ MeV, while green open circles denote those for $E_{\mathrm{lab}} = 249$ MeV. Cross sections calculated by the TDHF are denoted by red solid (green dotted) lines for $E_{\mathrm{lab}} = 235$ (249) MeV. As seen in the average number of transferred nucleons in Fig. 3.13 (a) and in the transfer probabilities in Fig. 3.14, the transfer cross sections toward the direction of the charge equilibrium dominate.

In (0p) and (-1p) panels of Fig. 3.15, the TDHF calculation is seen to reproduce the measured

---

**A mistake was found in Fig. 15 of Ref. [173]: In panel (-6p) in Ref. [173], cross sections for (-7p) channel are shown. Erratum will be published. Figure 3.15 shows correct cross sections.
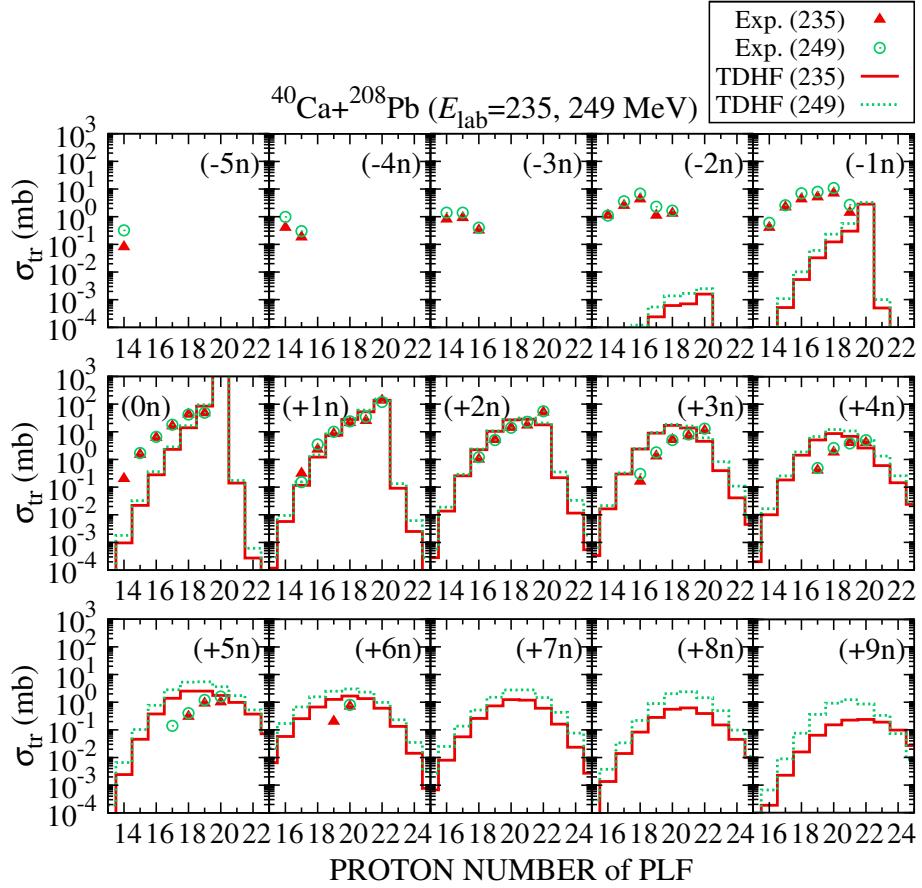
Figure 3.16: The same transfer cross sections for the ^{40}Ca+^{208}Pb reactions as those in Fig. 14. The number of transferred neutrons is indicated as (xn) $(-5 \leq x \leq +9)$. The figure was taken from Ref. [173].

cross sections up to six-neutron transfer. As the number of transferred protons increases, $(-2p)$ to $(-6p)$, the cross sections in the TDHF calculation show a maximum at a neutron number more than that of ^{40}Ca. Compared with measured cross sections, the TDHF results shift toward larger values of neutron number. This behavior is similar to the case of ^{40}Ca+^{124}Sn reaction. Looking at the transfer cross sections for a fixed number of transferred neutrons in Fig. 3.16, the TDHF calculations reproduce $(+1n)$ and $(+2n)$ panels rather well.

As seen in Fig. 3.15, the TDHF calculations provide substantial cross sections for proton pickup reactions, $(+1p)$ to $(+5p)$, which is the transfer toward the opposite direction of the charge equilibrium expected from the initial N/Z ratios. The cross sections show a peak around the neutron number 28. The TDHF calculations also provide substantial cross sections for many neutron pickup reactions (see bottom row of Fig. 3.16). The cross sections show a peak around the proton number 20. These cross sections come from an impact parameter region close to the fusion critical impact parameter. As seen in Fig. 3.13 (a), a large average number of transferred neutrons up to 10 is seen while the average number of transferred protons has small value. We note that the collision close to the fusion critical impact parameter accompanies large TKEL, and should suffer substantial evaporation effects which are not treated in the present analyses.

The TDHF calculation systematically underestimates the cross section of neutron transfer processes from ^{40}Ca to ^{208}Pb, $(-1n)$ to $(-5n)$ (see top row of Fig. 3.16). Although these processes are against the charge equilibrium, substantial cross sections are observed experimentally. In the TDHF calculation, cross sections of neutron transfer channels opposite to the charge equilibrium are several
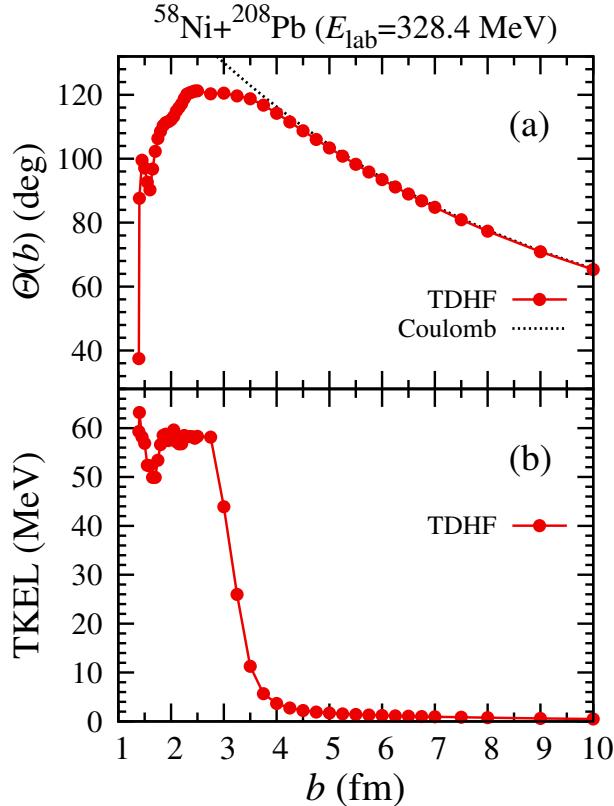
Figure 3.17:   Deflection function (a) and total kinetic energy loss (b) as functions of impact parameter b for the reactions of ^{58}Ni+^{208}Pb at $E_{lab} = 328.4$ MeV. In (a), we show a deflection function for the pure Coulomb trajectory by a dotted line. The figure was taken from Ref. [173].

orders of magnitude smaller than the measurements. In Ref. [50], it has been argued that the neutron evaporation after collision is responsible for these channels.

3.2.3 ^{58}Ni+^{208}Pb reaction

As a final case, we present results for the ^{58}Ni+^{208}Pb reaction at $E_{lab} = 328.4$ MeV ($E_{c.m.} \simeq$ 256.8 MeV), for which measurements are reported in Ref. [47]. Since this system has $Z_P Z_T = 2296$ exceeding the critical value 1600, we may expect an appearance of the QF process at a small impact parameter region. Using the frozen-density approximation, the Coulomb barrier height is estimated to be $V_B \approx 247.6$ MeV, which is lower than the center-of-mass energy. We find the fusion critical impact parameter b_f given by 1.38 fm for this reaction. To decide whether the nucleus once gets fused eventually decays into fragments or not, we continue to calculate the time evolution up to 4000 fm/c after two nuclei touches. If the fused system keeps a compact form for this period, we regard the process as fusion.

(a)   Overview of the reaction

We first present an overview of the reaction dynamics. In Fig. 3.17, we show the deflection function in (a) and the TKEL in (b), as functions of impact parameter. In (a), we also show a deflection function for the pure Coulomb trajectory by a dotted line. The Coulomb rainbow occurs at the impact parameter of 2.5 fm and the rainbow angle is $\theta_r \simeq 121°$. In Fig. 3.18, we compare the Coulomb rainbow angle with measured differential cross sections which have been reported in Ref. [47]. Red filled circles denote measured cross sections and blue solid vertical lines denote the Coulomb rainbow angle. From
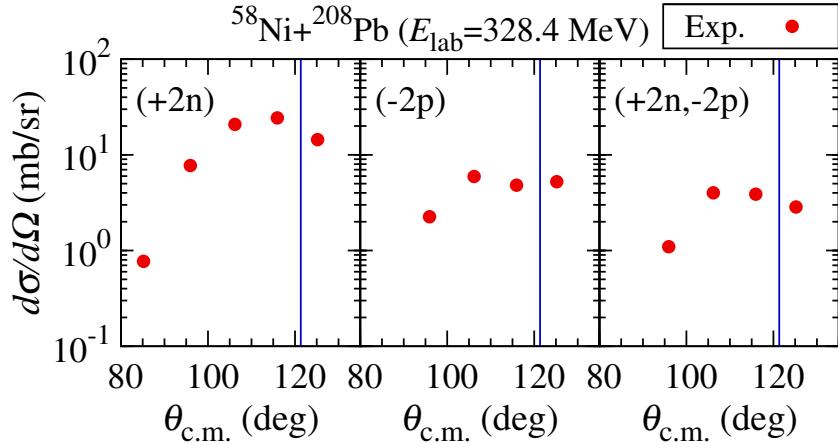
Figure 3.18: Differential cross sections of representative transfer channels as functions of scattering angle in the center-of-mass frame for the ^{58}Ni+^{208}Pb reaction at $E_{\rm lab} = 328.4$ MeV. The Coulomb rainbow angle obtained from the TDHF trajectories is denoted by blue solid vertical lines, and is compared with measured differential cross sections, red filled circles, which have been reported in Ref. [47]. The figure was taken from Ref. [173].

the figure, we find the measured differential cross sections show rather flat distributions compared with lighter systems. This may be related to a rather small curvature of the deflection function around the Coulomb rainbow angle obtained from the TDHF trajectories as seen in Fig. 3.17 (a).

The TKEL shows a behavior different from lighter systems. The maximum TKEL is about 50-60 MeV, similar to the value observed in ^{40}Ca+^{208}Pb reaction. However, there is a large impact parameter region, from 1.39 fm to 2.75 fm, in which the TKEL takes approximately the same value.

In Fig. 3.19, we show snapshots of density distribution for the ^{58}Ni+^{208}Pb reaction at the impact parameter of 1.39 fm, just outside the fusion critical impact parameter. In the course of the collision, colliding nuclei form a rather thick neck and excurse for a long period connected by the neck. We find the two nuclei are connected for a period as long as 3600 fm/c. For collisions in the impact parameter region where the TKEL takes values around 50-60 MeV, we find a formation of a similar thick neck which persists rather long period. These reactions are considered to correspond to the QF.

Figure 3.20 shows the average number of transferred nucleons in (a), the N/Z ratios of the PLF and the TLF in (b), the average number of nucleons emitted to the continuum in (c), and the fluctuation of the transferred nucleons in (d), as functions of impact parameter.

In Fig. 3.20 (a), the average number of transferred neutrons is shown by red filled circles connected with solid lines, while the average number of transferred protons is shown by green open circles connected with dotted lines. Positive numbers indicate the increase of the projectile nucleons (transfer from ^{208}Pb to ^{58}Ni) and negative numbers indicate the decrease (transfer from ^{58}Ni to ^{208}Pb). From the figure, we find the average number of transferred protons shows a minimum at $b = 2.75$ fm. We note that this value coincides with the impact parameter inside which the TKEL becomes almost constant in Fig. 3.17 (b). A similar minimum was also seen in the ^{40}Ca+^{208}Pb case, as shown in Fig. 3.13 (a). Outside this impact parameter, nucleons are transferred toward the direction of the charge equilibrium expected from the initial N/Z ratios. In the impact parameter region, 1.55 fm $\leq b \leq$ 2.75 fm, the average number of transferred nucleons increases as the impact parameter decreases for both neutrons and protons. A similar behavior was also seen in ^{40}Ca+^{208}Pb reaction as in Fig. 3.13 (a).

At the impact parameter region $b < 1.85$ fm, the average number of transferred protons becomes positive, opposite to the direction of the charge equilibrium of the initial system. However, the nucleon transfer still proceeds toward the charge equilibrium of both the PLF and the TLF after the collision.
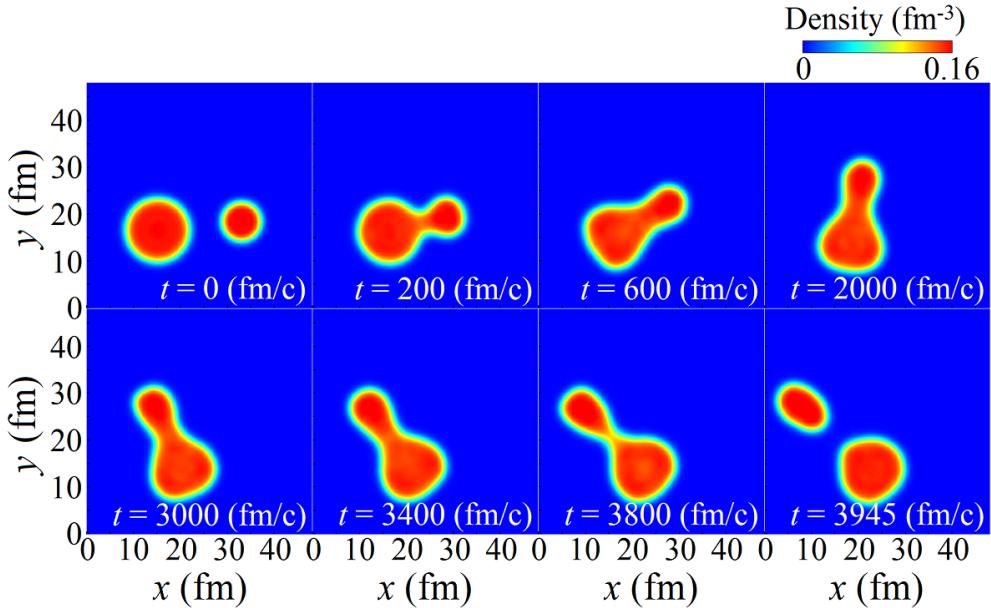
Figure 3.19: Snapshots of density distribution of the ^{58}Ni+^{208}Pb reaction at $E_{\text{lab}} = 328.4$ MeV and $b = 1.39$ fm, just outside the fusion critical impact parameter. The figure was taken from Ref. [173].

This is clearly seen in Fig. 3.20 (b) which shows the N/Z ratios of the PLF and the TLF after collision. The N/Z ratio of the PLF (TLF) is denoted by red filled (green open) circles connected with solid (dotted) lines. As seen from the figure, the N/Z ratios of both the PLF and the TLF become closer to the N/Z ratio of the total system, 1.42, which is represented by a horizontal dashed line.

As mentioned in the case of ^{40}Ca+^{208}Pb reactions, the change in the average number of transferred protons across the impact parameter $b \sim 3$ fm is related to the formation of the neck. Outside $b \sim 3$ fm, the neck is not formed and two nuclei are separated even at the closest approach. In such case, nucleons are transferred toward the direction of the charge equilibrium expected from the initial N/Z ratios. Inside $b \sim 3$ fm, the neck is formed between two nuclei. Then the transfer of nucleons proceeds in two steps. Before the formation of the neck, the transfer of nucleons proceeds toward the charge equilibrium of the initial system in the same way as that in $b > 3$ fm. After the formation of the neck, an exchange of a large number of nucleons occurs at the time of the breaking of the neck. Depending on the position of the neck breaking, the transfer of nucleons is expected in either directions, from the target to the projectile or the reverse. Since the neck is formed with both protons and neutrons, the nucleon transfer in the neck breaking process accompanies both protons and neutrons in the same direction.

Looking at Fig. 3.20 (a), we find the increase of the average numbers of transferred nucleons of both neutrons and protons as the impact parameter decreases below $b = 2.75$ fm. This indicates that the neck is broken at the position close to the target. Both protons and neutrons in the neck region are absorbed by the projectile. This mechanism explains the reason why the number of transferred protons increases as the impact parameter decreases in Fig. 3.20 (a). This transfer process associated with the neck breaking was also seen in the $^{40, 48}$Ca+^{124}Sn and the ^{40}Ca+^{208}Pb reactions.

At very small impact parameter region, 1.40 fm $\leq b \leq$ 1.50 fm, the average number of transferred neutrons shows a large fluctuation. The average number of transferred protons also shows the fluctuation, correlated with that of neutrons. These fluctuations occur by changes of the breaking point of the neck. When the neck is broken close to the target, a large number of nucleons are transferred from the target to the projectile, while the neck is broken at a midpoint between the projectile and the target, the number of transferred nucleons becomes small.
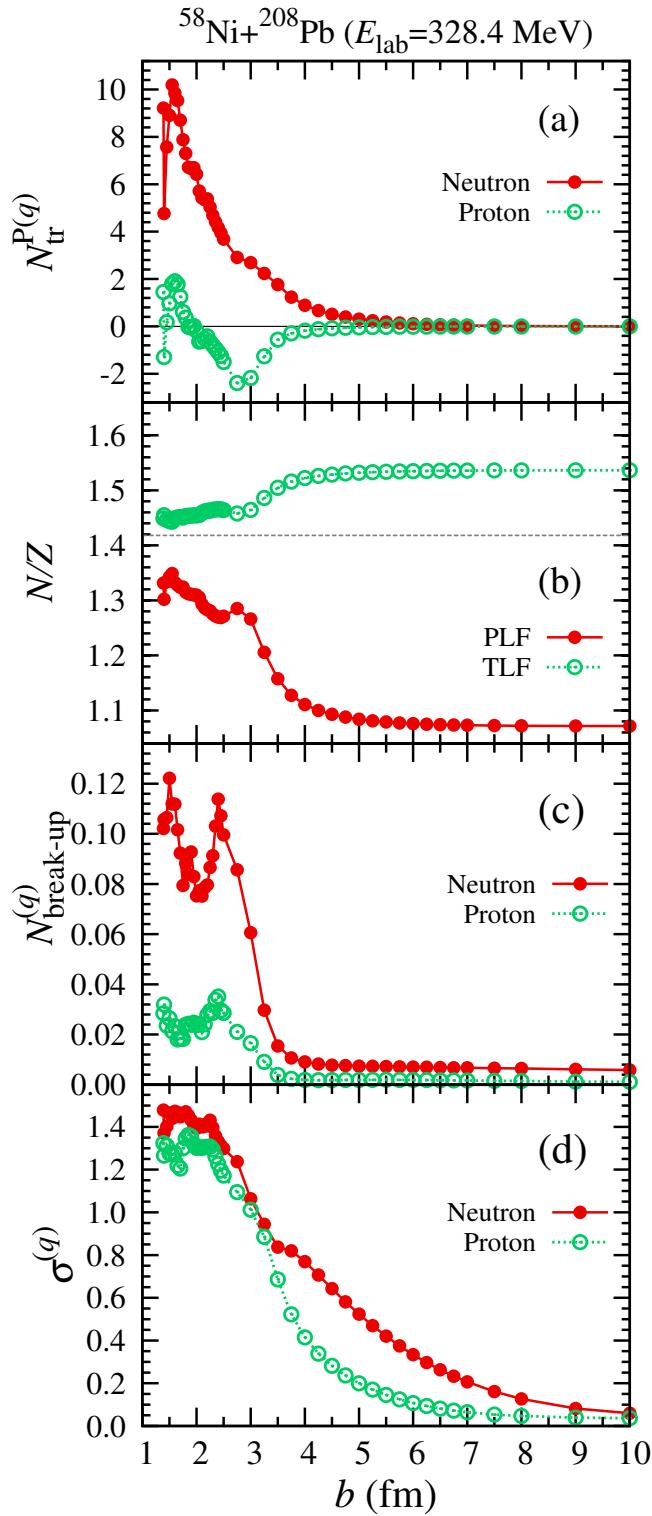
Figure 3.20: The ^{58}Ni+^{208}Pb reaction at $E_{\text{lab}} = 328.4$ MeV. (a): Average number of transferred nucleons from the target to the projectile. (b): Neutron-to-proton ratios, N/Z, of the PLF and the TLF after collision. (c): Average number of nucleons emitted to the continuum. (d): Fluctuation of transferred nucleon number. The horizontal axis is the impact parameter b. In (b), the equilibrium N/Z value of the total system, 1.42, is indicated by a horizontal dashed line. The figure was taken from Ref. [173].

^{58}Ni+^{208}Pb (E_{lab}=328.4 MeV)
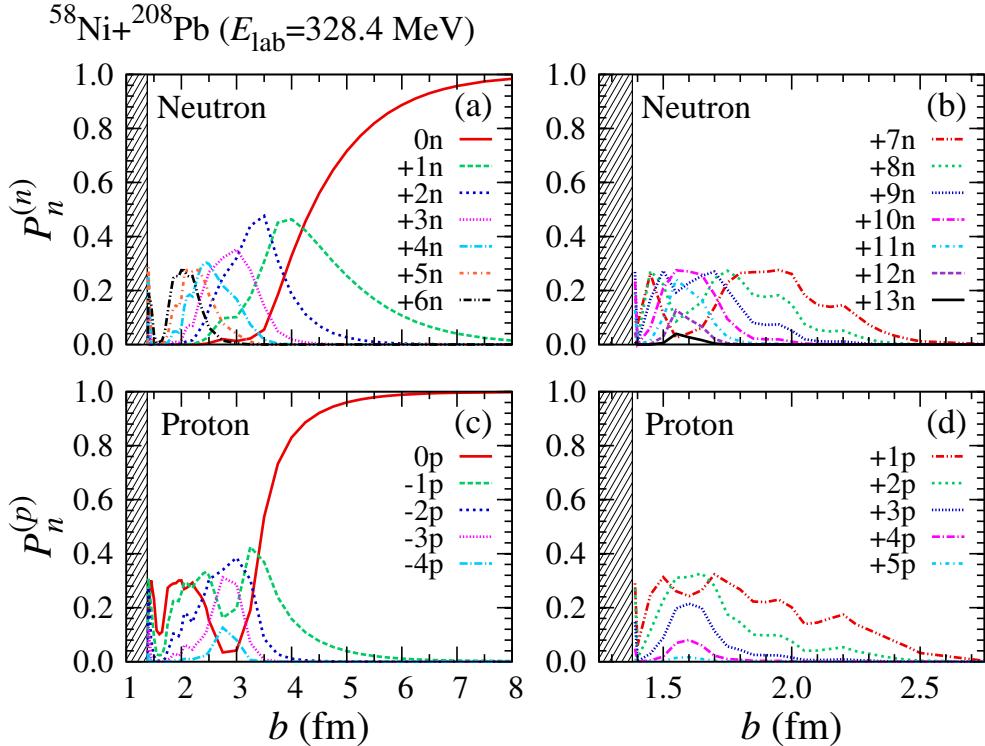
Figure 3.21: Neutron and proton transfer probabilities as functions of impact parameter b for the reactions of ^{58}Ni+^{208}Pb at $E_{\text{lab}} = 328.4$ MeV. Figure (a) and (b) show probabilities of neutrons, while figure (c) and (d) show those of protons. The positive (negative) number of transferred nucleons represents the number of nucleons added to (removed from) the projectile. Note that horizontal scales are different between the left and the right panels. A shaded region at small impact parameter ($b \leq 1.38$ fm) corresponds to the fusion reactions. The figure was taken from Ref. [173].

Figure 3.20 (c) shows the average number of nucleons emitted to the continuum during the time evolution. The average number of neutrons (protons) emitted to the continuum is denoted by red filled (green open) circles connected with solid (dotted) lines. As in other systems, we calculate it by subtracting the average number of nucleons inside a sphere of 14 fm for the TLF and that inside a sphere of 10 fm for the PLF from the total number of nucleons, 266. Again the number is rather small, about 0.12 at the maximum.

Figure 3.20 (d) shows the fluctuation of the transferred nucleon number. The fluctuation of transferred neutron (proton) number is denoted by red filled (green open) circles connected with solid (dotted) lines. They show a different behavior across the impact parameter around 3 fm, indicating a qualitative change of the dynamics. Outside this impact parameter where protons and neutrons are transferred in different directions, the fluctuation of transferred neutron number is larger than that of protons. Inside this impact parameter, although the average number of transferred neutrons is much larger than that of protons, the fluctuation is almost the same. This indicates that although the average number of transferred protons is small, there is a strong mixture of single-particle orbitals of protons because of the formation and breaking of the neck.

(b) Transfer probabilities

We next show transfer probabilities of the ^{58}Ni+^{208}Pb reaction as functions of impact parameter, which are shown in Fig. 3.21. The small impact parameter region ($b \leq 1.38$ fm) corresponding to the fusion reaction are shaded. The positive (negative) number of the transferred nucleons represents the
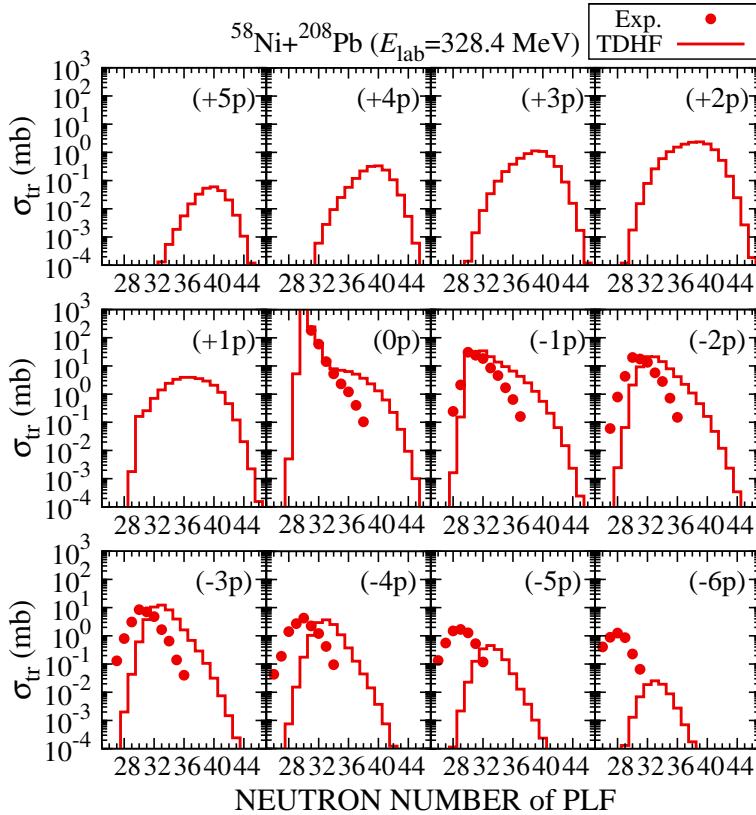
Figure 3.22: Transfer cross sections for the ^{58}Ni+^{208}Pb reaction at E_{lab} = 328.4 MeV. Red filled circles denote measured cross sections and red solid lines denote results of the TDHF calculations. The number of transferred protons (positive number for the transfer from ^{208}Pb to ^{58}Ni) is indicated as $(x\mathrm{p})$ ($-6 \leq x \leq +5$). The measured cross sections have been reported in Ref. [47]. The figure was taken from Ref. [173].

number of nucleons added to (removed from) the projectile. The upper (lower) panels show neutron (proton) transfer probabilities for each transfer channel. In the left panels ((a) and (c)), we show transfer probabilities, (0n) to (+6n) for neutrons and (0p) to (-4p) for protons. They correspond to the transfer processes toward the charge equilibrium of the initial system. In the right panels ((b) and (d)), we show transfer probabilities, (+7n) to (+13n) for neutrons and (+1p) to (+5p) for protons, which dominate in the small impact parameter region, $b \leq 2.75$ fm. Probabilities of neutron transfer from ^{58}Ni to ^{208}Pb are very small and are not shown.

In contrast to the previous cases of $^{40,\,48}$Ca+^{124}Sn and ^{40}Ca+^{208}Pb, probabilities of transfer processes involving more than 6 neutrons are seen in rather wide impact parameter region, 1.39 fm $\leq b \leq$ 2.75 fm, where the formation of the thick neck is observed. In Fig. 3.17 (b), a large value of TKEL was also seen in the impact parameter region of $b < 3$ fm, indicating the significance of the evaporation effects.

As in previous cases, probabilities of the processes accompanying small number of exchanged nucleons show large spatial tail. The transfer probabilities for channels toward the charge equilibrium are large in most cases. The zero-proton transfer probability (0p, red solid line) in Fig. 3.21 (c) decreases as the impact parameter decreases, shows minimum at $b \sim 3$ fm, and again increases at smaller impact parameter region. This behavior is consistent with the behavior of the average number of transferred protons seen in Fig. 3.20 (a). Although neutron transfer probabilities to the direction opposite to the charge equilibrium of the initial system are vanishingly small, we find appreciable probabilities of proton transfer opposite to the charge equilibrium of the initial system, as is seen from
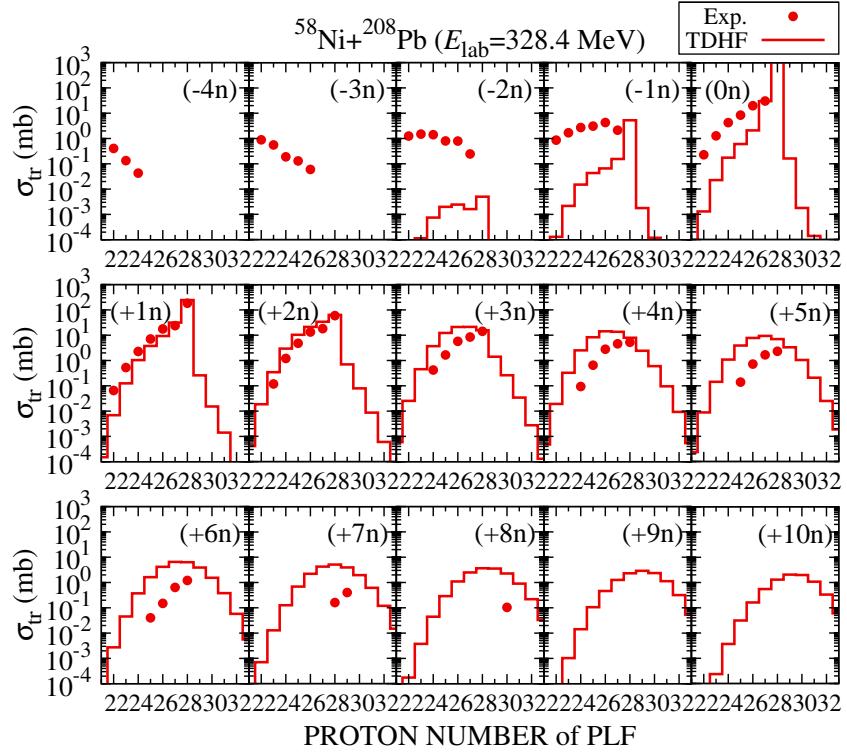
Figure 3.23:   The same transfer cross sections for the ^{58}Ni+^{208}Pb reaction as those in Fig. 21. The number of transferred neutrons is indicated as $(x\mathrm{n})$ $(-4 \leq x \leq +10)$. The figure was taken from Ref. [173].

Fig. 3.21 (d). This feature is again consistent with the behavior of the average number of transferred protons shown in Fig. 3.20 (a).

(c)   Transfer cross sections

We show transfer cross sections in Fig. 3.22 and Fig. 3.23. Each panel of Fig. 3.22 shows cross sections classified according to the change of the proton number of the PLF from ^{58}Ni, as functions of neutron number of the PLF. Each panels of Fig. 3.23 shows cross sections classified according to the change of the neutron number of the PLF from ^{58}Ni, as functions of proton number of the PLF. Red filled circles denote measured cross sections and red solid lines denote results of the TDHF calculations. Again, reaction cross sections with relatively large values, such as (0p) and $(-1\mathrm{p})$ panels of Fig. 3.22 and $(+1\mathrm{n})$ and $(+2\mathrm{n})$ panels of Fig. 3.23, are described reasonably well by the TDHF calculation.

In Fig. 3.22, as the transferred proton number increases, the calculation underestimates the measured cross section. The peak position of the cross section shifts toward larger neutron number compared with the measurements. A similar behavior was also seen in other systems. This discrepancy is considered to be partly originated from neutron evaporation processes which we have not yet taken into account.

In (0p) and $(-1\mathrm{p})$ panels of Fig. 3.22, the TDHF calculations overestimate the cross section for channels accompanying large number of transferred neutrons (neutron number of PLF more than 34). We also find abundant cross sections for $(+1\mathrm{p})$ to $(+5\mathrm{p})$ processes, opposite to the charge equilibrium direction for the initial system and accompanying a large number of transferred neutrons. They come from reactions at small impact parameter region, $b < 3$ fm, in which the transfer of nucleons associated with the neck breaking is appreciable.

In Fig. 3.23, we find an underestimation of cross sections for negative neutron transfer $(-x\mathrm{n})$
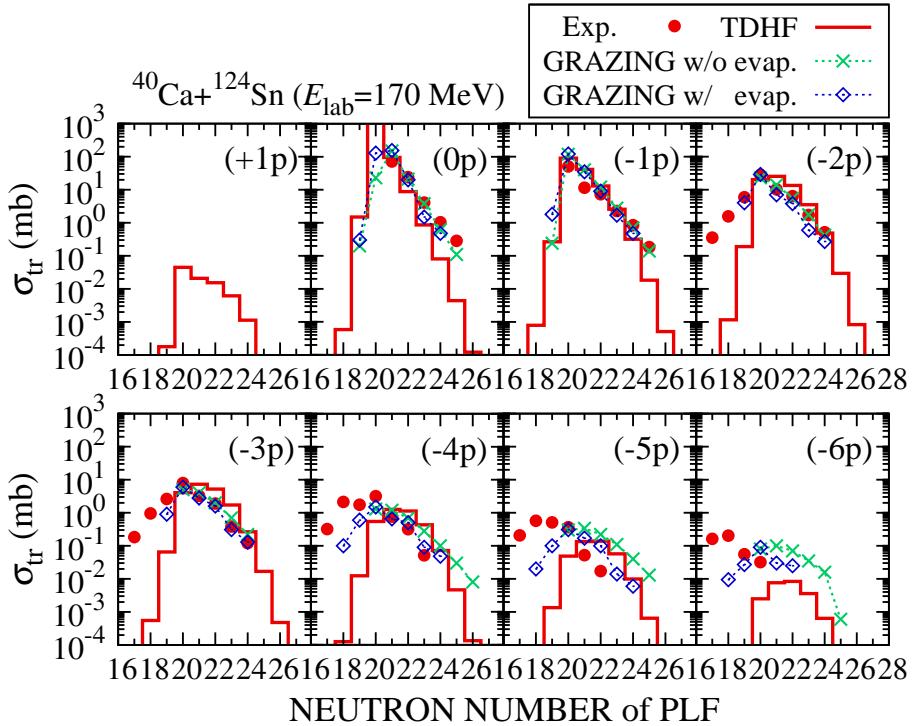
Figure 3.24: Transfer cross sections for the ^{40}Ca+^{124}Sn reaction at E_{lab} =170 MeV. Red filled circles denote measured cross sections, red solid lines denote results of the TDHF calculations, and green crosses (blue open diamonds) connected with dotted lines denote calculated results using the GRAZING code without (with) the neutron evaporation effect. The number of transferred protons is indicated as (xp) ($-6 \leq x \leq +1$). The measured cross sections and the GRAZING results have been reported in Ref. [40]. The figure was taken from Ref. [173].

(neutron transfer from ^{58}Ni to ^{208}Pb). On the other hand, almost constant cross sections are obtained for positive neutron transfer ($+x$n) (from ^{208}Pb to ^{58}Ni), up to the transfer of 10 neutrons. The underestimation of the negative neutron transfer channels may be explained by the evaporation effects as discussed in Ref. [47]. The cross sections for the positive neutron transfer channels originate from reactions at small impact parameter which accompany large TKEL. Therefore, they may also suffer the evaporation effects.

3.3 Comparison with Other Calculations

In this Section, we compare our results of the TDHF calculations with those by other theories. MNT cross sections have been extensively and successfully analyzed by direct reaction theories such as GRAZING [67] and CWKB [68]. In both theories, relative motion of colliding nuclei is treated in the semiclassical approximation. The probabilities of the MNT processes are treated with a statistical assumption using single-particle transfer probabilities evaluated with the time-dependent perturbation theory. We compare our results with those of the GRAZING for ^{40,48}Ca+^{124}Sn reactions which have been reported in Refs. [40, 43].

In Figs. 3.24 and 3.25, we show transfer cross sections for the reactions of ^{40}Ca+^{124}Sn and ^{48}Ca+^{124}Sn, respectively. Each panel of these figures shows cross sections for transfer channels classified according to the change of the proton number of the PLF as functions of neutron number of the PLF. Red filled circles denote measured cross sections and red solid lines denote results of our TDHF calculations. Green crosses and blue open diamonds connected with dotted lines denote results of
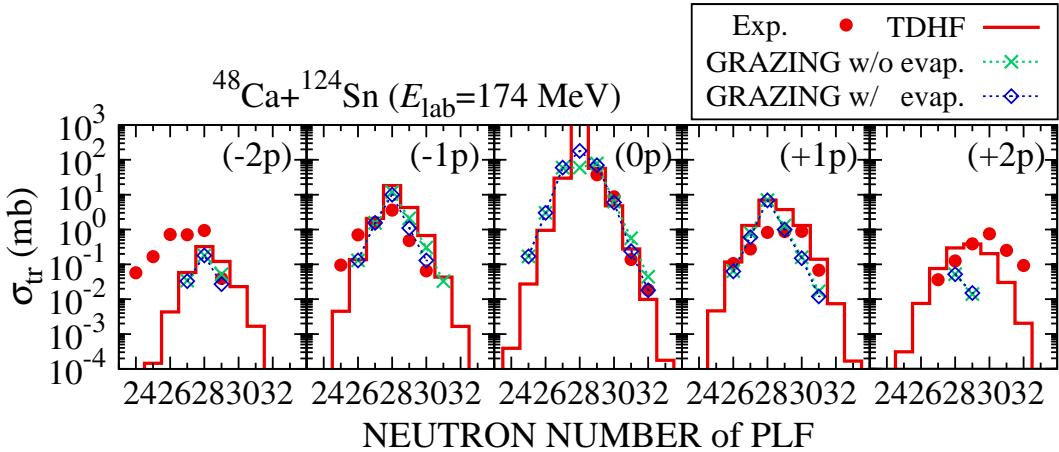
Figure 3.25:   Transfer cross sections for the ^{48}Ca+^{124}Sn reaction at E_{lab} =174 MeV. Red filled circles denote measured cross sections, red solid lines denote results of the TDHF calculations, and green crosses (blue open diamonds) connected with dotted lines denote calculated results using the GRAZING code without (with) the neutron evaporation effect. The number of transferred protons is indicated as $(x\text{p})$ $(-2 \leq x \leq +2)$. The measured cross sections and the GRAZING results have been reported in Ref. [43]. The figure was taken from Ref. [173].

the GRAZING calculation. The latter symbols, blue open diamonds, show cross sections including the neutron evaporation effect, while the former symbols, green crosses, without the evaporation effect.

For the ^{40}Ca+^{124}Sn reaction shown in Fig. 3.24, one find that the cross sections by our calculation and those by the GRAZING are very close to each other for the processes shown in the panels of (0p), (-1p), (-2p), (-3p), (-4p), and (-5p). Cross sections accompanying many proton transfer, (-6p), are better described by the GRAZING compared with the TDHF. In both TDHF and GRAZING calculations, the peak positions of the cross sections are shifted toward large number of neutrons in the (-5p) and (-6p) panels. The discrepancy is slightly remedied by including the neutron evaporation effect in the GRAZING calculation.

For the ^{48}Ca+^{124}Sn reaction shown in Fig. 3.25, we again find a good coincidence between the TDHF results and those of the GRAZING for (0p), $(\pm1\text{p})$, and (-2p) channels. For $(+2\text{p})$ channels, TDHF calculation gives better description than the GRAZING. In both TDHF and GRAZING calculations, the cross sections shift toward the direction of small neutron number for $(+2\text{p})$ panel compared with measurements, while toward the direction of large neutron number for (-2p) panel. In Ref. [43], the effect of the neutron evaporation has been evaluated to be small for this system.

We notice that there are similar failures in the TDHF and the GRAZING calculations for the cross sections of channels accompanying transfer of large number of protons. It seems that they are caused by a common problem, although two theories are relied upon very different basis. One possible origin of the failure is an insufficient inclusion of the correlation effects beyond the mean-field theory. In the TDHF calculation, the many-body wave function is always assumed to be a single Slater determinant and correlations beyond the mean-field is not included. In the GRAZING calculation, MNT probabilities are evaluated from single-nucleon transfer probabilities with a statistical assumption, ignoring correlation effects among nucleons.

We next consider an approach based on Langevin-type equations of motion which has been originally developed for and applied to fission dynamics [182, 183] and has been recently extended to apply to MNT reactions [69, 70]. We consider the ^{58}Ni+^{208}Pb reaction for which an application of the Langevin approach has been reported in Ref. [58].

In the Langevin approach, MNT processes are treated as sequential processes of single-nucleon

^{58}Ni+^{208}Pb (E_{lab}=328.4 MeV)
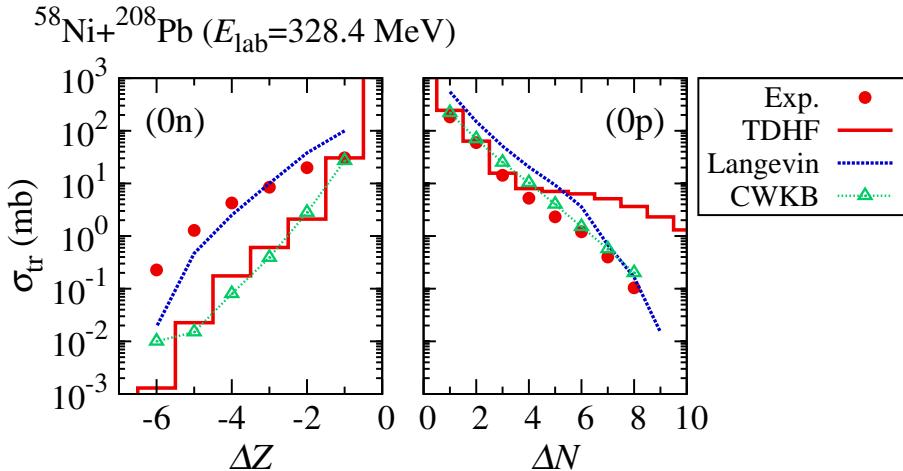
Figure 3.26: Cross sections for transfer channels of pure proton stripping without neutron transfer (left) and pure neutron pickup without proton transfer (right) for the ^{58}Ni+^{208}Pb reaction at E_{lab} = 328.4 MeV. Red filled circles denote measured cross sections [47], red solid lines denote results of the TDHF calculations, blue dotted lines denote results of the Langevin calculation [58], and green open triangles connected with dotted lines denote results of the CWKB calculation [47]. The figure was taken from Ref. [173].

transfers. In the theory, an empirical parameter describing nucleon transfer rate is introduced. Figure 3.26 shows cross sections for transfer channels of pure proton-stripping without neutron transfer (left) and pure neutron-pickup without proton transfer (right). Red filled circles denote measured cross sections, red solid lines denote results of our TDHF calculations, and blue dotted lines denote results of the Langevin approach reported in Ref. [58].

In the case of pure neutron-pickup channels, (0p), the TDHF calculation gives a better description than the Langevin theory for cross sections up to four-neutron transfer. The TDHF calculation overestimates the cross sections for more than three neutrons, because of the QF process at small impact parameter region as discussed in Sec. 3.2.3. On the other hand, cross sections of pure proton-stripping channels, (0n), are much better described by the Langevin theory than the TDHF, except for one-proton transfer channel.

Figure 3.27 shows transfer cross sections for several proton stripping channels. Again, red filled circles denote measured cross sections, red solid lines denote results of our TDHF calculations, and blue dotted lines denote results of the Langevin approach. For these channels, the Langevin calculation gives a much better description for the transfer cross sections than the TDHF calculation. We should, however, note that an adjustable parameter describing the nucleon transfer rate is introduced in the Langevin approach, while no empirical parameter is introduced in the TDHF calculation once the Skyrme interaction is specified. In the calculation of the Langevin theory, evaporation effects are already included in the calculation.

For the ^{58}Ni+^{208}Pb reaction, an analysis using the CWKB theory has also been reported in Ref. [47]. In the CWKB theory, the MNT processes are treated in a similar way to the GRAZING theory, evaluating statistically using single-nucleon transfer probabilities which are calculated by the first-order perturbation theory. In Figs. 3.26 and 3.27, the CWKB cross sections are shown by green open triangles connected with dotted lines. In Ref. [47], three results of cross sections have been reported: in a simple CWKB theory, adding the proton pair transfer effect, and taking account of evaporation effects in addition to the proton pair transfer effect. We show in these two figures the simplest version of the calculation without the proton pair transfer effect and the evaporation.

As seen from Fig. 3.26, the CWKB cross sections are very close to those of the TDHF except for
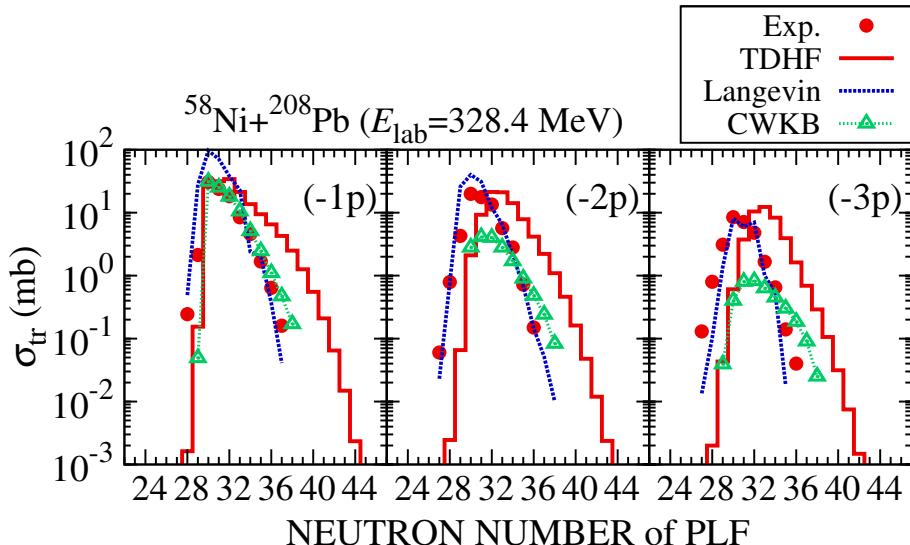
Figure 3.27: Cross sections for transfer channels of $(x\mathrm{p})$ $(-3 \leq x \leq -1)$ for the $^{58}\mathrm{Ni}+^{208}\mathrm{Pb}$ reaction at $E_{\mathrm{lab}} = 328.4$ MeV. The horizontal axis is the number of neutrons in the PLF. Red filled circles denote measured cross sections [47], red solid lines denote results of the TDHF calculations, blue dotted lines denote results of the Langevin calculation [58], and green open triangles connected with dotted lines denote results of the CWKB calculation [47]. The figure was taken from Ref. [173].

$\Delta N \geq 5$ in the (0p) panel. In Fig. 3.27, the CWKB cross sections are seen to be too small as the number of transferred protons increases. In Ref. [47], proton pair transfer processes are introduced and added to the simple CWKB cross sections to examine the effect as a possible origin of the discrepancy.

3.4 Summary and Concluding Remarks on Chapter 3

In this Chapter, we showed results of fully microscopic calculations for the MNT processes in low-energy heavy ion reactions in the TDHF theory. We performed calculations for the reactions of $^{40,48}\mathrm{Ca}+^{124}\mathrm{Sn}$ at $E_{\mathrm{lab}} = 170$, 174 MeV, $^{40}\mathrm{Ca}+^{208}\mathrm{Pb}$ at $E_{\mathrm{lab}} = 235$ and 249 MeV, and $^{58}\mathrm{Ni}+^{208}\mathrm{Pb}$ at $E_{\mathrm{lab}} = 328.4$ MeV, for which MNT cross sections were measured experimentally [40, 43, 47, 50]. We used the PNP technique [115] to calculate the transfer probabilities as functions of impact parameter from the TDHF wave function after collision. From the reaction probabilities, we evaluated cross sections for various transfer channels.

The systems we investigated, $^{40,48}\mathrm{Ca}+^{124}\mathrm{Sn}$, $^{40}\mathrm{Ca}+^{208}\mathrm{Pb}$, and $^{58}\mathrm{Ni}+^{208}\mathrm{Pb}$ showed different behaviors in the MNT processes characterized by the N/Z ratios of the projectile and the target, and by the product of the charge numbers, $Z_{\mathrm{P}}Z_{\mathrm{T}}$.

In the collisions with different N/Z ratios between the projectile and target nuclei ($^{40}\mathrm{Ca}+^{124}\mathrm{Sn}$, $^{40}\mathrm{Ca}+^{208}\mathrm{Pb}$, and $^{58}\mathrm{Ni}+^{208}\mathrm{Pb}$), we find a fast transfer of a few nucleons when the impact parameter is sufficiently large. The nucleons are transferred toward the direction of charge equilibrium expected from the N/Z ratios of the projectile and the target. This means that protons and neutrons are transferred in the opposite directions. When the N/Z ratios are almost equal between the projectile and target nuclei ($^{48}\mathrm{Ca}+^{124}\mathrm{Sn}$), we find a few nucleons are exchanged symmetrically.

As the impact parameter decreases, a neck is formed at the contact of two nuclei. Then the transfer process proceeds in two steps. At the beginning of the reaction before the formation of the neck, a few nucleons are transferred in the same way as described above. After forming the neck, the transfer of a number of nucleons occurs as a result of the neck breaking when two nuclei dissociate. Because

both neutrons and protons in the neck are transferred simultaneously in this mechanism, neutrons and protons are transferred in the same direction.

As the charge number product $Z_{\mathrm{P}}Z_{\mathrm{T}}$ increases, there appears an impact parameter region where a thick neck is formed. We may regard these reactions with a thick neck formation as an indication of emergence of the QF process reflecting the suppression of the fusion reaction. As mentioned above, both neutrons and protons are transferred in the same direction when the neck is broken at the time of dissociation. A large energy transfer is also accompanied from the nucleus-nucleus relative motion to the internal excitations.

Comparisons with measured cross sections show that the TDHF calculations describe cross sections reasonably well for transfer processes of a few nucleons between the projectile and the target. As the number of exchanged nucleons increases, the agreement becomes less accurate. When more than a few protons are transferred, cross sections as functions of the number of transferred neutrons show a peak at the neutron number more than that in the measurements. The magnitude of the calculated cross sections becomes too small compared with the measurements. This discrepancy is expected to be, to some extent, resolved when we introduce nucleon evaporation effects in our calculations. We will address this problem in the following Chapters (Chapters 4 and 5).

We have compared transfer cross sections of the TDHF calculations with those by other theories. We find that results of the TDHF calculations are rather close to those of direct reaction model calculations such as GRAZING and CWKB. We should note that the Skyrme Hamiltonian used in the TDHF calculation is entirely determined from the ground state calculations and there is no parameter introduced to describe nuclear dynamics. We thus conclude that the fully microscopic TDHF theory can describe the MNT cross sections in the quality comparable to existing direct reaction theories.

As mentioned above, there are several discrepancies between the calculated cross sections and the measurements. Among possible origins of the discrepancy, we should first take into account effects of particle evaporation. Because the evaporation processes take place in a much longer timescale than the reaction mechanism shown here, it is not realistic to achieve a direct evaluation of those deexcitation processes by following the TDHF time-evolution for such a long time. Instead, we will estimate them using a statistical model, using excitation energy of the final fragments calculated from the TDHF wave function after collision as inputs. To this end, in Chapter 4, we will develop a formalism to calculate excitation energy of reaction products in each transfer channel by extending the PNP technique. In Chapter 5, we will examine the effects of particle evaporation on MNT cross sections employing a statistical model using the excitation energy evaluated by the extended PNP method as an input.

Chapter 4

EXTENSION OF THE PNP METHOD TO STUDY PROPERTIES OF REACTION PRODUCTS

In Chapter 3, we have shown that MNT cross sections can be quantitatively described by the TDHF theory combined with the PNP technique with an accuracy comparable to calculations by other existing theories such as GRAZING [67] and CWKB [68], which are based on semiclassical approximation, and the dynamical model based on Langevin-type equations of motion [69, 70]. However, we have not taken into account effects of particle evaporation from primary reaction products. Since reaction products in MNT processes would have a substantial excitation energy, secondary deexcitation processes through transfer-induced fission, particle evaporation, and γ-particle emissions will take place before they are detected by an experimental apparatus. A significance of evaporation effects has been advocated both experimentally [40, 43, 47, 50] and theoretically [56, 57].

In this Chapter, we develop a theoretical framework to calculate excitation energy of produced nuclei which is needed to evaluate the effect of particle evaporation on production cross sections in the TDHF theory[†].

Since a timescale of particle evaporation is several orders of magnitude longer than the reaction timescale which is simulated in the usual TDHF calculation, a direct calculation of evaporation processes solving the TDHF time evolution would be computationally demanding. A possible alternative approach to include effects of particle evaporation is use of a statistical model of particle evaporation. The basic inputs of the statistical model are excitation energy and angular momentum of a decaying excited nucleus [185]. The above mentioned existing theories also use some statistical model to include effects of particle evaporation [67, 68, 69, 70].

To evaluate effects of particle evaporation on MNT cross sections in the TDHF theory, we need to calculate excitation energy and angular momentum of reaction products in the TDHF wave function after collision. In this Chapter, we develop a theoretical framework to calculate expectation values of arbitrary operators in the TDHF wave function after collision extending the PNP technique. The main idea of the method is to define an operator for one of reaction products in the TDHF wave function after collision. By taking an expectation value of the operator as commonly performed in nuclear structure calculations [136], we will get information on properties of reaction products in each transfer channel.

To show how our method works in practice, the method is applied to $^{24}O+^{16}O$ reactions for two quantities, angular momentum and excitation energy. From the results of PNP analysis, we

---

[†]This Chapter is essentially based on our publication of Ref. [184].

find reasonable transfer mechanisms in the TDHF calculation. These features could not be seen from ordinary expectation values without the PNP. Using the extended PNP method and a statistical model of particle evaporation, the effects of particle evaporation on MNT cross sections will be examined in Chapter 5.

This Chapter is organized as follows. In Sec. 4.1, we describe a general formalism to calculate expectation values of operators in the TDHF wave function after collision with the PNP. In Sec. 4.2, we apply the method to ^{24}O+^{16}O reactions, as an illustrative example. In Sec. 4.3, a summary and concluding remarks on this Chapter are presented.

4.1 Formulation

4.1.1 Particle-number projection method

We consider microscopic TDHF calculations of low-energy heavy ion reactions in which two fragments, a PLF and a TLF, are produced. In this Section, we develop a general formalism to calculate expectation values of operators for one of the fragments, either PLF or TLF, with the PNP. We first describe the formalism assuming that the system is composed of N identical fermions. An extension to include two kinds of fermions, neutrons and protons, is straightforward.

We assume that the fragments are well separated spatially after collision at the final stage of the TDHF calculation. We define two spatial regions, V and $\bar{V}$. The spatial region V includes a fragment to be analyzed. $\bar{V}$ is the complement of V, which includes the other fragment.

We denote the TDHF wave function after collision as $\Psi(x_1, \cdots, x_N)$, where x denotes a set of the spatial and the spin coordinates, $x \equiv (\boldsymbol{r}, \sigma)$. The wave function Ψ is, in general, not an eigenstate of the particle-number operator in the spatial region V but a superposition of states with different particle numbers in V. It can be expressed as

$$\Psi(x_1, \cdots, x_N) = \sum_{n=0}^{N} \Psi_n(x_1, \cdots, x_N), \tag{4.1.1}$$

where Ψ_n denotes a particle-number projected wave function,

$$\Psi_n(x_1, \cdots, x_N) = \hat{P}_n \Psi(x_1, \cdots, x_N). \tag{4.1.2}$$

Ψ_n is a component of Ψ having n particles in the spatial region V and $N - n$ particles in the spatial region $\bar{V}$. The operator $\hat{P}_n$ is the PNP operator defined by [115, 173]

$$\hat{P}_n = \sum_{s(\{\tau_i\}: V_P^n V_T^{N-n})} \Theta_{\tau_1}(\boldsymbol{r}_1) \cdots \Theta_{\tau_N}(\boldsymbol{r}_N) \tag{4.1.3}$$

$$= \frac{1}{2\pi} \int_0^{2\pi} d\theta \, e^{\mathrm{i}(n-\hat{N}_V)\theta}, \tag{4.1.4}$$

where $s(\{\tau_i\} : V_P^n V_T^{N-n})$ indicates that a sum over the sequence $\tau_1 \tau_2 \cdots \tau_N$ should be taken for all possible combinations that V appears n times and $\bar{V}$ appears $N - n$ times. We have introduced a space division function, $\Theta_\tau(\boldsymbol{r})$, and a particle-number operator in the spatial region τ, $\hat{N}_\tau$, which are defined by

$$\Theta_\tau(\boldsymbol{r}) = \begin{cases} 1 & \text{if} \quad \boldsymbol{r} \in \tau, \\ 0 & \text{if} \quad \boldsymbol{r} \notin \tau, \end{cases} \tag{4.1.5}$$

and

$$\hat{N}_\tau = \int_\tau d\boldsymbol{r} \sum_{i=1}^{N} \delta(\boldsymbol{r} - \boldsymbol{r}_i) = \sum_{i=1}^{N} \Theta_\tau(\boldsymbol{r}_i), \tag{4.1.6}$$

where τ represents the spatial region either V or $\bar{V}$.

We consider a general operator $\hat{\mathcal{O}}$ and decompose it into two operators according to the spatial regions:

$$\hat{\mathcal{O}} = \hat{\mathcal{O}}_V + \hat{\mathcal{O}}_{\bar{V}}. \tag{4.1.7}$$

The operator $\hat{\mathcal{O}}_V$ represents a part of the operator $\hat{\mathcal{O}}$ acting to the particle when it is in the spatial region V. The operator $\hat{\mathcal{O}}_{\bar{V}}$ represents the remaining part of the operator $\hat{\mathcal{O}}$. Any one-body operator which is local in space, $\hat{\mathcal{O}}^{(1)} = \sum_{i=1}^{N} \hat{o}^{(1)}(\boldsymbol{r}_i \sigma_i)$, can be decomposed as

$$\begin{aligned}
\hat{\mathcal{O}}^{(1)} &= \sum_{i=1}^{N} \Big(\Theta_V(\boldsymbol{r}_i) + \Theta_{\bar{V}}(\boldsymbol{r}_i) \Big) \hat{o}^{(1)}(\boldsymbol{r}_i \sigma_i) \\
&= \hat{\mathcal{O}}_V^{(1)} + \hat{\mathcal{O}}_{\bar{V}}^{(1)},
\end{aligned} \tag{4.1.8}$$

where σ_i denotes the spin coordinate of a particle i. In the same way, a two-body operator, $\hat{\mathcal{O}}^{(2)} = \sum_{i<j}^{N} \hat{o}^{(2)}(\boldsymbol{r}_i \sigma_i, \boldsymbol{r}_j \sigma_j)$, can be decomposed as

$$\begin{aligned}
\hat{\mathcal{O}}^{(2)} &= \sum_{i<j}^{N} \Big(\Theta_V(\boldsymbol{r}_i) + \Theta_{\bar{V}}(\boldsymbol{r}_i) \Big) \Big(\Theta_V(\boldsymbol{r}_j) + \Theta_{\bar{V}}(\boldsymbol{r}_j) \Big) \hat{o}^{(2)}(\boldsymbol{r}_i \sigma_i, \boldsymbol{r}_j \sigma_j) \\
&= \sum_{i<j}^{N} \Big(\Theta_V(\boldsymbol{r}_i) \Theta_V(\boldsymbol{r}_j) + \Theta_{\bar{V}}(\boldsymbol{r}_i) \Theta_{\bar{V}}(\boldsymbol{r}_j) \\
&\qquad + \Theta_V(\boldsymbol{r}_i) \Theta_{\bar{V}}(\boldsymbol{r}_j) + \Theta_{\bar{V}}(\boldsymbol{r}_i) \Theta_V(\boldsymbol{r}_j) \Big) \hat{o}^{(2)}(\boldsymbol{r}_i \sigma_i, \boldsymbol{r}_j \sigma_j) \\
&= \hat{\mathcal{O}}_V^{(2)} + \hat{\mathcal{O}}_{\bar{V}}^{(2)} + \hat{\mathcal{O}}_{V\bar{V}}^{(2)}.
\end{aligned} \tag{4.1.9}$$

The first (second) term represents two-body interactions which act when both particles i and j are in the spatial region V ($\bar{V}$). The third term represents two-body interactions which act when a particle i is in the spatial region V and a particle j is in the spatial region $\bar{V}$. For wave functions after collision in which two fragments are well separated, the third term can be ignored if the operator is short-range two-body interactions. When we calculate excitation energies of fragment nuclei, we ignore long-ranged Coulomb interactions acting protons belonging to different fragments.

The expectation value of the operator $\hat{\mathcal{O}}$ in the fragment which is composed of n particles and locates in the spatial region V is given by the expectation value of the operator $\hat{\mathcal{O}}_V$ in the wave function Ψ_n,

$$\mathcal{O}_n^V = \frac{\langle \Psi_n | \hat{\mathcal{O}}_V | \Psi_n \rangle}{\langle \Psi_n | \Psi_n \rangle}. \tag{4.1.10}$$

The bracket $\langle \Psi_n | \hat{O}_V | \Psi_n \rangle$ is defined by

$$\langle \Psi_n | \hat{\mathcal{O}}_V | \Psi_n \rangle \equiv \int dx_1 \cdots \int dx_N \, \Psi_n^*(x_1, \cdots, x_N) \, \hat{\mathcal{O}}_V \Psi_n(x_1, \cdots, x_N), \tag{4.1.11}$$

where the integral over x includes an integration over space and a sum over spin states, $\int dx \equiv \sum_\sigma \int d\boldsymbol{r}$. Here and hereafter, we often use the bracket notation to simplify equations.

The expectation value of the operator $\hat{\mathcal{O}}_V$ without PNP is given by $\mathcal{O}_V = \langle \Psi | \hat{\mathcal{O}}_V | \Psi \rangle$. It is related to $\hat{\mathcal{O}}_n^V$ by

$$\mathcal{O}_V = \sum_{n=0}^{N} P_n \mathcal{O}_n^V, \tag{4.1.12}$$

where P_n is defined by $P_n = \langle \Psi_n | \Psi_n \rangle = \langle \Psi | \hat{P}_n | \Psi \rangle$. To derive Eq. (4.1.12), we used identities $\sum_{n=0}^{N} \hat{P}_n = 1$, $\hat{P}_n \hat{P}_{n'} = \delta_{nn'} \hat{P}_n$, and $[\hat{\mathcal{O}}_V, \hat{P}_n] = 0$.

4.1.2 Formulae for the Slater determinant

We present formulae of expectation values which are useful for the TDHF wave function Ψ given by a single Slater determinant composed of single-particle wave functions $\psi_i(x)$,

$$\Psi(x_1, \cdots, x_N) = \frac{1}{\sqrt{N!}} \det\{\psi_i(x_j)\}. \tag{4.1.13}$$

Using the PNP operator of Eq. (4.1.4), the probability P_n can be calculated as [115, 173]

$$
\begin{aligned}
P_n &= \frac{1}{2\pi} \int_0^{2\pi} d\theta \, e^{in\theta} \langle \Psi | e^{-i\hat{N}_V \theta} | \Psi \rangle \\
&= \frac{1}{2\pi} \int_0^{2\pi} d\theta \, e^{in\theta} \det \mathcal{B}(\theta).
\end{aligned} \tag{4.1.14}
$$

$\mathcal{B}(\theta)$ denotes an N-dimensional matrix,

$$\left(\mathcal{B}(\theta)\right)_{ij} = \int dx \, \psi_i^*(x) \psi_j(x, \theta), \tag{4.1.15}$$

where $\psi_i(x, \theta)$ is defined by

$$\psi_i(x, \theta) \equiv \left(\Theta_{\bar{V}}(\boldsymbol{r}) + e^{-i\theta} \Theta_V(\boldsymbol{r})\right) \psi_i(x). \tag{4.1.16}$$

Using Eqs. (4.1.4) and (4.1.10), the expectation value $\mathcal{O}_n^V$ is expressed as

$$\mathcal{O}_n^V = \frac{1}{2\pi P_n} \int_0^{2\pi} d\theta \, e^{in\theta} \langle \Psi | \hat{\mathcal{O}}_V e^{-i\hat{N}_V \theta} | \Psi \rangle. \tag{4.1.17}$$

In the case of one- and two-body operators, $\hat{\mathcal{O}}_V^{(1)}$ and $\hat{\mathcal{O}}_V^{(2)}$, in Eqs. (4.1.8) and (4.1.9), expectation values can be calculated by [186]

$$\mathcal{O}_n^{V(1)} = \frac{1}{2\pi P_n} \int_0^{2\pi} d\theta \, e^{in\theta} \det \mathcal{B}(\theta) \sum_{i=1}^N \int_V dx \, \psi_i^*(x) \, \hat{o}^{(1)}(x) \tilde{\psi}_i(x, \theta), \tag{4.1.18}$$

$$
\begin{aligned}
\mathcal{O}_n^{V(2)} = \frac{1}{2\pi P_n} \int_0^{2\pi} d\theta \, e^{in\theta} \det \mathcal{B}(\theta) \sum_{i<j}^N \Bigg\{ &\int_V dx \int_V dx' \psi_i^*(x) \psi_j^*(x') \, \hat{o}^{(2)}(x, x') \, \tilde{\psi}_i(x, \theta) \tilde{\psi}_j(x', \theta) \\
&- \int_V dx \int_V dx' \psi_i^*(x) \psi_j^*(x') \, \hat{o}^{(2)}(x, x') \, \tilde{\psi}_j(x, \theta) \tilde{\psi}_i(x', \theta) \Bigg\},
\end{aligned} \tag{4.1.19}
$$

where $\tilde{\psi}_i(x, \theta)$ is defined by

$$\tilde{\psi}_i(x, \theta) \equiv \sum_{k=1}^N \psi_k(x, \theta) \left(\mathcal{B}^{-1}(\theta)\right)_{ki}. \tag{4.1.20}$$

We note that $\{\tilde{\psi}_i\}$ are biorthonormal to $\{\psi_i\}$, *i.e.* $\int dx \, \psi_i^*(x) \tilde{\psi}_j(x, \theta) = \delta_{ij}$, as described in Appendix A.6.

4.1.3 Application to the TDHF wave function

In actual TDHF calculations, the many-body wave function Ψ is given by a product of two Slater determinants, $\Psi = \Psi_\nu \Psi_\pi$, where Ψ_ν is for neutrons and Ψ_π is for protons. We present formulae of expectation values for this wave function. We denote the PNP operator for neutrons (protons) as $\hat{P}_N^{(n)}$

$(\hat{P}_Z^{(p)})$, where N (Z) is the number of neutrons (protons) in the spatial region V. The probability that N neutrons and Z protons are in the spatial region V is then given by a product of probabilities for neutrons and protons,

$$
\begin{aligned}
P_{N,Z} &= \langle\Psi|\hat{P}_N^{(n)}\hat{P}_Z^{(p)}|\Psi\rangle \\
&= \langle\Psi_\nu|\hat{P}_N^{(n)}|\Psi_\nu\rangle \langle\Psi_\pi|\hat{P}_Z^{(p)}|\Psi_\pi\rangle \\
&= P_N^{(n)}P_Z^{(p)}.
\end{aligned}
\tag{4.1.21}
$$

We first consider expectation values for a one-body operator. We note that any one-body operator can be written as a sum of operators for neutrons and for protons, $\hat{\mathcal{O}}_V^{(1)} = \hat{\mathcal{O}}_V^{(1,n)} + \hat{\mathcal{O}}_V^{(1,p)}$. Thus the expectation value of the one-body operator $\hat{\mathcal{O}}_V^{(1)}$ is given by a sum of two terms. For the fragment nucleus specified by N and Z, we have

$$
\begin{aligned}
\mathcal{O}_{N,Z}^{V(1)} &= \frac{\langle\Psi|\hat{\mathcal{O}}_V^{(1)}\hat{P}_N^{(n)}\hat{P}_Z^{(p)}|\Psi\rangle}{\langle\Psi|\hat{P}_N^{(n)}\hat{P}_Z^{(p)}|\Psi\rangle} \\
&= \frac{\langle\Psi_\nu|\hat{\mathcal{O}}_V^{(1,n)}\hat{P}_N^{(n)}|\Psi_\nu\rangle}{\langle\Psi_\nu|\hat{P}_N^{(n)}|\Psi_\nu\rangle} + \frac{\langle\Psi_\pi|\hat{\mathcal{O}}_V^{(1,p)}\hat{P}_Z^{(p)}|\Psi_\pi\rangle}{\langle\Psi_\pi|\hat{P}_Z^{(p)}|\Psi_\pi\rangle} \\
&= \mathcal{O}_N^{V(1,n)} + \mathcal{O}_Z^{V(1,p)}.
\end{aligned}
\tag{4.1.22}
$$

$\mathcal{O}_n^{V(1,q)}$ is defined by

$$
\mathcal{O}_n^{V(1,q)} = \frac{1}{2\pi P_n^{(q)}} \int_0^{2\pi} d\theta\, e^{in\theta}\langle\Psi_q|\hat{\mathcal{O}}_V^{(1,q)}e^{-i\hat{N}_V^{(q)}\theta}|\Psi_q\rangle,
\tag{4.1.23}
$$

where $\hat{N}_V^{(q)}$ denotes the particle-number operator for neutrons ($q=n$) and for protons ($q=p$) in the spatial region V. We will use these formulae, Eqs. (4.1.22) and (4.1.23), to calculate expectation values of the kinetic energy operator included in the Hamiltonian and of the angular momentum operator.

For a two-body operator, expectation values are not simply given by a sum of neutron and proton contributions, since two-body operators act between neutrons and protons. Therefore, we apply the PNP operators for both neutrons and protons simultaneously,

$$
\mathcal{O}_{N,Z}^{V(2)} = \frac{1}{(2\pi)^2 P_N^{(n)}P_Z^{(p)}} \int_0^{2\pi}d\theta \int_0^{2\pi}d\varphi\, e^{i(N\theta+Z\varphi)}\langle\Psi|\hat{\mathcal{O}}_V^{(2)}e^{-i(\hat{N}_V^{(n)}\theta+\hat{N}_V^{(p)}\varphi)}|\Psi\rangle.
\tag{4.1.24}
$$

We will use the above formula to evaluate excitation energy of nuclei produced through transfer processes.

To evaluate the excitation energy, we need to exclude the energy associated with the center-of-mass motion. For this purpose, we calculate the energy expectation value using Eqs. (4.1.21)-(4.1.24) in the coordinate system which moves with the fragment nucleus. In practice, we multiply all the single-particle wave functions by $e^{-i\boldsymbol{K}_\mu\cdot\boldsymbol{r}/A_\mu}$, where $\boldsymbol{K}_\mu$ is given by $\boldsymbol{K}_\mu = M_\mu\dot{\boldsymbol{R}}_\mu(t_f)/\hbar$, with M_μ, A_μ, and $\dot{\boldsymbol{R}}_\mu(t_f)$ being the average mass, the average nucleon number, and the average velocity of the fragment ($\mu =$ PLF or TLF) in the spatial region V at time t_f. We calculate the velocity of the fragment by $\dot{\boldsymbol{R}}_\mu(t_f) \equiv \left[\boldsymbol{R}_\mu(t_f+\Delta t) - \boldsymbol{R}_\mu(t_f-\Delta t)\right]/(2\Delta t)$.

We denote the calculated energy expectation value in the fragment nucleus composed of N neutrons and Z protons as $\mathcal{E}_{N,Z}^V$. We separately achieve ground state calculations for the fragment nucleus composed of N neutrons and Z protons, which we denote as $E_{N,Z}^{\text{g.s.}}$. We evaluate an excitation energy of the fragment nucleus by

$$
E_{N,Z}^{*V}(E,b) \equiv \mathcal{E}_{N,Z}^V(E,b) - E_{N,Z}^{\text{g.s.}},
\tag{4.1.25}
$$
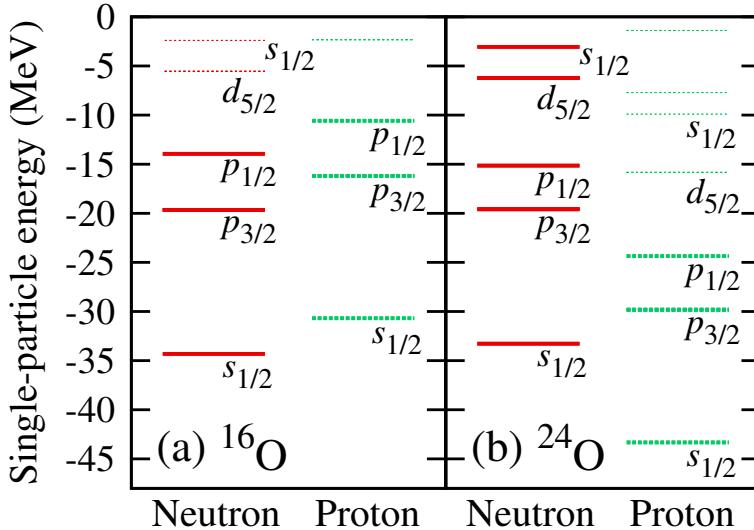
Figure 4.1: Single-particle energies of occupied orbitals for neutrons (thick red solid lines) and protons (thick green dotted lines) in ^{16}O and ^{24}O are shown in the panels (a) and (b), respectively. Single-particle energies of unoccupied orbitals are also shown by thin dotted lines. The figure was taken from Ref. [184].

where E and b denote the incident relative energy and the impact parameter, respectively.

In the ground state calculation, we employ a mass correction in the kinetic energy operator, $\frac{\hbar^2}{2m} \to \frac{\hbar^2}{2m}(1 - \frac{1}{N+Z})$, to take into account the center-of-mass correction. The same correction is applied in evaluating the expectation value of the kinetic energy operator using Eqs. (4.1.22) and (4.1.23), depending on numbers of neutrons and protons, N and Z, in the fragment nucleus.

4.2 An Illustrative Example: ^{24}O+^{16}O Reaction

To illustrate usefulness of the PNP method described in Sec. 4.1, we analyze properties of fragment nuclei in ^{24}O+^{16}O reactions described by the TDHF theory. For ^{24}O, pairing correlation may be important. In Ref. [187], the pairing interaction is reported to be negligible in the ground state, while finite contribution is reported in Ref. [188]. In this Chapter, we restrict ourselves to treatments ignoring pairing effects. We note that reactions including neutron-rich oxygen isotopes have been well-studied in the TDHF theory as a typical reaction involving light unstable nuclei [96, 97, 102, 189]. We will investigate expectation values of the angular momentum operator and average excitation energies.

We consider reactions in which two fragments are generated after collision. We call the ^{24}O-like fragment nucleus as the PLF and the ^{16}O-like fragment nucleus as the TLF. We describe the reaction in the center-of-mass frame. We choose xy-plane as the reaction plane setting the incident direction parallel to the x axis. The projectile, ^{24}O, moves toward the negative-x direction, while the target, ^{16}O, moves toward the positive-x direction. The impact parameter vector is set parallel to the positive-y direction.

4.2.1 Computational details

We use our own computational code of TDHF calculation for nuclear reactions, as in Ref. [173]. For this study, we use spatial grid points of $N_x \times N_y \times N_z = 90 \times 80 \times 26$ with 0.8-fm mesh spacing. As an initial condition, two nuclei are placed at the distance of 32 fm in the x direction. The initial wave functions of projectile and target nuclei are prepared in a box with $N_x \times N_y \times N_z = 40 \times 40 \times 26$ grid points. We calculate time evolution until a distance between the centers of the PLF and the TLF
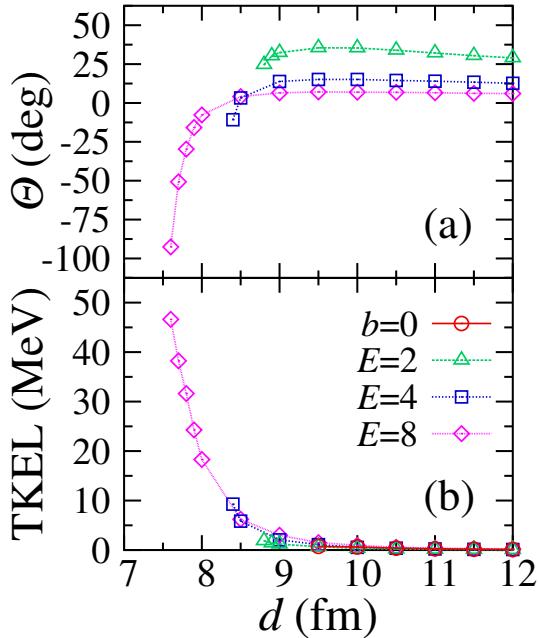
Figure 4.2: Deflection angle Θ in the center-of-mass frame (a) and total kinetic energy loss (b) are shown as functions of the distance of closest approach, $d = d(E, b)$. The figure was taken from Ref. [184].

exceeds 32 fm. For the PNP analysis, integrals over θ are performed by employing the trapezoidal rule discretizing the interval $[0, 2\pi]$ into M equal grids. We find that $M = 30$ is sufficient for the ^{24}O+^{16}O system. All the results reported here are calculated using the Skyrme SLyIII.0.8 parameter set [146].

4.2.2 Ground states

We calculate ground states of ^{16}O and ^{24}O nuclei, which are both spherical in the self-consistent solutions. Figure 4.1 shows single-particle energies of neutrons (red solid lines) and protons (green dotted lines) in ^{16}O in panel (a) and in ^{24}O in panel (b). Occupied orbitals are shown by thick lines, while unoccupied orbitals are shown by thin lines. As recognized from the figure, there are neutron orbitals characterized by small binding energies in neutron-rich ^{24}O nucleus. All proton orbitals in ^{24}O are deeply bound.

4.2.3 Reaction dynamics

We first provide an overview of the reaction dynamics in ^{24}O+^{16}O reactions. In Fig. 4.2, the deflection angle Θ in the center-of-mass frame and the TKEL are shown in the panels (a) and (b), respectively, as functions of the distance of closest approach, d. We evaluate Θ and TKEL from the momenta of two fragment nuclei and the Coulomb energy between them at the final stage of the TDHF calculation where two nuclei are well separated.

We employ the distance of closest approach d, instead of the impact parameter b. They are related by

$$d = \frac{Z_\mathrm{P} Z_\mathrm{T} e^2}{2E} + \sqrt{\left(\frac{Z_\mathrm{P} Z_\mathrm{T} e^2}{2E}\right)^2 + b^2}, \tag{4.2.1}$$

where E denotes the incident relative energy. Z_P and Z_T denote the proton numbers of the projectile and the target, respectively. We consider it is useful to use d, because transfer reactions take place at around the distance of closest approach. For head-on collisions, calculated results are indicated by $b = 0$ and are plotted against d which is related to the incident relative energy E by $d = Z_\mathrm{P} Z_\mathrm{T} e^2/E$.

We find the fusion reaction takes place at $d = 9.4$ fm for head-on collision ($b = 0$) which corresponds to the incident energy of $E_{\text{lab}} \sim 24.5$ MeV. For non-central collisions at incident energies of $E_{\text{lab}} = 2, 4,$ and 8 MeV/nucleon, the fusion reaction is found to take place at $d = 8.7, 8.3,$ and 7.5 fm, respectively.

The deflection angle is positive for reactions at the incident energy of 2 MeV/nucleon because of the Coulomb repulsion, as seen in Fig. 4.2 (a). As the distance of closest approach decreases, the nuclear attractive interaction acts to decrease the deflection angle. It becomes negative for $d < 8$ fm at the incident energy of 8 MeV/nucleon. In the panel (b), we see an increase of the TKEL at the small-d region where we observed negative deflection angles.

4.2.4 Transfer probability

In Fig 4.3, we show transfer probabilities calculated using Eq. (4.1.21). Red circles show probabilities for head-on collisions ($b = 0$) with several values of d. Green triangles, blue squares, and purple diamonds show probabilities as functions of d for incident energies $E_{\text{lab}} = 2, 4,$ and 8 MeV/nucleon, respectively.

In the calculations, we adopted two choices for the spatial region V. For the probabilities observing a PLF, which are shown in the right panels of Fig. 4.3, we adopted a sphere with a radius of 16 fm around the PLF for the spatial region V. For the probabilities observing a TLF shown in the left panels of Fig. 4.3, a sphere with a radius of 16 fm around the TLF is used. We have confirmed that obtained results are almost independent of the chosen radius R of the spatial region V, if R is taken in the range of 15 fm $< R < 20$ fm. We will use this radius for evaluation of expectation values of angular momentum and excitation energies.

Figure 4.3 (a) and (b) show probabilities of one-proton transfer processes, while (c) and (d) show probabilities of two-proton transfer processes. We note that, from the above choices of V for the PLF and the TLF, the probabilities of proton removal from ^{16}O ((a) and (c)) should be coincide with the probabilities of proton addition to ^{24}O ((b) and (d)), if the breakup processes can be neglected. As seen from the figure, (a) and (b) are very close to each other, indicating that the breakup processes are indeed negligible. We also find that (c) and (d) are close to each other. On the other hand, in the case of neutron transfer channels, one-neutron transfer in panels (e) and (f) and two-neutron transfer in panels (g) and (h), we find that the probability of neutron removal from ^{24}O is much larger than that of neutron addition to ^{16}O, especially for reactions at $E_{\text{lab}} = 8$ MeV/nucleon. This fact indicates that there are substantial probabilities of breakup processes for neutrons.

In Fig. 4.3, we find that transfer probabilities decrease as the incident energy increases. Comparing probabilities of neutron and proton transfer processes, neutron transfer probabilities are much larger than proton transfer probabilities at the same distance of closest approach and the same incident energy. We also find that the slope of probabilities for protons against the distance of closest approach is much steeper than that for neutrons. These features are consistent with orbital energies of the two colliding nuclei in their ground states which are shown in Fig. 4.1. Since there are neutrons bound weakly in ^{24}O, transfer probabilities of neutrons are much larger than those of protons. Since these weakly bound neutrons are spatially extended in ^{24}O, we find a long tail of neutron transfer probabilities.

At the highest incident energy of $E_{\text{lab}} = 8$ MeV/nucleon, the proton transfer probability is maximum around $d = 8$ fm. The probability decreases as the distance of closest approach decreases. The decrease at the small-d region indicates the increase of probabilities for other channels with transfers of a larger number of protons.
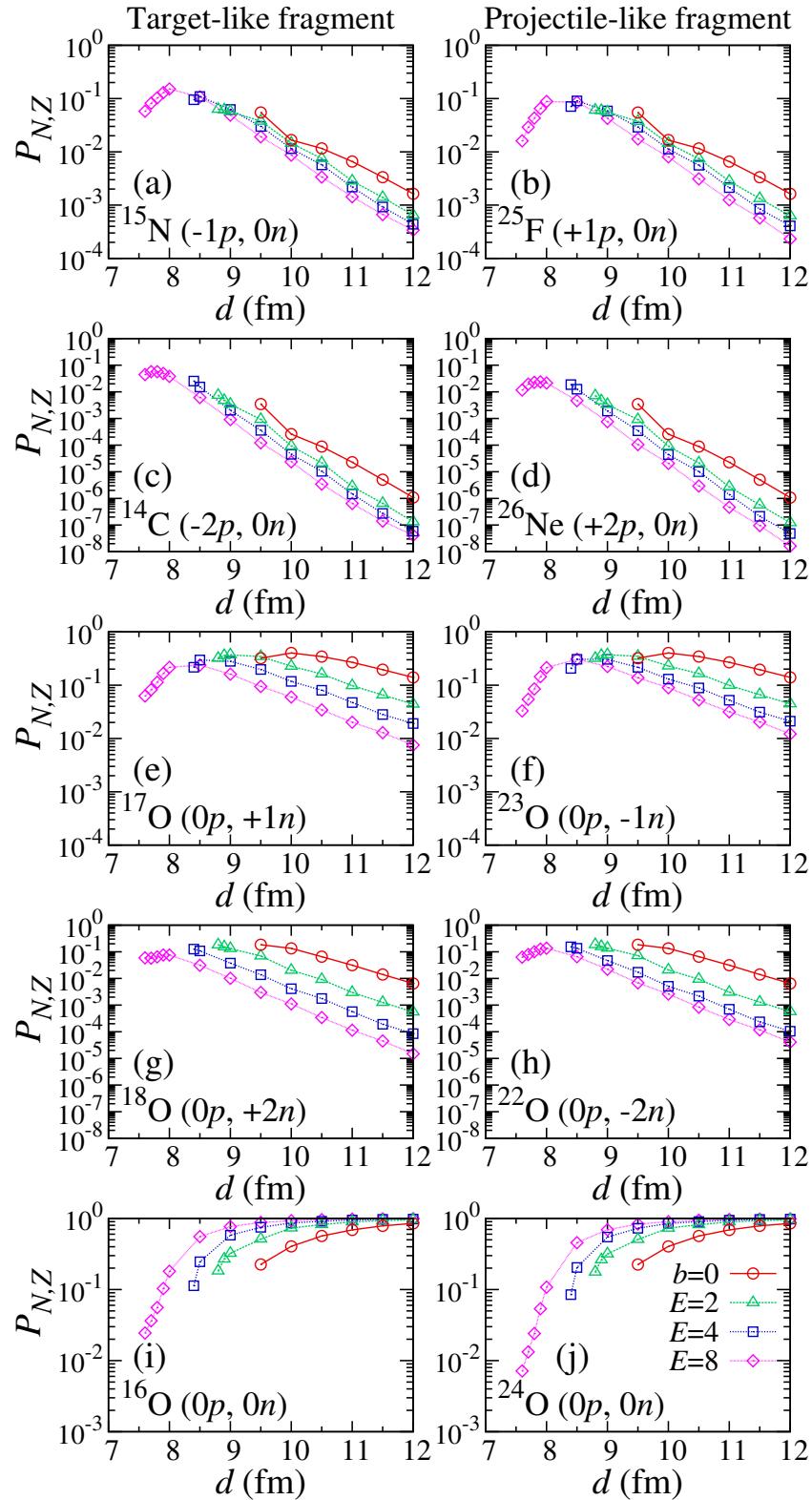
Figure 4.3: Transfer probabilities with respect to the TLF (left) and the PLF (right) are shown as functions of the distance of closest approach, $d = d(E, b)$. The figure was taken from Ref. [184].

4.2.5 Angular momentum

In this Subsection, we investigate expectation values of the angular momentum operator in the fragment nuclei. We will use the same definition for V as that in the previous Subsection, spheres with a radius of 16 fm around the center-of-mass of the PLF and the TLF. We consider the angular momentum operator in the spatial region V, $\hat{\boldsymbol{J}}_V = \hat{\boldsymbol{J}}_V^{(n)} + \hat{\boldsymbol{J}}_V^{(p)}$. The operator $\hat{\boldsymbol{J}}_V^{(q)}$ denotes the angular momentum operator for neutrons ($q = n$) and for protons ($q = p$) in the spatial region V, given by $\hat{\boldsymbol{J}}_V^{(q)} = \sum_{i \in q} \Theta_V(\boldsymbol{r}_i) \hat{\boldsymbol{j}}_i = \sum_{i \in q} \Theta_V(\boldsymbol{r}_i)\left[(\hat{\boldsymbol{r}}_i - \boldsymbol{R}_\mu) \times \hat{\boldsymbol{p}}_i + \hat{\boldsymbol{s}}_i\right]$. $\boldsymbol{R}_\mu$ is the center-of-mass coordinate of the fragment (μ = PLF or TLF).

Figure 4.4 shows expectation values of the angular momentum operators in the PLF and the TLF composed of specific numbers of neutrons and protons. A component perpendicular to the reaction plane is shown. Left panels show expectation values in the TLF, while right panels show those in the PLF. For reactions at $E_{\text{lab}} = 8$ MeV/nucleon, expectation values at the small-d region, $d < 8$ fm, are always positive irrespective of the numbers of transferred nucleons. This fact supports a macroscopic picture of a friction converting the angular momentum from the nucleus-nucleus relative motion to the internal ones.

In the following, we discuss results at relatively large-d region ($d > 9$ fm). In these reactions, the distance of closest approach is much larger than the sum of radii of two colliding nuclei, and transfer processes are considered to proceed as single-particle dynamics. TDHF calculations may describe either above-barrier transfer or quantum tunneling below the barrier. In nucleon removal channels ((a), (c), (f), and (h)), we find that the expectation values of the angular momentum operator are very small irrespective of either neutron(s) or proton(s) is(are) removed, either from ^{16}O or ^{24}O. This fact may be understood from properties of orbitals. For ^{16}O, orbitals of the smallest binding energy are $1p_{1/2}$ for both neutrons and protons. For ^{24}O, they are $2s_{1/2}$ for neutrons and $1p_{1/2}$ for protons. We thus find that the orbitals of the smallest binding energy are characterized by small angular momenta. Since nucleon removals from spatially extending single-particle orbitals are expected to take place for orbitals with the smallest binding energy, removal of nucleons from these orbitals may not leave large values of angular momentum in nucleon removed nuclei.

In nucleon addition channels ((b), (d), (e), and (g)), we find finite positive values of angular momentum in all channels. The expectation values increase as the incident energy increases. They do not depend much on the distance of closest approach d. These features may be understood by the following intuitive considerations. Let us consider a transfer of one nucleon from ^{24}O to ^{16}O. We assume that the nucleon transfer takes place when two nuclei are at the distance of closest approach. Ignoring the interaction potential by nuclear force, the relative velocity of two nuclei is approximately given by

$$v_{\text{rel}} = \sqrt{\frac{2}{\mu}\left(E - \frac{Z_{\text{P}} Z_{\text{T}} e^2}{d}\right)}, \tag{4.2.2}$$

where E and μ denote the incident relative energy and the reduced mass, respectively. In the rest frame of ^{16}O nucleus, we assume that the transferred nucleon has the same velocity as the relative velocity v_{rel}, ignoring the internal motion in ^{24}O. This may be reasonable, since we observed very small expectation values of the angular momentum in nucleon removed fragments, as seen in Fig. 4.4 (a), (c), (f), and (h). If the transferred nucleon stays at the surface of ^{16}O, the transferred nucleon brings the angular momentum,

$$l_z = R m v_{\text{rel}}, \tag{4.2.3}$$

into ^{16}O, where m is the nucleon mass and R is the radius of ^{16}O which we estimate by a simple formula, $R = r_0 A^{1/3}$, with $r_0 = 1.2$ fm and $A = 16$.

In Fig. 4.5, we show the angular momentum l_z evaluated using Eqs. (4.2.2) and (4.2.3) as functions of the distance of closest approach d for several energies. The estimated values of the angular
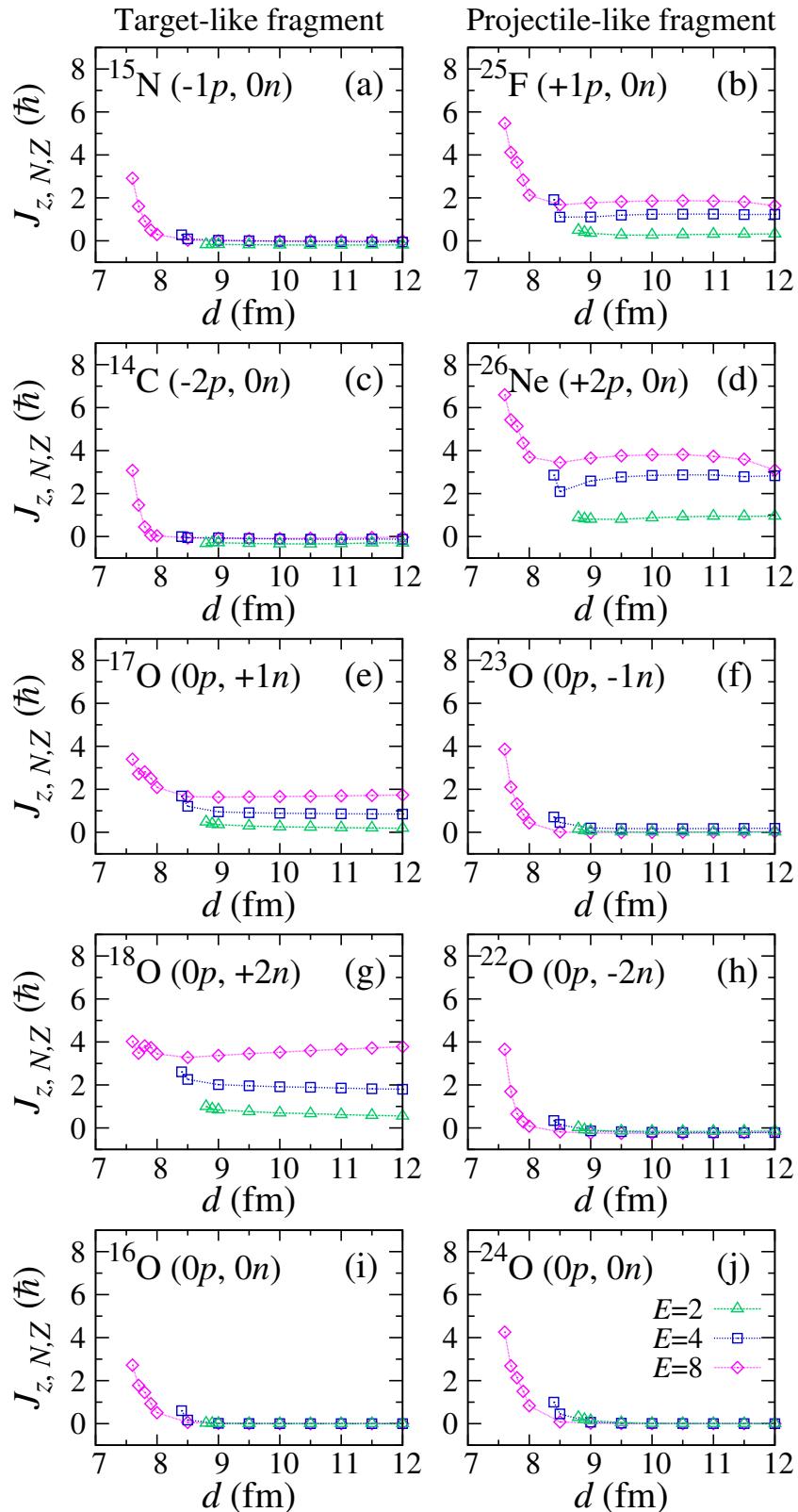
Figure 4.4: Expectation values of the angular momentum operator for fragment nuclei in each transfer channel are shown as functions of the distance of closest approach, $d = d(E, b)$. The figure was taken from Ref. [184].
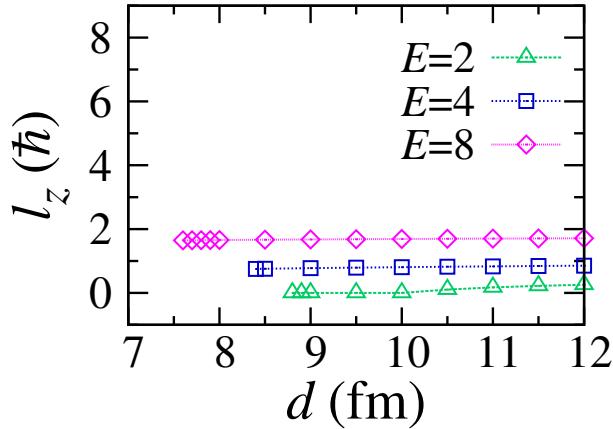
Figure 4.5: The angular momentum carried into ^{16}O by an added nucleon evaluated by Eqs. (4.2.2) and (4.2.3) is shown as a function of the distance of closest approach, $d = d(E, b)$. The figure was taken from Ref. [184].

momentum coincide quantitatively with the calculated results in channels of one-neutron addition to ^{16}O, shown in Fig. 4.4 (e). The estimated angular momentum depends little on the distance of closest approach d, since the Coulomb potential in Eq. (4.2.2) gives only a minor effect except for a case of very low incident energy. The angular momentum is roughly proportional to the square root of the energy. In the case of two-nucleon transfer, the angular momentum carried into ^{16}O is given by twice of l_z. This reasonably explains the observation in the panel (g).

4.2.6 Excitation energy

In Fig. 4.6, we show excitation energies of fragment nuclei evaluated using Eq. (4.1.25) as functions of the distance of closest approach d. Left panels show the excitation energies of the TLF, while right panels show the excitation energies of the PLF. As in previous figures, there are two kinds of calculations: Red circles show results of head-on collisions ($b = 0$) varying the incident energy. Green triangles, blue squares, and purple diamonds show results for fixed incident energies, $E_{\mathrm{lab}} = 2$, 4, and 8 MeV/nucleon, respectively, changing the impact parameter b.

As we mentioned below Eq. (4.1.25), we take into account the center-of-mass correction in calculating energies of fragment nuclei and reference energies of ground states in Eq. (4.1.25), while we ignore it in the time evolution calculations. For the quasielastic channels without nucleon transfer, we find very small average excitation energies at large-d region, $d > 9$ fm, as shown in the panels (i) and (j). This fact may indicate that the inconsistency between the treatments of the center-of-mass correction in evaluating excitation energies will not bring any serious problems.

In all channels, we find an increase of the excitation energy in a small-d region, $d < 8$ fm, where we find an appreciable TKEL in Fig. 4.2 (b). At a large-d region, $d > 9$ fm, we have found the small TKEL in Fig. 4.2 (b). However, behavior of the excitation energy depends much on the transfer channels, as is evident from Fig. 4.6.

In nucleon removal channels ((a), (c), (f), and (h)), we find that excitation energies are rather small. In either one-neutron removal from ^{24}O in (f) or one-proton removal from ^{16}O in (a), the average excitation energy is less than 3 MeV. This indicates that the nucleon is removed dominantly from the highest occupied orbital. In two-nucleon removal channels ((c) and (h)), the excitation energy becomes somewhat large, about 5-10 MeV in two-proton removal from ^{16}O in (c). The excitation energies after nucleon removal are almost independent of the incident energy. This suggests that nucleons are removed gently even at higher incident energies.

Contrarily, in nucleon addition channels ((b), (d), (e), and (g)), we find that excitation energies

depend much on the incident energy. A similar feature was also seen in the angular momentum shown in Fig. 4.4, where the added nucleon carries an angular momentum associated with the translational relative motion into the fragment. The expectation values of the angular momentum were also found to increase as the incident energy increases. This fact may be related to the increase of the excitation energies as the incident energy increases in nucleon addition channels: The transferred nucleons must stay at orbitals of higher angular momenta as the incident energy increases. The energies of orbitals with higher angular momenta are high.

For nucleon addition channels ((b), (d), (e), and (g)), we observe an increase of excitation energies as the distance of closest approach increases. One may consider that this fact contradicts to an intuitive picture that an excitation energy will be smaller as the distance of closest approach increases since two nuclei cannot collide violently. We examine this behavior for head-on collisions ($b = 0$). As shown by red circles in the panels (b), (d), (e), and (g), the excitation energies are very small at $d = 9.5$ fm. This distance of closest approach corresponds to slightly outside the boundary of the fusion reaction. As the distance of closest approach increases (this corresponds to a decrease of the incident energy in the head-on collision), the excitation energies increase.

This puzzling behavior can be understood by the following consideration. As we have shown in Fig. 4.1, the Fermi energies of neutrons and protons in ^{24}O and ^{16}O are rather different because of the excess neutrons in neutron-rich ^{24}O. When a nucleon is transferred at a large distance of closest approach which is much larger than the sum of the radius of two colliding nuclei, the nucleon transfer is expected to take place between orbitals which are close in energy. The energy-conserving transfer processes must cause excitations of produced fragments if a neutron-rich nuclei is involved in the reaction.

Let us consider one-proton transfer from ^{16}O to ^{24}O in head-on collisions, which are shown by red circles in the panel (b). The transfer takes place dominantly for a proton in the highest occupied orbital of ^{16}O, $1p_{1/2}$ at -10.6 MeV as shown in Fig. 4.1 (a). In Fig. 4.1 (b), we find proton orbitals at a similar orbital energy, $2s_{1/2}$ at -9.9 MeV. The proton highest occupied orbital of ^{24}O is $1p_{1/2}$ at -24.3 MeV and there are $1d_{5/2}$ unoccupied orbitals at -15.8 MeV. Since one of the $1d_{5/2}$ orbitals is occupied in the ground state of ^{25}F, we expect the excitation energy, $E^* \sim \varepsilon(^{24}\text{O}; \pi 2s_{1/2}) - \varepsilon(^{24}\text{O}; \pi 1d_{5/2}) = 5.9$ MeV. This energy difference almost coincides with the average excitation energy of ^{25}F shown in the panel (b) at the large-d region.

We next consider one-neutron transfer from ^{24}O to ^{16}O in head-on collisions, which are shown by red circles in the panel (e). The highest occupied neutron orbital in ^{24}O is $2s_{1/2}$ at -3.1 MeV as shown in Fig. 4.1 (b). In Fig. 4.1 (a), there are neutron unoccupied orbitals in ^{16}O at a similar energy, $2s_{1/2}$ at -2.4 MeV. Since the lowest neutron unoccupied orbital in ^{16}O is $1d_{5/2}$ orbital at -5.5 MeV which is occupied in the ground state of ^{17}O, we expect the excitation energy, $E^* \sim \varepsilon(^{16}\text{O}; \nu 2s_{1/2}) - \varepsilon(^{16}\text{O}; \nu 1d_{5/2}) = 3.1$ MeV. This energy difference almost coincides with the average excitation energy of ^{17}O shown in the panel (e) at the large-d region.

In the above considerations, we may understand the transfer mechanism in terms of orbital properties in the ground state: the highest occupied orbitals dominantly contribute to the transfer process. We note that, in Ref. [189], single-particle transfer dynamics in ^{24}O$+^{16}$O reaction has been examined analyzing density contributions from individual orbitals. The result reported in Ref. [189] is consistent with the above conclusion.

We make a final comment on an abrupt increase of excitation energy seen at the largest d value, 12 fm, and the highest incident energy, 8 MeV/nucleon in panels (b) and (d). We consider that they are due to a numerical failure. We note that probabilities of these processes are very small, as confirmed in Fig. 4.3.
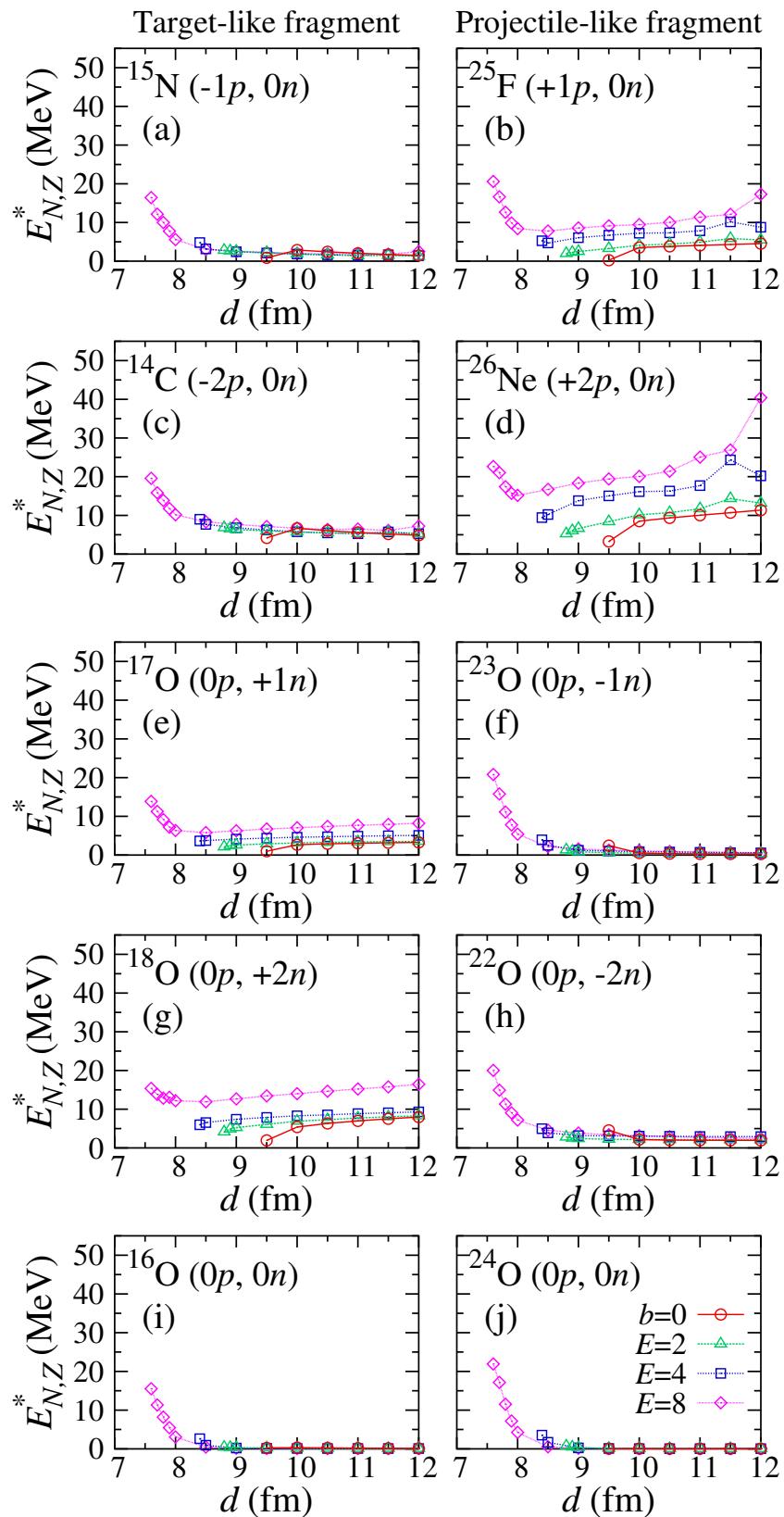
Figure 4.6: Average excitation energies of fragment nuclei in each transfer channel are shown as functions of the distance of closest approach, $d = d(E, b)$. The figure was taken from Ref. [184].

4.3 Summary and Concluding Remarks on Chapter 4

In the TDHF theory, low-energy heavy ion reactions are described by a time evolution of a single Slater-determinant wave function. At the final stage of calculation, the wave function can be regarded as a superposition of a number of channels with different particle numbers and quantum states. To obtain detailed information on reaction products, projection operator techniques will be useful. In this Chapter, we developed a method to calculate expectation values of operators with the PNP to investigate properties of reaction products after collision.

To demonstrate usefulness of our method, we applied the method to one- and two-nucleon transfer processes in ^{24}O+^{16}O reactions. We analyzed expectation values of the angular momentum operator and average excitation energies of produced nuclei. For fragment nuclei after nucleon removal, we found small values of angular momentum and excitation energy, suggesting a gentle removal of nucleons. For fragment nuclei with added nucleons, we found substantial expectation values of angular momentum and average excitation energies. We have found that the expectation value of the angular momentum of produced nuclei is proportional to the relative velocity of the two colliding nuclei at the turning point. The excitation energy can be understood by a transfer of nucleons between approximately degenerate orbitals of projectile and target nuclei.

The above example clearly shows the usefulness of the present method for microscopic investigations of reaction mechanisms in heavy ion reactions. The formalism will also be useful to estimate effects of particle evaporation after MNT processes, which are difficult to describe directly in the TDHF calculation because of the very long timescale of the evaporation processes. In the next Chapter (Chapter 5), we will examine effects of particle evaporation on MNT cross sections utilizing the method developed in this Chapter.

Chapter 5

EFFECTS OF PARTICLE EVAPORATION ON MNT CROSS SECTIONS

In Chapter 3, we presented results of the TDHF calculations for MNT processes in ^{40,48}Ca+^{124}Sn, ^{40}Ca+^{208}Pb, and ^{58}Ni+^{208}Pb reactions. From the results, we found that the TDHF calculations can reproduce measured cross sections quantitatively, when the number of transferred nucleons is small. However, as the number of transferred nucleons increases, a peak position of the calculated cross sections shifts toward larger neutron and proton number sides compared with the measurements. One of possible origins of the discrepancy is an insufficient description of particle evaporation processes in our TDHF calculations. Because we calculated the transfer probabilities and the cross sections from a TDHF wave function just after two nuclei reseparates (typically, order of 10^{-21} s after the reseparation), effects of secondary evaporation processes which occur in a much longer timescale were not included in the calculated cross sections.

To estimate how many nucleons are to be evaporated from produced fragment nuclei, we need to evaluate excitation energy of the fragment nuclei in each transfer channel. In Chapter 4, we have developed a formalism to calculate expectation values of operators in the TDHF wave function after collision with the PNP. The method enables us to evaluate the average excitation energy and the expectation value of the angular momentum operator, which are the basic inputs of statistical models of particle evaporation. In this Chapter, we evaluate effects of particle evaporation using a statistical model [190] in which the excitation energy obtained from the projection analysis can be used as an input quantity[‡].

It is certainly true that correlation effects included in the TDHF theory are somewhat limited. For example, isoscalar and isovector pair transfers, α-cluster transfer are not treated. We consider that MNT cross sections with improved treatment of evaporation processes will help us to uncover what is lacking and what is needed in our description of the MNT processes. The aim of this Chapter is to clarify to what extent the TDHF theory can describe MNT cross sections quantitatively, if we include the effects of particle evaporation.

This Chapter is organized as follows. In Sec. 5.1, we present an outline of our formalism to include the effects of particle evaporation in the calculation of the production cross sections. In Sec. 5.2, we show calculated production cross sections for ^{48}Ca+^{124}Sn and ^{58}Ni+^{208}Pb reactions with and without particle evaporation effects. Possible ways to improve the description of the MNT processes are discussed. In Sec. 5.3, a summary and concluding remarks on this Chapter are presented.

[‡] This Chapter is based on our analysis reported in Ref. [191].

5.1 How to Evaluate Effects of Particle Evaporation

5.1.1 Excitation energy of reaction products

In Chapter 4, we have extended the PNP technique to calculate expectation values of operators, in the particle-number projected TDHF wave function after collision. Using the method, we can calculate energy expectation value of a fragment nucleus composed of N neutrons and Z protons by

$$E_{N,Z}^{\mu} = \frac{\langle \Psi | \hat{H}_V \hat{P}_N^{(n)} \hat{P}_Z^{(p)} | \Psi \rangle}{\langle \Psi | \hat{P}_N^{(n)} \hat{P}_Z^{(p)} | \Psi \rangle}, \tag{5.1.1}$$

where μ denotes either PLF or TLF, a fragment nucleus to be analyzed included in the spatial region V. $\hat{H}_V \equiv \hat{T}_V + \hat{V}_V = \sum_i \Theta_V(\boldsymbol{r}_i) \hat{t}_i + \sum_{i<j} \Theta_V(\boldsymbol{r}_i)\Theta_V(\boldsymbol{r}_j) \hat{v}_{ij}$ denotes a Hamiltonian acting only for the fragment nucleus. As explained in Chapter 4, we remove the energy associated with the center-of-mass motion of the fragment nucleus by changing the coordinate system to the rest frame of the fragment.

We evaluate the energy expectation value using Eq. (5.1.1). The kinetic energy term for the fragment nucleus composed of N neutrons and Z protons can be calculated as

$$\mathcal{T}_{N,Z}^{\mu} = \mathcal{T}_N^{(n)\,\mu} + \mathcal{T}_Z^{(p)\,\mu}, \tag{5.1.2}$$

where

$$\mathcal{T}_n^{(q)\,\mu} \equiv \frac{1}{2\pi P_n^{(q)}} \int_0^{2\pi} d\theta\, e^{in\theta} \det \mathcal{B}^{(q)}(\theta) \frac{\hbar^2}{2m} \sum_{i\in q,\,\sigma} \int_V d\boldsymbol{r}\, \boldsymbol{\nabla}\psi_i^*(\boldsymbol{r}\sigma) \cdot \boldsymbol{\nabla}\tilde{\psi}_i(\boldsymbol{r}\sigma,\theta). \tag{5.1.3}$$

$\tilde{\psi}_i(\boldsymbol{r}\sigma,\theta)$ is defined by $\tilde{\psi}_i(\boldsymbol{r}\sigma,\theta) \equiv \sum_{k\in q_i} \left(\mathcal{B}^{(q_i)}(\theta) \right)_{ik}^{-1} \psi_k(\boldsymbol{r}\sigma)$. The center-of-mass correction is simply taken into account by considering the one-body term, replacing the coefficient of the kinetic energy operator $\frac{\hbar^2}{2m}$ with $\frac{\hbar^2}{2m}(1-\frac{1}{A})$, where $A = N+Z$ denotes the mass number of the fragment nucleus. The interaction part is calculated using transition densities, (e.g. the transition proton density is given by $\tilde{\rho}^{(p)}(\boldsymbol{r},\theta) \equiv \sum_{i\in p,\,\sigma} \psi_i^*(\boldsymbol{r}\sigma)\tilde{\psi}_i(\boldsymbol{r}\sigma,\theta)$). The two-body and three-body interaction terms for the fragment composed of N neutrons and Z protons are calculated as

$$\mathcal{E}_{N,Z,\text{int}}^{\mu} \equiv \frac{1}{(2\pi)^2 P_N^{(n)} P_Z^{(p)}} \int_0^{2\pi} d\theta \int_0^{2\pi} d\varphi\, e^{i(N\theta+Z\varphi)} \det \mathcal{B}(\theta,\varphi) \int_V d\boldsymbol{r}\, \tilde{\mathcal{V}}[\boldsymbol{r},\theta,\varphi], \tag{5.1.4}$$

where $\det \mathcal{B}(\theta,\varphi) \equiv \det \mathcal{B}^{(n)}(\theta) \det \mathcal{B}^{(p)}(\varphi)$. The Coulomb energy is evaluated using the transition proton density, $\tilde{\rho}^{(p)}(\boldsymbol{r},\theta)$, inside the spatial region V.

We then define the excitation energy of the PLF composed of N neutrons and Z protons by

$$E_{N,Z}^{*\,\mu}(E,b) \equiv \mathcal{E}_{N,Z}^{\mu}(E,b) - E_{N,Z}^{\text{g.s.}}, \tag{5.1.5}$$

where

$$\mathcal{E}_{N,Z}^{\mu} \equiv \mathcal{T}_{N,Z}^{\mu} + \mathcal{E}_{N,Z,\text{int}}^{\mu} + \mathcal{E}_{Z,\text{Coul}}^{\mu} \tag{5.1.6}$$

denotes the energy expectation value of the fragment nucleus. $E_{N,Z}^{\text{g.s.}}$ is the ground state energy of the nucleus composed of N neutrons and Z protons. In order to evaluate the excitation energy of reaction products in various transfer channels, we performed ground state calculations for isotopes with the atomic number $14 \leq Z \leq 35$ using the Skyrme SLy5 parameter set. Properties of the HF ground states for those nuclei are summarized in Appendix E.

In this Chapter, we will evaluate effects of particle evaporation on production cross sections for ^{48}Ca+^{124}Sn and ^{58}Ni+^{208}Pb reactions which were analyzed in Chapter 3. Thus, we have already calculated TDHF wave functions after collision using the SLy5 parameter set [141]. However, there is

a mathematical problem in evaluating $\mathcal{E}^{\mu}_{N,Z,\text{int}}$, Eq. (5.1.4), using a Skyrme EDF with the fractional-power density [148, 149, 150], as we mentioned in Sec. 2.1.2. Since the SLy5 parameter set contains a fractional-power density, we performed the following two types of calculations to examine reliability of our calculation:

(i) : We evaluate both $\mathcal{E}^{\mu}_{N,Z,\text{int}}$ and $E^{\text{g.s.}}_{N,Z}$ using the SLy5 parameter set. In this case, the Skyrme EDF used for the TDHF calculations and for the HF ground state calculations becomes the same. However, there remains the ambiguity because of the use of the fractional-power density.

(ii) : We evaluate $\mathcal{E}^{\mu}_{N,Z,\text{int}}$ with the SLyIII.0.8 parameter set [146] using the same TDHF wave function after collision as in the method (i) (calculated with SLy5). Correspondingly, we evaluate $E^{\text{g.s.}}_{N,Z}$ with the SLyIII.0.8 parameter set using the same HF ground state wave function as in the method (i) (calculated with SLy5). Since the SLyIII.0.8 parameter set contains only integer-power densities, we can avoid the mathematical problem in evaluating $\mathcal{E}^{\mu}_{N,Z,\text{int}}$.

Although the method (ii) avoid the problem, there arises a mismatch between the Skyrme EDF and the wave functions. As a result, we find constantly larger energy of $\mathcal{E}^{\mu}_{N,Z,\text{int}}$ (about 5-10 MeV) than the energy evaluated by the method (i) for all transfer channels. We thus also evaluate $E^{\text{g.s.}}_{N,Z}$ in a similar way to obtain consistently large ground state energies in the method (ii). The ground state energies evaluated by the methods (i) and (ii) are shown in 3rd and 11th columns of Tables E.1-E.20 in Appendix E, respectively. We note that the both methods (i) and (ii) give similar values of the excitation energy and resulting cross sections are almost the same. In the following, we will show results obtained by applying excitation energies evaluated by the method (ii).

5.1.2 Particle evaporation probabilities

We evaluate the effects of particle evaporation employing a statistical model developed by Dostrovsky and his coworkers [190]. In this model, evaporation of neutrons, protons, deuterons, tritons, ^{3}He, and α particles are taken into account. An input of the model is the excitation energy of a nucleus to be disintegrate by particle emission. For more detail explanation of the model, see Ref. [190] and references therein.

Using the average excitation energy evaluated from the TDHF wave function after collision using Eq. (5.1.5) as an input, we simulate evaporation processes. Starting from the excited fragment nucleus, all possible decay sequences are calculated until emissions of any particle are energetically prohibited. A decay chain of the evaporation processes from an initial excited state to a final state is called an *evaporation cascade*. In each evaporation cascade, kinds and energy of emitting particles are determined stochastically.

As an example, let us consider a case that we calculate evaporation processes from an excited fragment nucleus composed of N neutrons and Z protons with excitation energy of $E^{*\mu}_{N,Z}$. If a nucleus composed of N' neutrons and Z' protons is formed at the end of an evaporation cascade, the total numbers of evaporated neutrons and protons are given by $N - N'$ and $Z - Z'$, respectively. We count the number of cases in which n neutrons and z protons are evaporated until the end of an evaporation cascade among all the evaporation cascades examined. We then define the evaporation probability for n-neutron and z-proton emissions by

$$P^{\text{evap.}}_{n,z}\left[E^{*\mu}_{N,Z}(b)\right] = \frac{N_{n,z}}{N_{\text{cascade}}}. \tag{5.1.7}$$

$N_{n,z}$ denotes the total number of processes in which n neutrons and z protons were emitted until the end among all the evaporation cascades. N_{cascade} denotes the total number of evaporation cascades examined. We note that, because the excitation energy, $E^{*\mu}_{N,Z}$, depends on the impact parameter, resulting evaporation probabilities, $P^{\text{evap.}}_{n,z}$, also depend on the impact parameter.
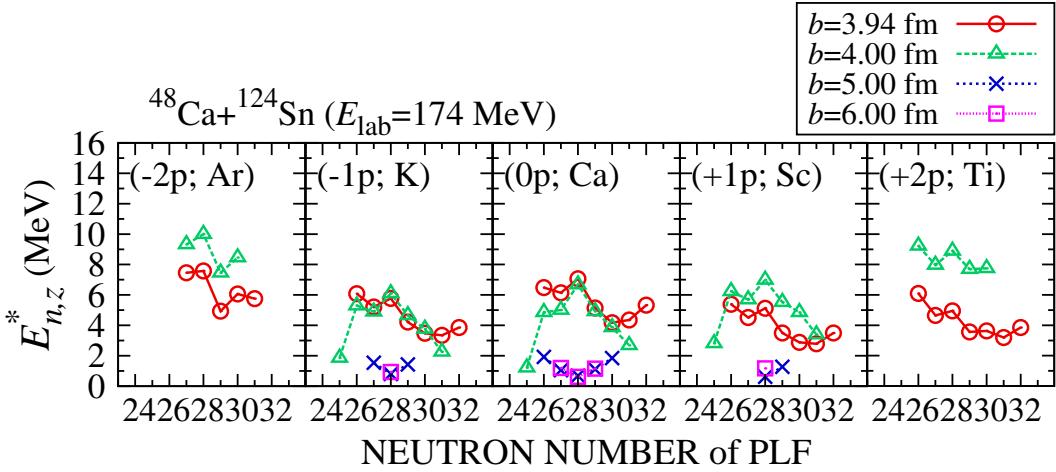
Figure 5.1: Average excitation energy of the PLF in the ^{48}Ca+^{124}Sn reaction at $E_{\mathrm{lab}} = 174$ MeV. Red open circles, green open triangles, blue crosses, purple open squares denote results at impact parameters $b = 3.94, 4, 5, 6$ fm, respectively. Results in transfer channels with small probabilities smaller than 10^{-4} are not shown.

5.1.3   Transfer cross sections with evaporaton effects

In Chapter 3, we calculated a transfer cross section for the channel in which a fragment nucleus is composed of N neutrons and Z protons by integrating the probability $P_{N,Z}(b)$ over the impact parameter,

$$\sigma_{\mathrm{tr}}(N, Z) = 2\pi \int_{b_{\min}}^{\infty} b \; P_{N,Z}(b) \, db. \tag{5.1.8}$$

The minimum impact parameter of the integration was taken to be a border dividing fusion and binary reactions. We assumed that both projectile and target nuclei are spherical, so that the reaction is specified by the incident energy E and the impact parameter b. In practice, we first examined the maximum impact parameter, b_{f}, in which fusion reactions take place for a given incident energy. We then repeated reaction calculations at various impact parameters for the region, $b > b_{\mathrm{f}}$, and calculated the cross section by numerical quadrature according to Eq. (5.1.8).

To include effects of particle evaporation into the cross sections, we simply extend the expression of the cross sections by using the evaporation probabilities obtained from the statistical calculation. Let us denote the evaporation probability for n-neutron and z-proton emission from a fragment μ composed of $N + n$ neutrons and $Z + z$ protons having excitation energy of $E_{N+n,Z+z}^{*\,\mu}$ as $P_{n,z}^{\mathrm{evap.}}\left[E_{N+n,Z+z}^{*\,\mathrm{PLF}}\right]$. The residual nucleus after the particle evaporation is composed of N neutrons and Z protons. We calculate the cross section for a channel where the fragment nucleus is composed of N neutrons and Z protons including effects of particle evaporation by

$$\sigma_{\mathrm{tr}}^{\mathrm{evap.}}(N, Z) = 2\pi \int_{b_{\min}}^{\infty} b \sum_{n,z} P_{N+n,Z+z}(b) \, P_{n,z}^{\mathrm{evap.}}\left[E_{N+n,Z+z}^{*\,\mu}(b)\right] db, \tag{5.1.9}$$

where the summation is taken for all possible n-neutron and z-proton evaporation processes.
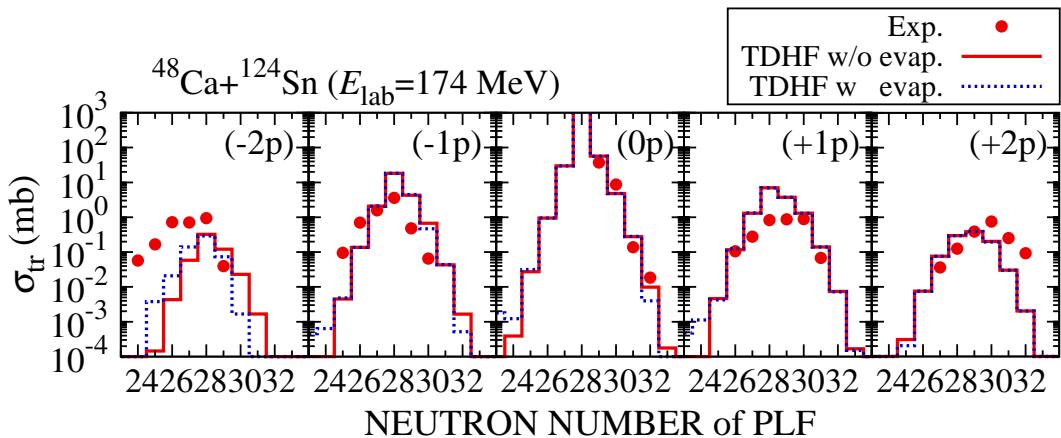
Figure 5.2: Production cross sections of the projectile (^{48}Ca) like fragments in ^{48}Ca+^{124}Sn reaction at $E_{\text{lab}} = 174$ MeV. Solid (dotted) line shows cross sections calculated by the TDHF theory without (with) evaporation effects. Measured cross sections [43] are also shown by filled circles.

5.2 Results and Discussion

We show the effects of particle evaporation on production cross sections in the ^{48}Ca+^{124}Sn and ^{58}Ni+^{208}Pb reactions which we analyzed in Chapter 3, as illustrative examples.

In Fig. 5.1, we show average excitation energy of the PLF in the ^{48}Ca+^{124}Sn reaction at $E_{\text{lab}} = 174$ MeV evaluated by Eq. (5.1.5). Each panel shows excitation energy of specific isotopes in each proton transfer channel. Horizontal axis is the neutron number of the PLF. Results for reactions at several impact parameters are shown for comparison. Red open circles, green open triangles, blue crosses, and purple open squares denote results at impact parameters, 3.94 fm, 4 fm, 5 fm, and 6 fm, respectively. Excitation energy of nuclei with a small production probability smaller than 10^{-4} is not shown.

When the impact parameter is small just outside the fusion critical impact parameter ($b = 3.94$ fm), we find a finite excitation energy of about 6 MeV for all transfer channels. We find a similar result for $b = 4$ fm case. As the impact parameter increases ($b = 5$ and 6 fm), excitation energy becomes very small at most 2 MeV. Because the excitation energy of the fragment nuclei for the ^{48}Ca+^{124}Sn reaction is not so large, we expect a small effect of particle evaporation for this system.

In Fig. 5.2, we show production cross sections of the PLF in the ^{48}Ca+^{124}Sn reaction with and without the effect of particle evaporation. Red filled circles show measured cross sections [43], while red solid (blue dotted) lines show results of the TDHF calculation without (with) the evaporation effect. Cross sections are classified according to the number of transferred protons indicated by ($\pm x$p) in the figure. Horizontal axis is the number of neutrons in the PLF.

From the figure, we find that the effects of particle evaporation are somewhat small as expected from the observation of small excitation energy in Fig. 5.1. We find a visible effect in the two-proton removal channel (-2p). Although the particle evaporation modifies the cross sections of the two-proton removal channel toward a direction consistent with the experimental data, the calculated cross sections still underestimate the measured cross sections when the number of neutrons in the PLF becomes small. We note that the GRAZING calculation reported in Ref. [43] shows similar results indicating a minor effect of particle evaporation (*cf.* Fig. 3.25).

Next, we show results for the ^{58}Ni+^{208}Pb reaction at $E_{\text{lab}} = 328.4$ MeV. In Fig. 5.3, we show average excitation energy of the PLF in the ^{58}Ni+^{208}Pb reaction evaluated by Eq. (5.1.5). As in Fig. 5.1, results for different proton transfer channels are shown in different panels and horizontal axis denotes the number of neutrons in the PLF. Results for reactions at typical impact parameters,
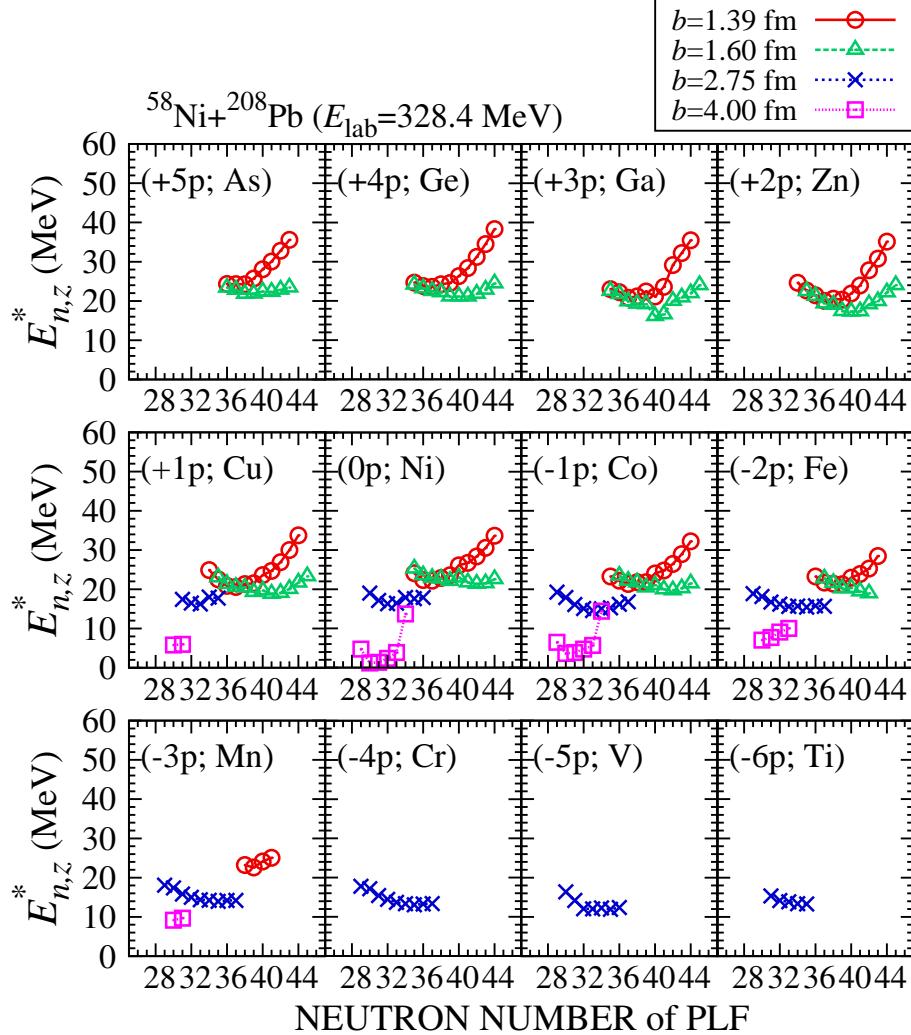
Figure 5.3:   Average excitation energy of PLF in ^{58}Ni+^{208}Pb reaction at $E_{\text{lab}} = 328.4$ MeV. Red open circles, green open triangles, blue crosses, purple open squares denote results at impact parameters $b = 1.39$, 1.6, 2.75, 4 fm, respectively. Results in transfer channels with small probabilities smaller than 10^{-4} are not shown.

$b = 1.39$, 1.60, 2.75, and 4 fm are shown. Excitation energy of nuclei with a small production probability smaller than 10^{-4} is not shown.

When the impact parameter is small just outside the fusion critical impact parameter ($b = 1.39$ fm), proton-pickup reactions occur through the neck breaking transfer dynamics. Because the neck breaking dynamics accompanies a large amount of TKEL as shown in Fig. 3.17 (b), we expect a substantial excitation in reaction products generated through the neck breaking dynamics. From the figure, we indeed find a large excitation energy up to around 40 MeV for those nuclei. When the impact parameter is slightly large ($b = 1.6$ fm), we find a similar excitation energy for reaction products in proton-pickup channels. As the impact parameter increases, excitation energy of reaction products decreases. At an impact parameter of 4 fm, we find somewhat small excitation energy of reaction products. We find that the average excitation energy is not so much dependent on the number of transferred nucleons in reactions at a given impact parameter.

In Fig. 5.4, we show production cross sections in the ^{58}Ni+^{208}Pb reaction classified according to the change of the proton number of the PLF from ^{58}Ni, as functions of the neutron number of the PLF. Red filled circles denote measured cross sections [47] and red solid (blue dotted) lines denote results of
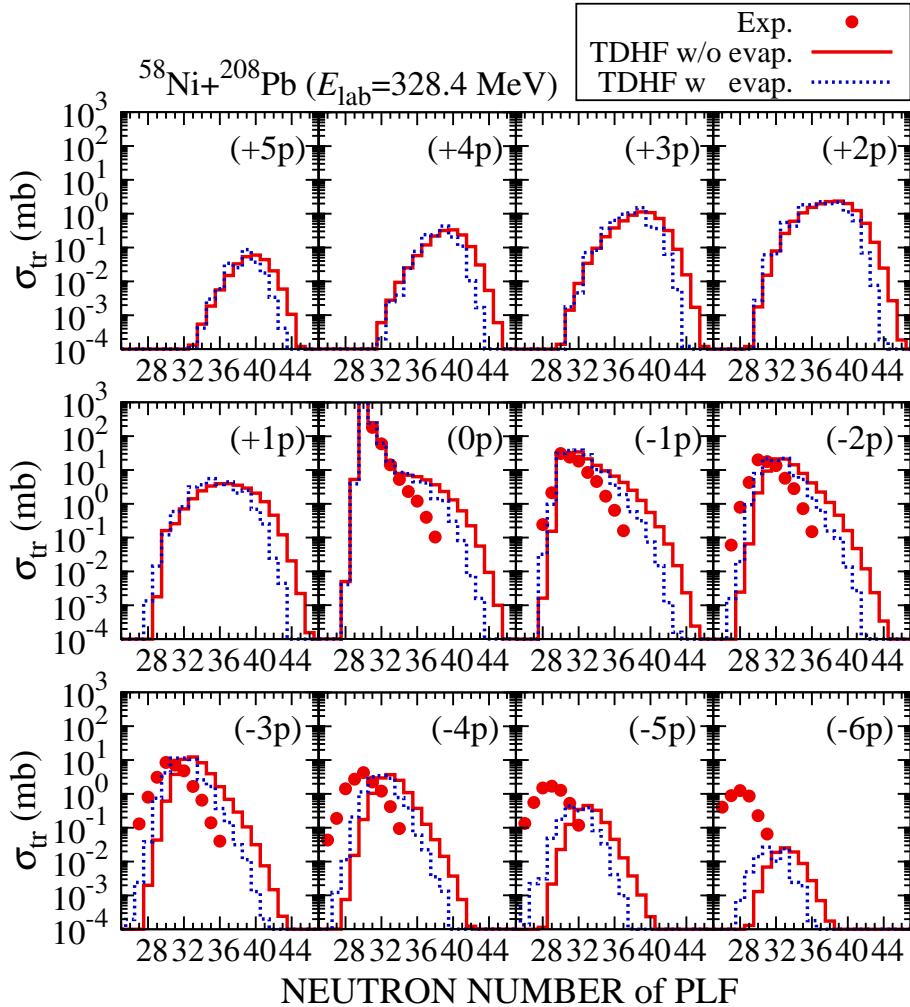
Figure 5.4: Production cross sections of the projectile (^{58}Ni) like fragments in ^{58}Ni+^{208}Pb reaction at $E_{lab} = 328.4$ MeV. Solid (dotted) line shows cross sections calculated by the TDHF theory without (with) evaporation effects. Measured cross sections [47] are also shown by filled circles.

the TDHF calculations without (with) effects of particle evaporation. As can be seen from the figure, the inclusion of effects of particle evaporation modifies the cross sections slightly toward lower neutron number side consistent with the experimental data. However, as the number of transferred nucleons increases, there appear discrepancies even when we include evaporation effects.

We conceive several possible origins of the discrepancy as follows. (*i*) We may consider that, if there were more particle evaporation of not only neutrons but also protons, the calculated cross sections would shift toward the desired direction indicated by the experimental data. Because we only performed the PNP when we evaluate excitation energy of reaction products, the evaluated excitation energy is averaged over all possible quantum states of the fragment nucleus. We anticipate that there are certain states having higher excitation energies compared with the average excitation energy. These states would emit more particles than the average state which we used to evaluate the evaporation effects. We note that to calculate an excitation-energy distribution by an *energy projection* is difficult and we could not investigate this possibility yet. In addition, we assumed that each primary reaction product becomes a CN keeping its mass and excitation energy. There would also be fast preequilibrium particle emissions which are not considered in our treatment. Such preequilibrium particle emissions may also increase the number of emitted particles.

Another possible origin of the discrepancy is (*ii*) an insufficient description of the MNT processes

because of the mean-field nature of the TDHF theory. In the TDHF theory, MNT processes are described by transfer of single-particle wave functions in a *single* time-dependent mean-field potential. In reality, we expect a transfer-channel dependent potential. That is, the depth of the potential would be changed depending on the number of transferred nucleons between two colliding nuclei. For example, in the ^{58}Ni+^{208}Pb case, when many protons are removed from ^{58}Ni, the depth of the potential for nucleons inside the projectile-like nucleus should become shallower and it would suppress neutron transfer from ^{208}Pb to ^{58}Ni. This kind of transfer-channel dependence of the mean-field potential is not sufficiently included in the description of the TDHF theory. A promising way to improve the description is a use of time-dependent generator coordinate method (TDGCM) [192, 193]. The TDGCM is a time-dependent extension of the generator coordinate method (GCM) which has widely succeeded in calculating static nuclear properties including many-body correlations beyond the mean-field level [136]. The method based on a time-dependent variational principle with a trial function which is given by a superposition of time-dependent many-body wave functions. The coefficients of those time-dependent basis functions (generator coordinates) are determined obeying the variational principle. By choosing the time-dependent basis functions as a superposition of TDHF wave functions with a constraint on average number of transferred nucleons or TDHF wave functions for different projectile-target combinations (*e.g.* ^{57}Co+^{209}Bi, ^{56}Fe+^{210}Po, and so on, for the ^{58}Ni+^{208}Pb system), we may get a more sufficient description of the MNT processes. Although we recognize a difficulty concerning the absence of the many-body Hamiltonian in the TDHF theory with a density-dependent Skyrme EDF [193], recently, a density-independent functional has been developed [194]. Since the TDGCM calculation requires only about 10 times larger computational cost compared with the TDHF theory (of course, it depends on how may generator coordinates we use) and there is a development of the density-independent functional, it will be a promising tool to improve our description of the MNT processes.

The other possible origin of the discrepancy is (*iii*) a luck of correlation effects beyond the mean-field level. For example, the pairing correlation is known to be important in nuclear structure at low excitation energy. Although effects of pairing correlations on reaction dynamics have not been fully understood yet, significant effects on MNT processes have been advocated [47, 50]. The time-dependent Hartree-Fock-Bogoliubov (TDHFB) theory would provide us a sufficient description of nuclear dynamics including effects of the pairing correlation [195, 196, 197, 198]. However, because it requires a tremendous computational cost, the application of the TDHFB theory to the nuclear collision dynamics is a challenging subject. Recently, a simplified version of the TDHFB theory, referred to as TDHF+BCS, has been developed and successfully applied to linear responses and nuclear reactions [199, 200, 201, 202, 203, 204, 205, 206, 207, 208]. A similar analysis of the MNT reaction using the TDHF+BCS to examine effects of pairing on reaction dynamics is of great interests. Another possibility is use of the Barian-Vénéroni variational principle which is equivalent to the time-dependent random phase approximation (TDRPA), which will give us a more better description of the width of mass distributions in the MNT reaction at a small impact parameter region [176]. Other sophisticated approaches such as time-dependent density matrix (TDDM) [209, 210, 211, 212] and stochastic mean-field (SMF) [179, 213, 214, 215] theories would provide us a promising foundation to include further many-body correlations into the description. Application of these theoretical models to the MNT reaction is one of the future subjects of this work.

5.3   Summary and Concluding Remarks on Chapter 5

In this Chapter, we have presented the effects of particle evaporation on MNT cross sections within the framework of the TDHF theory combined with the PNP. We evaluated excitation energy of a fragment nucleus in each transfer channel using the extended PNP technique which we have developed in Chapter 4. As illustrative examples, we showed MNT cross sections for ^{48}Ca+^{124}Sn and ^{58}Ni+^{208}Pb reactions with and without the effect of particle evaporation, and compared them with measured cross sections. We have found that the inclusion of the effects of particle evaporation improves the cross sections toward the direction that the experimental data suggested. However, calculations still underestimate measured cross sections when a number of protons are transferred. Possible origins of the discrepancy and some ways to improve the description were discussed.

In summary, in the first part of the thesis (Part I: Chapters 3, 4, and 5), we have examined whether or not the TDHF theory describes MNT cross sections quantitatively. From the results of the thorough analyses of MNT processes in several systems for which extensive experimental data are available, we draw a conclusion that the TDHF theory is capable of describing the MNT reaction in low-energy heavy ion reactions at energies around the Coulomb barrier reasonably well with an accuracy comparable to the existing theories, GRAZING, CWKB, and the Langevin-type dynamical model.

In the next part of the thesis (Part II: Chapters 6, 7, 8, and 9), we will extend the application of the TDHF theory to reactions involving more heavier nuclei such as ^{238}U. Because of the large charge product $Z_\mathrm{P} Z_\mathrm{T}$ of the system, we will find a substantial contribution from the QF process. Applicability of the TDHF theory to the MNT and QF processes in reactions of very heavy nuclei will be discussed in Part II.

Part II

Application of the TDHF theory to MNT and QF processes in reactions involving more heavier nuclei

Chapter 6

MNT AND QF PROCESSES IN ^{64}Ni$+^{238}$U REACTION

In the first part of the thesis (Part I: Chapters 3, 4, and 5), we have investigated MNT processes in low-energy heavy ion reactions for several systems employing the TDHF theory. In Chapter 3, we showed that MNT cross sections can be reasonably described by the TDHF theory combined with the PNP technique. In Chapter 4, we developed a formalism to calculate expectation values of operators in the TDHF wave function after collision with the PNP. This method enables us to examine properties of reaction products. In Chapter 5, we examined effects of particle evaporation on MNT cross sections by employing a statistical model using excitation energy of reaction products calculated from the TDHF wave function after collision as an input. From the thorough analyses of MNT processes, we concluded that the TDHF theory can quantitatively describe the MNT reaction with an accuracy comparable to other existing theories. Because the TDHF calculation can describe microscopic many-body dynamics without any artificial parameters adjustable for each colliding system, we consider that the TDHF theory will be a useful tool for providing a reliable prediction of MNT cross sections.

In this second part of the thesis (Part II: Chapters 6, 7, 8, and 9), we extend the application of the TDHF theory to reactions involving more heavier nuclei such as ^{238}U. In reactions of heavy nuclei, the QF process is expected to be a dominant process at a small impact parameter region, because of the substantial suppression of the fusion reaction by the strong Coulomb repulsion. The main purpose of this second part is to examine how feasibly the TDHF theory describes the MNT and QF processes in reactions involving heavy nuclei.

In this Chapter, we investigate MNT and QF processes in ^{64}Ni$+^{238}$U reaction as our first application to reactions involving ^{238}U. The ^{64}Ni$+^{238}$U reaction at energies around the Coulomb barrier has been extensively studied experimentally [45, 79, 216, 217]. MNT cross sections were measured by Corradi *et al.* [45] in INFN-LNL, Legnaro, Italy. In Fig. 6.1, we show the measured cross sections (black dots) classified according to the number of transferred protons indicated by ($\pm x$p). The minus sign corresponds to transfer from ^{64}Ni to ^{238}U, while the plus sign corresponds to transfer from ^{238}U to ^{64}Ni. Their precise experimental data show not only proton-stripping channels but also proton-pickup channels. The latter process is not expected from the N/Z ratios of the projectile and target nuclei before the collision. Theoretical analysis using the GRAZING code was also reported in Ref. [45], which are shown in Fig. 6.1 by histograms. The GRAZING calculation reproduced measured cross sections reasonably for (0p), (-1p), and (-2p) channels with a similar accuracy for lighter systems examined in Chapter 3. However, the GRAZING calculation underestimated measured cross sections for proton-pickup channels, may be due to an inappropriate assumption of the strong absorption in a small impact parameter region. The ^{64}Ni$+^{238}$U system has the charge product of $Z_\mathrm{P}Z_\mathrm{T} = 2576$ and the assumption would not be valid if a substantial suppression of the fusion reaction takes place.
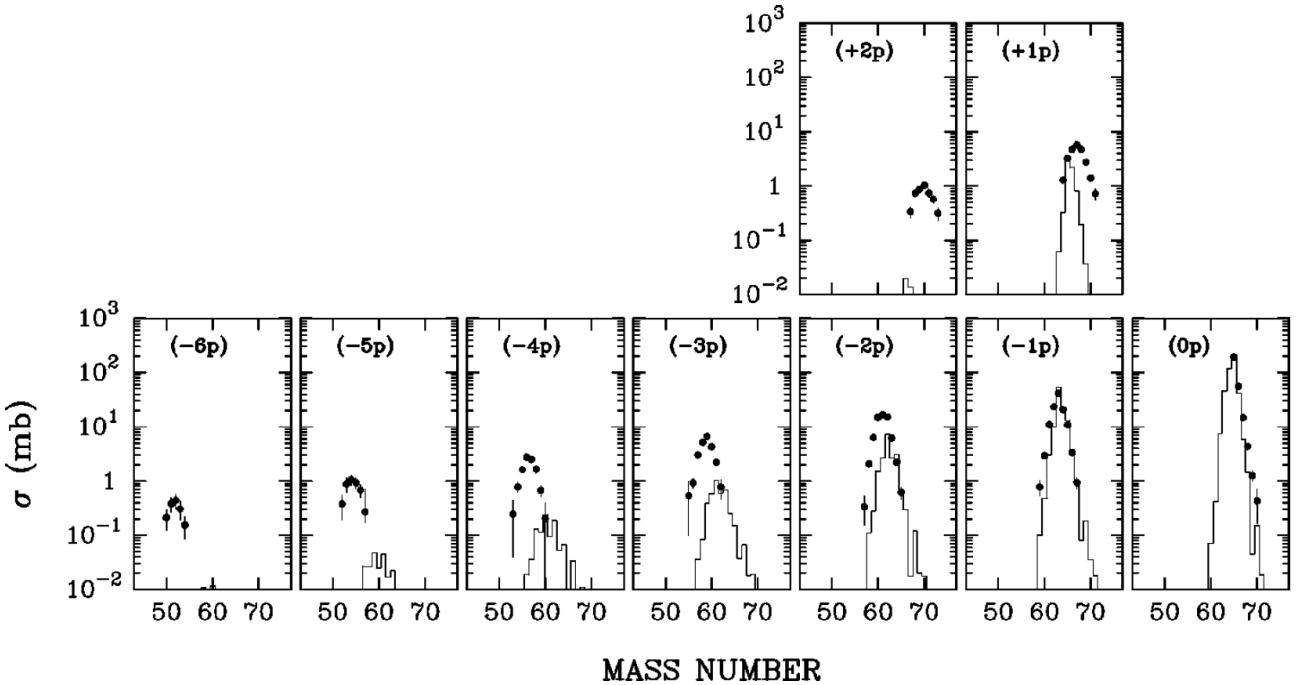
Figure 6.1: Production cross sections for the PLF in the ^{64}Ni+^{238}U reaction at $E_{lab} = 390$ MeV. Dots represent measured cross sections, while histograms represent results calculated by the GRAZING code. The figure was taken from Ref. [45].
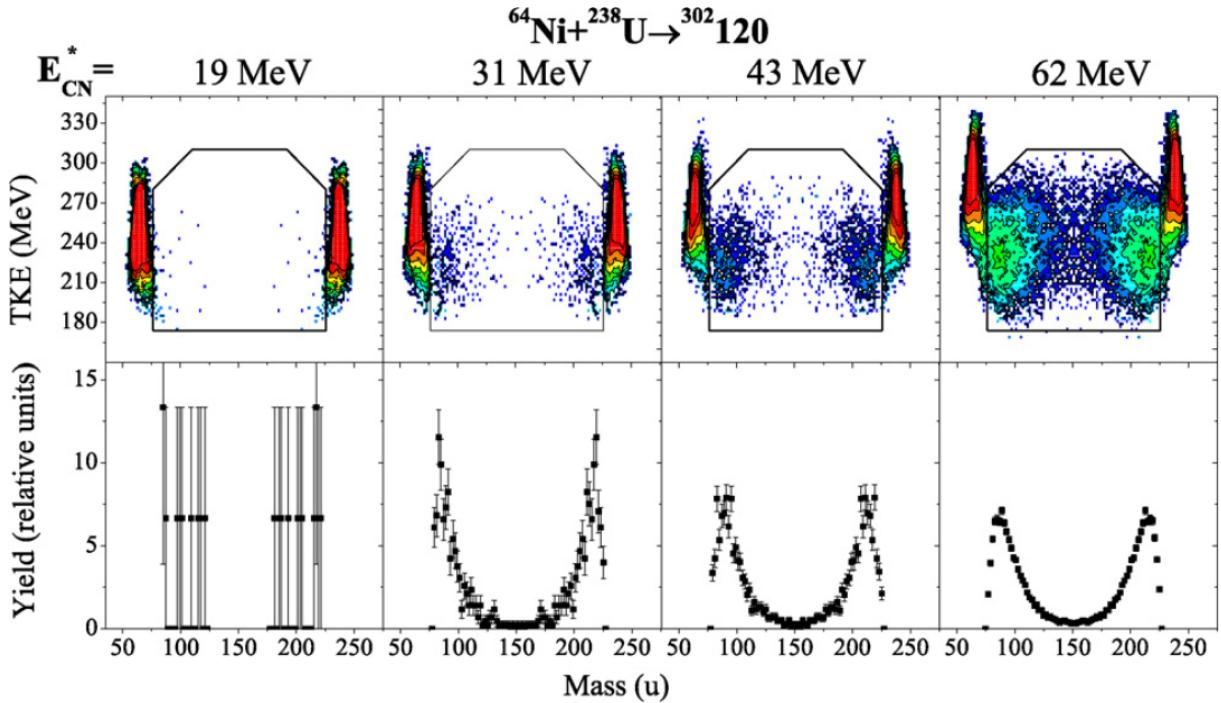
Figure 6.2: Yield of measured reaction products in TKE-A plane (upper panels) and a projection of the yield inside the contour lines in the TKE-A plots on to the A axis (lower panels) in the ^{64}Ni+^{238}U reactions at $E_{\text{lab}} = 330$, 343, 358, and 382 MeV. These energies correspond to excitation energies of the CN of 19, 31, 43, and 62 MeV, respectively. The figure was taken from Ref. [216].

Thus, if the TDHF theory can describe the cross sections for proton-pickup channels, it will be an indication of a better description of transfer dynamics in the small impact parameter region. To clarify this argument is one of the main motivations of this investigation.

The ^{64}Ni+^{238}U reaction has also attracted much interests as a possible candidate for producing a SH nucleus with atomic number $Z = 120$. To examine whether the reaction $^{64}_{28}$Ni$_{36}$+$^{238}_{92}$U$_{146}$ $\rightarrow^{302}_{120}$Ubn$_{182}$ is promising or not to produce the SH nucleus with $Z = 120$, fission fragment mass distributions were measured at several incident energies by Kozulin *et al.* [216]. In Fig. 6.2, we show the measured fragment mass distributions in the ^{64}Ni+^{238}U reaction at four incident energies. Upper panels show the fragment mass distributions in total kinetic energy (TKE) *vs.* fragment mass (A) plane. While lower panels show a projection of the yield inside the contour line in the TKE-A plot onto the A axis. As the incident energy increases, the measured mass distributions show a mass drift mode toward the mass symmetry. However, even at the highest incident energy examined, $E_{\text{lab}} = 382$ MeV, which corresponds to 62 MeV excitation energy of the CN, completely mass symmetric fragments around $A \sim 151$ were hardly produced. We may expect substantial yields of the mass symmetric fragments if the CN was formed. Therefore, regarding the experimental results, Kozulin *et al.* concluded that this reaction is not suitable for producing the SH nucleus with $Z = 120$. We are interested in to what extent the TDHF theory reproduces measured trends of QF processes. From comparisons of calculated cross sections and TKE-A distributions with those of measurements, we discuss reaction dynamics of MNT and QF processes in the TDHF theory.

This Chapter is organized as follows. In Sec. 6.1, we briefly describe some computational details of the TDHF calculations presented in this Chapter. In Sec. 6.2, we show MNT cross sections calculated by the TDHF theory combined with the PNP in comparison with the experimental data. In Sec. 6.3, we make a further comparison of the TKE-A distribution evaluated by the TDHF calculation with the measurements. In Sec. 6.4, we investigate energy dependence of the QF dynamics in head-on collisions of ^{64}Ni+^{238}U for two orientations of ^{238}U, the tip and side collisions. In Sec. 6.5, a summary and concluding remarks on this Chapter are presented.

6.1 Computational Details

We use our computational code of the TDHF calculation for heavy ion reactions as in Part I. We use a Skyrme EDF with the SLy5 parameter set [141]. We use a numerical box with $30 \times 30 \times 30$ grid points to calculate HF ground states of projectile and target nuclei. The mesh spacing is set to be 0.8 fm. For the TDHF calculation, a numerical box with $70 \times 70 \times 30$ grid points is used. The initial separation distance is set to be 24 fm in the incident direction (parallel to the x-axis). The impact parameter vector is set parallel to the positive-y direction. For the time evolution operator, the Taylor expansion method of 4th order is used with a small time step of $\Delta t = 0.2$ fm/c. We stop the time evolution calculation when the relative distance between two fragment nuclei exceeds a critical value, 26 fm. We have performed the TDHF calculations for an impact parameter region 0 fm $\leq b \leq$ 10 fm. We calculate the reaction with 0.5-fm step for 0 fm $\leq b \leq$ 5 fm, while we calculate the reaction with 1-fm step for $b > 5$ fm. For the PNP analysis, we discretize the integral over the phase factor θ into $M = 300$ equal grids and evaluate it utilizing the trapezoidal rule.

From the ground-state calculation, the HF ground state of ^{238}U turns out to be prolate shape with $\beta \sim 0.27$, while that of ^{64}Ni turns out to be oblate shape with $\beta \sim 0.11$. Concerning the relatively large deformation of ^{238}U, we performed the TDHF calculations of the ^{64}Ni+^{238}U reaction at three different initial orientations. We set the symmetry axis of ^{238}U parallel to the x-, y-, and z-axis, while the symmetry axis of ^{64}Ni is always set parallel to the z-axis (perpendicular to the collision plane). These initial configurations for the TDHF calculation are shown in Fig. 6.3.
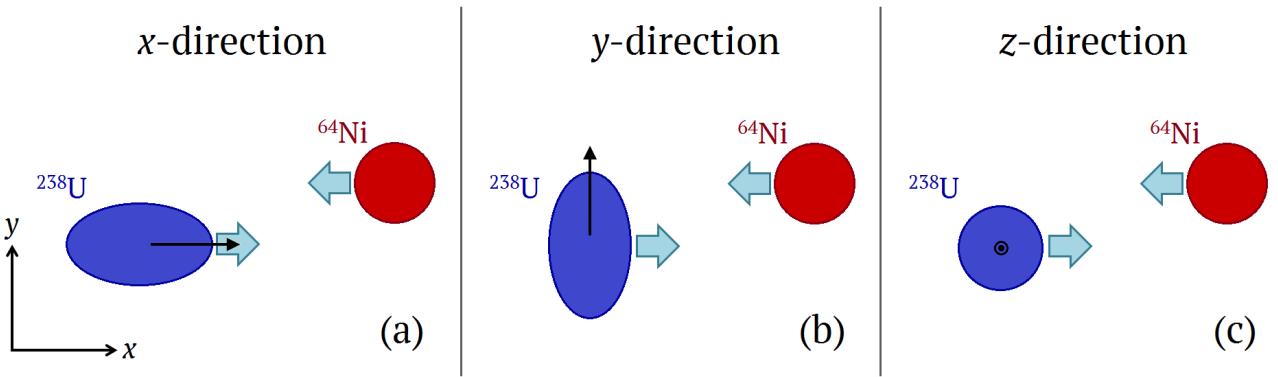
Figure 6.3: Schematic picture of the initial configurations of our TDHF calculations. We specify the relative orientation by the direction of symmetry axis of ^{238}U at the initial stage of the TDHF calculation. In this thesis, we investigate three initial orientations, denoted as x-, y-, and z-direction, as shown in the panels (a), (b), and (c), respectively.

6.2 MNT Processes

We first present MNT cross sections calculated by the TDHF theory combined with the PNP technique. Because both projectile and target nuclei are deformed in their HF ground states, we should take an orientation average to take full account of effects of deformation on MNT cross sections. However, since the orientation average requires a huge computational cost, we have not achieved the orientation average. Here we just show contributions from each initial configuration.

In Fig. 6.4, we show MNT cross sections obtained from the TDHF calculations combined with the PNP in comparison with the experimental data. Red filled circles denote measured cross sections reported in Ref. [45]. Red solid, green dashed, and blue dotted lines show results of the TDHF calculation for different initial configurations, the x-, y-, and z-direction configurations, respectively. Each panel shows cross sections for specific proton transfer channels. The ($-x$p) indicates that x protons are transferred from ^{64}Ni to ^{238}U (proton-stripping channels), while the ($+x$p) indicates that x protons are transferred from ^{238}U to ^{64}Ni (proton-pickup channels). The horizontal axis is the mass number A of the lighter (^{64}Ni-like) fragment.

From the figure, we find that the TDHF theory reasonably reproduces measured cross sections for both proton-stripping ($-x$p) and proton-pickup ($+x$p) channels. For the proton-stripping channels, the TDHF theory quantitatively describe measured cross sections up to around two-proton stripping reactions (-2p). As the number of removed protons increases, the peak position sifts toward larger neutron number side compared with that of the measured cross sections. For (-3p), (-4p), (-5p), and (-6p) channels, we find that cross sections contributed from the y- and z-direction configurations are much larger than those contributed from the x-direction configuration. When many protons are transferred, the TDHF calculation underestimates the measured cross sections (see (-4p), (-5p), and (-6p) panels). This behavior is similar to the cases of MNT processes in lighter systems shown in Chapter 3. By comparing transfer cross sections of proton-stripping channels ($-x$p) calculated by the TDHF theory with those of GRAZING shown in Fig. 6.1, we get the same conclusion as in Chapter 3 that the TDHF theory describes MNT cross sections reasonably well with an accuracy comparable to the GRAZING calculation.

In contrast, for the proton-pickup channels ($+x$p), the TDHF theory gives quantitatively much better descriptions compared with the GRAZING calculation (*cf*. Fig. 6.1). In the TDHF calculation, we obtain substantial cross sections not only for one-proton pickup ($+1$p) but also two-proton pickup ($+2$p) channels. The GRAZING calculation underestimates those cross sections, *e.g.* about two orders
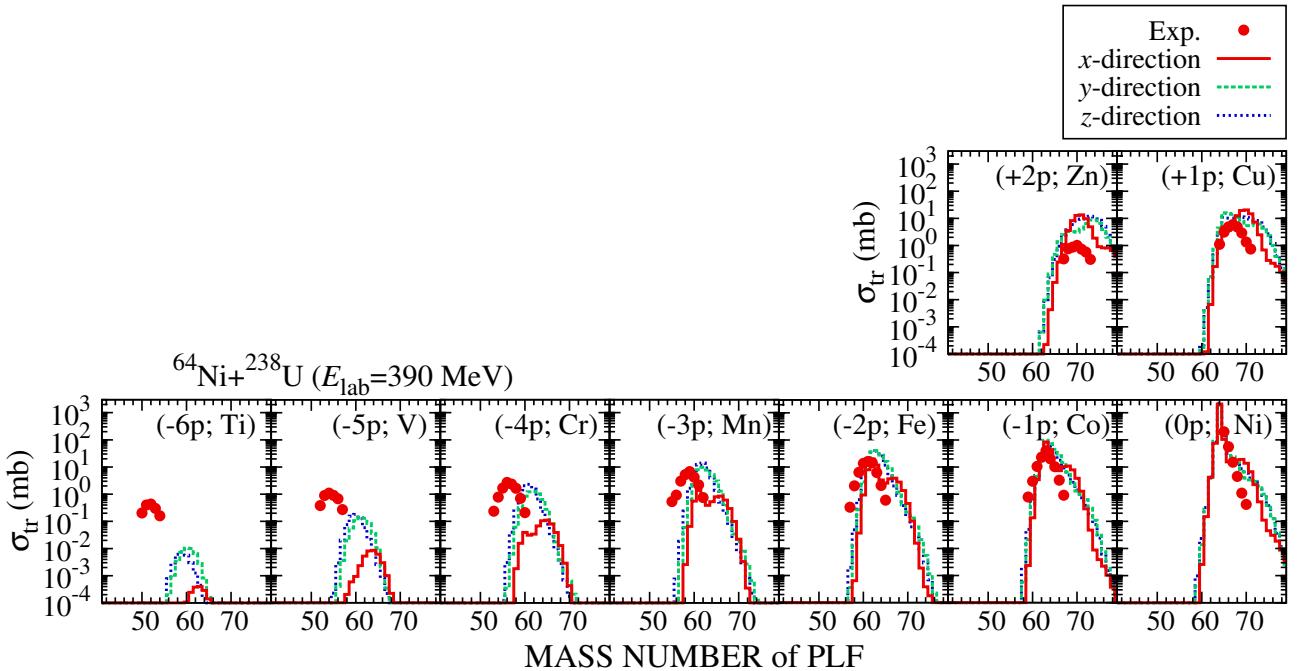
Figure 6.4: Transfer cross sections for the ^{64}Ni+^{238}U reaction at $E_{\mathrm{lab}} = 390$ MeV. Red filled circles denote measured cross sections reported in Ref. [45]. Red solid, green dashed, and blue dotted lines show results of the TDHF calculations for x-, y-, and z-direction configurations, respectively. Effects of particle evaporation were not taken into account in our calculation.

of magnitude smaller values than the measurements for the two-proton pickup channel (+2p). This fact may be caused by an insufficient description of a small impact parameter region in the GRAZING calculation. In the GRAZING code, contributions from the small impact parameter region are neglected assuming the strong absorption of the flux from MNT channels to more complex mechanisms. Because of the large charge product, $Z_P Z_T = 2576$, there may remain a significant contribution to MNT processes from the small impact parameter region. Because the TDHF theory dose not include any artificial assumption on the reaction dynamics, we expect more reliable descriptions of the reaction dynamics in the small impact parameter region. This is one of the advantages of our approach and we have got a confidence from the much better description of the cross sections of proton-pickup channels in the ^{64}Ni+^{238}U reaction.

6.3 QF Processes

As a matter of fact, the TDHF calculation gives much more abundant cross sections for proton-pickup channels not only the one- and two-proton pickup channels, (+1p) and (+2p) shown in Fig. 6.4, but also channels which correspond to transfer of many protons up to 12-20 from ^{238}U to ^{64}Ni producing nuclei with $Z \sim 40$-50. Transfer cross sections for such a many-proton transfer from ^{238}U to ^{64}Ni were not measured in the experiment of Ref. [45]. We note that, in Ref. [45], Corradi *et al.* mentioned that they actually observed reaction products with the atomic number around $Z \sim 40$. However, quantitative estimates of cross sections could not be achieved, since the experimental setup was not optimized for those fragments. These reaction products associated with the many-proton transfer from ^{238}U to ^{64}Ni were interpreted as a contribution from QF processes [45].

In Fig. 6.5, we show average numbers of nucleons in the lighter (^{64}Ni-like, upper panels) and the heavier (^{238}U-like, lower panels) fragments as functions of the impact parameter, b. Red open circles,
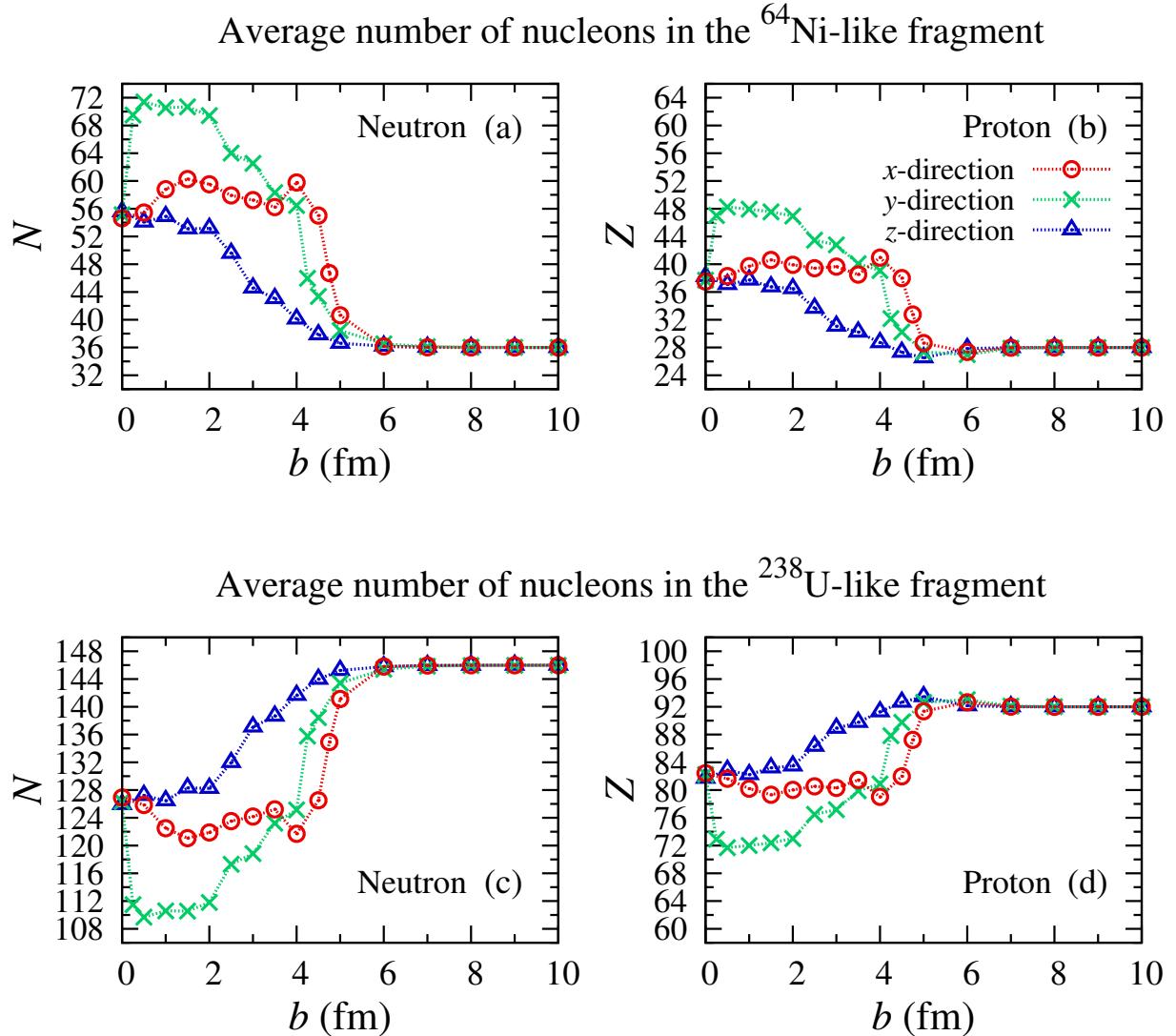
Figure 6.5: Average numbers of neutrons (left panels) and protons (right panels) in the lighter (^{64}Ni-like) fragment ((a) and (b)) and in the heavier (^{238}U-like) fragment ((c) and (d)) as functions of the impact parameter. Red open circles, green crosses, and blue open diamonds connected with lines show results for different initial configurations, x-, y-, and z-direction cases, respectively.

green crosses, blue open triangles denote results at different initial orientations, the x-, y-, and z-direction configurations, respectively. When the impact parameter is sufficiently large ($b > 5$ fm), the average numbers of nucleons almost coincide with the initial values, $N = 36$ and $Z = 28$ for the ^{64}Ni-like fragment shown in the panels (a) and (b), and $N = 146$ and $Z = 92$ for the ^{238}U-like fragment shown in the panels (c) and (d). What we observed in the cross sections shown in Fig. 6.4 would be contributions from this relatively large impact parameter region, $b \gtrsim 5$ fm. We note that the slightly different behavior at $b \sim 5$ fm shown in the panel (b) results in the difference of cross sections for $(-4p)$, $(-5p)$, and $(-6p)$ channels. The mass drift mode in the small impact parameter region $b < 5$ fm is regarded as the QF process.

As the impact parameter decreases, the average number of nucleons in the fragment nuclei changes suddenly at around $b \sim 5$ fm. Both neutrons and protons are transferred from ^{238}U to ^{64}Ni toward the mass symmetry in the small impact parameter region, $b \lesssim 5$ fm. The behavior of the average numbers of nucleons as functions of the impact parameter depends much on the initial orientations. When the symmetry axis of ^{238}U is set perpendicular to the collision plane (z-direction case, shown by blue open
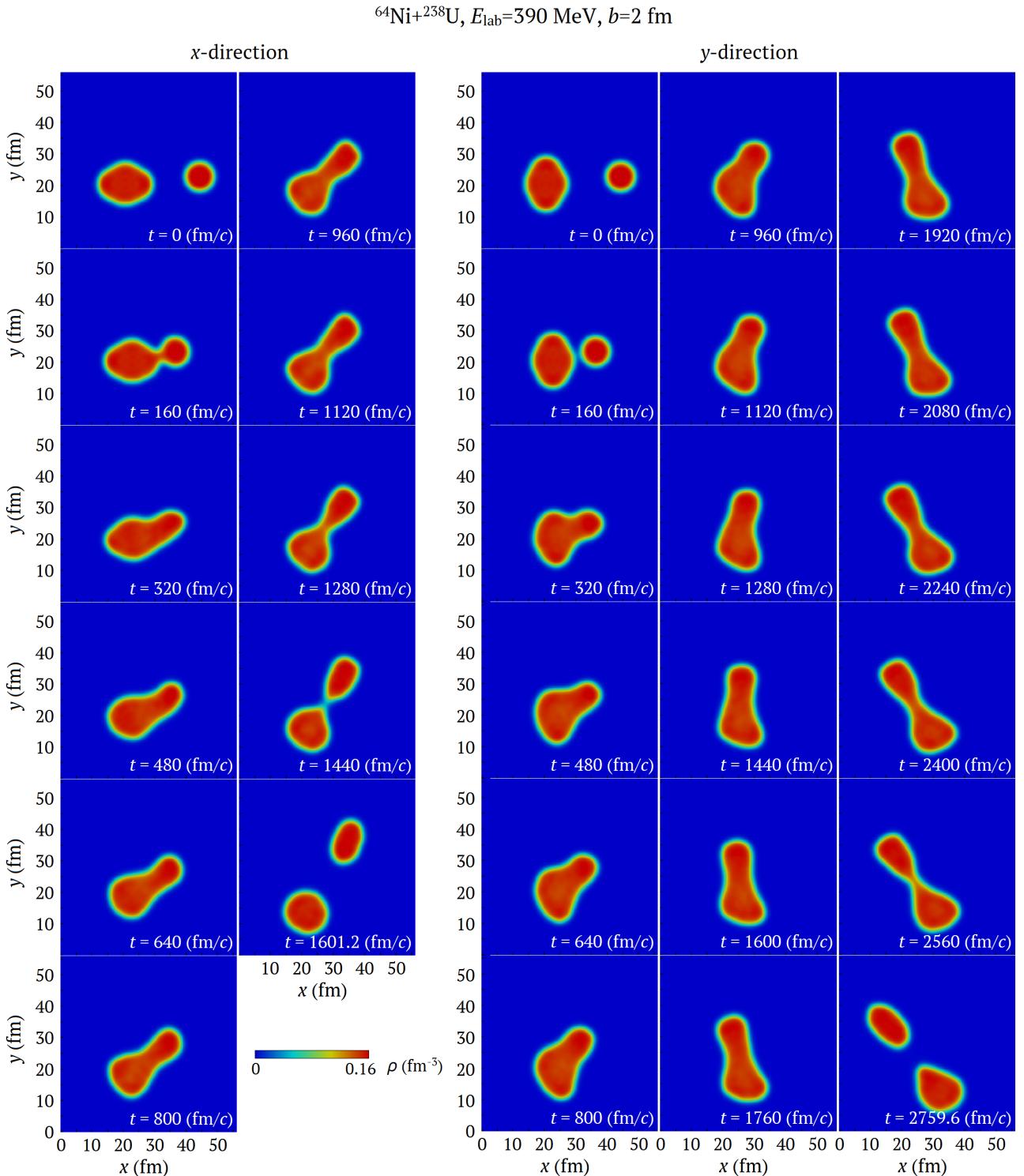
Figure 6.6: Time evolution of the density on the collision plane in the ^{64}Ni+^{238}U reaction at $E_{\text{lab}} =$ 390 MeV and $b = 2$ fm. Left panels show results for the x-direction configuration, while right panels show results for the y-direction configuration. The label '$t = x$ fm/c' denotes the elapsed time started from the initial stage of the TDHF calculation.
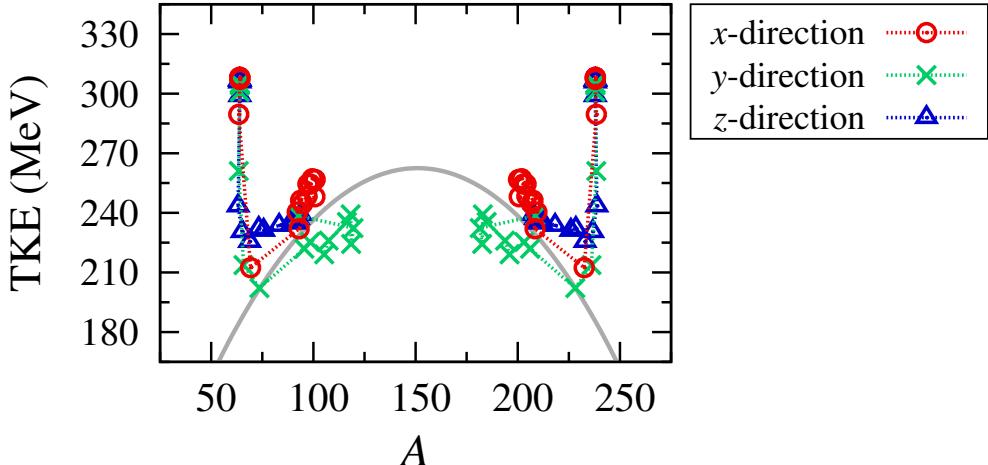
Figure 6.7:   The total kinetic energy (TKE) *vs.* average mass numbers (A) of the PLF and the TLF in the TDHF calculation of the ^{64}Ni+^{238}U reaction at $E_{\text{lab}} = 390$ MeV. Red open circles, green crosses, blue open triangles denote results at different initial configurations, x-, y-, and z-direction configurations, respectively. Gray solid line shows the TKE distribution evaluated by Eq. (6.3.1) which is based on the Viola systematics [223].

triangles), the change in the average nucleon number is moderate. On the other hand, in the case of x- and y-direction configurations, the change is dramatic. At around $b \sim 4$ fm, the average numbers of nucleons in the fragment nuclei jump up to $N \sim 56\text{-}60$ and $Z \sim 30\text{-}40$ in the lighter fragment and $N \sim 122\text{-}126$ and $Z \sim 80\text{-}82$ in the heavier fragment. In the x-direction case (red open circles), we find a prominent plateau persisting a wide impact parameter region smaller than 4 fm. A similar behavior was reported in Ref. [124]. We suspect that a substantial structural effect related to a relatively large binding energy of spherical ^{208}Pb and prolate $^{90-100}$Zr [218, 219, 220] may responsible for this process as mentioned in Ref. [125]. We note that, in the Langevin approach, substantial effects of structure were often observed, *e.g.* effects of large binding energy in doubly magic ^{208}Pb on fission fragment mass distributions [29, 69, 70, 71, 72, 84]. The substantial effect of doubly magic ^{208}Pb on QF dynamics is also observed experimentally [221, 222]. While in the y-direction case (green crosses), behavior is somewhat different showing a massive nucleon flow up to transfer of 56 nucleons from ^{238}U to ^{64}Ni. This trend is consistent with a statement in Ref. [125]. We note that, for head-on collision ($b = 0$ fm), the average number of nucleons changes suddenly in the y-direction configuration. These behaviors may be understood from a simple geometrical consideration with a very thick neck formation between two colliding nuclei. In the case of y-direction case, thickness of the neck can be much larger than that in x-direction case at the small impact parameter region (see, *e.g.*, panels with 800 fm/c in Fig. 6.6). The thick and long neck formation is substantially suppressed in the head-on collision, because the system keeps an initial spatial symmetry. Figure 6.6 shows snapshots of the density distribution on the collision plane for typical two cases of ^{64}Ni+^{238}U reaction at $b = 2$ fm, from which we may get an intuitive understanding of the above discussed behavior in x- and y-direction configurations.

To investigate the reality of the QF process obtained from the TDHF calculations, in Fig. 6.7, we show an average TKE-A plot obtained from the TDHF calculations. It can be compared with measured TKE-A plot shown in Fig. 6.2. The horizontal axis A is the average number of nucleons in the lighter (^{64}Ni-like) and the heavier (^{238}U-like) fragments. Red open circles, green crosses, and blue open triangles connected with lines show results for different initial orientations, the x-, y-, and z-direction configurations, respectively.

The incident energy of $E_{\text{lab}} = 390$ MeV corresponds to the incident relative energy of 307.4 MeV. Thus the maxima of TKE around $A_{\text{L}} \sim 64$ and $A_{\text{H}} \sim 238$ correspond to the quasielastic scattering.

Here we have introduced A_L and A_H which represent the average mass number of lighter and heavier fragments, respectively. From the figure, we find that, when the TKE becomes smaller than around 240 MeV, the average mass numbers change suddenly toward the direction of the mass symmetry.

For comparison, we also plot the TKE distribution evaluated based on the Viola systematics [223] including mass-asymmetry dependence [224, 225]. The formula is given by

$$\text{TKE}_{\text{Viola}} = \frac{0.755 Z_{\text{L}} Z_{\text{H}}}{A_{\text{L}}^{1/3} + A_{\text{H}}^{1/3}} + 7.3 \quad \text{MeV}, \tag{6.3.1}$$

where $Z_{\text{L(H)}}$ is the proton number of the lighter (heavier) fragment. We have assumed that the Z/A ratio of the fragment nuclei equals to that of the CN and any particle emissions are neglected. As seen from the figure, we find a reasonable agreement between the TKE obtained from the TDHF calculations and the Viola systematics. It indicates that the so called full momentum transfer from the relative energy to internal excitations is achieved and the TKE is roughly determined by the Coulomb energy at a scission configuration of the dinuclear system.

As shown in Fig. 6.2, we also find a similar mass drift mode in the forth column of the figure which corresponds to a similar incident energy of $E_{\text{lab}} = 382$ MeV. The two peaks in the measured fragment mass distributions correspond to $A_L \sim 90$ and $A_H \sim 210$. The TDHF calculation shows a similar mass drift mode in dissipative processes in the ^{64}Ni+^{238}U reaction at the small impact parameter region, $b \lesssim 5$ fm.

From the results, we conclude that the TDHF theory is capable of describing not only the MNT process but also the QF process in ^{64}Ni+^{238}U reaction. We have found a reasonable agreement of the TKE-A distribution obtained from the TDHF calculation with those of the Viola systematics and the experimental data, which indicates that a sufficient energy dissipation could be described by the so called one-body dissipation dynamics in the TDHF theory.

6.4 Energy Dependence of QF Dynamics

To get more deeper understandings of the QF processes, we examine energy dependence of the QF dynamics in ^{64}Ni+^{238}U reaction. For simplicity, we only consider head-on collisions ($b = 0$ fm). To examine orientation dependence of the QF dynamics, we calculate head-on collisions at two different configurations, the x-direction configuration in which the symmetry axis of ^{238}U is set parallel to the collision axis (corresponds to the tip collision) and the y-direction configuration in which the symmetry axis of ^{238}U is set parallel to the y-axis (corresponds to the side collision).

In Fig. 6.8, we show average numbers of neutrons and protons in the lighter (^{64}Ni-like) fragment ((a) and (b)) and the heavier (^{238}U-like) fragment ((c) and (d)) as functions of the incident energy. Red open circles connected with lines show results for the tip collisions, while green crosses connected with lines show results for the side collisions. The initial neutron and proton numbers of the projectile and target nuclei are represented by horizontal dotted lines.

As seen from the figure, we find a substantial orientation dependence as well as the incident energy dependence of the QF dynamics. When the incident energy is sufficiently small, the average numbers of neutrons and protons in reaction products almost coincide with the initial values. However, when the incident energy becomes higher than the Coulomb barrier, a drastic change of the neutron and proton numbers of the fragment nuclei is observed. In tip collisions (red open circles), the neutron and proton numbers of the fragment nuclei saturate at certain values. In tip collisions, two nuclei cannot form a compact configuration and the composite system always elongated forming an asymmetric dumbbell-like shape. Because of the asymmetric dumbbell-like shape, a neck is always developed forming mass asymmetric fragments.

On the other hand, results for the side collisions show different behavior. In side collisions (green crosses), the composite system of the projectile and target nuclei tends to form a compact configuration. In other words, the thickness of the neck formed between colliding nuclei becomes substantially large forming a mononuclear configuration. Because of the compact mononuclear configuration, a neck is developed forming mass symmetric fragments. We find a somewhat longer sticking time in side collisions compared with tip collisions. Especially, we observed capture processes in side collisions at $E_{\mathrm{lab}} \gtrsim 450$ MeV, while, we have never observed any capture processes in tip collisions.

To give an intuitive understanding of the QF dynamics, we show the time evolution of the density in reactions at typical two incident energies, $E_{\mathrm{lab}} = 362.1$ MeV and $E_{\mathrm{lab}} = 470.7$ MeV. Figure 6.9 shows typical QF dynamics for the tip and side collisions in reactions at $E_{\mathrm{lab}} = 362.1$ MeV. In both cases, a very thick neck is formed between two colliding nuclei (320-480 fm/c). In the side collision, the dinuclear system keeps its configuration up to around 1600 fm/c. After that, the neck structure starts shrinking and, eventually, it dissociates (2560 fm/c). On the other hand, in the tip collision, the dinuclear system forms an elongated neck (480-960 fm/c) and dissociates showing a relatively short sticking time. A similar dynamics is observed in the plateau region emerged at around 350 MeV $< E_{\mathrm{lab}} < 500$ MeV in Fig. 6.8.

In Fig. 6.10, we show a similar contour plots of the density in reactions at $E_{\mathrm{lab}} = 470.7$ MeV. As mentioned above, in the tip collision, we see a quite similar behavior of the QF dynamics as shown in Fig. 6.9. Not only the time-dependent shape evolution but also the sticking time are very similar to each other. On the other hand, in the side collision, we find a different behavior of reaction dynamics. Since the incident energy is higher than that of the previous example, two nuclei collides more deeply (320 fm/c). Then the composite system of the projectile and target nuclei forms a compact mononuclear configuration (480-6000 fm/c). It is remarkable that, in the side collision, we observed a capture process forming the SH composite system of $Z = 120$. We observed similar capture processes for side collisions at incident energy of $E_{\mathrm{lab}} \geq 470.7$ MeV. While any capture process has never been observed in the tip collisions, even if we increase the incident energy up to around 700 MeV.

From these results, we realize that the QF dynamics depends much on the relative orientation of the two colliding nuclei. In Refs. [226, 227, 228, 229, 230], it was argued that the side collision tends to form a compact shape leading to a CN formation, while the tip collision would form an elongated dinuclear system with substantial components of QF processes, consistent with our observed behavior in the TDHF calculations.

Average number of nucleons in the ^{64}Ni-like fragment

Average number of nucleons in the ^{238}U-like fragment
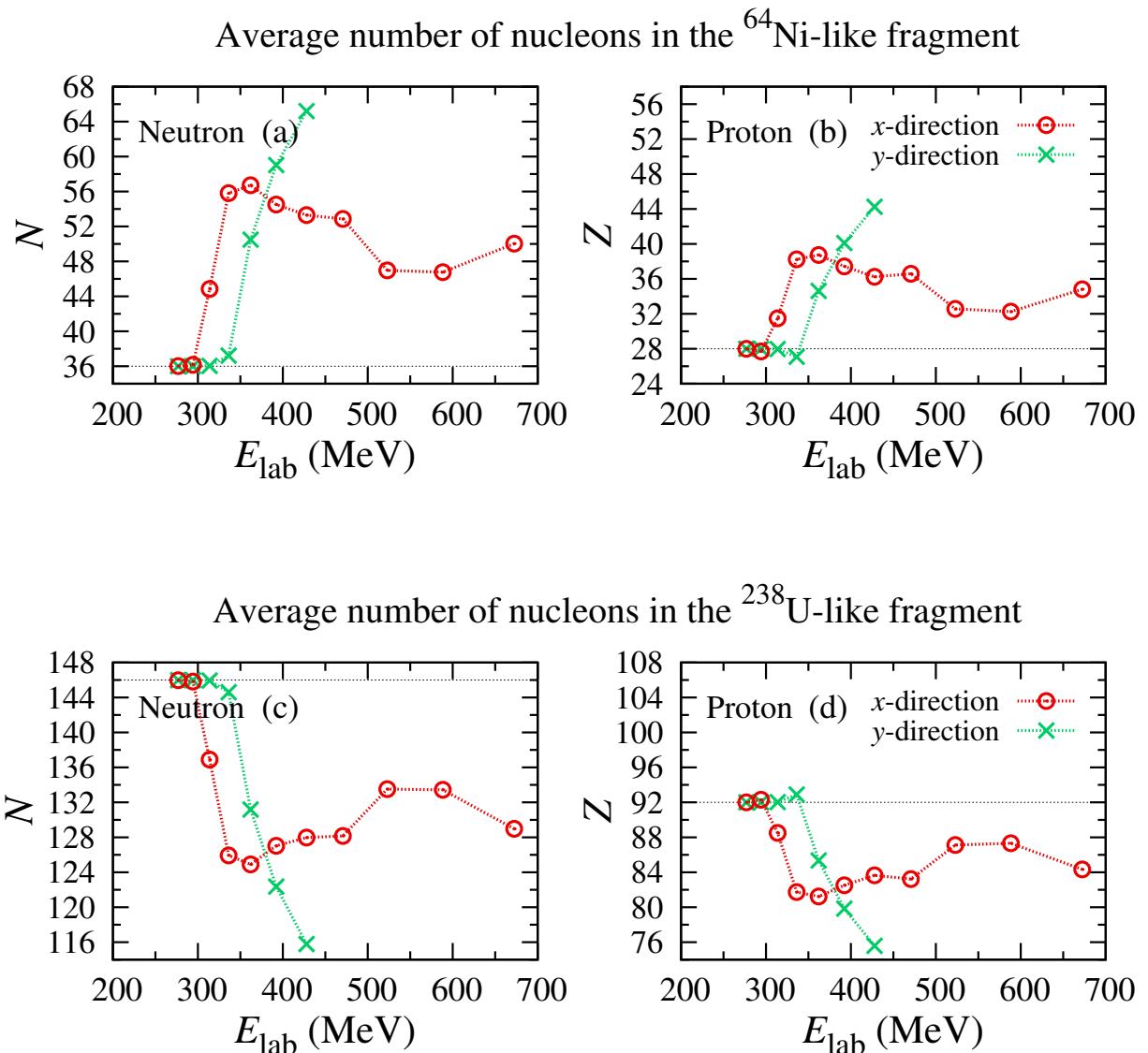
Figure 6.8: Incident energy dependence of the fragment's N and Z in head-on collisions of ^{64}Ni+^{238}U. The 'x-direction' means that symmetry axis of ^{238}U is set parallel to the collision axis (tip collision), while the 'y-direction' means that the symmetry axis is set perpendicular to the collision axis (side collision). Upper panels ((a) and (b)) show average numbers of nucleons in the lighter ($^{64}_{28}$Ni$_{36}$-like) fragment, while lower panels ((c) and (d)) show those in the heavier ($^{238}_{92}$U$_{146}$-like) fragment. The initial neutron and proton numbers in the projectile and target nuclei are represented by horizontal dotted lines.

6.5   Summary and Concluding Remarks on Chapter 6

In this Chapter, we have investigated ^{64}Ni+^{238}U reaction at energies around the Coulomb barrier to examine to what extent the TDHF theory is feasible in describing MNT and QF processes in such a heavier system. For the ^{64}Ni+^{238}U reaction, extensive measurements were performed for both MNT and QF processes [45, 79, 216, 217].

Because the HF ground state of ^{238}U is largely deformed in prolate shape, we performed TDHF calculations for an impact parameter region 0 fm $\leq b \leq$ 10 fm by taking three different initial orientations of ^{238}U. We applied the PNP technique to calculate MNT cross sections and compared them with experimental data [45]. From the comparison, we have found that the TDHF theory again nicely reproduces the experimental data with an accuracy comparable to the GRAZING calculation. A remarkable thing is that the TDHF theory quantitatively reproduce the measured cross sections not only for proton-stripping channels (^{64}Ni$\rightarrow^{238}$U) but also proton-pickup channels (^{64}Ni$\leftarrow^{238}$U), where the latter process is opposite to the direction expected from N/Z ratios of projectile and target nuclei. The semiclassical GRAZING calculation underestimates the measured cross sections of proton-pickup channels, because of neglected contributions from the small impact parameter region. This result will be an evidence of a reasonable description of a transitional regime from quasielastic to more complex reaction channels in the TDHF theory.

At a small impact parameter region, we found a mass drift mode toward the direction increasing the mass symmetry in the TDHF calculation. By comparing an average TKE-A distribution obtained from the TDHF calculations with available experimental data, we found that the mass numbers of the fragment nuclei in the mass drift mode roughly coincide with the measured TKE-A distribution. This fact indicates that the TDHF theory is capable of describing QF processes reasonably without any parameters specific to the reaction dynamics.

To get deeper insight into reaction mechanisms, we have investigated energy dependence of the QF dynamics in head-on collisions of ^{64}Ni+^{238}U. From the results, we found that the QF dynamics is strongly affected by the initial orientations of ^{238}U. In side collisions, the composite system of the projectile and target nuclei tends to form a compact mononuclear-type shape, while an asymmetric dumbbell-like elongated dinuclear shape is formed in tip collisions. Especially, in side collisions, we observed capture processes forming a SH nucleus with $Z = 120$ at incident energies larger than $E_{\mathrm{lab}} \sim 450$ MeV. Similar effects of the relative orientation on reaction dynamics were extensively discussed [226, 227, 228, 229, 230] and consistent with our calculations.

In the QF process, we observed some stabilizing effects which may be related to structure of fragment nuclei, $e.g.$ a large binding energy of doubly magic ^{208}Pb. In the dynamical model based on Langevin-type equations of motion, the QF dynamics is described by Langevin dynamics on a multidimensional potential energy surface (PES) of the composite system [69, 70]. In the model, significant effects of nuclear structure were observed, especially influence of a large binding energy of doubly magic nuclei such as ^{208}Pb or ^{78}Ni. Such structural effects generate some substantial valleys on the landscape of the PES [29, 69, 70, 71, 72, 84], which gather dynamical trajectories. We can calculate such a PES of the composite system employing the CHF method. We consider that a comparison between a landscape obtained from the static CHF calculation and the QF dynamics obtained from the TDHF calculation will be useful for developing further understanding of the QF process.

The results reported in this Chapter show the feasibility of the TDHF theory in describing not only MNT reactions at peripheral collisions but also QF dynamics in damped collisions at a small impact parameter region in a microscopic way without any adjustable parameter for the reaction dynamics. In the next Chapter (Chapter 7), we will show another application of the TDHF theory to reactions involving ^{238}U, $i.e.$ ^{238}U+^{100,124,132}Sn reactions.
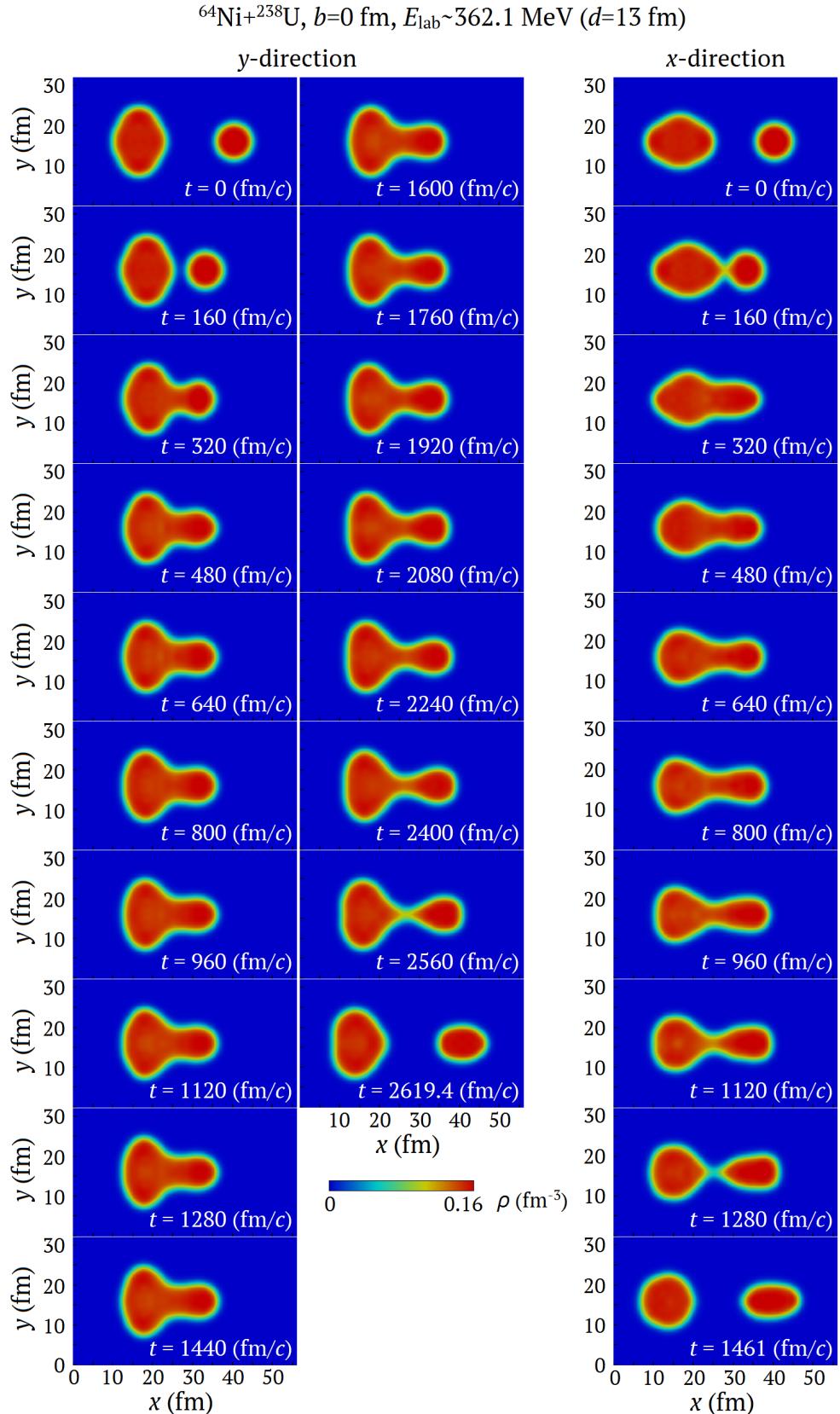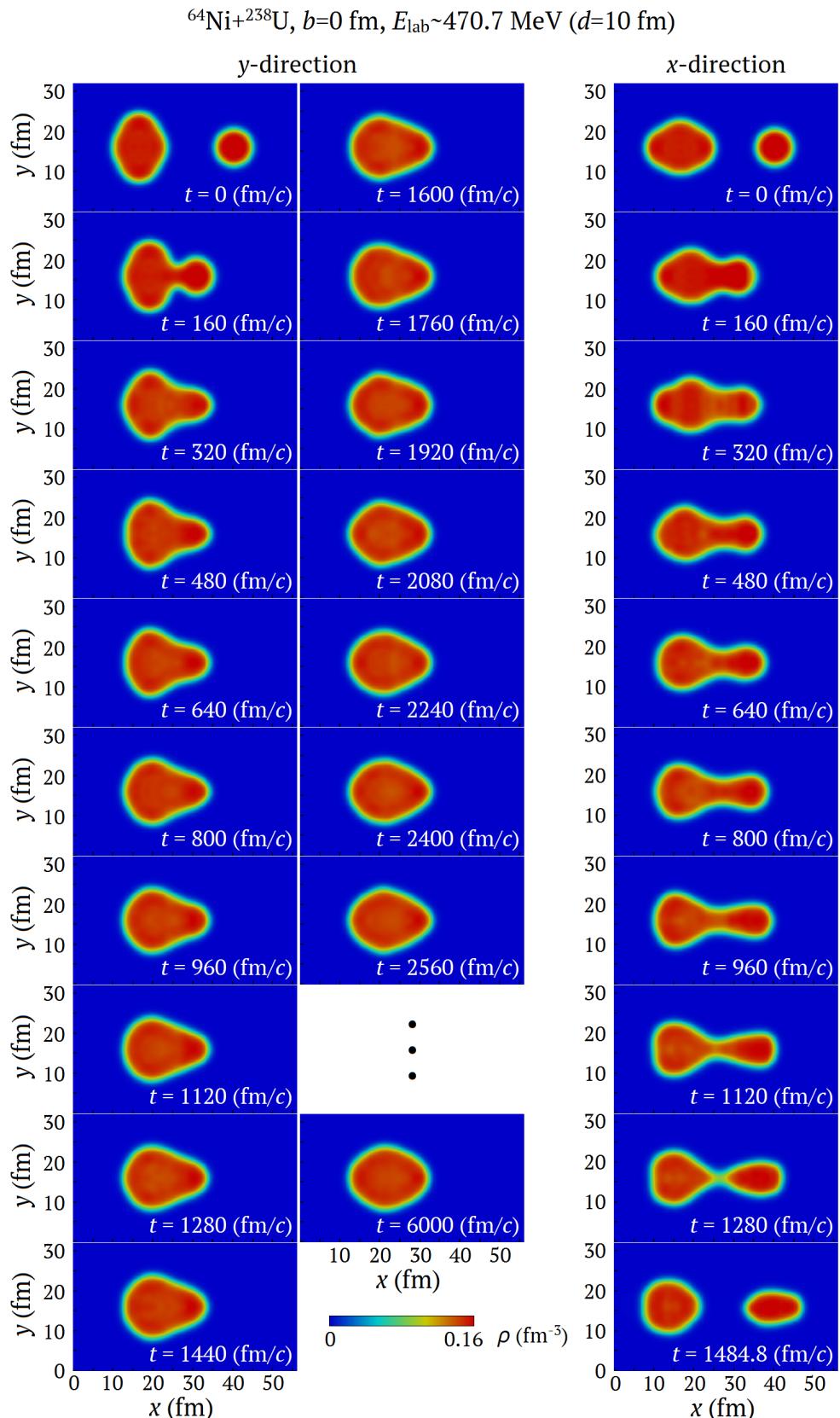
Figure 6.9: Time evolution of the density on the collision plane (xy-plane) in head-on collisions of ^{64}Ni+^{238}U at $E_{\text{lab}} \sim 362.1$ MeV. Results for the side collision (y-direction) are shown in left panels, while results for the tip collision (x-direction) are shown in right panels. Labels '$t = x$ fm/c' indicate an elapsed time from the initial stage of the TDHF calculation.

Figure 6.10: Same as Fig. 6.9 but for the case of $E_{lab} \sim 470.7$ MeV.

Chapter 7

MNT AND QF PROCESSES IN ^{238}U$+^{100,124,132}$Sn REACTIONS

In the second part of the thesis (Part II), we have examined to what extent the TDHF theory reasonably describes MNT and QF processes in reactions involving heavy nuclei. In Chapter 6, we have investigated ^{64}Ni$+^{238}$U reaction as the first consideration. From the results, we have found that the MNT processes are again quantitatively described by the TDHF theory combined with the PNP. It is worth emphasizing that the TDHF theory reasonably well describes not only proton-stripping channels, which are expected from N/Z ratios of the initial system, but also proton-pickup channels, which correspond to the opposite direction. From a comparison of TKE-A distributions obtained from the TDHF calculations and those of available experimental data, we have found a reasonable agreement between them. Because the TDHF theory nicely reproduces a measured mass drift mode toward the mass symmetry which has considered as QF processes, we have got a confidence that the TDHF theory is capable of describing both MNT and QF processes based on a unified microscopic description without any adjustable parameter specific to the reaction dynamics.

In this Chapter, we investigate ^{238}U$+^{100,124,132}$Sn reactions as a next example[§]. About 30 years ago, pioneering measurements of MNT cross sections in ^{238}U-induced dissipative collisions were achieved by Mayer *et al.* at GSI, Darmstadt, Germany [232]. In the measurements for ^{238}U$+^{124}$Sn reaction, MNT processes accompanying more than ten protons from ^{238}U to ^{124}Sn were observed. Possible structural effects were advocated to explain the fact that lighter fragments with neutron number approximately equal to $N = 82$ were produced abundantly. Although there have been extensive efforts to clarify the reaction mechanism both experimentally and theoretically, the origin of the transfer of many protons had not been clear. One of the main aims of this work is to clarify whether or not the TDHF theory can reproduce the measured many-proton transfer from ^{238}U to ^{124}Sn, which might be contributed from the QF induced MNT processes.

To get deeper understanding of the QF process, we also investigate energy dependence of head-on collisions in ^{238}U$+^{100,124,132}$Sn systems. Since the N/Z ratios of ^{100}Sn (1.00) , ^{124}Sn (1.48), and ^{132}Sn (1.64) are much smaller than, similar to, and larger than that of ^{238}U (1.59), respectively, we expect some different features in the QF dynamics. This analysis aims to obtain more information on microscopic reaction mechanisms of the QF dynamics.

This Chapter is organized as follows. In Sec. 7.1, we describe some computational details utilized for the TDHF calculations presented in this Chapter. In Sec. 7.2, we investigate MNT and QF processes in the ^{238}U$+^{124}$Sn reaction for which experimental data are available. In Sec. 7.3, results of TDHF calculations for head-on collisions of ^{238}U$+^{100,124,132}$Sn are shown. Incident energy dependence as well

---

[§]Part of this Chapter is based on results reported in our publication of Ref. [231].

as the system (N/Z ratio) dependence of the QF dynamics are discussed. In Sec. 7.4, a summary and concluding remarks on this Chapter are presented.

7.1 Computational Details

To describe ^{238}U+^{100,124,132}Sn reactions, we use the computational code of TDHF calculations for nuclear reactions as in Chapters 3-6. The projectile and target nuclei are calculated using a box with $30 \times 30 \times 30$ grid points. For reaction calculations, we use a box with $70 \times 70 \times 30$ grid points for non-central collisions and $90 \times 40 \times 30$ grid points for central collisions. We choose the incident direction parallel to the x-axis, and the direction of the impact parameter vector parallel to positive-y direction. The reaction plane is thus xy-plane. As the initial condition, we place wave functions of two nuclei separated by 24 fm in the incident direction. Because the total number of protons included in the projectile and target nuclei is very large, $Z = 92 + 50 = 142$, no fusion reactions have been observed at any impact parameters. At the final stage of calculations, there always appear two fragments, a PLF and a TLF. We continued time evolution calculations until the relative distance between the two fragments becomes larger than 28 fm. For all calculations reported in this Chapter, we use Skyrme SLy5 parameter set [141], as in Ref. [173].

The ground state of ^{238}U is prolately deformed with $\beta \sim 0.27$ and the ground state of ^{124}Sn is oblately deformed with $\beta \sim 0.11$. The ground state of doubly magic ^{100,132}Sn is of spherical shape. For the ^{238}U+^{124}Sn reaction, we performed TDHF calculations for three initial configurations characterized by different orientations of ^{238}U, as in Chapter 6: The symmetry axis of ^{238}U set parallel to the x-axis (parallel to the collision axis), y-axis (parallel to the impact parameter vector), and z-axis (perpendicular to the collision plane). The symmetry axis of a slightly deformed ^{124}Sn is always set parallel to the z-axis. For a quantitative comparison with the measured cross sections, we should take an average with respect to all possible orientations. However, since the orientation average requires excessive computational costs, we have not performed yet. Below, we show cross sections for each of the three initial conditions without the average, as in Chapter 6.

7.2 MNT and QF Processes

In Fig. 7.1, we show production cross sections of ^{124}Sn-like fragments in the A-Z plane. In Fig. 7.1 (a), (b), and (c), we show cross sections calculated using the PNP technique for different initial configurations. From the results shown in the panels (a), (b), and (c), we find that the distributions of the calculated cross sections depend much on the initial orientations of the deformed ^{238}U.

When the symmetry axis of ^{238}U is set parallel to the collision axis (x-direction in panel (a)), we find abundant cross sections widely spreading in the A-Z plane. For a fragment $^{116}_{44}$Ru$_{72}$ produced by a transfer of two neutrons and six protons from $^{124}_{50}$Sn$_{74}$, we find a cross section of 10^{-3} mb. For a fragment $^{150}_{64}$Gd$_{86}$ produced by a transfer of twelve neutrons and fourteen protons to $^{124}_{50}$Sn$_{74}$, the cross section is again the same order of magnitude, 10^{-3} mb.

When the symmetry axis of ^{238}U is set perpendicular to the collision axis (symmetry axis in y- and z-directions, shown in panels (b) and (c), respectively), the calculated cross sections do not so much extend in the A-Z plane compared with the case of x-direction shown in panel (a). Cross sections producing lighter nuclei in the transfer from ^{124}Sn to ^{238}U are almost the same as those in the x-direction case. However, cross sections to produce heavier nuclei in the transfer from ^{238}U to ^{124}Sn is substantially suppressed compared with the x-direction case. For example, we find a cross section of 10^{-3} mb for the production of $^{134}_{56}$Ba$_{78}$ which corresponds to a transfer of four neutrons and six

^{238}U+^{124}Sn (E_{lab}=5.70 MeV/A); w.r.t. the ^{124}Sn-like fragment
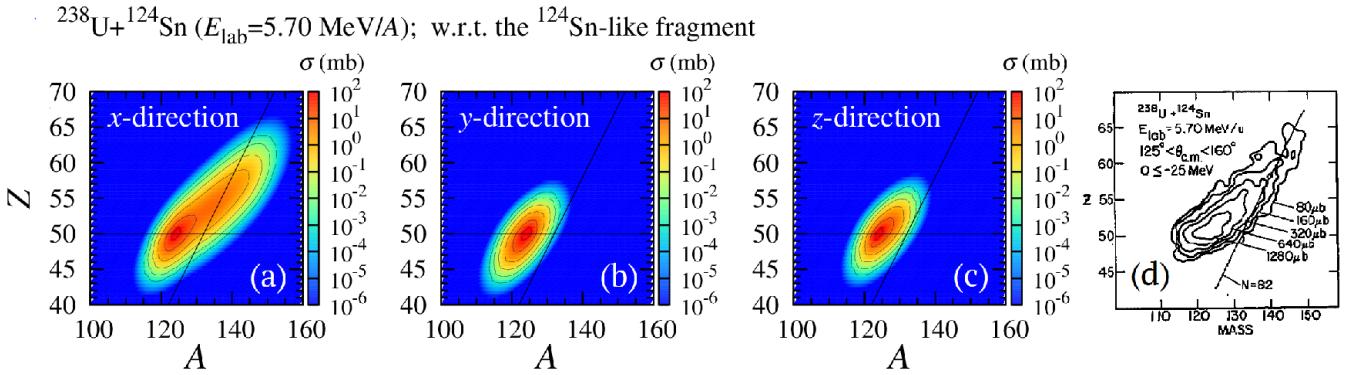
Figure 7.1:   Production cross sections of ^{124}Sn-like fragments in the ^{238}U+^{124}Sn reaction at $E_{\text{lab}} =$ 5.7 MeV/nucleon are shown in the A-Z plane. (a-c): Results of the TDHF calculations for three different relative orientations. (d): Experimentally measured cross sections, which was taken from Ref. [232]. The figure was taken from Ref. [231].

protons to $^{124}_{50}$Sn$_{74}$. The number of transferred nucleons with the similar magnitude of cross section is much smaller than the cross section shown in panel (a).

To obtain an intuitive picture for the reaction dynamics, we show, in Fig. 7.2, time evolutions of the calculated density distribution in the collision plane (xy-plane). We show results of head-on collisions ($b = 0$ fm) with two different initial orientations. In the x-direction case, the symmetry axis of ^{238}U is set parallel to the collision axis. In the y-direction case, symmetry axis of ^{238}U is set perpendicular to the collision axis. The top panels show initial configurations. We show several snapshots below.

In both x- and y-direction cases, two nuclei touch at around 320 fm/c. In the x-direction case (right panels), a thick neck is developed between the two colliding nuclei forming an elongated dinuclear system (480-800 fm/c). When the dinuclear system dissociates (~ 928 fm/c), the neck is cut at a position closer to the larger fragment. Consequently, a lot of nucleons in the neck region are absorbed by the smaller fragment. Since the neck region is composed of both neutrons and protons, the absorption of nucleons in the neck region results in the transfer of both neutrons and protons in the same direction. We find that about 11 neutrons and 7 protons are transferred on average in this reaction, producing fragments resembling $^{142}_{57}$La$_{85}$ and $^{219}_{85}$At$_{134}$. In the y-direction case (left panels), on the other hand, the neck is not so much developed compared with the x-direction case (320-640 fm/c). As a result, only one-neutron and one-proton are transferred on average from ^{238}U to ^{124}Sn.

In Fig. 7.1 (d), we show measured production cross sections for ^{124}Sn-like fragments in the ^{238}U+^{124}Sn reactions reported in Ref. [232]. As seen in Fig. 7.1 (d), measured cross sections extend to the mass number $A \sim 148$ and the proton number $Z \sim 64$. It corresponds to a transfer of 8 neutrons and 14 protons from ^{238}U to ^{124}Sn. As seen in Fig. 7.1 (a), (b), and (c), the large number of transferred nucleons from ^{238}U to ^{124}Sn in the measurement can only be explained by the x-direction configuration, the tip collision of a deformed ^{238}U, among the examined three configurations. Our TDHF calculations strongly suggest that the large number of transferred nucleons, more than ten protons, from ^{238}U to ^{124}Sn in the measured MNT processes can only be explained in the tip-collision-induced transfer, associated with the formation and absorption of the elongated thick neck during the collision.
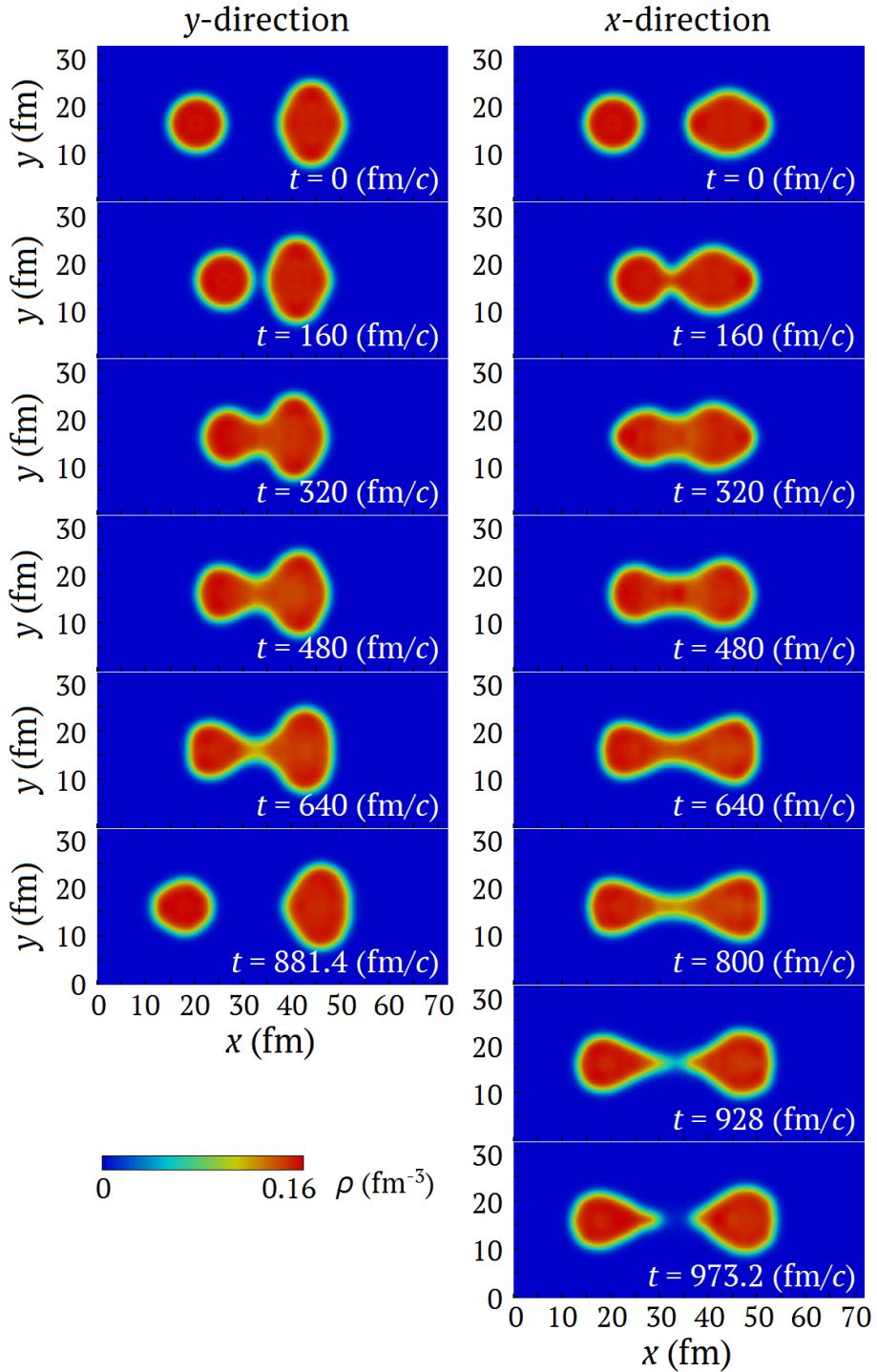
Figure 7.2: Time evolutions of the density distribution on the collision plane for head-on collisions of ^{238}U+^{124}Sn at $E_{\text{lab}} = 5.7$ MeV/nucleon at different initial configurations. (Left panels): A case of the side collision in which the symmetry axis of ^{238}U is set parallel to the y-axis. (Right panels): A case of the tip collision in which the symmetry axis of ^{238}U is set parallel to the x-axis. The figure was taken from Ref. [231].
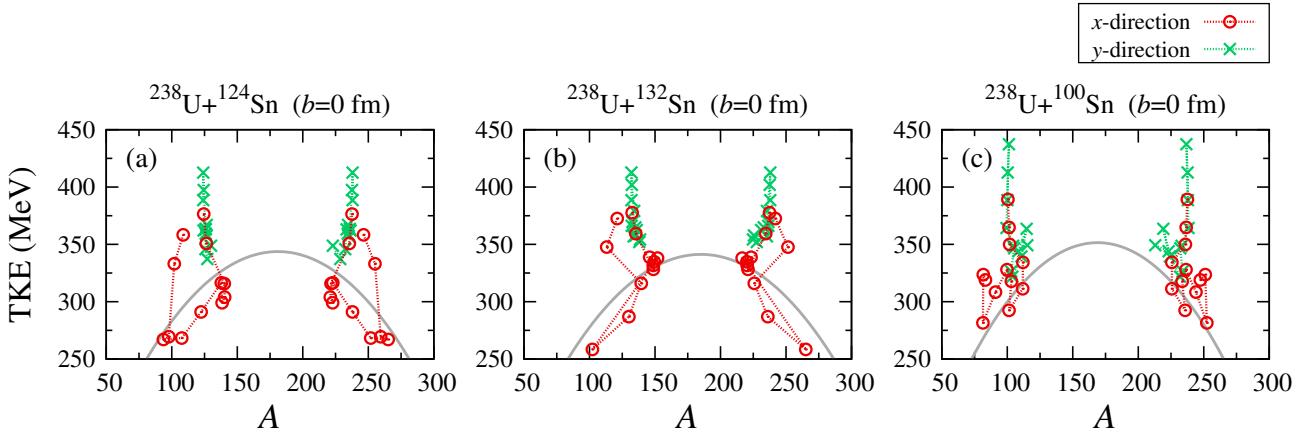
Figure 7.3: Total kinetic energy (TKE) and average fragment mass (A) in the TKE-A plane obtained from the TDHF calculations for head-on collisions of ^{238}U+^{100,124,132}Sn. Red circles show results for the x-direction configuration, while green crosses show results for the y-direction configuration. Gray solid line shows the TKE distribution evaluated by Eq. (6.3.1) which is based on the Viola systematics [223].

7.3 Energy and System Dependence of QF Dynamics

To get further information on reaction mechanisms of the QF process, we examine system as well as energy dependence of the QF dynamics. As in Chapter 6, for simplicity, we consider head-on collisions ($b = 0$ fm) at two different initial configurations, the x- and y-direction cases, corresponding to the tip and side collisions, respectively. We investigate three systems, ^{238}U+^{100,124,132}Sn, to examine, especially, the N/Z ratio dependence of the QF dynamics. We note that the N/Z ratios of ^{100}Sn, ^{124}Sn, and ^{132}Sn are 1.00, 1.48, and 1.64, respectively, while that of ^{238}U is 1.59. Therefore, we expect emergence of different features in the reaction dynamics.

7.3.1 Global trends

We performed many TDHF calculations of head-on collisions of ^{238}U+^{100,124,132}Sn by changing the incident energy. From the results, we can construct the average TKE-A plot from the TDHF calculations. In Fig. 7.3, we show obtained average TKE-A plot for each system. Red open circles show results for the tip collisions (x-direction), while green crosses show results for the side collisions (y-direction). The Viola systematics [223] evaluated by Eq. (6.3.1) is also shown by a gray solid curve.

From the figure, we can see a global trend of the reaction dynamics. In side collisions (green crosses), the average mass numbers of lighter and heavier fragments do not change largely and only a decrease of TKE is seen. On the other hand, in tip collisions (red open circles), we find that the average mass numbers of fragment nuclei show a substantial TKE dependence. As seen from the figure, the fragment mass tends to be more mass asymmetric compared with the initial mass asymmetry. This asymmetrizing trend indicates that there appear *inverse* QF processes in tip collisions of ^{238}U+^{100,124,132}Sn. We note that the average TKE-A distribution follows reasonably the Viola systematics. To get more deeper insight into the reaction dynamics, let us see in some detail the energy dependence of the reaction dynamics in respective systems.

7.3.2 ^{238}U+^{124}Sn reaction

In Fig. 7.4, we show the average numbers of nucleons in the fragment nuclei in head-on collisions of ^{238}U+^{124}Sn as functions of the incident energy. Upper panels show the average numbers of neutrons (a) and protons (b) in the heavier (^{238}U-like) fragment. Lower panels show the average numbers of neutrons (c) and protons (d) in the lighter (^{124}Sn-like) fragment. Red open circles show results for the tip collisions, while green crosses show results for the side collisions. The initial neutron and proton numbers of the projectile and target nuclei are shown by horizontal dotted lines.

Let us first focus on the side collisions represented by green crosses. From the figure (Fig. 7.4), we find that the average number of nucleons in side collisions (green crosses) is not so much dependent on the incident energy. The larger decrease in the neutron number of the heavier fragment shown in (a) compared with the increase in the lighter fragment shown in (c) indicates substantial neutron emissions to the continuum from ^{238}U. This behavior is very much different from the ^{64}Ni+^{238}U reaction examined in Chapter 6. For the ^{64}Ni+^{238}U reaction, we observed a substantial mass drift mode toward the direction increasing the mass symmetry (Fig. 6.8). This difference may come from the different total number of protons included in the system. Because, in the ^{64}Ni+^{238}U reaction, total number of protons of the system is $Z = 120$, the composite system still has a chance to form a mononuclear shape resulting in a capture process. Such a compact mononuclear shape eventually dissociates producing mass symmetric fragments. In contrast, the ^{238}U+^{124}Sn system contains 142 protons in total and the composite system may no longer have any chance to form a mononuclear system which corresponds to a capture process.

On the other hand, in the tip collision case, the situation is quite different. When the incident energy is sufficiently small, the average number of nucleons coincides with the initial values, $N = 146$ and $Z = 92$ in the heavier fragment and $N = 74$ and $Z = 50$ in the lighter fragment. As the incident energy increases, the average number of nucleons changes suddenly at around $E_{\mathrm{lab}} = 5.5$ MeV/nucleon. At an energy region, 5.5 MeV/nucleon $\lesssim E_{\mathrm{lab}} \lesssim 7$ MeV/nucleon, the average number of nucleons in the fragment nuclei shows a prominent plateau as a function of the incident energy. We observed a similar sudden jump and a plateau structure in ^{64}Ni+^{238}U reaction as shown in Figs. 6.5 and 6.8. Furthermore, in the ^{238}U+^{124}Sn reaction, the QF dynamics changes dramatically when the incident energy becomes higher than $E_{\mathrm{lab}} \sim 7$ MeV/nucleon. As the incident energy increases from $E_{\mathrm{lab}} \sim 7$ MeV/nucleon, the direction of transfer is inverted. At $E_{\mathrm{lab}} \sim 9$ MeV/nucleon, the average number of nucleons reaches a maxima/minima in the heavier/lighter fragment. In this case, the QF process proceeds toward the direction increasing the mass asymmetry, corresponding to the *inverse* QF process.

In Fig. 7.7, we show time evolution of the density on the collision plane in ^{238}U+^{124}Sn reaction at $E_{\mathrm{lab}} \sim 9$ MeV/nucleon, where we observed the inverse QF process for the tip collision. In the side collision (left panels), the neck structure is not so much developed as in lower incident energy case shown in Fig. 7.2. In this case, the average number of transferred nucleons is very small on average.

On the other hand, in the tip collision (right panels), we find completely different behavior in the transfer dynamics. After two nuclei collide, the surface of the density of the composite system vibrate strongly showing two nodes at different positions ($t = 320$ fm/c). Then, one of the nodes located at lighter nucleus side (the left side in the figure) develops suddenly to form a neck structure and it eventually dissociates at a position close to the lighter nucleus ($t = 320\text{-}960$ fm/c). In this case, about 16 neutrons and 12 protons are transferred from ^{124}Sn to ^{238}U producing $^{266}_{104}$Rf$_{162}$ on average. This is a typical dynamics of the *inverse* QF dynamics in ^{238}U+^{100,124,132}Sn reactions. We anticipate that there may be a substantial stabilizing effect for a large octopole deformation in $Z \sim 100$ region, which may partly responsible for the appearance of the inverse QF process.

To examine system dependence of the QF dynamics, let us next show results for other two systems, ^{238}U+^{100,132}Sn.
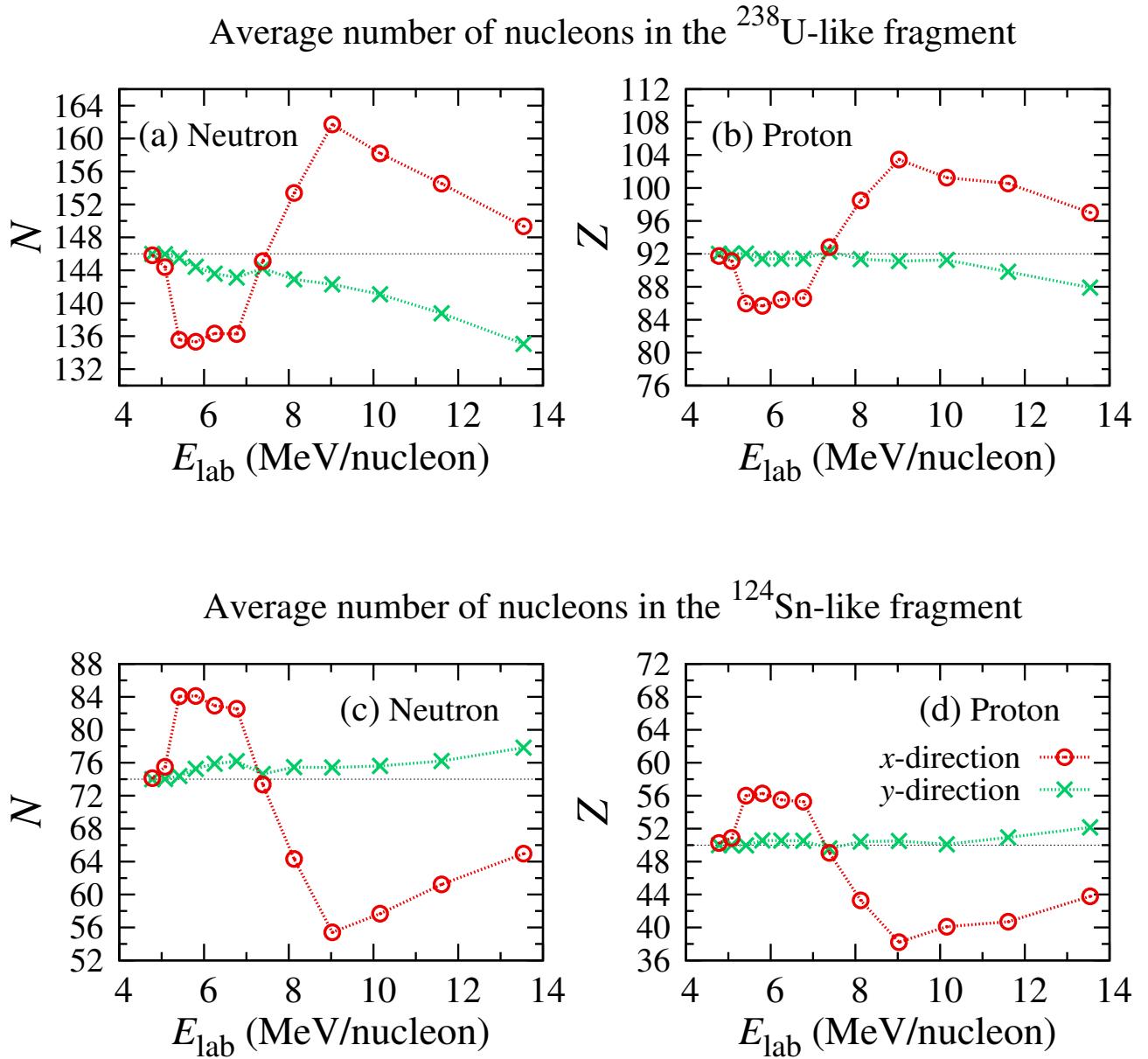
Figure 7.4: Incident energy dependence of the fragment's N and Z in head-on collisions of ^{238}U+^{124}Sn. The 'x-direction' means that symmetry axis of ^{238}U is set parallel to the collision axis (tip collision), while the 'y-direction' means that the symmetry axis is set perpendicular to the collision axis (side collision). Upper panels ((a) and (b)) show average numbers of nucleons in the heavier ($^{238}_{92}$U$_{146}$-like) fragment, while lower panels ((c) and (d)) show those in the lighter ($^{124}_{50}$Sn$_{74}$-like) fragment. The initial neutron and proton numbers in the projectile and target nuclei are represented by horizontal dotted lines.

7.3.3 ^{238}U+^{132}Sn reaction

In Fig. 7.5, we show the same quantities as in Fig. 7.4, but for ^{238}U+^{132}Sn reaction: Upper panels for the heavier (^{238}U-like) fragment, while lower panels for the lighter (^{132}Sn-like) fragment. Red open circles and green crosses show results for the tip and side collisions, respectively. Left panels show the average number of neutrons and right panels show the average number of protons in each fragment. The initial neutron and proton numbers in the projectile and target nuclei are represented by horizontal dotted lines.

From the figure (Fig. 7.5), in the side collision case, we again find that the average number of nucleons is not so much dependent on the incident energy, as in the ^{238}U+^{124}Sn system shown in Fig. 7.4. In the tip collision case, we find a similar behavior, a sudden jump and a plateau structure followed by inverse QF processes as in the ^{238}U+^{124}Sn system, except for two cases at $E_{\text{lab}} \sim 8.5$ and 10 MeV/nucleon. It is worth mentioning that, nevertheless the N/Z ratio of ^{132}Sn exceeds that of ^{238}U, the direction of nucleon transfer at the plateau region is the same as in the case of ^{238}U+^{124}Sn. It indicates that, in the QF process where two nuclei stick together for a relatively long timescale compared with that of nucleons' internuclear motions, the QF dynamics with a thick neck formation would responsible for the direction of nucleon transfer rather than the initial N/Z ratios of the projectile and target nuclei (Of course, the charge equilibration process takes place, but the neck breaking dynamics determines the direction of transfer of both neutrons and protons).

It is remarkable that a neutron-rich fermium isotope, $^{264}_{100}$Fm$_{164}$, is generated through the inverse QF process at $E_{\text{lab}} \sim 8$ MeV/nucleon, as a primary fragment in the TDHF calculation. Although such fragments produced by inverse QF processes must accompany huge excitation energy and suffer from disintegration processes, this result is encouraging for the further investigations to produce neutron-rich transuranium nuclei whose production is difficult by other reactions.

In Fig. 7.8, we show time evolution of the density on the collision plane in the tip collisions of ^{238}U+^{132}Sn at three different incident energies, $E_{\text{lab}} \sim 7$, 8, and 9 MeV/nucleon. As shown in Fig. 7.5, these incident energies show quite different numbers of nucleons in the fragment nuclei.

Let us first take a look at the $E_{\text{lab}} \sim 7$ MeV/nucleon case shown in the left panels of the figure. This reaction shows an ordinary QF process, a mass transfer toward the mass symmetry. We find that the shape evolution is very similar to the case of ^{238}U+^{124}Sn at $E_{\text{lab}} = 5.7$ MeV/nucleon shown in Fig. 7.2.

In the middle panels, we show the $E_{\text{lab}} \sim 8$ MeV/nucleon case which results in the inverse QF process. This shape evolution is very similar to the case of ^{238}U+^{124}Sn at $E_{\text{lab}} = 9$ MeV/nucleon shown in the right panels of Fig. 7.7. Again, the tip collision induces a rippling mode of the density and forms a neck structure at a position close to the smaller nucleus showing quite asymmetric structure during the collision ($t = 320$-1120 fm/c).

In the case of $E_{\text{lab}} \sim 9$ MeV/nucleon shown in the right panels of the figure, the dynamics is somewhat different from the previous case. After the collision, a similar surface rippling mode is seen ($t = 320$ fm/c). After that, up to around $t = 640$ fm/c, the system develops in a similar way to the previous case. However, at $t = 800$ fm/c, the neck structure changes slightly and starts to dissociate forming more mass symmetric fragments ($t = 960$-1280 fm/c).

In this way, appearance and disappearance of the inverse QF process show a sensitive incident energy dependence in the tip collisions of ^{238}U+^{132}Sn. From careful observations, we suspect that there are interplays between (i) the surface vibration mode induced by the collision which may responsible for a determination of the position of a neck formed at the initial stage of the dinuclear system formation, (ii) internuclear motions of nucleons inside the deformed mean-field potential, (iii) some structural effects of the composite system and those in the fragment nuclei. We note that Zagrebaev $et\ al.$ predicted an mechanism of inverse QF process which originates from a substantial stabilization
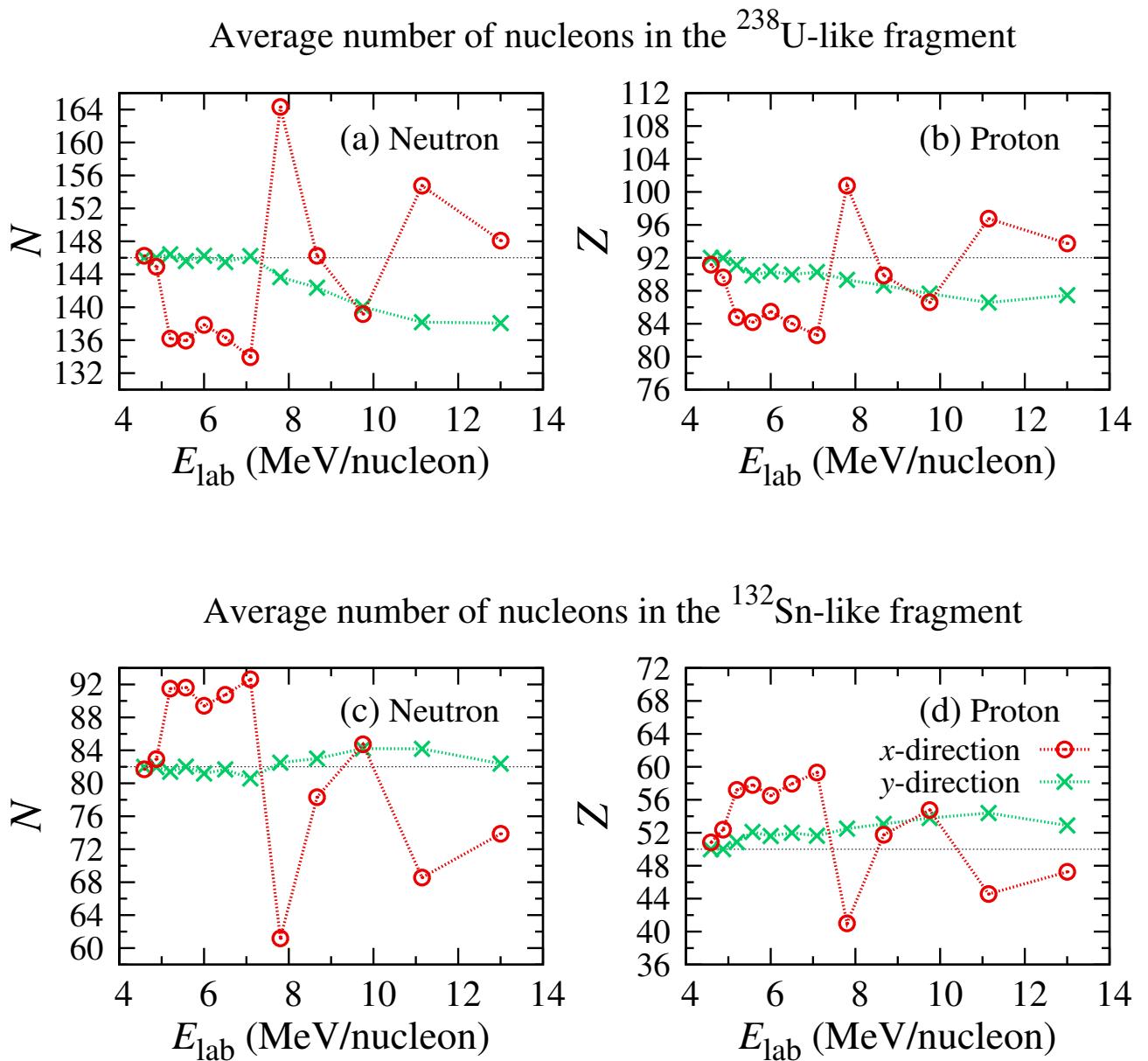
effect of doubly magic ^{208}Pb in the exit channel [29, 69, 70, 71, 72, 84]. Whereas the inverse QF dynamics we observed in the TDHF calculations for ^{238}U+^{100,124,132}Sn is expected to have a different origin which, to the author's knowledge, has not been investigated so far.
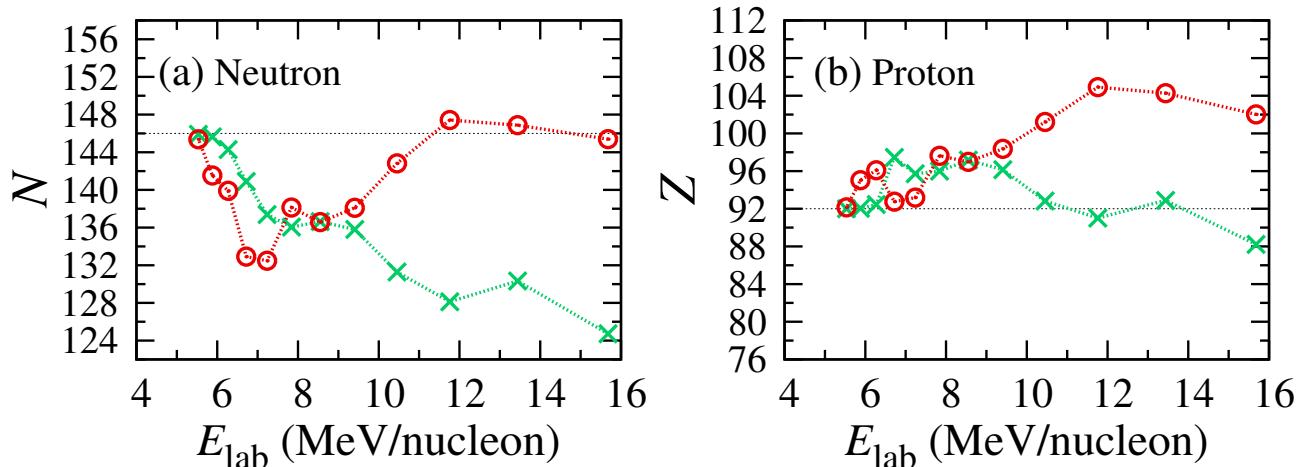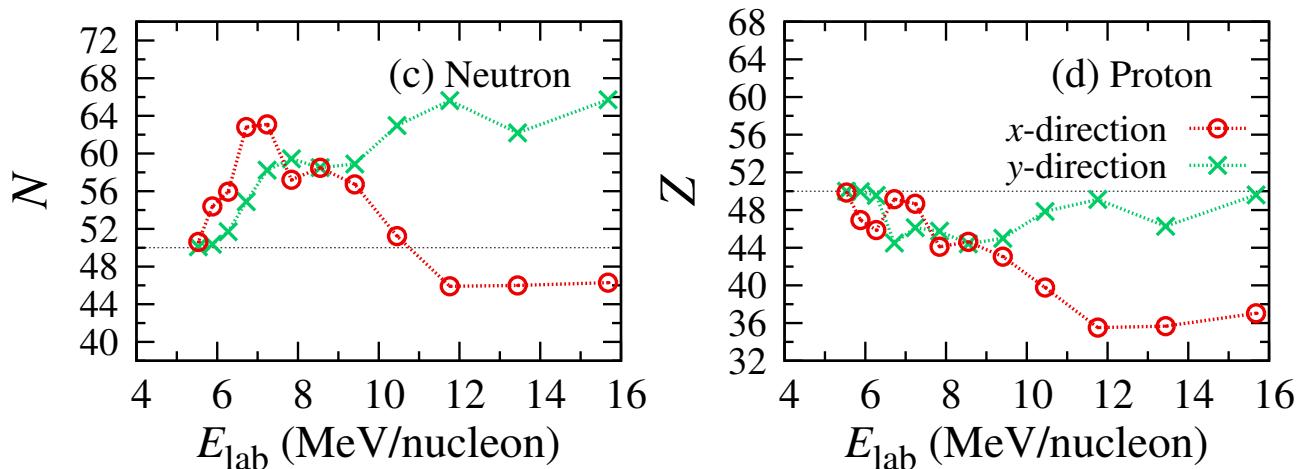
7.3.4 ^{238}U+^{100}Sn reaction

In Fig. 7.6, we show results of the TDHF calculation for head-on collisions of ^{238}U+^{100}Sn. Since the N/Z ratio of ^{100}Sn, $50/50 = 1.00$, is very much different from that of ^{238}U, $146/92 \sim 1.59$, we expect substantial transfer modes toward the direction of the charge equilibrium of the system.

First, we focus on results of the side collisions, where we have observed a week incident energy dependence in the previous ^{238}U+^{124,132}Sn cases shown in Figs. 7.4 and 7.5. From the figure (Fig. 7.6), we find different behavior of the average numbers of nucleons in the fragment nuclei as functions of the incident energy. In this case, we find that neutrons and protons tend to transfer toward the opposite directions, the direction of the charge equilibrium of the system (^{238}U$\rightarrow^{100}$Sn for neutrons, ^{238}U$\leftarrow^{100}$Sn for protons), at least for $E_{\text{lab}} \lesssim 10$ MeV/nucleons. As the incident energy increases, the proton transfer toward the direction of the charge equilibrium of the initial system is suppressed. A similar behavior has been observed in the case of MNT processes examined in Chapter 3, indicating a significant effect of the neck breaking dynamics after a sufficient charge equilibration, which induces transfer of both neutrons and protons in the same direction.

In the tip collision case, we find to some extent similar behavior to those in the ^{238}U+^{124,132}Sn systems, although the average number of protons looks different because of the substantial charge equilibration process. As the incident energy increases, the average number of neutrons shown in (a) and (c) changes rapidly as a function of the incident energy, while the change is somewhat small in the case of protons shown in (b) and (d). In the intermediate energy region, 6.5 MeV/nucleon $\lesssim E_{\text{lab}} \lesssim 9$ MeV/nucleon, the average number of nucleons takes a similar value (except for a hump at around $E_{\text{lab}} \sim 7$ MeV/nucleon). When we increase the incident energy further, inverse QF processes take place. Because ^{100}Sn is of neutron-deficient compared with ^{124,132}Sn and the neck breaking transfer dynamics takes place after a sufficient charge equilibration, the average number of neutrons is almost the same as that of the projectile and target nuclei in this inverse QF process. Therefore, only the proton number is changed drastically compared with the initial nuclei, ^{100}Sn and ^{238}U. It is worth mentioning that we find neutron-deficient transuranium nuclei, *e.g.* $^{252}_{104}$Rf$_{148}$ at $E_{\text{lab}} \sim 12$ MeV/nucleon, as a primary fragment in the TDHF calculation. In this way, we expect that the inverse QF process will be a unique tool to produce exotic unstable nuclei which have not been produced by other reactions.

Figure 7.5: Same as Fig. 7.4 but for the ^{238}U+^{132}Sn system.

Average number of nucleons in the ^{238}U-like fragment

Average number of nucleons in the ^{100}Sn-like fragment

Figure 7.6: Same as Figs. 7.4 and 7.5 but for the ^{238}U+^{100}Sn system.

^{238}U+^{124}Sn, b=0 fm, E_{lab}~2148.6 MeV (d=9 fm)
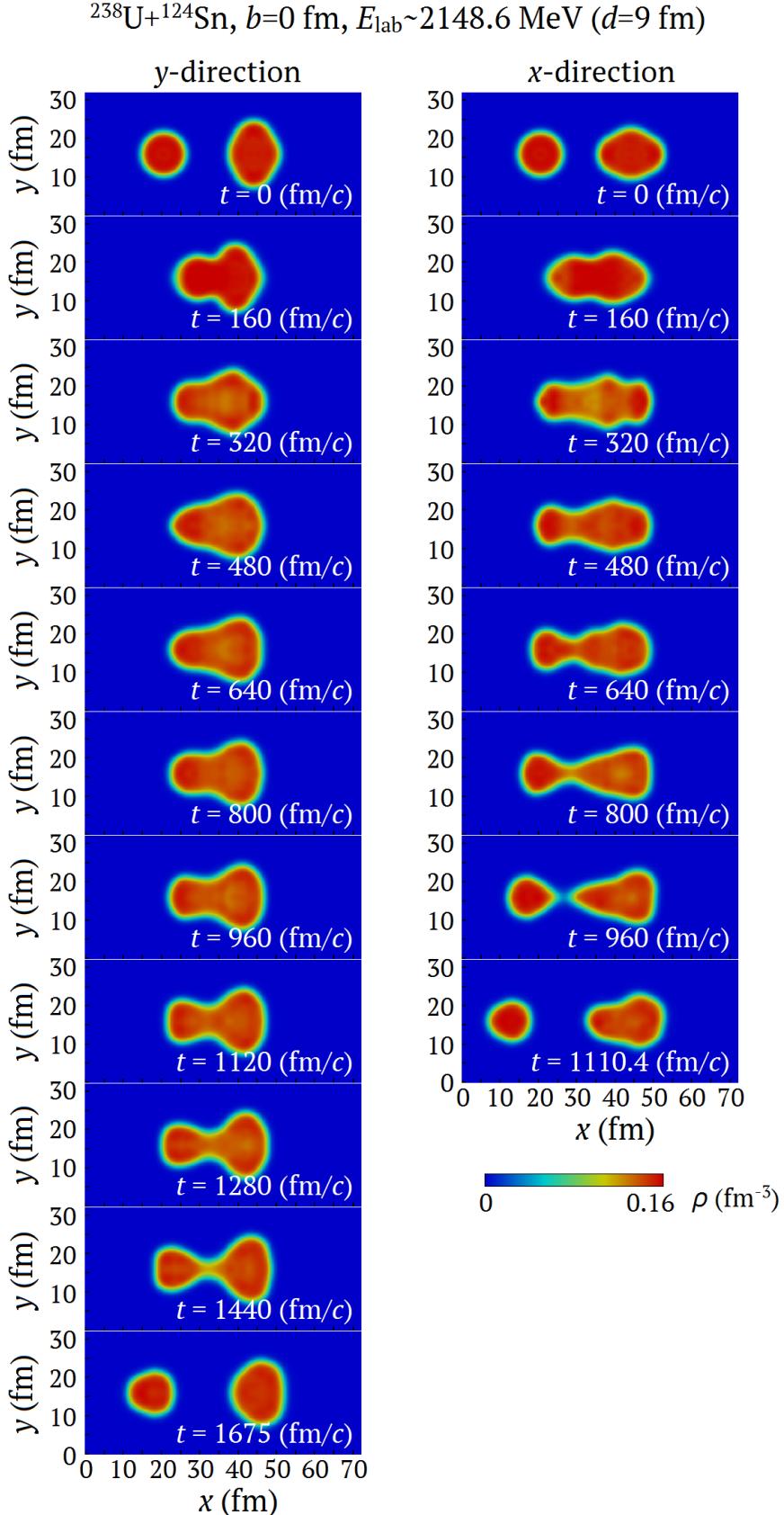
Figure 7.7: Time evolution of the density on the collision plane in head-on collisions of ^{238}U+^{124}Sn at $E_{\text{lab}} \sim 9$ MeV/nucleon ($d = 9$ fm). Left panels show result for the y-direction configuration (side collision), while right panels show results for the x-direction configuration (tip collision). Labels '$t = x$ fm/c' indicate an elapsed time from the initial stage of the TDHF calculation.

7.4   Summary and Concluding Remarks on Chapter 7

In this Chapter, we have investigated the MNT and QF processes in ^{238}U+^{100,124,132}Sn reactions, as a next application of the TDHF theory to reactions involving ^{238}U. For the ^{238}U+^{124}Sn reaction at $E_{\text{lab}} = 5.7$ MeV/nucleon, measurements of MNT processes were achieved [232], showing substantial MNT cross sections accompanying more than ten-proton transfer from ^{238}U to ^{124}Sn. From the calculation, we have found that the amount of transferred nucleons depends much on the relative orientation between the deformation axis of ^{238}U and the relative vector connecting centers of ^{238}U and ^{124}Sn nuclei. We have found a formation of thick neck when the ^{238}U collides from its tip with ^{124}Sn. However, the neck formation is substantially suppressed when ^{238}U collides from its side. We have found that a large number of protons are transferred in the tip collision. This is caused by the breaking of the neck and subsequent absorption of nucleons in the neck region. We thus conclude that the measured MNT processes involving about ten protons originate from the neck breaking transfer dynamics in the tip collisions of a deformed ^{238}U nucleus. This correspondence between the results of the TDHF calculations and experimental data will also be an evidence which shows the applicability of the TDHF theory in describing MNT and QF processes in reactions involving heavy nuclei.

To get further insight into the transfer dynamics associated with the neck breaking dynamics, we investigated incident energy dependence of head-on collisions of ^{238}U+^{124}Sn taking two different initial orientations of ^{238}U corresponding to the tip and side collisions. From the results, we have found that the neck formation is always suppressed irrespective of the incident energy when ^{238}U collides from its side. On the other hand, when ^{238}U collides from its tip, a drastic change in the transfer dynamics is observed. When we increase the incident energy, a breaking point of the neck changes suddenly resulting in a change of direction of nucleon transfer. A number of nucleons inside the neck region are transferred to heavier nucleus, the ^{238}U-like fragment, forming transuranium nuclei after the collision. It corresponds to the *inverse* QF process.

To investigate a projectile-target combination dependence, especially, the initial N/Z ratio dependence of the QF dynamics, we also performed similar calculations for head-on collisions of ^{238}U+^{100,132}Sn. ^{238}U and ^{124}Sn have a similar value of N/Z ratio, 1.59 and 1.48, respectively. Since ^{100}Sn has N/Z ratio of 1.00, we expect a significant effect of the charge equilibration process in the ^{238}U+^{100}Sn reaction. While, since ^{132}Sn has N/Z ratio of 1.64 which is greater than that of ^{238}U, we expect transfer of neutrons and protons toward the opposite direction to other two cases. From the results, we find that a globally similar behavior of the average number of nucleons in the fragment nuclei. In the ^{238}U+^{100}Sn system, we have found an emergence of the charge equilibration process as expected from the quite different N/Z ratios between the projectile and the target.

We note that for all three systems, ^{238}U+^{100,124,132}Sn, we have observed the *inverse* QF process in which reaction products become more mass asymmetric compared with initial masses of nuclei before the collision. In the inverse QF process, we have found productions of neutron-rich transuranium nuclei in ^{238}U+^{124,132}Sn and neutron-deficient transuranium nuclei in ^{238}U+^{100}Sn as primary reaction products in the TDHF calculations. We consider that these results are encouraging to search for a peculiar QF dynamics in the TDHF theory, which enables us to access exotic unstable nuclei whose production have not been achieved by other reactions.

^{238}U+^{132}Sn, b=0, x-direction
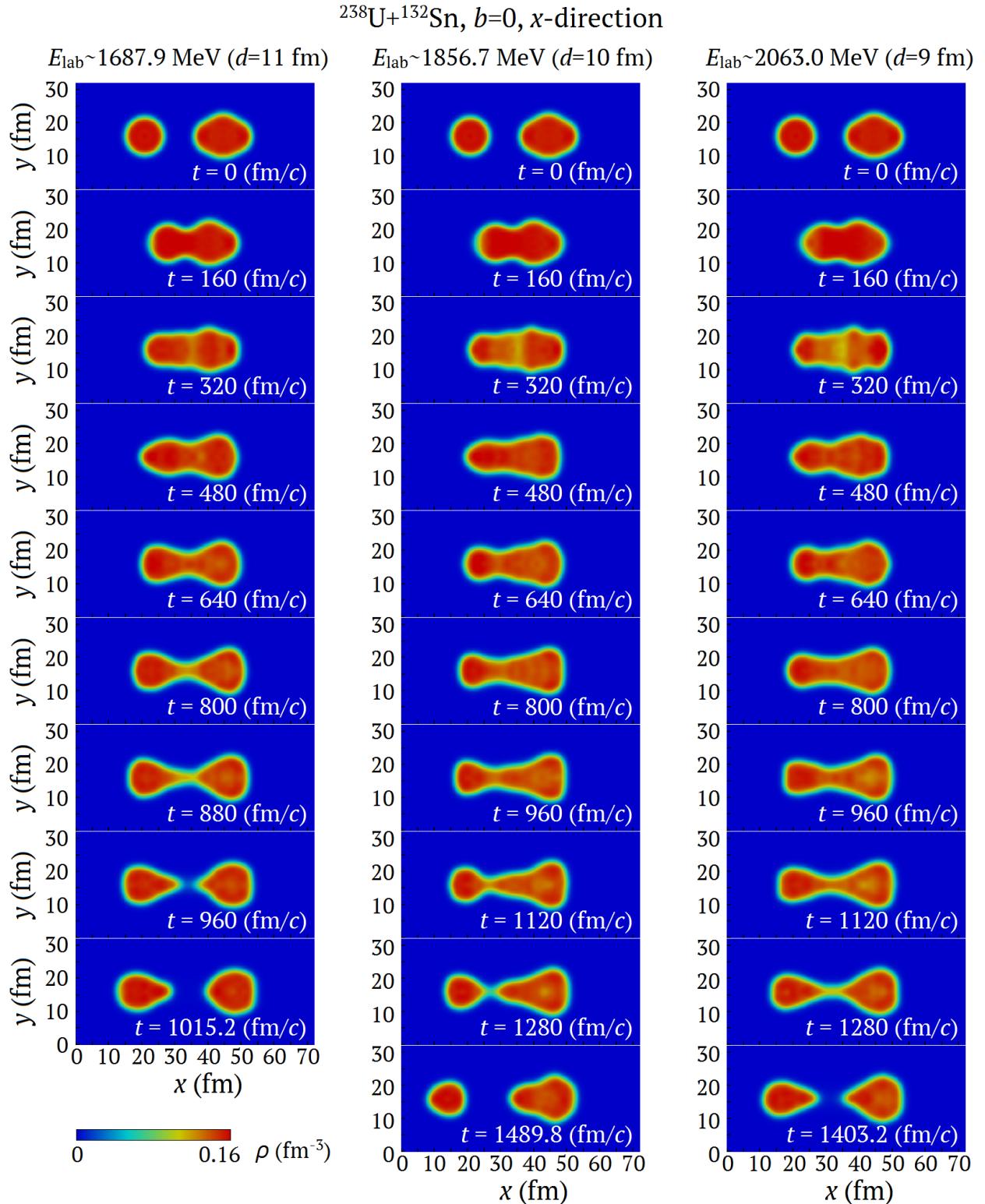
Figure 7.8: Time evolution of the density on the collision plane in head-on collisions of ^{238}U+^{132}Sn. Results for the x-direction configuration (tip collision) at three different incident energies are shown for comparison. Panels in the left and right columns show results at $E_{\mathrm{lab}} \sim 7$ and 9 MeV/nucleon, respectively, resulting in ordinary QF process. While panels in the middle column show results at $E_{\mathrm{lab}} \sim 8$ MeV/nucleon, resulting in an inverse QF process. Labels '$t = x$ fm/c' indicate an elapsed time from the initial stage of the TDHF calculation.

Chapter 8

SEARCH FOR OPTIMUM CONDITIONS FOR ^{136}Xe+^{198}Pt REACTION TO PRODUCE OBJECTIVE UNSTABLE NUCLEI

In this second part of the thesis (Part II), we have investigated MNT and QF processes in reactions involving heavy nuclei such as ^{238}U employing the TDHF theory. In Chapter 6, we analyzed ^{64}Ni+^{238}U reaction for which extensive experimental data of both MNT and QF processes are available [45, 79, 216, 217]. From the results, we found that the TDHF theory is capable of describing not only MNT reactions in peripheral collisions but also QF processes in dissipative collisions of heavy nuclei. The measured MNT cross sections for the ^{64}Ni+^{238}U reaction have been nicely reproduced by the TDHF theory combined with the PNP technique. By comparing an average TKE-A distribution obtained from the TDHF calculations with available experimental data, we found that the TDHF theory reasonably describes a mass drift mode toward the direction increasing the mass symmetry, which has been considered as QF processes. This fact shows the applicability of the TDHF theory to such dissipative collisions in reactions involving heavy nuclei.

In Chapter 7, we analyzed ^{238}U+^{100,124,132}Sn reactions. For the ^{238}U+^{124}Sn reaction, production cross sections for the lighter (^{124}Sn-like) fragment were measured experimentally [232]. The experimental data indicate that about 10 protons were transferred from ^{238}U to ^{124}Sn. From the TDHF calculations, we revealed that the measured many-proton transfer from ^{238}U to ^{124}Sn can be explained by a tip collision induced neck breaking transfer dynamics. When ^{238}U collides from its tip, a thick and long neck is formed between two colliding nuclei, while the neck formation is substantially suppressed when ^{238}U collides from its side. After the thick and long neck formation, the dinuclear system dissociate producing two individual nuclei. Depending on the scission point of the neck, nucleons involved in the neck structure are absorbed by one of the fragments. This neck breaking transfer dynamics explains the measured massive proton-flow from ^{238}U to ^{124}Sn.

From these analyses, we have gained a confidence that the TDHF theory gives us a reasonable description of both MNT and QF dynamics in dissipative collisions of heavy nuclei. Because the TDHF theory provides a unified microscopic description of the reaction dynamics without any adjustable parameters, the TDHF theory would be a promising tool for predicting optimum conditions to produce objective nuclei. As a final topic of the thesis, we present tentative results of the TDHF calculations on the way to achieve our main aim, a theoretical prediction of optimum conditions to produce objective nuclei. In this Chapter, we investigate ^{136}Xe+^{198}Pt reaction which is considered to be useful to

produce neutron-rich unstable nuclei around the neutron magic number $N = 126$ whose properties have a crucial impact on the r-process path of the nucleosynthesis.

This Chapter is organized as follows. In Sec. 8.1, we show some computational details utilized in the TDHF calculations shown in this Chapter. In Sec. 8.2, we show results of a systematic calculation of MNT and QF processes in ^{136}Xe+^{198}Pt reactions for various initial conditions. In Sec. 8.3, a summary and concluding remarks on this Chapter are presented.

8.1   Computational Details

We use our own computational code of the TDHF calculations of heavy ion reactions as in the previous Chapters. We discretize three-dimensional Cartesian coordinates into a uniform mesh to represent single-particle wave functions without any symmetry restriction. For the static HF calculation of projectile and target nuclei, we use $30 \times 30 \times 30$ grid points with a mesh spacing of 0.8 fm. The 11-point finite difference-formula is used to calculate first and second derivatives. For the TDHF calculations, we use a numerical box with $70 \times 70 \times 30$ grid points. The initial separation distance is set to be 25 fm in the incident direction parallel to the x-axis. For the time evolution operator, the fourth-order Taylor expansion method is utilized with $\Delta t = 0.2$ fm/c. Because the total number of protons in the ^{136}Xe+^{198}Pt system is very large, $Z = 54 + 78 = 132$, we have not observed any capture process at all initial conditions examined. We calculate the TDHF time evolution until the relative distance between centers of two fragment nuclei exceeds 27-30 fm, where two fragment nuclei are well separated spatially.

8.2   MNT and QF Processes

To find optimum conditions to produce objective nuclei, we performed a systematic TDHF calculation for ^{136}Xe+^{198}Pt reactions at various incident energies and impact parameters. We calculated reactions at $E_{\text{lab}} = 6$, 7, 8, 9, 9.5, and 10 MeV/nucleon and $b = 0$-10 fm.

In Fig. 8.1, we show the time evolution of the density of the two colliding nuclei in ^{136}Xe+^{198}Pt reactions at three typical initial conditions. From left to right, we show results at $E_{\text{lab}} = 8$, 9, 10 MeV/nucleon and $b = 5$, 4, 3 fm, respectively. The label 'x fm/c' in each panel indicates an elapsed time started from the initial stage of the TDHF calculation shown in the top panels (0 fm/c).

Let us first focus on the $E_{\text{lab}} = 8$ MeV/nucleon and $b = 5$ fm case shown in left panels of Fig. 8.1. After tow nuclei collide, a very thick neck structure is formed between tow colliding nuclei ($t = 200$-800 fm/c). When the composite system dissociates, the greater part of the neck is absorbed by the lighter nucleus located on the left-top side of the panel ($t = 800$-1000 fm/c). As a result of the absorption of nucleons inside the neck region, about 10 neutrons and 6 protons are transferred from ^{198}Pt to ^{136}Xe producing $^{152}_{60}$Nd$_{92}$ on average. This process would be regarded as an ordinary QF process, a mass drift mode toward the mass symmetry of the system.

Next, let us take a look at the $E_{\text{lab}} = 9$ MeV/nucleon and $b = 4$ fm case shown in middle panels of the figure. Compared with the previous case, the incident energy becomes higher and the impact parameter becomes smaller. Because of this change in the initial condition, two nuclei collide more deeply inducing a rippling mode on the surface of the density distribution of the composite system ($t = 200$-400 fm/c). After that, a neck structure start to develop at a position close to the lighter nucleus ($t = 400$-800 fm/c). When the neck dissociates, the most part of the neck structure is, in this case, absorbed by the heavier nucleus located on the right-bottom side in the panels ($t = 800$-1241 fm/c). As a result of the absorption of nucleons inside the neck region, about 5 neutrons and 4 protons are transferred from ^{136}Xe to ^{198}Pt producing $^{207}_{82}$Pb$_{125}$ on average. Thus, unlike the previous

case, there emerges an *inverse* QF process, a massive nucleon transfer toward the direction increasing the mass asymmetry.

The final typical example is the $E_{\text{lab}} = 10$ MeV/nucleon and $b = 3$ fm case shown in right panels of the figure. Compared with the previous two cases, again, the incident energy becomes higher and the impact parameter becomes smaller. Because of this change, two nuclei collide much more violently and form an almost mononuclear-type configuration as seen in panels $t = 200\text{-}600$ fm/c. That is, the composite system has no clear necking structure and we hardly regard it as a dinuclear system composed of two subsystems of projectile-like and target-like nuclei ($t = 600$ fm/c). Then the composite mononuclear system starts to dissociate making a neck structure at almost the middle point of the system ($t = 1000\text{-}1600$ fm/c). In this case, about 19 neutrons and 10 protons are transferred from ^{198}Pt to ^{136}Xe producing $^{165}_{64}$Gd$_{101}$ on average. In this case, the system approaches toward the mass symmetry reflecting the formation of the mononuclear configuration of the composite system, which may correspond to a deep QF process [233, 234, 235, 236, 237].

As we saw in the typical three examples, the direction of transfer as well as the amount of transferred nucleons depend much on the initial condition. In Fig. 8.2, we show the average number of nucleons in the heavier fragment obtained from the systematic TDHF calculation of ^{136}Xe+^{198}Pt reactions for various incident energies and impact parameters. Red open circles, orange down-pointing open triangles, green open triangles, blue open squares, magenta crosses, and purple open diamonds connected with lines show results at $E_{\text{lab}} = 10$, 9.5, 9, 8, 7, and 6 MeV/nucleon, respectively. The horizontal axis is the impact parameter, b, and results at the same incident energy are connected with lines and are represented by the same color.

From the figure, we find quite complex behavior of the average number of nucleons in the heavier fragment. Let us explain the results in order. Because the heavier nucleus, ^{198}Pt has $N = 120$ and $Z = 78$, the average numbers of neutrons and protons coincide with those values when the impact parameter is sufficiently large ($b \gtrsim 8$ fm), corresponding to the quasielastic reactions. As the impact parameter decreases, two colliding nuclei touch on the course of the reaction. Then, for all incident energies higher than 6 MeV/nucleon, the average numbers of nucleons in the heavier fragment decrease compared with the initial values $N = 120$ and $Z = 78$. The decrease of the number of nucleons in the heavier fragment means that those nucleons are transferred from ^{198}Pt to ^{136}Xe, from the heavier nucleus to the lighter one.

When the incident energy is lower than 9 MeV/nucleon, the average numbers of nucleons in the heavier fragment tend to approach to the initial values as the impact parameter decreases. On the other hand, when the incident energy is higher than or equal to 9 MeV/nucleon, the behavior is markedly different. As the impact parameter decreases, the average numbers of neutrons and protons in the heavier fragment increase suddenly and exceed the initial values at around $b \sim 5$ fm. This increase of the number of nucleons in the heavier fragment corresponds to the transfer of nucleons from ^{136}Xe to ^{198}Pt, from the lighter nucleus to the heavier one, corresponding to the *inverse* QF process.

At an impact parameter region around $b \sim 4\text{-}5$ fm, the average numbers of nucleons show a prominent plateau at around $N = 126$ and $Z = 82$. Although we need further detailed analyses to understand generation mechanisms of the inverse QF process, it would be worth mentioning that the plateau corresponds to a production of doubly magic ^{208}Pb on average. It may indicate that there exists certain influence of structural properties of the fragment nuclei in the exit channel on the QF dynamics. We note that, in analyses based on the dynamical Langevin calculation, substantial structural effects of the composite system are routinely observed [29, 69, 70, 71, 72, 84]. Also in some experiments, *e.g.* ^{34,36}S+^{238}U reactions reported in Refs. [228, 229], a peak at around $A \sim 208$ in fission fragment mass distributions was observed. It could be interpreted in the Langevin model as a substantial stabilization effect of ^{208}Pb producing a valley on a landscape of PES which gathers a
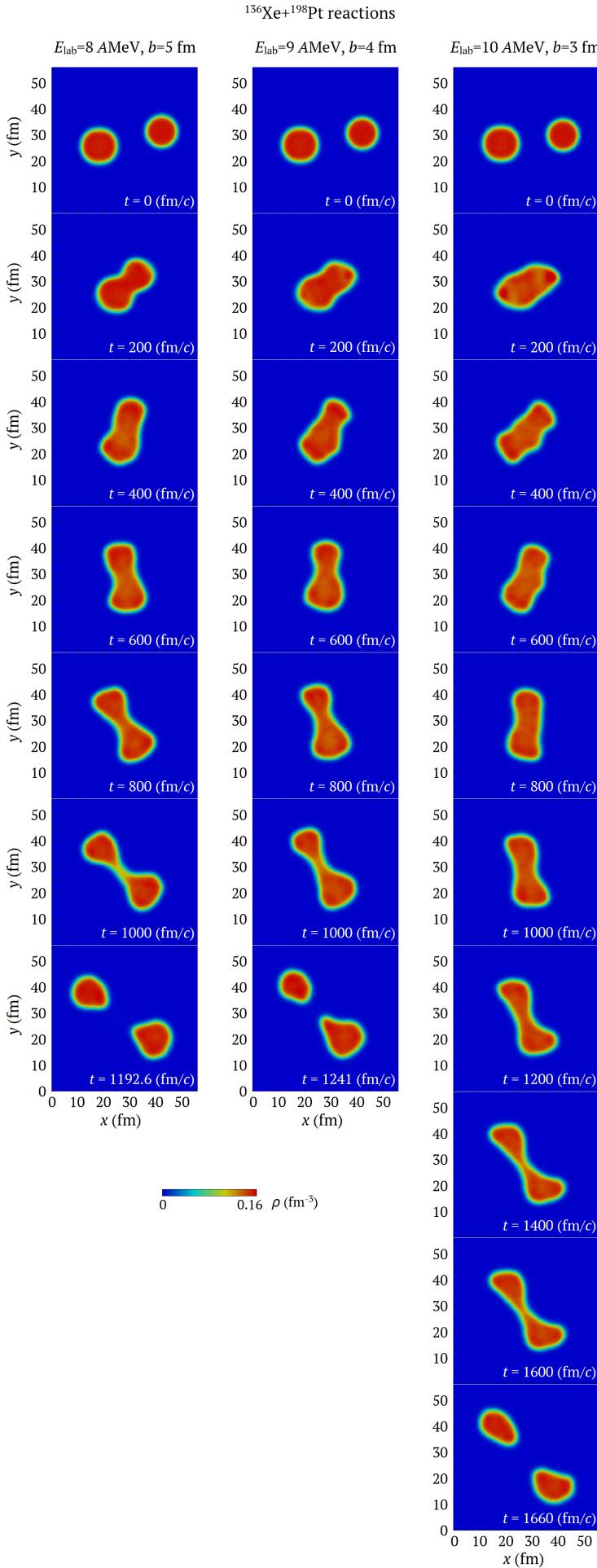
Figure 8.1: Time evolution of the density on the collision plane (xy-plane) in ^{136}Xe+^{198}Pt collisions at different initial conditions. Panels on the left column show results at $E_{\mathrm{lab}} =$ 8 MeV/nucleon and $b = 5$ fm. Panels on the middle column show results at $E_{\mathrm{lab}} = 9$ MeV/nucleon at $b = 4$ fm. Panels on the right column show results at $E_{\mathrm{lab}} = 10$ MeV/nucleon and $b = 3$ fm. Labels 'x fm/c' indicate an elapsed time from the initial stage of the TDHF calculation.
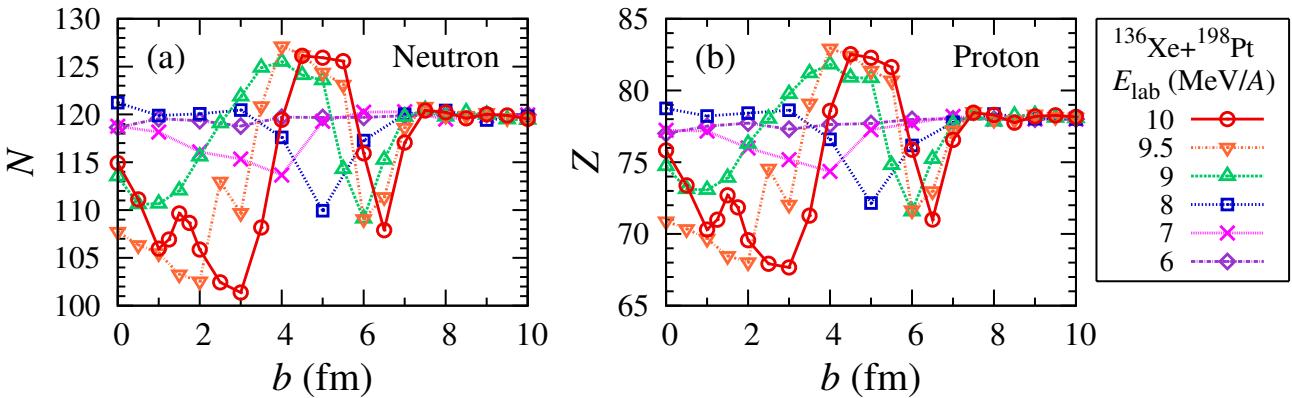
Figure 8.2: Average numbers of neutrons (left) and protons (right) in the heavier (^{198}Pt-like) fragment in ^{136}Xe+^{198}Pt reactions at various initial conditions. The horizontal axis is the impact parameter, b. Red open circles, orange down-pointing open triangles, green open triangles, blue open squares, magenta crosses, and purple open diamonds connected with lines show results at $E_{\text{lab}} = 10, 9.5, 9, 8, 7,$ and 6 MeV/nucleon, respectively.

bunch of dynamical trajectories. We note that, Zagrebaev $et\ al.$ extensively discussed similar inverse QF processes caused by structural effects of ^{208}Pb in ^{160}Gd+^{186}W reaction [72].

In a small impact parameter region ($b \lesssim 4$ fm), the direction of transfer again changes dramatically for $E_{\text{lab}} \geq 9$ MeV/nucleon cases. The average numbers of neutrons and protons in the heavier fragment decrease compared with the initial values $N = 120$ and $Z = 78$. This corresponds to the transfer of nucleons from ^{198}Pt to ^{136}Xe. These mass drift modes emerging in the small impact parameter region are originated from a mononuclear shape formation followed by a symmetric dissociation, the deep QF process, similar dynamics shown in right panels of Fig. 8.1.

Regarding the results shown above, we might conclude that the QF processes in ^{136}Xe+^{198}Pt reaction are very much complicated showing the complex initial condition dependence. We note that, however, we find another aspect of the QF process, which would provide us a much simplified picture of the reaction dynamics.

In Fig. 8.3, we show the same results as shown in Fig. 8.2, the average number of nucleons in the heavier fragment, but now, we have changed the horizontal axis from the impact parameter b to the distance of closest approach $d = d(E, b)$ (Eq. (4.2.1)) of the Rutherford trajectory. We then find that
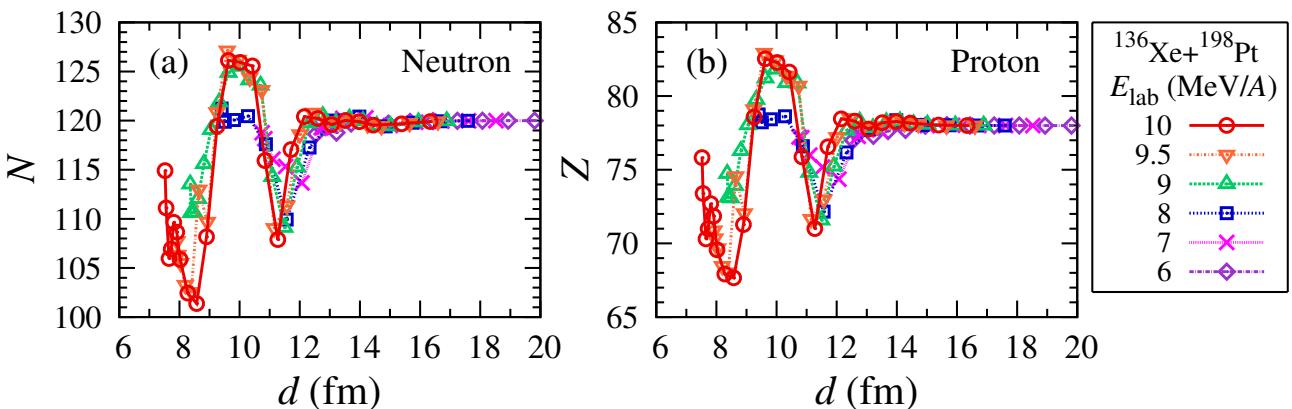
Figure 8.3: The same results as Fig. 8.2 but the horizontal axis is changed to the distance of closest approach of the Rutherford trajectory, d, specified by E_{lab} and b.
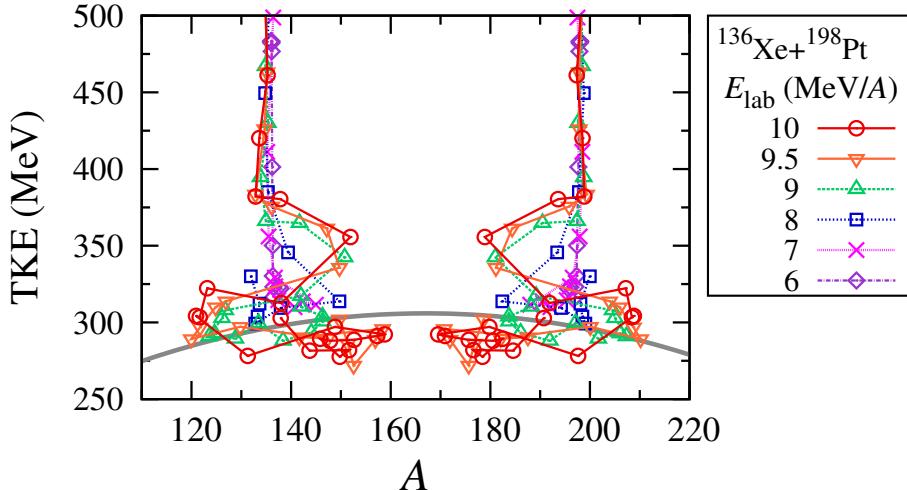
Figure 8.4: Total kinetic energy (TKE) and average fragment mass (A) in the TKE-A plane obtained from the TDHF calculations for ^{136}Xe+^{198}Pt reaction at various incident energies and impact parameters. Gray solid line shows the TKE distribution evaluated by Eq. (6.3.1) which is based on the Viola systematics [223].

the average numbers of nucleons at different incident energies and impact parameters show a similar behavior as a function of the distance of closest approach, d. As the distance of closest approach decreases, the direction of nucleon transfer changes at certain d-values, $d \sim 12$ fm (^{198}Pt→^{136}Xe), $d \sim 10$ fm (^{198}Pt←^{136}Xe), and $d \sim 9$ fm (^{198}Pt→^{136}Xe). This fact may indicate that the angular momentum carried into the composite system is not important in determining the QF dynamics.

The QF dynamics may be characterized by the radial motion of the two colliding nuclei. As we saw in Fig. 8.1, the shape of the composite system of the projectile and target nuclei depends on the violentness of the collision, reflecting induced rippling motion on the surface of the density distribution. Combined with the observation of the inverse QF processes producing ^{208}Pb-like nucleus and the systematic behavior shown in Fig. 8.3, we anticipate that some structural properties of the composite system at the turning point, $e.g.$ shape of vibrating surface of the composite system, elongation, thickness, and position of the necking structure, would determine the fate of the composite system dissociating in the QF dynamics. A possible way to examine such structural effects of the composite system is to calculate a PES of $^{334}_{132}$X$_{202}$, $e.g.$ in Q_{20}-Q_{30} plane, by the CHF method. Comparisons between the dynamical trajectories obtained from the TDHF calculations with the PES will provide us a more deeper understanding of the QF process. To understand microscopic reaction mechanisms and to predict optimum conditions to produce objective nuclei, we hope to try such analyses in future.

Next, let us take a look at the TKE-A distribution. In Fig. 8.4, we show the average TKE-A distribution in the ^{136}Xe+^{198}Pt reactions. Red open circles, orange down-pointing open triangles, green open triangles, blue open squares, magenta crosses, and purple open diamonds connected with lines show results at $E_{lab} = 10, 9.5, 9, 8, 7$, and 6 MeV/nucleon, respectively. Results at the same incident energy are connected with lines and are represented by the same color. We also show the Viola systematics [223] evaluated by Eq. (6.3.1) by a gray solid curve.

From the figure, we find a reasonable agreement between the TKE-A distributions obtained from the TDHF calculations and that of the Viola systematics. We find that the ordinary QF process observed at a relatively large-d region ($d \sim 11$ fm, see Fig. 8.3) occurs before the full momentum transfer is achieved. On the other hand, the inverse QF processes, the mass drift mode toward the direction increasing the mass asymmetry, and the deep QF process producing mass symmetric fragments take place after the full momentum transfer is achieved.
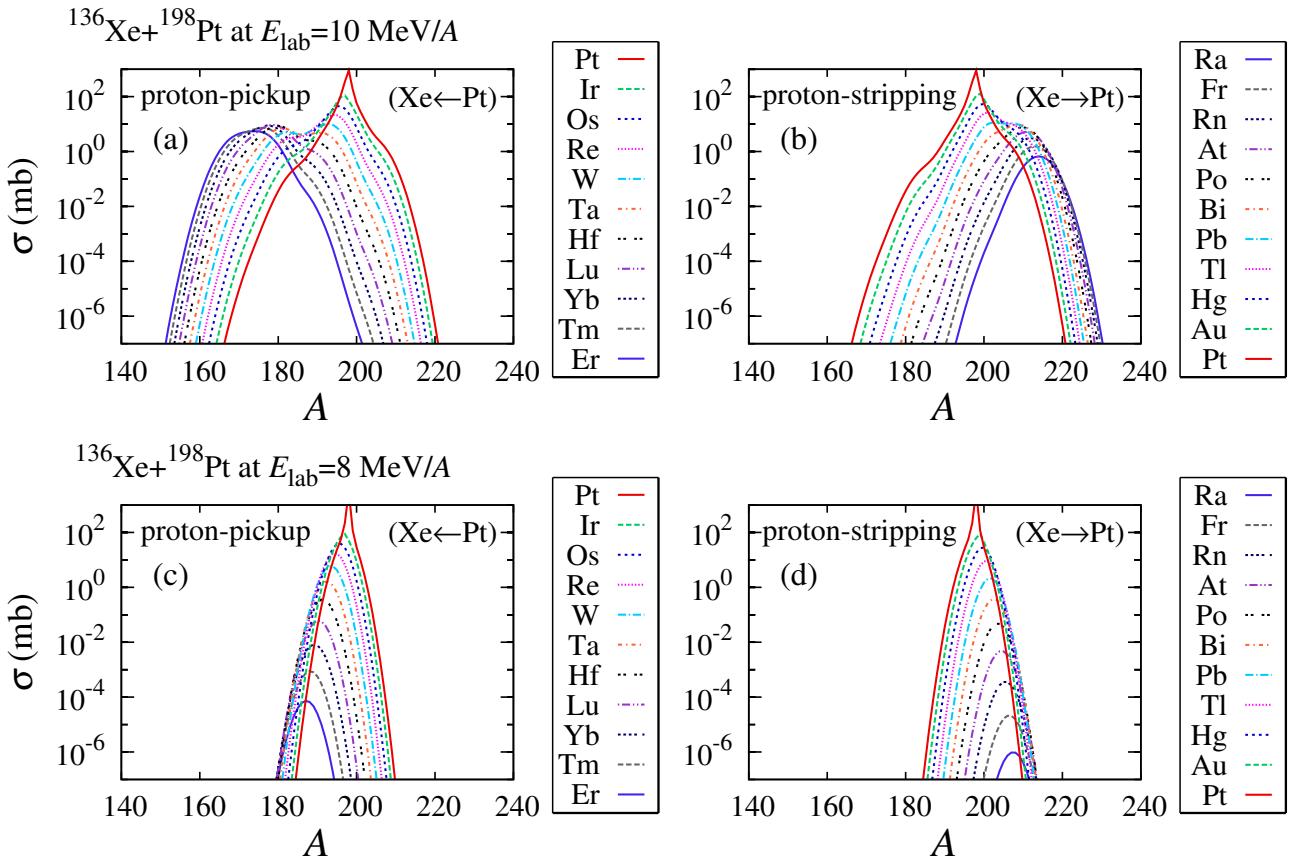
Figure 8.5: Primary production cross sections for the heavier (^{198}Pt-like) fragments in ^{136}Xe+^{198}Pt reaction at $E_{\text{lab}} = 8$ (lower panels) and 10 MeV/nucleon (upper panels) obtained from the TDHF calculation combined with the PNP. Left panels ((a) and (c)) show cross sections for proton-pickup channels, while right panels ((b) and (d)) show cross sections for proton-stripping channels. Horizontal axis denotes the mass number of the fragment. Cross sections of 0- to ±10-proton transfer channels are shown.

As a final topic of this Chapter, we show production cross sections for primary fragments of heavier (^{198}Pt-like) fragments in the ^{136}Xe+^{198}Pt reactions at typical two incident energies, $E_{\text{lab}} = 8$ and 10 MeV/nucleon. Figure 8.5 shows the cross sections calculated by the TDHF theory combined with the PNP technique. Upper panels show results at $E_{\text{lab}} = 10$ MeV/nucleon, while lower panels show results at $E_{\text{lab}} = 8$ MeV/nucleon. Left panels ((a) and (c)) show cross sections for proton-pickup channels (transfer from ^{198}Pt to ^{136}Xe), while right panels ((b) and (d)) show cross sections for proton-stripping channels (transfer from ^{136}Xe to ^{198}Pt). Horizontal axis is the mass number of the primary reaction products.

In the lower incident energy case ($E_{\text{lab}} = 8$ MeV/nucleon, lower panels), the cross sections distribute around the initial mass number, $A = 198$. Because of the ordinary QF process observed at a large-d region ($d \sim 11$ fm), the cross sections have larger values for proton-pickup channels shown in (c). On the other hand, in the higher incident energy case ($E_{\text{lab}} = 10$ MeV/nucleon, upper panels), the resulting cross sections for primary fragments show apparently different distributions. Because of the existence of the inverse QF process at an intermediate-d region ($d \sim 10$ fm) and the deep QF process at a small-d region ($d \lesssim 9$ fm), the cross sections extend much wider than those of the lower incident energy case. We note that, although the higher incident energy case shows much larger and abundant cross sections for various kinds of nuclei, the reaction products in the inverse and deep QF processes must have a high excitation energy and will suffer from subsequent disintegration processes.

Thus, we should consider a trade-off condition, smaller production cross sections with smaller effects of disintegration processes or larger production cross sections with larger effects of disintegration processes. To make a reliable prediction of the cross sections, we should estimate effects of subsequent decay processes not only particle evaporation but also induced fission. It is one of the subjects which we hope to investigate in future.

8.3   Summary and Concluding Remarks on Chapter 8

From the results shown in the other Chapters, we have obtained a confidence that the TDHF theory can reasonably describe not only MNT reactions at peripheral collisions but also QF processes in dissipative collisions of heavy nuclei at a small impact parameter region. In this Chapter, we presented tentative results toward the main goal of this study, a theoretical prediction of optimum conditions to produce objective nuclei. To this end, we performed a systematic TDHF calculation for ^{136}Xe+^{198}Pt reactions at various initial conditions. The ^{136}Xe+^{198}Pt reaction has been considered as a candidate to produce neutron-rich unstable nuclei around the neutron magic number $N = 126$ whose properties have a crucial impact on the r-process path of the nucleosynthesis.

From the results, we have found that the direction of nucleon transfer and the scission point of the neck structure depend much on the initial condition, incident energy and impact parameter. At a certain initial condition, we observed ordinary QF processes, the mass drift mode to produce mass symmetric fragments. In addition, we also observed inverse QF processes, where many nucleons are transferred from the lighter nucleus to the heavier one. The appearance of QF and inverse QF processes seemed to depend both incident energy and impact parameter, and the QF dynamics showed complex behavior as functions of the impact parameter.

A remarkable fact is that the average numbers of neutrons and protons in the fragment nuclei show a similar behavior as a function of the distance of closest approach of the Rutherford trajectory. This fact suggests us some important messages about mechanisms of the QF process. It indicates that the angular momentum carried into the composite system plays a minor role in determining a dynamical path of the QF process. In other words, it indicates that the radial motion of the two colliding nuclei is an important factor which characterizes a scission point of the neck. The value of distance of closest approach would be a measure of how deeply two nuclei collide. From careful observations of the density distribution, the violentness of the collision seems to be related to a surface vibration mode induced by the collision. We anticipate that the shape of the composite system at the turning point is one of the key ingredients which determines the path of the QF process. The QF dynamics seems also to be related to an interplay between such a macroscopic shape of the mean-field potential and microscopic internal degrees of freedom. Structural properties of the composite system as well as quantum states of nucleons and their dynamics would responsible for the QF path. We note that the inverse QF process in the ^{136}Xe+^{198}Pt reactions observed in the TDHF calculation would be related to doubly magic nature of ^{208}Pb in the exit channel, consistent with results of the successful Langevin calculations [72].

At present, still we have not understood the detailed underlying mechanisms of the QF and inverse QF processes, we expect that further investigations of QF dynamics in the TDHF theory will provide us useful information on the QF processes. Because the TDHF theory provides a parameter-free microscopic description of the complex reaction dynamics, we consider that the TDHF theory will be a promising tool to elucidate novel reaction dynamics which enables us to produce exotic unstable nuclei whose production has not been achieved by known reactions. To predict quantitative cross sections for reaction products of the QF processes, we should include not only effects of particle evaporation but also effects of induced fission, which we have not yet included in the present analyses.

Chapter 9

SUMMARY AND PROSPECT

The main aims of this work are (i) to develop microscopic understandings of multinucleon transfer (MNT) and quasifission (QF) processes which have recently been considered to be a useful means to produce unstable nuclei whose production is difficult by other methods and (ii) to theoretically predict optimum conditions, *i.e.* projectile-target combinations and incident energies, to produce those objective unstable nuclei.

To achieve these aims of this work, we have investigated MNT and QF processes in heavy ion reactions at low energies around the Coulomb barrier employing a microscopic framework of the time-dependent Hartree-Fock (TDHF) theory. The TDHF theory provides a fully microscopic description of nuclear dynamics and has been successfully applied to study giant resonances and heavy ion reactions. Although continuous and extensive efforts have been devoted for improving the method and for extending its applications, MNT and QF processes had not been studied seriously in the TDHF theory (very recently, some works on QF in TDHF were reported). It was not at all obvious whether the microscopic TDHF theory describes the MNT and QF processes reasonably. Therefore, we first tried to investigate the applicability of the TDHF theory in describing the MNT reaction.

To examine the feasibility of the TDHF theory in describing the MNT reaction, we investigated MNT processes in ^{40,48}Ca+^{124}Sn, ^{40}Ca+^{208}Pb, and ^{58}Ni+^{208}Pb reactions, for which precise measurements of MNT cross sections were achieved. In addition to the fact that the extensive experimental data are available for these systems, we considered it will be interesting to examine different features depending on the N/Z asymmetry and the charge product $Z_{\mathrm{P}}Z_{\mathrm{T}}$. It is well known that a charge equilibration process takes place in heavy ion reactions with a large N/Z asymmetry between projectile and target nuclei. Since the examined systems have different N/Z ratios (^{40}Ca+^{124}Sn, ^{40}Ca+^{208}Pb, and ^{58}Ni+^{208}Pb systems have large N/Z asymmetries, while ^{48}Ca+^{124}Sn does not), we expected different properties of the reaction dynamics. It is also well known that the charge product, $Z_{\mathrm{P}}Z_{\mathrm{T}}$, affects much on the reaction dynamics. When the value of $Z_{\mathrm{P}}Z_{\mathrm{T}}$ exceeds a critical value around 1600-1800, emergence of fusion reactions are substantially suppressed and the system needs an extra energy to get fused. Because the examined systems have different $Z_{\mathrm{P}}Z_{\mathrm{T}}$ values, 1000 for ^{40,48}Ca+^{124}Sn, 1640 for ^{40}Ca+^{208}Pb, and 2296 for ^{58}Ni+^{208}Pb, they are expected to show different features of the reaction dynamics.

From the results, we found different features of reaction dynamics as expected. When the N/Z asymmetry is small (^{48}Ca+^{124}Sn), transfer processes proceed symmetrically showing very small average numbers of transferred nucleons. On the other hand, when the N/Z asymmetry is large (^{40}Ca+^{124}Sn, ^{40}Ca+^{208}Pb, and ^{58}Ni+^{208}Pb), neutrons and protons are transferred in opposite directions, toward the direction of the charge equilibrium of the system. We also found that, as the charge product $Z_{\mathrm{P}}Z_{\mathrm{T}}$ increases, two nuclei are reseparated after a thick neck formation, indicating the suppression of fusion reaction. We found that, when the dinuclear system connected by the thick

neck dissociates, nucleons inside the neck region are absorbed by the smaller fragment. Because the neck region is composed of both neutrons and protons, the absorption of the neck region results in transfer of both neutrons and protons in the same direction. We regarded the appearance of the neck breaking dynamics as an indication of the QF process. We consider that this process is intimately related to the suppression of the fusion reaction.

To make a direct comparison between the results of the TDHF calculations and measurements, we need to calculate cross sections for each transfer channel. To calculate MNT cross sections, we extracted transfer probabilities from the TDHF wave function after collision using a particle-number projection (PNP) technique. By extending the PNP technique, we also evaluated average excitation energy of reaction products in each transfer channel. Combining transfer probabilities with evaporation probabilities which were evaluated by employing a statistical model using the excitation energy obtained from the TDHF wave function as an input, we calculated MNT cross sections including effects of particle evaporation. From the comparison, we concluded that the TDHF theory can describe MNT cross sections quantitatively with an accuracy comparable to the existing successful theories, GRAZING, complex WKB, and a dynamical model based on Langevin-type equations of motion.

The extended PNP method enables us to calculate expectation values of arbitrary operators for reaction products described by the particle-number projected TDHF wave function after collision. Using the method, we can analyze properties of reaction products, which could not be achieved by analyzing ordinary expectation values without the PNP. To show usefulness of the method, we analyzed ^{24}O+^{16}O reaction as an illustrative example. We calculated expectation values of the angular momentum operator and average excitation energies using the particle-number projected TDHF wave function after collision. From the results, we obtained following microscopic understanding of transfer processes. When nucleons are added to a nucleus, the transferred nucleon carries an angular momentum associated with the relative motion of colliding nuclei into the nucleus which received the transferred nucleons. When nucleons are removed from a nucleus, a very small change is found for angular momentum in the nucleus from which the nucleons are removed. This fact may be explained by a picture that the highest occupied nucleons, which are in $2s_{1/2}$ or $1p_{1/2}$ orbitals in the present case, are dominantly transferred in the nucleon removal processes. Because those highest occupied orbitals have a small orbital angular momentum, a gentle removal of those nucleons may not cause a large change of angular momentum in the nucleon removed nucleus.

From the average excitation energy, we obtained a picture for transfer processes consistent with that mentioned above, namely, the gentle removal of valence nucleons induces a very small excitation in the nucleon-removed nucleus. On the other hand, the nucleon-received nucleus gets a finite excitation energy, because the added nucleons stay at higher-energy single-particle orbitals compared with those of the ground state. We note that it is very difficult to obtain these microscopic transfer mechanisms in ordinary analyses using expectation values without the PNP.

Regarding the results described above, we are confident that it is feasible to study MNT processes in low-energy heavy ion reactions employing the TDHF theory. As a next step, we investigated the applicability of the TDHF theory to QF processes in reactions involving more heavier nuclei such as ^{238}U. We studied ^{64}Ni+^{238}U and ^{238}U+^{100,124,132}Sn reactions for which extensive measurements were performed (except for reactions involving ^{100,132}Sn).

For the ^{64}Ni+^{238}U reaction, precise experimental data of MNT cross sections are available. We calculated MNT cross sections using the TDHF theory combined with the PNP technique. Because ^{238}U nucleus is largely deformed in prolate shape, we performed TDHF calculations for three different initial orientations of ^{238}U. From the results, we again found that the TDHF theory reproduces measured MNT cross sections quantitatively with a similar accuracy to the lighter systems examined previously. In this case, the TDHF theory reasonably describes measured MNT cross sections not only proton stripping-channels, which are expected as a charge equilibration process, but also proton-pickup

channels, which are underestimated by the semiclassical GRAZING calculation. The underestimation of proton-pickup cross sections by the GRAZING calculation may be due to a neglected contribution from reactions at small impact parameters. Because the present system has a large charge product, $Z_P Z_T = 2576$, there could be certain contributions to MNT processes from reactions at small impact parameters. We consider that this result will be an evidence of a reasonable description of a transitional regime from quasielastic to more complex reaction channels in the TDHF theory.

For the ^{64}Ni+^{238}U reaction, measurements of fission fragment mass distributions including contributions from QF processes were achieved. In those experiments, a mass drift mode toward the mass symmetry was observed. We found that the TDHF theory describes the mass drift mode in reactions at small impact parameters. By comparing the total kinetic energy (TKE) $vs.$ the fragment mass (A) plots of measurements with those obtained from the TDHF calculations, we found a reasonable agreement between them. We also found that the TKE-A distribution obtained from the TDHF calculation follows nicely the well-known Viola systematics. This fact also supports that the TDHF theory can provide us a unified microscopic description of the dissipative QF process without any empirical parameters specific to the reaction dynamics. We note that results of the TDHF calculation showed a prominent plateau behavior in average number of nucleons of fragment nuclei as a function of the impact parameter, which might be related to a substantial stability of doubly magic ^{208}Pb in the exit channel.

To get further understandings of the QF process, we investigated incident energy dependence of the QF process in head-on collisions of ^{64}Ni+^{238}U. Calculations were performed for two orientations of ^{238}U, the tip collisions where the symmetry axis of prolately deformed ^{238}U is set parallel to the collision axis, and the side collisions where the symmetry axis of ^{238}U is set perpendicular to the collision axis. From the results, we found different nature of the QF dynamics depending on the orientations of ^{238}U. In the side collisions, the composite system of the projectile and target nuclei tends to form mass symmetric fragments. We found that, in side collisions, the composite system forms a compact configuration when two nuclei collide making a very thick neck structure. The formation of the very thick neck causes mass transfer from ^{238}U to ^{64}Ni through the neck breaking transfer dynamics. As the incident energy increases, we found occurrence of capture processes producing a superheavy nucleus with atomic number $Z = 120$, $^{64}_{28}$Ni$_{36}$+$^{238}_{92}$U$_{146}$ $\rightarrow$$^{302}_{120}Ubn_{182}$, consistent with the symmetrizing trend. On the other hand, in tip collisions, we observed different QF dynamics. The composite system cannot form a compact configuration. The composite system always has an elongated shape irrespective of the incident energy. As a result, we never observed any capture processes in the tip collisions. In this way, the QF dynamics in the TDHF theory shows a strong orientation dependence of the reaction dynamics.

For ^{238}U+^{124}Sn reaction, production cross sections were measured experimentally about 30 years ago. The experimental data show a mass drift mode toward the mass symmetry including about ten-proton transfer from ^{238}U to ^{124}Sn. However, the reaction mechanism of such proton transfer processes had not been clear. We thus performed the TDHF calculations for ^{238}U+^{124}Sn reaction at three different initial orientations of ^{238}U. From the results, we again found a strong orientation dependence of the reaction dynamics in ^{238}U+^{124}Sn. In the tip collisions, a thick and long neck structure is formed between the two colliding nuclei, while the neck formation is substantially suppressed in the side collisions. In the tip collisions, the thick and long neck formation and its breaking induce transfer of both neutrons and protons inside the neck structure from ^{238}U to ^{124}Sn. We concluded that the experimentally measured massive nucleon transfer from ^{238}U to ^{124}Sn is originated from the tip collision. That is, the neck breaking transfer dynamics, a thick and long neck formation followed by subsequent absorption of the nucleons inside the neck region, is responsible for the observed massive nucleon transfer.

We also investigated incident energy dependence of the QF dynamics in head-on collisions. To

investigate system dependence of the QF dynamics, especially initial N/Z ratio dependence, we performed the TDHF calculations for ^{238}U+^{100,124,132}Sn reactions for two initial orientations of ^{238}U, the tip collisions and the side collisions. From the results, we observed several new features of the QF dynamics. In the side collisions of ^{238}U+^{124,132}Sn, we found that the number of transferred nucleons is always small irrespective of the incident energy. Even when two nuclei collides violently, the neck is not so much developed. After the collision, nuclei similar to projectile and target, U- and Sn-like fragments, were produced. This trend is different from the ^{64}Ni+^{238}U system for which we observed a symmetrizing trend in side collisions. The difference may be due to the quite large total number of protons in the ^{238}U+^{124,132}Sn systems, $Z = 142$. In this case, the composite system may no longer have a chance to form a compact mononuclear configuration leading to a capture process because of the strong Coulomb repulsion.

In the tip collisions of ^{238}U+^{124,132}Sn, we observed different QF dynamics from that observed in the side collisions. As the incident energy increases, we found an emergence of an *inverse* QF process, a mass drift mode toward the direction increasing the mass asymmetry compared with that before the collision. Transfer of many (up to about 26) nucleons from ^{124,132}Sn to ^{238}U was observed, producing neutron-rich transuranium nuclei as primary reaction products, *e.g.* $^{264}_{100}$Fm$_{164}$ in the ^{238}U+^{132}Sn collision. Of course, the reaction products produced through the inverse QF process must be highly excited and suffer from substantial disintegration processes of fission and particle evaporation. However, we consider that this result is encouraging for extending the TDHF calculations further to find a novel reaction dynamics to produce exotic unstable nuclei.

In the case of ^{238}U+^{100}Sn, we observed substantial effects of charge equilibration processes at incident energies around and above the Coulomb barrier, because of the large N/Z asymmetry. In both tip and side collisions, neutrons and protons are transferred toward the direction of charge equilibrium of the system. As the incident energy increases, we again observed the inverse QF process. It is worth mentioning that, in this case, neutron-deficient transuranium nuclei, *e.g.* $^{252}_{104}$Rf$_{148}$, are produced as primary reaction products. In this way, the inverse QF process may provide us a unique opportunity to produce new transuranium nuclei which have not yet been produced by other reactions.

Finally, as one of main goals of this work, we have conducted a search for optimum conditions to produce objective unstable nuclei in ^{136}Xe+^{198}Pt reaction which has been considered to be a useful means to produce neutron-rich nuclei around the $N = 126$ region. We performed a systematic TDHF calculation for ^{136}Xe+^{198}Pt reactions at various incident energies and impact parameters. From the results, we found that the QF dynamics in the ^{136}Xe+^{198}Pt reaction depends much on the initial conditions. At certain initial conditions, we observed the inverse QF process producing ^{208}Pb-like heavier fragment on average. We also found that the results at different incident energies and impact parameters can be summarized into one figure if we plot them as a function of the distance of closest approach of the Rutherford trajectory. It indicates that the angular momentum carried into the composite system plays a minor role in determining a dynamical path of the QF process. We anticipate that the QF dynamics is characterized by some structural properties of the composite system of the projectile and target nuclei at the turning point, *e.g.* shape with vibrating surface, elongation, thickness of the neck, mass asymmetry, and so on. From these results, we consider that we should take into consideration not only initial N/Z ratios of the projectile and target nuclei but also structural properties of the composite system during the collision, to find optimum conditions for producing objective nuclei through QF processes.

There remain several subjects which we hope to address in future as natural extensions of the present work.

(i) Estimation of transfer induced fission. In this work, we only considered particle evaporation processes as deexcitation processes. However, reaction products, especially heavier ones, may also decay through fission. Because now we can calculate the expectation value of the angular momentum of

reaction products in each transfer channel using the extended PNP method, we can, in principle, adopt some statistical model to estimate effects of transfer induced fission as well as particle evaporation. In recent experiments, detections of both projectile-like and target-like fragments are becoming feasible, which enable us to estimate survival probability against fission [47]. Inclusion of transfer induced fission processes will provide us a more realistic prediction of cross sections. From detailed comparison between the prediction and measurements, we will be able to get further information on the reaction mechanisms.

(ii) Investigation of effects of structure of a composite system of projectile and target nuclei and reaction products. In the results for ^{238}U$+^{100,124,132}$Sn reactions, we observed the inverse QF process in which exotic transuranium nuclei were produced as a primary reaction product. From time evolution of the density of colliding nuclei, we found possible effects of surface vibration modes induced by the collision and a large octupole deformation of produced transuranium nuclei. We also observed inverse QF processes in ^{136}Xe$+^{198}$Pt reaction which may be related to a stabilization effect of doubly magic ^{208}Pb in the exit channel. These results indicate an importance of structural effects of the composite system and the fragment nuclei in the exit channel in determining dynamical paths of the QF processes. We consider that, to examine those structural effects on the QF dynamics, calculations of PES of the composite system by the CHF method will be useful. By comparing dynamical trajectories obtained from the TDHF calculations with the landscape of the PES, we may get further insight into microscopic mechanisms of the QF process.

(iii) Extension of the projection analysis to include the parity and angular momentum projections. We extended the PNP method to calculate expectation values of operators in the particle-number projected TDHF wave function after collision. The method enables us to examine properties of reaction products in each transfer channel. In principle, it would be possible to include not only the PNP but also the parity and angular momentum projections in our formalism. Recently, γ-ray spectroscopic study of reaction products of MNT processes were achieved [48, 51]. In the measurements reported in Ref. [51], reaction products with small total kinetic energy loss show γ-ray spectra from low-lying $J^\pi = 2^+$ and 4^+ states, while those with large total kinetic energy loss show much abundant spectra corresponding to transitions between high-spin states up to 16^+ state. We anticipate that if we include the parity and angular momentum projections in addition to the PNP in our formalism, we can investigate which states are populated through MNT processes directly from the TDHF wave function after collision. Such analyses will also provide us further information on the reaction mechanisms.

(iv) Extension of the theoretical framework. In the present work, we investigated the applicability of the TDHF theory to MNT and QF processes in low-energy heavy ion reactions. Of course, the TDHF theory is an approximate framework and the description is not fully realistic. We consider that we can develop more realistic theoretical frameworks. One of the most important missing physics in the TDHF theory is the pairing correlation. Although it is yet unclear to what extent the paired nucleons survive during the heavy ion reactions, their existence and importance have been well established in various properties of nuclei in their ground state and low-energy excited states. To include the pairing correlation in nuclear dynamics theoretically, the time-dependent Hartree-Fock-Bogoliubov (TDHFB) theory would be the best candidate, although it requires a vast computational cost. Recently, TDHF+BCS theory which is a simplified version of the TDHFB theory has been developed (BCS: Bardeen-Cooper-Schrieffer). Analyses of MNT and QF processes in low-energy heavy ion reactions including the pairing correlation employing these models would be an important subject. Other possible extensions of the theoretical framework are use of theories beyond the mean-field, *e.g.* Barian-Vénéroni variational principle which is equivalent to the time-dependent random phase approximation (TDRPA). The TDRPA method will improve the description of fluctuation of the number of transferred nucleons. The time-dependent generator coordinate method (TDGCM) is another candidate. The TDGCM would improve description of MNT processes by introducing different mean-field poten-

tials associated with time-dependent generator coordinates depending on the number of transferred nucleons. Other sophisticated formalisms such as time-dependent density matrix (TDDM) or the stochastic mean-field (SMF) theories which may contain rich many-body correlations in describing nuclear dynamics will also be a promising tool to get further insight into reaction mechanisms.

In conclusion, the TDHF theory turns out to be a valuable tool to study both MNT reactions and QF processes in low-energy heavy ion reactions at energies around the Coulomb barrier. As is well known, the TDHF theory provides a reasonable description of expectation values of a one-body operator such as the average number of transferred nucleons. With the aid of the PNP technique, we can get transfer probabilities around the average value. We can obtain transfer cross sections by integrating the transfer probabilities over the impact parameter. Thus, the calculated cross sections are expected to be reliable for main transfer channels with large probabilities around the average value. In reactions of very heavy nuclei, fusion processes become no longer possible because of the strong Coulomb repulsion. Then, the QF process becomes the most dominant process. Such a dominant process can be reasonably described by the average trajectory in the TDHF theory. In this way, the TDHF theory can provide us reasonable descriptions of MNT and QF processes, as demonstrated in the present thesis.

To appropriately describe the MNT and QF processes, various complex physics should be taken into account, *e.g.* time-dependent deformation of fragment nuclei as well as deformation of the composite system, dynamics of the neck formation and its breaking, nucleon transfer, energy dissipations, nuclear shell effects, and so on. Because the TDHF theory provides a parameter-free unified microscopic descriptions of nuclear many-body dynamics, it will be a promising tool to study complex low-energy nuclear dynamics. To get a microscopic understanding of reaction mechanisms and to find novel reaction dynamics for producing exotic unstable nuclei, we shall extend this study as far as possible. We hope readers will find something interesting from the thesis and this work will contribute to extend our understandings of the nature as well as the atomic nuclei.

Acknowledgments

DFT meetings were quite useful to conduct this work. I greatly appreciate them. I deeply appreciate L. Corradi for giving us the vivid experimental data. Discussions with him and valuable suggestions from him are also appreciated. I would also like to thank people in the Australian National University (ANU), especially, C. Simenel, M. Dasgupta, and D. J. Hinde, for giving me an opportunity to visit ANU in July-August 2014. It was a quite valuable experience for me. I would also like to thank J. A. Maruhn for valuable suggestions and for a special care paid for me when I visited Frankfurt am Main in November 2014. I am very much grateful to my best friend, T. Honda, for a number of stimulating discussions and encouragements.

Lastly, I would like to express my deepest gratitude to my family for their kind understanding, encouragements, and hearty supports. I dedicate this work to the memory of my beloved Petit, a cat she passed away in November 2011, as a token of my affection and gratitude.

Appendixes

Appendix A

Useful Formulae for the Slater Determinant

In the HF theory, a many-body wave function of the system with N particles are described by a single Slater determinant,

$$
\Phi(\boldsymbol{r}_1, \cdots, \boldsymbol{r}_N) = \frac{1}{\sqrt{N!}} \begin{vmatrix} \phi_1(\boldsymbol{r}_1) & \cdots & \phi_1(\boldsymbol{r}_N) \\ \vdots & & \vdots \\ \phi_N(\boldsymbol{r}_1) & \cdots & \phi_N(\boldsymbol{r}_N) \end{vmatrix}
$$

$$
= \frac{1}{\sqrt{N!}} \sum_\xi \mathrm{sgn}(\xi)\, \phi_{\xi_1}(\boldsymbol{r}_1) \cdots \phi_{\xi_N}(\boldsymbol{r}_N)
$$

$$
\equiv \frac{1}{\sqrt{N!}} \det\{\phi_i(\boldsymbol{r}_j)\},
$$

where the spatial functions $\phi_i(\boldsymbol{r})$ $(i = 1, \cdots, N)$ denote the single-particle wave functions which are orthonormal to each other. The spin and isospin degrees of freedom are neglected for simplicity. The notation $\det\{\phi_i(\boldsymbol{r}_j)\}$ appearing in the right hand side of above equation represents a determinant of an N-dimensional matrix which has a matrix element $\phi_i(\boldsymbol{r}_j)$ on ith row and jth column. In this Chapter, we present several treatments for the Slater determinant.

A.1 Overlap between two Slater determinants

We consider an overlap between two different Slater determinants, $\Phi(\boldsymbol{r}_1, \cdots, \boldsymbol{r}_N) = \frac{1}{\sqrt{N!}} \det\{\phi_i(\boldsymbol{r}_j)\}$ and $\Psi(\boldsymbol{r}_1, \cdots, \boldsymbol{r}_N) = \frac{1}{\sqrt{N!}} \det\{\psi_i(\boldsymbol{r}_j)\}$, which is given by

$$
\langle \Phi | \Psi \rangle = \frac{1}{N!} \int d\boldsymbol{r}_1 \cdots \int d\boldsymbol{r}_N \sum_\xi \mathrm{sgn}(\xi)\, \phi_{\xi_1}^*(\boldsymbol{r}_1) \cdots \phi_{\xi_N}^*(\boldsymbol{r}_N) \det\{\psi_i(\boldsymbol{r}_j)\}, \tag{A.1.1}
$$

where ξ represent a sequence of $\{\xi_1, \cdots, \xi_N\}$. The summation over ξ refers all possible permutations of the sequence $\{\xi_1, \cdots, \xi_N\}$, *i.e.*, $N!$ patterns. The $\mathrm{sgn}(\xi)$ multiplies (-1) when two single-particle wave functions are exchanged. Using the fact that the absolute value of a determinant is unchanged under the exchange of two rows or two columns, we can show that all $N!$ patterns of the permutations

have the same value of the integral of Eq. (A.1.1). We find

$$
\begin{aligned}
\langle \Phi | \Psi \rangle &= \int d\boldsymbol{r}_1 \cdots \int d\boldsymbol{r}_N \, \phi_1^*(\boldsymbol{r}_1) \cdots \phi_N^*(\boldsymbol{r}_N) \det\{\psi_i(\boldsymbol{r}_j)\} \\
&= \sum_{\xi} \operatorname{sgn}(\xi) \int d\boldsymbol{r}_1 \, \phi_1^*(\boldsymbol{r}_1) \psi_{\xi_1}(\boldsymbol{r}_1) \cdots \int d\boldsymbol{r}_N \, \phi_N^*(\boldsymbol{r}_N) \psi_{\xi_N}(\boldsymbol{r}_N) \\
&= \begin{vmatrix} \langle \phi_1 | \psi_1 \rangle & \cdots & \langle \phi_1 | \psi_N \rangle \\ \vdots & & \vdots \\ \langle \phi_N | \psi_1 \rangle & \cdots & \langle \phi_N | \psi_N \rangle \end{vmatrix} \\
&= \det\{\langle \phi_i | \psi_j \rangle\}.
\end{aligned}
\tag{A.1.2}
$$

In the case of $\Phi(\boldsymbol{r}_1, \cdots, \boldsymbol{r}_N) = \Psi(\boldsymbol{r}_1, \cdots, \boldsymbol{r}_N)$, Eq. (A.1.2) leads $\langle \Phi | \Phi \rangle = 1$ because of the orthonormality of the single-particle wave functions. It represents the normalization of the many-body wave function in the whole space.

A.2 Expectation value of a one-body operator

Let us denote an arbitrary one-body operator as $\hat{T} = \sum_{i=1}^{N} \hat{t}(\boldsymbol{r}_i)$. Here we consider the expectation value of the one-body operator for the Slater determinant,

$$
\langle \Phi | \hat{T} | \Phi \rangle = \frac{1}{N!} \int d\boldsymbol{r}_1 \cdots \int d\boldsymbol{r}_N \sum_{\xi} \operatorname{sgn}(\xi) \, \phi_{\xi_1}^*(\boldsymbol{r}_1) \cdots \phi_{\xi_N}^*(\boldsymbol{r}_N) \, \hat{T} \det\{\phi_i(\boldsymbol{r}_j)\}.
\tag{A.2.1}
$$

Since the one-body operator $\hat{T}$ has nothing to do with the exchange of coordinate indexes, we can show that the equivalence of the all possible terms in the summation over ξ because of the same reason that Eq. (A.1.1) could be Eq. (A.1.2). We find

$$
\begin{aligned}
\langle \Phi | \hat{T} | \Phi \rangle &= \int d\boldsymbol{r}_1 \cdots \int d\boldsymbol{r}_N \, \phi_1^*(\boldsymbol{r}_1) \cdots \phi_N^*(\boldsymbol{r}_N) \, \hat{T} \det\{\phi_i(\boldsymbol{r}_j)\} \\
&= \sum_{i=1}^{N} \sum_{\xi} \operatorname{sgn}(\xi) \, \langle \phi_1 | \phi_{\xi_1} \rangle \cdots \langle \phi_{i-1} | \phi_{\xi_{i-1}} \rangle \langle \phi_i | \hat{t} | \phi_{\xi_i} \rangle \langle \phi_{i+1} | \phi_{\xi_{i+1}} \rangle \cdots \langle \phi_N | \phi_{\xi_N} \rangle \\
&= \sum_{i=1}^{N} \sum_{\xi} \operatorname{sgn}(\xi) \, t_{i \xi_i} \, \delta_{1, \xi_1} \cdots \delta_{i-1, \xi_{i-1}} \delta_{i+1, \xi_{i+1}} \cdots \delta_{N, \xi_N},
\end{aligned}
\tag{A.2.2}
$$

with the one-body matrix elements,

$$
t_{ij} \equiv \int d\boldsymbol{r} \, \phi_i^*(\boldsymbol{r}) \hat{t}(\boldsymbol{r}) \phi_j(\boldsymbol{r}).
\tag{A.2.3}
$$

Eq. (A.2.2) has nonzero value only if $\xi_i = i$ $(i = 1, \cdots, N)$. We then obtain

$$
\langle \Phi | \hat{T} | \Phi \rangle = \sum_{i=1}^{N} t_{ii}.
\tag{A.2.4}
$$

In this way, the expectation value of the one-body operator for the Slater determinant is given by a sum of expectation values for the single-particle wave functions.

A.3   Expectation value of a two-body operator

Let us denote an arbitrary two-body operator as $\hat{V} = \sum_{i<j} \hat{v}(\boldsymbol{r}_i, \boldsymbol{r}_j)$. We next consider the expectation value of the two-body operator for the Slater determinant,

$$\langle \Phi | \, \hat{V} \, | \Phi \rangle = \frac{1}{N!} \int d\boldsymbol{r}_1 \cdots \int d\boldsymbol{r}_N \sum_{\xi} \text{sgn}(\xi) \, \phi_{\xi_1}^*(\boldsymbol{r}_1) \cdots \phi_{\xi_N}^*(\boldsymbol{r}_N) \, \hat{V} \det \phi_i(\boldsymbol{r}_j). \tag{A.3.1}$$

Assuming that the two-body operator $\hat{v}(\boldsymbol{r}_1, \boldsymbol{r}_2)$ equals to $\hat{v}(\boldsymbol{r}_2, \boldsymbol{r}_1)$, we obtain, in an analogous way for the one-body operator,

$$\begin{aligned}
\langle \Phi | \, \hat{V} \, | \Phi \rangle &= \int d\boldsymbol{r}_1 \cdots \int d\boldsymbol{r}_N \, \phi_1^*(\boldsymbol{r}_1) \cdots \phi_N^*(\boldsymbol{r}_N) \, \hat{V} \det\{\phi_i(\boldsymbol{r}_j)\} \\
&= \sum_{i<j} \sum_{\xi} \text{sgn}(\xi) \, v_{ij\xi_i\xi_j} \langle \phi_1 | \phi_{\xi_1} \rangle \cdots \langle \phi_{i-1} | \phi_{\xi_{i-1}} \rangle \langle \phi_{i+1} | \phi_{\xi_{i+1}} \rangle \\
&\qquad\qquad\qquad\qquad \cdots \langle \phi_{j-1} | \phi_{\xi_{j-1}} \rangle \langle \phi_{j+1} | \phi_{\xi_{j+1}} \rangle \cdots \langle \phi_N | \phi_{\xi_N} \rangle \\
&= \sum_{i<j} \sum_{\xi} \text{sgn}(\xi) \, v_{ij\xi_i\xi_j} \delta_{1,\xi_1} \cdots \delta_{i-1,\xi_{i-1}} \delta_{i+1,\xi_{i+1}} \cdots \delta_{j-1,\xi_{j-1}} \delta_{j+1,\xi_{j+1}} \cdots \delta_{N,\xi_N},
\end{aligned} \tag{A.3.2}$$

with the two-body matrix elements,

$$v_{ijkl} \equiv \int d\boldsymbol{r} \int d\boldsymbol{r}' \, \phi_i^*(\boldsymbol{r}) \phi_j^*(\boldsymbol{r}') \hat{v}(\boldsymbol{r}, \boldsymbol{r}') \phi_k(\boldsymbol{r}) \phi_l(\boldsymbol{r}'). \tag{A.3.3}$$

Eq. (A.3.2) has nonzero value for two cases: One is the case that $\xi_i = i$, $\xi_j = j$, and $\xi_k = k$ $(k \neq i, j)$ without permutation, the other is the case that $\xi_i = j$, $\xi_j = i$, and $\xi_k = k$ $(k \neq i, j)$ with one permutation. We then obtain

$$\langle \Phi | \, \hat{V} \, | \Phi \rangle = \sum_{i<j} \bar{v}_{ijij}, \tag{A.3.4}$$

where we introduce the anti-symmetrized two-body matrix elements, $\bar{v}_{ijkl} \equiv v_{ijkl} - v_{ijlk}$.

A.4   Derivation of the Hartree-Fock equation

Eqs. (A.2.4) and (A.3.4) show that the expectation value of the Hamiltonian,

$$\hat{H} = \sum_{i=1}^{N} \hat{t}(\boldsymbol{r}_i) + \sum_{i<j} \hat{v}(\boldsymbol{r}_i, \boldsymbol{r}_j), \tag{A.4.1}$$

for the Slater determinant takes the following form:

$$\langle \Phi | \, \hat{H} \, | \Phi \rangle = \sum_{i=1}^{N} t_{ii} + \sum_{i<j} \bar{v}_{ijij}. \tag{A.4.2}$$

We can derive the HF equation by performing a variation of Eq. (A.4.2) with respect to the single-particle wave functions, *i.e.*,

$$\frac{\delta}{\delta \phi_\alpha^*(\boldsymbol{r})} \left[\langle \Phi | \, \hat{H} \, | \Phi \rangle - \sum_{ij} \varepsilon_{ij} \Big(\langle \phi_i | \phi_j \rangle - \delta_{ij} \Big) \right] = 0, \tag{A.4.3}$$

where ε_{ij} are Lagrange multipliers to ensure the orthonormalization condition for the single-particle wave functions. The variation of the expectation value of the one-body operator Eq. (A.2.4) leads

$$
\begin{aligned}
\frac{\delta}{\delta\phi_i^*(\boldsymbol{r})} \langle\Phi| \hat{T} |\Phi\rangle &= \sum_{j=1}^{N} \int d\boldsymbol{r}' \frac{\delta\phi_j^*(\boldsymbol{r}')}{\delta\phi_i^*(\boldsymbol{r})} \hat{t}(\boldsymbol{r}')\phi_j(\boldsymbol{r}') \\
&= \sum_{j=1}^{N} \int d\boldsymbol{r}' \, \delta_{ij}\, \delta(\boldsymbol{r}-\boldsymbol{r}')\hat{t}(\boldsymbol{r}')\phi_j(\boldsymbol{r}') \\
&= \hat{t}(\boldsymbol{r})\phi_i(\boldsymbol{r}).
\end{aligned} \tag{A.4.4}
$$

In the same way, the variation of the expectation value of the two-body operator Eq. (A.3.4) is calculated as

$$
\begin{aligned}
\frac{\delta}{\delta\phi_i^*(\boldsymbol{r})} \langle\Phi| \hat{V} |\Phi\rangle &= \sum_{k<l} \int d\boldsymbol{r}' \int d\boldsymbol{r}'' \left\{ \frac{\delta\phi_k^*(\boldsymbol{r}')}{\delta\phi_i^*(\boldsymbol{r})}\phi_l^*(\boldsymbol{r}'') + \phi_k^*(\boldsymbol{r}')\frac{\delta\phi_l^*(\boldsymbol{r}'')}{\delta\phi_i^*(\boldsymbol{r})} \right\} \\
&\qquad \times \hat{v}(\boldsymbol{r}',\boldsymbol{r}'')\left(\phi_k(\boldsymbol{r}')\phi_l(\boldsymbol{r}'') - \phi_l(\boldsymbol{r}')\phi_k(\boldsymbol{r}'')\right) \\
&= \frac{1}{2}\sum_{k,l} \int d\boldsymbol{r}' \int d\boldsymbol{r}'' \left\{ \delta_{ki}\,\delta(\boldsymbol{r}-\boldsymbol{r}')\phi_l^*(\boldsymbol{r}'') + \delta_{li}\,\delta(\boldsymbol{r}-\boldsymbol{r}'')\phi_k^*(\boldsymbol{r}') \right\} \\
&\qquad \times \hat{v}(\boldsymbol{r}',\boldsymbol{r}'')\left(\phi_k(\boldsymbol{r}')\phi_l(\boldsymbol{r}'') - \phi_l(\boldsymbol{r}')\phi_k(\boldsymbol{r}'')\right) \\
&= \frac{1}{2}\sum_{j=1}^{N} \int d\boldsymbol{r}' \left\{ \phi_j^*(\boldsymbol{r}')\hat{v}(\boldsymbol{r},\boldsymbol{r}')\left(\phi_i(\boldsymbol{r})\phi_j(\boldsymbol{r}') - \phi_j(\boldsymbol{r})\phi_i(\boldsymbol{r}')\right) \right. \\
&\qquad \left. + \phi_j^*(\boldsymbol{r}')\hat{v}(\boldsymbol{r}',\boldsymbol{r})\left(\phi_j(\boldsymbol{r}')\phi_i(\boldsymbol{r}) - \phi_i(\boldsymbol{r}')\phi_j(\boldsymbol{r})\right) \right\}.
\end{aligned} \tag{A.4.5}
$$

Since the two terms appearing in the parentheses, { }, of the last row are equivalent to each other, we find

$$
\begin{aligned}
\frac{\delta}{\delta\phi_i^*(\boldsymbol{r})} \langle\Phi| \hat{V} |\Phi\rangle &= \sum_{j=1}^{N} \left\{ \int d\boldsymbol{r}' \, \hat{v}(\boldsymbol{r},\boldsymbol{r}')\phi_j^*(\boldsymbol{r}')\phi_j(\boldsymbol{r}')\phi_i(\boldsymbol{r}) - \int d\boldsymbol{r}' \, \hat{v}(\boldsymbol{r},\boldsymbol{r}')\phi_j(\boldsymbol{r})\phi_j^*(\boldsymbol{r}')\phi_i(\boldsymbol{r}') \right\} \\
&\equiv \hat{\Gamma}_{\mathrm{H}}(\boldsymbol{r})\phi_i(\boldsymbol{r}) - \int d\boldsymbol{r}' \, \hat{\Gamma}_{\mathrm{F}}(\boldsymbol{r},\boldsymbol{r}')\phi_i(\boldsymbol{r}').
\end{aligned} \tag{A.4.6}
$$

We have introduced the so called Hartree potential $\Gamma_{\mathrm{H}}(\boldsymbol{r})$ and Fock potential $\Gamma_{\mathrm{F}}(\boldsymbol{r},\boldsymbol{r}')$ as follows:

$$
\Gamma_{\mathrm{H}}(\boldsymbol{r}) \equiv \int d\boldsymbol{r}'\hat{v}(\boldsymbol{r},\boldsymbol{r}')\rho(\boldsymbol{r}'), \qquad \rho(\boldsymbol{r}) \equiv \sum_{i=1}^{N}\left|\phi_i(\boldsymbol{r})\right|^2, \tag{A.4.7}
$$

$$
\Gamma_{\mathrm{F}}(\boldsymbol{r},\boldsymbol{r}') \equiv \hat{v}(\boldsymbol{r},\boldsymbol{r}')\rho(\boldsymbol{r},\boldsymbol{r}'), \qquad \rho(\boldsymbol{r},\boldsymbol{r}') \equiv \sum_{i=1}^{N}\phi_i(\boldsymbol{r})\phi_i^*(\boldsymbol{r}'). \tag{A.4.8}
$$

In this way, we obtain the relation

$$
\hat{t}(\boldsymbol{r})\phi_i(\boldsymbol{r}) + \hat{\Gamma}_{\mathrm{H}}(\boldsymbol{r})\phi_i(\boldsymbol{r}) - \int d\boldsymbol{r}' \, \hat{\Gamma}_{\mathrm{F}}(\boldsymbol{r},\boldsymbol{r}')\phi_i(\boldsymbol{r}') = \sum_{j}\varepsilon_{ij}\phi_i(\boldsymbol{r}), \tag{A.4.9}
$$

where the term appearing on the right hand side is originated from the term for the constraint on the orthonormalization condition. We note that the many-body wave function is unchanged under arbitrary unitary transformations for the single-particle wave functions. We thus use this gauge degree of freedom to diagonalize the single-particle Hamiltonian. As a result, we obtain the HF equation

$$
\int d\boldsymbol{r}' \, \hat{h}_{\mathrm{HF}}(\boldsymbol{r},\boldsymbol{r}')\phi_i(\boldsymbol{r}') = \varepsilon_i\phi_i(\boldsymbol{r}), \tag{A.4.10}
$$

where $\varepsilon_i \equiv \varepsilon_{ii}$. The single-particle Hamiltonian is defined by

$$\hat{h}_{\mathrm{HF}}(\boldsymbol{r}, \boldsymbol{r}') \equiv \left[\hat{t}(\boldsymbol{r}') + \hat{\Gamma}_{\mathrm{H}}(\boldsymbol{r}') \right] \delta(\boldsymbol{r} - \boldsymbol{r}') - \hat{\Gamma}_{\mathrm{F}}(\boldsymbol{r}, \boldsymbol{r}'). \tag{A.4.11}$$

A.5 Average number of transferred nucleons and its fluctuation

To evaluate the average number of transferred nucleons, we introduce the number operator in a spacial region V as

$$\hat{N}_V \equiv \int_N d\boldsymbol{r}\, \hat{n}(\boldsymbol{r}) = \sum_{i=1}^{N} \Theta_V(\boldsymbol{r}_i). \tag{A.5.1}$$

The $\hat{n}(\boldsymbol{r})$ represents the number density operator,

$$\hat{n}(\boldsymbol{r}) = \sum_{i=1}^{N} \delta(\boldsymbol{r} - \boldsymbol{r}_i). \tag{A.5.2}$$

The $\Theta_V(\boldsymbol{r})$ is a space division function defined by

$$\Theta_\tau(\boldsymbol{r}) = \begin{cases} 1 & \text{for} \quad \boldsymbol{r} \in \tau, \\ 0 & \text{for} \quad \boldsymbol{r} \notin \tau. \end{cases} \tag{A.5.3}$$

Because the number density operator is a one-body operator, we can evaluate the expectation value for the Slater determinant in the same way as Eq. (A.2.4). We find

$$\begin{aligned} \langle \Phi | \, \hat{N}_V \, | \Phi \rangle &= \int_V d\boldsymbol{r} \, \langle \Phi | \, \hat{n}(\boldsymbol{r}) \, | \Phi \rangle \\ &= \sum_{i=1}^{N} \langle \phi_i | \, \Theta_V \, | \phi_i \rangle \\ &= \int_V d\boldsymbol{r} \, \rho(\boldsymbol{r}). \end{aligned} \tag{A.5.4}$$

The average number of transferred nucleons is evaluated by comparing the expectation value of Eq. (A.5.4) with the number of nucleons of the nucleus before the collision. If we take the spacial region V as the whole space, Eq. (A.5.4) becomes

$$\langle \Phi | \, \hat{N} \, | \Phi \rangle = \sum_{i=1}^{N} \langle \phi_i | \phi_i \rangle = N. \tag{A.5.5}$$

That is, it coincides with the total number of nucleons of the system.

We can also evaluate the fluctuation in the average number of transferred nucleons,

$$\sigma \equiv \sqrt{\langle \Phi | \left(\hat{N}_V \right)^2 | \Phi \rangle - \langle \Phi | \, \hat{N}_V \, | \Phi \rangle^2}. \tag{A.5.6}$$

The expectation value of the square of the number operator in the spatial region V is evaluated as

$$\begin{aligned} \langle \Phi | \left(\hat{N}_V \right)^2 | \Phi \rangle &= \sum_{i,j=1}^{N} \langle \Phi | \, \Theta_V(\boldsymbol{r}_i) \Theta_V(\boldsymbol{r}_j) \, | \Phi \rangle \\ &= \sum_{i=1}^{N} \langle \Phi | \, \Theta_V(\boldsymbol{r}_i) \, | \Phi \rangle + \sum_{i \neq j}^{N} \langle \Phi | \, \Theta_V(\boldsymbol{r}_i) \Theta_V(\boldsymbol{r}_j) \, | \Phi \rangle, \end{aligned} \tag{A.5.7}$$

where the first term after the last equality represents the $i = j$ part, which coincides with Eq. (A.5.4). We have used a relation $\left[\Theta_V(\boldsymbol{r}_i)\right]^2 = \Theta_V(\boldsymbol{r}_i)$. The second term in the last row of Eq. (A.5.7) can be regarded as a two-body operator. We find

$$
\begin{aligned}
\sum_{i\neq j}^{N} \langle\Phi|\,\Theta_V(\boldsymbol{r}_i)\Theta_V(\boldsymbol{r}_j)\,|\Phi\rangle &= \sum_{ij}\int d\boldsymbol{r}\int d\boldsymbol{r}'\phi_i^*(\boldsymbol{r})\phi_j^*(\boldsymbol{r})\left\{\phi_i(\boldsymbol{r})\phi_j(\boldsymbol{r}') - \phi_j(\boldsymbol{r})\phi_i(\boldsymbol{r}')\right\} \\
&\qquad\qquad\qquad\times\Theta_V(\boldsymbol{r})\Theta_V(\boldsymbol{r}') \\[6pt]
&= \int d\boldsymbol{r}\rho(\boldsymbol{r})\Theta_V(\boldsymbol{r})\int d\boldsymbol{r}'\rho(\boldsymbol{r}')\Theta_V(\boldsymbol{r}') \\[4pt]
&\quad - \sum_{ij}\int d\boldsymbol{r}\phi_i^*(\boldsymbol{r})\phi_j(\boldsymbol{r})\Theta_V(\boldsymbol{r})\int d\boldsymbol{r}'\phi_j^*(\boldsymbol{r}')\phi_i(\boldsymbol{r}')\Theta_V(\boldsymbol{r}') \\[6pt]
&= \langle\Phi|\,\hat{N}_V\,|\Phi\rangle^2 - \sum_{ij}\left|\langle\phi_i|\phi_j\rangle_V\right|^2.
\end{aligned}
\tag{A.5.8}
$$

From Eqs. (A.5.7) and (A.5.8), we obtain

$$
\sigma = \sqrt{\int_V d\boldsymbol{r}\,\rho(\boldsymbol{r}) - \sum_{ij}\left|\langle\phi_i|\phi_j\rangle_V\right|^2}.
\tag{A.5.9}
$$

Let us slightly rewrite Eq. (A.5.9) as

$$
\begin{aligned}
\sigma &= \left\{\sum_{i=1}^{N}\langle\phi_i|\phi_i\rangle_V - \sum_{i,j}\left|\langle\phi_i|\phi_j\rangle_V\right|^2\right\}^{-\frac{1}{2}} \\[6pt]
&= \left\{\sum_{i=1}^{N}\langle\phi_i|\phi_i\rangle\left(1 - \langle\phi_i|\phi_i\rangle_V\right) - \sum_{i\neq j}\left|\langle\phi_i|\phi_j\rangle_V\right|^2\right\}^{-\frac{1}{2}},
\end{aligned}
\tag{A.5.10}
$$

which has maximum value $\sigma = \sqrt{\frac{N}{4}}$ when $\langle\phi_i|\phi_j\rangle_V = 0$ $(i \neq j)$ and $\langle\phi_i|\phi_i\rangle_V = 0.5$ $(i = 1, \cdots, N)$. Experimentally, widths of fragment mass distribution were measured which exceed the upper limit. Thus this upper limit of the fluctuation of an expectation value of a one-body operator is known as one of the drawbacks of the HF theory. If we take the spatial region V as the whole space, Eq. (A.5.9) becomes

$$
\sigma = \sqrt{\langle\Phi|\,\hat{N}_V\,|\Phi\rangle - \sum_{ij}\left|\langle\phi_i|\phi_j\rangle\right|^2} = \sqrt{\langle\Phi|\,\hat{N}_V\,|\Phi\rangle - N} = 0.
\tag{A.5.11}
$$

A.6   Formulae for two different Slater determinants

We consider two Slater determinants Φ and Ψ, which are composed of different sets of single-particle wave functions $\{\phi_i\}$ and $\{\psi_i\}$, respectively. When these two sets of single-particle wave functions are not orthonormal to each other, $i.e.$ $\langle\phi_i|\psi_j\rangle \neq \delta_{ij}$, we cannot adopt formulae presented in the previous Sections. We actually encounter such a situation, for example, when we calculate expectation values of operators in a particle-number projected TDHF wave function after collision. It is then useful to introduce a transformation for single-particle wave functions $\{\psi_i\}$ to be orthonormal to $\{\phi_i\}$, as follows.

We introduce a new set of single-particle wave functions $\{\tilde{\psi}_i\}$. They are related to $\{\psi_i\}$ by a transformation,

$$
\tilde{\psi}_i(\boldsymbol{r}) \equiv \sum_{j=1}^{N}\psi_j(\boldsymbol{r})\mathcal{B}_{ji}^{-1},
\tag{A.6.1}
$$

where $\mathcal{B}$ is an N-dimensional matrix. $\mathcal{B}^{-1}$ denotes the inverse matrix of the $\mathcal{B}$. At present, we do not know the explicit form of the matrix $\mathcal{B}$. We shall determine the form of $\mathcal{B}$ so as to fulfill the relation,

$$\langle \phi_i | \tilde{\psi}_i \rangle = \delta_{ij}. \tag{A.6.2}$$

Recalling the identity

$$
\mathcal{B}^{-1}\mathcal{B} =
\begin{pmatrix}
\mathcal{B}_{11}^{-1} & \mathcal{B}_{12}^{-1} & \cdots & \mathcal{B}_{1N}^{-1} \\
\mathcal{B}_{21}^{-1} & \mathcal{B}_{22}^{-1} & \cdots & \mathcal{B}_{2N}^{-1} \\
\vdots & \vdots & \ddots & \vdots \\
\mathcal{B}_{N1}^{-1} & \mathcal{B}_{N2}^{-1} & \cdots & \mathcal{B}_{NN}^{-1}
\end{pmatrix}
\begin{pmatrix}
\mathcal{B}_{11} & \mathcal{B}_{12} & \cdots & \mathcal{B}_{1N} \\
\mathcal{B}_{21} & \mathcal{B}_{22} & \cdots & \mathcal{B}_{2N} \\
\vdots & \vdots & \ddots & \vdots \\
\mathcal{B}_{N1} & \mathcal{B}_{N2} & \cdots & \mathcal{B}_{NN}
\end{pmatrix}
$$

$$
=
\begin{pmatrix}
\sum_k \mathcal{B}_{1k}^{-1}\mathcal{B}_{k1} & \sum_k \mathcal{B}_{1k}^{-1}\mathcal{B}_{k2} & \cdots & \sum_k \mathcal{B}_{1k}^{-1}\mathcal{B}_{kN} \\
\sum_k \mathcal{B}_{2k}^{-1}\mathcal{B}_{k1} & \sum_k \mathcal{B}_{2k}^{-1}\mathcal{B}_{k2} & \cdots & \sum_k \mathcal{B}_{2k}^{-1}\mathcal{B}_{kN} \\
\vdots & \vdots & \ddots & \vdots \\
\sum_k \mathcal{B}_{Nk}^{-1}\mathcal{B}_{k1} & \sum_k \mathcal{B}_{Nk}^{-1}\mathcal{B}_{k2} & \cdots & \sum_k \mathcal{B}_{Nk}^{-1}\mathcal{B}_{kN}
\end{pmatrix} = I, \tag{A.6.3}
$$

we see $\sum_k \mathcal{B}_{ik}^{-1}\mathcal{B}_{kj} = \delta_{ij}$. Multiplying Eq. (A.6.1) by $\mathcal{B}_{ik}$ and taking a summation over the index i, we find

$$\sum_{i=1}^{N} \tilde{\psi}_i(\boldsymbol{r})\mathcal{B}_{ik} = \sum_{j=1}^{N} \psi_j(\boldsymbol{r}) \underbrace{\sum_{i=1}^{N} \mathcal{B}_{ji}^{-1}\mathcal{B}_{ik}}_{=\delta_{jk}} = \psi_k(\boldsymbol{r}). \tag{A.6.4}$$

We then multiply $\phi_l^*(\boldsymbol{r})$ from the left side of Eq. (A.6.4) and integrate over the coordinate $\boldsymbol{r}$ to determine the matrix elements of $\mathcal{B}$:

$$\sum_{i=1}^{N} \langle \phi_l | \tilde{\psi}_i \rangle \mathcal{B}_{ik} = \mathcal{B}_{lk} = \langle \phi_l | \psi_k \rangle, \tag{A.6.5}$$

where the first equality follows from the requirement, Eq. (A.6.2).

Ones we get the explicit form of the matrix $\mathcal{B}$, we can construct a set of biorthonormal single-particle wave functions $\{\tilde{\psi}_i\}$ by Eq. (A.6.1). The Slater determinant Ψ turns out to be

$$
\begin{aligned}
\Psi(\boldsymbol{r}_1, \cdots, \boldsymbol{r}_N) &= \frac{1}{\sqrt{N!}} \det\{\psi_i(\boldsymbol{r}_j)\} = \frac{1}{\sqrt{N!}} \det\{\textstyle\sum_k \tilde{\psi}_k(\boldsymbol{r}_j)\mathcal{B}_{ki}\} \\
&= \frac{1}{\sqrt{N!}} \det\{{}^t\mathcal{A}\mathcal{B}\} = \frac{1}{\sqrt{N!}} \det {}^t\mathcal{A} \det \mathcal{B} = \frac{1}{\sqrt{N!}} \det \mathcal{A} \det \mathcal{B} \\
&= \det \mathcal{B}\, \tilde{\Psi}(\boldsymbol{r}_1, \cdots, \boldsymbol{r}_N),
\end{aligned} \tag{A.6.6}
$$

where we introduced an N-dimensional matrix $\mathcal{A}$ composed of matrix elements $\mathcal{A}_{ij} = \tilde{\psi}_i(\boldsymbol{r}_j)$, just for convenience. $\tilde{\Psi}$ is defined by

$$\tilde{\Psi}(\boldsymbol{r}_1, \cdots, \boldsymbol{r}_N) = \frac{1}{\sqrt{N!}} \det\{\tilde{\psi}_i(\boldsymbol{r}_j)\}. \tag{A.6.7}$$

Using Eq. (A.6.6), we can rewrite any transition matrix elements as

$$\langle \Phi | \hat{\mathcal{O}} | \Psi \rangle = \det \mathcal{B}\, \langle \Phi | \hat{\mathcal{O}} | \tilde{\Psi} \rangle. \tag{A.6.8}$$

Because now Φ and $\tilde{\Psi}$ are composed of single-particle wave functions $\{\phi_i\}$ and $\{\tilde{\psi}_i\}$, respectively, which are biorthonormal to each other, we can evaluate $\langle \Phi | \hat{\mathcal{O}} | \tilde{\Psi} \rangle$ using formulae given in the previous Sections.

Appendix B

Detailed Derivation of the Skyrme Hartree-Fock Equation

In this Chapter, we present a detailed derivation of the HF equation with a Skyrme-type effective interaction. In Sec. B.1, we give definitions of various densities and relations between them which are useful to derive the Skyrme HF equation. In Sec. B.2, we derive the expression of the expectation value of the Skyrme Hamiltonian, the Skyrme EDF. In Sec. B.3, we perform a variation of the energy expectation value to derive the Skyrme HF equation.

B.1 Preparation

Before deriving the Skyrme EDF and the Skyrme HF equation, we first define the following densities:

$$
\begin{align}
\rho(\boldsymbol{r}) &\equiv \sum_{i\,\sigma} \phi_i^*(\boldsymbol{r}\sigma)\phi_i(\boldsymbol{r}\sigma), \tag{B.1.1} \\
\boldsymbol{s}(\boldsymbol{r}) &\equiv \sum_{i\,\sigma_1\,\sigma_2} \phi_i^*(\boldsymbol{r}\sigma_1)\phi_i(\boldsymbol{r}\sigma_2) \langle \sigma_1 | \hat{\boldsymbol{\sigma}} | \sigma_2 \rangle, \tag{B.1.2} \\
\tau(\boldsymbol{r}) &\equiv \sum_{i\,\sigma} \boldsymbol{\nabla}\phi_i^*(\boldsymbol{r}\sigma) \cdot \boldsymbol{\nabla}\phi_i(\boldsymbol{r}\sigma), \tag{B.1.3} \\
\boldsymbol{T}(\boldsymbol{r}) &\equiv \sum_{i\,\sigma_1\,\sigma_2} \{\boldsymbol{\nabla}\phi_i^*(\boldsymbol{r}\sigma_1) \cdot \boldsymbol{\nabla}\phi_i(\boldsymbol{r}\sigma_2)\} \langle \sigma_1 | \hat{\boldsymbol{\sigma}} | \sigma_2 \rangle, \tag{B.1.4} \\
\boldsymbol{j}(\boldsymbol{r}) &\equiv \frac{1}{2\mathrm{i}} \sum_{i\,\sigma} \{\phi_i^*(\boldsymbol{r}\sigma)\boldsymbol{\nabla}\phi_i(\boldsymbol{r}\sigma) - \phi_i(\boldsymbol{r}\sigma)\boldsymbol{\nabla}\phi_i^*(\boldsymbol{r}\sigma)\}, \tag{B.1.5} \\
J_{\mu\nu}(\boldsymbol{r}) &\equiv \frac{1}{2\mathrm{i}} \sum_{i\,\sigma_1\,\sigma_2} \{\phi_i^*(\boldsymbol{r}\sigma_1)\partial_\mu\phi_i(\boldsymbol{r}\sigma_2) - \phi_i(\boldsymbol{r}\sigma_2)\partial_\mu\phi_i^*(\boldsymbol{r}\sigma_1)\} \langle \sigma_1 | \hat{\sigma_\nu} | \sigma_2 \rangle, \tag{B.1.6} \\
\boldsymbol{J}(\boldsymbol{r}) &\equiv \Big(J_{23}(\boldsymbol{r}) - J_{32}(\boldsymbol{r}),\ J_{31}(\boldsymbol{r}) - J_{13}(\boldsymbol{r}),\ J_{12}(\boldsymbol{r}) - J_{21}(\boldsymbol{r}) \Big). \tag{B.1.7}
\end{align}
$$

The function $\phi_i(\boldsymbol{r}\sigma)$ denotes a spin σ ($\uparrow$ or $\downarrow$) component of the single-particle wave function of i th nucleon ($i = 1, \cdots, A$),

$$
\begin{pmatrix} \phi_i(\boldsymbol{r}\ \uparrow) \\ \phi_i(\boldsymbol{r}\ \downarrow) \end{pmatrix} = \phi_i(\boldsymbol{r}\ \uparrow) \begin{pmatrix} 1 \\ 0 \end{pmatrix} + \phi_i(\boldsymbol{r}\ \downarrow) \begin{pmatrix} 0 \\ 1 \end{pmatrix} = \sum_\sigma \phi_i(\boldsymbol{r}\sigma)\chi_\sigma(i). \tag{B.1.8}
$$

$\chi_\sigma(i)$ denotes the spin part of the single-particle wave function of ith nucleon, which is an eigenstate of $\hat{S}_z = \hat{\sigma}_z/2$ with eigenvalues $\sigma = \pm 1/2$:

$$|\sigma\rangle \equiv \chi_\sigma = \begin{cases} \begin{pmatrix} 1 \\ 0 \end{pmatrix} & \text{for} \quad \sigma = +1/2 \ (\uparrow), \\[2em] \begin{pmatrix} 0 \\ 1 \end{pmatrix} & \text{for} \quad \sigma = -1/2 \ (\downarrow). \end{cases} \tag{B.1.9}$$

The operator $\hat{\boldsymbol{\sigma}} = (\hat{\sigma}_x, \hat{\sigma}_y, \hat{\sigma}_z)$ denotes the Pauli spin matrices,

$$\hat{\sigma}_x = \begin{pmatrix} 0 & 1 \\ 1 & 0 \end{pmatrix}, \qquad \hat{\sigma}_y = \begin{pmatrix} 0 & \mathrm{i} \\ -\mathrm{i} & 0 \end{pmatrix}, \qquad \hat{\sigma}_z = \begin{pmatrix} 1 & 0 \\ 0 & -1 \end{pmatrix}, \tag{B.1.10}$$

which act only on the spin space. From these definitions, we find the following relations:

$$\hat{\sigma}_x |\sigma\rangle = |-\sigma\rangle, \tag{B.1.11}$$

$$\hat{\sigma}_y |\sigma\rangle = 2\mathrm{i}\sigma|-\sigma\rangle, \tag{B.1.12}$$

$$\hat{\sigma}_z |\sigma\rangle = 2\sigma|\sigma\rangle. \tag{B.1.13}$$

The bracket in $\boldsymbol{s}$, $\boldsymbol{T}$, and $J_{\mu\nu}$ is defined as $\langle\sigma_1|\hat{\boldsymbol{\sigma}}|\sigma_2\rangle \equiv \chi_{\sigma_1}^\dagger \hat{\boldsymbol{\sigma}} \chi_{\sigma_2}$. For each component of the Pauli spin matrix, we find

$$\langle\sigma_1|\hat{\boldsymbol{\sigma}}|\sigma_2\rangle = \left(\delta_{\sigma_1-\sigma_2}, \quad -2\mathrm{i}\sigma_1\delta_{\sigma_1-\sigma_2}, \quad 2\sigma_1\delta_{\sigma_1\sigma_2} \right). \tag{B.1.14}$$

In the standard HF theory, each single-particle wave function is assumed to have its own intrinsic isospin q_i, where $q_i = n$ for neutrons or $q_i = p$ for protons. It is crucial when we calculate the exchange term in the expectation value of a two-body operator, because this assumption eliminates exchange terms between nucleons with different isospins. We will comeback to this point later. The operator $\boldsymbol{\nabla} = (\partial/\partial x, \partial/\partial y, \partial/\partial z)$ denotes a nabla operator which acts only on a neighboring spatial function sitting on its right side, $i.e.$ $\boldsymbol{\nabla} f(\boldsymbol{r})g(\boldsymbol{r}) = g(\boldsymbol{r})\boldsymbol{\nabla} f(\boldsymbol{r})$. These densities ρ, τ, $\boldsymbol{j}$, $\boldsymbol{s}$, $\boldsymbol{T}$, and $J_{\mu\nu}$ are referred to as (matter) density, kinetic energy density, current (density), spin density, spin kinetic energy density, and spin current pseudotensor (density), respectively. $\boldsymbol{J}(\boldsymbol{r})$ denotes the antisymmetric part of the spin current pseudotensor $J_{\mu\nu}$ having components $J_\lambda(\boldsymbol{r}) = \sum_{\mu\nu} \varepsilon_{\lambda\mu\nu}J_{\mu\nu}(\boldsymbol{r})$. All these densities are real by definition.

We also define following densities with isospin dependence

$$\rho^{(q)}(\boldsymbol{r}) \equiv \sum_{i \in q\,\sigma} \phi_i^*(\boldsymbol{r}\sigma)\phi_i(\boldsymbol{r}\sigma), \tag{B.1.15}$$

$$\boldsymbol{s}^{(q)}(\boldsymbol{r}) \equiv \sum_{i \in q\,\sigma_1\,\sigma_2} \phi_i^*(\boldsymbol{r}\sigma_1)\phi_i(\boldsymbol{r}\sigma_2) \langle\sigma_1| \hat{\boldsymbol{\sigma}} |\sigma_2\rangle, \tag{B.1.16}$$

$$\tau^{(q)}(\boldsymbol{r}) \equiv \sum_{i \in q\,\sigma} \boldsymbol{\nabla}\phi_i^*(\boldsymbol{r}\sigma) \cdot \boldsymbol{\nabla}\phi_i(\boldsymbol{r}\sigma), \tag{B.1.17}$$

$$\boldsymbol{T}^{(q)}(\boldsymbol{r}) \equiv \sum_{i \in q\,\sigma_1\,\sigma_2} \{\boldsymbol{\nabla}\phi_i^*(\boldsymbol{r}\sigma_1) \cdot \boldsymbol{\nabla}\phi_i(\boldsymbol{r}\sigma_2)\} \langle\sigma_1| \hat{\boldsymbol{\sigma}} |\sigma_2\rangle, \tag{B.1.18}$$

$$\boldsymbol{j}^{(q)}(\boldsymbol{r}) \equiv \frac{1}{2\mathrm{i}} \sum_{i \in q\,\sigma} \{\phi_i^*(\boldsymbol{r}\sigma)\boldsymbol{\nabla}\phi_i(\boldsymbol{r}\sigma) - \phi_i(\boldsymbol{r}\sigma)\boldsymbol{\nabla}\phi_i^*(\boldsymbol{r}\sigma)\}, \tag{B.1.19}$$

$$J_{\mu\nu}^{(q)}(\boldsymbol{r}) \equiv \frac{1}{2\mathrm{i}} \sum_{i \in q\,\sigma_1\,\sigma_2} \{\phi_i^*(\boldsymbol{r}\sigma_1)\partial_\mu\phi_i(\boldsymbol{r}\sigma_2) - \phi_i(\boldsymbol{r}\sigma_2)\partial_\mu\phi_i^*(\boldsymbol{r}\sigma_1)\} \langle\sigma_1| \hat{\sigma_\nu} |\sigma_2\rangle, \tag{B.1.20}$$

$$\boldsymbol{J}^{(q)}(\boldsymbol{r}) \equiv \Big(J_{23}^{(q)}(\boldsymbol{r}) - J_{32}^{(q)}(\boldsymbol{r}),\ J_{31}^{(q)}(\boldsymbol{r}) - J_{13}^{(q)}(\boldsymbol{r}),\ J_{12}^{(q)}(\boldsymbol{r}) - J_{21}^{(q)}(\boldsymbol{r})\Big), \tag{B.1.21}$$

and with spin dependence

$$\rho_{\sigma_1\sigma_2}(\boldsymbol{r}) \equiv \sum_i \phi_i^*(\boldsymbol{r}\sigma_1)\phi_i(\boldsymbol{r}\sigma_2), \tag{B.1.22}$$

$$\rho_{\sigma_1\sigma_2}^{(q)}(\boldsymbol{r}) \equiv \sum_{i \in q} \phi_i^*(\boldsymbol{r}\sigma_1)\phi_i(\boldsymbol{r}\sigma_2), \tag{B.1.23}$$

$$\tau_{\sigma_1\sigma_2}(\boldsymbol{r}) \equiv \sum_{i\,\sigma_1\,\sigma_2} \boldsymbol{\nabla}\phi_i^*(\boldsymbol{r}\sigma_1) \cdot \boldsymbol{\nabla}\phi_i(\boldsymbol{r}\sigma_2), \tag{B.1.24}$$

$$\tau_{\sigma_1\sigma_2}^{(q)}(\boldsymbol{r}) \equiv \sum_{i \in q\,\sigma_1\,\sigma_2} \boldsymbol{\nabla}\phi_i^*(\boldsymbol{r}\sigma_1) \cdot \boldsymbol{\nabla}\phi_i(\boldsymbol{r}\sigma_2), \tag{B.1.25}$$

$$\boldsymbol{j}_{\sigma_1\sigma_2}(\boldsymbol{r}) \equiv \frac{1}{2\mathrm{i}} \sum_i \{\phi_i^*(\boldsymbol{r}\sigma_1)\boldsymbol{\nabla}\phi_i(\boldsymbol{r}\sigma_2) - \phi_i(\boldsymbol{r}\sigma_2)\boldsymbol{\nabla}\phi_i^*(\boldsymbol{r}\sigma_1)\}, \tag{B.1.26}$$

$$\boldsymbol{j}_{\sigma_1\sigma_2}^{(q)}(\boldsymbol{r}) \equiv \frac{1}{2\mathrm{i}} \sum_{i \in q} \{\phi_i^*(\boldsymbol{r}\sigma_1)\boldsymbol{\nabla}\phi_i(\boldsymbol{r}\sigma_2) - \phi_i(\boldsymbol{r}\sigma_2)\boldsymbol{\nabla}\phi_i^*(\boldsymbol{r}\sigma_1)\}, \tag{B.1.27}$$

where the summation $\sum_{i \in q}$ is taken over particle index i with a condition that the isospin of ith particle should coincide with the isospin q, *i.e.* $q_i = q$.

We next derive relations among these densities which are useful to derive the Skyrme EDF and the Skyrme HF equation. From Eq. (B.1.14), there follows a relation

$$
\begin{aligned}
\langle\sigma_1| \hat{\boldsymbol{\sigma}} |\sigma_2\rangle \cdot \langle\sigma_3| \hat{\boldsymbol{\sigma}} |\sigma_4\rangle &= \sum_\mu \langle\sigma_1|\hat{\sigma}_\mu|\sigma_2\rangle\langle\sigma_3|\hat{\sigma}_\mu|\sigma_4\rangle \\
&= \delta_{\sigma_1-\sigma_2}\delta_{\sigma_3-\sigma_4} - 4\sigma_1\sigma_3\delta_{\sigma_1-\sigma_2}\delta_{\sigma_3-\sigma_4} + 4\sigma_1\sigma_3\delta_{\sigma_1\sigma_2}\delta_{\sigma_3\sigma_4} \\
&= 2\delta_{\sigma_1-\sigma_2-\sigma_3\sigma_4} + \delta_{\sigma_1\sigma_2\sigma_3\sigma_4} - \delta_{\sigma_1\sigma_2-\sigma_3-\sigma_4}, \tag{B.1.28}
\end{aligned}
$$

where we have introduced a shorthand notation, $\delta_{\sigma_1\sigma_2\sigma_3\sigma_4} = \delta_{\sigma_1\sigma_2}\delta_{\sigma_3\sigma_4}\delta_{\sigma_1\sigma_3}$. Using Eq. (B.1.28), we can rewrite a squared spin density $\boldsymbol{s}^2(\boldsymbol{r})$ as

$$
\begin{aligned}
\boldsymbol{s}^2(\boldsymbol{r}) &= \sum_{i\sigma_1\sigma_2} \phi_i^*(\boldsymbol{r}\sigma_1)\phi_i(\boldsymbol{r}\sigma_2)\langle\sigma_1|\hat{\boldsymbol{\sigma}}|\sigma_2\rangle \cdot \sum_{j\sigma_3\sigma_4} \phi_j^*(\boldsymbol{r}\sigma_3)\phi_j(\boldsymbol{r}\sigma_4)\langle\sigma_3|\hat{\boldsymbol{\sigma}}|\sigma_4\rangle \\
&= \sum_{ij\sigma}\Big\{ 2\phi_i^*(\boldsymbol{r}\sigma)\phi_i(\boldsymbol{r}-\sigma)\phi_j^*(\boldsymbol{r}-\sigma)\phi_j(\boldsymbol{r}\sigma) + \phi_i^*(\boldsymbol{r}\sigma)\phi_i(\boldsymbol{r}\sigma)\phi_j^*(\boldsymbol{r}\sigma)\phi_j(\boldsymbol{r}\sigma) \\
&\quad -\phi_i^*(\boldsymbol{r}\sigma)\phi_i(\boldsymbol{r}\sigma)\phi_j^*(\boldsymbol{r}-\sigma)\phi_j(\boldsymbol{r}-\sigma)\Big\} \\
&= 2\sum_{ij\sigma}\Big\{ \phi_i^*(\boldsymbol{r}\sigma)\phi_i(\boldsymbol{r}-\sigma)\phi_j^*(\boldsymbol{r}-\sigma)\phi_j(\boldsymbol{r}\sigma) + \phi_i^*(\boldsymbol{r}\sigma)\phi_i(\boldsymbol{r}\sigma)\phi_j^*(\boldsymbol{r}\sigma)\phi_j(\boldsymbol{r}\sigma)\Big\} \\
&\quad -\sum_{ij\sigma}\Big\{ \phi_i^*(\boldsymbol{r}\sigma)\phi_i(\boldsymbol{r}\sigma)\phi_j^*(\boldsymbol{r}-\sigma)\phi_j(\boldsymbol{r}-\sigma) + \phi_i^*(\boldsymbol{r}\sigma)\phi_i(\boldsymbol{r}\sigma)\phi_j^*(\boldsymbol{r}\sigma)\phi_j(\boldsymbol{r}\sigma)\Big\} \\
&= 2\sum_{ij\sigma_1\sigma_2}\Big\{ \phi_i^*(\boldsymbol{r}\sigma_1)\phi_i(\boldsymbol{r}\sigma_2)\phi_j^*(\boldsymbol{r}\sigma_2)\phi_j(\boldsymbol{r}\sigma_1)\Big\} \\
&\quad -\sum_{ij\sigma}\phi_i^*(\boldsymbol{r}\sigma)\phi_i(\boldsymbol{r}\sigma)\Big\{ \phi_j^*(\boldsymbol{r}-\sigma)\phi_j(\boldsymbol{r}-\sigma) + \phi_j^*(\boldsymbol{r}\sigma)\phi_j(\boldsymbol{r}\sigma)\Big\} \\
&= 2\sum_{\sigma_1\sigma_2}\sum_i \phi_i^*(\boldsymbol{r}\sigma_1)\phi_i(\boldsymbol{r}\sigma_2)\sum_j \phi_j^*(\boldsymbol{r}\sigma_2)\phi_j(\boldsymbol{r}\sigma_1) \\
&\quad -\sum_{i\sigma_1}\phi_i^*(\boldsymbol{r}\sigma_1)\phi_i(\boldsymbol{r}\sigma_1)\sum_{j\sigma_2}\phi_j^*(\boldsymbol{r}\sigma_2)\phi_j(\boldsymbol{r}\sigma_2) \\
&= 2\sum_{\sigma_1\sigma_2}\rho_{\sigma_1\sigma_2}(\boldsymbol{r})\rho_{\sigma_2\sigma_1}(\boldsymbol{r}) - \rho^2(\boldsymbol{r}),
\end{aligned}
$$

where, in the forth equality, we changed a summation over σ to summations over σ_1 and σ_2. We then obtain following relations:

$$
\begin{aligned}
\boldsymbol{s}^2(\boldsymbol{r}) &= 2\sum_{\sigma_1\,\sigma_2}\rho_{\sigma_1\sigma_2}(\boldsymbol{r})\rho_{\sigma_2\sigma_1}(\boldsymbol{r}) - \rho^2(\boldsymbol{r}), && \text{(B.1.29)}
\end{aligned}
$$

$$
\begin{aligned}
\boldsymbol{s}^{(q)2}(\boldsymbol{r}) &= 2\sum_{\sigma_1\,\sigma_2}\rho_{\sigma_1\sigma_2}^{(q)}(\boldsymbol{r})\rho_{\sigma_2\sigma_1}^{(q)}(\boldsymbol{r}) - \rho^{(q)2}(\boldsymbol{r}). && \text{(B.1.30)}
\end{aligned}
$$

In the same way, we can also obtain

$$
\begin{aligned}
\boldsymbol{T}^2(\boldsymbol{r}) &= 2\sum_{\sigma_1\,\sigma_2}\tau_{\sigma_1\sigma_2}(\boldsymbol{r})\tau_{\sigma_2\sigma_1}(\boldsymbol{r}) - \tau^2(\boldsymbol{r}), && \text{(B.1.31)}
\end{aligned}
$$

$$
\begin{aligned}
\boldsymbol{T}^{(q)2}(\boldsymbol{r}) &= 2\sum_{\sigma_1\,\sigma_2}\tau_{\sigma_1\sigma_2}^{(q)}(\boldsymbol{r})\tau_{\sigma_2\sigma_1}^{(q)}(\boldsymbol{r}) - \tau^{(q)2}(\boldsymbol{r}), && \text{(B.1.32)}
\end{aligned}
$$

$$
\begin{aligned}
\boldsymbol{s}(\boldsymbol{r})\cdot\boldsymbol{T}(\boldsymbol{r}) &= 2\sum_{\sigma_1\,\sigma_2}\rho_{\sigma_1\sigma_2}(\boldsymbol{r})\tau_{\sigma_2\sigma_1}(\boldsymbol{r}) - \rho(\boldsymbol{r})\tau(\boldsymbol{r}), && \text{(B.1.33)}
\end{aligned}
$$

$$
\begin{aligned}
\boldsymbol{s}^{(q)}(\boldsymbol{r})\cdot\boldsymbol{T}^{(q)}(\boldsymbol{r}) &= 2\sum_{\sigma_1\,\sigma_2}\rho_{\sigma_1\sigma_2}^{(q)}(\boldsymbol{r})\tau_{\sigma_2\sigma_1}^{(q)}(\boldsymbol{r}) - \rho^{(q)}(\boldsymbol{r})\tau^{(q)}(\boldsymbol{r}). && \text{(B.1.34)}
\end{aligned}
$$

Noting the following expressions of tensor components

$$
\partial_\mu s_\nu(\boldsymbol{r}) = \sum_{\sigma_1\sigma_2}\partial_\mu\rho_{\sigma_1\sigma_2}(\boldsymbol{r})\langle\sigma_1|\hat{\sigma}_\nu|\sigma_2\rangle, \qquad\qquad \text{(B.1.35)}
$$

$$
J_{\mu\nu}(\boldsymbol{r}) = \sum_{\sigma_1\sigma_2}j_{\mu,\sigma_1\sigma_2}(\boldsymbol{r})\langle\sigma_1|\hat{\sigma}_\nu|\sigma_2\rangle, \qquad\qquad \text{(B.1.36)}
$$

we find similar relations for the sum of square of these tensor components,

$$
\begin{aligned}
\sum_{\mu\nu}\Big(\partial_\mu s_\nu(\boldsymbol{r})\Big)^2 &= \sum_\mu\Bigg\{\sum_{\sigma_1\sigma_2}\partial_\mu\rho_{\sigma_1\sigma_2}(\boldsymbol{r})\langle\sigma_1|\hat{\boldsymbol{\sigma}}|\sigma_2\rangle\cdot\sum_{\sigma_3\sigma_4}\partial_\mu\rho_{\sigma_3\sigma_4}(\boldsymbol{r})\langle\sigma_3|\hat{\boldsymbol{\sigma}}|\sigma_4\rangle\Bigg\} \\
&= \sum_\mu\Bigg\{2\sum_{\sigma_1\sigma_2}\partial_\mu\rho_{\sigma_1\sigma_2}(\boldsymbol{r})\partial_\mu\rho_{\sigma_2\sigma_1}(\boldsymbol{r})-\Big(\partial_\mu\rho(\boldsymbol{r})\Big)^2\Bigg\} \\
&= 2\sum_{\sigma_1\sigma_2}\boldsymbol{\nabla}\rho_{\sigma_1\sigma_2}(\boldsymbol{r})\cdot\boldsymbol{\nabla}\rho_{\sigma_2\sigma_1}(\boldsymbol{r})-\Big(\boldsymbol{\nabla}\rho(\boldsymbol{r})\Big)^2.
\end{aligned}
\tag{B.1.37}
$$

We can rewrite $\sum_{\mu\nu}\big(J_{\mu\nu}(\boldsymbol{r})\big)^2$ in the same way. We then obtain

$$
\begin{aligned}
\sum_{\mu\nu}\Big(\partial_\mu s_\nu(\boldsymbol{r})\Big)^2 &= 2\sum_{\sigma_1\sigma_2}\boldsymbol{\nabla}\rho_{\sigma_1\sigma_2}(\boldsymbol{r})\cdot\boldsymbol{\nabla}\rho_{\sigma_2\sigma_1}(\boldsymbol{r})-\Big(\boldsymbol{\nabla}\rho(\boldsymbol{r})\Big)^2, &\text{(B.1.38)} \\
\sum_{\mu\nu}\Big(\partial_\mu s_\nu^{(q)}(\boldsymbol{r})\Big)^2 &= 2\sum_{\sigma_1\sigma_2}\boldsymbol{\nabla}\rho_{\sigma_1\sigma_2}^{(q)}(\boldsymbol{r})\cdot\boldsymbol{\nabla}\rho_{\sigma_2\sigma_1}^{(q)}(\boldsymbol{r})-\Big(\boldsymbol{\nabla}\rho^{(q)}(\boldsymbol{r})\Big)^2, &\text{(B.1.39)} \\
\sum_{\mu\nu}\Big(J_{\mu\nu}(\boldsymbol{r})\Big)^2 &= 2\sum_{\sigma_1\sigma_2}\boldsymbol{j}_{\sigma_1\sigma_2}(\boldsymbol{r})\cdot\boldsymbol{j}_{\sigma_2\sigma_1}(\boldsymbol{r})-\boldsymbol{j}^2(\boldsymbol{r}), &\text{(B.1.40)} \\
\sum_{\mu\nu}\Big(J_{\mu\nu}^{(q)}(\boldsymbol{r})\Big)^2 &= 2\sum_{\sigma_1\sigma_2}\boldsymbol{j}_{\sigma_1\sigma_2}^{(q)}(\boldsymbol{r})\cdot\boldsymbol{j}_{\sigma_2\sigma_1}^{(q)}(\boldsymbol{r})-\boldsymbol{j}^{(q)2}(\boldsymbol{r}). &\text{(B.1.41)}
\end{aligned}
$$

From equations for the gradient of the matter densities $\rho(\boldsymbol{r})$ and $\rho_{\sigma_1\sigma_2}(\boldsymbol{r})$ and the spin density $\boldsymbol{s}(\boldsymbol{r})$,

$$
\begin{aligned}
\boldsymbol{\nabla}\rho(\boldsymbol{r}) &= \sum_{i\,\sigma}\big\{\phi_i(\boldsymbol{r}\sigma)\boldsymbol{\nabla}\phi_i^*(\boldsymbol{r}\sigma)+\phi_i^*(\boldsymbol{r}\sigma)\boldsymbol{\nabla}\phi_i(\boldsymbol{r}\sigma)\big\}, &\text{(B.1.42)} \\
\boldsymbol{\nabla}\rho_{\sigma_1\sigma_2}(\boldsymbol{r}) &= \sum_{i}\big\{\phi_i(\boldsymbol{r}\sigma_2)\boldsymbol{\nabla}\phi_i^*(\boldsymbol{r}\sigma_1)+\phi_i^*(\boldsymbol{r}\sigma_1)\boldsymbol{\nabla}\phi_i(\boldsymbol{r}\sigma_2)\big\}, &\text{(B.1.43)} \\
\partial_\mu s_\nu(\boldsymbol{r}) &= \sum_{i\,\sigma_1\sigma_2}\big\{\phi_i(\boldsymbol{r}\sigma_2)\partial_\mu\phi_i^*(\boldsymbol{r}\sigma_1)+\phi_i^*(\boldsymbol{r}\sigma_1)\partial_\mu\phi_i(\boldsymbol{r}\sigma_2)\big\}\langle\sigma_1|\hat{\sigma}_\nu|\sigma_2\rangle, &\text{(B.1.44)}
\end{aligned}
$$

combined with the definitions of $\boldsymbol{j}(\boldsymbol{r})$ Eq. (B.1.5), $\boldsymbol{j}_{\sigma_1\sigma_2}(\boldsymbol{r})$ Eq. (B.1.26), and $J_{\mu\nu}(\boldsymbol{r})$ Eq. (B.1.6), we find

$$
\begin{aligned}
\frac{1}{2}\boldsymbol{\nabla}\rho(\boldsymbol{r})+\mathrm{i}\boldsymbol{j}(\boldsymbol{r}) &= \sum_{i\,\sigma}\phi_i^*(\boldsymbol{r}\sigma)\boldsymbol{\nabla}\phi_i(\boldsymbol{r}\sigma), &\text{(B.1.45)} \\
\frac{1}{2}\boldsymbol{\nabla}\rho(\boldsymbol{r})-\mathrm{i}\boldsymbol{j}(\boldsymbol{r}) &= \sum_{i\,\sigma}\phi_i(\boldsymbol{r}\sigma)\boldsymbol{\nabla}\phi_i^*(\boldsymbol{r}\sigma), &\text{(B.1.46)} \\
\frac{1}{2}\boldsymbol{\nabla}\rho_{\sigma_1\sigma_2}(\boldsymbol{r})+\mathrm{i}\boldsymbol{j}_{\sigma_1\sigma_2}(\boldsymbol{r}) &= \sum_{i}\phi_i^*(\boldsymbol{r}\sigma_1)\boldsymbol{\nabla}\phi_i(\boldsymbol{r}\sigma_2), &\text{(B.1.47)} \\
\frac{1}{2}\boldsymbol{\nabla}\rho_{\sigma_1\sigma_2}(\boldsymbol{r})-\mathrm{i}\boldsymbol{j}_{\sigma_1\sigma_2}(\boldsymbol{r}) &= \sum_{i}\phi_i(\boldsymbol{r}\sigma_2)\boldsymbol{\nabla}\phi_i^*(\boldsymbol{r}\sigma_1), &\text{(B.1.48)} \\
\frac{1}{2}\partial_\mu s_\nu(\boldsymbol{r})+\mathrm{i}J_{\mu\nu}(\boldsymbol{r}) &= \sum_{i\,\sigma_1\sigma_2}\phi_i^*(\boldsymbol{r}\sigma_1)\partial_\mu\phi_i(\boldsymbol{r}\sigma_2)\langle\sigma_1|\hat{\sigma}_\nu|\sigma_2\rangle, &\text{(B.1.49)} \\
\frac{1}{2}\partial_\mu s_\nu(\boldsymbol{r})-\mathrm{i}J_{\mu\nu}(\boldsymbol{r}) &= \sum_{i\,\sigma_1\sigma_2}\phi_i(\boldsymbol{r}\sigma_2)\partial_\mu\phi_i^*(\boldsymbol{r}\sigma_1)\langle\sigma_1|\hat{\sigma}_\nu|\sigma_2\rangle. &\text{(B.1.50)}
\end{aligned}
$$

We denote a Laplacian operator as $\triangle = \boldsymbol{\nabla}^2 = \partial^2/\partial x^2 + \partial^2/\partial y^2 + \partial^2/\partial z^2$ which acts only on a neighboring spatial function sitting on its right side, *i.e.* $\triangle f(\boldsymbol{r})g(\boldsymbol{r}) = g(\boldsymbol{r}) \triangle f(\boldsymbol{r})$. Using an equation for the Laplacian of the matter density,

$$\triangle \rho(\boldsymbol{r}) = \sum_{i\,\sigma} \big\{ \phi_i(\boldsymbol{r}\sigma) \triangle \phi_i^*(\boldsymbol{r}\sigma) + \phi_i^*(\boldsymbol{r}\sigma) \triangle \phi_i(\boldsymbol{r}\sigma) + 2\boldsymbol{\nabla}\phi_i^*(\boldsymbol{r}\sigma) \cdot \boldsymbol{\nabla}\phi_i(\boldsymbol{r}\sigma) \big\}, \qquad (\text{B.1.51})$$

and the definition of $\tau(\boldsymbol{r})$, Eq. (B.1.3), we find

$$\triangle \rho(\boldsymbol{r}) - 2\tau(\boldsymbol{r}) = \sum_{i\,\sigma} \big\{ \phi_i^*(\boldsymbol{r}\sigma) \triangle \phi_i(\boldsymbol{r}\sigma) + \phi_i(\boldsymbol{r}\sigma) \triangle \phi_i^*(\boldsymbol{r}\sigma) \big\}, \qquad (\text{B.1.52})$$

$$\triangle \rho_{\sigma_1\sigma_2}(\boldsymbol{r}) - 2\tau_{\sigma_1\sigma_2}(\boldsymbol{r}) = \sum_{i} \big\{ \phi_i^*(\boldsymbol{r}\sigma_1) \triangle \phi_i(\boldsymbol{r}\sigma_2) + \phi_i(\boldsymbol{r}\sigma_2) \triangle \phi_i^*(\boldsymbol{r}\sigma_1) \big\}. \qquad (\text{B.1.53})$$

Recalling the formulae of the vector analysis

$$\boldsymbol{\nabla} \times (f\boldsymbol{A}) = f(\boldsymbol{\nabla} \times \boldsymbol{A}) - \boldsymbol{A} \times (\boldsymbol{\nabla} f), \qquad (\text{B.1.54})$$

$$\boldsymbol{\nabla} \times (\boldsymbol{\nabla} f) = 0, \qquad (\text{B.1.55})$$

where $f = f(\boldsymbol{r})$ and $\boldsymbol{A} = \boldsymbol{A}(\boldsymbol{r})$ denote arbitrary scalar and vector spatial functions, respectively, we find

$$
\begin{aligned}
\boldsymbol{\nabla} \times \boldsymbol{j}(\boldsymbol{r}) &= \frac{1}{2\mathrm{i}} \sum_{i\,\sigma} \boldsymbol{\nabla} \times \big\{ \phi_i^*(\boldsymbol{r}\sigma)\boldsymbol{\nabla}\phi_i(\boldsymbol{r}\sigma) - \phi_i(\boldsymbol{r}\sigma)\boldsymbol{\nabla}\phi_i^*(\boldsymbol{r}\sigma) \big\} \\
&= \frac{1}{2\mathrm{i}} \sum_{i\,\sigma} \big\{ \phi_i^*(\boldsymbol{r}\sigma)\boldsymbol{\nabla} \times \big(\boldsymbol{\nabla}\phi_i(\boldsymbol{r}\sigma)\big) - \boldsymbol{\nabla}\phi_i(\boldsymbol{r}\sigma) \times \boldsymbol{\nabla}\phi_i^*(\boldsymbol{r}\sigma) \\
&\qquad\qquad - \phi_i(\boldsymbol{r}\sigma)\boldsymbol{\nabla} \times \big(\boldsymbol{\nabla}\phi_i^*(\boldsymbol{r}\sigma)\big) + \boldsymbol{\nabla}\phi_i^*(\boldsymbol{r}\sigma) \times \boldsymbol{\nabla}\phi_i(\boldsymbol{r}\sigma) \big\} \\
&= \frac{1}{\mathrm{i}} \sum_{i\,\sigma} \boldsymbol{\nabla}\phi_i^*(\boldsymbol{r}\sigma) \times \boldsymbol{\nabla}\phi_i(\boldsymbol{r}\sigma)
\end{aligned}
$$

and

$$
\begin{aligned}
\boldsymbol{\nabla} \cdot \boldsymbol{J}(\boldsymbol{r}) &= \sum_{\lambda\mu\nu} \varepsilon_{\lambda\mu\nu}\partial_\lambda J_{\mu\nu}(\boldsymbol{r}) \\
&= \frac{1}{2\mathrm{i}} \sum_{\lambda\mu\nu} \varepsilon_{\lambda\mu\nu} \sum_{i\,\sigma_1\sigma_2} \partial_\lambda \big\{ \phi_i^*(\boldsymbol{r}\sigma_1)\partial_\mu\phi_i(\boldsymbol{r}\sigma_2) - \phi_i(\boldsymbol{r}\sigma_2)\partial_\mu\phi_i^*(\boldsymbol{r}\sigma_1) \big\} \langle\sigma_1|\,\hat{\sigma}_\nu\,|\sigma_2\rangle \\
&= \frac{1}{2\mathrm{i}} \sum_{\lambda\mu\nu} \varepsilon_{\lambda\mu\nu} \sum_{i\,\sigma_1\sigma_2} \big\{ \partial_\lambda\phi_i^*(\boldsymbol{r}\sigma_1)\partial_\mu\phi_i(\boldsymbol{r}\sigma_2) + \phi_i^*(\boldsymbol{r}\sigma_1)\partial_\lambda\partial_\mu\phi_i(\boldsymbol{r}\sigma_2) \\
&\qquad\qquad - \partial_\lambda\phi_i(\boldsymbol{r}\sigma_2)\partial_\mu\phi_i^*(\boldsymbol{r}\sigma_1) - \phi_i(\boldsymbol{r}\sigma_2)\partial_\lambda\partial_\mu\phi_i^*(\boldsymbol{r}\sigma_1) \big\} \langle\sigma_1|\,\hat{\sigma}_\nu\,|\sigma_2\rangle \\
&= \frac{1}{\mathrm{i}} \sum_{i\,\sigma_1\sigma_2} \sum_{\lambda\mu\nu} \varepsilon_{\lambda\mu\nu}\partial_\lambda\phi_i^*(\boldsymbol{r}\sigma_1)\partial_\mu\phi_i(\boldsymbol{r}\sigma_2) \langle\sigma_1|\,\hat{\sigma}_\nu\,|\sigma_2\rangle \\
&= \frac{1}{\mathrm{i}} \sum_{i\,\sigma_1\sigma_2} \big\{ \boldsymbol{\nabla}\phi_i^*(\boldsymbol{r}\sigma_1) \times \boldsymbol{\nabla}\phi_i(\boldsymbol{r}\sigma_2) \big\} \cdot \langle\sigma_1|\,\hat{\boldsymbol{\sigma}}\,|\sigma_2\rangle,
\end{aligned}
$$

where, in the fourth equality, we used anti-symmetric nature of the Levi-Civita tensor, which leads $\varepsilon_{\lambda\mu\nu}\partial_\mu\partial_\nu f(\boldsymbol{r}) = 0$. To summarize, we have

$$
\mathrm{i}\boldsymbol{\nabla} \times \boldsymbol{j}(\boldsymbol{r}) = \sum_{i\,\sigma} \boldsymbol{\nabla}\phi_i^*(\boldsymbol{r}\sigma) \times \boldsymbol{\nabla}\phi_i(\boldsymbol{r}\sigma), \tag{B.1.56}
$$

$$
\mathrm{i}\boldsymbol{\nabla} \times \boldsymbol{j}^{(q)}(\boldsymbol{r}) = \sum_{i\in q\,\sigma} \boldsymbol{\nabla}\phi_i^*(\boldsymbol{r}\sigma) \times \boldsymbol{\nabla}\phi_i(\boldsymbol{r}\sigma), \tag{B.1.57}
$$

$$
\mathrm{i}\boldsymbol{\nabla} \cdot \boldsymbol{J}(\boldsymbol{r}) = \sum_{i\,\sigma_1\,\sigma_2} \left\{ \boldsymbol{\nabla}\phi_i^*(\boldsymbol{r}\sigma_1) \times \boldsymbol{\nabla}\phi_i(\boldsymbol{r}\sigma_2) \right\} \cdot \langle\sigma_1| \,\hat{\boldsymbol{\sigma}}\, |\sigma_2\rangle, \tag{B.1.58}
$$

$$
\mathrm{i}\boldsymbol{\nabla} \cdot \boldsymbol{J}^{(q)}(\boldsymbol{r}) = \sum_{i\in q\,\sigma_1\,\sigma_2} \left\{ \boldsymbol{\nabla}\phi_i^*(\boldsymbol{r}\sigma_1) \times \boldsymbol{\nabla}\phi_i(\boldsymbol{r}\sigma_2) \right\} \cdot \langle\sigma_1| \,\hat{\boldsymbol{\sigma}}\, |\sigma_2\rangle. \tag{B.1.59}
$$

B.2 Derivation of the Skyrme energy density functional

In this Section, we derive the Skyrme EDF using the relations presented in the previous Section. We describe the expectation value of the Skyrme effective interaction, Eq. (2.1.12), for the Slater determinant. What we need to calculate is the expectation value of a two-body interaction operator given by

$$
\langle\Phi|\hat{V}|\Phi\rangle = \frac{1}{2}\sum_{ij} \Big\{ \underbrace{\langle\phi_i\phi_j| \,\hat{v}\, |\phi_i\phi_j\rangle}_{\text{direct term}} - \underbrace{\langle\phi_i\phi_j| \,\hat{v}\, |\phi_j\phi_i\rangle}_{\text{exchange term}} \Big\}, \tag{B.2.1}
$$

where we refer to the first (second) term as the direct (exchange) term.

Here we use a bracket notation defined as follows: We suppose that each single-particle wave function is represented by a two-component spinor,

$$
\tilde{\phi}_i^\dagger(\boldsymbol{r}) = \Big(\phi_i^*(\boldsymbol{r}\uparrow)\ \ \phi_i^*(\boldsymbol{r}\downarrow) \Big), \quad \tilde{\phi}_i(\boldsymbol{r}) = \begin{pmatrix} \phi_i(\boldsymbol{r}\uparrow) \\ \phi_i(\boldsymbol{r}\downarrow) \end{pmatrix}. \tag{B.2.2}
$$

We define a bracket notation for the single-particle expectation value of arbitrary one- and two-body operators, respectively, as

$$
\langle\phi_i|\hat{o}|\phi_j\rangle \equiv \int d\boldsymbol{r}\, \tilde{\phi}_i^\dagger(\boldsymbol{r})\, \hat{o}\, \tilde{\phi}_j(\boldsymbol{r}), \tag{B.2.3}
$$

$$
\langle\phi_i\phi_j|\hat{o}|\phi_k\phi_l\rangle \equiv \int d\boldsymbol{r} \int d\boldsymbol{r}'\, \tilde{\phi}_i^\dagger(\boldsymbol{r})\tilde{\phi}_j^\dagger(\boldsymbol{r}')\, \hat{o}\, \tilde{\phi}_k(\boldsymbol{r})\tilde{\phi}_l(\boldsymbol{r}'). \tag{B.2.4}
$$

When those operators have no spin-dependence, we have

$$
\langle\phi_i|\hat{o}|\phi_j\rangle = \sum_{\sigma} \int d\boldsymbol{r}\, \phi_i^*(\boldsymbol{r}\sigma)\hat{o}(\boldsymbol{r})\phi_j(\boldsymbol{r}\sigma), \tag{B.2.5}
$$

$$
\langle\phi_i\phi_j|\hat{o}|\phi_k\phi_l\rangle = \sum_{\sigma_1\sigma_2} \int d\boldsymbol{r}_1 \int d\boldsymbol{r}_2\, \phi_i^*(\boldsymbol{r}_1\sigma_1)\phi_j^*(\boldsymbol{r}_2\sigma_2)\, \hat{o}(\boldsymbol{r}_1,\boldsymbol{r}_2)\, \phi_k(\boldsymbol{r}_1\sigma_1)\phi_l(\boldsymbol{r}_2\sigma_2). \tag{B.2.6}
$$

When those operators have spin-dependence, *e.g.* $\hat{o}(\boldsymbol{r})\hat{\boldsymbol{\sigma}}$ and $\hat{o}(\boldsymbol{r},\boldsymbol{r}')(\hat{\boldsymbol{\sigma}} + \hat{\boldsymbol{\sigma}}')$, we have

$$
\langle\phi_i|\hat{o}\,\hat{\boldsymbol{\sigma}}|\phi_j\rangle = \sum_{\sigma_1\sigma_2} \int d\boldsymbol{r}\, \phi_i^*(\boldsymbol{r}\sigma_1)\, \hat{o}(\boldsymbol{r})\, \phi_j(\boldsymbol{r}\sigma_2)\langle\sigma_1|\hat{\boldsymbol{\sigma}}|\sigma_2\rangle, \tag{B.2.7}
$$

$$
\langle\phi_i\phi_j| \,\hat{o}\big(\hat{\boldsymbol{\sigma}} + \hat{\boldsymbol{\sigma}}'\big)\, |\phi_k\phi_l\rangle = \sum_{\sigma_1\sigma_1'\sigma_2\sigma_2'} \int d\boldsymbol{r}_1 \int d\boldsymbol{r}_2\, \phi_i^*(\boldsymbol{r}_1\sigma_1)\phi_j^*(\boldsymbol{r}_2\sigma_2)\, \hat{o}(\boldsymbol{r}_1,\boldsymbol{r}_2)\, \phi_k(\boldsymbol{r}_1\sigma_1')\phi_l(\boldsymbol{r}_2\sigma_2')
$$
$$
\times \Big(\langle\sigma_1|\hat{\boldsymbol{\sigma}}|\sigma_1'\rangle\delta_{\sigma_2\sigma_2'} + \delta_{\sigma_1\sigma_1'}\langle\sigma_2|\hat{\boldsymbol{\sigma}}|\sigma_2'\rangle \Big). \tag{B.2.8}
$$

In the following, we calculate the expectation value Eq. (B.2.1) for the Skyrme effective interaction given in Eq. (2.1.12).

The t_0 and t_3 terms (central and density-dependent terms, respectively)

First, we calculate the expectation values of the t_0 and t_3 terms,

$$\hat{V}_0 \equiv \sum_{i<j} t_0(1 + x_0\hat{P}_\sigma)\,\delta(\boldsymbol{r}_i - \boldsymbol{r}_j),$$

$$\hat{V}_3 \equiv \sum_{i<j} \frac{1}{6}t_3\,\rho^\alpha\Big(\frac{\boldsymbol{r}_i + \boldsymbol{r}_j}{2}\Big)\big(1 + x_3\hat{P}_\sigma\big)\delta(\boldsymbol{r}_i - \boldsymbol{r}_j).$$

We first calculate the direct term in $\langle\Phi|\hat{V}_0|\Phi\rangle$. The first and second terms in $\hat{V}_0$ without and with the spin exchange operator $\hat{P}_\sigma$ lead, respectively,

$$
\begin{aligned}
\sum_{i<j}\langle\phi_i\phi_j|\delta(\boldsymbol{r}-\boldsymbol{r}')|\phi_i\phi_j\rangle &= \frac{1}{2}\sum_{ij\sigma\sigma'}\int d\boldsymbol{r}\int d\boldsymbol{r}'\,\phi_i^*(\boldsymbol{r}\sigma)\phi_j^*(\boldsymbol{r}'\sigma')\,\delta(\boldsymbol{r}-\boldsymbol{r}')\,\phi_i(\boldsymbol{r}\sigma)\phi_j(\boldsymbol{r}'\sigma') \\
&= \frac{1}{2}\int d\boldsymbol{r}\sum_{i\sigma}\phi_i^*(\boldsymbol{r}\sigma)\phi_i(\boldsymbol{r}\sigma)\sum_{j\sigma'}\phi_j^*(\boldsymbol{r}\sigma')\phi_j(\boldsymbol{r}\sigma') \\
&= \frac{1}{2}\int d\boldsymbol{r}\rho^2(\boldsymbol{r}), \tag{B.2.9}
\end{aligned}
$$

and

$$
\begin{aligned}
\sum_{i<j}\langle\phi_i\phi_j|\delta(\boldsymbol{r}-\boldsymbol{r}')\hat{P}_\sigma|\phi_i\phi_j\rangle &= \frac{1}{2}\sum_{ij\sigma\sigma'}\int d\boldsymbol{r}\int d\boldsymbol{r}'\,\phi_i^*(\boldsymbol{r}\sigma)\phi_j^*(\boldsymbol{r}'\sigma')\,\delta(\boldsymbol{r}-\boldsymbol{r}')\,\phi_i(\boldsymbol{r}\sigma')\phi_j(\boldsymbol{r}'\sigma) \\
&= \frac{1}{2}\int d\boldsymbol{r}\sum_{\sigma\sigma'}\sum_i\phi_i^*(\boldsymbol{r}\sigma)\phi_i(\boldsymbol{r}\sigma')\sum_j\phi_j^*(\boldsymbol{r}\sigma')\phi_j(\boldsymbol{r}\sigma) \\
&= \frac{1}{2}\int d\boldsymbol{r}\sum_{\sigma\sigma'}\rho_{\sigma\sigma'}(\boldsymbol{r})\rho_{\sigma'\sigma}(\boldsymbol{r}) \\
&= \frac{1}{4}\int d\boldsymbol{r}\Big[\,\boldsymbol{s}^2(\boldsymbol{r}) + \rho^2(\boldsymbol{r})\Big]. \tag{B.2.10}
\end{aligned}
$$

In the last equality, we have used Eq. (B.1.29). When we calculate the exchange term, we use the identity, $|\phi_j\phi_i\rangle = \hat{P}_{\boldsymbol{r}}\hat{P}_\sigma\hat{P}_\tau|\phi_i\phi_j\rangle = \hat{P}_{\boldsymbol{r}}\hat{P}_\sigma\delta_{q_iq_j}|\phi_i\phi_j\rangle$. The last equality reflects the fact that, in our formalism, each nucleon has its own intrinsic isospin and the exchange term can act only for nucleons with the same isospin. The exchange term in $\langle\Phi|\hat{V}_0|\Phi\rangle$ without and with the spin exchange operator $\hat{P}_\sigma$ are, respectively, calculated as

$$
\begin{aligned}
\sum_{i<j}\langle\phi_i\phi_j|\delta(\boldsymbol{r}-\boldsymbol{r}')|\phi_j\phi_i\rangle &= \sum_{i<j}\langle\phi_i\phi_j|\delta(\boldsymbol{r}-\boldsymbol{r}')\hat{P}_{\boldsymbol{r}}\hat{P}_\sigma\delta_{q_iq_j}|\phi_i\phi_j\rangle \\
&= \frac{1}{4}\int d\boldsymbol{r}\sum_q\Big\{\boldsymbol{s}^{(q)2}(\boldsymbol{r}) + \rho^{(q)2}(\boldsymbol{r})\Big\}, \tag{B.2.11}
\end{aligned}
$$

where we have used Eq. (B.1.30), and

$$
\begin{aligned}
\sum_{i<j}\langle\phi_i\phi_j|\delta(\boldsymbol{r}-\boldsymbol{r}')\hat{P}_\sigma|\phi_j\phi_i\rangle &= \sum_{i<j}\langle\phi_i\phi_j|\delta(\boldsymbol{r}-\boldsymbol{r})\hat{P}_{\boldsymbol{r}}\delta_{q_iq_j}|\phi_i\phi_j\rangle \\
&= \frac{1}{2}\int d\boldsymbol{r}\sum_q\rho^{(q)2}(\boldsymbol{r}). \tag{B.2.12}
\end{aligned}
$$

We have used the identity, $\big(\hat{P}_\sigma\big)^2 = 1$. We note that the existence of the spatial coordinates exchange operator, $\hat{P}_{\boldsymbol{r}}$, does not affect the calculation, because now interactions are symmetric under the exchange of the spatial coordinates.

Although the t_3 term, $\hat{V}_3$, contains an additional density dependence ρ^α compared with the $\hat{V}_0$, we can calculate the expectation value of the $\hat{V}_3$ in the same way as the t_0 term case. By summing up these results, Eqs. (B.2.9)-(B.2.12), multiplying by proper coefficients, the expectation values of the t_0 and t_3 terms are found to be

t_0 term :

$$
\begin{aligned}
\left\langle \Phi \middle| \hat{V}_0 \middle| \Phi \right\rangle &= \left\langle \Phi \middle| \sum_{i<j} t_0(1 + x_0\hat{P}_\sigma)\delta(\boldsymbol{r}_i - \boldsymbol{r}_j) \middle| \Phi \right\rangle \\
&= \frac{1}{2}t_0 \int d\boldsymbol{r} \left[\left(1 + \frac{1}{2}x_0\right)\rho^2(\boldsymbol{r}) + \frac{1}{2}x_0\boldsymbol{s}^2(\boldsymbol{r}) - \sum_q \left\{ \left(\frac{1}{2} + x_0\right)\rho^{(q)2}(\boldsymbol{r}) + \frac{1}{2}\boldsymbol{s}^{(q)2}(\boldsymbol{r}) \right\} \right],
\end{aligned}
\tag{B.2.13}
$$

t_3 term :

$$
\begin{aligned}
\left\langle \Phi \middle| \hat{V}_3 \middle| \Phi \right\rangle &= \left\langle \Phi \middle| \sum_{i<j} \frac{1}{6}t_3\, \rho^\alpha\!\left(\frac{\boldsymbol{r}_i + \boldsymbol{r}_j}{2}\right)\left(1 + x_3\hat{P}_\sigma\right)\delta(\boldsymbol{r}_i - \boldsymbol{r}_j) \middle| \Phi \right\rangle \\
&= \frac{1}{12}t_3 \int d\boldsymbol{r}\, \rho^\alpha(\boldsymbol{r}) \left[\left(1 + \frac{1}{2}x_3\right)\rho^2(\boldsymbol{r}) + \frac{1}{2}x_3\boldsymbol{s}^2(\boldsymbol{r}) - \sum_q \left\{ \left(\frac{1}{2} + x_3\right)\rho^{(q)2}(\boldsymbol{r}) + \frac{1}{2}\boldsymbol{s}^{(q)2}(\boldsymbol{r}) \right\} \right].
\end{aligned}
\tag{B.2.14}
$$

The t_1 term (one of the non-local term)

We next consider the expectation value of the t_1 term,

$$\hat{V}_1 \equiv \sum_{i<j} \frac{1}{2} t_1 (1 + x_1 \hat{P}_\sigma) \Big\{ \delta(\boldsymbol{r}_i - \boldsymbol{r}_j) \, \hat{\boldsymbol{k}}^2 + \hat{\boldsymbol{k}}'^2 \, \delta(\boldsymbol{r}_i - \boldsymbol{r}_j) \Big\}. \tag{B.2.15}$$

Again, we first calculate the direct term in $\langle \Phi | \hat{V}_1 | \Phi \rangle$. The direct term of the first term without the spin exchange operator $\hat{P}_\sigma$ is calculated as

$$\sum_{i<j} \langle \phi_i \phi_j | \Big\{ \delta(\boldsymbol{r} - \boldsymbol{r}')\hat{\boldsymbol{k}}^2 + \hat{\boldsymbol{k}}'^2 \delta(\boldsymbol{r} - \boldsymbol{r}') \Big\} | \phi_i \phi_j \rangle$$

$$= -\frac{1}{8} \sum_{ij\sigma\sigma'} \int d\boldsymbol{r} \int d\boldsymbol{r}' \Big\{ \phi_i^*(\boldsymbol{r}\sigma)\phi_j^*(\boldsymbol{r}'\sigma') \, \delta(\boldsymbol{r} - \boldsymbol{r}') \Big(\overrightarrow{\nabla}^2 + \overrightarrow{\nabla}'^2 - 2\overrightarrow{\nabla}\cdot\overrightarrow{\nabla}' \Big) \phi_i(\boldsymbol{r}\sigma)\phi_j(\boldsymbol{r}'\sigma')$$

$$\qquad\qquad + \phi_i^*(\boldsymbol{r}\sigma)\phi_j^*(\boldsymbol{r}'\sigma') \Big(\overleftarrow{\nabla}^2 + \overleftarrow{\nabla}'^2 - 2\overleftarrow{\nabla}\cdot\overleftarrow{\nabla}' \Big) \delta(\boldsymbol{r} - \boldsymbol{r}') \, \phi_i(\boldsymbol{r}\sigma)\phi_j(\boldsymbol{r}'\sigma') \Big\}$$

$$= -\frac{1}{4} \sum_{ij\sigma\sigma'} \int d\boldsymbol{r} \Big\{ \phi_i^*(\boldsymbol{r}\sigma) \triangle \phi_i(\boldsymbol{r}\sigma) \, \phi_j^*(\boldsymbol{r}\sigma')\phi_j(\boldsymbol{r}\sigma') - \phi_i^*(\boldsymbol{r}\sigma)\boldsymbol{\nabla}\phi_i(\boldsymbol{r}\sigma) \cdot \phi_j^*(\boldsymbol{r}\sigma')\boldsymbol{\nabla}\phi_j(\boldsymbol{r}\sigma')$$

$$\qquad\qquad + \triangle \phi_i^*(\boldsymbol{r}\sigma)\phi_i(\boldsymbol{r}\sigma) \, \phi_j^*(\boldsymbol{r}\sigma')\phi_j(\boldsymbol{r}\sigma') - \boldsymbol{\nabla}\phi_i^*(\boldsymbol{r}\sigma)\phi_i(\boldsymbol{r}\sigma) \cdot \boldsymbol{\nabla}\phi_j^*(\boldsymbol{r}\sigma')\phi_j(\boldsymbol{r}\sigma') \Big\}$$

$$= -\frac{1}{4} \int d\boldsymbol{r} \Big\{ \sum_{i\sigma} \Big(\phi_i^*(\boldsymbol{r}\sigma) \triangle \phi_i(\boldsymbol{r}\sigma) + \phi_i(\boldsymbol{r}\sigma) \triangle \phi_i^*(\boldsymbol{r}\sigma) \Big) \sum_{j\sigma'} \phi_j^*(\boldsymbol{r}\sigma')\phi_j(\boldsymbol{r}\sigma')$$

$$\qquad\qquad - \sum_{i\sigma} \phi_i^*(\boldsymbol{r}\sigma)\boldsymbol{\nabla}\phi_i(\boldsymbol{r}\sigma) \cdot \sum_{j\sigma'} \phi_j^*(\boldsymbol{r}\sigma')\boldsymbol{\nabla}\phi_j(\boldsymbol{r}\sigma')$$

$$\qquad\qquad - \sum_{i\sigma} \phi_i(\boldsymbol{r}\sigma)\boldsymbol{\nabla}\phi_i^*(\boldsymbol{r}\sigma) \cdot \sum_{j\sigma'} \phi_j(\boldsymbol{r}\sigma')\boldsymbol{\nabla}\phi_j^*(\boldsymbol{r}\sigma') \Big\}$$

$$= -\frac{1}{4} \int d\boldsymbol{r} \Big\{ \Big(\triangle\rho(\boldsymbol{r}) - 2\tau(\boldsymbol{r}) \Big)\rho(\boldsymbol{r}) - \Big(\frac{1}{2}\boldsymbol{\nabla}\rho(\boldsymbol{r}) + \mathrm{i}\boldsymbol{j}(\boldsymbol{r}) \Big)^2 - \Big(\frac{1}{2}\boldsymbol{\nabla}\rho(\boldsymbol{r}) - \mathrm{i}\boldsymbol{j}(\boldsymbol{r}) \Big)^2 \Big\}$$

$$= -\frac{1}{4} \int d\boldsymbol{r} \Big\{ \rho(\boldsymbol{r}) \triangle \rho(\boldsymbol{r}) - 2\rho(\boldsymbol{r})\tau(\boldsymbol{r}) - \frac{1}{2}\Big(\boldsymbol{\nabla}\rho(\boldsymbol{r}) \Big)^2 + 2\boldsymbol{j}^2(\boldsymbol{r}) \Big\}$$

$$= \frac{1}{2} \int d\boldsymbol{r} \Big[-\frac{3}{4} \rho(\boldsymbol{r}) \triangle \rho(\boldsymbol{r}) + \rho(\boldsymbol{r})\tau(\boldsymbol{r}) - \boldsymbol{j}^2(\boldsymbol{r}) \Big], \tag{B.2.16}$$

where, in the fourth equality, we have used Eqs. (B.1.52), (B.1.45), and (B.1.46). In the last equality, we have taken integration by parts

$$\int d\boldsymbol{r} \, \boldsymbol{\nabla}\rho(\boldsymbol{r}) \cdot \boldsymbol{\nabla}\rho(\boldsymbol{r}) = \rho(\boldsymbol{r})\boldsymbol{\nabla}\rho(\boldsymbol{r})\Big|_{\boldsymbol{r}\to\infty} - \int d\boldsymbol{r} \, \rho(\boldsymbol{r}) \triangle \rho(\boldsymbol{r}), \tag{B.2.17}$$

where the first term vanishes because of the finiteness of the density distribution, $\rho(\boldsymbol{r}) \xrightarrow{r\to\infty} 0$. The

direct term of the second term with the spin exchange operator $\hat{P}_\sigma$ is calculated as

$$\sum_{i<j}\langle\phi_i\phi_j|\Big\{\delta(\boldsymbol{r}-\boldsymbol{r}')\hat{\boldsymbol{k}}^2+\hat{\boldsymbol{k}}'^2\delta(\boldsymbol{r}-\boldsymbol{r}')\Big\}\hat{P}_\sigma|\phi_i\phi_j\rangle$$

$$=\ -\frac{1}{8}\sum_{ij\sigma\sigma'}\int d\boldsymbol{r}\int d\boldsymbol{r}'\Big\{\phi_i^*(\boldsymbol{r}\sigma)\phi_j^*(\boldsymbol{r}'\sigma')\,\delta(\boldsymbol{r}-\boldsymbol{r}')\Big(\overrightarrow{\boldsymbol{\nabla}}^2+\overrightarrow{\boldsymbol{\nabla}}'^2-2\overrightarrow{\boldsymbol{\nabla}}\cdot\overrightarrow{\boldsymbol{\nabla}}'\Big)\phi_i(\boldsymbol{r}\sigma')\phi_j(\boldsymbol{r}'\sigma)$$

$$+\phi_i^*(\boldsymbol{r}\sigma)\phi_j^*(\boldsymbol{r}'\sigma')\Big(\overleftarrow{\boldsymbol{\nabla}}^2+\overleftarrow{\boldsymbol{\nabla}}'^2-2\overleftarrow{\boldsymbol{\nabla}}\cdot\overleftarrow{\boldsymbol{\nabla}}'\Big)\delta(\boldsymbol{r}-\boldsymbol{r}')\,\phi_i(\boldsymbol{r}\sigma')\phi_j(\boldsymbol{r}'\sigma)\Big\}$$

$$=\ -\frac{1}{4}\sum_{\sigma\sigma'}\int d\boldsymbol{r}\Big\{\sum_i\Big(\phi_i^*(\boldsymbol{r}\sigma)\,\triangle\,\phi_i(\boldsymbol{r}\sigma')+\phi_i(\boldsymbol{r}\sigma')\,\triangle\,\phi_i^*(\boldsymbol{r}\sigma)\Big)\sum_j\phi_j^*(\boldsymbol{r}\sigma')\phi_j(\boldsymbol{r}\sigma)$$

$$-\sum_i\phi_i^*(\boldsymbol{r}\sigma)\boldsymbol{\nabla}\phi_i(\boldsymbol{r}\sigma')\cdot\sum_j\phi_j^*(\boldsymbol{r}\sigma')\boldsymbol{\nabla}\phi_j(\boldsymbol{r}\sigma)$$

$$-\sum_i\phi_i(\boldsymbol{r}\sigma')\boldsymbol{\nabla}\phi_i^*(\boldsymbol{r}\sigma)\cdot\sum_j\phi_j(\boldsymbol{r}\sigma)\boldsymbol{\nabla}\phi_j^*(\boldsymbol{r}\sigma')\Big\}$$

$$=\ -\frac{1}{4}\sum_{\sigma\sigma'}\int d\boldsymbol{r}\Big\{\Big(\triangle\rho_{\sigma\sigma'}(\boldsymbol{r})-2\tau_{\sigma\sigma'}(\boldsymbol{r})\Big)\rho_{\sigma'\sigma}(\boldsymbol{r})$$

$$-\Big(\frac{1}{2}\boldsymbol{\nabla}\rho_{\sigma\sigma'}(\boldsymbol{r})+\mathrm{i}\boldsymbol{j}_{\sigma\sigma'}(\boldsymbol{r})\Big)\Big(\frac{1}{2}\boldsymbol{\nabla}\rho_{\sigma'\sigma}(\boldsymbol{r})+\mathrm{i}\boldsymbol{j}_{\sigma'\sigma}(\boldsymbol{r})\Big)$$

$$-\Big(\frac{1}{2}\boldsymbol{\nabla}\rho_{\sigma\sigma'}(\boldsymbol{r})-\mathrm{i}\boldsymbol{j}_{\sigma\sigma'}(\boldsymbol{r})\Big)\Big(\frac{1}{2}\boldsymbol{\nabla}\rho_{\sigma'\sigma}(\boldsymbol{r})-\mathrm{i}\boldsymbol{j}_{\sigma'\sigma}(\boldsymbol{r})\Big)\Big\}$$

$$=\ -\frac{1}{4}\sum_{\sigma\sigma'}\int d\boldsymbol{r}\Big\{\rho_{\sigma'\sigma}(\boldsymbol{r})\,\triangle\,\rho_{\sigma\sigma'}(\boldsymbol{r})-2\rho_{\sigma'\sigma}(\boldsymbol{r})\tau_{\sigma\sigma'}(\boldsymbol{r})-\frac{1}{2}\boldsymbol{\nabla}\rho_{\sigma\sigma'}(\boldsymbol{r})\cdot\boldsymbol{\nabla}\rho_{\sigma'\sigma}(\boldsymbol{r})+2\boldsymbol{j}_{\sigma\sigma'}(\boldsymbol{r})\cdot\boldsymbol{j}_{\sigma'\sigma}(\boldsymbol{r})\Big\}$$

$$=\ -\frac{1}{4}\sum_{\sigma\sigma'}\int d\boldsymbol{r}\Big\{-\frac{3}{2}\boldsymbol{\nabla}\rho_{\sigma\sigma'}(\boldsymbol{r})\cdot\boldsymbol{\nabla}\rho_{\sigma'\sigma}(\boldsymbol{r})-2\rho_{\sigma'\sigma}(\boldsymbol{r})\tau_{\sigma\sigma'}(\boldsymbol{r})+2\boldsymbol{j}_{\sigma\sigma'}(\boldsymbol{r})\cdot\boldsymbol{j}_{\sigma'\sigma}(\boldsymbol{r})\Big\}$$

$$=\ -\frac{1}{4}\int d\boldsymbol{r}\Big\{-\frac{3}{4}\Big[\Big(\boldsymbol{\nabla}\rho(\boldsymbol{r})\Big)^2+\sum_{\mu\nu}\Big(\partial_\mu s_\nu(\boldsymbol{r})\Big)^2\Big]$$

$$-\Big[\rho(\boldsymbol{r})\tau(\boldsymbol{r})+\boldsymbol{s}(\boldsymbol{r})\cdot\boldsymbol{T}(\boldsymbol{r})\Big]+\Big[\boldsymbol{j}^2(\boldsymbol{r})+\sum_{\mu\nu}\Big(J_{\mu\nu}(\boldsymbol{r})\Big)^2\Big]\Big\}$$

$$=\ \frac{1}{4}\int d\boldsymbol{r}\Big[-\frac{3}{4}\rho(\boldsymbol{r})\,\triangle\,\rho(\boldsymbol{r})-\frac{3}{4}\boldsymbol{s}(\boldsymbol{r})\cdot\triangle\boldsymbol{s}(\boldsymbol{r})$$

$$+\Big(\rho(\boldsymbol{r})\tau(\boldsymbol{r})-\boldsymbol{j}^2(\boldsymbol{r})\Big)+\Big(\boldsymbol{s}(\boldsymbol{r})\cdot\boldsymbol{T}(\boldsymbol{r})-\overleftrightarrow{\mathcal{J}}^2(\boldsymbol{r})\Big)\Big], \tag{B.2.18}$$

where, in the third equality, we have used Eqs. (B.1.53), (B.1.47), and (B.1.48) and, in the sixth equality, we have used Eqs. (B.1.38), (B.1.33), and (B.1.40). In the last equality, we have taken integration by parts of Eq. (B.2.17) and

$$\int d\boldsymbol{r}\sum_{\mu\nu}\partial_\mu s_\nu(\boldsymbol{r})\partial_\mu s_\nu(\boldsymbol{r})\ =\ \sum_{\mu\nu}s_\nu(\boldsymbol{r})\partial_\mu s_\nu(\boldsymbol{r})\Big|_{\boldsymbol{r}\to\infty}-\int d\boldsymbol{r}\sum_{\mu\nu}s_\nu(\boldsymbol{r})\partial_\mu^2 s_\nu(\boldsymbol{r})$$

$$=\ -\int d\boldsymbol{r}\,\boldsymbol{s}(\boldsymbol{r})\cdot\triangle\boldsymbol{s}(\boldsymbol{r}). \tag{B.2.19}$$

The Laplacian of the spin density, $\triangle\boldsymbol{s}(\boldsymbol{r})$, denotes the spin density with components $\triangle s_\nu(\boldsymbol{r})$, that is, the Laplacian is considered to act to each component of $\boldsymbol{s}(\boldsymbol{r})$. The exchange terms in $\langle\Phi|\hat{V}_1|\Phi\rangle$

without and with the spin exchange operator $\hat{P}_\sigma$ are, respectively, calculated as

$$\sum_{i<j}\langle\phi_i\phi_j|\Big\{\delta(\boldsymbol{r}-\boldsymbol{r}')\hat{\boldsymbol{k}}^2+\hat{\boldsymbol{k}}'^2\delta(\boldsymbol{r}-\boldsymbol{r}')\Big\}|\phi_j\phi_i\rangle$$

$$=\sum_{i<j}\langle\phi_i\phi_j|\Big\{\delta(\boldsymbol{r}-\boldsymbol{r}')\hat{\boldsymbol{k}}^2+\hat{\boldsymbol{k}}'^2\delta(\boldsymbol{r}-\boldsymbol{r}')\Big\}\hat{P}_{\boldsymbol{r}}\hat{P}_\sigma\delta_{q_iq_j}|\phi_i\phi_j\rangle$$

$$=\frac{1}{4}\int d\boldsymbol{r}\sum_q\Big\{-\frac{3}{4}\rho^{(q)}(\boldsymbol{r})\,\triangle\,\rho^{(q)}(\boldsymbol{r})-\frac{3}{4}\boldsymbol{s}^{(q)}(\boldsymbol{r})\cdot\triangle\boldsymbol{s}^{(q)}(\boldsymbol{r})$$

$$+\Big(\rho^{(q)}(\boldsymbol{r})\tau^{(q)}(\boldsymbol{r})-\boldsymbol{j}^{(q)2}(\boldsymbol{r})\Big)+\Big(\boldsymbol{s}^{(q)}(\boldsymbol{r})\cdot\boldsymbol{T}^{(q)}(\boldsymbol{r})-\overleftrightarrow{J}^{(q)2}(\boldsymbol{r})\Big)\Big\}\quad\text{(B.2.20)}$$

and

$$\sum_{i<j}\langle\phi_i\phi_j|\Big\{\delta(\boldsymbol{r}-\boldsymbol{r}')\hat{\boldsymbol{k}}^2+\hat{\boldsymbol{k}}'^2\delta(\boldsymbol{r}-\boldsymbol{r}')\Big\}\hat{P}_\sigma|\phi_j\phi_i\rangle$$

$$=\sum_{i<j}\langle\phi_i\phi_j|\Big\{\delta(\boldsymbol{r}-\boldsymbol{r}')\hat{\boldsymbol{k}}^2+\hat{\boldsymbol{k}}'^2\delta(\boldsymbol{r}-\boldsymbol{r}')\Big\}\hat{P}_{\boldsymbol{r}}\delta_{q_iq_j}|\phi_i\phi_j\rangle$$

$$=\frac{1}{2}\int d\boldsymbol{r}\sum_q\Big\{-\frac{3}{4}\rho^{(q)}(\boldsymbol{r})\,\triangle\,\rho^{(q)}(\boldsymbol{r})+\rho^{(q)}(\boldsymbol{r})\tau^{(q)}(\boldsymbol{r})-\boldsymbol{j}^{(q)2}(\boldsymbol{r})\Big\}.\quad\text{(B.2.21)}$$

We note that the existence of the spatial coordinates exchange operator, $\hat{P}_{\boldsymbol{r}}$, does not affect the calculation, because the operator is symmetric under the exchange of the spatial coordinates as in the case of t_0 and t_3 terms.

By summing up these results, Eqs. (B.2.16), (B.2.18), (B.2.20), and (B.2.21), multiplying by proper coefficients, the expectation value of the t_1 term of the Skyrme effective interaction is found to be

t_1 **term :**

$$\langle\Phi|\hat{V}_1|\Phi\rangle = \langle\Phi|\sum_{i<j}\frac{1}{2}t_1(1+x_1\hat{P}_\sigma)\Big\{\delta(\boldsymbol{r}_i-\boldsymbol{r}_j)\hat{\boldsymbol{k}}^2+\hat{\boldsymbol{k}}'^2\delta(\boldsymbol{r}_i-\boldsymbol{r}_j)\Big\}|\Phi\rangle$$

$$=\frac{1}{4}t_1\int d\boldsymbol{r}\Big[-\frac{3}{4}\Big(1+\frac{1}{2}x_1\Big)\rho(\boldsymbol{r})\,\triangle\,\rho(\boldsymbol{r})-\frac{3}{8}x_1\boldsymbol{s}(\boldsymbol{r})\cdot\triangle\boldsymbol{s}(\boldsymbol{r})$$

$$+\Big(1+\frac{1}{2}x_1\Big)\{\rho(\boldsymbol{r})\tau(\boldsymbol{r})-\boldsymbol{j}^2(\boldsymbol{r})\}+\frac{1}{2}x_1\{\boldsymbol{s}(\boldsymbol{r})\cdot\boldsymbol{T}(\boldsymbol{r})-\overleftrightarrow{J}^2(\boldsymbol{r})\}$$

$$-\sum_q\Big\{-\frac{3}{4}\Big(\frac{1}{2}+x_1\Big)\rho^{(q)}(\boldsymbol{r})\,\triangle\,\rho^{(q)}(\boldsymbol{r})-\frac{3}{8}\boldsymbol{s}^{(q)}(\boldsymbol{r})\cdot\triangle\boldsymbol{s}^{(q)}(\boldsymbol{r})$$

$$+\Big(\frac{1}{2}+x_1\Big)\{\rho^{(q)}(\boldsymbol{r})\tau^{(q)}(\boldsymbol{r})-\boldsymbol{j}^{(q)2}(\boldsymbol{r})\}$$

$$+\frac{1}{2}\{\boldsymbol{s}^{(q)}(\boldsymbol{r})\cdot\boldsymbol{T}^{(q)}(\boldsymbol{r})-\overleftrightarrow{J}^{(q)2}(\boldsymbol{r})\}\Big\}\Big].\quad\text{(B.2.22)}$$

The t_2 term (the other non-local term)

We next calculate the expectation value of the t_2 term,

$$\hat{V}_2 \equiv \sum_{i<j} t_2(1 + x_2\hat{P}_\sigma)\hat{\boldsymbol{k}}' \cdot \delta(\boldsymbol{r}_i - \boldsymbol{r}_j)\,\hat{\boldsymbol{k}}. \tag{B.2.23}$$

We first consider the direct term in $\langle\Phi|\hat{V}_2|\Phi\rangle$. The direct term of the first term in $\hat{V}_2$ without the spin exchange operator $\hat{P}_\sigma$ is calculated as

$$\sum_{i<j}\langle\phi_i\phi_j|\hat{\boldsymbol{k}}' \cdot \delta(\boldsymbol{r} - \boldsymbol{r}')\hat{\boldsymbol{k}}|\phi_i\phi_j\rangle$$

$$= \frac{1}{8}\sum_{ij\sigma\sigma'}\int d\boldsymbol{r}\int d\boldsymbol{r}'\phi_i^*(\boldsymbol{r}\sigma)\phi_j^*(\boldsymbol{r}'\sigma')(\overleftarrow{\boldsymbol{\nabla}} - \overleftarrow{\boldsymbol{\nabla}}') \cdot \delta(\boldsymbol{r} - \boldsymbol{r}')(\overrightarrow{\boldsymbol{\nabla}} - \overrightarrow{\boldsymbol{\nabla}}')\phi_i(\boldsymbol{r}\sigma)\phi_j(\boldsymbol{r}'\sigma')$$

$$= \frac{1}{8}\sum_{ij\sigma\sigma'}\int d\boldsymbol{r}\left\{\left(\boldsymbol{\nabla}\phi_i^*(\boldsymbol{r}\sigma)\phi_j^*(\boldsymbol{r}\sigma') - \phi_i^*(\boldsymbol{r}\sigma)\boldsymbol{\nabla}\phi_j^*(\boldsymbol{r}\sigma')\right)\right.$$

$$\left. \cdot\left(\boldsymbol{\nabla}\phi_i(\boldsymbol{r}\sigma)\phi_j(\boldsymbol{r}\sigma') - \phi_i(\boldsymbol{r}\sigma)\boldsymbol{\nabla}\phi_j(\boldsymbol{r}\sigma')\right)\right\}$$

$$= \frac{1}{8}\sum_{ij\sigma\sigma'}\int d\boldsymbol{r}\left\{\boldsymbol{\nabla}\phi_i^*(\boldsymbol{r}\sigma) \cdot \boldsymbol{\nabla}\phi_i(\boldsymbol{r}\sigma)\,\phi_j^*(\boldsymbol{r}\sigma')\phi_j(\boldsymbol{r}\sigma') - \boldsymbol{\nabla}\phi_i^*(\boldsymbol{r}\sigma)\phi_i(\boldsymbol{r}\sigma) \cdot \phi_j^*(\boldsymbol{r}\sigma')\boldsymbol{\nabla}\phi_j(\boldsymbol{r}\sigma')\right.$$

$$\left. -\phi_i^*(\boldsymbol{r}\sigma)\boldsymbol{\nabla}\phi_i(\boldsymbol{r}\sigma) \cdot \boldsymbol{\nabla}\phi_j^*(\boldsymbol{r}\sigma')\phi_j(\boldsymbol{r}\sigma') + \phi_i^*(\boldsymbol{r}\sigma)\phi_i(\boldsymbol{r}\sigma)\,\boldsymbol{\nabla}\phi_j^*(\boldsymbol{r}\sigma') \cdot \boldsymbol{\nabla}\phi_j(\boldsymbol{r}\sigma')\right\}$$

$$= \frac{1}{8}\int d\boldsymbol{r}\left\{\sum_{i\sigma}\boldsymbol{\nabla}\phi_i^*(\boldsymbol{r}\sigma) \cdot \boldsymbol{\nabla}\phi_i(\boldsymbol{r}\sigma)\sum_{j\sigma'}\phi_j^*(\boldsymbol{r}\sigma')\phi_j(\boldsymbol{r}\sigma')\right.$$

$$-\sum_{i\sigma}\phi_i(\boldsymbol{r}\sigma)\boldsymbol{\nabla}\phi_i^*(\boldsymbol{r}\sigma) \cdot \sum_{j\sigma'}\phi_j^*(\boldsymbol{r}\sigma')\boldsymbol{\nabla}\phi_j(\boldsymbol{r}\sigma')$$

$$-\sum_{i\sigma}\phi_i^*(\boldsymbol{r}\sigma)\boldsymbol{\nabla}\phi_i(\boldsymbol{r}\sigma) \cdot \sum_{j\sigma'}\phi_j(\boldsymbol{r}\sigma')\boldsymbol{\nabla}\phi_j^*(\boldsymbol{r}\sigma')$$

$$\left. +\sum_{i\sigma}\phi_i^*(\boldsymbol{r}\sigma)\phi_i(\boldsymbol{r}\sigma)\sum_{j\sigma'}\boldsymbol{\nabla}\phi_j^*(\boldsymbol{r}\sigma') \cdot \boldsymbol{\nabla}\phi_j(\boldsymbol{r}\sigma')\right\}$$

$$= \frac{1}{4}\int d\boldsymbol{r}\left\{\rho(\boldsymbol{r})\tau(\boldsymbol{r}) - \left(\frac{1}{2}\boldsymbol{\nabla}\rho(\boldsymbol{r}) - \mathrm{i}\boldsymbol{j}(\boldsymbol{r})\right) \cdot \left(\frac{1}{2}\boldsymbol{\nabla}\rho(\boldsymbol{r}) + \mathrm{i}\boldsymbol{j}(\boldsymbol{r})\right)\right\}$$

$$= \frac{1}{4}\int d\boldsymbol{r}\left[\rho(\boldsymbol{r})\tau(\boldsymbol{r}) - \boldsymbol{j}^2(\boldsymbol{r}) + \frac{1}{4}\rho(\boldsymbol{r})\triangle\rho(\boldsymbol{r})\right], \tag{B.2.24}$$

where, in the fifth equality, we have utilized the relations of Eqs. (B.1.46) and (B.1.45). In the last equality, we have taken the integration by parts of Eq. (B.2.17). The direct term of the second term

in $\hat{V}_2$ with the spin exchange operator $\hat{P}_\sigma$ is calculated as

$$
\sum_{i<j}\langle\phi_i\phi_j|\hat{\boldsymbol{k}}'\cdot\delta(\boldsymbol{r}-\boldsymbol{r}')\hat{\boldsymbol{k}}\,\hat{P}_\sigma|\phi_i\phi_j\rangle
$$

$$
= \frac{1}{8}\sum_{ij\sigma\sigma'}\int d\boldsymbol{r}\int d\boldsymbol{r}'\phi_i^*(\boldsymbol{r}\sigma)\phi_j^*(\boldsymbol{r}'\sigma')(\overleftarrow{\boldsymbol{\nabla}}-\overleftarrow{\boldsymbol{\nabla}}')\cdot\delta(\boldsymbol{r}-\boldsymbol{r}')(\overrightarrow{\boldsymbol{\nabla}}-\overrightarrow{\boldsymbol{\nabla}}')\phi_i(\boldsymbol{r}\sigma')\phi_j(\boldsymbol{r}'\sigma)
$$

$$
= \frac{1}{8}\int d\boldsymbol{r}\Big\{\sum_{i\sigma}\boldsymbol{\nabla}\phi_i^*(\boldsymbol{r}\sigma)\cdot\boldsymbol{\nabla}\phi_i(\boldsymbol{r}\sigma')\sum_{j\sigma'}\phi_j^*(\boldsymbol{r}\sigma')\phi_j(\boldsymbol{r}\sigma)
$$

$$
-\sum_{i\sigma}\phi_i(\boldsymbol{r}\sigma')\boldsymbol{\nabla}\phi_i^*(\boldsymbol{r}\sigma)\cdot\sum_{j\sigma'}\phi_j^*(\boldsymbol{r}\sigma')\boldsymbol{\nabla}\phi_j(\boldsymbol{r}\sigma)
$$

$$
-\sum_{i\sigma}\phi_i^*(\boldsymbol{r}\sigma)\boldsymbol{\nabla}\phi_i(\boldsymbol{r}\sigma')\cdot\sum_{j\sigma'}\phi_j(\boldsymbol{r}\sigma)\boldsymbol{\nabla}\phi_j^*(\boldsymbol{r}\sigma')
$$

$$
+\sum_{i\sigma}\phi_i^*(\boldsymbol{r}\sigma)\phi_i(\boldsymbol{r}\sigma')\sum_{j\sigma'}\boldsymbol{\nabla}\phi_j^*(\boldsymbol{r}\sigma')\cdot\boldsymbol{\nabla}\phi_j(\boldsymbol{r}\sigma)\Big\}
$$

$$
= \frac{1}{8}\sum_{\sigma\sigma'}\int d\boldsymbol{r}\Big\{\rho_{\sigma'\sigma}(\boldsymbol{r})\tau_{\sigma\sigma'}(\boldsymbol{r})-\Big(\frac{1}{2}\boldsymbol{\nabla}\rho_{\sigma\sigma'}(\boldsymbol{r})-\mathrm{i}\boldsymbol{j}_{\sigma\sigma'}(\boldsymbol{r})\Big)\cdot\Big(\frac{1}{2}\boldsymbol{\nabla}\rho_{\sigma'\sigma}(\boldsymbol{r})+\mathrm{i}\boldsymbol{j}_{\sigma'\sigma}(\boldsymbol{r})\Big)
$$

$$
-\Big(\frac{1}{2}\boldsymbol{\nabla}\rho_{\sigma\sigma'}(\boldsymbol{r})+\mathrm{i}\boldsymbol{j}_{\sigma\sigma'}(\boldsymbol{r})\Big)\cdot\Big(\frac{1}{2}\boldsymbol{\nabla}\rho_{\sigma'\sigma}(\boldsymbol{r})-\mathrm{i}\boldsymbol{j}_{\sigma'\sigma}(\boldsymbol{r})\Big)+\rho_{\sigma\sigma'}(\boldsymbol{r})\tau_{\sigma'\sigma}(\boldsymbol{r})\Big\}
$$

$$
= \frac{1}{4}\sum_{\sigma\sigma'}\int d\boldsymbol{r}\Big\{\rho_{\sigma\sigma'}(\boldsymbol{r})\tau_{\sigma'\sigma}(\boldsymbol{r})-\frac{1}{4}\boldsymbol{\nabla}\rho_{\sigma\sigma'}(\boldsymbol{r})\cdot\boldsymbol{\nabla}\rho_{\sigma'\sigma}(\boldsymbol{r})-\boldsymbol{j}_{\sigma\sigma'}(\boldsymbol{r})\cdot\boldsymbol{j}_{\sigma'\sigma}(\boldsymbol{r})\Big\}
$$

$$
= \frac{1}{4}\int d\boldsymbol{r}\Big[\frac{1}{2}\Big\{\rho(\boldsymbol{r})\tau(\boldsymbol{r})+\boldsymbol{s}(\boldsymbol{r})\cdot\boldsymbol{T}(\boldsymbol{r})\Big\}
$$

$$
-\frac{1}{8}\Big\{\big(\boldsymbol{\nabla}\rho(\boldsymbol{r})\big)^2+\sum_{\mu\nu}\big(\partial_\mu s_\nu(\boldsymbol{r})\big)^2\Big\}-\frac{1}{2}\Big\{\boldsymbol{j}^2(\boldsymbol{r})+\sum_{\mu\nu}\big(J_{\mu\nu}(\boldsymbol{r})\big)^2\Big\}\Big]
$$

$$
= \frac{1}{8}\int d\boldsymbol{r}\Big[\rho(\boldsymbol{r})\tau(\boldsymbol{r})-\boldsymbol{j}^2(\boldsymbol{r})+\boldsymbol{s}(\boldsymbol{r})\cdot\boldsymbol{T}(\boldsymbol{r})-\overleftrightarrow{\mathcal{J}}^2(\boldsymbol{r})+\frac{1}{4}\big(\rho(\boldsymbol{r})\triangle\rho(\boldsymbol{r})+\boldsymbol{s}(\boldsymbol{r})\cdot\triangle\boldsymbol{s}(\boldsymbol{r})\big)\Big],
$$

$$(\text{B.2.25})$$

where, in the third equality, we have used the relations of Eqs. (B.1.48) and (B.1.47). In the fifth equality, we have used the relations of Eqs. (B.1.33), (B.1.38), and (B.1.40). The exchange terms of the first and second terms in $\hat{V}_2$ without and with the spin exchange operator are calculated as

$$
\sum_{i<j}\langle\phi_i\phi_j|\hat{\boldsymbol{k}}'\cdot\delta(\boldsymbol{r}-\boldsymbol{r}')\hat{\boldsymbol{k}}|\phi_j\phi_i\rangle
$$

$$
= \sum_{i<j}\langle\phi_i\phi_j|\hat{\boldsymbol{k}}'\cdot\delta(\boldsymbol{r}-\boldsymbol{r}')\hat{\boldsymbol{k}}\,\hat{P}_{\boldsymbol{r}}\hat{P}_\sigma\delta_{q_iq_j}|\phi_i\phi_j\rangle
$$

$$
= -\int d\boldsymbol{r}\sum_q\Big\{\frac{1}{8}\big(\rho^{(q)}(\boldsymbol{r})\tau^{(q)}(\boldsymbol{r})-\boldsymbol{j}^{(q)2}(\boldsymbol{r})\big)+\frac{1}{8}\big(\boldsymbol{s}^{(q)}(\boldsymbol{r})\cdot\boldsymbol{T}^{(q)}(\boldsymbol{r})-\overleftrightarrow{\mathcal{J}}^{(q)2}(\boldsymbol{r})\big)
$$

$$
+\frac{1}{32}\big(\rho^{(q)}(\boldsymbol{r})\triangle\rho^{(q)}(\boldsymbol{r})+\boldsymbol{s}^{(q)}(\boldsymbol{r})\cdot\triangle\boldsymbol{s}^{(q)}(\boldsymbol{r})\big)\Big\}
$$

$$(\text{B.2.26})$$

and

$$\sum_{i<j}\langle\phi_i\phi_j|\hat{\boldsymbol{k}}'\cdot\delta(\boldsymbol{r}-\boldsymbol{r}')\hat{\boldsymbol{k}}\,\hat{P}_\sigma|\phi_i\phi_j\rangle$$

$$=\sum_{i<j}\langle\phi_i\phi_j|\hat{\boldsymbol{k}}'\cdot\delta(\boldsymbol{r}-\boldsymbol{r}')\hat{\boldsymbol{k}}\,\hat{P}_{\boldsymbol{r}}\delta_{q_iq_j}|\phi_i\phi_j\rangle$$

$$=-\frac{1}{4}\int d\boldsymbol{r}\sum_q\Big\{\rho^{(q)}(\boldsymbol{r})\tau^{(q)}(\boldsymbol{r})-\boldsymbol{j}^{(q)2}(\boldsymbol{r})+\frac{1}{4}\rho^{(q)}(\boldsymbol{r})\triangle\rho^{(q)}(\boldsymbol{r})\Big\}. \tag{B.2.27}$$

We note that the existence of the spatial coordinates exchange operator, $\hat{P}_{\boldsymbol{r}}$, in this case, generates an additional minus sign for the whole result compared with the direct term, because now the operator $\hat{V}_2$ contains $\hat{\boldsymbol{k}}$ acting to the right which is antisymmetric under the exchange of the spatial coordinates in the ket states.

By summing up these results, Eqs. (B.2.24)-(B.2.27), multiplying by proper coefficients, the expectation value of the t_2 term of the Skyrme effective interaction is found to be

---

t_2 term :

$$\langle\Phi|\hat{V}_2|\Phi\rangle=\langle\Phi|\sum_{i<j}t_2(1+x_2\hat{P}_\sigma)\hat{\boldsymbol{k}}'\cdot\delta(\boldsymbol{r}_i-\boldsymbol{r}_j)\hat{\boldsymbol{k}}|\Phi\rangle$$

$$=\frac{1}{2}t_2\int d\boldsymbol{r}\bigg[\frac{1}{8}\Big(1+\frac{1}{2}x_2\Big)\rho(\boldsymbol{r})\triangle\rho(\boldsymbol{r})+\frac{1}{16}x_2\boldsymbol{s}(\boldsymbol{r})\cdot\triangle\boldsymbol{s}(\boldsymbol{r})$$

$$+\frac{1}{2}\Big(1+\frac{1}{2}x_2\Big)\big\{\rho(\boldsymbol{r})\tau(\boldsymbol{r})-\boldsymbol{j}^2(\boldsymbol{r})\big\}+\frac{1}{4}x_2\big\{\boldsymbol{s}(\boldsymbol{r})\cdot\boldsymbol{T}(\boldsymbol{r})-\overleftrightarrow{\mathcal{J}}^2(\boldsymbol{r})\big\}$$

$$+\sum_q\Big\{\frac{1}{8}\Big(\frac{1}{2}+x_2\Big)\rho^{(q)}(\boldsymbol{r})\triangle\rho^{(q)}(\boldsymbol{r})+\frac{1}{16}\boldsymbol{s}^{(q)}(\boldsymbol{r})\cdot\triangle\boldsymbol{s}^{(q)}(\boldsymbol{r})$$

$$+\frac{1}{2}\Big(\frac{1}{2}+x_2\Big)\big\{\rho^{(q)}(\boldsymbol{r})\tau^{(q)}(\boldsymbol{r})-\boldsymbol{j}^{(q)2}(\boldsymbol{r})\big\}$$

$$+\frac{1}{4}\big\{\boldsymbol{s}^{(q)}(\boldsymbol{r})\cdot\boldsymbol{T}^{(q)}(\boldsymbol{r})-\overleftrightarrow{\mathcal{J}}^{(q)2}(\boldsymbol{r})\big\}\Big\}\bigg]. \tag{B.2.28}$$

The W_0 (or t_4) term (the spin-orbit term)

Finally, we consider the expectation value of the spin-orbit term,

$$\hat{V}_{\mathrm{so}} \equiv \sum_{i<j} \mathrm{i} W_0 (\hat{\boldsymbol{\sigma}}_i + \hat{\boldsymbol{\sigma}}_j) \cdot \{\hat{\boldsymbol{k}}' \times \delta(\boldsymbol{r}_i - \boldsymbol{r}_j)\hat{\boldsymbol{k}}\}. \tag{B.2.29}$$

The direct term in $\langle \Phi | \hat{V}_{\mathrm{so}} | \Phi \rangle$ is calculated as

$$
\begin{aligned}
&\sum_{i<j} \langle \phi_i \phi_j | (\hat{\boldsymbol{\sigma}} + \hat{\boldsymbol{\sigma}}') \cdot \{\hat{\boldsymbol{k}}' \times \delta(\boldsymbol{r} - \boldsymbol{r}')\hat{\boldsymbol{k}}\} | \phi_i \phi_j \rangle \\
&= \frac{1}{8} \sum_{ij\sigma_1\sigma_1'\sigma_2\sigma_2'} \int d\boldsymbol{r} \int d\boldsymbol{r}' \{\phi_i^*(\boldsymbol{r}\sigma_1)\phi_j^*(\boldsymbol{r}'\sigma_2)(\overleftarrow{\boldsymbol{\nabla}} - \overleftarrow{\boldsymbol{\nabla}}') \times \delta(\boldsymbol{r}-\boldsymbol{r}')(\overrightarrow{\boldsymbol{\nabla}} - \overrightarrow{\boldsymbol{\nabla}}') \phi_i(\boldsymbol{r}\sigma_1')\phi_j(\boldsymbol{r}'\sigma_2')\} \\
&\qquad\qquad\qquad \cdot \left(\langle\sigma_1|\hat{\boldsymbol{\sigma}}|\sigma_1'\rangle\langle\sigma_2|\sigma_2'\rangle + \langle\sigma_1|\sigma_1'\rangle\langle\sigma_2|\hat{\boldsymbol{\sigma}}|\sigma_2'\rangle \right) \\
&= \frac{1}{8} \sum_{ij\sigma_1\sigma_1'\sigma_2\sigma_2'} \int d\boldsymbol{r} \left(\boldsymbol{\nabla}\phi_i^*(\boldsymbol{r}\sigma_1)\phi_j^*(\boldsymbol{r}\sigma_2) - \phi_i^*(\boldsymbol{r}\sigma_1)\boldsymbol{\nabla}\phi_j^*(\boldsymbol{r}\sigma_2) \right) \\
&\qquad\qquad\qquad \times \left(\boldsymbol{\nabla}\phi_i(\boldsymbol{r}\sigma_1')\phi_j(\boldsymbol{r}\sigma_2') - \phi_i(\boldsymbol{r}\sigma_1')\boldsymbol{\nabla}\phi_j(\boldsymbol{r}\sigma_2') \right) \cdot \left(\langle\sigma_1|\hat{\boldsymbol{\sigma}}|\sigma_1'\rangle\delta_{\sigma_2\sigma_2'} + \delta_{\sigma_1\sigma_1'}\langle\sigma_2|\hat{\boldsymbol{\sigma}}|\sigma_2'\rangle \right) \\
&= \frac{1}{4} \sum_{ij\sigma_1\sigma_1'\sigma_2\sigma_2'} \int d\boldsymbol{r} \Big\{ \boldsymbol{\nabla}\phi_i^*(\boldsymbol{r}\sigma_1) \times \boldsymbol{\nabla}\phi_i(\boldsymbol{r}\sigma_1')\, \phi_j^*(\boldsymbol{r}\sigma_2)\phi_j(\boldsymbol{r}\sigma_2') \\
&\qquad\qquad\qquad\quad - \boldsymbol{\nabla}\phi_i^*(\boldsymbol{r}\sigma_1)\phi_i(\boldsymbol{r}\sigma_1') \times \phi_j^*(\boldsymbol{r}\sigma_2)\boldsymbol{\nabla}\phi_j(\boldsymbol{r}\sigma_2') \Big\} \\
&\qquad\qquad\qquad \cdot \left(\langle\sigma_1|\hat{\boldsymbol{\sigma}}|\sigma_1'\rangle\delta_{\sigma_2\sigma_2'} + \delta_{\sigma_1\sigma_1'}\langle\sigma_2|\hat{\boldsymbol{\sigma}}|\sigma_2'\rangle \right) \\
&= \frac{1}{4} \int d\boldsymbol{r} \Big\{ \sum_{i\sigma_1\sigma_1'} \boldsymbol{\nabla}\phi_i^*(\boldsymbol{r}\sigma_1) \times \boldsymbol{\nabla}\phi_i(\boldsymbol{r}\sigma_1')\langle\sigma_1|\hat{\boldsymbol{\sigma}}|\sigma_1'\rangle \sum_{j\sigma_2} \phi_j^*(\boldsymbol{r}\sigma_2)\phi_j(\boldsymbol{r}\sigma_2) \\
&\qquad\qquad + \sum_{i\sigma_1} \boldsymbol{\nabla}\phi_i^*(\boldsymbol{r}\sigma_1) \times \boldsymbol{\nabla}\phi_i(\boldsymbol{r}\sigma_1) \sum_{j\sigma_2\sigma'} \phi_j^*(\boldsymbol{r}\sigma_2)\phi_j(\boldsymbol{r}\sigma_2')\langle\sigma_2|\hat{\boldsymbol{\sigma}}|\sigma_2'\rangle \\
&\qquad\qquad + \sum_{i\sigma_1\sigma_1'} \phi_i(\boldsymbol{r}\sigma_1')\boldsymbol{\nabla}\phi_i^*(\boldsymbol{r}\sigma_1) \times \langle\sigma_1|\hat{\boldsymbol{\sigma}}|\sigma_1'\rangle \cdot \sum_{j\sigma_2} \phi_j^*(\boldsymbol{r}\sigma_2)\boldsymbol{\nabla}\phi_j(\boldsymbol{r}\sigma_2) \\
&\qquad\qquad - \sum_{j\sigma_2\sigma_2'} \phi_j^*(\boldsymbol{r}\sigma_2)\boldsymbol{\nabla}\phi_j(\boldsymbol{r}\sigma_2') \times \langle\sigma_2|\hat{\boldsymbol{\sigma}}|\sigma_2'\rangle \cdot \sum_{i\sigma_1} \phi_i(\boldsymbol{r}\sigma_1)\boldsymbol{\nabla}\phi_i^*(\boldsymbol{r}\sigma_1) \Big\} \\
&= \frac{1}{4} \int d\boldsymbol{r} \Big\{ \mathrm{i}\rho(\boldsymbol{r})\boldsymbol{\nabla} \cdot \boldsymbol{J}(\boldsymbol{r}) + \mathrm{i}\boldsymbol{s}(\boldsymbol{r})\boldsymbol{\nabla} \times \boldsymbol{j}(\boldsymbol{r}) \\
&\qquad\qquad + \sum_{\lambda\mu\nu} \varepsilon_{\lambda\mu\nu} \left(\frac{1}{2}\partial_\mu s_\nu(\boldsymbol{r}) - \mathrm{i}J_{\mu\nu}(\boldsymbol{r}) \right) \left(\frac{1}{2}\partial_\lambda \rho(\boldsymbol{r}) + \mathrm{i}j_\lambda(\boldsymbol{r}) \right) \\
&\qquad\qquad - \sum_{\lambda\mu\nu} \varepsilon_{\lambda\mu\nu} \left(\frac{1}{2}\partial_\mu s_\nu(\boldsymbol{r}) + \mathrm{i}J_{\mu\nu}(\boldsymbol{r}) \right) \left(\frac{1}{2}\partial_\lambda \rho(\boldsymbol{r}) - \mathrm{i}j_\lambda(\boldsymbol{r}) \right) \Big\} \\
&= \frac{\mathrm{i}}{4} \int d\boldsymbol{r} \Big\{ \rho(\boldsymbol{r})\boldsymbol{\nabla} \cdot \boldsymbol{J}(\boldsymbol{r}) + \boldsymbol{s}(\boldsymbol{r}) \cdot \boldsymbol{\nabla} \times \boldsymbol{j}(\boldsymbol{r}) + \sum_{\lambda\mu\nu} \varepsilon_{\lambda\mu\nu} \big\{ \partial_\mu s_\nu(\boldsymbol{r})j_\lambda(\boldsymbol{r}) - J_{\mu\nu}(\boldsymbol{r})\partial_\lambda\rho(\boldsymbol{r}) \big\} \Big\} \\
&= \frac{\mathrm{i}}{4} \int d\boldsymbol{r} \Big\{ \rho(\boldsymbol{r})\boldsymbol{\nabla} \cdot \boldsymbol{J}(\boldsymbol{r}) + \boldsymbol{s}(\boldsymbol{r}) \cdot \boldsymbol{\nabla} \times \boldsymbol{j}(\boldsymbol{r}) + \sum_{\lambda\mu\nu} \varepsilon_{\lambda\mu\nu} \big\{ s_\lambda(\boldsymbol{r})\partial_\mu j_\nu(\boldsymbol{r}) + \partial_\lambda J_{\mu\nu}(\boldsymbol{r})\rho(\boldsymbol{r}) \big\} \Big\} \\
&= \frac{\mathrm{i}}{2} \int d\boldsymbol{r} \Big\{ \rho(\boldsymbol{r})\boldsymbol{\nabla} \cdot \boldsymbol{J}(\boldsymbol{r}) + \boldsymbol{s}(\boldsymbol{r}) \cdot \boldsymbol{\nabla} \times \boldsymbol{j}(\boldsymbol{r}) \Big\}, \tag{B.2.30}
\end{aligned}
$$

where, in the fourth equality, we have used the identity of triple vector products, $(\boldsymbol{A} \times \boldsymbol{B}) \cdot \boldsymbol{C} = (\boldsymbol{B} \times \boldsymbol{C}) \cdot \boldsymbol{A} = (\boldsymbol{C} \times \boldsymbol{A}) \cdot \boldsymbol{B}$. In the fifth equality, we have used the relations, Eqs. (B.1.58), (B.1.56), (B.1.50), and (B.1.49). In the seventh equality, we have taken two integrations by parts.

The exchange term in $\langle\Phi|\hat{V}_{\text{so}}|\Phi\rangle$ can be calculated in the same way as the direct term. We note that the existence of the spatial coordinates exchange operator, $\hat{P}_{\boldsymbol{r}}$, generates an additional minus sign for the whole result compared with the direct term, because the operator $\hat{V}_{\text{so}}$ contains $\hat{\boldsymbol{k}}$ acting to the right which is antisymmetric under the exchange of the spatial coordinates in the ket states. We also note that the spin exchange operator $\hat{P}_{\sigma}$ does not affect the calculation, because the spin part of the operator $\hat{V}_{\text{so}}$ is $(\hat{\boldsymbol{\sigma}}_i + \hat{\boldsymbol{\sigma}}_j)$ which is symmetric under the exchange of the spin coordinates in the ket states. Thus the result is given by

$$
\sum_{i<j}\big\langle\phi_i\phi_j\big|(\hat{\boldsymbol{\sigma}}+\hat{\boldsymbol{\sigma}}')\cdot\big\{\hat{\boldsymbol{k}}'\times\delta(\boldsymbol{r}-\boldsymbol{r}')\hat{\boldsymbol{k}}\big\}\big|\phi_j\phi_i\big\rangle
$$

$$
=\ \sum_{i<j}\big\langle\phi_i\phi_j\big|(\hat{\boldsymbol{\sigma}}+\hat{\boldsymbol{\sigma}}')\cdot\big\{\hat{\boldsymbol{k}}'\times\delta(\boldsymbol{r}-\boldsymbol{r}')\hat{\boldsymbol{k}}\big\}\hat{P}_{\boldsymbol{r}}\hat{P}_{\sigma}\hat{P}_{q_i q_j}\big|\phi_i\phi_j\big\rangle
$$

$$
=\ -\frac{\mathrm{i}}{2}\int d\boldsymbol{r}\sum_q\Big\{\rho^{(q)}(\boldsymbol{r})\boldsymbol{\nabla}\cdot\boldsymbol{J}^{(q)}(\boldsymbol{r})+\boldsymbol{s}^{(q)}(\boldsymbol{r})\cdot\boldsymbol{\nabla}\times\boldsymbol{j}^{(q)}(\boldsymbol{r})\Big\}. \tag{B.2.31}
$$

The expectation value of the spin-orbit term of the Skyrme effective interaction, which proportional to the coefficient W_0, leads

spin-orbit term :

$$
\Big\langle\Phi\Big|\sum_{i<j}\mathrm{i}W_0(\hat{\boldsymbol{\sigma}}_i+\hat{\boldsymbol{\sigma}}_j)\cdot\big\{\hat{\boldsymbol{k}}'\times\delta(\boldsymbol{r}_i-\boldsymbol{r}_j)\hat{\boldsymbol{k}}\big\}\Big|\Phi\Big\rangle
$$

$$
=-\frac{1}{2}W_0\int d\boldsymbol{r}\bigg[\,\rho(\boldsymbol{r})\boldsymbol{\nabla}\cdot\boldsymbol{J}(\boldsymbol{r})+\boldsymbol{s}(\boldsymbol{r})\cdot\boldsymbol{\nabla}\times\boldsymbol{j}(\boldsymbol{r})
$$

$$
+\sum_q\Big\{\rho^{(q)}(\boldsymbol{r})\boldsymbol{\nabla}\cdot\boldsymbol{J}^{(q)}(\boldsymbol{r})+\boldsymbol{s}^{(q)}(\boldsymbol{r})\cdot\boldsymbol{\nabla}\times\boldsymbol{j}^{(q)}(\boldsymbol{r})\Big\}\bigg]. \tag{B.2.32}
$$

The kinetic and Coulomb terms

In the HF theory, the Hamiltonian of the system contains the kinetic energy operator $\hat{T} = \sum_i \hat{t}(\boldsymbol{r}_i) = \sum_i \frac{-\hbar^2}{2m} \triangle_i$, where m denotes the nucleon mass and $\triangle_i$ is a Laplacian operator for the coordinates $\boldsymbol{r}_i$. Since $\hat{T}$ is a one-body operator, its expectation value is calculated as

$$
\begin{aligned}
\langle \Phi | \hat{T} | \Phi \rangle &= -\frac{\hbar^2}{2m} \int d\boldsymbol{r} \sum_{i\sigma} \phi_i^*(\boldsymbol{r}\sigma) \triangle \phi_i(\boldsymbol{r}\sigma) \\
&= \frac{\hbar^2}{2m} \int d\boldsymbol{r} \sum_{i\sigma} \boldsymbol{\nabla} \phi_i^*(\boldsymbol{r}\sigma) \cdot \boldsymbol{\nabla} \phi_i(\boldsymbol{r}\sigma) \\
&= \frac{\hbar^2}{2m} \int d\boldsymbol{r}\, \tau(\boldsymbol{r}),
\end{aligned}
\tag{B.2.33}
$$

where, in the second equality, we have taken an integration by parts.

In addition to the nuclear force, the Coulomb interaction acts between protons. The Coulomb interaction is given by

$$
\hat{V}_{\mathrm{Coul}} = \sum_{i<j} \hat{v}_{\mathrm{Coul}}(\boldsymbol{r}_i, \boldsymbol{r}_j) = \sum_{i<j} \frac{e^2}{|\boldsymbol{r}_i - \boldsymbol{r}_j|} \delta_{q_i p} \delta_{q_j p}.
\tag{B.2.34}
$$

The direct term in $\langle \Phi | \hat{V}_{\mathrm{Coul}} | \Phi \rangle$ is calculated as

$$
\begin{aligned}
E_{\mathrm{Coul}}^{\mathrm{dir}} &\equiv \sum_{i<j} \langle \phi_i \phi_j | \hat{v}_{\mathrm{Coul}} | \phi_i \phi_j \rangle \\
&= \frac{e^2}{2} \sum_{i,j \in p,\, \sigma\sigma'} \int d\boldsymbol{r} \int d\boldsymbol{r}' \frac{\phi_i^*(\boldsymbol{r}\sigma)\phi_j^*(\boldsymbol{r}'\sigma')\phi_i(\boldsymbol{r}\sigma)\phi_j(\boldsymbol{r}'\sigma')}{|\boldsymbol{r}-\boldsymbol{r}'|} \\
&= \frac{e^2}{2} \int d\boldsymbol{r} \sum_{i \in p,\, \sigma} \phi_i^*(\boldsymbol{r}\sigma)\phi_i(\boldsymbol{r}\sigma) \int d\boldsymbol{r}' \frac{1}{|\boldsymbol{r}-\boldsymbol{r}'|} \sum_{j \in p,\, \sigma'} \phi_j^*(\boldsymbol{r}'\sigma')\phi_j(\boldsymbol{r}'\sigma') \\
&= \frac{e^2}{2} \int d\boldsymbol{r}\, \rho^{(p)}(\boldsymbol{r}) \int d\boldsymbol{r}' \frac{\rho^{(p)}(\boldsymbol{r}')}{|\boldsymbol{r}-\boldsymbol{r}'|}.
\end{aligned}
\tag{B.2.35}
$$

The exchange term in $\langle \Phi | \hat{V}_{\mathrm{Coul}} | \Phi \rangle$,

$$
E_{\mathrm{Coul}}^{\mathrm{exc}} \equiv \sum_{i<j} \langle \phi_i \phi_j | \hat{v}_{\mathrm{Coul}} | \phi_j \phi_i \rangle = \frac{e^2}{2} \sum_{i,j \in p,\, \sigma\sigma'} \int d\boldsymbol{r} \int d\boldsymbol{r}' \frac{\phi_i^*(\boldsymbol{r}\sigma)\phi_j^*(\boldsymbol{r}'\sigma')\phi_j(\boldsymbol{r}\sigma)\phi_i(\boldsymbol{r}'\sigma')}{|\boldsymbol{r}-\boldsymbol{r}'|},
$$

is usually approximated by the so called Slater approximation [151]. By using the Coulomb exchange energy for a homogeneous nuclear matter which is corresponding to the so called local-density approximation (LDA), we obtain

$$
E_{\mathrm{Coul}}^{\mathrm{exc, LDA}} = -\frac{3}{4} \left(\frac{3}{\pi} \right)^{\frac{1}{3}} e^2 \int d\boldsymbol{r} \left[\rho^{(p)}(\boldsymbol{r}) \right]^{\frac{4}{3}}.
\tag{B.2.36}
$$

We thus calculate the Coulomb energy as

$$
E_{\mathrm{Coul}} \equiv \int d\boldsymbol{r}\, \mathcal{H}_{\mathrm{Coul}}(\boldsymbol{r}),
\tag{B.2.37}
$$

where the Coulomb energy density, $\mathcal{H}_{\mathrm{Coul}}(\boldsymbol{r})$, is defined by

$$
\mathcal{H}_{\mathrm{Coul}}(\boldsymbol{r}) = \frac{e^2}{2} \rho^{(p)}(\boldsymbol{r}) \left\{ \int d\boldsymbol{r}' \frac{\rho^{(p)}(\boldsymbol{r}')}{|\boldsymbol{r}-\boldsymbol{r}'|} - \frac{3}{2} \left(\frac{3}{\pi} \right)^{\frac{1}{3}} [\rho^{(p)}(\boldsymbol{r})]^{\frac{1}{3}} \right\}.
\tag{B.2.38}
$$

The resulting Skyrme EDF

By summing up these equations derived above, we obtain the Skyrme EDF:

$$E_{\mathrm{SHF}}[\rho, \tau, \boldsymbol{j}, \boldsymbol{s}, \boldsymbol{T}, \overleftrightarrow{J}] = \langle \Phi | \hat{H}_{\mathrm{Skyrme}} | \Phi \rangle = \int d\boldsymbol{r}\, \mathcal{H}(\boldsymbol{r}), \tag{B.2.39}$$

with the Skyrme Hamiltonian density, $\mathcal{H}(\boldsymbol{r})$, which takes the following form:

$$
\begin{aligned}
\mathcal{H}(\boldsymbol{r}) = {} & \frac{\hbar^2}{2m}\tau(\boldsymbol{r}) + B_1\rho^2(\boldsymbol{r}) + B_2 \sum_q \rho^{(q)2}(\boldsymbol{r}) \\
& + B_3\Big[\rho(\boldsymbol{r})\tau(\boldsymbol{r}) - \boldsymbol{j}^2(\boldsymbol{r})\Big] + B_4 \sum_q \Big[\rho^{(q)}(\boldsymbol{r})\tau^{(q)}(\boldsymbol{r}) - \boldsymbol{j}^{(q)2}(\boldsymbol{r})\Big] \\
& + B_5\rho(\boldsymbol{r}) \triangle \rho(\boldsymbol{r}) + B_6 \sum_q \rho^{(q)}(\boldsymbol{r}) \triangle \rho^{(q)}(\boldsymbol{r}) + B_7\rho^\alpha(\boldsymbol{r})\rho^2(\boldsymbol{r}) + B_8\rho^\alpha(\boldsymbol{r}) \sum_q \rho^{(q)2}(\boldsymbol{r}) \\
& + B_9\Big[\rho(\boldsymbol{r})\boldsymbol{\nabla}\cdot\boldsymbol{J}(\boldsymbol{r}) + \boldsymbol{s}(\boldsymbol{r})\cdot(\boldsymbol{\nabla}\times\boldsymbol{j}(\boldsymbol{r})) + \sum_q\Big\{\rho^{(q)}(\boldsymbol{r})\boldsymbol{\nabla}\cdot\boldsymbol{J}^{(q)}(\boldsymbol{r}) + \boldsymbol{s}^{(q)}(\boldsymbol{r})\cdot\Big(\boldsymbol{\nabla}\times\boldsymbol{j}^{(q)}(\boldsymbol{r})\Big)\Big\}\Big] \\
& + B_{10}\boldsymbol{s}^2(\boldsymbol{r}) + B_{11}\sum_q \boldsymbol{s}^{(q)2}(\boldsymbol{r}) + B_{12}\rho^\alpha(\boldsymbol{r})\boldsymbol{s}^2(\boldsymbol{r}) + B_{13}\sum_q \rho^{(q)\alpha}(\boldsymbol{r})\boldsymbol{s}^{(q)2}(\boldsymbol{r}) \\
& + B_{14}\Big[\boldsymbol{s}(\boldsymbol{r})\cdot\boldsymbol{T}(\boldsymbol{r}) - \overleftrightarrow{J}^2(\boldsymbol{r})\Big] + B_{15}\boldsymbol{s}(\boldsymbol{r})\cdot\triangle\boldsymbol{s}(\boldsymbol{r}) \\
& + B_{16}\sum_q\Big[\boldsymbol{s}^{(q)}(\boldsymbol{r})\cdot\boldsymbol{T}^{(q)}(\boldsymbol{r}) - \overleftrightarrow{J}^{(q)2}(\boldsymbol{r})\Big] + B_{17}\sum_q \boldsymbol{s}^{(q)}(\boldsymbol{r})\cdot\triangle\boldsymbol{s}^{(q)}(\boldsymbol{r}) + \mathcal{H}_{\mathrm{Coul}}(\boldsymbol{r}). \tag{B.2.40}
\end{aligned}
$$

The coefficients $B_1, \cdots, B_{17}$ are defined as follows:

$$B_1 = \frac{1}{2}t_0\Big(1 + \frac{1}{2}x_0\Big), \quad B_2 = -\frac{1}{2}t_0\Big(\frac{1}{2} + x_0\Big), \quad B_3 = \frac{1}{4}\Big\{t_1\Big(1 + \frac{1}{2}x_1\Big) + t_2\Big(1 + \frac{1}{2}x_2\Big)\Big\},$$

$$B_4 = -\frac{1}{4}\Big\{t_1\Big(\frac{1}{2} + x_1\Big) - t_2\Big(\frac{1}{2} + x_2\Big)\Big\}, \quad B_5 = -\frac{1}{16}\Big\{3t_1\Big(1 + \frac{1}{2}x_1\Big) - t_2\Big(1 + \frac{1}{2}x_2\Big)\Big\},$$

$$B_6 = \frac{1}{16}\Big\{3t_1\Big(\frac{1}{2} + x_1\Big) + t_2\Big(\frac{1}{2} + x_2\Big)\Big\}, \quad B_7 = \frac{1}{12}t_3\Big(1 + \frac{1}{2}x_3\Big), \quad B_8 = -\frac{1}{12}t_3\Big(\frac{1}{2} + x_3\Big),$$

$$B_9 = -\frac{1}{2}W_0, \quad B_{10} = \frac{1}{4}t_0x_0, \quad B_{11} = -\frac{1}{4}t_0, \quad B_{12} = \frac{1}{24}t_3x_3, \quad B_{13} = -\frac{1}{24}t_3,$$

$$B_{14} = \frac{1}{8}\left(t_1x_1 + t_2x_2\right), \quad B_{15} = -\frac{1}{32}\left(3t_1x_1 - t_2x_2\right), \quad B_{16} = -\frac{1}{8}\left(t_1 - t_2\right), \quad B_{17} = \frac{1}{32}\left(3t_1 + t_2\right).$$

In the following, we shall perform the variation of Eq. (A.4.3) with the Skyrme EDF, Eq. (B.2.39), to derive the Skyrme HF equation.

B.3   Derivation of the Skyrme Hartree-Fock equations

In this Section, we perform the variation calculations for the Skyrme EDF Eq. (B.2.40) for each term.

The kinetic term

The kinetic term is proportional to the kinetic energy density $\tau(\boldsymbol{r})$. The variation of the kinetic energy density $\tau(\boldsymbol{r})$ is calculated as

$$
\begin{aligned}
\frac{\delta}{\delta\phi_i^*(\boldsymbol{r}\sigma)} \int d\boldsymbol{r}'\, \tau(\boldsymbol{r}') &= \frac{\delta}{\delta\phi_i^*(\boldsymbol{r}\sigma)} \int d\boldsymbol{r}' \sum_{j\,\sigma'} \boldsymbol{\nabla}\phi_j^*(\boldsymbol{r}'\sigma') \cdot \boldsymbol{\nabla}\phi_j(\boldsymbol{r}'\sigma') \\
&= -\int d\boldsymbol{r}' \sum_{j\,\sigma'} \frac{\delta\phi_j^*(\boldsymbol{r}'\sigma')}{\delta\phi_i^*(\boldsymbol{r}\sigma)} \triangle \phi_j(\boldsymbol{r}'\sigma') \\
&= -\triangle\, \phi_i(\boldsymbol{r}\sigma),
\end{aligned}
\tag{B.3.1}
$$

where, in the second equality, we have taken an integration by parts to remove a nabla operator, $\boldsymbol{\nabla}$, from the $\phi_j^*(\boldsymbol{r}'\sigma')$. Here and hereafter, we frequently employ an identity,

$$
\frac{\delta\phi_j^*(\boldsymbol{r}'\sigma')}{\delta\phi_i^*(\boldsymbol{r}\sigma)} = \delta(\boldsymbol{r} - \boldsymbol{r}')\delta_{ij}\delta_{\sigma\sigma'}.
$$

The Coulomb term

From the variation of the Coulomb term, we readily obtain

$$
\frac{\delta}{\delta\phi_i^*(\boldsymbol{r}\sigma)} \int d\boldsymbol{r}'\, \mathcal{H}_{\text{Coul}}(\boldsymbol{r}') = e^2 \left\{ \int d\boldsymbol{r}' \frac{\rho^{(p)}(\boldsymbol{r}')}{|\boldsymbol{r} - \boldsymbol{r}'|} - \left(\frac{3}{\pi}\right)^{\frac{1}{3}} \left[\rho^{(p)}(\boldsymbol{r})\right]^{\frac{1}{3}} \right\} \delta_{q_i p}\, \phi_i(\boldsymbol{r}\sigma).
\tag{B.3.2}
$$

The B_1, B_2, B_{5-8} terms

The B_1 and B_2 terms are proportional to the square of the densities, $\rho^2(\boldsymbol{r})$ and $\sum_q \rho^{(q)2}(\boldsymbol{r})$, respectively. The B_5 and B_6 terms are proportional to the product of the matter density and its Laplacian, $\rho(\boldsymbol{r})\triangle\rho(\boldsymbol{r})$ and $\sum_q \rho^{(q)}(\boldsymbol{r})\triangle\rho^{(q)}(\boldsymbol{r})$, respectively. The B_7 and B_8 terms are proportional to the product of αth power of the matter density and the squared density, $\rho^\alpha(\boldsymbol{r})\rho^2(\boldsymbol{r})$ and $\rho^\alpha(\boldsymbol{r})\sum_q \rho^{(q)2}(\boldsymbol{r})$, respectively. Since they are composed only of the product of densities $\rho(\boldsymbol{r})$, we can simply evaluate variations of them using a formula for the variation of the density. The variation of the density $\rho(\boldsymbol{r}') = \sum_{j\sigma'} \phi_j^*(\boldsymbol{r}'\sigma')\phi_j(\boldsymbol{r}'\sigma')$ is calculated as

$$
\frac{\delta}{\delta\phi_i^*(\boldsymbol{r}\sigma)}\rho(\boldsymbol{r}') = \delta(\boldsymbol{r} - \boldsymbol{r}')\, \phi_i(\boldsymbol{r}\sigma),
\tag{B.3.3}
$$

$$
\frac{\delta}{\delta\phi_i^*(\boldsymbol{r}\sigma)}\rho^{(q)}(\boldsymbol{r}') = \delta(\boldsymbol{r} - \boldsymbol{r}')\delta_{qq_i}\, \phi_i(\boldsymbol{r}\sigma).
\tag{B.3.4}
$$

Then, using the Eq. (B.3.3), the variation of the squared density $\rho^2(\boldsymbol{r})$ is calculated as

$$
\begin{aligned}
\frac{\delta}{\delta\phi_i^*(\boldsymbol{r}\sigma)} \int d\boldsymbol{r}'\rho^2(\boldsymbol{r}') &= 2\int d\boldsymbol{r}'\rho(\boldsymbol{r}')\frac{\delta\rho(\boldsymbol{r}')}{\delta\phi_i^*(\boldsymbol{r}\sigma)} \\
&= 2\rho(\boldsymbol{r})\, \phi_i(\boldsymbol{r}\sigma).
\end{aligned}
\tag{B.3.5}
$$

In the same way, using the Eq. (B.3.4), we obtain

$$\frac{\delta}{\delta\phi_i^*(\boldsymbol{r}\sigma)} \int d\boldsymbol{r}' \sum_q \rho^{(q)2}(\boldsymbol{r}') = 2\rho^{(q_i)}(\boldsymbol{r})\,\phi_i(\boldsymbol{r}\sigma). \tag{B.3.6}$$

The variation of $\rho(\boldsymbol{r}) \triangle \rho(\boldsymbol{r})$ and $\sum_q \rho^{(q)}(\boldsymbol{r}) \triangle \rho^{(q)}(\boldsymbol{r})$ are, respectively, calculated as

$$\frac{\delta}{\delta\phi_i^*(\boldsymbol{r}\sigma)} \int d\boldsymbol{r}' \rho(\boldsymbol{r}') \triangle \rho(\boldsymbol{r}') = \int d\boldsymbol{r}' \left\{ \frac{\delta\rho(\boldsymbol{r}')}{\delta\phi_i^*(\boldsymbol{r}\sigma)} \triangle \rho(\boldsymbol{r}') + \triangle\rho(\boldsymbol{r}') \frac{\delta\rho(\boldsymbol{r}')}{\delta\phi_i^*(\boldsymbol{r}\sigma)} \right\}$$

$$= 2 \triangle \rho(\boldsymbol{r})\,\phi_i(\boldsymbol{r}\sigma), \tag{B.3.7}$$

$$\frac{\delta}{\delta\phi_i^*(\boldsymbol{r}\sigma)} \int d\boldsymbol{r}' \sum_q \rho^{(q)}(\boldsymbol{r}') \triangle \rho^{(q)}(\boldsymbol{r}') = 2 \triangle \rho^{(q_i)}(\boldsymbol{r})\,\phi_i(\boldsymbol{r}\sigma), \tag{B.3.8}$$

where, in the first equality, we have taken an integration by parts to remove the Laplacian operator $\triangle$ from $\rho(\boldsymbol{r}')$ sitting on the right side. Lastly, the variation of $\rho^\alpha(\boldsymbol{r})\rho^2(\boldsymbol{r})$ and $\rho^\alpha(\boldsymbol{r})\rho^{(q)2}(\boldsymbol{r})$ are, respectively, calculated as

$$\frac{\delta}{\delta\phi_i^*(\boldsymbol{r}\sigma)} \int d\boldsymbol{r}' \rho^{(\alpha+2)}(\boldsymbol{r}') = (\alpha+2) \int d\boldsymbol{r}' \rho^{(\alpha+1)}(\boldsymbol{r}') \frac{\delta\rho(\boldsymbol{r}')}{\delta\phi_i^*(\boldsymbol{r}\sigma)}$$

$$= (\alpha+2)\rho^{(\alpha+1)}(\boldsymbol{r})\,\phi_i(\boldsymbol{r}\sigma), \tag{B.3.9}$$

$$\frac{\delta}{\delta\phi_i^*(\boldsymbol{r}\sigma)} \int d\boldsymbol{r}' \rho^\alpha(\boldsymbol{r}') \sum_q \rho^{(q)2}(\boldsymbol{r}') = \int d\boldsymbol{r}' \left\{ \alpha\rho^{(\alpha-1)}(\boldsymbol{r}') \frac{\delta\rho(\boldsymbol{r}')}{\delta\phi_i^*(\boldsymbol{r}\sigma)} \sum_q \rho^{(q)2}(\boldsymbol{r}') \right.$$

$$\left. + 2\rho^\alpha(\boldsymbol{r}') \sum_q \rho^{(q)}(\boldsymbol{r}') \frac{\delta\rho^{(q)}(\boldsymbol{r}')}{\delta\phi_i^*(\boldsymbol{r}\sigma)} \right\}$$

$$= \alpha\rho^{(\alpha-1)}(\boldsymbol{r}) \sum_q \rho^{(q)2}(\boldsymbol{r})\,\phi_i(\boldsymbol{r}\sigma) + 2\rho^\alpha(\boldsymbol{r})\rho^{(q_i)}(\boldsymbol{r})\,\phi_i(\boldsymbol{r}\sigma). \tag{B.3.10}$$

In this way, we have obtained the following expressions for the variations of B_1, B_2, and B_{5-8} terms:

B_1 **term :**
$$\frac{\delta}{\delta\phi_i^*(\boldsymbol{r}\sigma)}\int d\boldsymbol{r}'\rho^2(\boldsymbol{r}') = 2\rho(\boldsymbol{r})\phi_i(\boldsymbol{r}\sigma), \tag{B.3.11}$$

B_2 **term :**
$$\frac{\delta}{\delta\phi_i^*(\boldsymbol{r}\sigma)}\int d\boldsymbol{r}'\sum_q\rho^{(q)2}(\boldsymbol{r}') = 2\rho^{(q_i)}(\boldsymbol{r})\phi_i(\boldsymbol{r}\sigma), \tag{B.3.12}$$

B_5 **term :**
$$\frac{\delta}{\delta\phi_i^*(\boldsymbol{r}\sigma)}\int d\boldsymbol{r}'\rho(\boldsymbol{r}')\triangle\rho(\boldsymbol{r}') = 2\triangle\rho(\boldsymbol{r})\phi_i(\boldsymbol{r}\sigma), \tag{B.3.13}$$

B_6 **term :**
$$\frac{\delta}{\delta\phi_i^*(\boldsymbol{r}\sigma)}\int d\boldsymbol{r}'\sum_q\rho^{(q)}(\boldsymbol{r}')\triangle\rho^{(q)}(\boldsymbol{r}') = 2\triangle\rho^{(q_i)}(\boldsymbol{r})\phi_i(\boldsymbol{r}\sigma), \tag{B.3.14}$$

B_7 **term :**
$$\frac{\delta}{\delta\phi_i^*(\boldsymbol{r}\sigma)}\int d\boldsymbol{r}'\rho^{(\alpha+2)}(\boldsymbol{r}') = (\alpha+2)\rho^{(\alpha+1)}(\boldsymbol{r})\phi_i(\boldsymbol{r}\sigma), \tag{B.3.15}$$

B_8 **term :**
$$\frac{\delta}{\delta\phi_i^*(\boldsymbol{r}\sigma)}\int d\boldsymbol{r}'\rho^\alpha(\boldsymbol{r}')\sum_q\rho^{(q)2}(\boldsymbol{r}') = \alpha\rho^{(\alpha-1)}(\boldsymbol{r})\sum_q\rho^{(q)2}(\boldsymbol{r})\phi_i(\boldsymbol{r}\sigma)$$
$$+2\rho^\alpha(\boldsymbol{r})\rho^{(q_i)}(\boldsymbol{r})\phi_i(\boldsymbol{r}\sigma). \tag{B.3.16}$$

The B_{10-13}, B_{15}, and B_{17} terms

In the above Subsection, we have calculated the variations of $B_{1,2,5-8}$ terms in the Skyrme EDF, where we just used a formula of the variation of the density $\rho(\boldsymbol{r})$. There are similar terms in the Skyrme EDF for the spin density $\boldsymbol{s}(\boldsymbol{r})$. The B_{10} and B_{11} terms are proportional to the square of the spin densities, $\boldsymbol{s}^2(\boldsymbol{r})$ and $\sum_q\boldsymbol{s}^{(q)2}(\boldsymbol{r})$, respectively. The B_{15} and B_{17} terms are proportional to the product of the spin density and its Laplacian, $\boldsymbol{s}(\boldsymbol{r})\triangle\boldsymbol{s}(\boldsymbol{r})$ and $\sum_q\boldsymbol{s}^{(q)}(\boldsymbol{r})\triangle\boldsymbol{s}^{(q)}(\boldsymbol{r})$, respectively. The B_{12} and B_{13} terms are proportional to the product of αth power of the matter density and the squared spin density, $\rho^\alpha(\boldsymbol{r})\boldsymbol{s}^2(\boldsymbol{r})$ and $\rho^\alpha(\boldsymbol{r})\sum_q\boldsymbol{s}^{(q)2}(\boldsymbol{r})$, respectively. Since they are composed only of the product of matter and spin densities, $\rho(\boldsymbol{r})$ and $\boldsymbol{s}(\boldsymbol{r})$, we can again simply evaluate variations of them using the formulae for the variation of the matter density and that of the spin density. The variation of the spin density $\boldsymbol{s}(\boldsymbol{r}')=\sum_{j\sigma_1\sigma_2}\phi_j^*(\boldsymbol{r}'\sigma_1)\phi_j(\boldsymbol{r}'\sigma_2)\langle\sigma_1|\hat{\boldsymbol{\sigma}}|\sigma_2\rangle$ is calculated as

$$\frac{\delta}{\delta\phi_i^*(\boldsymbol{r}\sigma)}\boldsymbol{s}(\boldsymbol{r}') = \delta(\boldsymbol{r}-\boldsymbol{r}')\sum_{\sigma'}\langle\sigma|\hat{\boldsymbol{\sigma}}|\sigma'\rangle\phi_i(\boldsymbol{r}\sigma'), \tag{B.3.17}$$

$$\frac{\delta}{\delta\phi_i^*(\boldsymbol{r}\sigma)}\boldsymbol{s}^{(q)}(\boldsymbol{r}') = \delta(\boldsymbol{r}-\boldsymbol{r}')\delta_{qq_i}\sum_{\sigma'}\langle\sigma|\hat{\boldsymbol{\sigma}}|\sigma'\rangle\phi_i(\boldsymbol{r}\sigma'). \tag{B.3.18}$$

Using these equations, Eqs. (B.3.17) and (B.3.18), we calculate the variation of $\boldsymbol{s}^2(\boldsymbol{r})$ and $\sum_q\boldsymbol{s}^{(q)2}(\boldsymbol{r})$ as

$$\frac{\delta}{\delta\phi_i^*(\boldsymbol{r}\sigma)}\int d\boldsymbol{r}'\boldsymbol{s}^2(\boldsymbol{r}') = 2\int d\boldsymbol{r}'\boldsymbol{s}(\boldsymbol{r}')\frac{\delta\boldsymbol{s}(\boldsymbol{r}')}{\delta\phi_i^*(\boldsymbol{r}\sigma)}$$
$$= 2\boldsymbol{s}(\boldsymbol{r})\cdot\sum_{\sigma'}\langle\sigma|\hat{\boldsymbol{\sigma}}|\sigma'\rangle\phi_i(\boldsymbol{r}\sigma'), \tag{B.3.19}$$

$$\frac{\delta}{\delta\phi_i^*(\boldsymbol{r}\sigma)}\int d\boldsymbol{r}'\sum_q\boldsymbol{s}^{(q)2}(\boldsymbol{r}') = 2\boldsymbol{s}^{(q_i)}(\boldsymbol{r})\cdot\sum_{\sigma'}\langle\sigma|\hat{\boldsymbol{\sigma}}|\sigma'\rangle\phi_i(\boldsymbol{r}\sigma'). \tag{B.3.20}$$

In the same way, the variations of $s(r) \cdot \triangle s(r)$ and $\sum_q s^{(q)}(r) \cdot \triangle s^{(q)}(r)$ are calculated as

$$
\frac{\delta}{\delta \phi_i^*(r\sigma)} \int dr' s(r') \cdot \triangle s(r') = \int dr' \left\{ \frac{\delta s(r')}{\delta \phi_i^*(r\sigma)} \cdot \triangle s(r') + \triangle s(r') \cdot \frac{\delta s(r')}{\delta \phi_i^*(r\sigma)} \right\}
$$

$$
= 2 \triangle s(r) \cdot \sum_{\sigma'} \langle \sigma | \hat{\sigma} | \sigma' \rangle \phi_i(r\sigma'), \qquad (B.3.21)
$$

$$
\frac{\delta}{\delta \phi_i^*(r\sigma)} \int dr' \sum_q s^{(q)}(r') \cdot \triangle s^{(q)}(r') = 2 \triangle s^{(q_i)}(r) \cdot \sum_{\sigma'} \langle \sigma | \hat{\sigma} | \sigma' \rangle \phi_i(r\sigma'), \qquad (B.3.22)
$$

where, in the first equality, we have taken two integrations by parts to remove the Laplacian operator from $s(r')$ sitting on the right side. Lastly, the variations of $\rho^\alpha(r)s^2(r)$ and $\rho^\alpha(r)\sum_q s^{(q)2}(r)$ are calculated as follows:

$$
\frac{\delta}{\delta \phi_i^*(r\sigma)} \int dr' \rho^\alpha(r') s^2(r') = \int dr' \left\{ \alpha \rho^{(\alpha-1)}(r') \frac{\delta \rho(r')}{\delta \phi_i^*(r\sigma)} s^2(r') + 2\rho^\alpha(r')s(r') \cdot \frac{\delta s(r')}{\delta \phi_i^*(r\sigma)} \right\}
$$

$$
= \alpha \rho^{(\alpha-1)}(r) s^2(r) \phi_i(r\sigma)
$$

$$
+ 2\rho^\alpha(r)s(r) \cdot \sum_{\sigma'} \langle \sigma | \hat{\sigma} | \sigma' \rangle \phi_i(r\sigma'), \qquad (B.3.23)
$$

$$
\frac{\delta}{\delta \phi_i^*(r\sigma)} \int dr' \rho^\alpha(r') \sum_q s^{(q)2}(r') = \alpha \rho^{(\alpha-1)}(r) \sum_q s^{(q)2}(r) \phi_i(r\sigma)
$$

$$
+ 2\rho^\alpha(r)s^{(q_i)}(r) \cdot \sum_{\sigma'} \langle \sigma | \hat{\sigma} | \sigma' \rangle \phi_i(r\sigma'). \qquad (B.3.24)
$$

In this way, we have obtained the following expressions for the variations of $B_{10-13,15,17}$ terms:

$$
\boxed{
\begin{aligned}
\textbf{B}_{10} \textbf{ term :} \qquad & \frac{\delta}{\delta \phi_i^*(r\sigma)} \int dr' s^2(r') = 2s(r) \cdot \sum_{\sigma'} \langle \sigma | \hat{\sigma} | \sigma' \rangle \phi_i(r\sigma'), \qquad (B.3.25) \\[2mm]
\textbf{B}_{11} \textbf{ term :} \qquad & \frac{\delta}{\delta \phi_i^*(r\sigma)} \int dr' \sum_q s^{(q)2}(r') = 2s^{(q_i)}(r) \cdot \sum_{\sigma'} \langle \sigma | \hat{\sigma} | \sigma' \rangle \phi_i(r\sigma'), \qquad (B.3.26) \\[2mm]
\textbf{B}_{12} \textbf{ term :} \qquad & \frac{\delta}{\delta \phi_i^*(r\sigma)} \int dr' \rho^\alpha(r') s^2(r') = \alpha \rho^{(\alpha-1)}(r) s^2(r) \phi_i(r\sigma) \\
& \qquad\qquad\qquad\qquad + 2\rho^\alpha(r)s(r) \cdot \sum_{\sigma'} \langle \sigma | \hat{\sigma} | \sigma' \rangle \phi_i(r\sigma'), \\
\textbf{B}_{13} \textbf{ term :} \qquad & \qquad\qquad\qquad\qquad\qquad\qquad\qquad\qquad (B.3.27) \\
& \frac{\delta}{\delta \phi_i^*(r\sigma)} \int dr' \rho^\alpha(r') \sum_q s^{(q)2}(r') = \alpha \rho^{(\alpha-1)}(r) \sum_q s^{(q)2}(r) \phi_i(r\sigma) \\
& \qquad\qquad\qquad\qquad + 2\rho^\alpha(r)s^{(q_i)}(r) \cdot \sum_{\sigma'} \langle \sigma | \hat{\sigma} | \sigma' \rangle \phi_i(r\sigma'), \\
& \qquad\qquad\qquad\qquad\qquad\qquad\qquad\qquad (B.3.28) \\[2mm]
\textbf{B}_{15} \textbf{ term :} \qquad & \frac{\delta}{\delta \phi_i^*(r\sigma)} \int dr' s(r') \cdot \triangle s(r') = 2 \triangle s(r) \cdot \sum_{\sigma'} \langle \sigma | \hat{\sigma} | \sigma' \rangle \phi_i(r\sigma'), \qquad (B.3.29) \\[2mm]
\textbf{B}_{17} \textbf{ term :} \qquad & \\
& \frac{\delta}{\delta \phi_i^*(r\sigma)} \int dr' \sum_q s^{(q)}(r') \cdot \triangle s^{(q)}(r') = 2 \triangle s^{(q_i)}(r) \cdot \sum_{\sigma'} \langle \sigma | \hat{\sigma} | \sigma' \rangle \phi_i(r\sigma'). \qquad (B.3.30)
\end{aligned}
}
$$

The B_3 and B_4 terms

The B_3 and B_4 terms in the Skyrme EDF are proportional to $\rho(\boldsymbol{r})\tau(\boldsymbol{r}) - \boldsymbol{j}^2(\boldsymbol{r})$ and $\sum_q \rho^{(q)}(\boldsymbol{r})$ $\tau^{(q)}(\boldsymbol{r}) - \boldsymbol{j}^{(q)2}(\boldsymbol{r})$, respectively. Here we consider the first term, $\rho(\boldsymbol{r})\tau(\boldsymbol{r})$, and the second term, $\boldsymbol{j}^2(\boldsymbol{r})$, separately. The variation of the first term can be expressed as

$$\frac{\delta}{\delta\phi_i^*(\boldsymbol{r}\sigma)} \int d\boldsymbol{r}' \rho(\boldsymbol{r}')\tau(\boldsymbol{r}') = \int d\boldsymbol{r}' \left\{ \frac{\delta\rho(\boldsymbol{r}')}{\delta\phi_i^*(\boldsymbol{r}\sigma)}\tau(\boldsymbol{r}') + \rho(\boldsymbol{r}')\frac{\delta\tau(\boldsymbol{r}')}{\delta\phi_i^*(\boldsymbol{r}\sigma)} \right\}. \tag{B.3.31}$$

Using the variation of $\rho(\boldsymbol{r})$ Eq. (B.3.3), the first term in the curly brackets is calculated as

$$\int d\boldsymbol{r}' \frac{\delta\rho(\boldsymbol{r}')}{\delta\phi_i^*(\boldsymbol{r}\sigma)}\tau(\boldsymbol{r}') = \tau(\boldsymbol{r})\,\phi_i(\boldsymbol{r}\sigma). \tag{B.3.32}$$

The second term in the curly bracket in Eq. (B.3.31) is calculated as follows:

$$\begin{aligned}
\int d\boldsymbol{r}' \rho(\boldsymbol{r}')\frac{\delta\tau(\boldsymbol{r}')}{\delta\phi_i^*(\boldsymbol{r}\sigma)} &= \int d\boldsymbol{r}' \rho(\boldsymbol{r}')\frac{\delta}{\delta\phi_i^*(\boldsymbol{r}\sigma)} \sum_{j\sigma'} \left\{ \boldsymbol{\nabla}\phi_j^*(\boldsymbol{r}'\sigma') \cdot \boldsymbol{\nabla}\phi_j(\boldsymbol{r}'\sigma') \right\} \\
&= -\int d\boldsymbol{r}' \sum_{j\sigma'} \left\{ \frac{\delta\phi_j^*(\boldsymbol{r}'\sigma')}{\delta\phi_i^*(\boldsymbol{r}\sigma)} \boldsymbol{\nabla} \cdot \left(\rho(\boldsymbol{r}')\boldsymbol{\nabla}\phi_j(\boldsymbol{r}'\sigma') \right) \right\} \\
&= -\left\{ \overrightarrow{\boldsymbol{\nabla}}\rho(\boldsymbol{r}) \cdot \overrightarrow{\boldsymbol{\nabla}} \right\} \phi_i(\boldsymbol{r}\sigma),
\end{aligned} \tag{B.3.33}$$

where we have introduced the operator $\overrightarrow{\boldsymbol{\nabla}}$ which acts on all the spatial functions sitting on the right side, i.e. $\overrightarrow{\boldsymbol{\nabla}}f(\boldsymbol{r})g(\boldsymbol{r}) = \boldsymbol{\nabla}f(\boldsymbol{r})\,g(\boldsymbol{r}) + f(\boldsymbol{r})\,\boldsymbol{\nabla}g(\boldsymbol{r})$. The variation of the remaining second term $\boldsymbol{j}^2(\boldsymbol{r})$ is calculated as

$$\begin{aligned}
\frac{\delta}{\delta\phi_i^*(\boldsymbol{r}\sigma)} \int d\boldsymbol{r}' \boldsymbol{j}^2(\boldsymbol{r}') &= 2\int d\boldsymbol{r}' \boldsymbol{j}(\boldsymbol{r}') \cdot \frac{\delta\boldsymbol{j}(\boldsymbol{r}')}{\delta\phi_i^*(\boldsymbol{r}\sigma)} \\
&= \frac{1}{\mathrm{i}} \int d\boldsymbol{r}' \boldsymbol{j}(\boldsymbol{r}') \cdot \frac{\delta}{\delta\phi_i^*(\boldsymbol{r}\sigma)} \sum_{j\sigma'} \left\{ \phi_j^*(\boldsymbol{r}'\sigma')\boldsymbol{\nabla}\phi_j(\boldsymbol{r}'\sigma') - \phi_j(\boldsymbol{r}'\sigma')\boldsymbol{\nabla}\phi_j^*(\boldsymbol{r}'\sigma') \right\} \\
&= \frac{1}{\mathrm{i}}\boldsymbol{j}(\boldsymbol{r}) \cdot \boldsymbol{\nabla}\phi_i(\boldsymbol{r}\sigma) + \frac{1}{\mathrm{i}} \int d\boldsymbol{r}' \sum_{j\sigma'} \left\{ \frac{\delta\phi_j^*(\boldsymbol{r}'\sigma')}{\delta\phi_i^*(\boldsymbol{r}\sigma)} \boldsymbol{\nabla} \cdot \left(\boldsymbol{j}(\boldsymbol{r}')\phi_j(\boldsymbol{r}'\sigma') \right) \right\} \\
&= -\mathrm{i}\left\{ \overrightarrow{\boldsymbol{\nabla}} \cdot \boldsymbol{j}(\boldsymbol{r}) + \boldsymbol{j}(\boldsymbol{r}) \cdot \overrightarrow{\boldsymbol{\nabla}} \right\} \phi_i(\boldsymbol{r}\sigma).
\end{aligned} \tag{B.3.34}$$

The B_4 term can be calculated in the same way as the B_3 term. Summarizing above equations, the variation of B_3 and B_4 is expressed as

$$\boxed{\begin{aligned}
&\boldsymbol{B_3}\ \textbf{term}: \quad \frac{\delta}{\delta\phi_i^*(\boldsymbol{r}\sigma)} \int d\boldsymbol{r}' \left\{ \rho(\boldsymbol{r}')\tau(\boldsymbol{r}') - \boldsymbol{j}^2(\boldsymbol{r}') \right\} \\
&\qquad = \left[-\overrightarrow{\boldsymbol{\nabla}}\rho(\boldsymbol{r}) \cdot \overrightarrow{\boldsymbol{\nabla}} + \tau(\boldsymbol{r}) + \mathrm{i}\left\{ \overrightarrow{\boldsymbol{\nabla}} \cdot \boldsymbol{j}(\boldsymbol{r}) + \boldsymbol{j}(\boldsymbol{r}) \cdot \overrightarrow{\boldsymbol{\nabla}} \right\} \right] \phi_i(\boldsymbol{r}\sigma), \qquad (\text{B.3.35}) \\[2ex]
&\boldsymbol{B_4}\ \textbf{term}: \quad \frac{\delta}{\delta\phi_i^*(\boldsymbol{r}\sigma)} \int d\boldsymbol{r}' \sum_q \left\{ \rho^{(q)}(\boldsymbol{r}')\tau^{(q)}(\boldsymbol{r}') - \boldsymbol{j}^{(q)2}(\boldsymbol{r}') \right\} \\
&\qquad = \left[-\overrightarrow{\boldsymbol{\nabla}}\rho^{(q_i)}(\boldsymbol{r}) \cdot \overrightarrow{\boldsymbol{\nabla}} + \tau^{(q_i)}(\boldsymbol{r}) + \mathrm{i}\left\{ \overrightarrow{\boldsymbol{\nabla}} \cdot \boldsymbol{j}^{(q_i)}(\boldsymbol{r}) + \boldsymbol{j}^{(q_i)}(\boldsymbol{r}) \cdot \overrightarrow{\boldsymbol{\nabla}} \right\} \right] \phi_i(\boldsymbol{r}\sigma).
\end{aligned}}$$
$$(\text{B.3.36})$$

The spin-orbit term (the B_9 term)

The spin-orbit term in the Skyrme EDF, $E_{\mathrm{LS}} = \int d\boldsymbol{r}\mathcal{H}_{\mathrm{LS}}(\boldsymbol{r})$, contains a Hamiltonian density,

$$\mathcal{H}_{\mathrm{LS}}(\boldsymbol{r}) \equiv B_9\Big\{\rho(\boldsymbol{r})\boldsymbol{\nabla}\cdot\boldsymbol{J}(\boldsymbol{r}) + \boldsymbol{s}(\boldsymbol{r})\cdot\boldsymbol{\nabla}\times\boldsymbol{j}(\boldsymbol{r}) + \sum_q \rho^{(q)}(\boldsymbol{r})\boldsymbol{\nabla}\cdot\boldsymbol{J}^{(q)}(\boldsymbol{r}) + \boldsymbol{s}^{(q)}(\boldsymbol{r})\cdot\boldsymbol{\nabla}\times\boldsymbol{j}^{(q)}(\boldsymbol{r})\Big\}. \quad \text{(B.3.37)}$$

The variation of the first term in E_{LS} can be expressed as

$$\frac{\delta}{\delta\phi_i^*(\boldsymbol{r}\sigma)}\int d\boldsymbol{r}'\rho(\boldsymbol{r}')\boldsymbol{\nabla}\cdot\boldsymbol{J}(\boldsymbol{r}') = \int d\boldsymbol{r}'\left\{\frac{\delta\rho(\boldsymbol{r}')}{\delta\phi_i^*(\boldsymbol{r}\sigma)}\boldsymbol{\nabla}\cdot\boldsymbol{J}(\boldsymbol{r}') - \boldsymbol{\nabla}\rho(\boldsymbol{r}')\cdot\frac{\delta\boldsymbol{J}(\boldsymbol{r}')}{\delta\phi_i^*(\boldsymbol{r}\sigma)}\right\}. \quad \text{(B.3.38)}$$

Using the variation of $\rho(\boldsymbol{r})$ Eq. (B.3.3), the first term in the curly brackets is calculated as

$$\int d\boldsymbol{r}'\frac{\delta\rho(\boldsymbol{r}')}{\delta\phi_i^*(\boldsymbol{r}\sigma)}\boldsymbol{\nabla}\cdot\boldsymbol{J}(\boldsymbol{r}') = \boldsymbol{\nabla}\cdot\boldsymbol{J}(\boldsymbol{r})\,\phi_i(\boldsymbol{r}\sigma). \quad \text{(B.3.39)}$$

The second term in the curly bracket in Eq. (B.3.38) is calculated as

$$\begin{aligned}
-\int d\boldsymbol{r}'\boldsymbol{\nabla}\rho(\boldsymbol{r}')\cdot\frac{\delta\boldsymbol{J}(\boldsymbol{r}')}{\delta\phi_i^*(\boldsymbol{r}\sigma)} &= -\frac{1}{2\mathrm{i}}\int d\boldsymbol{r}'\sum_{\lambda\mu\nu}\varepsilon_{\lambda\mu\nu}\partial_\lambda\rho(\boldsymbol{r}')\sum_{j\sigma_1\sigma_2}\langle\sigma_1|\hat{\sigma}_\nu|\sigma_2\rangle \\
&\qquad \frac{\delta}{\delta\phi_i^*(\boldsymbol{r}\sigma)}\Big\{\phi_j^*(\boldsymbol{r}'\sigma_1)\partial_\mu\phi_j(\boldsymbol{r}'\sigma_2) - \phi_j(\boldsymbol{r}'\sigma_2)\partial_\mu\phi_j^*(\boldsymbol{r}'\sigma_1)\Big\} \\
&= -\frac{1}{\mathrm{i}}\sum_{\lambda\mu\nu}\varepsilon_{\lambda\mu\nu}\partial_\lambda\rho(\boldsymbol{r})\sum_{\sigma'}\langle\sigma|\hat{\sigma}_\nu|\sigma'\rangle\partial_\mu\phi_i(\boldsymbol{r}\sigma') \\
&= -\mathrm{i}\boldsymbol{\nabla}\rho(\boldsymbol{r})\cdot\sum_{\sigma'}\langle\sigma|\hat{\boldsymbol{\sigma}}|\sigma'\rangle\times\boldsymbol{\nabla}\phi_i(\boldsymbol{r}\sigma'), \quad \text{(B.3.40)}
\end{aligned}$$

where, in the second equality, we have taken an integration by parts for the second term in the curly bracket and used the antisymmetric nature of the Levi-Civita tensor which leads $\varepsilon_{\lambda\mu\nu}\partial_\mu\partial_\lambda\rho(\boldsymbol{r}') = 0$. The variation of the second term in E_{LS} is expressed as

$$\begin{aligned}
\frac{\delta}{\delta\phi_i^*(\boldsymbol{r}\sigma)}\int d\boldsymbol{r}'\boldsymbol{s}(\boldsymbol{r}')\cdot\boldsymbol{\nabla}\times\boldsymbol{j}(\boldsymbol{r}') &= \frac{\delta}{\delta\phi_i^*(\boldsymbol{r}\sigma)}\int d\boldsymbol{r}'\sum_{\lambda\mu\nu}\varepsilon_{\lambda\mu\nu}s_\lambda(\boldsymbol{r}')\partial_\mu j_\nu(\boldsymbol{r}') \\
&= \int d\boldsymbol{r}'\sum_{\lambda\mu\nu}\varepsilon_{\lambda\mu\nu}\left\{\frac{\delta s_\lambda(\boldsymbol{r}')}{\delta\phi_i^*(\boldsymbol{r}\sigma)}\partial_\mu j_\nu(\boldsymbol{r}') - \partial_\mu s_\lambda(\boldsymbol{r}')\frac{\delta j_\nu(\boldsymbol{r}')}{\delta\phi_i^*(\boldsymbol{r}\sigma)}\right\}.
\end{aligned}$$

$$\text{(B.3.41)}$$

The first term in the curly bracket in Eq. (B.3.41) is calculated by using the variation of $\boldsymbol{s}(\boldsymbol{r})$ Eq. (B.3.17) as

$$\begin{aligned}
\int d\boldsymbol{r}'\sum_{\lambda\mu\nu}\varepsilon_{\lambda\mu\nu}\frac{\delta s_\lambda(\boldsymbol{r}')}{\delta\phi_i^*(\boldsymbol{r}\sigma)}\partial_\mu j_\nu(\boldsymbol{r}') &= \sum_{\lambda\mu\nu}\varepsilon_{\lambda\mu\nu}\partial_\mu j_\nu(\boldsymbol{r})\sum_{\sigma'}\langle\sigma|\hat{\sigma}_\lambda|\sigma'\rangle\phi_i(\boldsymbol{r}\sigma') \\
&= \boldsymbol{\nabla}\times\boldsymbol{j}(\boldsymbol{r})\cdot\sum_{\sigma'}\langle\sigma|\hat{\boldsymbol{\sigma}}|\sigma'\rangle\phi_i(\boldsymbol{r}\sigma'). \quad \text{(B.3.42)}
\end{aligned}$$

The second term in the curly bracket in Eq. (B.3.41) is calculated as

$$
\begin{aligned}
-\int d\boldsymbol{r}' \sum_{\lambda\mu\nu} \varepsilon_{\lambda\mu\nu} \partial_\mu s_\lambda(\boldsymbol{r}') \frac{\delta j_\nu(\boldsymbol{r}')}{\delta\phi_i^*(\boldsymbol{r}\sigma)} &= -\frac{1}{2\mathrm{i}} \int d\boldsymbol{r}' \sum_{\lambda\mu\nu} \varepsilon_{\lambda\mu\nu} \partial_\mu s_\lambda(\boldsymbol{r}') \sum_{j\sigma'} \\
&\quad \frac{\delta}{\delta\phi_i^*(\boldsymbol{r}\sigma)} \Big\{ \phi_j^*(\boldsymbol{r}'\sigma')\partial_\nu\phi_j(\boldsymbol{r}'\sigma') - \phi_j(\boldsymbol{r}'\sigma')\partial_\nu\phi_j^*(\boldsymbol{r}'\sigma') \Big\} \\
&= -\frac{1}{\mathrm{i}} \sum_{\lambda\mu\nu} \varepsilon_{\lambda\mu\nu} \partial_\mu s_\lambda(\boldsymbol{r})\partial_\nu\phi_i(\boldsymbol{r}\sigma) \\
&= -\mathrm{i}\boldsymbol{\nabla} \times \boldsymbol{s}(\boldsymbol{r}) \cdot \boldsymbol{\nabla}\phi_i(\boldsymbol{r}\sigma), \quad (\mathrm{B}.3.43)
\end{aligned}
$$

where, in the second equality, we have taken an integration by parts and used the antisymmetric nature of the Levi-Civita tensor. The variations of the third and forth terms in E_{LS} can be calculated in the same way. By combining the above results, we obtain

B_9 term :

$$
\begin{aligned}
\frac{\delta}{\delta\phi_i^*(\boldsymbol{r}\sigma)} \int d\boldsymbol{r}' \hat{\mathcal{H}}_{\mathrm{LS}}(\boldsymbol{r}') &= B_9 \sum_{\sigma'} \Bigg[\Big\{ \boldsymbol{\nabla}\cdot\boldsymbol{J}(\boldsymbol{r}) + \boldsymbol{\nabla}\cdot\boldsymbol{J}^{(q_i)}(\boldsymbol{r}) \Big\}\delta_{\sigma\sigma'} \\
&\quad -\mathrm{i}\Big\{ \boldsymbol{\nabla}\rho(\boldsymbol{r}) + \boldsymbol{\nabla}\rho^{(q_i)}(\boldsymbol{r}) \Big\}\cdot\langle\sigma|\hat{\boldsymbol{\sigma}}|\sigma'\rangle \times \boldsymbol{\nabla} \\
&\quad +\Big\{ \boldsymbol{\nabla}\times\boldsymbol{j}(\boldsymbol{r}) + \boldsymbol{\nabla}\times\boldsymbol{j}^{(q_i)}(\boldsymbol{r}) \Big\}\cdot\langle\sigma|\hat{\boldsymbol{\sigma}}|\sigma'\rangle \\
&\quad -\mathrm{i}\Big\{ \boldsymbol{\nabla}\times\boldsymbol{s}(\boldsymbol{r}) + \boldsymbol{\nabla}\times\boldsymbol{s}^{(q_i)}(\boldsymbol{r}) \Big\}\cdot\boldsymbol{\nabla}\delta_{\sigma\sigma'} \Bigg] \phi_i(\boldsymbol{r}\sigma').
\end{aligned}
$$

$$(\mathrm{B}.3.44)$$

The B_{14} and B_{16} terms

Lastly, we consider the B_{14} and B_{16} terms in the Skyrme EDF, which are proportional to $\boldsymbol{s}(\boldsymbol{r})\cdot\boldsymbol{T}(\boldsymbol{r}) - \overleftrightarrow{J}^2(\boldsymbol{r})$ and $\sum_q \boldsymbol{s}^{(q)}(\boldsymbol{r})\cdot\boldsymbol{T}^{(q)}(\boldsymbol{r}) - \overleftrightarrow{J}^{(q)2}(\boldsymbol{r})$, respectively. The variation of the first term $\boldsymbol{s}(\boldsymbol{r})\cdot\boldsymbol{T}(\boldsymbol{r})$ is expressed as

$$
\frac{\delta}{\delta\phi_i^*(\boldsymbol{r}\sigma)} \int d\boldsymbol{r}' \boldsymbol{s}(\boldsymbol{r}')\cdot\boldsymbol{T}(\boldsymbol{r}') = \int d\boldsymbol{r}' \left\{ \frac{\delta\boldsymbol{s}(\boldsymbol{r}')}{\delta\phi_i^*(\boldsymbol{r}\sigma)}\cdot\boldsymbol{T}(\boldsymbol{r}') + \boldsymbol{s}(\boldsymbol{r}')\cdot\frac{\delta\boldsymbol{T}(\boldsymbol{r}')}{\delta\phi_i^*(\boldsymbol{r}\sigma)} \right\}. \quad (\mathrm{B}.3.45)
$$

The variation of the first term in the curly bracket in Eq. (B.3.45) is calculated by using Eq. (B.3.17) as

$$
\int d\boldsymbol{r}' \frac{\delta\boldsymbol{s}(\boldsymbol{r}')}{\delta\phi_i^*(\boldsymbol{r}\sigma)}\cdot\boldsymbol{T}(\boldsymbol{r}') = \boldsymbol{T}(\boldsymbol{r})\cdot\sum_{\sigma'} \langle\sigma|\hat{\boldsymbol{\sigma}}|\sigma'\rangle \phi_i(\boldsymbol{r}\sigma'). \quad (\mathrm{B}.3.46)
$$

The variation of the second term in the curly bracket in Eq. (B.3.45) is calculated as

$$
\begin{aligned}
\int d\boldsymbol{r}' \boldsymbol{s}(\boldsymbol{r}')\cdot\frac{\delta\boldsymbol{T}(\boldsymbol{r}')}{\delta\phi_i^*(\boldsymbol{r}\sigma)} &= \int d\boldsymbol{r}' \sum_\nu s_\nu(\boldsymbol{r}') \frac{\delta}{\delta\phi_i^*(\boldsymbol{r}\sigma)} \sum_{j\sigma_1\sigma_2} \Big\{ \boldsymbol{\nabla}\phi_j^*(\boldsymbol{r}'\sigma_1)\cdot\boldsymbol{\nabla}\phi_j(\boldsymbol{r}'\sigma_2) \Big\}\langle\sigma_1|\hat{\sigma}_\nu|\sigma_2\rangle \\
&= -\int d\boldsymbol{r}' \sum_\nu \sum_{j\sigma_1\sigma_2} \frac{\delta\phi_j^*(\boldsymbol{r}'\sigma_1)}{\delta\phi_i^*(\boldsymbol{r}\sigma)}\boldsymbol{\nabla}\cdot\Big(s_\nu(\boldsymbol{r}')\boldsymbol{\nabla}\phi_j(\boldsymbol{r}'\sigma_2) \Big)\langle\sigma_1|\hat{\sigma}_\nu|\sigma_2\rangle \\
&= -\sum_{\sigma'} \sum_\nu \boldsymbol{\nabla}\cdot\Big(s_\nu(\boldsymbol{r}')\boldsymbol{\nabla} \Big)\langle\sigma|\hat{\sigma}_\nu|\sigma'\rangle \phi_i(\boldsymbol{r}\sigma'). \quad (\mathrm{B}.3.47)
\end{aligned}
$$

The variation of the second term is calculated as follows:

$$
\begin{aligned}
-\frac{\delta}{\delta\phi_i^*(\boldsymbol{r}\sigma)} \int d\boldsymbol{r}'\overleftrightarrow{J}^2(\boldsymbol{r}') &= -2\int d\boldsymbol{r}' \sum_{\mu\nu} J_{\mu\nu}(\boldsymbol{r}')\frac{\delta J_{\mu\nu}(\boldsymbol{r}')}{\delta\phi_i^*(\boldsymbol{r}\sigma)} \\
&= -\frac{1}{\mathrm{i}}\int d\boldsymbol{r}' \sum_{\mu\nu} J_{\mu\nu}(\boldsymbol{r}') \sum_{j\sigma_1\sigma_2}\langle\sigma_1|\hat{\sigma}_\nu|\sigma_2\rangle \\
&\quad \frac{\delta}{\delta\phi_i^*(\boldsymbol{r}\sigma)}\Big\{\phi_j^*(\boldsymbol{r}'\sigma_1)\partial_\mu\phi_j(\boldsymbol{r}'\sigma_2) - \phi_j(\boldsymbol{r}'\sigma_2)\partial_\mu\phi_j^*(\boldsymbol{r}'\sigma_1)\Big\} \\
&= \mathrm{i}\sum_{\mu\nu} J_{\mu\nu}(\boldsymbol{r})\sum_{\sigma'}\langle\sigma|\hat{\sigma}_\nu|\sigma'\rangle\,\partial_\mu\phi_i(\boldsymbol{r}\sigma') \\
&\quad +\mathrm{i}\sum_{\mu\nu}\sum_{\sigma'}\langle\sigma|\hat{\sigma}_\nu|\sigma'\rangle\partial_\mu\Big(J_{\mu\nu}(\boldsymbol{r})\phi_j(\boldsymbol{r}\sigma')\Big) \\
&= \mathrm{i}\sum_{\mu\nu}\Big\{\overrightarrow{\nabla}_\mu J_{\mu\nu}(\boldsymbol{r}) + J_{\mu\nu}(\boldsymbol{r})\overrightarrow{\nabla}_\mu\Big\}\sum_{\sigma'}\langle\sigma|\hat{\sigma}_\nu|\sigma'\rangle\,\phi_i(\boldsymbol{r}\sigma'),
\end{aligned}
$$

$$(\text{B.3.48})$$

where, in the third equality, we have taken an integration by parts for the second term in the curly brackets. The B_{16} term can be calculated in the same way as the B_{14} term. We then obtain the following expressions for the variations of the B_{14} and B_{16} terms in the Skyrme EDF:

B_{14} **term :**

$$
\frac{\delta}{\delta\phi_i^*(\boldsymbol{r}\sigma)}\int d\boldsymbol{r}\Big\{\boldsymbol{s}(\boldsymbol{r})\cdot\boldsymbol{T}(\boldsymbol{r}) - \overleftrightarrow{J}^2(\boldsymbol{r})\Big\}
$$

$$
= \sum_{\nu\,\sigma}\Big[-\overrightarrow{\nabla}s_\nu(\boldsymbol{r}')\cdot\overrightarrow{\nabla} + T_\nu(\boldsymbol{r}') + \mathrm{i}\sum_\mu\Big\{\overrightarrow{\nabla}_\mu J_{\mu\nu}(\boldsymbol{r}) + J_{\mu\nu}(\boldsymbol{r})\overrightarrow{\nabla}_\mu\Big\}\Big]\langle\sigma|\hat{\sigma}_\nu|\sigma'\rangle\,\phi_i(\boldsymbol{r}\sigma'),
$$

$$(\text{B.3.49})$$

B_{16} **term :**

$$
\frac{\delta}{\delta\phi_i^*(\boldsymbol{r}\sigma)}\int d\boldsymbol{r}\sum_q\Big\{\boldsymbol{s}^{(q)}(\boldsymbol{r})\cdot\boldsymbol{T}^{(q)}(\boldsymbol{r}) - \overleftrightarrow{J}^{(q)2}(\boldsymbol{r})\Big\}
$$

$$
= \sum_{\nu\,\sigma}\Big[-\overrightarrow{\nabla}s_\nu^{(q_i)}(\boldsymbol{r}')\cdot\overrightarrow{\nabla} + T_\nu^{(q_i)}(\boldsymbol{r}') + \mathrm{i}\sum_\mu\Big\{\overrightarrow{\nabla}_\mu J_{\mu\nu}^{(q_i)}(\boldsymbol{r}) + J_{\mu\nu}^{(q_i)}(\boldsymbol{r})\overrightarrow{\nabla}_\mu\Big\}\Big]\langle\sigma|\hat{\sigma}_\nu|\sigma'\rangle\,\phi_i(\boldsymbol{r}\sigma').
$$

$$(\text{B.3.50})$$

The resulting Skyrme HF equation

As a result, we obtain the Skyrme Hartree-Fock equations for single-particle wave functions:

$$\sum_{\sigma'} \hat{h}_{\text{SHF}}^{(q_i)}(\boldsymbol{r}\sigma\sigma')\phi_i(\boldsymbol{r}\sigma') = \varepsilon_i\,\phi_i(\boldsymbol{r}\sigma), \tag{B.3.51}$$

where the single-particle Hamiltonian is given by

$$\hat{h}_{\text{SHF}}^{(q)}(\boldsymbol{r}\sigma\sigma') = -\frac{\hbar^2}{2m}\,\triangle\,\delta_{\sigma\sigma'} + \hat{h}_{\text{even}}^{(q)}(\boldsymbol{r}\sigma\sigma') + \hat{h}_{\text{odd}}^{(q)}(\boldsymbol{r}\sigma\sigma'). \tag{B.3.52}$$

The time-even and time-odd parts of the single-particle Hamiltonian are defined by

$$\hat{h}_{\text{even}}^{(q)}(\boldsymbol{r}\sigma\sigma') = -\overrightarrow{\boldsymbol{\nabla}}\cdot M^{(q)}(\boldsymbol{r})\overrightarrow{\boldsymbol{\nabla}}\delta_{\sigma\sigma'} + U^{(q)}(\boldsymbol{r})\delta_{\sigma\sigma'} + \frac{1}{2\mathrm{i}}\left(\overleftrightarrow{\boldsymbol{\nabla}\boldsymbol{\sigma}}_{\sigma\sigma'}\cdot\overleftrightarrow{\boldsymbol{B}}^{(q)}(\boldsymbol{r}) + \overleftrightarrow{\boldsymbol{B}}^{(q)}(\boldsymbol{r})\cdot\overleftrightarrow{\boldsymbol{\nabla}\boldsymbol{\sigma}}_{\sigma\sigma'}\right), \tag{B.3.53}$$

$$\hat{h}_{\text{odd}}^{(q)}(\boldsymbol{r}\sigma\sigma') = -\overrightarrow{\boldsymbol{\nabla}}\cdot\left(\boldsymbol{\sigma}_{\sigma\sigma'}\cdot\boldsymbol{C}^{(q)}(\boldsymbol{r})\right)\overrightarrow{\boldsymbol{\nabla}} + \boldsymbol{\sigma}_{\sigma\sigma'}\cdot\boldsymbol{\Sigma}^{(q)}(\boldsymbol{r}) + \frac{1}{2\mathrm{i}}\left(\overrightarrow{\boldsymbol{\nabla}}\cdot\boldsymbol{I}^{(q)}(\boldsymbol{r}) + \boldsymbol{I}^{(q)}(\boldsymbol{r})\cdot\overrightarrow{\boldsymbol{\nabla}}\right)\delta_{\sigma\sigma'}. \tag{B.3.54}$$

We introduced a shorthand notation, $\boldsymbol{\sigma}_{\sigma\sigma'} \equiv \langle\sigma|\hat{\boldsymbol{\sigma}}|\sigma'\rangle$. We defined two rank-2 tensors, $\overleftrightarrow{\boldsymbol{\nabla}}$ which denotes a tensor having components $\nabla_{\mu\nu} \equiv \sum_\lambda \varepsilon_{\mu\nu\lambda}\overrightarrow{\boldsymbol{\nabla}}_\lambda$ and $\overleftrightarrow{\boldsymbol{\nabla}\boldsymbol{\sigma}}_{\sigma\sigma'}$ which denotes a tensor having components $\nabla_\mu\sigma_{\nu,\sigma\sigma'}$. We note that the differential operators, $\boldsymbol{\nabla}$ and $\triangle$, act only on a neighboring spatial function, while $\overrightarrow{\boldsymbol{\nabla}}$ acts all the spatial functions sitting on the right side of $\overrightarrow{\boldsymbol{\nabla}}$. Time-even mean-field potentials are defined by

$$M^{(q)}(\boldsymbol{r}) = B_3\rho(\boldsymbol{r}) + B_4\rho^{(q)}(\boldsymbol{r}), \tag{B.3.55}$$

$$\begin{aligned}
U^{(q)}(\boldsymbol{r}) =\ & 2\left\{B_1\rho(\boldsymbol{r}) + B_2\rho^{(q)}(\boldsymbol{r})\right\} + B_3\tau(\boldsymbol{r}) + B_4\tau^{(q)}(\boldsymbol{r}) \\
& + 2\left\{B_5\triangle\rho(\boldsymbol{r}) + B_6\triangle\rho^{(q)}(\boldsymbol{r})\right\} + B_9\boldsymbol{\nabla}\cdot\left\{\boldsymbol{J}(\boldsymbol{r}) + \boldsymbol{J}^{(q)}(\boldsymbol{r})\right\} \\
& + B_7(\alpha+2)\rho^{\alpha+1}(\boldsymbol{r}) + B_8\left\{\alpha\rho^{\alpha-1}(\boldsymbol{r})\left(\rho^{(n)2}(\boldsymbol{r}) + \rho^{(p)2}(\boldsymbol{r})\right) + 2\rho^\alpha(\boldsymbol{r})\rho^{(q)}(\boldsymbol{r})\right\} \\
& + \alpha\rho^{\alpha-1}(\boldsymbol{r})\left\{B_{12}\boldsymbol{s}^2(\boldsymbol{r}) + B_{13}\left(\boldsymbol{s}^{(n)2}(\boldsymbol{r}) + \boldsymbol{s}^{(p)2}(\boldsymbol{r})\right)\right\} + V_{\text{Coul}}(\boldsymbol{r})\,\delta_{qp},
\end{aligned} \tag{B.3.56}$$

$$\overleftrightarrow{\boldsymbol{B}}^{(q)}(\boldsymbol{r}) = -2\left\{B_{14}\overleftrightarrow{\boldsymbol{J}}(\boldsymbol{r}) + B_{16}\overleftrightarrow{\boldsymbol{J}}^{(q)}(\boldsymbol{r})\right\} - B_9\overleftrightarrow{\boldsymbol{\nabla}}\left\{\rho(\boldsymbol{r}) + \rho^{(q)}(\boldsymbol{r})\right\}, \tag{B.3.57}$$

where the Coulomb potential $V_{\text{Coul}}(\boldsymbol{r})$ is given by

$$V_{\text{Coul}}(\boldsymbol{r}) = e^2\left\{\int d\boldsymbol{r}'\,\frac{\rho^{(p)}(\boldsymbol{r}')}{|\boldsymbol{r} - \boldsymbol{r}'|} - \left(\frac{3}{\pi}\right)^{\frac{1}{3}}\left[\rho^{(p)}(\boldsymbol{r})\right]^{\frac{1}{3}}\right\}. \tag{B.3.58}$$

While time-odd mean-field potentials are defined by

$$\boldsymbol{I}^{(q)}(\boldsymbol{r}) = -2\{B_3\boldsymbol{j}(\boldsymbol{r}) + B_4\boldsymbol{j}^{(q)}(\boldsymbol{r})\} + B_9\boldsymbol{\nabla} \times \{\boldsymbol{s}(\boldsymbol{r}) + \boldsymbol{s}^{(q)}(\boldsymbol{r})\}, \tag{B.3.59}$$

$$\boldsymbol{C}^{(q)}(\boldsymbol{r}) = B_{14}\boldsymbol{s}(\boldsymbol{r}) + B_{16}\boldsymbol{s}^{(q)}(\boldsymbol{r}), \tag{B.3.60}$$

$$\boldsymbol{\Sigma}^{(q)}(\boldsymbol{r}) = 2\left\{B_{10}\boldsymbol{s}(\boldsymbol{r}) + B_{11}\boldsymbol{s}^{(q)}(\boldsymbol{r})\right\} + B_{14}\boldsymbol{T}(\boldsymbol{r}) + B_{16}\boldsymbol{T}^{(q)}(\boldsymbol{r})$$

$$+ 2\left\{B_{15}\triangle\boldsymbol{s}(\boldsymbol{r}) + B_{17}\triangle\boldsymbol{s}^{(q)}(\boldsymbol{r})\right\} + B_9\boldsymbol{\nabla}\times\left\{\boldsymbol{j}(\boldsymbol{r}) + \boldsymbol{j}^{(q)}(\boldsymbol{r})\right\}$$

$$+ 2\rho^{\alpha}(\boldsymbol{r})\left\{B_{12}\boldsymbol{s}(\boldsymbol{r}) + B_{13}\boldsymbol{s}^{(q)}(\boldsymbol{r})\right\}. \tag{B.3.61}$$

To simplify the notation of the single-particle Hamiltonian, we have used relations for tensorial functions. As a matter of principle, we describe below some notations used to define the Skyrme single-particle Hamiltonian.

The scalar product between two tensors, $\overset{\leftrightarrow}{A}$ and $\overset{\leftrightarrow}{B}$, having components, $A_{\mu\nu}$ and $B_{\mu\nu}$, respectively, is defined by

$$\overset{\leftrightarrow}{A} \cdot \overset{\leftrightarrow}{B} \equiv \sum_{\mu\nu} A_{\mu\nu}B_{\mu\nu}. \tag{B.3.62}$$

We have introduced two tensors, $\overset{\leftrightarrow}{\nabla}\overset{\rightarrow}{\sigma}_{\sigma\sigma'}$ and $\overset{\leftrightarrow}{\nabla}$. The $\overset{\leftrightarrow}{\nabla}\overset{\rightarrow}{\sigma}_{\sigma\sigma'}$ has components $\overset{\rightarrow}{\nabla}_{\mu}\sigma_{\nu,\sigma\sigma'}$, while the tensor $\overset{\leftrightarrow}{\nabla}$ has components

$$\nabla_{\mu\nu} \equiv \sum_{\lambda} \varepsilon_{\mu\nu\lambda}\overset{\rightarrow}{\nabla}_{\lambda}. \tag{B.3.63}$$

There follows the following relation:

$$\overset{\leftrightarrow}{\nabla} \cdot \overset{\leftrightarrow}{A} = \sum_{\mu\nu} \nabla_{\mu\nu}A_{\mu\nu} = \sum_{\mu\nu\lambda} \varepsilon_{\mu\nu\lambda}\nabla_{\lambda}A_{\mu\nu} = \boldsymbol{\nabla}\cdot\boldsymbol{A}, \tag{B.3.64}$$

where $\boldsymbol{A} = \big(A_{23} - A_{32},\ A_{31} - A_{13},\ A_{12} - A_{21}\big)$ is the antisymmetric part of the tensor $\overset{\leftrightarrow}{A}$. Using above relations, we find

$$\frac{1}{2\mathrm{i}}\left(\overset{\leftrightarrow}{\nabla}\overset{\rightarrow}{\sigma}_{\sigma\sigma'} \cdot \overset{\leftrightarrow}{B}^{(q)}(\boldsymbol{r}) + \overset{\leftrightarrow}{B}^{(q)}(\boldsymbol{r}) \cdot \overset{\leftrightarrow}{\nabla}\overset{\rightarrow}{\sigma}_{\sigma\sigma'}\right)$$

$$= \frac{1}{2\mathrm{i}}\sum_{\mu\nu}\left\{\overset{\rightarrow}{\nabla}_{\mu}\sigma_{\nu,\sigma\sigma'}\,B^{(q)}_{\mu\nu}(\boldsymbol{r}) + B^{(q)}_{\mu\nu}(\boldsymbol{r})\,\overset{\rightarrow}{\nabla}_{\mu}\sigma_{\nu,\sigma\sigma'}\right\}$$

$$= \frac{1}{2\mathrm{i}}\sum_{\mu\nu}\sigma_{\nu,\sigma\sigma'}\left\{\overset{\rightarrow}{\nabla}_{\mu}B^{(q)}_{\mu\nu}(\boldsymbol{r}) + B^{(q)}_{\mu\nu}(\boldsymbol{r})\overset{\rightarrow}{\nabla}_{\mu}\right\}$$

$$= \mathrm{i}\sum_{\mu\nu}\left\{B_{14}\overset{\rightarrow}{\nabla}_{\mu}J_{\mu\nu}(\boldsymbol{r}) + B_{16}\overset{\rightarrow}{\nabla}_{\mu}J^{(q)}_{\mu\nu}(\boldsymbol{r}) + B_{14}J_{\mu\nu}(\boldsymbol{r})\overset{\rightarrow}{\nabla}_{\mu} + B_{16}J^{(q)}_{\mu\nu}(\boldsymbol{r})\overset{\rightarrow}{\nabla}_{\mu}\right\}\sigma_{\nu,\sigma\sigma'}$$

$$-\frac{1}{2\mathrm{i}}\sum_{\mu\nu\lambda}B_9\,\varepsilon_{\mu\nu\lambda}\left\{\overset{\rightarrow}{\nabla}_{\mu}\nabla_{\lambda}\big(\rho(\boldsymbol{r}) + \rho^{(q)}(\boldsymbol{r})\big) + \nabla_{\lambda}\big(\rho(\boldsymbol{r}) + \rho^{(q)}(\boldsymbol{r})\big)\overset{\rightarrow}{\nabla}_{\mu}\right\}\sigma_{\nu,\sigma\sigma'}$$

$$= \mathrm{i}B_{14}\sum_{\mu\nu}\left\{\overset{\rightarrow}{\nabla}_{\mu}J_{\mu\nu}(\boldsymbol{r}) + J_{\mu\nu}(\boldsymbol{r})\overset{\rightarrow}{\nabla}_{\mu}\right\} + \mathrm{i}B_{16}\sum_{\mu\nu}\left\{\overset{\rightarrow}{\nabla}_{\mu}J^{(q)}_{\mu\nu}(\boldsymbol{r}) + J^{(q)}_{\mu\nu}(\boldsymbol{r})\overset{\rightarrow}{\nabla}_{\mu}\right\}$$

$$-\mathrm{i}B_9\boldsymbol{\nabla}\big(\rho(\boldsymbol{r}) + \rho^{(q)}(\boldsymbol{r})\big)\cdot\boldsymbol{\sigma}_{\sigma\sigma'}\times\boldsymbol{\nabla}, \tag{B.3.65}$$

which coincide with the third terms in Eqs. (B.3.49) and (B.3.50) and the second term in Eq. (B.3.44).

Finally, we make a small proof for the notation of the single-particle Hamiltonian containing the mean-field $\boldsymbol{I}(\boldsymbol{r})$:

$$\frac{1}{2\mathrm{i}}\left(\overrightarrow{\boldsymbol{\nabla}}\cdot\boldsymbol{I}^{(q)}(\boldsymbol{r})+\boldsymbol{I}^{(q)}(\boldsymbol{r})\cdot\overrightarrow{\boldsymbol{\nabla}}\right)$$

$$=\ \mathrm{i}B_3\left\{\overrightarrow{\boldsymbol{\nabla}}\cdot\boldsymbol{j}(\boldsymbol{r})+\boldsymbol{j}(\boldsymbol{r})\cdot\overrightarrow{\boldsymbol{\nabla}}\right\}+\mathrm{i}B_4\left\{\overrightarrow{\boldsymbol{\nabla}}\cdot\boldsymbol{j}^{(q)}(\boldsymbol{r})+\boldsymbol{j}(\boldsymbol{r})^{(q)}\cdot\overrightarrow{\boldsymbol{\nabla}}\right\}$$

$$+\frac{1}{2\mathrm{i}}B_9\Big(\underbrace{\boldsymbol{\nabla}\cdot\boldsymbol{\nabla}\times\left\{\boldsymbol{s}(\boldsymbol{r})+\boldsymbol{s}^{(q)}(\boldsymbol{r})\right\}}_{=0}+2\boldsymbol{\nabla}\times\left\{\boldsymbol{s}(\boldsymbol{r})+\boldsymbol{s}^{(q)}(\boldsymbol{r})\right\}\cdot\boldsymbol{\nabla}\Big),\qquad\text{(B.3.66)}$$

which coincide with the third terms in Eqs. (B.3.35) and (B.3.36) and the fourth term in Eq. (B.3.44). Other mean-field potentials, $M^{(q)}(\boldsymbol{r})$, $U^{(q)}(\boldsymbol{r})$, $\boldsymbol{C}^{(q)}(\boldsymbol{r})$, and $\boldsymbol{\Sigma}^{(q)}(\boldsymbol{r})$, are defined straightforwardly.

Appendix C

Constrained Hartree-Fock Method

We are interested in not only a ground state of nuclei but also states with different properties such as energies, deformations, angular momenta, and so on. For example, to investigate adiabatic fission paths, we calculate a multidimensional PES as functions of $e.g.$ nuclear elongation, asymmetry, deformation of fragments, and thickness of a neck. To calculate such a PES, we need to minimize energy with certain constraints, namely, we minimize energy requiring some expectation values to be specific values. In this Chapter, we explain how to achieve such a Hartree-Fock calculation with certain constraints.

C.1 Linear constraint

The most simple way to minimize energy with certain constraints is a variational calculation with Lagrange multipliers. Here, we consider the case where we require expectation values of one-body operators $\hat{Q}_k = \sum_{i=1}^{N} \hat{q}_k(\boldsymbol{r}_i)$ become q_k, $(k = 1, \cdots, N_\mathrm{c})$

$$\langle \Phi | \hat{\boldsymbol{Q}} | \Phi \rangle = \boldsymbol{q}, \tag{C.1.1}$$

where $|\Phi\rangle$ is a many-body wave function of the system. To achieve this, we transform a Hamiltonian of the system, $\hat{H}$, as follows:

$$\hat{H}' = \hat{H} - \boldsymbol{\lambda} \cdot \hat{\boldsymbol{Q}}, \tag{C.1.2}$$

where $\boldsymbol{\lambda} = (\lambda_1, \cdots, \lambda_{N_\mathrm{c}})$ is a set of the Lagrange multipliers. Denoting the expectation value of transformed Hamiltonian as $E'(\boldsymbol{\lambda})$, there follows

$$\begin{aligned} E'(\boldsymbol{\lambda}) &= \langle \Phi(\boldsymbol{\lambda}) | \hat{H}' | \Phi(\boldsymbol{\lambda}) \rangle \\ &= \langle \Phi(\boldsymbol{\lambda}) | \hat{H} | \Phi(\boldsymbol{\lambda}) \rangle - \boldsymbol{\lambda} \cdot \langle \Phi(\boldsymbol{\lambda}) | \hat{\boldsymbol{Q}} | \Phi(\boldsymbol{\lambda}) \rangle \\ &= E(\boldsymbol{\lambda}) - \boldsymbol{\lambda} \cdot \boldsymbol{Q}(\boldsymbol{\lambda}), \end{aligned} \tag{C.1.3}$$

where $\boldsymbol{Q} = \sum_{i=1}^{N} \langle \phi_i | \hat{\boldsymbol{q}} | \phi_i \rangle$ and ϕ_i denotes the single-particle wave function. According to the variational principle, we require E' to be stationary under any variations,

$$\delta E' = \delta \langle \Phi(\boldsymbol{\lambda}) | \hat{H} | \Phi(\boldsymbol{\lambda}) \rangle - \boldsymbol{\lambda} \cdot \delta \langle \Phi(\boldsymbol{\lambda}) | \hat{\boldsymbol{Q}} | \Phi(\boldsymbol{\lambda}) \rangle = 0. \tag{C.1.4}$$

If we conduct variations of E' for q_k, we find

$$\frac{\partial E}{\partial q_k} = \lambda_k \frac{\partial Q_k}{\partial q_k} = \lambda_k. \tag{C.1.5}$$

At the last equality, we used the required relation, $\langle \Phi | \hat{Q}_k | \Phi \rangle = q_k$. Above relation indicates that, in the CHF approach with liner constraints, we calculate a state which satisfies $\partial E / \partial q_k = \lambda_k$ for a given

Figure C.1:   Schematic picture for the constrained Hartree-Fock calculation with a linear constraint. A solid curve denotes energy surface of the original system.

fixed value of λ_k. Figure C.1 shows a schematic picture of CHF calculation with a linear constraint. In the figure, we show an energy surface $E(q)$ as a function of q. For a fixed value of $\lambda = \lambda_{\mathrm{c}}$, we can calculate a state at $\partial E(q)/\partial q = \lambda_{\mathrm{c}}$. It corresponds to an energy minimization calculation on a new potential energy surface E' rotated by $\alpha = \tan \lambda_{\mathrm{c}}$.

We note that, in the CHF calculation with linear constraints, what we can adjust is not the expectation values $\boldsymbol{q} = \langle \Phi | \hat{\boldsymbol{Q}} | \Phi \rangle$ but the slope of energy surface, $\partial E/\partial \boldsymbol{q}$. According to this fact, the CHF approach with linear constraints no longer works, when the fixed λ locates at a vicinity of the inflection point or the energy surface $E(q)$ has a positive second derivative. In the former case, there are many solutions with same λ having slightly different values of q. In the latter case, there is no stationary solution around such an energy maximum.

C.2   Quadratic constraint

Contrary to the case of linear constraints, we can calculate the energy for any values of $\boldsymbol{q}$ by adopting quadratic constraints. In the CHF approach with quadratic constraints, we consider a minimization problem of the following energy:

$$E''(\boldsymbol{q}) = \langle \Phi(\boldsymbol{q}) | \hat{H} | \Phi(\boldsymbol{q}) \rangle + \frac{1}{2} C \Big(\langle \Phi(\boldsymbol{q}) | \hat{\boldsymbol{Q}} | \Phi(\boldsymbol{q}) \rangle - \boldsymbol{\mu} \Big)^2, \tag{C.2.1}$$

where $\boldsymbol{\mu} = (\mu_1, \cdots, \mu_{N_{\mathrm{c}}})$ is a set of arbitrary parameters. In Fig. C.2, we schematically show the new energy surface E'' as a function of q. As seen in the figure, we can calculate a state with $q_k = \langle \Phi | \hat{Q}_k | \Phi \rangle \sim \mu_k$. By conducting a variation of E'' for q_k, we find

$$\frac{\partial E''(\boldsymbol{q})}{\partial q_k} = \frac{\partial E(\boldsymbol{q})}{\partial q_k} + C \Big(\langle \Phi(\boldsymbol{q}) | \hat{Q}_k | \Phi(\boldsymbol{q}) \rangle - \mu_k \Big) = 0, \tag{C.2.2}$$

where we again used the required relation, $\langle \Phi | \hat{Q}_k | \Phi \rangle = q_k$. The above equation is equivalent to the linear constraints with $\boldsymbol{\lambda} = -C \big(\langle \Phi | \hat{\boldsymbol{Q}} | \Phi \rangle - \boldsymbol{\mu} \big)$. Thus this CHF calculation with quadratic constraints gives the same energy surface to that calculated with linear constraints. Calculating variation of

Figure C.2: Same as Fig. C.1 but for a quadratic constraint.

Eq. (C.2.2) for q_k, we obtain

$$\frac{\partial \mu_k}{\partial q_k} = 1 + \frac{1}{C} \frac{\partial^2 E''(\boldsymbol{q})}{\partial q_k^2}, \tag{C.2.3}$$

where $1 = \partial Q_k / \partial q_k$. Therefore, for sufficiently large value of C satisfying $C > \left| \partial^2 E / \partial q_k^2 \right|$, μ_k becomes monotonic function of q_k. It ensures the existence of stable solution at a given μ_k.

C.3 Constrained imaginary-time method

Another way to achieve minimization with certain constraints is the constrained imaginary time method. In the method, we determine the Lagrange multipliers so as to satisfy $\langle \Phi | \hat{\boldsymbol{Q}} | \Phi \rangle = \boldsymbol{q}$ at every imaginary-time step. As we done in practice, we give formulae for the constrained imaginary time method putting constraints on $\langle \Phi | \hat{\boldsymbol{Q}} | \Phi \rangle = \boldsymbol{q}$ and orthonormality of single-particle wave functions, $\langle \phi_i | \phi_j \rangle = \delta_{ij}$. The variational principle with these constraints requires the following relation:

$$\delta \left[\frac{\langle \Phi | \hat{H} | \Phi \rangle}{\langle \Phi | \Phi \rangle} - \sum_k \eta_k \left(\langle \Phi | \hat{Q}_k | \Phi \rangle - Q_k \right) - \sum_{ij} \varepsilon_{ij} \left(\langle \phi_i | \phi_j \rangle - \delta_{ij} \right) \right] = 0, \tag{C.3.1}$$

where η_k and ε_{ij} are the Lagrange multipliers. By conducing the variation Eq. (C.3.1) with respect to the single-particle wave function, $\phi_i^*(\boldsymbol{r}\sigma)$, we find

$$\frac{\delta E}{\delta \phi_i^*(\boldsymbol{r}\sigma)} - \sum_k \eta_k \hat{q}_k(\boldsymbol{r}) \phi_i(\boldsymbol{r}\sigma) - \sum_j \varepsilon_{ij} \phi_j(\boldsymbol{r}\sigma) = 0, \tag{C.3.2}$$

where E denotes the total energy, $E = \langle \Phi | \hat{H} | \Phi \rangle / \langle \Phi | \Phi \rangle$. Then, the infinitesimal imaginary time evolution is given by

$$\phi_i^{(n+1)}(x) = \phi_i^{(n)}(x) - \Delta\tau \, g_i^{(n)}(x), \tag{C.3.3}$$

where x denotes a set of the spatial and the spin coordinates, $x = (\boldsymbol{r}, \sigma)$. The superscript (n) indicates imaginary time, $\tau = \mathrm{i}n\Delta t$. The function $g_i^{(n)}(x)$ is defined as

$$g_i^{(n)}(x) \equiv f_i^{(n)}(x) - \sum_k \eta_k \hat{q}_k(\boldsymbol{r}) \phi_i^{(n)}(x) - \sum_j \varepsilon_{ij} \phi_j^{(n)}(x), \tag{C.3.4}$$

$$f_i^{(n)}(x) \equiv \frac{\delta E^{(n)}}{\delta \phi_i^*(x)} = \frac{\delta}{\delta \phi_i^*(x)} \frac{\langle \Phi^{(n)} | \hat{H} | \Phi^{(n)} \rangle}{\langle \Phi^{(n)} | \Phi^{(n)} \rangle}, \tag{C.3.5}$$

where $E^{(n)}$ and $\Phi^{(n)}$ are the total energy and the many-body wave function at imaginary time $\tau = \mathrm{i}n\Delta t$. In the following, we shall determine the Lagrange multipliers η_k and ε_{ij} so as to satisfy subsidiary conditions, $\langle \Phi | \hat{Q}_k | \Phi \rangle = Q_k$ and $\langle \phi_i | \phi_j \rangle = \delta_{ij}$.

We first require that the condition $\langle \Phi | \hat{Q}_k | \Phi \rangle = Q_k$ is satisfied after an imaginary time evolution:

$$
\begin{aligned}
\langle \Phi^{(n+1)} | \hat{Q}_k | \Phi^{(n+1)} \rangle &= \sum_{i=1}^A \langle \phi_i^{(n+1)} | \hat{q}_k | \phi_i^{(n+1)} \rangle \\
&= \sum_{i=1}^A \Bigl\{ \langle \phi_i^{(n)} | \hat{q}_k | \phi_i^{(n)} \rangle - \Delta\tau \Bigl(\langle \phi_i^{(n)} | \hat{q}_k | g_i^{(n)} \rangle + \langle g_i^{(n)} | \hat{q}_k | \phi_i^{(n)} \rangle \Bigr) \\
&\qquad\qquad + (\Delta\tau)^2 \langle g_i^{(n)} | \hat{q}_k | g_i^{(n)} \rangle \Bigr\} \\
&= \langle Q_k^{(n)} \rangle - \Delta\tau \sum_{i=1}^A \Bigl(\langle \phi_i^{(n)} | \hat{q}_k | f_i^{(n)} \rangle + \langle f_i^{(n)} | \hat{q}_k | \phi_i^{(n)} \rangle \Bigr) \\
&\qquad + \Delta\tau \sum_{i=1}^A \sum_l \Bigl(\eta_l \langle \phi_i^{(n)} | \hat{q}_k \hat{q}_l | \phi_i^{(n)} \rangle + \eta_l^* \langle \phi_i^{(n)} | \hat{q}_l \hat{q}_k | \phi_i^{(n)} \rangle \Bigr) \\
&\qquad + \Delta\tau \sum_{ij} \Bigl(\varepsilon_{ij} \langle \phi_i^{(n)} | \hat{q}_k | \phi_j^{(n)} \rangle + \varepsilon_{ij}^* \langle \phi_j^{(n)} | \hat{q}_k | \phi_i^{(n)} \rangle \Bigr) \\
&= \langle Q_k^{(n)} \rangle - \Delta\tau \sum_{i=1}^A \Bigl(\langle \phi_i^{(n)} | \hat{q}_k | f_i^{(n)} \rangle + \langle f_i^{(n)} | \hat{q}_k | \phi_i^{(n)} \rangle \Bigr) \\
&\qquad + 2\Delta\tau \sum_l \eta_l \sum_{i=1}^A \langle \phi_i^{(n)} | \hat{q}_k \hat{q}_l | \phi_i^{(n)} \rangle + 2\Delta\tau \sum_{ij} \varepsilon_{ij} \langle \phi_i^{(n)} | \hat{q}_k | \phi_j^{(n)} \rangle \\
&\equiv Q_k, \tag{C.3.6}
\end{aligned}
$$

where, in the third equality, we have assumed that η_k is real, $\eta_k^* = \eta_k$. In the fourth equality, we have assumed that constraint operators commute each other, $[\hat{q}_k, \hat{q}_l] = 0$, and ε_{ij} is hermitian, $\varepsilon_{ij} = \varepsilon_{ji}^*$. In the same way, we require that the condition $\langle \phi_i | \phi_j \rangle = \delta_{ij}$ is satisfied after the imaginary time

evolution:

$$
\begin{aligned}
\langle\phi_i^{(n+1)}|\phi_j^{(n+1)}\rangle &= \underbrace{\langle\phi_i^{(n)}|\phi_j^{(n)}\rangle}_{=\delta_{ij}} -\Delta\tau\Big(\langle\phi_i^{(n)}|f_j^{(n)}\rangle+\langle f_i^{(n)}|\phi_j^{(n)}\rangle\Big) \\
&\quad +2\Delta\tau\sum_k \eta_k\langle\phi_i^{(n)}|\hat{q}_k|\phi_j^{(n)}\rangle \\
&\quad +\Delta\tau\sum_{k=1}^{A}\Big(\varepsilon_{jk}\underbrace{\langle\phi_i^{(n)}|\phi_k^{(n)}\rangle}_{=\delta_{ik}}+\varepsilon_{ik}^{*}\underbrace{\langle\phi_k^{(n)}|\phi_j^{(n)}\rangle}_{=\delta_{kj}}\Big) \\
&= \delta_{ij}-\Delta\tau\Big(\langle\phi_i^{(n)}|f_j^{(n)}\rangle+\langle f_i^{(n)}|\phi_j^{(n)}\rangle\Big) \\
&\quad +2\Delta\tau\sum_k \eta_k\langle\phi_i^{(n)}|\hat{q}_k|\phi_j^{(n)}\rangle + 2\Delta\tau\,\varepsilon_{ji} \\
&\equiv \delta_{ij},
\end{aligned}
\tag{C.3.7}
$$

where we have assumed that the orthonormality of single-particle wave functions at imaginary time $\tau = \mathrm{i}n\Delta t$, $\langle\phi_i^{(n)}|\phi_j^{(n)}\rangle = \delta_{ij}$, is satisfied. Because of this assumption, in practical calculations, we have to ensure the orthonormality employing the Schmidt's orthogonalization method at every imaginary-time step.

We make small modifications for Eqs. (C.3.6) and (C.3.7). From the requirement for the expectation values of $\hat{Q}_k$, Eq. (C.3.6), we find

$$
\begin{aligned}
\sum_l \eta_l \sum_{i=1}^{A}\langle\phi_i^{(n)}|\hat{q}_k\hat{q}_l|\phi_i^{(n)}\rangle &= \frac{1}{2\Delta\tau}\Big(Q_k-\langle\hat{Q}_k\rangle^{(n)}\Big)+\frac{1}{2}\sum_{i=1}^{A}\Big(\langle\phi_i^{(n)}|\hat{q}_k|f_i^{(n)}\rangle+\langle f_i^{(n)}|\hat{q}_k|\phi_i^{(n)}\rangle\Big) \\
&\quad -\sum_{ij}\varepsilon_{ji}\langle\phi_j^{(n)}|\hat{q}_k|\phi_i^{(n)}\rangle.
\end{aligned}
\tag{C.3.8}
$$

From the requirement for the orthonormal relation, Eq. (C.3.7), we find

$$
\varepsilon_{ji} = \frac{1}{2}\Big(\langle\phi_i^{(n)}|f_j^{(n)}\rangle+\langle f_i^{(n)}|\phi_j^{(n)}\rangle\Big)-\sum_k \eta_k\langle\phi_i^{(n)}|\hat{q}_k|\phi_j^{(t)}\rangle.
\tag{C.3.9}
$$

By substituting Eq. (C.3.9) into Eq. (C.3.8) to eliminate ε_{ji}, we obtain a linear equation to determine the Lagrange multipliers η_k which ensures the requirements, Eqs. (C.3.6) and (C.3.7):

$$
\begin{aligned}
\sum_l \eta_l \sum_{i=1}^{A}\langle\phi_i^{(n)}|\hat{q}_k\hat{q}_l|\phi_i^{(n)}\rangle &= \frac{1}{2\Delta\tau}\Big(Q_k-\langle\hat{Q}_k\rangle^{(n)}\Big)+\frac{1}{2}\sum_{i=1}^{A}\Big(\langle\phi_i^{(n)}|\hat{q}_k|f_i^{(n)}\rangle+\langle f_i^{(n)}|\hat{q}_k|\phi_i^{(n)}\rangle\Big) \\
&\quad -\sum_{ij}\bigg[\frac{1}{2}\Big(\langle\phi_i^{(n)}|f_j^{(n)}\rangle+\langle f_i^{(n)}|\phi_j^{(n)}\rangle\Big)-\sum_l \eta_l\langle\phi_i^{(n)}|\hat{q}_l|\phi_j^{(n)}\rangle\bigg]\langle\phi_j^{(n)}|\hat{q}_k|\phi_i^{(n)}\rangle \\
\Leftrightarrow \sum_l \eta_l\bigg\{\sum_{i=1}^{A}&\langle\phi_i^{(n)}|\hat{q}_k\hat{q}_l|\phi_i^{(n)}\rangle-\sum_{ij}\langle\phi_i^{(n)}|\hat{q}_k|\phi_j^{(n)}\rangle\langle\phi_j^{(n)}|\hat{q}_l|\phi_i^{(t)}\rangle\bigg\} \\
= \frac{1}{2\Delta\tau}\Big(Q_k-\langle\hat{Q}_k\rangle^{(n)}\Big)&+\sum_{i=1}^{A}\Re\Big[\langle\phi_i^{(n)}|\hat{q}_k|f_i^{(n)}\rangle\Big]-\sum_{ij}\frac{1}{2}\Big(\langle\phi_i^{(n)}|f_j^{(n)}\rangle+\langle f_i^{(n)}|\phi_j^{(n)}\rangle\Big)\langle\phi_j^{(n)}|\hat{q}_k|\phi_i^{(n)}\rangle \\
&\Leftrightarrow \sum_l A_{kl}\,\eta_l = B_k,
\end{aligned}
\tag{C.3.10}
$$

where

$$A_{kl} \equiv \sum_{i=1}^{A}\langle\phi_i^{(n)}|\hat{q}_k\hat{q}_l|\phi_i^{(n)}\rangle - \sum_{ij}\langle\phi_i^{(n)}|\hat{q}_k|\phi_j^{(n)}\rangle\langle\phi_j^{(n)}|\hat{q}_l|\phi_i^{(t)}\rangle \tag{C.3.11}$$

$$B_k \equiv \frac{1}{2\Delta\tau}\Big(Q_k - \langle\hat{Q}_k\rangle^{(n)}\Big) + \sum_{i=1}^{A}\Re\Big[\langle\phi_i^{(n)}|\hat{q}_k|f_i^{(n)}\rangle\Big]$$
$$- \sum_{ij}\frac{1}{2}\Big(\langle\phi_i^{(n)}|f_j^{(n)}\rangle + \langle f_i^{(n)}|\phi_j^{(n)}\rangle\Big)\langle\phi_j^{(n)}|\hat{q}_k|\phi_i^{(n)}\rangle. \tag{C.3.12}$$

By solving Eq. (C.3.10) for η_k, we can get the Lagrange multipliers which ensure requirements, $\langle\Phi^{(n+1)}|\hat{\boldsymbol{Q}}|\Phi^{(n+1)}\rangle = \boldsymbol{Q}$ and $\langle\phi_i|\phi_j\rangle = \delta_{ij}$, at each imaginary-time step. In practice, we calculate the inverse of the matrix A to solve the equation Eq. (C.3.10) for $\boldsymbol{\eta}$.

C.4 Constraint operators

We have used the following constraint operators in practical calculations.

- Center-of-mass coordinates:

$$\hat{x}, \quad \hat{y}, \quad \hat{z}. \tag{C.4.1}$$

These constraints are used to fix a nucleus at the center of a numerical box.

- Principal axes:

$$\hat{x}\hat{y}, \quad \hat{y}\hat{z}, \quad \hat{z}\hat{x}. \tag{C.4.2}$$

We usually require $\langle\hat{x}\hat{y}\rangle = \langle\hat{y}\hat{z}\rangle = \langle\hat{z}\hat{x}\rangle = 0$ in order to set principal axes of a nucleus parallel to the x-, y-, and z-axis.

- Multipole moments:

$$\hat{Q}_{20} = \sqrt{\frac{5}{16\pi}}\Big(2\hat{z}^2 - \hat{x}^2 - \hat{y}^2\Big), \tag{C.4.3}$$

$$\hat{Q}_{22} = \sqrt{\frac{15}{16\pi}}\Big(\hat{x}^2 - \hat{y}^2\Big), \tag{C.4.4}$$

$$\hat{Q}_{30} = \sqrt{\frac{7}{16\pi}}\Big(2\hat{z}^2 - 3\hat{x}^2 - 3\hat{y}^2\Big)\hat{z}, \tag{C.4.5}$$

$$\vdots$$

In practice, we use constraints on $\hat{Q}_{20}$ and $\hat{Q}_{22}$ in order to impose constraints on deformation parameters, β and γ. They are given by

$$\beta = \frac{4\pi}{5}\frac{1}{A\langle r\rangle^2}\sqrt{\langle\hat{Q}_{20}\rangle^2 + \langle\hat{Q}_{22}\rangle^2}, \tag{C.4.6}$$

$$\gamma = \arctan\left[\frac{\langle\hat{Q}_{22}\rangle}{\langle\hat{Q}_{20}\rangle}\right]\frac{360}{2\pi} \quad [\text{deg}], \tag{C.4.7}$$

where $\langle r\rangle$ denotes the root-mean-square radius. In a static HF calculation, we first calculate states imposing constraints on $\beta = 0$ and $\beta = 0.1$ and 0.2 with $\gamma = 0°, 30°$, and $60°$. We then release those constraints and re-minimize the energy. After getting convergent results, we regard a least energy state as a HF ground state.

Appendix D

Calculation of the Coulomb Potential for an Isolated System

In this Chapter, we present a method to calculate the Coulomb potential $V(\boldsymbol{r})$ of a charge density distribution $\rho_p(\boldsymbol{r})$ in the finite numerical box of

$$0 < x \le L_x,\ 0 < y \le L_y,\ 0 < z \le L_z.$$

The Coulomb potential takes the form

$$V(\boldsymbol{r}) = \int d\boldsymbol{r}' \frac{e^2}{|\boldsymbol{r} - \boldsymbol{r}'|} \rho_p(\boldsymbol{r}').$$

This method is known as Hockney's method [152].

D.1 Preparation

D.1.1 Decomposition of the Coulomb potential

We decompose the Coulomb potential into two parts, the long-range part and the short-range part. Using error function, we define these two parts as follows:

$$\frac{1}{r} = \frac{1}{r} \mathrm{erf}(\frac{r}{R_c}) + \frac{1}{r}\left\{1 - \mathrm{erf}(\frac{r}{R_c})\right\}$$

$$\equiv G^L(r) + G^S(r) \tag{D.1.1}$$

with

$$G^L(r) = \frac{1}{r}\mathrm{erf}(\frac{r}{R_c}), \tag{D.1.2}$$

$$G^S(r) = \frac{1}{r}\mathrm{erfc}(\frac{r}{R_c}). \tag{D.1.3}$$

The error functions are defined by

$$\mathrm{erf}(r) = \frac{2}{\sqrt{\pi}} \int_0^x e^{-t^2} dt, \tag{D.1.4}$$

$$\mathrm{erfc}(r) = 1 - \mathrm{erf}(r). \tag{D.1.5}$$

D.1.2   Assumption of periodicity

We assume that $\rho_p(\boldsymbol{r})$ is a periodic function of a length $2L$,

$$\rho(\boldsymbol{r}) \equiv \begin{cases} \rho_p(\boldsymbol{r}) & (0 < r \le L), \\ 0 & (L < r \le 2L). \end{cases} \tag{D.1.6}$$

Then we can represent $\rho(\boldsymbol{r})$ and $G^L(r)$ as a Fourier series

$$\rho(x) = \sum_{k=-\infty}^{\infty} \tilde{\rho}_k e^{\mathrm{i}\frac{2\pi k}{2L}x} \quad , \quad \tilde{\rho}_k = \frac{1}{2L}\int_0^{2L} dx\, \rho(x) e^{-\mathrm{i}\frac{2\pi k}{2L}x}, \tag{D.1.7}$$

$$G^L(x) = \sum_{k=-\infty}^{\infty} \tilde{G}_k^L e^{\mathrm{i}\frac{2\pi k}{2L}x} \quad , \quad \tilde{G}_k^L = \frac{1}{2L}\int_{-L}^{L} dx\, G^L(x) e^{-\mathrm{i}\frac{2\pi k}{2L}x}. \tag{D.1.8}$$

Here, we consider one-dimensional case for simplicity. An extension to three-dimensional case is straightforward. Actually, the spatial integral for the inverse transformation is performed by discretizing the interval of the integral. Defining these quantities,

$$\rho_i \equiv \rho(x_i) \quad , \quad G_i^L \equiv G^L(x_i), \tag{D.1.9}$$

$$i = 1, \cdots, 2N \quad , \quad x_i = iH \quad , \quad 2NH = 2L \quad , \tag{D.1.10}$$

we find

$$\begin{aligned}
\tilde{\rho}_k &= \frac{1}{2L}\sum_{i=1}^{N} \rho_i e^{-\mathrm{i}\frac{2\pi k}{2L}x_i} H \\
&= \frac{1}{2N}\sum_{i=1}^{N} \rho_i e^{-\mathrm{i}\frac{2\pi ki}{2N}},
\end{aligned} \tag{D.1.11}$$

$$G_k^L = \frac{1}{2N}\sum_{i=-N+1}^{N} G_i^L e^{-\mathrm{i}\frac{2\pi ki}{2N}}. \tag{D.1.12}$$

Since $\rho_i = 0$ ($N < i \le 2N$), the summation over grid points i takes $i = 1, \cdots, N$.

D.2   Calculation of the long-range part of the Coulomb potential

We denote the long-range part of the Coulomb potential as $V^L(x)$ which takes the form

$$V^L(x) = e^2 \int_0^{2L} dx'\, G^L(x - x')\rho(x'). \tag{D.2.1}$$

It is difficult to evaluate the spatial integral in the infinitely large space because of the long-range nature of the Coulomb interaction. We thus substitute the Fourier series representation of $\rho(x)$ and $G^L(x)$ into Eq. (D.2.1). We find

$$\begin{aligned}
V^L(x) &= e^2 \int_0^{2L} dx' \left\{ \sum_{k=-\infty}^{\infty} \tilde{G}_k^L e^{\mathrm{i}\frac{2\pi k}{2L}(x-x')} \right\} \left\{ \sum_{l=-\infty}^{\infty} \tilde{\rho}_l e^{\mathrm{i}\frac{2\pi l}{2L}x'} \right\} \\
&= e^2 \sum_{k=-\infty}^{\infty} \sum_{l=-\infty}^{\infty} \tilde{G}_k^L \tilde{\rho}_l e^{\mathrm{i}\frac{2\pi k}{2L}x} \int_0^{2L} dx' e^{-\mathrm{i}\frac{2\pi(k-l)}{2L}x'} \\
&= 2Le^2 \sum_{k=-\infty}^{\infty} \tilde{G}_k^L \tilde{\rho}_k e^{\mathrm{i}\frac{2\pi k}{2L}x}.
\end{aligned} \tag{D.2.2}$$

D.3   Calculation of the short-range part of the Coulomb potential

We denote the short-range part of the Coulomb potential as $V^S(x)$ which takes the form

$$V^S(x) = e^2 \int dx' G^S(x-x')\rho(x'). \tag{D.3.1}$$

In this case, we first perform the Fourier transformation for $\rho(x)$ and $G^S(x)$

$$\rho(x) = \frac{1}{2\pi} \int dq\, \tilde{\rho}(q)e^{iqx} \quad,\quad \tilde{\rho}(q) = \int dx\, \rho(x)e^{-iqx}, \tag{D.3.2}$$

$$G^S(x) = \frac{1}{2\pi} \int dq\, \tilde{G}^S(q)e^{iqx} \quad,\quad \tilde{G}^S(q) = \int dx\, G^S(x)e^{-iqx}. \tag{D.3.3}$$

We also use the Fourier series representation of Eq. (D.1.11) for the inverse transformation of $\rho(\boldsymbol{r})$. We then find

$$
\begin{aligned}
\tilde{\rho}(q) &= \sum_{k=-\infty}^{\infty} \tilde{\rho}_k \int dx e^{-i(q-\frac{2\pi k}{2L}x)} \\
&= 2\pi \sum_{k=-\infty}^{\infty} \tilde{\rho}_k \delta(q - \pi k/L). \tag{D.3.4}
\end{aligned}
$$

Using Eqs. (D.3.2), (D.3.3), and (D.3.4), the short-range part of the Coulomb potential is calculated as

$$
\begin{aligned}
V^S(x) &= e^2 \int_0^{2L} dx' \left\{ \int dq\, \tilde{G}^S(q)e^{iq(x-x')} \right\} \left\{ \int dq'\, \tilde{\rho}(q')e^{iq'x'} \right\} \\
&= \frac{e^2}{(2\pi)^2} \int dq \int dq'\, \tilde{G}^S(q)\tilde{\rho}(q')e^{iqx} \int dx' e^{-i(q-q')x'} \\
&= \frac{e^2}{2\pi} \int dq\, \tilde{G}^S(q)\tilde{\rho}(q)e^{iqx} \\
&= e^2 \sum_{k=-\infty}^{\infty} \tilde{\rho}_k \int dq\, \tilde{G}^S(q)e^{iqx}\delta(q - \frac{\pi k}{L}) \\
&= e^2 \sum_{k=-\infty}^{\infty} \tilde{G}^S(\frac{\pi k}{L})\tilde{\rho}_k e^{i\frac{\pi k}{L}x} \\
&= 2Le^2 \sum_{k=-\infty}^{\infty} \tilde{G}^S_k \tilde{\rho}_k e^{i\frac{\pi k}{L}x}. \tag{D.3.5}
\end{aligned}
$$

We have introduced a notation

$$\tilde{G}^S_k \equiv \frac{1}{2L}\tilde{G}^S(\frac{\pi k}{L}). \tag{D.3.6}$$

D.4   Calculation of the Coulomb potential for the isolated system

To summarize, the Coulomb potential $V(x)$ can be calculated as

$$
\begin{aligned}
V(x) &= V^L(x) + V^S(x) \\
&= 2Le^2 \sum_{k=-\infty}^{\infty} (\tilde{G}^L_k + \tilde{G}^S_k)\tilde{\rho}_k e^{i\frac{\pi k}{L}x}. \tag{D.4.1}
\end{aligned}
$$

For three-dimensional calculation, the Coulomb potential of the charge density $\rho_q(\boldsymbol{r})$ is calculated as follows:

$$i_x = 1, \cdots, N_x \quad, \quad i_y = 1, \cdots, N_y \quad, \quad i_z = 1, \cdots, N_z, \tag{D.4.2}$$

$$L_x = N_x H \quad, \quad L_y = N_y H \quad, \quad L_z = N_z H, \tag{D.4.3}$$

$$V(\boldsymbol{r}) = (2L_x 2L_y 2L_z)e^2 \sum_{\vec{k}=-\vec{N}+1}^{\vec{N}} (\tilde{G}_{\vec{k}}^L + \tilde{G}_{\vec{k}}^S)\tilde{\rho}_{\vec{k}} \exp\left[i\pi\left(\frac{k_x i_x}{N_x} + \frac{k_y i_y}{N_y} + \frac{k_z i_z}{N_z}\right)\right], \tag{D.4.4}$$

$$\tilde{\rho}_{\vec{k}} = \frac{1}{2N_x 2N_y 2N_z} \sum_{\vec{i}=1}^{\vec{N}} \rho_{\vec{i}} \exp\left[-i\pi\left(\frac{k_x i_x}{N_x} + \frac{k_y i_y}{N_y} + \frac{k_z i_z}{N_z}\right)\right], \tag{D.4.5}$$

$$\tilde{G}_{\vec{k}}^L = \frac{1}{2N_x 2N_y 2N_z} \sum_{\vec{i}=-\vec{N}+1}^{\vec{N}} G_{\vec{i}}^L \exp\left[-i\pi\left(\frac{k_x i_x}{N_x} + \frac{k_y i_y}{N_y} + \frac{k_z i_z}{N_z}\right)\right], \tag{D.4.6}$$

$$\tilde{G}_{\vec{k}}^S = \frac{1}{2L_x 2L_y 2L_z} \tilde{G}^S\left(\frac{\pi\vec{k}}{\vec{L}}\right). \tag{D.4.7}$$

In practice, we work with the following relations:

$$\begin{aligned} G^L(r) &= \frac{1}{r}\mathrm{erf}\left(\frac{r}{R_c}\right) = \frac{1}{r}\frac{2}{\sqrt{\pi}}\int_0^{r/R_c} e^{-t^2}\,dt \\ &\xrightarrow{r\to 0} \frac{2}{\sqrt{\pi}R_c}, \end{aligned} \tag{D.4.8}$$

$$\begin{aligned} \tilde{G}^S(\boldsymbol{q}) &= \int d\boldsymbol{r}\, G^S(r)e^{-\boldsymbol{q}\cdot\boldsymbol{r}} \\ &= \int dr \int r\,d\theta \int r\sin\theta\,d\varphi\, \frac{1}{r}\mathrm{erfc}\left(\frac{r}{R_c}\right)e^{-iqr\cos\theta} \\ &= \frac{4\pi}{q}\int_0^\infty dr\,\sin(qr)\,\mathrm{erfc}\left(\frac{r}{R_c}\right) \\ &= \frac{4\pi R_c}{q}\int_0^\infty dr\,\sin(qR_c x)\,\mathrm{erfc}(x) \quad (x \equiv r/R_c), \end{aligned} \tag{D.4.9}$$

$$\tilde{G}^S(\boldsymbol{q}) \xrightarrow{q\to 0} 4\pi R_c^2 \int_0^\infty dx\, x\,\mathrm{erfc}(x). \tag{D.4.10}$$

Appendix E

Ground State Properties Calculated with the Skyrme SLy5 Parameter Set

In Chapter 5, we examined effects of particle evaporation on MNT cross sections for ^{48}Ca+^{124}Sn and ^{58}Ni+^{208}Pb reactions. To calculate average excitation energies of reaction products in each transfer channel, we calculated the energy of HF ground state for each nucleus. Here, we present properties of HF ground states obtained from the calculations.

To calculate HF ground states, we performed β-γ CHF calculations. We first minimize the total energy imposing constraints of $\beta = 0$ and $\beta = 0.1$ and 0.2 with $\gamma = 0°, 30°$, and $60°$. We then release those constraints on β and γ and re-minimize the energy. We regarded a least energy state as the HF ground state.

For odd-even, even-odd, and odd-odd nuclei, we adopted the so called equal-filling approximation, where the occupation probability of the last occupied nucleon is forced be 0.5 so as to equally fill both the highest occupied orbital and its time-reversal partner. We then calculate densities with the occupation probability, _e.g._ $\rho(\boldsymbol{r}) = \sum_{i\sigma} n_i \big|\phi_i(\boldsymbol{r}\sigma)\big|^2$, where n_i denotes the occupation probability of ith orbital.

In Tables E.1-E.20, we summarize obtained results for every nucleus. We denote the ground state energy calculated by using SLy5 parameter set [141] as $E_{\text{g.s.}}$ which is shown in 4th column in the table. The $E_{g.s.}$(SLyIII.0.8) shown in 11th column of the table is defined by

$$E_{\text{g.s.}}(\text{SLyIII.0.8}) \equiv \big\langle \Phi_{\text{g.s.}}(\text{SLy5}) \big| \hat{H}_{\text{Skyrme}}(\text{SLyIII.0.8}) \big| \Phi_{\text{g.s.}}(\text{SLy5}) \big\rangle, \qquad \text{(E.0.1)}$$

where $\big| \Phi_{\text{g.s.}}(\text{SLy5}) \big\rangle$ denotes the wave function in the HF ground state calculated by using SLy5 parameter set. $\hat{H}_{\text{Skyrme}}(\text{SLyIII.0.8})$ denotes the Skyrme Hamiltonian with SLyIII.0.8 parameter set [146]. The energy $E_{\text{g.s.}}(\text{SLyIII.0.8})$ was used to evaluate the average excitation energy of reaction products presented in Chapter 5.

Table E.1:   Ground state properties of silicon (upper table) and phosphors (lower table) isotopes calculated with Skyrme SLy5 parameter set [141]. We use $N_x \times N_y \times N_z = 26 \times 26 \times 26$ grid points with 0.8-fm mesh. The 11-point high-order finite difference method is used for derivatives. The one-body center-of-mass correction was taken into account.

										$_{14}$Si
Z	N	A	$E_{\text{g.s.}}$	β	γ (deg)	$\varepsilon_n(1)$	$\varepsilon_p(1)$	$\varepsilon_n(N)$	$\varepsilon_p(Z)$	$E_{\text{g.s.}}$(SLyIII.0.8)
14	14	28	-234.324	0.274	60.0	-45.751	-39.587	-15.723	-10.434	-230.223
14	15	29	-244.242	0.179	60.0	-46.538	-41.257	-11.036	-11.268	-239.873
14	16	30	-255.705	0.002		-47.392	-42.729	-12.253	-12.832	-249.875
14	17	31	-263.305	0.087	60.0	-46.628	-43.242	-8.382	-13.546	-258.047
14	18	32	-271.244	0.137	60.0	-45.846	-43.664	-8.578	-14.556	-266.427
14	19	33	-278.141	0.051	60.0	-45.642	-44.559	-7.765	-15.774	-273.317
14	20	34	-285.612	0.000		-45.187	-45.198	-8.141	-17.044	-280.840
14	21	35	-288.995	0.067	60.0	-45.307	-45.933	-4.087	-17.753	-284.245
14	22	36	-292.927	0.163	0.2	-45.311	-46.472	-5.033	-17.606	-287.868
14	23	37	-297.143	0.201	0.4	-45.416	-47.146	-4.748	-18.174	-291.979
14	24	38	-301.510	0.237	0.0	-45.515	-47.794	-4.915	-18.718	-296.154
14	25	39	-304.743	0.230	11.3	-45.703	-48.508	-3.796	-19.873	-299.254
14	26	40	-308.351	0.247	25.1	-45.652	-48.895	-4.281	-21.051	-302.343
14	27	41	-311.129	0.243	45.2	-45.672	-49.332	-3.745	-23.068	-304.673
14	28	42	-314.935	0.265	60.0	-45.606	-49.694	-4.472	-24.703	-307.716
14	29	43	-315.640	0.233	59.8	-45.991	-50.455	-1.284	-25.268	-308.043
14	30	44	-316.777	0.208	44.5	-46.287	-51.166	-1.864	-25.451	-308.620

										$_{15}$P
Z	N	A	$E_{\text{g.s.}}$	β	γ (deg)	$\varepsilon_n(1)$	$\varepsilon_p(1)$	$\varepsilon_n(N)$	$\varepsilon_p(Z)$	$E_{\text{g.s.}}$(SLyIII.0.8)
15	14	29	-238.859	0.184	60.0	-47.330	-39.804	-16.505	-5.422	-233.984
15	15	30	-251.050	0.000		-47.833	-41.202	-12.878	-7.287	-245.870
15	16	31	-263.312	0.000		-47.776	-41.887	-12.822	-7.905	-256.627
15	17	32	-272.102	0.074	59.5	-47.146	-42.452	-9.478	-9.050	-266.062
15	18	33	-281.144	0.120	59.9	-46.495	-42.941	-9.643	-10.126	-275.676
15	19	34	-289.276	0.048	59.2	-46.206	-43.706	-8.895	-11.283	-283.866
15	20	35	-297.855	0.000		-45.788	-44.326	-9.202	-12.341	-292.573
15	21	36	-302.222	0.061	59.4	-45.952	-45.088	-4.983	-13.314	-297.053
15	22	37	-307.258	0.169	0.6	-45.927	-45.620	-6.056	-14.445	-302.207
15	23	38	-312.590	0.209	0.3	-46.014	-46.283	-5.859	-15.563	-307.633
15	24	39	-318.081	0.245	0.0	-46.098	-46.922	-6.021	-16.680	-313.098
15	25	40	-322.348	0.234	0.0	-46.332	-47.694	-4.676	-17.710	-317.407
15	26	41	-326.602	0.235	13.6	-46.443	-48.298	-4.836	-18.516	-321.440
15	27	42	-329.512	0.216	34.3	-46.592	-48.882	-3.799	-18.703	-323.860
15	28	43	-333.461	0.227	59.5	-46.652	-49.344	-4.923	-18.768	-326.805
15	29	44	-335.437	0.206	46.4	-46.867	-49.988	-2.611	-20.074	-328.507
15	30	45	-337.937	0.193	30.6	-47.067	-50.630	-3.174	-21.402	-330.417

Table E.2: Same as Table E.1 but for sulfur (upper table) and chlorine (lower table) isotopes.

| | | | | | | | | | | $_{16}$S |
Z	N	A	$E_{\text{g.s.}}$	β	γ (deg)	$\varepsilon_n(1)$	$\varepsilon_p(1)$	$\varepsilon_n(N)$	$\varepsilon_p(Z)$	$E_{\text{g.s.}}$(SLyIII.0.8)
16	14	30	-244.497	0.000		-48.815	-40.125	-18.145	-6.275	-237.732
16	15	31	-257.545	0.000		-48.414	-40.656	-13.503	-6.873	-250.423
16	16	32	-270.433	0.000		-48.225	-41.233	-13.398	-7.461	-262.091
16	17	33	-280.369	0.069	59.3	-47.673	-41.804	-10.568	-8.560	-272.873
16	18	34	-290.496	0.111	59.7	-47.114	-42.314	-10.693	-9.606	-283.852
16	19	35	-299.761	0.048	59.4	-46.794	-43.031	-9.953	-10.692	-293.019
16	20	36	-309.392	0.000		-46.410	-43.648	-10.223	-11.705	-302.759
16	21	37	-314.752	0.081	1.3	-46.558	-44.350	-6.155	-12.706	-308.683
16	22	38	-320.926	0.179	0.2	-46.524	-44.845	-7.126	-13.812	-315.687
16	23	39	-327.392	0.220	0.2	-46.588	-45.478	-6.981	-14.940	-322.508
16	24	40	-334.009	0.256	0.0	-46.654	-46.098	-7.125	-16.055	-329.278
16	25	41	-339.303	0.246	0.0	-46.863	-46.838	-5.672	-17.065	-334.711
16	26	42	-344.523	0.237	0.0	-47.059	-47.538	-5.616	-18.040	-340.001
16	27	43	-348.332	0.262	0.0	-46.940	-47.942	-4.337	-19.035	-342.977
16	28	44	-351.713	0.181	45.2	-47.614	-48.973	-4.929	-18.637	-345.883
16	29	45	-355.456	0.236	0.0	-47.301	-49.215	-3.612	-20.580	-348.876
16	30	46	-358.881	0.185	0.0	-47.765	-50.065	-4.022	-21.094	-351.991

| | | | | | | | | | | $_{17}$Cl |
Z	N	A	$E_{\text{g.s.}}$	β	γ (deg)	$\varepsilon_n(1)$	$\varepsilon_p(1)$	$\varepsilon_n(N)$	$\varepsilon_p(Z)$	$E_{\text{g.s.}}$(SLyIII.0.8)
17	14	31	-246.224	0.091	59.7	-49.175	-39.030	-18.747	-2.373	-239.489
17	15	32	-260.432	0.076	59.3	-48.849	-39.690	-14.623	-3.437	-253.418
17	16	33	-274.445	0.068	59.6	-48.677	-40.342	-14.478	-4.497	-266.432
17	17	34	-286.200	0.109	59.9	-48.077	-40.861	-12.265	-6.194	-279.194
17	18	35	-297.962	0.135	60.0	-47.517	-41.366	-12.239	-7.740	-291.786
17	19	36	-308.147	0.074	60.0	-47.244	-42.111	-10.888	-8.629	-301.876
17	20	37	-318.752	0.027	58.3	-46.886	-42.748	-11.195	-9.561	-312.569
17	21	38	-325.417	0.076	60.0	-47.042	-43.478	-7.147	-10.848	-319.684
17	22	39	-332.248	0.151	0.9	-47.087	-44.080	-7.679	-11.510	-326.887
17	23	40	-339.427	0.187	0.6	-47.187	-44.741	-7.642	-12.239	-334.380
17	24	41	-346.686	0.221	0.2	-47.280	-45.381	-7.732	-12.884	-341.799
17	25	42	-352.925	0.212	0.2	-47.499	-46.121	-6.593	-13.814	-348.211
17	26	43	-359.062	0.204	0.3	-47.707	-46.824	-6.509	-14.717	-354.454
17	27	44	-363.837	0.171	28.5	-47.959	-47.540	-5.482	-16.288	-359.216
17	28	45	-369.283	0.159	59.9	-48.232	-48.250	-6.237	-17.645	-364.056
17	29	46	-373.032	0.163	42.5	-48.231	-48.706	-4.288	-18.160	-367.310
17	30	47	-377.094	0.173	29.2	-48.253	-49.173	-4.614	-18.507	-370.470
17	31	48	-379.894	0.153	42.4	-48.331	-49.632	-3.329	-19.498	-372.213
17	32	49	-383.026	0.139	59.2	-48.425	-50.082	-3.583	-20.275	-373.917

Table E.3: Same as Tables E.1 and E.2 but for argon isotopes.

						$_{18}$Ar				
Z	N	A	$E_{\text{g.s.}}$	β	γ (deg)	$\varepsilon_n(1)$	$\varepsilon_p(1)$	$\varepsilon_n(N)$	$\varepsilon_p(Z)$	$E_{\text{g.s.}}$(SLyIII.0.8)
18	14	32	-248.047	0.144	60.0	-49.417	-37.910	-19.680	-2.317	-241.193
18	15	33	-263.303	0.123	59.8	-49.197	-38.706	-15.654	-3.333	-256.302
18	16	34	-278.363	0.111	59.9	-49.057	-39.448	-15.487	-4.343	-270.667
18	17	35	-291.748	0.135	60.0	-48.461	-39.959	-13.807	-5.883	-285.039
18	18	36	-305.027	0.153	60.0	-47.911	-40.465	-13.692	-7.334	-299.152
18	19	37	-316.101	0.096	60.0	-47.672	-41.230	-11.774	-8.197	-310.183
18	20	38	-327.625	0.048	59.3	-47.345	-41.889	-12.128	-9.078	-321.789
18	21	39	-335.560	0.092	59.8	-47.474	-42.594	-8.355	-10.315	-330.286
18	22	40	-343.479	0.128	60.0	-47.575	-43.245	-8.335	-11.467	-338.803
18	23	41	-351.073	0.150	29.6	-47.731	-43.976	-8.116	-12.140	-346.410
18	24	42	-358.954	0.189	0.2	-47.892	-44.712	-8.357	-12.477	-353.721
18	25	43	-366.129	0.182	10.7	-48.094	-45.425	-7.526	-13.448	-361.255
18	26	44	-373.235	0.183	20.5	-48.235	-46.057	-7.487	-14.434	-368.716
18	27	45	-379.534	0.162	42.0	-48.435	-46.724	-6.894	-15.894	-375.344
18	28	46	-386.197	0.164	60.0	-48.612	-47.366	-7.063	-16.961	-381.891
18	29	47	-389.649	0.105	0.1	-48.943	-48.136	-4.882	-17.064	-384.203
18	30	48	-395.114	0.159	59.9	-48.787	-48.407	-4.876	-18.365	-389.232
18	31	49	-398.843	0.158	59.8	-48.710	-48.816	-4.127	-19.040	-391.953
18	32	50	-402.664	0.158	60.0	-48.666	-49.222	-4.216	-19.692	-394.593
18	33	51	-404.969	0.183	60.0	-48.158	-49.399	-2.764	-20.772	-396.930
18	34	52	-407.507	0.203	60.0	-47.686	-49.585	-2.974	-21.715	-399.338

Table E.4: Same as Tables E.1-E.3 but for potassium isotopes.

					$_{19}$K					
Z	N	A	$E_{\text{g.s.}}$	β	γ (deg)	$\varepsilon_n(1)$	$\varepsilon_p(1)$	$\varepsilon_n(N)$	$\varepsilon_p(Z)$	$E_{\text{g.s.}}$(SLyIII.0.8)
19	14	33	-248.466	0.054	57.8	-50.249	-37.370	-20.874	-1.160	-241.010
19	15	34	-264.964	0.050	59.5	-49.872	-38.066	-16.812	-2.282	-257.462
19	16	35	-281.162	0.047	59.7	-49.679	-38.766	-16.577	-3.335	-272.840
19	17	36	-295.452	0.074	60.0	-49.123	-39.311	-14.684	-4.255	-288.108
19	18	37	-309.616	0.097	60.0	-48.596	-39.837	-14.556	-5.128	-303.162
19	19	38	-322.796	0.054	60.0	-48.223	-40.478	-13.678	-7.036	-316.699
19	20	39	-336.085	0.021	60.0	-47.829	-41.067	-13.736	-8.666	-330.414
19	21	40	-344.593	0.059	60.0	-47.980	-41.804	-8.868	-9.272	-339.393
19	22	41	-352.998	0.092	59.8	-48.108	-42.492	-8.775	-9.788	-348.324
19	23	42	-361.404	0.119	5.1	-48.275	-43.242	-8.938	-10.627	-356.704
19	24	43	-369.924	0.148	0.2	-48.412	-43.926	-8.910	-11.225	-365.402
19	25	44	-378.032	0.140	0.3	-48.626	-44.655	-8.415	-12.155	-373.794
19	26	45	-385.985	0.133	0.4	-48.830	-45.349	-8.279	-13.057	-381.964
19	27	46	-393.308	0.085	0.2	-49.125	-46.096	-7.783	-14.423	-389.575
19	28	47	-400.896	0.056	59.9	-49.347	-46.768	-8.059	-15.466	-397.435
19	29	48	-405.761	0.082	58.9	-49.350	-47.259	-5.274	-15.732	-401.545
19	30	49	-410.731	0.105	32.9	-49.379	-47.740	-5.459	-16.148	-405.355
19	31	50	-415.183	0.089	59.1	-49.450	-48.224	-4.850	-16.896	-408.847
19	32	51	-419.729	0.073	59.7	-49.562	-48.704	-4.930	-17.765	-412.067
19	33	52	-422.844	0.047	58.6	-49.418	-49.037	-3.498	-18.723	-414.119
19	34	53	-426.057	0.038	50.4	-49.250	-49.334	-3.573	-19.453	-416.010

Table E.5: Same as Tables E.1-E.4 but for calcium isotopes.

					$_{20}$Ca					
Z	N	A	$E_{\text{g.s.}}$	β	γ (deg)	$\varepsilon_n(1)$	$\varepsilon_p(1)$	$\varepsilon_n(N)$	$\varepsilon_p(Z)$	$E_{\text{g.s.}}$(SLyIII.0.8)
20	14	34	-249.225	0.000		-50.775	-36.584	-22.078	-1.294	-241.231
20	15	35	-266.805	0.010		-50.379	-37.309	-17.846	-2.327	-258.860
20	16	36	-284.036	0.001		-50.187	-38.036	-17.575	-3.317	-275.285
20	17	37	-299.278	0.027	59.5	-49.662	-38.599	-15.598	-4.268	-291.481
20	18	38	-314.347	0.049	59.5	-49.168	-39.148	-15.426	-5.186	-307.424
20	19	39	-329.293	0.021	59.4	-48.718	-39.722	-15.306	-6.795	-323.072
20	20	40	-344.125	0.000		-48.292	-40.278	-15.182	-8.241	-338.533
20	21	41	-353.274	0.032	59.9	-48.452	-41.031	-9.444	-8.905	-348.147
20	22	42	-362.231	0.061	59.9	-48.599	-41.743	-9.278	-9.480	-357.595
20	23	43	-371.489	0.081	3.0	-48.756	-42.467	-9.580	-10.342	-367.194
20	24	44	-380.629	0.107	0.0	-48.901	-43.157	-9.485	-10.969	-376.653
20	25	45	-389.665	0.100	0.0	-49.100	-43.874	-9.320	-11.885	-386.055
20	26	46	-398.521	0.094	0.0	-49.292	-44.558	-9.157	-12.775	-395.208
20	27	47	-407.187	0.047	0.0	-49.543	-45.269	-9.090	-14.083	-404.229
20	28	48	-415.991	0.000		-49.760	-45.938	-9.264	-15.335	-413.273
20	29	49	-421.191	0.033	0.1	-49.794	-46.474	-5.640	-15.722	-417.691
20	30	50	-426.578	0.067	0.4	-49.845	-46.986	-5.865	-16.078	-421.900
20	31	51	-431.858	0.033	0.2	-49.962	-47.516	-5.706	-16.972	-426.292
20	32	52	-437.326	0.001		-50.096	-48.025	-5.896	-17.829	-430.530
20	33	53	-441.157	0.000		-49.849	-48.322	-4.168	-18.469	-433.119
20	34	54	-445.015	0.002		-49.650	-48.618	-4.191	-19.089	-435.591
20	35	55	-447.822	0.037	59.1	-49.323	-48.906	-3.248	-19.529	-438.511
20	36	56	-450.870	0.064	60.0	-48.992	-49.182	-3.463	-19.937	-441.597

Table E.6:   Same as Tables E.1-E.5 but for scandium isotopes.

										$_{21}$Sc
Z	N	A	$E_{\text{g.s.}}$	β	γ (deg)	$\varepsilon_n(1)$	$\varepsilon_p(1)$	$\varepsilon_n(N)$	$\varepsilon_p(Z)$	$E_{\text{g.s.}}$(SLyIII.0.8)
21	17	38	-299.023	0.763	59.5	-50.275	-38.356	-16.892	-0.097	-291.105
21	18	39	-315.372	0.092	59.8	-49.762	-38.881	-16.670	-1.309	-308.435
21	19	40	-330.884	0.059	59.8	-49.360	-39.477	-15.911	-1.811	-324.558
21	20	41	-346.361	0.032	59.6	-48.958	-40.041	-15.852	-2.391	-340.662
21	21	42	-357.187	0.061	59.5	-49.102	-40.775	-11.088	-4.031	-351.929
21	22	43	-367.835	0.118	0.8	-49.180	-41.429	-11.256	-5.971	-362.800
21	23	44	-378.462	0.144	0.5	-49.312	-42.125	-10.943	-7.343	-373.772
21	24	45	-388.967	0.169	0.4	-49.439	-42.796	-10.849	-8.696	-384.536
21	25	46	-398.629	0.158	0.1	-49.654	-43.528	-9.943	-9.273	-394.622
21	26	47	-408.119	0.147	0.4	-49.860	-44.226	-9.790	-9.858	-404.477
21	27	48	-417.004	0.096	2.3	-50.125	-44.951	-9.319	-10.030	-413.828
21	28	49	-426.166	0.056	60.0	-50.349	-45.629	-9.682	-10.412	-423.334
21	29	50	-432.365	0.074	59.5	-50.371	-46.174	-6.557	-11.359	-428.756
21	30	51	-438.813	0.112	0.5	-50.353	-46.647	-6.934	-12.403	-433.982
21	31	52	-444.410	0.078	58.8	-50.482	-47.203	-6.174	-12.749	-438.702
21	32	53	-450.270	0.067	59.9	-50.572	-47.694	-6.207	-13.254	-443.269
21	33	54	-454.632	0.051	59.3	-50.393	-48.040	-4.709	-13.639	-446.624
21	34	55	-459.123	0.077	2.5	-50.134	-48.339	-4.921	-14.484	-450.490
21	35	56	-462.913	0.070	58.2	-49.855	-48.632	-4.261	-15.131	-453.927
21	36	57	-466.950	0.092	59.9	-49.498	-48.892	-4.445	-16.084	-458.155

Table E.7:   Same as Tables E.1-E.6 but for titanium isotopes.

										$_{22}$Ti
Z	N	A	$E_{\text{g.s.}}$	β	γ (deg)	$\varepsilon_n(1)$	$\varepsilon_p(1)$	$\varepsilon_n(N)$	$\varepsilon_p(Z)$	$E_{\text{g.s.}}$(SLyIII.0.8)
22	17	39	-298.744	0.157	1.4	-50.740	-38.006	-17.504	-0.436	-290.553
22	18	40	-316.122	0.129	60.0	-50.293	-38.592	-17.823	-1.034	-309.195
22	19	41	-332.103	0.092	59.8	-49.944	-39.216	-16.416	-1.454	-325.718
22	20	42	-348.136	0.060	0.1	-49.583	-39.797	-16.596	-2.017	-342.276
22	21	43	-360.651	0.119	0.1	-49.660	-40.463	-13.022	-3.941	-355.031
22	22	44	-373.470	0.184	0.0	-49.666	-41.048	-13.408	-6.095	-367.933
22	23	45	-385.460	0.207	0.1	-49.791	-41.731	-12.288	-7.432	-380.247
22	24	46	-397.311	0.231	0.0	-49.911	-42.391	-12.173	-8.750	-392.325
22	25	47	-407.509	0.216	0.1	-50.142	-43.140	-10.479	-9.247	-403.011
22	26	48	-417.549	0.202	0.1	-50.363	-43.854	-10.339	-9.755	-413.488
22	27	49	-426.572	0.151	1.8	-50.637	-44.596	-9.455	-9.862	-423.079
22	28	50	-436.125	0.112	60.0	-50.834	-45.289	-10.291	-10.228	-433.025
22	29	51	-443.206	0.124	31.0	-50.842	-45.819	-7.589	-11.040	-439.377
22	30	52	-450.744	0.161	0.1	-50.776	-46.258	-7.992	-12.163	-445.928
22	31	53	-456.649	0.128	34.9	-50.868	-46.822	-6.566	-12.433	-450.890
22	32	54	-463.069	0.117	59.8	-50.914	-47.305	-6.773	-12.982	-455.984
22	33	55	-467.919	0.143	59.8	-50.434	-47.511	-5.238	-14.014	-461.149
22	34	56	-473.200	0.128	0.1	-50.544	-47.997	-5.814	-14.279	-465.452
22	35	57	-477.571	0.118	38.1	-50.217	-48.284	-5.001	-14.851	-469.679
22	36	58	-482.441	0.117	60.0	-49.964	-48.587	-5.289	-15.499	-474.190
22	37	59	-486.384	0.108	59.3	-49.673	-48.870	-4.280	-16.006	-478.101
22	38	60	-490.420	0.099	60.0	-49.383	-49.142	-4.370	-16.514	-482.036
22	39	61	-493.918	0.064	59.0	-49.183	-49.448	-4.021	-16.710	-485.080
22	40	62	-497.873	0.029	6.3	-48.951	-49.739	-4.532	-17.006	-488.592

Table E.8: Same as Tables E.1-E.7 but for vanadium isotopes.

										$_{23}$V
Z	N	A	$E_{\text{g.s.}}$	β	γ (deg)	$\varepsilon_n(1)$	$\varepsilon_p(1)$	$\varepsilon_n(N)$	$\varepsilon_p(Z)$	$E_{\text{g.s.}}$(SLyIII.0.8)
23	20	43	-349.899	0.083	0.4	-50.208	-39.556	-17.285	-1.943	-343.859
23	21	44	-363.780	0.146	0.0	-50.264	-40.199	-14.400	-3.304	-357.921
23	22	45	-377.977	0.209	0.0	-50.258	-40.774	-14.770	-4.664	-372.180
23	23	46	-391.218	0.232	0.1	-50.366	-41.440	-13.522	-5.899	-385.759
23	24	47	-404.299	0.256	0.0	-50.470	-42.083	-13.384	-7.110	-399.085
23	25	48	-415.372	0.242	0.0	-50.698	-42.826	-11.340	-7.976	-410.628
23	26	49	-426.268	0.228	0.2	-50.915	-43.534	-11.182	-8.824	-421.945
23	27	50	-435.692	0.179	0.7	-51.187	-44.277	-9.841	-9.217	-431.964
23	28	51	-445.332	0.120	59.2	-51.406	-44.999	-11.044	-9.229	-442.070
23	29	52	-453.669	0.158	3.2	-51.345	-45.462	-8.789	-10.569	-449.759
23	30	53	-462.206	0.188	0.0	-51.257	-45.910	-8.959	-11.542	-457.370
23	31	54	-468.462	0.175	15.7	-51.189	-46.381	-6.792	-12.027	-463.023
23	32	55	-475.151	0.128	59.7	-51.421	-47.005	-7.423	-12.087	-467.911
23	33	56	-480.890	0.150	17.9	-51.133	-47.294	-6.245	-13.122	-474.003
23	34	57	-487.028	0.156	0.8	-50.991	-47.660	-6.686	-13.903	-479.733
23	35	58	-491.805	0.141	25.1	-50.685	-47.958	-5.391	-14.316	-484.348
23	36	59	-497.121	0.125	59.5	-50.468	-48.297	-5.854	-14.661	-489.130
23	37	60	-501.704	0.115	59.9	-50.175	-48.578	-4.914	-15.290	-493.771
23	38	61	-506.375	0.105	59.8	-49.883	-48.847	-4.999	-15.914	-498.436
23	39	62	-510.284	0.069	59.8	-49.703	-49.166	-4.469	-16.312	-501.909
23	40	63	-514.708	0.038	6.3	-49.475	-49.458	-5.003	-16.790	-505.953

Table E.9: Same as Tables E.1-E.8 but for chromium isotopes.

							$_{24}$Cr			
Z	N	A	$E_{\text{g.s.}}$	β	γ (deg)	$\varepsilon_n(1)$	$\varepsilon_p(1)$	$\varepsilon_n(N)$	$\varepsilon_p(Z)$	$E_{\text{g.s.}}$(SLyIII.0.8)
24	22	46	-382.068	0.233	0.0	-50.824	-40.500	-16.107	-4.274	-375.923
24	23	47	-396.537	0.257	0.0	-50.916	-41.150	-14.732	-5.483	-390.750
24	24	48	-410.821	0.280	0.0	-51.005	-41.779	-14.569	-6.668	-405.305
24	25	49	-422.758	0.266	0.0	-51.231	-42.515	-12.190	-7.521	-417.696
24	26	50	-434.502	0.253	0.0	-51.444	-43.216	-12.014	-8.360	-429.846
24	27	51	-444.316	0.205	0.6	-51.713	-43.959	-10.217	-8.743	-440.282
24	28	52	-454.281	0.153	0.0	-51.966	-44.670	-10.424	-9.102	-450.852
24	29	53	-463.658	0.185	0.1	-51.836	-45.128	-9.773	-10.087	-459.576
24	30	54	-473.169	0.214	0.0	-51.719	-45.561	-9.913	-11.056	-468.278
24	31	55	-480.103	0.222	3.2	-51.454	-45.895	-7.295	-11.826	-475.077
24	32	56	-487.165	0.225	11.1	-51.255	-46.265	-7.462	-12.461	-481.777
24	33	57	-493.695	0.209	2.7	-51.265	-46.754	-6.944	-13.054	-487.779
24	34	58	-500.402	0.186	0.0	-51.374	-47.290	-7.071	-13.486	-493.564
24	35	59	-505.697	0.173	0.1	-51.129	-47.605	-5.608	-14.076	-498.874
24	36	60	-511.263	0.154	28.5	-50.822	-47.906	-6.073	-14.324	-504.055
24	37	61	-516.391	0.121	60.0	-50.653	-48.282	-5.538	-14.668	-508.795
24	38	62	-521.687	0.111	60.0	-50.360	-48.550	-5.618	-15.287	-514.173
24	39	63	-525.995	0.074	59.5	-50.197	-48.880	-4.895	-15.666	-518.072
24	40	64	-530.911	0.050	0.5	-49.974	-49.171	-5.428	-16.164	-522.646
24	41	65	-534.688	0.232	0.0	-50.535	-49.551	-4.823	-18.149	-526.054
24	42	66	-539.346	0.260	0.1	-50.555	-49.889	-5.032	-19.083	-530.610

Table E.10: Same as Tables E.1-E.9 but for manganese isotopes.

| | | | | | | | | | | $_{25}$Mn |
Z	N	A	$E_{\text{g.s.}}$	β	γ (deg)	$\varepsilon_n(1)$	$\varepsilon_p(1)$	$\varepsilon_n(N)$	$\varepsilon_p(Z)$	$E_{\text{g.s.}}$(SLyIII.0.8)
25	24	49	-414.728	0.268	0.0	-51.658	-41.595	-15.441	-4.015	-409.085
25	25	50	-427.827	0.255	0.0	-51.860	-42.309	-13.333	-5.159	-422.638
25	26	51	-440.704	0.243	0.0	-52.052	-42.988	-13.129	-6.274	-435.924
25	27	52	-451.415	0.194	0.1	-52.318	-43.726	-11.112	-7.159	-447.247
25	28	53	-462.283	0.142	0.4	-52.566	-44.429	-11.330	-8.054	-458.710
25	29	54	-472.374	0.176	0.1	-52.433	-44.892	-10.491	-8.752	-468.095
25	30	55	-482.613	0.206	0.2	-52.315	-45.327	-10.643	-9.467	-477.445
25	31	56	-490.304	0.216	3.8	-52.022	-45.646	-8.045	-10.211	-485.111
25	32	57	-498.147	0.220	14.3	-51.819	-46.012	-8.261	-10.997	-492.618
25	33	58	-505.324	0.207	2.8	-51.772	-46.475	-7.616	-11.629	-499.463
25	34	59	-512.695	0.188	0.0	-51.835	-46.990	-7.717	-12.303	-506.070
25	35	60	-518.661	0.171	0.1	-51.629	-47.326	-6.275	-12.950	-511.994
25	36	61	-524.801	0.158	24.4	-51.330	-47.613	-6.652	-13.525	-517.827
25	37	62	-530.345	0.129	32.5	-51.157	-47.977	-5.980	-14.008	-523.034
25	38	63	-536.189	0.107	57.5	-50.888	-48.281	-6.245	-14.456	-528.925
25	39	64	-541.225	0.076	0.0	-50.763	-48.617	-5.727	-15.270	-533.283
25	40	65	-546.825	0.047	0.0	-50.487	-48.903	-6.033	-15.862	-538.984
25	41	66	-550.983	0.082	4.2	-50.525	-49.265	-4.571	-16.349	-543.264
25	42	67	-555.934	0.252	0.0	-51.094	-49.647	-5.544	-16.549	-547.600
25	43	68	-560.316	0.219	0.0	-50.859	-49.958	-4.833	-17.130	-552.183
25	44	69	-565.084	0.186	0.0	-50.618	-50.258	-5.221	-17.726	-557.039

Table E.11:   Same as Tables E.1-E.10 but for iron isotopes.

Z	N	A	$E_{\text{g.s.}}$	β	γ (deg)	$\varepsilon_n(1)$	$\varepsilon_p(1)$	$\varepsilon_n(N)$	$\varepsilon_p(Z)$	$E_{\text{g.s.}}$(SLyIII.0.8)
						$_{26}$Fe				
26	24	50	-418.160	0.256	0.0	-52.272	-41.405	-16.291	-3.561	-412.348
26	25	51	-432.390	0.244	0.0	-52.452	-42.097	-14.445	-4.673	-427.035
26	26	52	-446.372	0.233	0.0	-52.621	-42.755	-14.215	-5.760	-441.426
26	27	53	-457.964	0.184	0.1	-52.885	-43.487	-11.993	-6.632	-453.619
26	28	54	-469.724	0.130	0.1	-53.126	-44.182	-12.220	-7.514	-465.958
26	29	55	-480.512	0.167	0.1	-52.995	-44.653	-11.195	-8.197	-475.992
26	30	56	-491.467	0.198	0.0	-52.879	-45.092	-11.418	-8.898	-485.971
26	31	57	-499.908	0.209	9.1	-52.580	-45.408	-8.863	-9.652	-494.437
26	32	58	-508.548	0.220	16.2	-52.311	-45.722	-9.041	-10.438	-502.928
26	33	59	-516.349	0.204	6.0	-52.273	-46.206	-8.256	-11.051	-510.459
26	34	60	-524.406	0.188	0.0	-52.280	-46.693	-8.393	-11.726	-517.938
26	35	61	-531.015	0.170	0.1	-52.098	-47.041	-6.920	-12.356	-524.486
26	36	62	-537.755	0.160	20.3	-51.822	-47.325	-7.207	-12.944	-530.980
26	37	63	-543.791	0.132	24.1	-51.655	-47.692	-6.466	-13.447	-536.661
26	38	64	-550.102	0.108	31.2	-51.435	-48.015	-6.705	-13.940	-542.799
26	39	65	-555.908	0.074	0.0	-51.255	-48.349	-6.312	-14.663	-548.244
26	40	66	-562.102	0.046	0.3	-50.976	-48.632	-6.612	-15.227	-554.641
26	41	67	-566.747	0.076	8.6	-51.017	-48.999	-5.019	-15.735	-559.448
26	42	68	-571.924	0.243	0.3	-51.604	-49.401	-6.060	-15.964	-563.963
26	43	69	-576.910	0.146	0.7	-51.088	-49.675	-5.513	-16.646	-569.563
26	44	70	-582.256	0.176	0.2	-51.125	-50.008	-5.703	-17.139	-574.783

Table E.12: Same as Tables E.1-E.11 but for cobalt isotopes.

							$_{27}$Co			
Z	N	A	$E_{\text{g.s.}}$	β	γ (deg)	$\varepsilon_n(1)$	$\varepsilon_p(1)$	$\varepsilon_n(N)$	$\varepsilon_p(Z)$	$E_{\text{g.s.}}$(SLyIII.0.8)
27	28	55	-476.256	0.074	0.1	-53.727	-43.979	-14.030	-6.796	-472.389
27	29	56	-487.165	0.118	0.1	-53.647	-44.496	-11.343	-6.860	-482.474
27	30	57	-498.296	0.154	1.2	-53.570	-44.963	-11.555	-6.996	-492.499
27	31	58	-507.424	0.157	19.3	-53.406	-45.369	-9.600	-7.830	-501.216
27	32	59	-516.799	0.164	28.7	-53.261	-45.755	-9.747	-8.666	-509.869
27	33	60	-525.258	0.144	19.3	-53.233	-46.246	-8.850	-9.312	-518.068
27	34	61	-534.005	0.140	0.1	-53.110	-46.657	-9.158	-9.817	-526.531
27	35	62	-541.437	0.134	18.3	-52.783	-46.915	-7.863	-10.643	-534.183
27	36	63	-549.139	0.133	36.3	-52.462	-47.165	-8.055	-11.588	-541.807
27	37	64	-556.123	0.110	40.3	-52.239	-47.499	-7.349	-12.418	-548.826
27	38	65	-563.291	0.093	57.6	-51.944	-47.776	-7.498	-13.194	-556.305
27	39	66	-569.907	0.050	1.4	-51.784	-48.125	-7.274	-13.994	-562.436
27	40	67	-577.049	0.022	0.7	-51.482	-48.386	-7.538	-14.927	-569.914
27	41	68	-581.986	0.050	24.6	-51.522	-48.757	-5.281	-15.256	-575.074
27	42	69	-587.128	0.082	24.9	-51.549	-49.093	-5.525	-15.528	-580.360
27	43	70	-592.531	0.115	2.9	-51.593	-49.446	-5.731	-15.642	-585.737
27	44	71	-598.096	0.145	0.0	-51.628	-49.779	-6.111	-15.846	-591.222
27	45	72	-603.088	0.150	0.0	-51.691	-50.156	-5.227	-16.304	-596.317
27	46	73	-608.055	0.157	0.0	-51.748	-50.519	-5.212	-16.747	-601.313

Table E.13:   Same as Tables E.1-E.12 but for nickel isotopes.

										$_{28}$Ni
Z	N	A	$E_{\text{g.s.}}$	β	γ (deg)	$\varepsilon_n(1)$	$\varepsilon_p(1)$	$\varepsilon_n(N)$	$\varepsilon_p(Z)$	$E_{\text{g.s.}}$(SLyIII.0.8)
28	28	56	-482.762	0.000		-54.269	-43.748	-16.019	-6.936	-478.680
28	29	57	-493.654	0.061	0.1	-54.254	-44.324	-11.398	-6.779	-488.779
28	30	58	-504.871	0.105	0.1	-54.228	-44.831	-11.680	-6.808	-498.788
28	31	59	-515.146	0.091	59.3	-54.284	-45.386	-10.771	-8.319	-508.071
28	32	60	-525.682	0.000		-54.531	-46.064	-11.069	-9.550	-517.491
28	33	61	-534.565	0.154	59.6	-53.595	-45.841	-9.530	-9.442	-526.956
28	34	62	-543.891	0.187	60.0	-53.052	-45.917	-9.698	-10.105	-537.014
28	35	63	-551.941	0.144	58.7	-53.120	-46.514	-8.560	-10.694	-544.711
28	36	64	-560.366	0.112	60.0	-53.092	-46.999	-8.822	-11.351	-552.311
28	37	65	-568.099	0.095	60.0	-52.788	-47.285	-8.053	-11.986	-560.582
28	38	66	-575.919	0.081	60.0	-52.474	-47.547	-8.126	-12.606	-568.885
28	39	67	-583.401	0.034	59.6	-52.254	-47.873	-8.074	-13.531	-576.289
28	40	68	-591.446	0.000		-51.958	-48.127	-8.439	-14.393	-584.591
28	41	69	-596.741	0.032	59.6	-51.998	-48.500	-5.643	-14.769	-590.155
28	42	70	-602.239	0.063	59.7	-52.023	-48.835	-5.859	-15.164	-595.872
28	43	71	-607.690	0.083	1.7	-52.069	-49.204	-5.969	-15.183	-601.398
28	44	72	-613.466	0.112	0.0	-52.102	-49.539	-6.100	-15.401	-607.173
28	45	73	-618.920	0.118	0.0	-52.163	-49.913	-5.680	-15.864	-612.750
28	46	74	-624.336	0.124	0.0	-52.218	-50.275	-5.649	-16.317	-618.222

Table E.14: Same as Tables E.1-E.13 but for copper isotopes.

										$_{29}$Cu
Z	N	A	$E_{\text{g.s.}}$	β	γ (deg)	$\varepsilon_n(1)$	$\varepsilon_p(1)$	$\varepsilon_n(N)$	$\varepsilon_p(Z)$	$E_{\text{g.s.}}$(SLyIII.0.8)
29	28	57	-484.593	0.060	0.2	-54.751	-43.330	-15.837	-2.192	-479.182
29	29	58	-496.550	0.109	0.1	-54.600	-43.786	-12.402	-3.204	-490.569
29	30	59	-508.812	0.157	0.0	-54.360	-44.126	-12.744	-4.336	-502.285
29	31	60	-519.413	0.159	24.5	-54.252	-44.572	-11.068	-4.842	-512.179
29	32	61	-530.239	0.162	33.5	-54.152	-44.991	-11.151	-5.381	-522.064
29	33	62	-540.143	0.166	57.9	-53.910	-45.308	-10.329	-5.672	-531.726
29	34	63	-550.248	0.192	59.7	-53.411	-45.416	-10.436	-6.428	-542.660
29	35	64	-558.885	0.157	58.0	-53.445	-45.960	-9.094	-7.012	-550.948
29	36	65	-567.855	0.128	53.7	-53.420	-46.435	-9.353	-7.569	-559.235
29	37	66	-576.143	0.111	59.6	-53.150	-46.730	-8.592	-8.091	-568.014
29	38	67	-584.499	0.098	59.8	-52.857	-46.992	-8.652	-8.620	-576.893
29	39	68	-592.139	0.051	59.3	-52.674	-47.339	-8.281	-8.776	-584.351
29	40	69	-600.455	0.016	0.4	-52.417	-47.616	-8.797	-9.016	-592.757
29	41	70	-606.595	0.045	59.4	-52.453	-47.977	-6.465	-9.840	-599.259
29	42	71	-612.931	0.088	6.9	-52.390	-48.257	-6.829	-11.010	-606.071
29	43	72	-619.544	0.116	2.1	-52.391	-48.580	-6.914	-11.968	-612.956
29	44	73	-626.279	0.144	0.0	-52.396	-48.896	-7.184	-12.913	-619.834
29	45	74	-632.392	0.151	0.0	-52.452	-49.258	-6.332	-13.574	-626.129
29	46	75	-638.462	0.157	0.0	-52.505	-49.609	-6.300	-14.232	-632.305

Table E.15:   Same as Tables E.1-E.14 but for zinc isotopes.

						$_{30}$Zn				
Z	N	A	$E_{\text{g.s.}}$	β	γ (deg)	$\varepsilon_n(1)$	$\varepsilon_p(1)$	$\varepsilon_n(N)$	$\varepsilon_p(Z)$	$E_{\text{g.s.}}$(SLyIII.0.8)
30	28	58	-486.469	0.105	0.2	-55.165	-42.904	-15.822	-2.198	-479.358
30	29	59	-499.482	0.158	0.0	-54.817	-43.175	-13.542	-3.284	-492.448
30	30	60	-512.892	0.200	0.0	-54.474	-43.430	-13.877	-4.422	-505.927
30	31	61	-524.086	0.206	15.4	-54.268	-43.799	-11.663	-5.035	-516.866
30	32	62	-535.527	0.214	22.3	-54.059	-44.142	-11.793	-5.650	-528.009
30	33	63	-545.840	0.192	12.8	-54.082	-44.665	-10.768	-6.253	-537.962
30	34	64	-556.541	0.179	0.2	-54.078	-45.144	-11.124	-6.836	-548.103
30	35	65	-565.748	0.164	0.5	-53.876	-45.478	-9.467	-7.286	-557.408
30	36	66	-575.226	0.164	28.5	-53.548	-45.713	-9.840	-7.623	-566.740
30	37	67	-583.759	0.131	39.6	-53.460	-46.160	-8.980	-7.796	-574.944
30	38	68	-592.638	0.112	57.9	-53.241	-46.477	-9.168	-8.187	-584.235
30	39	69	-600.434	0.067	59.3	-53.085	-46.840	-8.460	-8.340	-591.776
30	40	70	-608.991	0.036	0.1	-52.854	-47.133	-9.086	-8.596	-600.181
30	41	71	-616.083	0.078	3.6	-52.768	-47.403	-7.545	-9.663	-608.141
30	42	72	-623.631	0.235	16.3	-52.998	-47.603	-8.223	-12.125	-617.100
30	43	73	-631.140	0.146	0.5	-52.667	-47.972	-7.844	-11.695	-624.308
30	44	74	-638.799	0.172	0.0	-52.659	-48.279	-7.962	-12.607	-632.232
30	45	75	-645.577	0.179	0.0	-52.710	-48.627	-6.994	-13.278	-639.256
30	46	76	-652.311	0.186	0.0	-52.760	-48.968	-6.957	-13.938	-646.151

Table E.16:   Same as Tables E.1-E.15 but for gallium isotopes.

										$_{31}$Ga
Z	N	A	$E_{\text{g.s.}}$	β	γ (deg)	$\varepsilon_n(1)$	$\varepsilon_p(1)$	$\varepsilon_n(N)$	$\varepsilon_p(Z)$	$E_{\text{g.s.}}$(SLyIII.0.8)
31	28	59	-487.220	0.094	56.7	-55.624	-42.539	-17.214	-1.094	-478.621
31	29	60	-500.584	0.164	25.3	-55.146	-42.670	-14.065	-1.459	-492.343
31	30	61	-514.593	0.205	14.8	-54.750	-42.880	-14.486	-2.030	-506.817
31	31	62	-526.933	0.218	22.2	-54.452	-43.170	-12.699	-3.085	-519.273
31	32	63	-539.382	0.228	25.6	-54.173	-43.459	-12.761	-4.056	-531.887
31	33	64	-550.127	0.216	33.9	-54.066	-43.881	-11.150	-4.644	-542.101
31	34	65	-561.293	0.214	50.6	-53.791	-44.202	-11.808	-5.252	-553.245
31	35	66	-571.190	0.191	36.7	-53.820	-44.676	-10.457	-5.784	-562.854
31	36	67	-581.453	0.180	31.3	-53.652	-45.026	-10.562	-6.372	-573.226
31	37	68	-590.442	0.150	37.5	-53.565	-45.463	-9.428	-6.808	-582.027
31	38	69	-599.752	0.130	46.4	-53.363	-45.799	-9.678	-7.239	-591.637
31	39	70	-608.275	0.157	53.5	-53.265	-46.076	-8.804	-8.088	-601.201
31	40	71	-617.204	0.006		-53.306	-46.674	-10.130	-8.362	-607.267
31	41	72	-624.629	0.074	22.8	-53.133	-46.885	-8.055	-8.658	-616.145
31	42	73	-633.386	0.237	22.1	-53.181	-46.972	-8.684	-9.912	-627.227
31	43	74	-640.893	0.246	21.7	-53.205	-47.313	-7.732	-10.602	-635.018
31	44	75	-649.061	0.175	0.4	-52.956	-47.727	-8.711	-10.297	-642.318
31	45	76	-656.492	0.181	1.9	-53.008	-48.075	-7.641	-10.947	-650.027
31	46	77	-663.870	0.188	2.0	-53.059	-48.414	-7.595	-11.586	-657.599

Table E.17:   Same as Tables E.1-E.16 but for germanium isotopes.

					$_{32}$Ge					
Z	N	A	$E_{\text{g.s.}}$	β	γ (deg)	$\varepsilon_n(1)$	$\varepsilon_p(1)$	$\varepsilon_n(N)$	$\varepsilon_p(Z)$	$E_{\text{g.s.}}$(SLyIII.0.8)
32	30	62	-516.300	0.216	22.3	-54.972	-42.310	-15.102	-1.941	-507.713
32	31	63	-529.653	0.230	25.1	-54.608	-42.542	-13.667	-2.911	-521.689
32	32	64	-543.071	0.240	27.7	-54.299	-42.805	-13.709	-3.865	-535.527
32	33	65	-554.420	0.230	36.0	-54.135	-43.190	-11.782	-4.451	-546.535
32	34	66	-566.157	0.229	46.1	-53.876	-43.513	-12.228	-4.998	-558.270
32	35	67	-576.622	0.208	38.9	-53.864	-43.969	-10.942	-5.565	-568.573
32	36	68	-587.438	0.194	33.1	-53.761	-44.362	-11.181	-6.116	-579.387
32	37	69	-597.177	0.222	33.4	-53.658	-44.620	-10.016	-6.928	-589.949
32	38	70	-606.973	0.248	32.9	-53.572	-44.885	-10.076	-7.647	-600.407
32	39	71	-616.011	0.222	35.8	-53.477	-45.301	-9.510	-8.157	-609.564
32	40	72	-625.469	0.199	40.6	-53.332	-45.670	-9.874	-8.638	-619.223
32	41	73	-634.130	0.216	33.3	-53.350	-46.011	-8.957	-9.229	-628.136
32	42	74	-642.926	0.238	26.3	-53.376	-46.365	-9.123	-9.680	-637.011
32	43	75	-651.117	0.248	25.2	-53.401	-46.710	-8.412	-10.343	-645.452
32	44	76	-659.285	0.260	24.2	-53.424	-47.051	-8.404	-10.996	-653.753
32	45	77	-667.021	0.184	8.5	-53.271	-47.519	-8.297	-10.641	-660.518
32	46	78	-675.060	0.192	8.9	-53.311	-47.851	-8.258	-11.298	-668.810

Table E.18:   Same as Tables E.1-E.17 but for arsenic isotopes.

					$_{33}$As					
Z	N	A	$E_{\text{g.s.}}$	β	γ (deg)	$\varepsilon_n(1)$	$\varepsilon_p(1)$	$\varepsilon_n(N)$	$\varepsilon_p(Z)$	$E_{\text{g.s.}}$(SLyIII.0.8)
33	32	65	-544.505	0.232	36.5	-54.573	-42.276	-14.300	-1.757	-536.073
33	33	66	-557.223	0.229	45.5	-54.329	-42.593	-13.141	-3.092	-548.783
33	34	67	-570.291	0.231	55.7	-54.042	-42.890	-13.562	-4.357	-562.101
33	35	68	-580.943	0.210	49.3	-54.040	-43.360	-11.117	-4.571	-572.484
33	36	69	-591.977	0.191	43.2	-54.001	-43.806	-11.489	-4.785	-583.341
33	37	70	-602.275	0.216	43.7	-53.880	-44.039	-10.547	-5.391	-594.606
33	38	71	-612.791	0.153	59.4	-53.658	-44.518	-10.918	-6.373	-604.928
33	39	72	-622.852	0.176	59.9	-53.599	-44.785	-10.296	-7.015	-615.748
33	40	73	-632.892	0.196	59.7	-53.549	-45.055	-10.283	-7.652	-626.462
33	41	74	-641.882	0.206	50.7	-53.557	-45.370	-9.198	-8.080	-635.806
33	42	75	-650.787	0.218	44.5	-53.561	-45.688	-9.152	-8.390	-645.032
33	43	76	-659.214	0.233	36.4	-53.626	-46.079	-8.702	-8.452	-653.458
33	44	77	-668.066	0.173	0.3	-53.506	-46.646	-9.615	-9.183	-661.255
33	45	78	-676.768	0.181	1.4	-53.532	-46.976	-8.901	-9.805	-670.401
33	46	79	-685.408	0.188	1.5	-53.567	-47.304	-8.844	-10.429	-679.362

Table E.19: Same as Tables E.1-E.18 but for selenium isotopes.

						$_{34}$Se				
Z	N	A	$E_{\text{g.s.}}$	β	γ (deg)	$\varepsilon_n(1)$	$\varepsilon_p(1)$	$\varepsilon_n(N)$	$\varepsilon_p(Z)$	$E_{\text{g.s.}}$(SLyIII.0.8)
34	32	66	-546.057	0.230	46.1	-54.785	-41.685	-14.829	-1.925	-537.074
34	33	67	-560.101	0.232	56.9	-54.500	-41.959	-14.448	-3.345	-551.420
34	34	68	-574.273	0.236	60.0	-54.263	-42.302	-14.641	-4.370	-565.412
34	35	69	-585.444	0.246	59.8	-54.216	-42.635	-11.359	-4.678	-577.219
34	36	70	-596.526	0.193	53.5	-54.242	-43.254	-11.698	-4.785	-587.253
34	37	71	-607.578	0.173	58.6	-54.142	-43.648	-11.355	-5.596	-598.309
34	38	72	-618.732	0.161	60.0	-53.945	-43.947	-11.415	-6.032	-609.986
34	39	73	-629.432	0.181	60.0	-53.887	-44.218	-10.924	-6.657	-621.431
34	40	74	-640.108	0.201	60.0	-53.826	-44.477	-10.892	-7.255	-632.942
34	41	75	-647.714	0.083	59.8	-53.876	-45.238	-10.005	-7.368	-638.673
34	42	76	-659.115	0.216	60.0	-53.799	-45.082	-9.616	-8.395	-652.981
34	43	77	-667.777	0.221	60.0	-53.831	-45.431	-8.831	-8.937	-661.919
34	44	78	-676.835	0.171	0.0	-53.735	-46.097	-10.278	-8.814	-670.300
34	45	79	-686.164	0.179	0.0	-53.747	-46.416	-9.523	-9.441	-680.159
34	46	80	-695.430	0.186	0.0	-53.768	-46.734	-9.462	-10.057	-689.831

Table E.20: Same as Tables E.1-E.19 but for bromine isotopes.

						$_{35}$Br				
Z	N	A	$E_{\text{g.s.}}$	β	γ (deg)	$\varepsilon_n(1)$	$\varepsilon_p(1)$	$\varepsilon_n(N)$	$\varepsilon_p(Z)$	$E_{\text{g.s.}}$(SLyIII.0.8)
35	32	67	-546.177	0.211	39.1	-55.150	-41.306	-15.412	-0.454	-536.459
35	33	68	-560.418	0.211	49.2	-54.891	-41.602	-14.623	-0.637	-550.825
35	34	69	-574.942	0.219	59.9	-54.654	-41.940	-14.912	-0.848	-565.407
35	35	70	-587.123	0.196	52.2	-54.570	-42.333	-12.647	-2.172	-577.691
35	36	71	-599.657	0.180	46.4	-54.481	-42.742	-12.940	-3.395	-590.338
35	37	72	-611.283	0.162	50.7	-54.379	-43.124	-11.981	-3.953	-602.069
35	38	73	-623.155	0.146	59.3	-54.255	-43.477	-12.230	-4.546	-614.107
35	39	74	-634.094	0.166	55.5	-54.189	-43.745	-11.188	-4.829	-625.832
35	40	75	-645.028	0.186	55.3	-54.124	-44.009	-11.156	-5.107	-637.646
35	41	76	-655.064	0.194	53.9	-54.108	-44.314	-10.205	-5.597	-648.280
35	42	77	-664.975	0.206	54.3	-54.077	-44.627	-10.120	-6.022	-658.785
35	43	78	-674.507	0.238	59.5	-54.023	-45.052	-9.547	-6.729	-668.795
35	44	79	-684.308	0.151	0.1	-54.095	-45.640	-10.403	-7.553	-677.244
35	45	80	-694.021	0.158	0.1	-54.125	-45.967	-9.894	-7.936	-687.454
35	46	81	-703.653	0.165	0.0	-54.159	-46.292	-9.819	-8.300	-697.475

Bibliography

[1] E. Rutherford, Philos. Mag. **21**, 669 (1911).

[2] A. Bohr and B. R. Mottelson, *Nuclear Structure*, Vol. **I**: *Single-Particle Motion* (W. A. Benjamin, 1969); Vol. **II**: *Nuclear Deformations* (W. A. Benjamin, 1975).

[3] M. G. Mayer, Phys. Rev. **75**, 1969 (1949).

[4] O. Haxel, J. H. D. Jensen, and H. E. Suess, Phys. Rev. **75**, 1766 (1949).

[5] M. G. Mayer, Phys. Rev. **78**, 16 (1950).

[6] P. Ring and P. Schuck, *"The Nuclear Many-Body Problem"*, (Springer-Verlag, 1980).

[7] T. Nakatsukasa, Prog. Theor. Exp. Phys. **2012**, 01A207.

[8] A. Nasirov, K. Kim, G. Mandaglio, G. Giardina, A. Muminov, and Y. Kim, Eur. Phys. J. A **49**, 147 (2013).

[9] Website: RIKEN Nishina Center for Accelerator-Based Science, `http://www.rarf.riken.jp/facility/RIBFabout_e.html`.

[10] I. Tanihata, H. Hamagaki, O. Hashimoto, Y. Shida, N. Yoshikawa, K. Sugimoto, O. Yamakawa, T. Kobayashi, and N. Takahashi, Phys. Rev. Lett. **55**, 2676 (1985).

[11] I. Tanihata, J. Phys. G: Nucl. Part. Phys. **22**, 157 (1996).

[12] K. Hagino, H. Sagawa, J. Carbonell, and P. Schuck, Phys. Rev. Lett. **99**, 022506 (2007).

[13] H. Sakurai, S. M. Lukyanov, M. Notani, N. Aoi, D. Beaumel, N. Fukuda, M. Hirai, E. Ideguchi, N. Imai, M. Ishihara, H. Iwasaki, T. Kubo, K. Kusaka, H. Kumagai, T. Nakamura, H. Ogawa, Yu. E. Penionzhkevich, T. Teranishi, Y. X. Watanabe, K. Yoneda, A. Yoshida, Phys. Lett. B **448**, 180 (1999).

[14] A. Ozawa, T. Kobayashi, T. Suzuki, K. Yoshida, and I. Tanihata, Phys. Rev. Lett. **84**, 5493 (2000).

[15] D. Steppenbeck, S. Takeuchi, N. Aoi, P. Doornenbal, M. Matsushita, H. Wang, H. Baba, N. Fukuda, S. Go, M. Honma, J. Lee, K. Matsui, S. Michimasa, T. Motobayashi, D. Nishimura, T. Otsuka, H. Sakurai, Y. Shiga, P.-A. Soderstrom, T. Sumikama, H. Suzuki, R. Taniuchi, Y. Utsuno, J. J. Valiente-Dobon, and K. Yoneda, Nature **502**, 207 (2013).

[16] C. Thibault, R. Klapisch, C. Rigaud, A. M. Poskanzer, R. Prieels, L. Lessard and W. Reisdorf, Phys. Rev. C **12**, 644 (1975).

[17] E. K. Warburton, J. A. Becker, and B. A. Brown, Phys. Rev. C **41**, 1147 (1990).

[18] N. A. Orr, W. Mittig, L. K. Fifield, M. Lewitowicz, E. Plagnol, Y. Schutz, Zhan Wen Long, L. Bianchi, A. Gillibert, A. V. Belozyorov, S. M. Lukyanov, Yu. E. Penionzhkevich, A. C. C. Villari, A. Cunsolo, A. Foti, G. Audi, C. Stephan, L. Tassan-Got, Phys. Lett. B **258**, 29 (1991).

[19] T. Otsuka, T. Suzuki, M. Honma, Y. Utsuno, N. Tsunoda, K. Tsukiyama, and M. Hjorth-Jensen Phys. Rev. Lett. **104**, 012501 (2010).

[20] T. Otsuka, Phys. Scr. **T152**, 014007 (2013).

[21] Y. Tsunoda, T. Otsuka, N. Shimizu, M. Honma, and Y. Utsuno, Phys. Rev. C **89**, 031301(R) (2014).

[22] M. Bender, K. Rutz, P.-G. Reinhard, J. A. Maruhn, and W. Greiner, Phys. Rev. C **60**, 034304 (1999).

[23] S. Ćwiok, P.-H. Heenen, and W. Nazarewicz, Nature **433**, 705 (2005).

[24] A. Staszczak, A. Baran, and W. Nazarewicz, Phys. Rev. C **87**, 024320 (2013).

[25] S. Hofmann and G. Münzenberg, Rev. Mod. Phys. **72**, 733 (2000).

[26] K. Morita, K. Morimoto, D. Kaji, H. Haba, E. Ideguchi, J. C. Peter, R. Kanungo, K. Katori, H. Koura, H. Kudo, T. Ohnishi, A. Ozawa, T. Suda, K. Sueki, I. Tanihata, H. Xu, A. V. Yeremin, A. Yoneda, A. Yoshida, Y.-L. Zhao, T. Zheng, S. Goto, and F. Tokanai, Jour. Phys. Soc. Japan, **73**, 1738 (2004).

[27] K. Morita, K. Morimoto, D. Kaji, T. Akiyama, S. Goto, H. Haba, E. Ideguchi, R. Kanungo, K. Katori, H. Koura, H. Kudo, T. Ohnishi, A. Ozawa, T. Suda, K. Sueki, H. Xu, T. Yamaguchi, A. Yoneda, A. Yoshida, and Y.-L. Zhao, Jour. Phys. Soc. Japan, **73**, 2593 (2004).

[28] Yu. Ts. Oganessian, J. Phys. G: Nucl. Part. Phys. **34**, R165 (2007).

[29] V. I. Zagrebaev and W. Greiner, Phys. Rev. C **83**, 044618 (2011).

[30] Website: EurekAlert! The Global Source for Science News, PUBLIC RELEASE: 6-APR-2008, `http://www.eurekalert.org/pub_releases/2008-04/acs-nse031108.php`.

[31] K. Sapotta, R. Bass, V. Hartmann, H. Noll, R. E. Renfordt, and K. Stelzer, Phys. Rev. C **31**, 1297 (1985).

[32] K. E. Rehm, A. M. van den Berg, J. J. Kolata, D. G. Kovar, W. Kutschera, G. Rosner, G. S. F. Stephans, and J. L. Yntema, Phys. Rev. C **37**, 2629 (1988).

[33] R. Künkel, W. von Oertzen, B. Gebauer, H. G. Bohlen, H. A. Bösser, B. Kohlmeyer, F. Pühlhofer, and D. Schüll, Phys. Lett. B **208**, 355 (1988).

[34] U. W. Scherer, W. Brüchle, M. Brügger, C. Frink, H. Gäggeler, G. Herrmann, J. V. Kratz, K. J. Moody, M. Schädel, K. Sümmerer, N. Trautmann, and G. Wirth, Z. Phys. A **335**, 421 (1990).

[35] J. Speer, W. von Oertzen, D. Schüll, M. Wilpert, H. G. Bohlen, B. Gebauer, B. Kohlmeyer, and F. Pühlhofer, Phys. Lett. B **259**, 422 (1991).

[36] M. Wilpert, B. Gebauer, W. von Oertzen, Th. Wilpert, E. Stiliaris, and H. G. Bohlen, Phys. Rev. C **44**, 1081 (1991).

[37] W. von Oertzen, Z. Phys. A **342**, 177 (1992).

[38] C. L. Jiang, K. E. Rehm, J. Gehring, B. Glagola, W. Kutschera, M. Rhein, and A.H. Wuosmaa, Phys. Lett. B **337**, 59 (1994).

[39] L. Corradi, A. M. Stefanini, D. Ackermann, S. Beghini, G. Montagnoli, C. Petrache, F. Scarlassara, C. H. Dasso, G. Pollarolo, and A. Winther, Phys. Rev. C **49**, R2875 (1994).

[40] L. Corradi, J. H. He, D. Ackermann, A. M. Stefanini, A. Pisent, S. Beghini, G. Montagnoli, F. Scarlassara, G. F. Segato, G. Pollarolo, C. H. Dasso, and A. Winther, Phys. Rev. C **54**, 201 (1996).

[41] G. Montagnoli, S. Beghini, F. Scarlassara, G. F. Segato, L. Corradi, C. J. Lin, and A. M. Stefanini, J. Phys. G: Nucl. Part. Phys. **23**, 1431 (1997).

[42] L. Corradi, A. M. Stefanini, J. H. He, C. Lin, S. Beghini, G. Montagnoli, F. Scarlassara, G. F. Segato, G. Pollarolo, C. H. Dasso, and A. Winther, J. Phys. G: Nucl. Part. Phys. **23**, 1485 (1997).

[43] L. Corradi, A. M. Stefanini, J. H. He, S. Beghini, G. Montagnoli, F. Scarlassara, G. F. Segato, G. Pollarolo, and C. H. Dasso, Phys. Rev. C **56**, 938 (1997).

[44] C. L. Jiang, K. E. Rehm, H. Esbensen, D. J. Blumenthal, B. Crowell, J. Gehring, B. Glagola, J. P. Schiffer, and A. H. Wuosmaa, Phys. Rev. C **57**, 2393 (1998).

[45] L. Corradi, A. M. Stefanini, C. J. Lin, S. Beghini, G. Montagnoli, F. Scarlassara, G. Pollarolo, and A. Winther, Phys. Rev. C **59**, 261 (1999).

[46] L. Corradi, A. M. Vinodkumar, A. M. Stefanini, D. Ackermann, M. Trotta, S. Beghini, G. Montagnoli, F. Scarlassara, G. Pollarolo, F. Cerutti, and A. Winther, Phys. Rev. C **63**, 021601(R) (2001).

[47] L. Corradi, A. M. Vinodkumar, A. M. Stefanini, E. Fioretto, G. Prete, S. Beghini, G. Montagnoli, F. Scarlassara, G. Pollarolo, F. Cerutti, and A. Winther, Phys. Rev. C **66**, 024606 (2002).

[48] W. Królas, R. Broda, B. Fornal, T. Pawlat, H. Grawe, K. H. Maier, M. Schramm, and R. Schubart, Nucl. Phys. **A724**, 289 (2003).

[49] S. Szilner, L. Corradi, F. Haas, G. Pollarolo, S. Beghini, B. R. Behera, E. Caurier, E. Fioretto, A. Gadea, A. Latina, G. Montagnoli, F. Nowacki, F. Scarlassara, A. M. Stefanini, M. Trotta, A. M. Vinodkumar, and Y. W. Wu, Eur. Phys. J. A **21**, 87 (2004).

[50] S. Szilner, L. Corradi, G. Pollarolo, S. Beghini, B. R. Behera, E. Fioretto, A. Gadea, F. Haas, A. Latina, G. Montagnoli, F. Scarlassara, A. M. Stefanini, M. Trotta, A. M. Vinodkumar, and Y. Wu, Phys. Rev. C **71**, 044610 (2005).

[51] S. Szilner, C. A. Ur, L. Corradi, N. Mărginean, G. Pollarolo, A. M. Stefanini, S. Beghini, B. R. Behera, E. Fioretto, A. Gadea, B. Guiot, A. Latina, P. Mason, G. Montagnoli, F. Scarlassara, M. Trotta, G. de Angelis, F. Della Vedova, E. Farnea, F. Haas, S. Lenzi, S. Lunardi, R. Mărginean, R. Menegazzo, D. R. Napoli, M. Nespolo, I. V. Pokrovsky, F. Recchia, M. Romoli, M.-D. Salsac, N. Soić, and J. J. Valiente-Dobón, Phys. Rev. C **76**, 024604 (2007).

[52] Sunil Kalkal, S. Mandal, N. Madhavan, A. Jhingan, E. Prasad, Rohit Sandal, S. Nath, J. Gehlot, Ritika Garg, Gayatri Mohanto, Mansi Saxena, Savi Goyal, S. Verma, B. R. Behera, Suresh Kumar, U. D. Pramanik, A. K. Sinha, and R. Singh, Phys. Rev. C **83**, 054607 (2011).

[53] L. Corradi, S. Szilner, G. Pollarolo, G. Colò, P. Mason, E. Farnea, E. Fioretto, A. Gadea, F. Haas, D. Jelavić-Malenica, N. Mărginean, C. Michelagnoli, G. Montagnoli, D. Montanari, F. Scarlassara, N. Soić, A. M. Stefanini, C. A. Ur, and J. J. Valiente-Dobón, Phys. Rev. C **84**, 034603 (2011).

[54] W. von Oertzen and A. Vitturi, Rep. Prog. Phys. **64**, 1247 (2001).

[55] L. Corradi, G. Pollarolo, and S. Szilner, J. Phys. G: Nucl. Part. Phys. **36**, 113101 (2009).

[56] C. H. Dasso, G. Pollarolo, and A. Winther, Phys. Rev. Lett. **73**, 1907 (1994).

[57] C. H. Dasso, G. Pollarolo, and A. Winther, Phys. Rev. C **52**, 2264 (1995).

[58] V. Zagrebaev and W. Greiner, Phys. Rev. Lett. **101**, 122701 (2008).

[59] E. M. Kozulin, E. Vardaci, G. N. Knyazheva, A. A. Bogachev, S. N. Dmitriev, I. M. Itkis, M. G. Itkis, A. G. Knyazev, T. A. Loktev, K. V. Novikov, E. A. Razinkov, O. V. Rudakov, S. V. Smirnov, W. Trzaska, and V. I. Zagrebaev, Phys. Rev. C **86**, 044611 (2012).

[60] H. Grawe, K. Langanke, and G. Martínez-Pinedo, Rep. Prog. Phys. **70**, 1525 (2007).

[61] M. Arnould, S. Goriely, and K. Takahashi, Phys. Rep. **450**, 97 (2007).

[62] S. C. Jeong, N. Imai, H. Ishiyama, Y. Hirayama, H. Miyatake, and Y. X. Watanabe, KEK Rep. **2010-2** (2010).

[63] V. I. Zagrebaev, B. Fornal, S. Leoni, and W. Greiner, Phys. Rev. C **89**, 054608 (2014).

[64] T. Kurtukian-Nieto, Ph.D. Thesis, Santiago de Compostela, 2007.

[65] E. Kwan, Dissertation on degree of Doctor of Phil., Department od Physics, Michigan State University, 2006.

[66] http://www.nishina.riken.jp/RIBF/BigRIPS/intensity.html; H. Suzuki *et al.*, Nucl. Inst. Methods Phys. Res. B **317**, 756 (2013).

[67] A. Winther, Nucl. Phys. **A572**, 191 (1994); **A594**, 203 (1995).

[68] E. Vigezzi and A. Winther, Ann. Phys. (N.Y.) **192**, 432 (1989).

[69] V. Zagrebaev and W. Greiner, J. Phys. G: Nucl. Part. Phys. **31**, 825 (2005).

[70] V. Zagrebaev and W. Greiner, J. Phys. G: Nucl. Part. Phys. **34**, 1 (2007).

[71] V. I. Zagrebaev, Yu. Ts. Oganessian, M. G. Itkis, and W. Greiner, Phys. Rev. C **73**, 031602(R) (2006).

[72] V. Zagrebaev and W. Greiner, J. Phys. G: Nucl. Part. Phys. **34**, 2265 (2007).

[73] V. Zagrebaev and W. Greiner, Phys. Rev. C **78**, 034610 (2008).

[74] W. J. Swiatecki, Nucl. Phys. **A376**, 275 (1982).

[75] H. Gäggeler, T. Sikkeland, G. Wirth, W. Brüchle, W. Bögl, G. Franz, G. Herrmann, J. V. Kratz, M. Schädel, K. Sümmerer, and W. Weber, Z. Phys. A **316**, 291 (1984).

[76] C.-C. Sham and H.-G. Clerc, Z. Phys. A **319**, 113 (1984).

[77] R. du Rietz, D. J. Hinde, M. Dasgupta, R. G. Thomas, L. R. Gasques, M. Evers, N. Lobanov, and A. Wakhle, Phys. Rev. Lett. **106**, 052701 (2011).

[78] R. Bock, Y. T. Chu, M. Dakowski, A. Gobbi, E. Grosse, A. Olmi, H. Sann, D. Schwalm, U. Lynen, W. Müller, S. Bjørnholm, H. Esbensen, W. Wölfli, and E. Morenzoni, Nucl. Phys. **A388**, 334 (1982).

[79] J. Tōke, R. Bock, G. X. Dai, A. Gobbi, S. Gralla, K. D. Hildenbrand, J. Kuzminski, W. F. J. Müller, A. Olmi, H. Stelzer, B. B. Back, and S. Bjørnholm, Nucl. Phys. **A440**, 327 (1985).

[80] R. du Rietz, E. Williams, D. J. Hinde, M. Dasgupta, M. Evers, C. J. Lin, D. H. Luong, C. Simenel, and A. Wakhle, Phys. Rev. C **88**, 054618 (2013).

[81] J. U. Andersen, J. Chevallier, J. S. Forster, S. A. Karamian, C. R. Vane, J. R. Beene, A. Galindo-Uribarri, J. Gomez del Campo, C. J. Gross, H. F. Krause, E. Padilla-Rodal, D. Radford, D. Shapira, C. Broude, F. Malaguti, and A. Uguzzoni, Phys. Rev. C **78**, 064609 (2008).

[82] F. Goldenbaum, M. Morjean, J. Galin, E. Liénard, B. Lott, A. Péghaire, Y. Périer, M. Chevallier, D. Dauvergne, R. Kirsch, J. C. Poizat, J. Remillieux, C. Cohen, A. L'Hoir, G. Prévot, D. Schmaus, J. Dural, M. Toulemonde, and D. Jacquet, Phys. Rev. Lett. **82**, 5012 (1999); **83**, 2094 (1999).

[83] A. Ray, EPJ Web of Conferences **86**, 00038 (2015).

[84] V. I. Zagrebaev and W. Greiner, Phys. Rev. C **87**, 034608 (2013).

[85] P. A. M. Dirac, Proc. Cambridge Philos. Soc. **26**, 376 (1930).

[86] P. Bonche, S. Koonin, and J. W. Negele, Phys. Rev. C **13**, 1226 (1976).

[87] R. Y. Cusson, R. K. Smith, and J. A. Maruhn, Phys. Rev. Lett. **36**, 1166 (1976).

[88] S. E. Koonin, K. T. R. Davies, V. Maruhn-Rezwani, H. Feldmeier, S. J. Krieger, and J. W. Negele, Phys. Rev. C **15**, 1359 (1977).

[89] K. T. R. Davies, V. Maruhn-Rezwani, S. E. Koonin, and J. W. Negele, Phys. Rev. Lett. **41**, 632 (1978).

[90] H. Flocard, S. E. Koonin, and M. S. Weiss, Phys. Rev. C **17**, 1682 (1978).

[91] S. J. Krieger and K. T. R. Davies, Phys. Rev. C **18**, 2567 (1978).

[92] K. T. R. Davies, K. R. Sandhya Devi, and M. R. Strayer, Phys. Rev. C **20**, 1372 (1979).

[93] C. H. Dasso, T. Døssing, and H. C. Pauli, Z. Phys. A **289**, 395 (1979).

[94] J. W. Negele, Rev. Mod. Phys. **54**, 913 (1982).

[95] A. S. Umar, M. R. Strayer, and P.-G. Reinhard, Phys. Rev. Lett. **56**, 2793 (1986).

[96] K.-H. Kim, T. Otsuka, and M. Tohyama, Phys. Rev. C **50**, R566 (1994).

[97] K.-H. Kim, T. Otsuka, and P. Bonche, J. Phys. G: Nucl. Part. Phys. **23**, 1267 (1997).

[98] C. Simenel and Ph. Chomaz, Phys. Rev. C **68**, 024302 (2003).

[99] T. Nakatsukasa and K. Yabana, Phys. Rev. C **71**, 024301 (2005).

[100] A. S. Umar and V. E. Oberacker, Phys. Rev. C **71**, 034314 (2005).

[101] J. A. Maruhn, P. G. Reinhard, P. D. Stevenson, J. Rikovska Stone, and M. R. Strayer, Phys. Rev. C **71**, 064328 (2005).

[102] A. S. Umar and V. E. Oberacker, Phys. Rev. C **73**, 054607 (2006).

[103] J. A. Maruhn, P.-G. Reinhard, P. D. Stevenson, and M. R. Strayer, Phys. Rev. C **74**, 027601 (2006).

[104] A. S. Umar and V. E. Oberacker, Phys. Rev. C **74**, 021601(R) (2006).

[105] Lu Guo, J. A. Maruhn, and P.-G. Reinhard, Phys. Rev. C **76**, 014601 (2007).

[106] A. S. Umar and V. E. Oberacker, Phys. Rev. C **76**, 014614 (2007).

[107] Lu Guo, J. A. Maruhn, P.-G. Reinhard, and Y. Hashimoto, Phys. Rev. C **77**, 041301(R) (2008).

[108] A. S. Umar, V. E. Oberacker, and J. A. Maruhn, Eur. Phys. J. A **37**, 245 (2008).

[109] A. S. Umar and V. E. Oberacker, Phys. Rev. C **77**, 064605 (2008).

[110] K. Washiyama and D. Lacroix, Phys. Rev. C **78**, 024610 (2008).

[111] K. Washiyama, D. Lacroix, and S. Ayik, Phys. Rev. C **79**, 024609 (2009).

[112] C. Golabek and C. Simenel, Phys. Rev. Lett. **103**, 042701 (2009).

[113] D. J. Kedziora and C. Simenel, Phys. Rev. C **81**, 044613 (2010).

[114] Y. Iwata, T. Otsuka, J. A. Maruhn, and N. Itagaki, Phys. Rev. Lett. **104**, 252501 (2010).

[115] C. Simenel, Phys. Rev. Lett. **105**, 192701 (2010).

[116] Y. Iwata and J. A. Maruhn, Phys. Rev. C **84**, 014616 (2011).

[117] Lu Guo and T. Nakatsukasa, EPJ Web of Conferences **38**, 09003 (2012).

[118] R. Keser, A. S. Umar, and V. E. Oberacker, Phys, Rev. C **85**, 044606 (2012).

[119] Y. Iwata, J. Mod. Phys. **3**, 476 (2012).

[120] C. Simenel, A. Wakhle, B. Avez, D. J. Hinde, R. du Rietz, M. Dasgupta, M. Evers, C. J. Lin, and D. H. Luong, EPJ Web of Conferences **38**, 09001 (2012).

[121] C. Simenel, Eur. Phys. J. A **48**, 152 (2012).

[122] C. Simenel, M. Dasgupta, D. J. Hinde, and E. Williams, Phys. Rev. C **88**, 064604 (2013).

[123] C. Simenel and A. S. Umar, Phys. Rev. C **89**, 031601(R) (2014).

[124] A. Wakhle, C. Simenel, D. J. Hinde, M. Dasgupta, M. Evers, D. H. Luong, R. du Rietz, and E. Williams, Phys. Rev. Lett. **113**, 182502 (2014).

[125] V. E. Oberacker, A. S. Umar, and C. Simenel, Phys. Rev. C **90**, 054605 (2014).

[126] G.-F. Dai, Lu Guo, E.-G. Zhao, and S.-G. Zhou, Phys. Rev. C **90**, 044609 (2014).

[127] T. H. R. Skyrme, Philos. Mag. **1**, 1043 (1956).

[128] A. Bonaccorso, D. M. Brink, and L. Lo Monaco, J. Phys. G: Nucl. Part. Phys. **13**, 1407 (1987).

[129] A. Bonaccorso and D. M. Brink, Phys. Rev. C **38**, 1776 (1988).

[130] A. Bonaccorso and D. M. Brink, Phys. Rev. C **43**, 299 (1991).

[131] D. R. Hartree, Proc. Camb. Phil. Soc. **24**, 89 (1928).

[132] V. A. Fock, Z. Phys. **61**, 126 (1930).

[133] T. H. R. Skyrme, Nucl. Phys. **9**, 615 (1959).

[134] D. Vautherin and D. M. Brink, Phys. Lett. B **32**, 149 (1970).

[135] D. Vautherin and D. M. Brink, Phys. Rev. C **5**, 626 (1972).

[136] M. Bender, P.-H. Heenen, and P.-G. Reinhard, Rev. Mod. Phys. **75**, 121 (2003).

[137] D. Lunney, J. M. Pearson, and C. Thibault, Rev. Mod. Phys. **75**, 1021 (2003).

[138] M. Beiner, H. Flocard, N. van Giai, and P. Quentin, Nucl. Phys. **A238**, 29 (1975).

[139] J. Bartel, P. Quentin, M. Brack, C. Guet, and H.-B. Håkansson, Nucl. Phys. **A386**, 79 (1982).

[140] J. Dobaczewski, H. Flocard, and J. Treiner, Nucl. Phys. **A422**, 103 (1984).

[141] E. Chabanat, P. Bonche, P. Haensel, J. Meyer, and R. Schaeffer, Nucl. Phys. **A635**, 231 (1998); **A643**, 441 (1998).

[142] J. R. Stone, Prog. Part. Nucl. Phys. **58**, 587 (2007).

[143] M. Kortelainen, T. Lesinski, J. Moré, W. Nazarewicz, J. Sarich, N. Schunck, M. V. Stoitsov, and S. Wild, Phys. Rev. C **82**, 024313 (2010).

[144] N. Nikolov, N. Schunck, W. Nazarewicz, M. Bender, and J. Pei, Phys. Rev. C **83**, 034305 (2011).

[145] M. Kortelainen, J. McDonnell, W. Nazarewicz, P.-G. Reinhard, J. Sarich, N. Schunck, M. V. Stoitsov, and S. M. Wild, Phys. Rev. C **85**, 024304 (2012).

[146] K. Washiyama, K. Bennaceur, B. Avez, M. Bender, P.-H. Heenen, and V. Hellemans, Phys. Rev. C **86**, 054309 (2012).

[147] M. Kortelainen, J. McDonnell, W. Nazarewicz, E. Olsen, P.-G. Reinhard, J. Sarich, N. Schunck, S. M. Wild, D. Davesne, J. Erler, and A. Pastore, Phys. Rev. C **89**, 054314 (2014).

[148] D. Lacroix, T. Duguet, and M. Bender, Phys. Rev. C **79**, 044318 (2009).

[149] M. Bender, T. Duguet, and D. Lacroix, Phys. Rev. C **79**, 044319 (2009).

[150] T. Duguet, M. Bender, K. Bennaceur, D. Lacroix, and T. Lesinski, Phys. Rev. C **79**, 044320 (2009).

[151] J. C. Slater, Phys. Rev. **81**, 385 (1950).

[152] J. W. Eastwood and D. R. K. Brownrigg, J. Compt. Phys. **32**, 24 (1979).

[153] Y. M. Engel, D. M. Brink, K. Goeke, S. J. Kreiger, and D. Vautherin, Nucl. Phys. **A249**, 215 (1975).

[154] J. Dobaczewski and J. Dudek, Phys. Rev. C **52**, 1827 (1995).

[155] P. Hohenberg and W. Kohn, Phys. Rev. B **136**, 864 (1964).

[156] M. Levy, Proc. Natl. Acad. Sci. U.S.A. **76**, 6062 (1979).

[157] W. Khon and L. J. Sham, Phys. Rev. A **140**, 1133 (1965).

[158] M. Levy, Phys. Rev. A **26**, 1200 (1982).

[159] T. L. Gilbert, Phys. Rev. B **12**, 2111 (1975).

[160] J. E. Harriman, Phys. Rev. A **24**, 680 (1981).

[161] J. Engel, Phys. Rev. C **75**, 014306 (2007).

[162] B. G. Giraud, Phys. Rev. C **77**, 014311 (2008).

[163] B. G. Giraud, Phys. Rev. C **78**, 014307 (2008).

[164] B. G. Giraud, Phys. Rev. A **78**, 032507 (2008).

[165] T. Nakatsukasa, J. Phys.: Conf. Ser. **302**, 012050 (2011).

[166] E. Runge and E. K. U. Gross, Phys. Rev. Lett. **52**, 997 (1984).

[167] R. van Leeuwen, Phys. Rev. Lett. **82**, 3863 (1999).

[168] M. A. L. Marques, C. A. Ullrich, F. Nogueira, A. Rubio, K. Burke, and E. U. K. Gross, *"Time-Dependent Density Functional Theory"*, Lect. Notes Phys. **706** (Springer, Berlin Heidelberg, 2006).

[169] P. C. Martin, Phys. Rev. **115**, 1342 (1959).

[170] W. Greiner and J. A. Maruhn, *"Nuclear Models"* (Springer, Berlin Heidelberg, 1996).

[171] H. Goldstein, *Classical Mechanics*, 2nd edition (Addison-Wesley, 1980).

[172] N. Tajima, Prog. Theor. Phys. Suppl. **142**, 265 (2001).

[173] K. Sekizawa and K. Yabana, Phys. Rev. C **88**, 014614 (2013).

[174] H. Freiesleben and J. V. Kratz, Phys. Rep. **106**, 1 (1984).

[175] R. Balian and M. Vénéroni, Phys. Rev. Lett. **47**, 1353 (1981).

[176] C. Simenel, Phys. Rev. Lett. **106**, 112502 (2011).

[177] H. J. Lüdde and R. M. Dreizler, J. Phys. B **16**, 3973 (1983).

[178] R. Nagano, K. Yabana, T. Tazawa, and Y. Abe, Phys. Rev. A **62**, 062721 (2000).

[179] K. Washiyama, S. Ayik, and D. Lacroix, Phys. Rev. C **80**, 031602(R) (2009).

[180] K. A. Brueckner, J. R. Buchler, and M. M. Kelly, Phys. Rev. **173**, 944 (1968).

[181] V. Yu. Denisov and W. Nörenberg, Eur. Phys. J. A **15**, 375 (2002).

[182] Y. Abe, S. Ayik, P.-G. Reinhard, and E. Suraud, Phys. Rep. **275**, 49 (1996).

[183] P. Fröbrich and I. I. Gontchar, Phys. Rep. **292**, 131 (1998).

[184] K. Sekizawa and K. Yabana, Phys. Rev. C **90**, 064614 (2014).

[185] M. B. Tsang, R. Bougault, R. Charity, D. Durand, W. A. Friedman, F. Gulminelli, A. Le Fèvre, Al. H. Raduta, Ad. R. Raduta, S. Souza, W. Trautmann, R. Wada, Eur. Phys. J. A **30**, 129 (2006).

[186] S. Shinohara, H. Ohta, T. Nakatsukasa, and K. Yabana, Phys. Rev. C **74**, 054315 (2006).

[187] S. Hilaire and M. Girod, Eur. Phys. J. A **33**, 237 (2007); http://www-phynu.cea.fr/science_en_ligne/carte_potentiels_microspiques/carte_potentiel_nucleaire_eng.htm.

[188] M. Tohyama and A. S. Umar, Phys. Lett. B **549**, 72 (2002).

[189] A. S. Umar, V. E. Oberacker, and J. A. Maruhn, Eur. Phys. J. A **37**, 245 (2008).

[190] I. Dostrovsky and Z. Fraenkei, Phys. Rev. **116**, 683 (1959); **119** 2098 (1960).

[191] K. Sekizawa and K. Yabana, EPJ Web of Conferences **86**, 00043 (2015).

[192] J. F. Berger, M. Girod, and D. Gogny, Nucl. Phys. **A428** 23 (1984).

[193] C. Simenel, J. Phys. G: Nucl. Part. Phys. **41**, 094007 (2014).

[194] J. Sadoudi, M. Bender, K. Bennaceur, D. Davesne, R. Jodon, and T. Duguet, Phys. Scr. **T154**, 014013 (2013).

[195] Y. Hashimoto and K. Nodeki, arXiv:0707.3083 [nucl-th].

[196] B. Avez, C. Simenel, and Ph. Chomaz, Phys. Rev. C **78**, 044318 (2008).

[197] I. Stetcu, A. Bulgac, P. Magierski, and K. J. Roche, Phys. Rev. C **84**, 051309(R) (2011).

[198] Y. Hashimono, Eur. Phys. J. A **48**, 55 (2012).

[199] J. Blocki and H. Flocard, Nucl. Phys. **A273**, 45 (1976).

[200] S. Ebata, T. Nakatsukasa, T. Inakura, K. Yoshida, Y. Hashimoto, and K. Yabana, Phys. Rev. C **82**, 034306 (2010).

[201] G. Scamps, D. Lacroix, G. F. Bertsch, and K. Washiyama, Phys. Rev. C **85**, 034328 (2012).

[202] S. Ebata, J. Phys.: Conf. Ser. **454**, 012054 (2013).

[203] G. Scamps and D. Lacroix, Phys. Rev. C **87**, 014605 (2013).

[204] G. Scamps and D. Lacroix, Phys. Rev. C **88**, 044310, (2013).

[205] G. Scamps and D. Lacroix, Phys. Rev. C **89**, 034314, (2014).

[206] S. Ebata and T. Nakatsukasa, arXiv:1408.2495 [nucl-th].

[207] S. Ebata, T. Nakatsukasa, and T. Inakura, Phys. Rev. C **90**, 024303 (2014).

[208] S. Ebata and M. Kimura, Phys. Rev. C **91**, 014309 (2015).

[209] S. J. Wang and W. Cassing, Ann. Phys. **159**, 328 (1985).

[210] W. Cassing and S. J. Wang, Z. Phys. A **328**, 423 (1987).

[211] M. Tohyama and M. Gong, Z. Phys. A **332**, 269 (1989).

[212] M. Gong and M. Tohyama, Z. Phys. A **335**, 153 (1990).

[213] S. Ayik, Phys. Lett. B **658**, 174 (2008).

[214] S. Ayik, K. Washiyama, and D. Lacroix, Phys. Rev. C **79**, 054606 (2009).

[215] B. Yilmaz, S. Ayik, D. Lacroix, and K. Washiyama, Phys. Rev. C **83**, 064615 (2011).

[216] E. M. Kozulin, G. N. Knyazheva, I. M. Itkis, M. G. Itkis, A. A. Bogachev, L. Krupa, T. A. Loktev, S. V. Smirnov, V. I. Zagrebaev, J. Aysto, W. H. Trzaska, V. A. Rubchenya, E. Vardaci, A. M. Stefanini, M. Cinausero, L. Corradi, E. Fioretto, P. Mason, G. F. Prete, R. Silvestri, S. Beghini, G. Montagnoli, F. Scarlassara, F. Hanappe, S. V. Khlebnikov, J. Kliman, A. Brondi, A. Di Nitto, R. Moro, N. Gelli, and S. Szilner, Phys. Lett. B **686**, 227 (2010).

[217] M. O. Freégeau, D. Jacquet, M. Morjean, E. Bonnet, A. Chbihi, J. D. Frankland, M. F. Rivet, L. Tassan-Got, F. Dechery, A. Drouart, L. Nalpas, X. Ledoux, M. Parlog, C. Ciortea, D. Dumitriu, D. Fluerasu, M. Gugiu, F. Gramegna, V. L. Kravchuk, T. Marchi, D. Fabris, A. Corsi, and S. Barlini, Phys. Rev. Lett. **108**, 122701 (2012).

[218] G. A. Lalazissis, S. Raman, and P. Ring, At. Data Nucl. Data Tables **71**, 1 (1999).

[219] A. Blazkiewicz, V. E. Oberacker, A. S. Umar, and M. Stoitsov, Phys. Rev. C **71**, 054321 (2005).

[220] J. K. Hwang, A. V. Ramayya, J. H. Hamilton, Y. X. Luo, A. V. Daniel, G. M. Ter-Akopian, J. D. Cole, and S. J. Zhu, Phys. Rev. C **73**, 044316 (2006).

[221] M. G. Itkis, J. Äystö, S. Beghini, A. A. Bogachev, L. Corradi, O. Dorvaux, A. Gadea, G. Giardina, F. Hanappe, I. M. Itkis, M. Jandel, J. Kliman, S. V. Khlebnikov, G. N. Kniajeva, N. A. Kondratiev, E. M. Kozulin, L. Krupa, A. Latina, T. Materna, G. Montagnoli, Yu. Ts. Oganessian, I. V. Pokrovsky, E. V. Prokhorova, N. Rowley, V. A. Rubchenya, A. Ya. Rusanov, R. N. Sagaidak, F. Scarlassara, A. M. Stefanini, L. Stuttge, S. Szilner, M. Trotta, W. H. Trzaska, D. N. Vakhtin, A. M. Vinodkumar, V. M. Voskressenski, V. I. Zagrebaev, Nucl. Phys. **A734**, 136 (2004).

[222] E. M. Kozulin, G. N. Knyazheva, I. M. Itkis, M. G. Itkis, A. A. Bogachev, E. V. Chernysheva, L. Krupa, F. Hanappe, O. Dorvaux, L. Stuttgé, W. H. Trzaska, C. Schmitt, and G. Chubarian, Phys. Rev. C **90**, 054608 (2014).

[223] V. E. Viola, K. Kwiatkowski, and M. Walker, Phys. Rev. C **31**, 1550 (1985).

[224] D. J. Hinde, J. R. Leigh, J. J. M. Bokhorst, J. O. Newton, R. L. Walsh, and J. W. Boldeman, Nucl. Phys. **A472**, 318 (1987).

[225] D. J. Hinde, D. Hilscher, H. Rossner, B. Gebauer, M. Lehmann, and M. Wilpert, Phys. Rev. C **45**, 1229 (1992).

[226] D. J. Hinde, M. Dasgupta, J. Leigh, J. Mein, C. Morton, J. Newton, and H. Timmers, Phys. Rev. C **53**, 1290 (1996).

[227] J. Mein, D. Hinde, M. Dasgupta, J. Leigh, J. Newton, and H. Timmers, Phys. Rev. C **55**, R995 (1997).

[228] K. Nishio, H. Ikezoe, S. Mitsuoka, I. Nishinaka, Y. Nagame, Y. Watanabe, T. Ohtsuki, K. Hirose, and S. Hofmann, Phys. Rev. C **77**, 064607 (2008).

[229] K. Nishio, S. Hofmann, F. Heßberger, D. Ackermann, S. Antalic, Y. Aritomo, V. Comas, Ch. Düllmann, A. Gorshkov, R. Graeger, K. Hagino, S. Heinz, J. Heredia, K. Hirose, H. Ikezoe, J. Khuyagbaatar, B. Kindler, I. Kojouharov, B. Lommel, R. Mann, S. Mitsuoka, Y. Nagame, I. Nishinaka, T. Ohtsuki, A. Popeko, S. Saro, M. Schädel, A. Türler, Y. Watanabe, A. Yakushev, and A. Yeremin, Phys. Rev. C **82**, 024611 (2010).

[230] K. Nishio, H. Ikezoe, I. Nishinaka, S. Mitsuoka, K. Hirose, T. Ohtsuki, Y. Watanabe, Y. Aritomo, and S. Hofmann, Phys. Rev. C **82**, 044604 (2010).

[231] K. Sekizawa and K. Yabana, to appear in JPS Conference Proceedings; arXiv:1403.8612 [nucl-th].

[232] W. Mayer, G. Beier, J. Friese, W. Henning, P. Kienle, H. J. Körner, W. A. Mayer, L. Müller, G. Rosner, and W. Wagner, Phys. Lett. B **152**, 162 (1985).

[233] Y. Aritomo and M. Ohta, Nucl. Phys. **A744**, 3 (2004).

[234] Y. Aritomo and M. Ohta, Nucl. Phys. **A753**, 152 (2005).

[235] Y. Aritomo, Phys. Rev. C **80**, 064604 (2009).

[236] Y. Aritomo, K. Hagino, K. Nishio, S. Chiba, Phys. Rev. C **85**, 044614 (2012).

[237] K. Nishio, S. Mitsuoka, I. Nishinaka, H. Makii, Y. Wakabayashi, H. Ikezoe, K. Hirose, T. Ohtsuki, Y. Aritomo, and S. Hofmann, Phys. Rev. C **86**, 034608 (2012).